



**Universiteit
Antwerpen**

Faculty of Science
Department of Physics

**Microstructural investigation of irradiation
assisted stress corrosion cracking mechanism
based on focused ion beam analysis**

Thesis submitted for the degree in Doctor of Science: Physics
at the University of Antwerp, to be defended by:

Aäron G. Penders

University Supervisor:

Prof. Dr. D. Schryvers

SCKCEN Mentors:


Dr. M. Konstantinović

Dr. R.W. Bosch


Antwerp, 2022

Individual Doctorate Committee (IDC) and IDC Jury Members

Committee chairman


Prof. Dr. Dirk Lamoen 
 dirk.lamoen@uantwerpen.be
 University of Antwerp
 Belgium

Committee members:


Prof. Dr. Erik Neyts 
 erik.neyts@uantwerpen.be
 University of Antwerp
 Belgium

Prof. Dr. Anna Hojná
 anna.hojna@cvrez.cz
 Centrum výzkumu Řež (CVR)
 Czech Republic

University Supervisor:

Prof. Dr. D. Schryvers 
 nick.schryvers@uantwerpen.be
 University of Antwerp
 Belgium

SCKCEN Promotors:

Dr. M. Konstantinović 
 milan.konstantinovic@sckcen.be
 SCKCEN
 Belgium

Dr. R.W. Bosch 
 rik-wouter.bosch@sckcen.be
 SCKCEN
 Belgium

ENGIE Sponsorship:

F. Somville 
 frederic.somville@tractebel.engie.com
 Tractebel Engineering
 Belgium

Thesis Author:

Penders Aäron 
 aaron.penders@sckcen.be
 aaron.penders@uantwerpen.be
 pendersaaron@gmail.com
 University of Antwerp & SCKCEN
 Belgium



UA | University of Antwerp
 Groenenborgerlaan 171 – 2020 Antwerp – Belgium
<https://www.uantwerpen.be/en/>



SCKCEN | Belgian Nuclear Research Centre
 Boeretang 200 - 2400 Mol – Belgium
<https://www.sckcen.be/en/>



EMAT | Electron microscopy for materials science
 Groenenborgerlaan 171 – 2020 Antwerp – Belgium
<https://www.uantwerpen.be/en/research-groups/emat/>

ENGIE Electrabel
 Boulevard Simon Bolivarlaan 34 – 1000 Brussels
<https://www.engie.be/nl/>

*The image of stress corrosion I see,
is that of a huge unwanted tree,
against whose trunk we chop and chop,
but which outgrows the chips that drop.*

*From each gash made in its bark,
a new branch grows to make more dark,
the shade of ignorance around its base,
where scientists toil with puzzled face.*

-S. P. Rideout, 1967

Acknowledgements

This Ph.D. manuscript is the culmination of four challenging but rewarding years of work. None of these efforts were made possible without the assistance of a long list of individuals who I wish to thank for their participation, guidance and moral support. I feel grateful towards all those who have contributed either directly or indirectly to this endeavor. This experience could not have been successful without those who took part in this formidable scientific and personal undertaking.

First and foremost, I wish to acknowledge **Mr. Robert Gérard** and **Mr. Frédéric Somville** at ENGIE-Tractebel for overseeing the sponsorship by ENGIE awarded to this doctorate research. Together with the Belgian Nuclear Research Centre SCKCEN, allowable budgets were dispensed so that this work was made possible at SCKCEN's research facilities in Mol. Secondly, I would like to thank **Prof. Dr. Dominique Schryvers**, staff member of the electron microscopy research group EMAT at the University of Antwerp, for that his mail addressed towards the whole Physics Master's students started everything. I am grateful for your support and thank you for this unique opportunity. To my SCKCEN scientific supervisors and mentors, **Dr. Milan Konstantinović** and **Dr. Rik-Wouter Bosch**, thank you truly for your guidance throughout these years. I appreciate your involvement and wish to thank you for being able to pass on your interests for the material and corrosion sciences. My deepest appreciation goes to Milan with whom I had the great pleasure to discuss his multiple ideas and insights surrounding the internal oxidation concept. I find it interesting to reflect on how our lengthy talks and heated discussions, especially during the writing of our scientific papers, helped me improve both on an academical but also personal front. I would also like to express my gratitude towards **Dr. Wouter Van Renterghem** and **Jelle Van Eycken** for their assistance regarding the experimental work using the SEM, FIB-SEM and (S)TEM instruments. To Wouter, thank you for your availability in answering all of my technical and electron microscopy related questions. I also appreciate the assistance of Ms. **Tong Yang** and **Dr. Lars Riekehr** in operating the STEM instrument at the EMAT facilities at the University of Antwerp. Concerning some FEM analyses calculations which were performed on request, I wish to thank **Dr. Alexander Bakaev** and **Dr. Marc Vankeerberghen** for their efforts and dedication. For their assistance in handling the irradiated materials and preparation of my specimens, my sincerest thanks goes out to SCKCEN's specialized hot-cell operators **Kris Kaers** and **Yves Heymans**. Finally, to **Dr. Michèle Coeck**, as director of the SCKCEN Academy I wish to thank you for your efforts for all of us PhD students.

I would like to thank **Prof. Dr. Dirk Lamoen** for overseeing the role of committee chairman of the individual doctorate commission (IDC) in evaluation of this thesis. Towards all members of the IDC commission, thank you for your interest and taking the time to read and review my work. My gratitude is also extended towards **Dr. Anna Hojná**, senior material expert at the Centrum výzkumu Řež (CVR) of the ÚJV group in Husinec-Řež (Czech Republic), for joining the thesis jury as a scientific expert in the fields of material science and corrosion.

To my closest family members who knew how to support me during these long lasting years, I wish to express a very heartfelt thank you. I consider my parents, **Patricia** and **Michel**, to be my main sources of guidance and support. To you two, I look up to the most when achieving my life goals. Although

you may not have understood every line of detail regarding the content of my thesis work, I still chuckle when you can proudly say the abbreviations and functions of the FIB and TEM instruments aloud. To my brother **Eli** and my sister **Hannah**, thanks for moving out of the house during my doctorate. It got a lot quieter at home since you've been gone. In all seriousness though, I would like to think that together, we complete the package of the best family our mum and dad could hope for. You all are the best. Thank you for being a part of my life.

Words fail me in thanking my close friends from high school and university for their continued support and encouragement. Thank you for the many laughs we had together, my *dates-friends*: **Dries Verst.** and **Yenthe**, **Sofie** and **Dries Verh.**, **Nick** and **Julie**, **Sven** and **Michon**, and of course **Yanice**. Others who I dare not forget, are of course **Gianni** and **Roman**, and of course my *kot-friends*: **Charlotte**, **Tim**, **Jens**, **Wim**, **Anouk**, and **Dieter**. Also, these years would not have been the same without the presence of my fellow other Ph.D. students. To those of you that have already graduated, I commend you for your hard work. To all others, I'll definitely be there to support you just as you are there to support me during this period. In no particular ranking order, thank you to **Dr. Andrew Cea**, **Dr. Daniele Salvato**, **Dr. Alexander Zinovyev**, **Amke Lescur**, **Dr. Jonas Vande Pitte**, **Meng Li**, **Liese Vandewalle**, **Tymofii Khvan**, **Olga Kachko**, **Selim Uyger**, **Dr. Niels Cautsaerts**, **Dr. Chao Yin**, **Lilly Charalampopoulou**, **Dr. Sultan Mahmood**, **Moni Kuster**, **Dr. Maja Koblar** and of course **Dr. Annesha Das**.

I cannot conclude these words without acknowledging my ever-loving girlfriend **Liesbeth**. For someone I only met during my final two years of my Ph.D., you were, and still are, someone I can always rely upon. You are my constant source of encouragement, and a daily source of inspiration. You never stop to astound me with your availability, your kindness, and your willingness to make my everyday life more enjoyable. Your smile and your ability to lift my spirits and restore my confidence are invaluable.

English abstract

Irradiation assisted stress corrosion cracking (IASCC) is an intergranular cracking effect which can occur in heavily irradiated structural components of nuclear reactor cores. Internal components of nuclear reactor pressure vessels are fabricated primarily from austenitic stainless steels because of their relatively high strength, ductility, and fracture toughness. Nevertheless, the operating conditions may cause severe material degradation and component failure, which is extremely important for nuclear power plant safety and lifetime managements. IASCC is a complex phenomenon not yet fully understood because it occurs through an interplay of several material degradation processes. The factors that influence the IASCC susceptibility of materials include irradiation damage (neutrons and other irradiation particles), temperature, water corrosion, stress and material composition.

Despite much accumulated data in the literature, contemporary crack initiation and propagation mechanisms still need to be further elucidated, modelled and experimentally verified. Evaluation of crack initiation processes is usually performed on the basis of the mechanical constant load compression tests. In the last few years, over 80 O-ring specimens were made from the neutron-irradiated flux thimble tube of the Tihange nuclear power plant (NPP). These specimens have been subjected to compression tests to initiate stress corrosion cracking. In these tests, the samples are loaded to different stress levels, typically a significant fraction of irradiated yield stress, in order to measure their corresponding time-to-failure. These results have demonstrated that: (i) the O-ring samples fail faster when being subjected to higher stress values, (ii) with an increasing neutron dose, the applied compression stresses required for the O-rings to fail tend to decrease, and (iii) estimation of the stress threshold under which no IASCC cracking occurred, yielded about 40% of the irradiated yield stress. However, a large uncertainty is observed in the time-to-failure data which somewhat limits the application of the proposed stress threshold. Similar uncertainties regarding the cracking aspects of industrial specimens like baffle-to-former bolts have been observed in the NPP field of experience. Some baffle bolts are observed to crack while one would not expect them to crack, according to relatively low accumulated dose and low temperature. On the contrary, some bolts do not crack while one would expect them to crack, because of their symmetrical positions with respect of the cracked bolts (the same material, dose, stress and temperature). Because of that, it is of crucial importance to understand the origin of scatter in these types of experiments and to know what drives the cracking and its uncertainty that ultimately leads to the specimen failure.

To that end, a probabilistic fracture model was recently developed and applied to IASCC, assuming that the oxidized part of the stainless steel sample plays the most essential role for crack initiation, propagation, and ultimate sample failure. A Weibull statistical distribution is employed, to estimate the time-to-failures through a correlation with the statistical distribution of oxide strengths. Large failure uncertainties in these type of tests were explained as originating from an intrinsic stochastic behavior of the oxide cracking due to a subcritical crack propagation (SCP) process. The results of the probabilistic fracture model indicate that the parameters governing subcritical crack growth in the oxidized part of stainless steel are expected to play the most important role in IASCC. The model successfully explained several important experimental observations: (i) The scatter in IASCC time-to-failure data originates from an intrinsic oxide failure uncertainty, (ii) no significant difference between

the time-to-failures of 40 dpa and 80 dpa samples occurs because the oxidation has reached quasi steady state thickness, (iii) the critical irradiation dose for the cracking might be very low if other parameters (such as the exposure time to the corrosive environment and the applied stress during testing) provide conditions for subcritical crack growth (the cracking of NPP baffle bolts is observed to occur even at the dose of about 3 dpa).

Still, despite a very good agreement with experimental observations, the SCP model but also other contemporary models favored within the literature, require further experimental verification to what concerns the investigation of (IA)SCC. In particular, the characterization of the microstructure and morphology of trans- and intergranular cracks and crack tips nucleated within the oxide on the fracture surface and along oxidized grain boundaries of stainless steels are deemed important. To that end, the main objective of this study was to utilize experimental instrumentations like SEM, FIB-SEM and (S)TEM to conduct the investigation of the crack initiation and propagation processes in both tested and industrial specimens. Some of the investigated materials were retrieved within a nuclear reactor and are thus considered as unique test material to investigate the material degradation processes relevant for cracking. Other specimens were tailor-made to simulate the cracking processes of irradiated materials in otherwise un-irradiated materials.

Within the interest of this thesis, analyzes were performed both on un-irradiated tapered tensile and on neutron-irradiated O-ring compression tested samples. Both types of specimens were subjected to constant load experiments with known testing conditions in order to induce specimen cracking and ultimate specimen failure. Subsequent operation of the FIB-SEM instrument allowed for an accurate sample extraction from relevant specimen regions, e.g. close to and beyond the propagating crack tips. Microstructural analysis was then conducted using the numerous characterization techniques employed in SEM and TEM microscopy.

1. To what concerns the tapered tensile specimens, a methodology was firstly developed for an accurate detection of SCC cracks. These measurements allowed for the formulation of crack density graphs which were considered very useful for the determination of a so-called critical SCC threshold, i.e., a stress threshold value below which no occurrence of cracking in the material is observed. TEM examination illustrated that the oxide assembly formed within the SCC cracks appertained to both a chromite and a magnetite oxide structure. Based upon the mechanical load data, the crack morphology analyzes, and the microstructural investigation surrounding the SCC cracks, the transgranular cracking was found to be associated to two dominant failure regimes. The first regime appertained specifically to low strain-rates and was dominated by the film-induced cleavage mechanism, while the secondary regime illustrated a strain-induced failure at high strain-rates.
2. Alternatively, regarding the analyses performed on the neutron-irradiated O-ring specimens, close examination was performed on the deformation field and the oxide assembly associated with intergranular IASCC cracking. Clear evidence of displacive transformations, amongst which deformation twinning and stress-induced martensitic phases, were unveiled at different stress states extending from and adjacent to the crack tips. Chemical investigation of the grain boundaries in several specimens also provided arguments for known neutron-induced material deteriorating effects that may increase the susceptibility to intergranular cracking. In investigating the morphology of the IASCC crack tips, at all times, cracking was observed to extend within the priorly oxidized grain boundary, which was deemed to be in full-agreement with the internal oxidation and SCP models. All investigated cracks exhibited grain boundary oxidation in front of the crack tip, the extent of which was found to be proportional to the applied macroscopic stress to the O-ring specimen. These findings clearly demonstrated that, under the SCP regime, the grain boundary oxide grew faster than the crack. In investigating crack tips from specimens with

an initially removed outer surface oxide layer prior to the initiation of the constant load tests, comparatively less oxidation was observed in front of the crack tip. This difference was attributed to the initiation of cracking from regions like the O-ring's inner surface, where effectively a lower stress-enhanced effect was reasoned. Considering O-ring specimens loaded specifically under cyclic conditions, a more pronounced effect on the crack tip microstructure was observed, which demonstrated an increased deformation in the bulk material in front of the crack tip. The extent of crack tip oxidation in front of cyclic loaded tips still agreed well with expected values for maximum stress applied during cyclic loading. This result illustrated that the peak stresses play the most essential role for crack propagation in cyclic loaded specimens.

The results obtained in this investigation provide crucial information in order to elucidate the complex mechanism responsible for IASCC. The newly acquired experimental results help rationalize some existing models and methodologies used in the literature to analyze the failure of structural materials of reactor components. All results are in full agreement with the recently proposed SCP model based on a stress-assisted internal oxidation mechanism assuming brittle fractures in the internally oxidized grain boundaries of stainless steels.

Dutch abstract

Bestraling-geassisteerde spanningscorrosie (IASCC) is een intergranulair scheureffect dat kan optreden in het zwaar bestraald materiaal van de structurele componenten van kernreactoren. Interne onderdelen van de drukvaten van kernreactoren worden voornamelijk gemaakt uit austenitisch roestvrij staal vanwege hun relatief hoge sterkte, vervormbaarheid, en scheur-resistentie. Nochtans kunnen de interne omstandigheden van de drukvaten ernstige vormen van materiaaldegradatie en het falen van componenten veroorzaken, wat natuurlijk uiterst belangrijk is voor de veiligheid en het beheer van kerncentrales. IASCC is een complex fenomeen dat nog niet volledig wordt begrepen omdat het plaatsvindt door een samenspel van verschillende materiaaldegradatieprocessen. De factoren die de IASCC-gevoeligheid van materialen beïnvloeden, zijn onder meer stralingschade (door middel van neutronen en andere stralingsdeeltjes), temperatuur, watercorrosie, stress en materiaalsamenstelling.

Ondanks alle verzamelde gegevens in de literatuur, moeten de hedendaagse scheurinitiatie- en propagatiemechanismen nog verder opgeklaard, gemodelleerd en experimenteel geverifieerd worden. Evaluatie van scheurinitiatieprocessen wordt meestal uitgevoerd op basis van mechanische compressietesten met constante belasting. In de afgelopen jaren zijn meer dan 80 O-ring stalen gemaakt uit een bestraalde neutron- moderatorbuis van één van de kerncentrale van Tihange. Deze stalen zijn onderworpen aan de compressietesten om de spanningscorrosie-scheuren te laten initiëren. Bij deze tests worden de stalen belast met verschillende spanningsniveaus, typisch tot een aanzienlijk deel van de bestraalde vloeispanning, om hun overeenkomstige tijd tot breken te meten. Deze resultaten hebben aangetoond dat: (i) de O-ring stalen sneller breken wanneer ze worden blootgesteld aan hogere spanningswaarden, (ii) met een toenemende bestraalde neutronendosis, hebben de compressiespanningen die nodig zijn om de O-ringen te doen laten falen, de neiging om af te nemen, en (iii) de schatting van de stressdrempel waaronder geen IASCC-scheuring optrad, leverde ongeveer 40% van de bestraalde vloeispanning op. Echter, er wordt een grote spreiding waargenomen in de verschillende tijden-tot-falen. Deze spreiding beperkt enigszins de toepassing van de functie van de voorgestelde stressdrempel. Deze onzekerheden zijn gelijkwaardig aan de spreiding in falen van industriële componenten uit kerncentrales, zoals bijvoorbeeld het scheuren van onder meer de baffle-to-former-bouten. Namelijk, sommige bouten barsten onder condities waarvan je initieel niet zou verwachten dat ze zouden barsten, zoals bij relatief laag geaccumuleerde stralingsdosis en lage temperaturen. Integendeel, sommige bouten barsten niet terwijl je juist wél zou verwachten dat ze moeten barsten, bijvoorbeeld bij hun symmetrische positie ten opzichte van reeds wel gescheurde bouten die hetzelfde materiaal, geaccumuleerde dosis, spanning en temperatuur hebben opgelopen. Daarom is het van cruciaal belang om de oorsprong van de spreiding in dit soort experimenten te begrijpen en te weten wat de scheuronzekerheid veroorzaakt die uiteindelijk tot het falen van het staal leidt.

Om dit probleem aan te kaarten, is er onlangs een probabilistisch scheurmodel ontwikkeld en toegepast op IASCC. Dit model gaat ervan uit dat het geoxideerde deel van het roestvrije staal de meest essentiële rol speelt voor het ontstaan van scheuren, de propagatie ervan, en het uiteindelijk falen van het monster. Er wordt gebruik gemaakt van een statistische Weibull-verdeling om de tijden-tot-falen in te schatten door middel van een correlatie met de statistische verdeelde oxidesterkten. De grote

spreiding uit de compressietesten worden reeds verklaard als komende uit een intrinsiek stochastisch gedrag van de oxidelaag als gevolg van een subkritisch scheurpropagatieproces (SCP). De resultaten van het probabilistische scheurmodel geven aan dat de parameters die de subkritische scheurgroei in het geoxideerde deel van roestvrij staal bepalen naar verwachting de belangrijkste rol spelen voor IASCC. Het model verklaart met succes enkele verschillende belangrijke experimentele waarnemingen: (i) De spreiding in de tijd-tot-falen-gegevens van IASCC komt voort uit een intrinsieke onzekerheid in het falen van de oxides, (ii) er treedt geen significant verschil tussen de tijd-tot-falen van 40 of 80 dpa-monsters op omdat de oxidatie een quasi stationaire dikte heeft bereikt na deze bestralingsdosissen, en (iii) de kritische stralingsdosis voor het scheuren van stalen kan erg laag zijn als andere parameters (zoals de blootstelling aan het corrosief milieu en toegepaste stress gedurende het testen) voorwaarden bieden voor de subkritische scheurgroei (het barsten van NPP-schotbouten wordt waargenomen zelfs bij een dosis van ongeveer 3 dpa).

Ondanks zeer goede overeenkomsten met experimentele waarnemingen in de literatuur, vereisen het SCP-model maar ook andere hedendaagse scheur modellen die de voorkeur krijgen in de literatuur, verdere experimentele onderzoek naar wat betreft (IA)SCC. In het bijzonder, worden de karakterisering van de microstructuur en de morfologie van trans- en intergranulaire scheuren die geïnitieerd zijn in de oxide op het breukoppervlak óf langs geoxideerde korrelgrenzen van roestvast staal, belangrijk geacht. Om dit te volbrengen, werden experimentele instrumenten zoals SEM, FIB-SEM en (S)TEM gebruikt om de scheur initiatie- en propagatieprocessen in zowel geteste als industriële monsters te onderzoeken. Sommige van de onderzochte materialen zijn verworven van binnenin een nucleaire reactor. Omwille van deze reden worden ze dus als uniek testmateriaal beschouwd om de degradatie processen die relevant zijn voor het scheuren van materialen te onderzoeken. Andere onderzochte materialen werden dan weer op maat gemaakt om de scheurprocessen van bestraalde materialen te simuleren in anders, juist niet-bestraalde, materialen.

In het kader van dit proefschrift, werden er analyses uitgevoerd op niet-bestraalde versmallende trekmonsters én op met neutronen-bestraalde O-ring compressie monsters. Beide stalen werden onderworpen aan constante belastingexperimenten waarvan de testparameters gekend zijn, om het scheuren van de monsters en ook het uiteindelijke falen ervan te veroorzaken. Vervolgens werd er gebruik gemaakt van het FIB-SEM-instrument om plaatsnauwkeurige extracties mogelijk te maken uit relevante gebieden van de monsters. Interessante gebieden zijn bijvoorbeeld de voortgeplante scheurtip en het materiaal dat er juist naast volgt. Hierna werd er een uitgebreide microstructurele analyse uitgevoerd met behulp van verschillende karakteriseringstechnieken binnen de SEM en TEM microscopie.

1. Wat betreft de versmalde trekmonsters, werd er allereerst een methodologie ontwikkeld voor het nauwkeurige detecteren van SCC-scheuren. Deze metingen maakten het mogelijk om scheurdichtheidsgrafieken te formuleren die zeer nuttig werden geacht voor het bepalen van een zogenaamde kritische SCC-drempelwaarde, d.w.z., een drempelwaarde waaronder het materiaal niet meer scheurt als gevolg van stress. Volgend TEM-onderzoek illustreerde dat de oxide die gevormd wordt in SCC-scheuren zowel bestaat uit een chromiet als een magnetiet oxidestructuur. Op basis van de mechanische testdata, de scheurmorfologie-analyse en het microstructurele onderzoek rond de SCC-scheuren, bleek dat transgranulaire scheuren geassocieerd te zijn met twee dominante faalregimes. Het eerste regime was specifiek geldig voor een lage treksnelheid en werd gedomineerd door een film-geïnduceerde scheurmechanisme. Anderzijds, wordt het secundaire regime bepaald door een spanningsgeïnduceerd falen bij hoge treksnelheden.
2. Met betrekking tot de analyses die werden uitgevoerd op neutronen-bestraalde O-ringmonsters, werden het vervormingsveld rond de samenstelling van de oxides in de intergranulaire IASCC-scheuren grondig onderzocht. Er werd duidelijk bewijs vastgesteld van deformatie-tweelingen en spanning-geïnduceerde martensitische fasen, d.w.z. microstructurele vervormingstransformaties,

naast maar ook vertrekkende vanuit de scheurtippen bij verschillende stressgehalten. Chemisch onderzoek van de korrelgrenzen in verschillende O-ringmonsters bracht ook elementen aan het licht die aanwijzingen gaven naar gekende materiaaldegradatie effecten die geïnduceerd worden door neutronen bestraling. Deze vormen van materiaaldegradatie kunnen de gevoeligheid voor intergranulaire scheuren vergroten. Bij het onderzoeken van de morfologie van de IASCC-scheurtippen werd ten allen tijden waargenomen dat scheuren zich uitstrekken binnen geoxideerde korrelgrens. Dit werd volledig in overeenstemming geacht met de interne oxidatie- en SCP-scheurmodellen. Alle onderzochte scheuren vertoonden een korrelgrensoxidatie vóór de scheurtip, waarvan de uiteindelijke omvang evenredig bleek te zijn met de uitgeoefende macroscopische stress op het O-ringmonster. Deze bevindingen toonden duidelijk aan dat, onder het SCP-scheurmodel, de korrelgrensoxide sneller groeit dan de eigenlijke scheur zelf. Bij het onderzoeken van de scheurtippen van de monsters met een aanvankelijk verwijderde oxidelaag aan de buitenkant van de O-ring aan de start van de constante belastingtests, werd er relatief minder oxidatie waargenomen voor de scheurtip dan initieel werd verwacht. Dit verschil werd toegeschreven aan het ontstaan van de scheuren uit gebieden van de O-ring waar een effectief lager stress-verhogend effect werd waargenomen, zoals bijvoorbeeld aan de binnenkant van de O-ring. In wat betreft de analyses van O-ringmonsters die specifiek onder cyclische omstandigheden zijn belast, werd er een meer uitgesproken effect op de microstructuur van de scheurtip waargenomen, wat een verhoogde vervorming in het bulkmateriaal voor de scheurtip aantoonde. De mate van oxidatie voor een cyclisch geladen scheurtip kwam goed overeen met de verwachte waarden voor maximale stress die werd uitgeoefend tijdens cyclische belasting. Dit resultaat illustreerde dat enkel de piekstressen in cyclisch belaste monsters de meest essentiële rol spelen voor scheurpropagatie.

De resultaten die in dit onderzoek zijn verkregen, bieden nieuwe cruciale informatie aan om het complexe mechanisme dat verantwoordelijk is voor IASCC op te helderen. De verworven experimentele resultaten helpen bij het rationaliseren van enkele bestaande scheurmodellen en methodologieën die in de literatuur worden gebruikt om het falen van structurele materialen van reactorcomponenten te analyseren. Alle resultaten zijn in volledige overeenstemming met het recentelijk voorgestelde SCP-model dat gebaseerd is op een stress-ondersteund intern oxidatiemechanisme, waarbij er wordt uitgegaan van brosse breuken in de intern geoxideerde korrelgrenzen van roestvast staal.

List of Publications

This doctoral work produced the following list of original peer-reviewed publications, internally published technical reports and conference and workshop contributions:

Academic publications:

- [1] **A. Penders**, M.J. Konstantinović, R.W. Bosch, and D. Schryvers (2020) *Crack initiation in tapered high Si stainless steel specimens – stress threshold analyses*, *Corrosion Engineering, Science and Technology*, 55:8, 721-728, DOI: <http://doi.org/10.1080/1478422X.2020.1785651>
- [2] **A. Penders**, M.J. Konstantinović, W. Van Renterghem, R.W. Bosch, and D. Schryvers (2021) *TEM investigation of SCC crack tips in high Si stainless steel tapered specimens*, *Corrosion Engineering, Science and Technology*, 56:8, 767-777, DOI: <http://doi.org/10.1080/1478422X.2021.1961665>
- [3] **A.G. Penders**, M.J. Konstantinović, T. Yang, R.W. Bosch, and D. Schryvers, and F. Somville (2022) *Microstructural investigation of IASCC crack tips extracted from thimble tube O-ring specimens*. *Journal Nuclear Materials*, 565, 153727, DOI: <http://doi.org/10.1016/j.jnucmat.2022.153727>
- [4] **A.G. Penders**, M.J. Konstantinović, W. Van Renterghem, R.W. Bosch, D. Schryvers & F. Somville (2022) *Characterization of IASCC crack tips extracted from neutron-irradiated flux thimble tube specimens in view of a probabilistic fracture model*. *Journal of Nuclear Materials*, 571, 154015, DOI: <https://doi.org/10.1016/j.jnucmat.2022.154015>
- [5] R.W. Bosch, M.J. Konstantinović, **A.G. Penders**, M. Vankeerberghen & F. Somville, *IASCC crack initiation testing of thimble tube material under PWR conditions: effect of oxide layer, stress and load form*. In *FRONTEND 10: International Symposium Contribution of Materials Investigations and Operating Experience to LWRs' Safety, Performance and Reliability*, 19-22 September 2022, Avignon, France.

Technical reports (SCKCEN):

- [1] M.J. Konstantinovic, **A.G. Penders**, W. Van Renterghem, R.-W. Bosch (2021) *Microstructural investigation of IASCC crack tips from tested O-ring specimens*. Report no. R-8289, Nuclear Materials Science Institute (NMS)-MNA-MCA, Mol.
- [2] M.J. Konstantinovic, **A.G. Penders**, W. Van Renterghem, R.-W. Bosch (2021) *Final report task 3.1: Microstructural analysis of cracks/crack tips in support of the probabilistic fracture model*. Report no. R-8899, NMS-HLB-MNA, Mol.

Conference Presentations & Workshop participations:

- [1] **A.G. Penders**, M.J. Konstantinović, R.-W. Bosch, and D. Schryvers. *Crack Initiation in Tapered Specimens - High Si Stainless Steels*, *EUROCORR2019*, Seville (Spain), 9-13th September, 2019 (Poster)
- [2] **A.G. Penders**, M.J. Konstantinović, R.-W. Bosch, and D. Schryvers. *TEM investigation of SCC crack tips in high Si stainless steel tapered specimens*, *EUROCORR2020*, 7-11th September, 2020 (Oral)
- [3] **A.G. Penders**, M.J. Konstantinović, R.-W. Bosch, and D. Schryvers. *TEM investigation of SCC crack tips in high Si stainless steel tapered specimens*, *NUMAT2020*, 26-29th October, 2020 (Oral)
- [4] **A.G. Penders**, M.J. Konstantinović, R.-W. Bosch, and D. Schryvers. *Microstructural investigation of IASCC crack tips extracted from Thimble Tube O-ring specimens*, *virtual EUROCORR2021*, 20-24th September, 2021 (Oral)
- [5] Safe and longterm Operation of LWRs based on improved understanding of radiation effects in nuclear structural materials - SOTERA workshop, Valencia (Spain), 3-7th September, 2018
- [6] Nuclear corrosion summer school - NuCoSS19, Gozd Martuljek (Slovenia), 7-12th June, 2019
- [7] EMAT workshop on TEM - A complete training on HRTEM and TEM spectroscopy focused on hands-on experience, Antwerp (Belgium), 11-21st June, 2019

List of Figures

1.1	Evolution of the total gross electricity production in Belgium (TWh), from 2007 up to 2020. Redrawn from reference [10].	6
1.2	Illustration of a PWR NPP, separating the reactor primary water coolant system (yellow) from the secondary water coolant system (blue). Redrawn from reference [14]. . .	8
1.3	(A) Diagram of the internal structure of an RPV core of a PWR NPP. (B) Illustration of the baffle-former assembly with in-placed BFBs. (C) Visual and metallographic examination of an extracted BFB. Redrawn from references [32, 33].	11
2.1	Schematic of the primary contributors that affect the underlying crack tip processes that control IASCC. The effects of neutron-irradiation is also shown, amongst which: (ir)radiation-induced segregation (RIS), -hardening (RH) and embrittlement (RE), and -creep (IC). Redrawn from reference [22].	18
2.2	Ball-and-stick and hard-sphere representations of the unit cells for the austenite (FCC), ferrite (BCC), and martensite (HCP) and (BCT) lattices, respectively.	19
2.3	Schaeffler diagram illustrating the stable allotrope phases of SSs according to their equivalent ferrite and austenite stabilizers. Amongst others, types 316L and high-Si A078 duplex steel employed in this study are added for reference. Redrawn according to references [48, 49].	20
2.4	(A) Visual representation of the orientation of an edge- and screw dislocation, defined by their respective Burger \vec{b} and line vectors \vec{l} . (B) Atomistic representation of the process of dislocation slip. Redrawn according to reference [59].	22
2.5	(A) Stacking sequence of $\{111\}$ -type FCC lattice planes, illustrating how (B) dislocations with a perfect Burgers vector b_1 may dissociate into two partial dislocations with vectors b_2 and b_3 . Redrawn in accordance to reference [59].	23
2.6	Atomistic model of the generation of a finite thickness coherent twin orientated in a $\langle 112 \rangle$ direction between two $\{111\}$ mirror twin boundaries. According to reference [59].	25
2.7	Schematic illustration of the stacking of an FCC lattice, leading to the formation of (A) twinning, and (B) HCP ϵ -martensite. Redrawn in accordance to the schematics in reference [48].	26
2.8	Schematic of the ballistic damage cascade following the impact of neutron irradiation in structural nuclear materials. Redrawn from references [111, 112].	31
2.9	DF-TEM of typical Frank loops and precipitates observed within the microstructure of baffle bolt C47 at dose values and irradiation temperatures of (A) 18 dpa and 337-348 °C, (B) 27 dpa and 340-343 °C, and (C) 45 dpa and 340-345 °C. Figures adopted from reference [113].	33
2.10	Under-focused BF-TEM of typical void clusters observed within the microstructure of baffle bolt C47 at dose values and irradiation temperatures of (A) 18 dpa and 337-348 °C, (B) 27 dpa and 340-343 °C, and (C) 45 dpa and 340-345 °C. Figures adopted from reference [113].	34

2.11	Illustration of the effects of radiation induced segregation. (A) Point defect concentrations profiles and fluxes of vacancies (C_v, \vec{J}_v) and interstitials (C_i, \vec{J}_i) in close vicinity to microstructural sinks. (B) Concentration profiles and corresponding element fluxes ($C_{A,B}, \vec{J}_{A,B}$) of elements A and B being enriched or depleted in association to the point defect flux.	35
2.12	Radiation induced segregation mechanisms: (A) low binding enthalpy vacancy-exchange mechanism for FCC lattices, (B) formation of high symmetry interstitial dumbbells in FCC lattices, (C) solute drag vacancy-exchange mechanism, illustrating either enrichment or depletion respectively, depending on the vacancy-interstitial binding enthalpy, and (D) interstitial transport mechanism, illustrating either enrichment or depletion depending on the stability of the dumbbell configuration.	37
2.13	(A) First principle description of the stress distribution at the crack tip whereat σ and τ represent the normal and shear stress components in the (x,y)-directions at the crack tip. (B) Illustration of the distinct cracking modes for cracks subjected to external load. Redrawn from reference [155].	43
2.14	Description of SCC models according to (A) Parkin's model [159], (B) Staehle's model [160]. Redrawn according to each separate reference.	44
2.15	Evan's diagram for the corrosion of Fe in a cathodic solution. Redrawn from reference [182].	48
2.16	Evan's diagram illustrating the effect of passivation and Cr addition on the corrosion potential. Redrawn from reference [183].	50
2.17	Schematic illustration of the successive events described by the film-induced cleavage (FIC) model for transgranular SCC. Redrawn according to references [184, 195].	53
2.18	Schematic illustration of the successive events described by the film-rupture (slip-dissolution) model. Adopted and redrawn according to reference [204].	54
2.19	Schematic diagram of SCC sub-processes for quantitative analysis of the FRM. Adopted and redrawn according to reference [104].	56
2.20	(A) Weibull cumulative failure distribution for several σ_i 's. (B) Depiction of the volume-thickness effect on the Weibull cumulative safety distribution calculated for several V/V_i 's. Calculated from equations 2.25 and 2.31.	61
2.21	Schematic depiction of the normal stress-variation along an oxidized intrusion tip ($0 \gg x \gg \ell$) in front of a stationary crack ($x \leq 0$). Adopted and redrawn according to reference [233].	65
3.1	A diagram of a typical SEM illumination column. Adopted and redrawn in accordance to reference [242].	75
3.2	A diagram illustrating the individual components of the FIB-SEM DualBeam set-up. Adopted and redrawn from reference [243].	76
3.3	Schematic overview of the TEM-lamella FIB preparation of IASCC crack tips.	77
3.4	Comparison between the different imaging modes during the TEM specimen thinning operation: (A) SEM secondary electron using the ETD-detector, (B) SEM ordinary backscattered-secondary electron using T1-detector, and (C) SEM OptiTilt backscattered-secondary electron image using the T1-detector.	79
3.5	A schematic diagram of the JEOL 3010 LaB ₆ (S)TEM. Redrawn in accordance to reference [251].	80
3.6	Schematic overview of the ray diagram projector stage consisting of the objective lens (OL), three intermediate lenses (ILs) and the projector lens (PL). Redrawn in accordance to reference [252].	83

3.7	Illustration of the (A) Bragg diffraction condition where the incoming and scattered waves constructively interfere when the path length difference δ equals an integer multiple of the wavelength. (B) Geometric construction of the Ewald's sphere, or otherwise known as the sphere of reflection. Redrawn from reference [253].	84
3.8	Ray diagram illustrating the operation to produce: (A) a BF-image, (B) a DADF-image from a specific off-axis scattered electron beam, and (C) a CDF image from a scattered electron beam onto the optic axis by tilting the primary incident beam onto the specimen. The DP seen on the viewing screen, is shown below each ray diagram. Redrawn from reference [252].	86
3.9	Electron diffraction through TEM investigation: (A) BF-TEM of grain boundary separating two opposing grains, (B) Centralized DF-TEM of grain 1, (C) corresponding DP, and (D) indexed DP, illustrating that the grain was tilted into the 013 austenitic zone axis.	87
3.10	Electron ring-diffraction through TEM investigation: (A) BF-TEM of SCC arrested at the metal-oxide interface, (B) illustration of the different concentric circles of the Ewald's sphere represented in the reciprocal lattice (redrawn from reference [252]), (C) corresponding oxide DP, and (D) corresponding Pt DP in A.	88
3.11	(A) Oxide ring-DP. (B) Application the rotationally averaging and integrating of the diffracted ring intensities, and (C) its corresponding signal ring intensity signal.	89
3.12	Schematic diagram of (A) Bohr's atomic model illustrating the principle of EDS, and (B) the electronic transitions related to X-ray emission. An electron hole in the inner K-shell is filled by an electron from an outer L ₃ -shell.	89
3.13	(A) BF-TEM image of an oxide intrusion leading into a grain boundary of an IASCC crack. (B) HR-TEM of the intergranular oxide at the crack tip. (C) HR-TEM Moiré pattern at the oxide-metal overlap.	90
3.14	Schematic diagram illustrative of the geometric arrangement of the STEM-BF, -ADF and -HAADF detectors. The (semi-) collection angles of the BF- and DF-detector are representative for a 200 kV non-corrected STEM and may vary depending on the mode of operations. Redrawn from reference [257].	92
3.15	(A) BF-TEM and (B) CDF-TEM of an intergranular crack tip and its leading grain boundary. More magnified images are respectively displayed in images (C-D), which attract a lot of interest for analytical TEM and STEM investigations.	93
3.16	Overview of a typical tapered tensile specimen, (A) pre and (B) post CERT-testing after specimen failure. The distances are given in mm.	97
3.17	Functionality of the MATLAB script file handling the improved detection based on several filtering algorithms. (A) Flowchart of the algorithm. (B) Performance of the mean crack angle and segmented length filters on SEM BSE images. Indications highlight various false-detected surface features, excluded from the detection in the next filter (as indicated by arrows). (C) Performance of the crack clustering algorithm. Nearby clusters indicate similar and overcounted cracks (as indicated by crosses).	98
3.18	O-ring compression test rig. (A) Autoclave pressure unit installed in one of SCKCEN's hot-cell facilities. (B) The compression loading unit capable of compressing five O-rings to failure. (C) Schematic representation of the tensile and compressive surface stresses on the inner and outer surfaces of the O-ring. Fracture typically occurs in the middle plane in between the bending points. (D) COMSOL Multiphysics stress calculations.	100
3.19	O-ring cutting procedure. (A) Operation of the hot-cell mechanical arms during the process of sample preparation. (B) Inside view of SCKCEN's hot-cell 37. (C) Irradiated O-ring prior to cutting, and (D) post-cutting.	102

3.20	TTO-1-053 O-ring cutting scheme. (A) Intact O-ring specimen prior to constant load testing. (B) O-ring post constant load compression testing. Indications of the loading points and transversal cut along the middle of the specimen are depicted. (C) Second cut of the remaining piece, close to the primary fracture surface. (D) Secondary electron SEM view of the fracture surface illustrating the full intergranular mode. (E) Backscattered electron SEM view in edge-on orientation illustrating the extent of branched cracking from the inner surface.	103
4.1	Autoclave load-elongation curves for high Si stainless steels obtained after CERT-testing, under (a) PWR and (b) inert N ₂ conditions. The curves are corrected for an initial load offset due the small load oscillations before the CERT deformation. . .	106
4.2	Main fracture surface of a tapered specimen tested under $\dot{\epsilon} = 5.00 \text{ E-}8 \text{ s}^{-1}$ in a simulated PWR environment. (A) General overview of the transgranular fracture, with (B) its brittle- and (C) its ductile-aspect of the fracture regions.	107
4.3	Main fracture surface of a tapered specimen tested under $\dot{\epsilon} = 5.00 \text{ E-}6 \text{ s}^{-1}$ in a simulated PWR environment. (A) General overview of the transgranular fracture with (B-C) its ductile-aspects of the fracture regions.	109
4.4	Main fracture surface of a tapered specimen tested under $\dot{\epsilon} = 5.00 \text{ E-}7 \text{ s}^{-1}$ in an inert N ₂ environment. (A) General overview of the transgranular fracture with (B-C) its ductile-aspects of the fracture regions.	110
4.5	Overview of several EDS spectral maps of the tapered gauge length of a specimen tested to $\dot{\epsilon} = 5.00 \text{ E-}7 \text{ s}^{-1}$	111
4.6	Point EDS spectra of the (A) austenite (γ) and (B) ferrite (α) phases of the tapered gauge length of a specimen tested to $\dot{\epsilon} = 5.00 \text{ E-}7 \text{ s}^{-1}$	112
4.7	SCC crack detection on a tapered gauge length of a specimen strained to $\dot{\epsilon} = 5.00 \text{ E-}8 \text{ s}^{-1}$. (A) Original SEM frame, (B) crack detection (prior to filtering), (C) crack detection (post filtering), (D) crack angle distribution (prior to filtering, (E-F) crack length and crack angle distributions (post filtering).	113
4.8	Process of phase recognition of the duplex surface composition of a single SEM frame in the crack detection algorithm. (A) Original SEM frame, (B) probability map, (C) threshold masked map and (D) phase recognition map of the austenite-ferrite phases. .	114
4.9	Total variation of the duplex surface composition of a typical tapered specimen's gauge length.	115
4.10	Crack density distributions of CERT-strained tapered specimens with strain-rates: (A) $\dot{\epsilon} = 1.00 \text{ E-}6 \text{ s}^{-1}$, (B) $\dot{\epsilon} = 1.00 \text{ E-}7 \text{ s}^{-1}$ and (C) $\dot{\epsilon} = 5.00 \text{ E-}8 \text{ s}^{-1}$ and (D) FEM stress intensity after simulating the load history of the sample tested under $\dot{\epsilon} = 5.00 \text{ E-}8 \text{ s}^{-1}$. The critical gauge lengths ℓ_c and the FEM simulated critical stress threshold are shown.	116
4.11	FEM calculations of the stress intensities along the tapered gauge length. (A) Zero, (B) one, (C) two, and (D) ultimately six triangular crack prisms of size $0.4 \times 0.15 \times 0.15 \text{ mm}^3$ were consecutively simulated in the mesh as being representative of dense crack regions.	117
4.12	Stress thresholds $\sigma_{\text{thr},i}$ for high Si stainless steel tapered specimens in a simulated PWR environment. Extrapolation through the individual stress thresholds determines the stress threshold under which constant load conditions are independent of the applied nominal strain-rate i.e., the critical stress threshold which is evaluated as $\sigma_{\text{thr}} = 581 \pm 16 \text{ MPa}$	118
4.13	FIB-SEM images illustrating the methodology of SCC crack tip extraction from a bulk specimen surface.	119
4.14	Low-voltage BSE grain contrast imaging of a TEM-lamella with SCC cracks. The dashed lines illustrate the compositional grain structure of the lamella cross-section. .	120

4.15	Low-magnification BF-TEM image of the lamella cross-sections of strained tapered specimens with respective strain-rates of (A) $\dot{\epsilon} = 5.00 \text{ E-}8 \text{ s}^{-1}$ (slow) and (B) $\dot{\epsilon} = 5.00 \text{ E-}6 \text{ s}^{-1}$ (fast).	121
4.16	Cross-sectional crack morphologies of SCC cracks appertaining to (A) $\dot{\epsilon} = 5.00 \text{ E-}8 \text{ s}^{-1}$, and (B) $\dot{\epsilon} = 5.00 \text{ E-}6 \text{ s}^{-1}$	122
4.17	Comparison of the SCC crack length-to-width ratio as an indicator for the crack morphology variation in terms of the applied nominal strain-rate. The morphology of the crack tip becomes more rounded with increasing strain-rate.	123
4.18	Two-beam micrographs of an embedded microcleavage crack tip for a lamella belonging to a specimen slowly strained to $\dot{\epsilon} = 5.00 \text{ E-}7 \text{ s}^{-1}$. (A) BF-TEM overview, (B,C) respective BF- and CDF-TEM of the magnified crack tip. The metal and oxide reciprocal reflections are indexed in the inset diffraction pattern, and the experimental objective aperture is illustrated with the small circle.	124
4.19	Twinned microstructure of the deformed metal matrix for a specimen appertaining to the sample strained to $\dot{\epsilon} = 5.00 \text{ E-}6 \text{ s}^{-1}$. (A) BF-TEM, (B) CDF-TEM and (C) corresponding SAED diffraction pattern of twinned structure. The objective aperture is shown by the small circle. The indexing of the matrix (M) and twin (T) diffraction spots demonstrates that the twins predominantly occur along the $\{111\}$ austenitic planes.	124
4.20	BF-TEM appertaining to specimens strained to (A,B) $\dot{\epsilon} = 5.00 \text{ E-}7 \text{ s}^{-1}$, and (C,D) $\dot{\epsilon} = 5.00 \text{ E-}6 \text{ s}^{-1}$. See also Fig. 4.20 (continued).	125
4.21	(A) BF-TEM SCC crack from a specimen strained to $\dot{\epsilon} = 5.00 \text{ E-}7 \text{ s}^{-1}$. (B) Corresponding EDS spectra of different features surrounding the crack tip. The Cu signal originates from the TEM support grid.	127
4.22	External and crack tip oxide thickness measurements obtained from the BF- and CDF-TEM images for the varying strain-rates.	128
4.23	(A) Inner oxide experimental ring diffraction pattern. (B) Application of the radial sampling method i.e. taking rotational integrations of the diffraction pattern and subsequently normalizing the resulting intensities. (C) Corresponding line trace of the radial sampling method.	129
4.24	Inner oxide for a specimen strained to $\dot{\epsilon} = 1.00 \text{ E-}6 \text{ s}^{-1}$. (A) BF- and (B) corresponding CDF-TEM of the inner oxide in between two crack tips, with (C) their indexed ring-like diffraction pattern matching FeCr_2O_4	129
4.25	Outer oxide for a specimen strained to $\dot{\epsilon} = 1.00 \text{ E-}6 \text{ s}^{-1}$. (A) BF- and (B) corresponding CDF-TEM of an outer oxide grain in between two crack tips, with (C) their indexed spot-like diffraction pattern matching $(\text{Fe,Ni})_3\text{O}_4$	130
4.26	Outer oxide (A) experimental, and (B) simulated diffraction pattern analysis of the FCC-type spinel oxide $\text{Fd}\bar{3}m(227)$ $(\text{Fe,Ni})_3\text{O}_4$ [281]. All systematic absences of the space group along the zone-axis $[113]$ are indicated with little blue crosses.	131
4.27	STEM-HAADF EDS spectral maps acquired from a $\dot{\epsilon} = 5.00 \text{ E-}7 \text{ s}^{-1}$ CERT-strained tapered specimen illustrating the SCC initiation within the austenite phase of the duplex microstructure.	132
4.28	STEM-HAADF EDS spectral maps acquired from a $\dot{\epsilon} = 5.00 \text{ E-}7 \text{ s}^{-1}$ CERT-strained tapered specimen illustrating the different metallic and oxide composition of a typical SCC crack.	132
5.1	Mechanical load O-ring compression testing. Stress versus time to failure of O-rings tested under the constant load condition. Time to failure of O-rings that are investigated in this study are indicated in the figure.	136

5.2	(A) Reconstruction of the failure of TTO-1-053 (390 MPa). (B) BSE-SEM imaging of the crack initiation along the inner surface. (C) SE-SEM of the as-received O-ring's outer surface.	138
5.3	(A) Reconstruction of the failure of TTO-1-001 (690 MPa). (B-C) SEM imaging of the crack initiation along the outer surface.	138
5.4	SEM SE investigation of the primary fracture surface of specimens (A) TTO-1-053 (390 MPa), (B) TTO-1-071 (500 MPa), (C) TTO-1-001 (690 MPa).	139
5.5	FIB-SEM images illustrating the methodology of IASCC crack tip extraction from an O-ring's specimen piece polished primary fracture surface.	141
5.6	SEM images of IASCC crack initiation at the (A) primary fracture surface of TTO-1-090 and (B) at the outer surface of TTO-1-001.	142
5.7	TTO-1-053 (390 MPa) L03 (A) BF-TEM overview of a main IASCC branch leading up to a completely oxidized grain boundary triple junction. Inset image depicts the corresponding low-magnification CDF-TEM view of the oxidized grain boundary. (B) Magnified view of the metal-oxide interface cracking. (C) Representation of the strong crack branching nature within the intergranular oxide. Darker contrast bands represent intentionally thicker strokes of material that are left behind during the process of FIB-milling in order to mitigate the strong curtaining effect underneath the oxidized triple junction.	144
5.8	TTO-1-001 (690 MPa) L06 (A) BF-TEM and (B) corresponding CDF-TEM overview of a main completely oxidized IASCC branch.	145
5.9	TTO-1-053 (390 MPa) L06 (A) BF-TEM and (B) CDF-TEM of an IASCC crack imaged from an intergranular oxide reflection. Respectively, the (C,E) DPs and (D,F) EDS spectra of the corresponding chromite spinel $(\text{Fe,Cr})_3\text{O}_4$ and the magnetite deposit $(\text{Fe,Ni})_3\text{O}_4$ oxides are depicted. The strong Cu-signal originates from the TEM grid holder.	146
5.10	TTO-1-090 (700 MPa - non-native oxide) L06 (A) BF-TEM and (B) corresponding CDF-TEM of the general crack morphology imaged from an internal chromite reflection. (C) BF-TEM of narrow oxidized crack flanks. (D) EDS spectra of the duplex oxide formation inside the crack flank of C. (E-F) Chromite $(\text{Fe,Cr})_3\text{O}_4$ and (G-H) Magnetite $(\text{Fe,Ni})_3\text{O}_4$ CDF-TEM and corresponding DPs relating to C.	147
5.11	TTO-1-053 (390 MPa) L05 (A) BF-TEM overview of a typical intergranular IASCC crack extending into the bulk. (B,C) BF-TEM deformation structures identified as deformation band and twin bands, respectively. (D,E) Corresponding CDF-TEM and DP of the deformation twin bands, respectively.	148
5.12	TTO-1-001 (690 MPa) L16 (A) Magnified BF-TEM overview of a broad IASCC crack. (B) BF-TEM of (111) orientated deformation twins extending from the crack tip. Corresponding CDF-TEM of (C) parent austenite and (D) deformation twin.	149
5.13	TTO-1-090 (700 MPa - Non-native oxide) L06 (A) BF-TEM overview of tapered IASCC crack. (B) Magnified BF-TEM of (111) orientated deformation twins extending from the crack tip. Corresponding CDF-TEM with inset DPs shown for (C) the parent austenite and (D) the deformation twin structures.	150
5.14	TTO-1-090 (700 MPa - non-native oxide) L01 (A) BF-TEM, and (B) CDF-TEM of twinned microstructure ahead of an IASCC crack tip. (C) BF-TEM of double twin-systems leading to grain boundary migration. (D) Corresponding twin-related DP.	151
5.15	TTO-1-066 (280 MPa - cyclic loading) L09 (A) BF-TEM overview of twinned microstructure in the crack's vicinity. (B) BF-TEM and (C,D) CDF-TEM of the austenitic and twinned microstructure, respectively. (E) Grain boundary migration. (F) BF-TEM of twins and (G) its corresponding DP.	152

5.16	TTO-1-053 (390 MPa) L06 (A) BF-TEM overview of the microstructure alongside a crack. (B) CDF-TEM of microstructural twins extending from the crack flanks. (C) Corresponding DP of twinned structure. (D) Magnified BF-TEM of stress-induced martensitic laths. (E) CDF-TEM of laths extending from the crack tip. (F) Corresponding martensitic DP illustrating the BCC nature of the stress-induced α' -martensite from a $[011]$ zone-axis.	153
5.17	TTO-1-053 (390 MPa) L05 (A) BF-TEM and (B) corresponding CDF-TEM of martensitic laths extending across the grain close to the crack initiation. (C) Corresponding DP of the martensitic laths. (D) Analyzed DP matching the Nishiyama-Wasserman orientation relationship between FCC γ - austenite and BCC α' -martensite. This figure corresponds to the top-left grain beside the crack displayed in Fig. 5.11.	154
5.18	TTO-1-053 (390 MPa) L05 (A) BF-TEM and (B,C) corresponding CDF-TEM with associated DP of α' -martensite extending from the leading grain boundary in $[\bar{1}11]\alpha'$ zone-axis orientation. (D,E) Retained γ -austenite located at martensite interfaces with associated DP. (F) Analyzed DP matching the Kurdjumov-Sachs orientation relationship between FCC γ - austenite and BCC α' -martensite. This figure depicts the leading grain boundary imaged in Fig. 5.11.	155
5.19	TTO-1-066 (280 MPa - cyclic loading) L08 (A) BF-TEM of ϵ -martensite laths extending from the crack flanks into the bulk interior. Deeper into the bulk, phase transformation of austenite to martensite is observed in accordance to Olsen-Cohen's model [86] from a (B) BF-TEM, and (C-E) CDF-TEM γ -austenite, ϵ -martensite and α' -martensite perspective. The overall DP is illustrated and indexed in (F).	156
5.20	TTO-1-053 (390 MPa) L03 (A) BF-TEM imaged IASCC intergranular crack propagating along an oxidized grain boundary. (B) Corresponding CDF-TEM from an inner oxide reflection. (C) BF-TEM crack tip extending from the triple junction illustrating the presence of deformation twinning at the crack tip. (D) Corresponding CDF-TEM illustrating the extent of intergranular oxide penetration in front of the crack tip. (E) BF-TEM underfocus Fresnel contrast image of the same crack tip from edge-on orientation. (F) HR-TEM of the oxide near the crack tip seen in C, with a reduced FFT diffractogram as an inset matching the largest d-spacings of the chromite.	157
5.21	TTO-1-053 (390 MPa) L08 (A) BF-TEM and (B) corresponding CDF-TEM of the integral chromite oxide, of an IASCC crack tip propagating along an oxidized grain boundary.	158
5.22	TTO-1-066 (280 MPa - cyclic loading) L09 (A) BF-TEM overview of grain boundary cracking whereat the oxide intrusion is seen to penetrate the leading grain boundary in front of the propagating crack tip. (B) BF-TEM underfocus Fresnel contrast image illustrating apparent fracture bands within the intergranular oxide. (C) BF-TEM of oxidized crack tip. (D) Corresponding HR-TEM of the crack tip. Inset FFT diffractogram illustrates the 111_γ austenite planes, while the oxidized tip remained amorphous. . . .	159
5.23	BF-TEM of the oxidation in front of several crack tips corresponding to (A) TTO-1-053 (390 MPa) L03, (B) TTO-1-071 (500 MPa) L07, (C,F) TTO-1-001 (690 MPa) L16 and L23, (D) (A) TTO-1-090 (700 MPa - non-native oxide) L08, and (E) TTO-1-066 (280 MPa - cyclic loading) L07.	160
5.24	TTO-1-053 (390 MPa) L08 HAADF-STEM EDS chemical mapping of a selected IASCC crack tip.	162
5.25	TTO-1-053 (390 MPa) L08 HAADF-STEM EDS chemical mapping of enriched and depleted elements closer to a selected IASCC crack tip.	163

5.26	TTO-1-090 (700 MPa - non-native oxide) L01 HAADF-STEM EDS chemical mapping of enriched and depleted elements close to a selected IASCC crack tip. Regions of high to low STEM intensities are indicated by the color scheme varying from white to black, respectively.	164
5.27	TTO-1-090 (700 MPa - non-native oxide) L01 HAADF-STEM EDS line scan along the IASCC crack tip (A) propagation direction and (B) opening direction illustrated in Fig. 5.26A.	165
5.28	HAADF-STEM EDS line scans of edge-on unimpaired grain boundaries appertaining to specimens (A) TTO-1-053 (390 MPa) L08 and (B) TTO-1-090 (700 MPa) L01. . .	165
5.29	TTO-1-053 (390 MPa) L01 (A) BF-TEM of an intergranular IASCC crack arrested at a (B) EDS-confirmed MnS inclusion particle in close vicinity to the grain boundary. (C) BF-TEM of the crack tip illustrating a heavy deformation field in close vicinity to the particle. (D) CDF-TEM displaying the intergranular oxide deflection away from the grain boundary towards the inclusion particle.	167
5.30	TTO-1-090 (700 MPa - non-native oxide) L01 (A) BF-TEM overview of IASCC leading grain boundary. (B-C) CDF-TEM of adjacent grain boundary structures. (D) CDF-TEM of intergranular inclusion particles. Inset shows a CDF-TEM from a CT oxidation reflection, illustrating oxide intrusion up to the inclusion particle. (E) Magnified BF-TEM of intergranular inclusions. (F) Corresponding DP.	168
5.31	TTO-1-090 (700 MPa - non-native oxide) L01 (A) BF-TEM image of, and (B) STEM-HAADF line scan across, the intergranular inclusion particle. (C) HR-TEM and (D) reduced FFT of C of the inclusion particle.	169
5.32	TTO-1-053 L03 (A) BF-TEM of an intergranular crack propagating in cleavage mode in relation to the tensile stress direction. (B) CDF-TEM of oxidized grain boundary triple junction. (C-D) CDF-TEM of the opposing grains.	170
5.33	TTO-1-001 (690 MPa) L20 (A) BF-TEM and (B) corresponding CDF-TEM of inner oxide reflection along oxidized outer surface. (C) Magnified BF-TEM with (D) corresponding CDF-TEM of oxidized crack tip arrested at microstructural interface.	171
5.34	TTO-1-001 (690 MPa) L23 (A) BF-TEM and (B) corresponding oxide reflection CDF-TEM of the overview of a typical IASCC crack. (C-D) CDF-TEM and corresponding oxide DP of the crack flank oxide. (E-F) CDF-TEM and corresponding DP of adjacent metallic phase aside of the crack. (G-H) BF-TEM and corresponding oxide CDF-TEM of preferential oxidation along deformation bands.	172
5.35	Mean intergranular oxidation lengths with corresponding standard errors on the oxide intrusions measurements, normalized to the specimen with the lowest macroscopic stress, for crack tips extracted from O-rings tested under increased stress conditions. .	177
5.36	(A) Overview of the TTFs of the constant load native, non-native, and cyclic loaded O-ring data in terms of stress [294]. Model analysis of data is performed through equation 2.37, statistically optimized to match the most ideal SCC corrosion susceptibility parameter n . (B) Adjusted stress interpretation of the non-native oxide and cyclic loaded O-ring failures on the account of possible crack initiation from the O-ring's inner surface and peak stress intensity values, respectively.	179
5.37	Time-to-failure data of constant vs. non-native oxide O-ring data in evaluation of the oxide strength volume-effect. Model curves and corresponding 90% coincidence intervals are drawn to both native and non-native oxide specimens relating to equation 2.37, optimized to match the most ideal SCC corrosion susceptibility parameter n . . .	183

Acronyms

ADF	<i>Annular DF</i>	DP	<i>Diffraction pattern</i>
ASTM	<i>American society for testing and materials</i>	DPA	<i>Displacements-per-atom</i>
BCC	<i>Body-centered cubic</i>	DSA	<i>Dynamic strain ageing</i>
BCT	<i>Body-centered tetragonal</i>	EBS	<i>Electron backscatter diffraction</i>
BD	<i>Black dot</i>	ECP	<i>Electrochemical potential</i>
BF	<i>Bright-field</i>	ED(S/X)	<i>Electron-dispersive X-ray spectroscopy</i>
BFB	<i>Baffle-former bolt</i>	FAC	<i>Flow-assisted corrosion</i>
BFP	<i>Back-focal plane</i>	FCC	<i>Face-centered cubic</i>
BSE	<i>Backscattered electron</i>	FEG	<i>Field-emission gun</i>
BWR	<i>Boiling-water reactor</i>	FEM	<i>Finite-element analysis</i>
C(A)DF	<i>Centralized (aperture) DF</i>	FFT	<i>Fast-fourier transform</i>
CAD	<i>Crack angle distribution</i>	FIB	<i>Focused-ion beam</i>
CCD	<i>Charged-coupled device</i>	FIC	<i>Film-induced cleavage</i>
CCG	<i>Climb-controlled glide</i>	FRM	<i>Film-rupture model</i>
CERT	<i>Constant elongation rate tensile</i>	GIS	<i>Gas injection system</i>
CEFM	<i>Coupled Environmental Fracture Model</i>	HAADF	<i>High-angle annular DF</i>
CGR	<i>Crack growth rate</i>	HAB	<i>High-angle grain boundary</i>
CLD	<i>Crack length distribution</i>	HAC	<i>Hydrogen-assisted cracking</i>
CSL(B)	<i>Coincident site lattice (boundaries)</i>	HCF	<i>High-cycle fatigue</i>
CW	<i>Cold-work(ed)</i>	HCP	<i>Hexagonally-close packed</i>
D1-4	<i>NPP reactors Doel 1 through 4</i>	HE	<i>Hydrogen embrittlement</i>
D(A)DF	<i>Displaced (aperture) DF</i>	HELP	<i>Hydrogen-enhanced localized plasticity</i>
DIGM	<i>Diffusion-induced grain boundary migration</i>	HR-TEM	<i>High resolution TEM</i>
DF	<i>Dark-field</i>	(IA)SCC	<i>(Irradiation-assisted) Stress corrosion cracking</i>

IC	<i>Irradiation creep</i>	RPV	<i>Reactor pressure vessel</i>
IGSCC	<i>Intergranular SCC</i>	SADP	<i>Selected area diffraction pattern</i>
IL	<i>Intermediate lens</i>	SAED	<i>Selected area electron diffraction</i>
IO	<i>Internal oxidation</i>	SAGBO	<i>Stress-assisted grain boundary oxidation</i>
IPCC	<i>International panel of climate change</i>	SCP	<i>Subcritical crack propagation</i>
LCF	<i>Low-cycle fatigue</i>	SE	<i>Secondary electron</i>
LCOE	<i>Levelized costs of electricity</i>	SEM	<i>Secondary electron microscop(e/y)</i>
LOCA	<i>Loss of coolant accident</i>	SFE	<i>Stacking fault energy</i>
LMIS	<i>Liquid-metal ion source</i>	SFT	<i>Stacking fault tetrahedron</i>
LTE	<i>Lifetime extension</i>	SIA	<i>Self-interstitial atom</i>
LTO	<i>Lifetime operation</i>	SIPA	<i>Stress-induced preferential absorption</i>
LWR	<i>Light water reactor</i>	SMR	<i>Small modular reactor</i>
NPP	<i>Nuclear power plant</i>	SPECT	<i>Single-photon emission computerized tomography</i>
OL	<i>Objective lens</i>	SS	<i>Stainless steel</i>
OS	<i>Outer surface</i>	(S)TEM	<i>(Scanning) Transmission Electron Microscop(e/y)</i>
PB	<i>Pilling-Bedworth</i>	T1-3	<i>NPP reactors Tihange 1 through 3</i>
PET	<i>Positron emission tomography</i>	TGSCC	<i>Transgranular SCC</i>
PFS	<i>Primary fracture surface</i>	TTF	<i>Time-to-failure</i>
PL	<i>Projector lens</i>	TTO	<i>Thimble tube O-ring</i>
PV	<i>Photovoltaic</i>	UNFCC	<i>United Nations Framework Convention on Climate Change</i>
PWR	<i>Pressurized-water reactor</i>	XRD	<i>X-ray powder diffraction</i>
RE	<i>Radiation embrittlement</i>		
RH	<i>Radiation hardening</i>		
RIS	<i>Radiation-induced segregation</i>		

Table of contents

Acknowledgments	vii
English abstract	ix
Dutch abstract	xv
List of publications	xix
List of figures	xx
Acronyms	xxix
1 Introduction	1
1.1 Climate change	1
1.1.1 European Commission's Green Deal	1
1.2 The role of nuclear industry	2
1.2.1 Nuclear policy in Belgium	3
1.2.2 Cost and benefits of nuclear power	5
1.2.3 NPP designs	7
1.2.4 Pressurized-water reactors	8
1.3 Material challenges in PWRs	9
1.3.1 Material degradation after LTE	9
1.3.2 IASCC cracking of baffle bolts	10
1.4 Thesis structure and objectives	12
2 Irradiation-assisted stress corrosion cracking	17
2.1 Introduction	17
2.1.1 Characteristics of (IA)SCC	17
2.2 Stainless steels	18
2.2.1 Crystal structure	19
2.2.2 Lattice structure and defects	20
2.2.3 Deformation behavior	24
2.2.3.1 Strain-hardening	25
2.2.3.2 Deformation twinning	25
2.2.3.3 Martensite transformation	27
2.2.4 Oxidation kinetics	28
2.3 Irradiation of stainless steels	30
2.3.1 Microstructural alterations	32
2.3.1.1 Radiation-induced microstructural defects	32
2.3.2 Microchemical alterations	34
2.3.2.1 Radiation-induced segregation	35

2.3.2.2	Phase precipitation	38
2.3.2.3	Transmutation reactions	38
2.3.3	Metallurgical effects	39
2.3.3.1	Radiation hardening and embrittlement	39
2.3.3.2	Localized deformation in irradiated steels	40
2.3.3.3	Irradiation Creep	41
2.4	(IA)SCC crack development	42
2.4.1	Stress intensity factor	42
2.4.2	Crack growth stages	44
2.4.3	Additional factors affecting crack growth rate	45
2.4.3.1	Stress	45
2.4.3.2	Cold-work	45
2.4.3.3	Dynamic loading	46
2.4.3.4	Corrosion potential	47
2.4.3.5	Passivation layer	49
2.5	(IA)SCC mechanisms	51
2.5.1	Film-induced cleavage	52
2.5.2	Film-rupture or slip-dissolution model	54
2.5.3	Internal oxidation	57
2.5.3.1	Subcritical crack propagation model	59
2.5.3.2	Stress-assisted grain boundary oxidation model	64
2.5.3.3	The local model	66
2.5.4	Hydrogen-assisted cracking degradation	67
2.6	Synthesis: (IA)SCC	69
3	Experimental Methods	71
3.1	Scanning Electron Microscopy	72
3.2	Focused-ion beam analysis	74
3.2.1	FIB-SEM instrument	74
3.2.2	Operational Techniques	75
3.2.2.1	TEM-lamella preparation	76
3.2.2.2	Low-voltage electron contrast imaging	78
3.3	Transmission electron microscopy (TEM)	79
3.3.1	TEM instrument	80
3.3.2	Electron diffraction in TEM	82
3.3.2.1	Bragg's Law	82
3.3.3	Operational techniques	83
3.3.3.1	Selected area electron diffraction (SAED)	84
3.3.3.2	Bright-(BF) and dark-field (DF) imaging	84
3.3.3.3	Ring-diffraction characterization	85
3.3.3.4	Energy dispersive X-ray Spectroscopy	88
3.3.3.5	Phase contrast and High-resolution TEM (HR-TEM)	90
3.4	Scanning TEM (STEM)	91
3.4.1	STEM Image formation	91
3.4.2	High-angle annular dark field (HAADF)	92
3.5	Material investigation	93
3.5.1	High Si SS tapered specimens	94
3.5.1.1	Tapered specimens and CERT-testing	94
3.5.1.2	Crack detection algorithm	96
3.5.2	Flux thimble tube	99

3.5.2.1	Constant load compression testing	99
3.5.2.2	Sample preparation for microstructural analysis	101
3.6	Synthesis: Experimental Techniques	102
4	Tapered Specimens	105
4.1	SEM investigation	105
4.1.1	CERT load-elongation curves	105
4.1.2	Main fracture surface investigation	108
4.1.3	EDS-spectra	109
4.1.4	SCC crack detection	111
4.1.5	Crack density distributions	112
4.1.6	Finite-element analysis	113
4.1.7	Critical stress threshold	115
4.2	FIB analysis	118
4.2.1	SCC crack extraction	118
4.2.2	Grain contrast imaging	119
4.3	TEM investigation	120
4.3.1	Low-magnification imaging	120
4.3.2	SCC crack tips	121
4.3.3	Crack tip oxidation	123
4.3.4	STEM-HAADF analysis	127
4.3.5	Transgranular SCC mechanism	129
5	Thimble Tube O-ring Specimens	135
5.1	Prior SEM investigations	137
5.1.1	O-ring crack initiation studies	137
5.1.1.1	TTO-1-053	137
5.1.1.2	TTO-1-001	139
5.1.1.3	Primary fracture surface analyses	139
5.2	FIB analysis	140
5.2.1	IASCC crack extraction	140
5.3	TEM investigation	142
5.3.1	Intergranular oxidation	143
5.3.1.1	Overview of grain boundary cracking	143
5.3.1.2	Native oxide characterization	145
5.3.1.3	Non-native oxide characterization	146
5.3.2	Microstructural characterization	148
5.3.2.1	Crack deformation field	148
5.3.2.2	LCF-induced deformation field	152
5.3.2.3	Martensite transformation	152
5.3.3	Crack tip characterization	156
5.3.3.1	SAED investigations of several IASCC tips	156
5.3.3.2	Oxide intrusions comparison	159
5.3.4	STEM-HAADF analysis	161
5.3.4.1	Crack tip mapping	162
5.3.4.2	RIS at unimpaired grain boundaries	165
5.3.5	Interesting cases surrounding IASCC cracking	166
5.3.5.1	MnS inclusion particles	166
5.3.5.2	Intergranular inclusion particles	167
5.3.5.3	Tensile stress direction	169

	5.3.5.4 Preferential oxidation	170
5.4	Discussion	173
	5.4.1 On the effect of applied external stress	173
	5.4.1.1 Deformation twinning	173
	5.4.1.2 Martensite transformation	174
	5.4.2 Stress-assisted oxidation at the crack tip	176
	5.4.3 In broader perspective with the literature	178
	5.4.4 Mechanical failure data	180
	5.4.4.1 On the effect of oxide abrasion	180
	5.4.4.2 On the effect of cyclic loading	182
	5.4.5 Microchemical investigations	184
	5.4.5.1 Regarding the role of RIS	184
	5.4.5.2 Regarding the role of MnS inclusions	185
	5.4.5.3 Regarding the role of intergranular inclusions	186
	5.4.6 IASCC cracking mechanisms	187
6	Conclusions	189
6.1	Research outcomes	190
	6.1.1 Tapered specimens	190
	6.1.2 Thimble tube O-rings	192
6.2	Future outlook	196
	6.2.1 IASCC-resistant alloys	198
	Bibliography	200

Chapter 1

Introduction

1.1 Climate change

Comprehensive studies regarding climate change all indicate towards the trend of global warming as a result of human activity since the industrial age mid twentieth century. As of November 2021, in association with the United Nations Framework Convention on Climate Change (UNFCCC), the Paris Agreement was signed by 195¹ (including the European Union (EU)) UNFCCC member states to pledge all common national efforts into undertaking the impact of climate change, adapting to its aftermath, and assisting developing countries in doing the same. Consistent with the agreed upon pledges on greenhouse gas emissions, all member states vow to take measures for global warming not to increase beyond 1.5 °C above pre-industrial levels. The consequences of such average temperature increases have been assessed in a special report of the Intergovernmental Panel on Climate Change (IPCC) for both 1.5 °C, and an upper limit of 2 °C [1]. Regional climate change impacts may include higher mean temperatures, temperature extremes, increased mean precipitation followed by consecutive periods of drought (especially in the Northern hemisphere), flooding, sea level rises, specific species extinctions, and an increase in tropical storms and cyclones. The consequences and aggregated impacts as a result of reducing the warming only up to 1.5 °C are severely lessened when compared to the more drastic impact of a 2 °C scenario. Avoided impacts and reduced risks in a less than 2 °C temperature increase, include regional economic benefits, decreased climate change hotspots, and specifically, the reduced endangerment of threatened systems such as less adaptive species and ecosystems. It was reported that anthropic induced warming likely transcended the 1 °C threshold by the end of 2017, with a steady increase of 0.2 °C with each passing decade. Increased measures in accordance with the Paris Agreement would require a net zero CO₂ emission cycle, and a global reduction in non-CO₂ forcings such as methane, by around 2050.

1.1.1 European Commission's Green Deal

To address the extensive impacts of climate change, several transformative pathways were outlined with the aim to prevent, or limit, an overshoot of a 1.5 °C. A reduction in energy demand, accompanied

¹ Technically 194 member states for a only a few months, after the withdrawal of the United States from the accord on the 4th of November 2020. Fortunately, within hours of president Biden's presidency, the United States formerly rejoined the initiative on February 19th, 2020.

with the undertaking of carbon capture and storage, plus measures taken on agricultural, housing and transport sectors, have all been revolutionary on that front. However, such commitments require the decarbonization of the contemporary energy market and transport sector. Consequently, a lot of attention has been drawn to renewable energy sources such as photovoltaics, wind and hydroelectric power, in addition to the new and improved forms of energy storage. Emission-free energy sources have become strong contenders in the past decades thanks to continuous innovation and extensive investments. Solar photovoltaics and on- or offshore wind power have become cost-competitive with respect to fossil fuel counterparts, with respective levelized costs of electricity (LCOE) in Europe of 85 \$/MWh (solar PV), 90 \$/MWh (on- and offshore wind) and 120-145 \$/MWh for fossil fuel power (natural gas and supercritical coal) [2]. The LCOE is a measure that accommodates for the net sum of lifetime costs to the sum of electrical power generation for a specific power source in that lifetime. Recent developments in renewable energy technology indicate that these costs have been in steady decline for the past decade, which sparks further interest especially in the private sector. For good reasons namely, because of the recent investments, beneficial and sustainable cost structures, economic development and manufacturing jobs and so on. However, the unreliability of weather patterns and the fact that its technology is still in its infancy in terms of deployment and innovation, make it so that renewables are still facing challenges which are yet to be overcome. Additionally, renewable energy sources are greatly dependent on geographical locations that generally require a large land area in order to become cost-effective.

To reach the intermediate climate goals by 2030 and ultimate climate-neutrality around 2050, the European Commission has declared both nuclear and gas-fired power plants to be considered as sustainable bridging technologies² towards a fully renewable energy mix. Specifically in times when the global energy demand rises significantly, the EU's regulation supports the retention of nuclear and gas-fired power plants as a backstop until renewables become indispensable to the energy-mix. Notably, this decision relies on the condition that gas-fired power plants switch to low-carbon or renewable gases (such as biomass or hydrogen produced gas) short of 2035, and that nuclear power plants have a detailed plan in place to securely dispose of its radioactive waste by 2050. While so far no permanent disposal sites have gone into operation, all nuclear-invested countries have considered their options for nuclear waste storage. In the interest of Belgium³, potential geological disposal sites for nuclear waste are primarily considered within Boom and Ypresian clay deposits [3]. Among the various benefits for waste storage within deep clay layers, primarily the impermeability of clay to water is considered to prevent the worst-case scenario of radiation leakage to ground water.

1.2 The role of nuclear industry

Nevertheless, the fact that both nuclear- and gas-powered energy plants are considered sustainable by the EU commission's regulatory taxonomy act leaves room for all EU member states to choose their own energy mix for the coming decades. While some nations consider, or reinvest into existing, nuclear facilities, other member states are strongly opposed and prefer to opt for fossil gas-fired powered

² As of February 2nd 2022, issued in the EU Taxonomy Complementary Climate Delegation Act covering certain nuclear and gas activities: https://ec.europa.eu/commission/presscorner/detail/en/qanda_22_712.

³ The legislature committed the management of radioactive waste in Belgium, is the Agency for Radioactive Waste and Enriched Fissile Materials, abbreviated as NIRAS/ONDRAF. Contemporary research and development programs in the field of long-term nuclear waste management in close collaboration with the Belgian Nuclear Research Centre (SCKCEN), have lead to the construction of a dedicated underground demonstration facility within the Boom clay in Mol. NIRAS/ONDRAF drafted a complete nuclear waste plan in accordance to all available research in line with legislative frameworks, which is currently available for governmental policy decisions [4].

plants instead. Leading parties on both fronts include France, which due to its 56 NPP reactors is heavily invested in nuclear altogether, while in the aftermath of the Fukushima Daiichi accident, Germany decided on a complete nuclear phase-out to pursue a path of high-carbon polluting power until renewables may fill the gap on a later date. The collective weight of energy stakeholders and the considerations of national political parties are important factors to consider within this controversy. Still, it is apparent how several countries, including the Netherlands, Finland, Estonia, the Czech Republic, Bulgaria, Romania and Poland have announced plans to (re-)invest into nuclear technology⁴. Most interests are specifically related to development of small modular reactors (SMRs) projects and technologies. This is mostly due to SMR's flexible ability to adapt real-time to the required energy needs, so that they may nicely adopt within the nation's current energy mix. Despite this, a third category of member state competitors are those front-running nations that are already further along in the race of towards renewable energy. Such member states include the Nordic/Scandinavian countries (Norway, Sweden, Finland, Denmark and Iceland), which have met their 2020 renewable targets already two years before the deadline. Their renewable energy is strongly reliant on hydro-electric and wind, supported by biomass power, to support a sustainable long term energy mix for the future. To this end, these Nordic countries may serve as lead figureheads in adopting their resources and geographical locations for the sake of renewables.

1.2.1 Nuclear policy in Belgium

In comparison to most other EU member states, Belgium on the other hand remained largely undecided for the past quadranscentennial on whether a complete (plan A) or partial (plan B) nuclear phase-out was in order. Dating back from July 1999, Belgium's plan A complete nuclear phase-out legislation was passed under the direction of Verhofstadt I, consisting of the Liberal (VLD & MR), Socialist (SP.A & PS) and Green (Groen! & Ecolo) parties. On January 2003, Verhofstadt II without the green parties, delineated the terms of the nuclear phase-out, issuing the closure of all nuclear reactors (Doel(D) 1-4, Tihange(T) 1-3) after a lifetime of 40 years and banning the construction of any new reactors altogether. This policy decision would mean a gradual nuclear phase-out, starting with D1-2 and T1 in 2015, D3 and T2 respectively in 2022 and 2023, and ultimately closing D4 and T3 in 2025. However, according to an analysis report issued by the Federal Planning Bureau in 2005 [6], replacement of Belgium's nuclear capacity for the sake of renewables (which constituted of a few mere percentages of the total energy mix) would be deemed impossible in such short time-frame. Additionally, in 2007 the Belgian Commission of Energy stated that⁵: (i) the use of nuclear energy is required to achieve CO₂ standards issued by the Kyoto Protocol in order to maintaining economic stability, (ii) if nuclear were not employed, energy prices would be estimated to rise significantly, and (iii) the lifespan of all seven nuclear power reactors is proposed to be extended. In a study issued by Belgium's federal minister for Climate and Energy at the time, Maignette (PS), the GEMIX group recommended a ten-year lifetime extension (LTE) for the three oldest NPP reactors (D1-2, T1) until 2025, and another 20 years for all others (D3-4, T2-3). Therefore, as of October 2009, Van Rompuy I consisting of the Liberals (Open VLD & MR), Christian Democrats (CD&V and cdH) and Socialists (PS), extended the life-time of operation, achieving an accord with operator GDF Suez (former ENGIE as of 2015, which previously merged with its subsidiary Electrabel) with an added annual nuclear tax for the privilege of continued operation. In deciding to postpone to nuclear phase-out, Belgium aligned its views with other EU member states at the time. Sweden's government overturned previous regulations for the construction

⁴ Although not bound anymore to EU's regulations, the United Kingdom additionally joins the nuclear front in supporting the development of its new Sizewell C NPP.

⁵ As analyzed in a study issued by the Commission for Electricity and Gas Regulation (CREG) [5]: <https://www.creg.be/nl/publicaties/studie-over-het-voorlopige-rapport-van-de-commissie-energie-2030-met-als-titel-belgiums>.

of a new NPP, while Italy effectively plans new operations for a reactor, ending its previously motivated phase-out.

However, turning over the previous turn-overs, energy secretary of state Whatelet (cd&H) under the federal government of Di Rupo I, announced in June 2012 to close D1-2 in 2015 recanting the previous agreement with GDF Suez despite the favorable ruling of the FANC⁶ for the agreed ten-years extension. After firm debate amongst stakeholders with state regulations, government Michel I announced in 2014 to revert this legislation and align the phase-out of D1-2 again with other NPPs to the final deadline of 2025⁷. Interestingly, it was during this period that D3 and T2 were shut down twice due to concerns about hydrogen flakes and its consequence on the structural integrity of the reactor pressure vessel. Additionally, D4 remained temporarily unavailable due to the leaking of lubricant oil from the turbine generator, which was later deemed as intentional sabotage that remains unsolved as of today. Still, in a final evaluation report [7], D3 and T2 were approved for restart in May 2013 by the FANC, after immediately being shut down in 2014 again due to maintenance outages. In a consecutive report [8] based on preliminary microstructural analyses and assessments, the FANC concluded that the impact of these flakes had an "acceptable impact on the serviceability of Doel 3 and Tihange 2" and thus approved the restart of operations in November 2015. Due to these subsequent outages of both units, the possibility of blackouts were not implausible during the winter months of 2014–2015 as indicated by the considerable loss of overall electricity production in Belgium, see Fig. 1.1. Given the near constant shares of renewables and gas-fired powered plants, it can be concluded that the volatility in Belgium's electricity production at the time was directly related to the total share of nuclear-generated electricity. This is also evident by the near-equal increase in electricity production in the subsequent year 2016 when comparing the nuclear share versus the total gross electricity production.

In accordance to the final agreed upon deadlines of the NPPs as of 2015 (D3 in 2022, T2 in 2023, and D1-2,4 and T1,3 in 2025), PricewaterhouseCoopers (PwC) Enterprise Advisory Belgium published in October 2016 a technical analysis report outlining the feasibility of Belgium's 2050 climate goals without the contribution from nuclear energy after the phase-out of 2025 [9]. In this report, PwC states that the (i) energy mix between renewables with nuclear not only offers the best combination to meet the national energy requirement, but also offers the best pathway to competitive and low-carbon energy. Furthermore, it explicitly states that (ii) in the absence of Belgium's nuclear capacity, more expensive options and foreign import of energy should be considered. Ultimately, the final conclusion states that (iii) nuclear power does not oppose renewable technology, as is claimed in the policies of the Green party (Groen). Consequently, in November 2017, technology federation Agoria and two other Belgian business associations issued that a complete nuclear phase out (plan A) as planned in 2025 was not affordable; therefore requesting a partial closure of only the oldest NPPs instead⁸.

As of February 16th 2022⁹, the employers' federations VBO, VoKa, UWE and Beci issued a joint statement in an open letter to Belgian's federal government, referring to the technical report outlined by the Federal Agency for Nuclear Control (FANC), to reconvene again on the decision of a complete nuclear phase-out. In the joint statement, all employer federations collectively opt for Belgium's so-

⁶ FANC's favourable ruling of Doel 1 and 2, given required reinvestments: https://www.standaard.be/cnt/dmf20140917_01272747.

⁷ LTE of Doel 1 and 2 for another ten years, up to 2025: https://www.standaard.be/cnt/dmf20141218_01436041.

⁸ Agoria, essenscia and Febeliec's request for a partial phase-out in 2025: <https://www.agoria.be/nl/marktontwikkeling/internationaal/energy-technology-club/sluit-niet-alle-kerncentrales-in-2025>.

⁹ Joint statement from VBO, VoKa, UWE and Beci: <https://www.vrt.be/vrtnws/nl/2022/02/16/werkgeversorganisaties-uitstel-kernuitstap/>.

called plan B option: defining the course of a partial closure of the oldest nuclear power plants, leaving D4 and T3 in operation, supported by the operation of several gas-fired power plants. Defining a plan B course of action would additionally limit Belgium's ties to the international gas prices, which at the time of a reviving post-pandemic economy and the aggressive geopolitical expansion policies of Russia (especially after its invasion of Ukraine, February 24th 2022) remain increasingly high. The FANC issued in their statement that a long-term extension of both NPPs remains feasible under the assumption that: (i) the required regulatory adjustments and (ii) safety improvements are met, in addition to (iii) a clear policy decision from the federal government is taken in the first trimester of 2022 (that is, before March 18th), and that (iv) ENGIE Electrabel, operator of the Doel and Tihange NPP sites, decides from own company policies to continue investing in Belgium's NPP installations. Though, in a previous statement dating back towards September 2020, ENGIE Electrabel readily stated that the actions outlined in a plan B model do not correspond to their corporate vision, given the uncertainty and the indecisiveness of the Belgian government. If the government decides to pursue a definite plan B course of action, immediate discussions on policies and conditions should be summarized before ENGIE Electrabel can conduct its own risk-benefit analysis.

Coming closer to recent events, the highly controversial decision on the role of nuclear power in Belgium was pushed back to March 18th, 2022. In this ruling, minister of energy Van Der Straeten of the federal government De Croo I received the political mandate to engage in discussions with ENGIE on the prolongation of D4 and T3. The federal government issued three principal red lines, namely that (i) only 2 GW's of the Belgian nuclear power capacity may be extended in a coming period of ten years (i.e., no other NPP apart from D4 and T3), (ii) no nationalization of the NPPs is of the order, and (iii) the federal government will not be held responsible for any additional costs (that is, costs associated with the storing of the produced nuclear waste over the extended lifetime or from the decommissioning of the NPPs in question). These negotiations led to a disputed principal-agreement on July 22nd wherein which the latter two deal breakers are overturned. At present, D4 and T3 are scheduled to become operational again in 2026; that is one year overdue, past their prior closure date in 2025. Additional costs associated with the production of nuclear waste during their extended lifetime are shared amongst the federal government and ENGIE group. What concerns the decommissioning of the NPPs, it is agreed that any expenses above a yet to be determined maximum cost attributed to ENGIE, are also ascribed to the federal government. A final agreement is in the making, scheduled to be signed by the European Commission at the end of 2022.

1.2.2 Cost and benefits of nuclear power

There are great many things to be said about nuclear and its place in the global energy industry. As explained above, nuclear remains among the most controversial topics for politicians and governments, not only in Belgium but also across the world. Still, advocates rightfully claim that the nuclear industry is a nearly carbon emission free source of energy¹⁰, with a very efficient throughput of resources, able to produce electricity in a much more inexpensive manner than any other fuel source currently available. In this way, nuclear-generated electricity is among the most responsible sources of energy, able to combat climate change and limit the emissions of greenhouse polluting gasses. Furthermore, as displayed in Fig. 1.1, the nuclear share in Belgium's gross electricity production remained significant for the past decade. In fact, from the updated de-rating factors declared to the

¹⁰ Of course, as one would with all forms of industry and technology, the carbon footprint of a nuclear power plant should be put into perspective over the entire lifetime of the facility. Aside from its general operation during service, this includes the build and decommissioning of the plant, the transport and storage of the radioactive waste, and also the mining and production processes of enriched uranium.

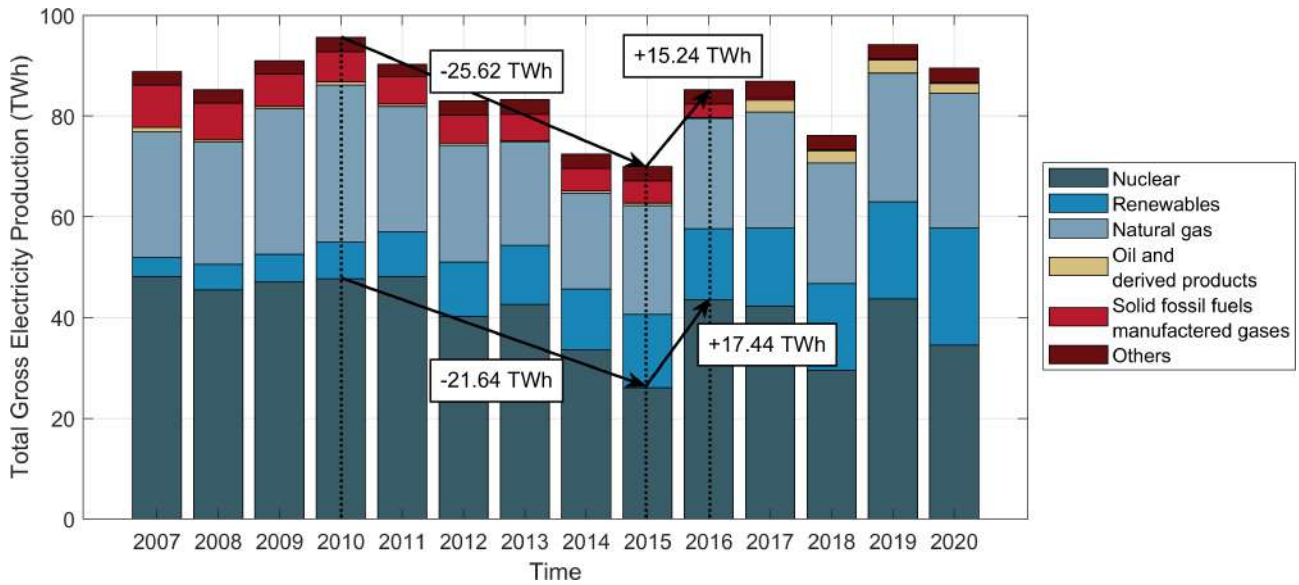


Figure 1.1: Evolution of the total gross electricity production in Belgium (TWh), from 2007 up to 2020. Redrawn from reference [10].

European Commission [11], which state the reliability and contribution of a certain technology to the security of supply during so-called simulated scarcity moments, it may be concluded that nuclear's de-rating factor is the highest to-date i.e. 96%. This statistic implies the reliability of nuclear is higher than a full capacity of gas-fired power plant alternatives, which would constitute to a plan A phase-out scenario. Moreover, aside from previous benefits, nuclear fission is additionally used for the production of radio-isotopes, which are indispensable within medical applications such as medical imaging, cancer treatments and pain control¹¹. Of secondary importance is the thermal heat that is generated from this fission process, which is often regarded as a secondary by-product. Nuclear-generated heat may be used to decarbonize other resource intensive sectors, such as local housing districts and local industry sectors. Finally, during its construction, operation and dismantling of NPPs, the nuclear sector offers quality jobs contributing to the regional and national economy.

Antagonists on the other hand point towards the high upfront and end-of-life costs of nuclear power plants, the indisputable challenge of radioactive waste, the non-renewability aspect of its fuel source, and the well-known accidents such as Chernobyl (Ukrainian SSR, 1986) and Fukushima Daiichi (Japan, 2011) in the past. Additionally, uranium enrichment and spent-fuel reprocessing have led to the fear of nuclear proliferation, a well-known issue that motivated the Iraq crisis in 2003 and the Iran Proliferation Deal in 2013. Of secondary importance might be the dependency on uranium-producing countries of which, given the recent geopolitical tensions, Russia and post-Soviet Kazakhstan are major contenders. But above all, in relation to the subject of this thesis, nuclear antagonists indicate towards the concerning material degradation issues that are related to NPPs. As previously discussed, the unplanned maintenance outages caused by potential loss of structural integrity due to hydrogen flaking was a worrying safety problem. In relation to this issue, Fig. 1.1 may illustrate Belgium's reliance on nuclear power, as the energy output dropped significantly during the outages of D3 and T2 in 2014-2015. As a result, the concern on material degradation should not only be considered

¹¹ Interestingly, Belgium, through the SCKCEN, is amongst the world's top-ranked global players in the production and distribution of medical radio-isotopes. Amongst others, the relatively short-lived technetium-99m isotope is used for PET/SPECT imaging in cardiology and oncology applications.

as a safety issue, but a significant economic issue as well. In a statement from ENGIE's subsidiary Electrabel, operator of the Doel and Tihange plants, the impact of the outage of these two units on the net recurring income of the ENGIE group was estimated to be around 40 million euro's per month¹².

1.2.3 NPP designs

In a breakdown of four illustrative pathways for future development (P1-P4), the 2018 IPCC report [12] illustrates that, in order to limit global warming to 1.5°C by 2100, all four pathways involve a drastic increase in nuclear power. It is estimated that a global increase between +[98 – 501]% (P3) is required between the years (2030, 2050) respectively, in order to achieve a no- or limited overshoot of the current climate goals¹³.

The increase in global nuclear capacity can be achieved either through existing nuclear technologies, or through exploring new options such as: Gen III/Gen IV nuclear reactors, SMRs, or other nuclear developments. Amongst all of the +440 worldwide NPPs [13], most reactors are of the type Gen II which are considered to be the first improvement reactors on the general proof-of concept (Gen I) reactor developed during the 1950s-1960s. Gen II reactors mostly entail pressurized-water (PWR) and boiling-water reactor (BWR) designs (aside from Russian and Canadian variants), collectively labeled as light water reactors (LWRs). These type of designs employ active safety features, both mechanically and automatically initiated. Whereas on average the world's fleet of NPP is about 20 years old, the operational life-time of these reacts averages around 40 years. Even LTEs of many currently operating NPPs up to 60 years and beyond are nowadays not uncommon. Gen III reactors entail design improvements upon the previous version which extend its lifetime beyond 60 years of operation, and mostly differ in terms of fuel efficiency, modularized constructions, and safety features. Gen IV designs would imply a system of active reactors with a fuel fabrication and a fuel reprocessing facility alongside. This overhaul would make the complete design much more fuel-efficient, without the production of long-lived radioactive waste, and without the usage of uranium or plutonium to cause concerns about proliferation. Gen IV designs prolong the usage of nuclear fuel through recycling either today's spent fuel or recycling the used stockpiles of depleted uranium from enriching plants. Another major benefit relates to the elimination of long-lived nuclear waste actinides through reprocessing them as fuel active fuel material so that they end up as short-lived fission products instead. Of the Gen IV types, the sodium fast and molten-salt reactor models have been found to show the most potential in terms of reliability and inherent safety, however any functional design is still conceptual.

From the viewpoint of most governments, there is a strong interest in smaller and simpler designed reactor units which can be ideally integrated within urban regions for the benefits of reliable power and fission-generated heat. Such reactor designs are required to have a strongly reduced initial cost, faster construction, scalable and modular design, and a large power flexibly so that they can be easily adapted to smaller energy grids. These so-called small modular reactors (SMRs) are attractive for all of the reasons above and offer enhanced safety integrations over prior and larger designs.

¹² ENGIE: Unavailability of Doel 3 and Tihange 2 - Press Release May 13th 2015, <https://www.zonebourse.com/actua-lite-bourse/ENGIE-Unavailability-of-Doel-3-and-Tihange-2-Press-Release-May-13-2015--20366199/>.

¹³ Among the possible pathways (P1-P4), P3 delineates a course of action wherein the future developments follow societal and technological advancements along the same trend as they have in the past. The reduction in global emissions is realized not so much by way of reducing energy demand, but more in the way how energy and products are being produced. Other pathways, among the least (P1) and most resource intensive (P4) scenario's, equally illustrate an increase of nuclear power with an interquartile range of [+44, +102]% by the 2030s, and a [+91, +190]% by the 2050s.

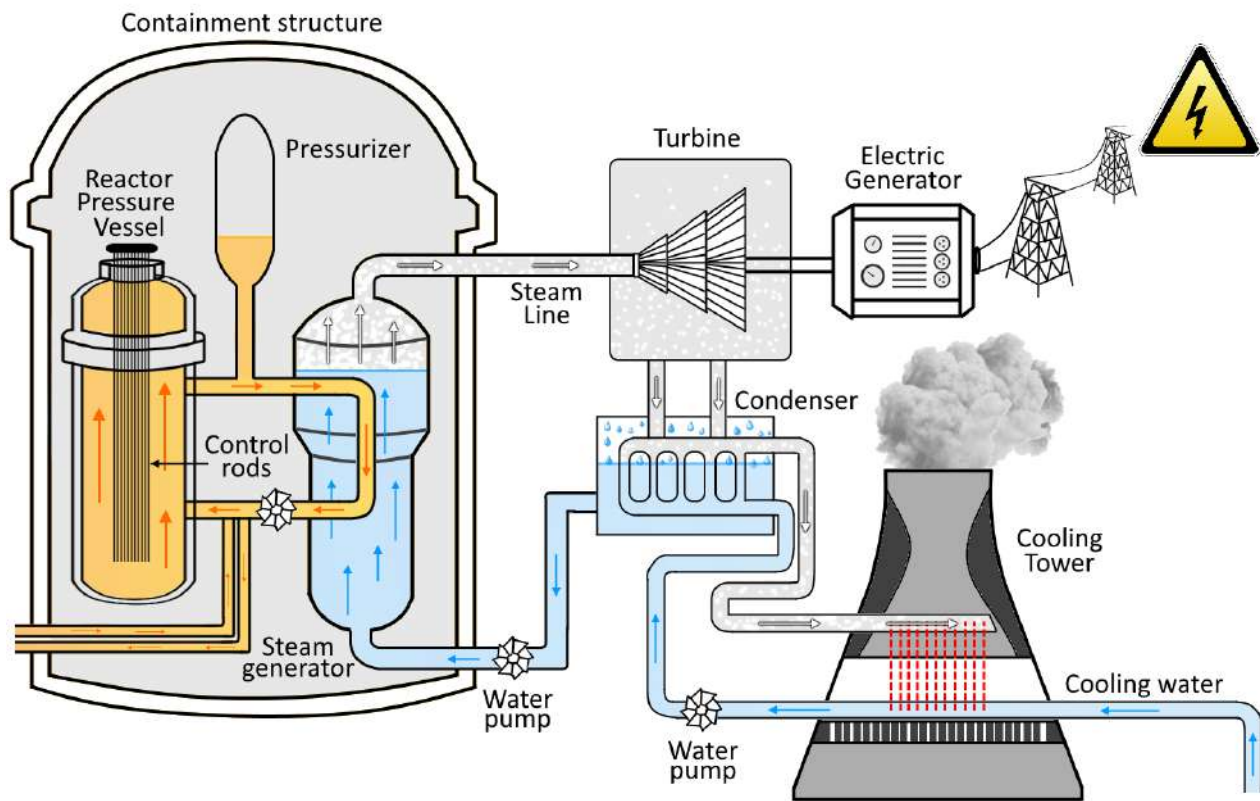


Figure 1.2: Illustration of a PWR NPP, separating the reactor primary water coolant system (yellow) from the secondary water coolant system (blue). Redrawn from reference [14].

1.2.4 Pressurized-water reactors

All seven nuclear power plants built in Belgium are of the Generation II PWR type, explained above. The typical operation of a PWR NPP is illustrated in Fig. 1.2. The reactor core inside the reactor pressure vessel (RPV) generates heat through nuclear fission. This heat is carried away from the reactor core through the connected heat transport loops, which circulate coolant water controlled by installed pressurizer systems. The coolant is pumped from the bottom end into the pressure vessel, bringing it into contact with the fuel elements inside the core. Ultimately, the transported heat is circulated through heat exchangers i.e., steam generators, where it is transferred to a secondary coolant. Heat transfer to a secondary coolant loop is important in order to prevent the primary coolant, which is radioactive, from leaving the containment structure altogether. For the most efficient transfer of heat, the primary coolant enters the steam generator through bundles of U-tubes. Steam produced from the secondary coolant rises through interconnected moisture separators and passes through the top of the steam generator.

During the second stage of operation, the thermal energy produced from the nuclear fission reaction is converted into electrical energy. The vaporized water from the secondary coolant loop expands into steam, where it will flow under great pressure towards the turbine generator. Excess steam is exhausted to a condenser, where it is cooled either from the secondary coolant system or from a tertiary coolant loop attached to nearby water reservoir (usually a river or lake). The condenser serves to transmit the remaining excess steam and heat from the reactor and converts it into water. The pressure and temperature of the exit steam must be as low as possible in order to increase the

efficiency of the steam turbine. The turbine generator converts this steam into electricity and supplies this to the transmission system attached to the electrical grid.

Interestingly, the main difference of a PWR compared to a BWR NPP, is that the coolant water in the primary reactor loop is held under high temperature and pressure when entering the RPV of a PWR while it is allowed to boil when operating a BWR instead. This means that, in a BWR power plant, there is no need for a subsequent heat exchanger (steam generator) and thus only a single coolant loop is required. While this implies that a BWR reactor can operate at a substantially lower pressure and have a greater thermal efficiency, it comes at the cost of observed radioactive contamination of the turbine generators.

1.3 Material challenges in PWRs

Numerous LWR NPPs in Europe [15] and the U.S. [16] are considering LTEs beyond their designed operational life-times. To that end, many NPPs should anticipate operation and radiation exposures that exceed their designated life-time and experience. In fact, the original design criteria only accounted for material degradation through corrosion and fatigue processes, aimed for a life-time of about 30 to 40 years. Still, material degradation can occur through a number of processes. For instance, considering phenomena that occur during mid- to long-term operation, neutron-irradiation induced microstructural and microchemical effects, material radiation hardening (RH) and embrittlement (RE) [17, 18], material swelling [19–21], and other related microstructural effects have been observed. Furthermore, in addition to the aspect of the harsh operating conditions, reactor components and structural materials must be able to withstand the environmental exposure of the reactor (e.g., the pressurized-water conditions, high operating temperature) and the high degree of operating stresses. When acting upon susceptible materials, the influence of the water-environment in combination with stress may lead to a reduced material performance or sudden operational failures. Amongst such failures, stress corrosion cracking (SCC) possibly assisted by the aspect of neutron-irradiation (IASCC), are the most prominent failures [22–25]. Other types of nuclear corrosion that have been observed in the field are related to the high flow-rates within coolant piping leading towards flow-assisted corrosion (FAC) [26, 27], or as a consequence of a local attack referred to as pitting corrosion [28, 29].

1.3.1 Material degradation after LTE

It is to the benefit of all current and advanced nuclear systems to get a better understanding of the governing degradation phenomena so that the performances, security and reliability of all NPPs can be improved. However, material degradation in a nuclear environment remains still poorly understood due to the complex interplay of various factors, such as the considerable amount of different material compositions, impact of various environmental conditions, and the aspect of different stress states imposed under operating conditions. In fact, in the case of PWRs, the water within the primary and secondary coolant circuits is held under different pressures, temperatures and chemical purities. Furthermore, NPP reactors employ, amongst others, different grades of stainless steel and carbon steel for the internal components and reactor pressure vessel respectively, zircalloy for the fuel cladding and high nickel-based alloys primarily for the steam generator and welds. Supposedly, these materials retain high mechanical properties and corrosion resistance, though over time, they remain susceptible to degradation nonetheless [30, 31].

Core support structures of LWRs are expected to remain structurally stable for their entire designed life-time. Thus, as a result, these structures should be able to sustain considerable amount of neutron doses during their operation. In PWRs, the accumulated doses after about 40 years may be of the

order of 80 – 100 displacements-per-atom (dpa) in the most affected zones. This neutron-irradiation causes large cascades of atomic displacements, resulting in a number of produced vacancy and interstitial sites within the original crystallographic lattice. Although many of the generated defects initially recombine while under the influence of high operating temperatures, a significant portion persists and diffuses towards microstructural trap sites such as grain boundaries and other interfaces. During that process, a number of defects may agglomerate into nanoscale proportions, which cause severe changes on the metallurgical properties of affected materials. Apart from radiation-induced hardening (RH) and embrittlement (RE), a potentially more problematic modification may occur at grain boundary sites where the chemical composition may be altered. Neutron irradiation may well induce local depletion of known oversized elements like Fe and Cr, or enrichment of under-sized elements like Ni or Si, mutually referred to as radiation-induced segregation (RIS). Further concerns are expressed about the collection of possible fission and transmutation reactions that produce energetic gamma-rays or gases like hydrogen or helium. Helium, which due to its low reactivity, persists for long periods of time within the material, and may potentially accumulate at material interfaces such as grain boundaries or defects like voids or nanocavities. Excess helium may then collect to form helium bubbles, which contribute to helium-embrittlement or even swelling of the material. Especially the combination of heavily irradiated materials subjected to heat-deposition induced by fission-released gamma rays (γ -heating), may increase the risk of void swelling. Furthermore, such high temperature materials are additionally susceptible to thermal aging effects caused by specific metallic impurities. These impurities may include the formation of hardening phases like copper-rich precipitates or phosphorus-induced temper embrittlement, which then again results in a decrease in ductility and material toughness. On top of that, nuclear materials not only have to face with metallic impurities caused at the consequence of LWR operation, but also have to contend with pre-existing forging anomalies that originated during the manufacturing, castings, or steel forging processes during the material's fabrication. While some degradation effects are related to the macro-segregation of carbon and sulphur, others may have resulted from the inadequate control of elements like hydrogen. Inhomogeneity in structural element compositions may have severe consequences for the metallurgical properties of internal reactor components, first and foremost leading to hardening and embrittlement. Finally, in combination with all of the above, core materials (mostly austenitic stainless steels) have shown sudden structural failures in the presence of oxidizing environments. Intergranular cracks at the consequence of radiation-induced material changes and localized stress conditions are otherwise known as irradiation-induced stress corrosion cracking (IASCC), which is the leading interest of this investigation.

1.3.2 IASCC cracking of baffle bolts

Most industrial failures are observed within the internal components of the reactor pressure vessel where the materials face the harshest conditions, see Fig. 1.3A. Dedicated towards PWRs specifically, the most frequently recurring type of failure is the IASCC cracking of 316L grade stainless steel baffle-former bolts (BFB) [34]. BFBs screw together the so-called baffle- and former plates i.e., metallic support plates of the RPV lower internal structure, in order to maintain the coolant water around the reactor core and to provide lateral support to the reactor fuel assemblies, see Fig. 1.3B. BFBs are reported to experience intergranular cracks, known as IASCC failures, which have been first observed in 1989 in French NPPs. Since then, IASCC BFB cracking has been similarly observed around the world, including in Belgium. A typical example of a fractured BFB after visual and metallographic examination is displayed in Fig. 1.3C. Typically, the reported failures are found in NPPs operating for 15 years or longer, wherein no continuous coolant water flow occurred through a drill hole onto the bolt's shank. Because this coolant water flow is the case in all other reactors, it questions Belgium's T1 and D1-2 units in particular. Indeed, since the beginning of ultrasonic inspections planned during maintenance outages of T1, a total of 37 (resp. 53) bolts in 1995, 5 (resp. 1) bolts in 2002, and 23 (resp.

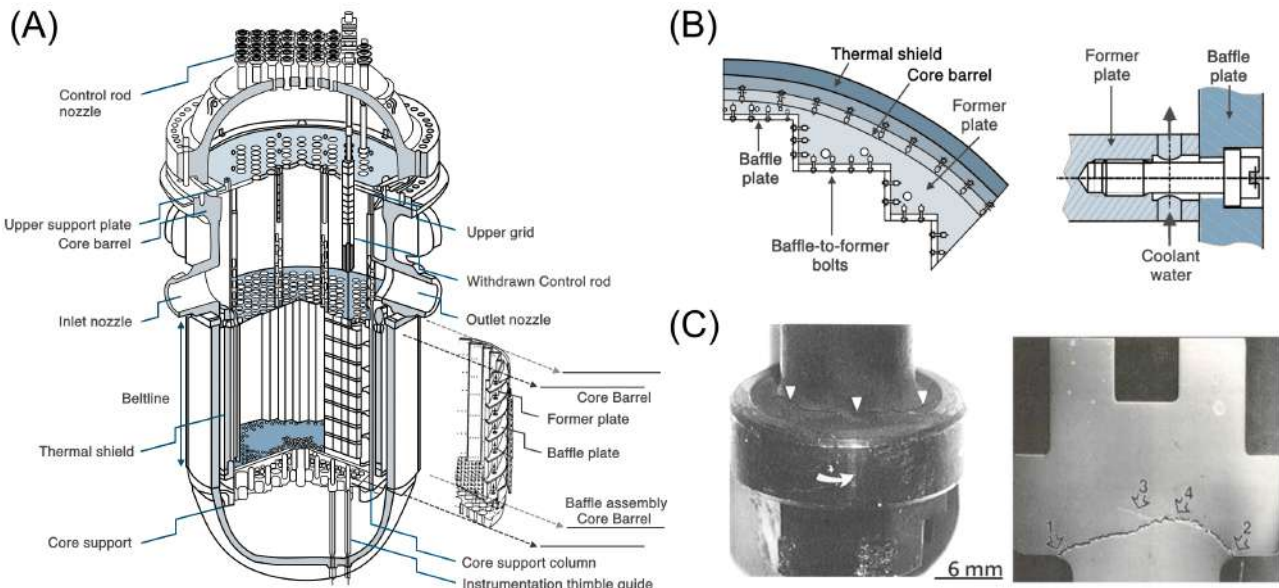


Figure 1.3: (A) Diagram of the internal structure of an RPV core of a PWR NPP. (B) Illustration of the baffle-former assembly with in-placed BFBs. (C) Visual and metallographic examination of an extracted BFB. Redrawn from references [32,33].

13) bolts in 2010, were considered as cracked (respectively deemed uninterpretable or speculative) and were since then preventively replaced. Conversely for D1-2 where the operating conditions and construction of the reactor assembly were considered as more favorable to cracking, no cracks in 1991, 8 (1) bolts (D1) in 2005, and only 5 bolts (D2) in 2006 were found and replaced accordingly. Some references suggest that it takes about two thirds of the 900-1000 BFBs, depending on the design of the RPV, to fail in order to endanger RPV structural integrity [33].

Although the locations of fractured BFBs generally correlated well with sensitive locations in the reactor assembly whereat higher irradiation doses and ambient temperatures were observed, the situation in practice is typically more complicated. Several of the cracked bolts failed in locations with a lower accumulated radiation dose or temperature. On the other hand, some bolts at deemed sensitive locations, did not crack while the expected susceptibility to cracking was considered high. Therefore, it remains uncertain why some bolts crack under certain operating conditions while others in symmetrical positions and comparable conditions remain unaffected. It is reasoned that several conditions may influence the probability of bolt cracking. In the first place, irradiation-induced swelling, especially in LTE NPPs older than 40 years, remains a concern for BFBs that are securely fastened. Swelling could generate significant deformation caused by localized contact stress with the assembly structure. Therefore, the general stress conditions and the susceptibility of the baffle bolt material to deformation are deemed important. On the other hand, the lower temperature conditions at the bolt's locations in D1-2 compared to T1 due to placement of certain coolant water flow holes, might explain lower instances of BFB failures in D1-2 as compared to T1. Thirdly, from tensile specimens retrieved from low and highly irradiated baffle bolts, results showed that the fracture toughness decreased with increasing radiation dose. The observations indicated that the fracture toughness entered a saturation regime at higher doses. Nevertheless, the role of radiation dose is considered influential at lower dose values still, considering that other parameters such as the stress, temperature, water corrosion and other operating conditions, remain comparable.

Structural failure of an important number of BFBs could lead to the opening of a gap between the

baffle-former assembly plates and therefore transfer the primary load to neighboring bolts, causing a increased chance of successive failure of adjacent BFBs. On the other hand, it could also induce fuel damage or compromise the fuel assembly as a whole. In the unlikely event when the coolant flow which transports the reactor fission heat is reduced or lost all together i.e., a loss of coolant accident (LOCA), the resultant pressure wave in the RPV subjects the baffle plates to significantly higher differential pressure, which could also cause a successive failure of adjacent bolts [34]. Such occurrences might cause significant deformations in baffle plates, which could bend fuel assemblies and jeopardize the insertion of control rods. One conclusion may be that the observed variability in BFB cracking indicates an intrinsic stochastic behavior of the cracking process, wherein external factors influence to global failure probability of the BFBs. To that end, a general understanding of the mechanisms that drive crack propagation is important for NPP safety and lifetime management. Interpretation of BFB cracking in the light of predictive probabilistic models may not only ensure the safety issue, but ultimately prevent a large economic impact as well. Unexpected NPP outages in combination with inspection and component replacement costs may drive maintenance costs upwards. A general understanding of structural component failure due to cracking, may therefore provide oversight in the preemptive replacement of susceptible components, thereby decreasing the risk to unplanned safety and cost issues.

1.4 Thesis structure and objectives

It is within the interest of this doctoral thesis, to formerly analyze the material degradation phenomena in stainless steels that ultimately lead to the initiation and propagation of trans- and intergranular cracks. For this purpose, the materials investigated in this thesis stem from tested surrogate materials and industrial specimens, respectively:

- The surrogate material considers a tailor-made *high Si model-type stainless steel alloy* that has been shown to be susceptible to transgranular SCC [35, 36]. This alloy has been designed to simulate the grain boundary composition indicative to irradiated stainless steels in an otherwise unirradiated material. Hence, this alloy can be considered as a useful test material to investigate the initiation of SCC without being irradiated itself in the first place. The objective of this material investigation is to obtain measurements for a so-called SCC threshold under which no SCC can occur, as well as investigate the SCC crack initiation processes that may ultimately lead to specimen failure.
- On the other hand, the other investigated material within this study was retrieved from an internal component inside of a nuclear reactor. This component i.e., a *316L stainless steel flux thimble tube*, was retrieved from the Belgian PWR NPP T2 stemming from the Tihange site. A thimble tube is a long and slender steel component that is mounted to the reactor fuel assembly from the lower internal component side of the RPV structure. Its function is to moderate the fission reaction by providing a way for the neutron flux detector to detect the neutron fluence of the internal reactor core. This acquired flux thimble tube remained operational for some 25 years at T2. It is considered as unique test material to investigate and characterize the phenomenon of IASCC.

The objectives of this research and the purpose of this thesis are to formerly understand the driving mechanisms of trans- and intergranular cracks in tested and industrial materials. Not only the crack morphology along its length, but also the state and chemistry at the crack tip, are deemed important. Investigation of the deformed microstructure around that crack and crack tip is further investigated, as it may assist or impede on further propagation of the crack. These microstructural results, in

contemplation of the mechanical test data, may assist in understanding the origin of scatter related to IASCC in the field i.e. BFB cracking, and in time-to-failure crack initiation experiments discussed later on. IASCC is investigated on the basis of several factors that may drive the cracking, including on the applied stress intensity, but also on the state of material parameters including the intergranular oxide, and the form of loading; constant or cyclic conditions. Practically, this is achieved by utilizing experimental instrumentations like scanning electron microscopy (SEM), focused-ion beam SEM (FIB-SEM) and (scanning) transmission electron microscopy (S)TEM.

The intent of this thesis is to provide additional experimental results that could aid in rationalizing existing failure mechanisms used for the interpretation of internal RPV component failures. To that end, FIB-SEM is employed for the purpose of accurate sample extractions from relevant specimen positions e.g., close to and beyond initiated cracks and crack tips. Investigating the main morphology and the surrounding deformation features of extracted trans- and intergranular crack tips with the use of TEM is expected to lead to a better understanding of the degradation phenomena that take place inside the above materials. Microstructural analyses at the crack tip provide more crucial information that could elucidate on the complex mechanism responsible for (IA)SCC. These investigations may then lead to the advancement of predictive methodologies and mitigation strategies of industrial specimen failures, like the BFB cracking in commercial PWR NPPs. The obtained results are analyzed in the light of the known failure models, including the probabilistic fracture model developed by Konstantinović, being one of SCKCEN's promoters of this thesis.

1 Thesis structure

The general structure of this thesis is outlined as follows:

1. In this first chapter, the European Commission's energy policies on renewables and supporting energy technologies to combat climate change were presented. Of significance, was its declaration on February 2nd 2022 wherein both nuclear fission and gas-fired power plants were considered as sustainable bridging technologies towards a fully renewable energy mix. While certain EU member states decide to reinvest into their nuclear power facilities, Belgium on the other hand has a long history of policies on a complete nuclear phase-out. However, on July 22nd 2022, the Belgian federal government reached an agreement with ENGIE-Electrabel to prolong the operation of its two youngest NPPs, i.e., D4 and T3 for an extended period of 10 years. Though nuclear power offers great benefits towards a sustainable energy to meet the 2030 and 2050 climate goals, it has been greatly controversial amongst policy makers and the general public opinion. The controversy emanates partially from the concern about material degradation, especially on (irradiation-assisted) stress corrosion cracking (IA)SCC, on which this thesis is based.
2. Chapter 2 presents a complete summary of the literature review on (IA)SCC in austenitic stainless steels. The focus is given to stainless steel's crystallographic structure and its deformation behavior, wherein dislocation motion, twinning and phase transformation were considered important. The chapter goes on about the role of steel's passivating oxide layer, and its importance towards (IA)SCC. Intergranular failure has been implicated to be among the main limiting factors to the integrity of NPPs. Therefore, in regards to rationalizing the microstructural results obtained in subsequent chapters, the different contributing mechanisms are discussed, together with three failure mechanisms believed to be relevant to IASCC: the slip-dissolution, internal oxidation, and hydrogen-related failure models.
3. In chapter 3, we summarize the main experimental methods applied during this thesis. Fundamentally, the thesis is based on scanning electron microscopy (SEM), focused-ion beam SEM (FIB-SEM) and (scanning (S)TEM) transmission electron microscopy (TEM). Besides

an overview on several imaging techniques, this chapter also outlines the methodology to extract (IA)SCC cracks from a specimen's fracture surface. Relevant crack tips may be extracted by means of FIB-analysis from the specimen's bulk material, after which they can be investigated using TEM microscopy. The chapter concludes with an overview of the investigated materials and the performed testing techniques that were employed to produce relevant test samples.

4. Chapter 4 is entirely based on the first set of materials investigated during this research i.e., high-Si duplex stainless steels tapered specimens, and their susceptibility to stress corrosion cracking (SCC). Constant elongation rate tensile testing was employed as an accelerated test technique to study the crack initiation along the gauge surface of these tapered specimens. By means of applying a novel crack detection algorithm on iteratively displaced SEM pictures, detailed crack density distributions were obtained from which the critical stress threshold value for SCC in duplex high Si stainless steel was derived. The results based on microstructural analyses were supported by means of finite-element analysis and the interpretation of the mechanical load history of the sample sets.

Subsequent TEM analyses on FIB-extracted SCC crack tips were additionally performed. Microstructural investigations in the near vicinity of SCC crack tips illustrate a strain-rate dependency in SCC mechanisms. Detailed analyses of the crack tip morphology, that include the crack tip oxidation and the surrounding deformation field, indicate the existence of an interplay between corrosion- and deformation-driven failure as a function of the strain rate. Slow strain-rate crack tips exhibit a narrow cleavage failure which can be linked to the film-induced failure mechanism, while rounded shaped crack tips for faster strain rates could be related to the strain-induced failure. As a result, two nominal strain-rate-dependent failure regimes dominated either by corrosion or deformation-driven cracking mechanisms can be distinguished. This observation is in agreement with the previously performed SEM observations during the first half of this chapter.

5. Contrary to the previous one, chapter 5 is based on the investigation of IASCC cracking on industrial specimens. During this chapter, the microstructural features of IASCC crack tips from a redeemed neutron-irradiated flux thimble tube are investigated using FIB-analysis and (S)TEM microscopy. This work presents a close examination of the deformation field and oxide assembly associated with intergranular cracking, in addition to the analysis of chemical segregation in front of leading crack tips and unimpaired grain boundaries. Furthermore, the effect of the imposed stress level, removal of the internal oxide, and cyclic versus tensile loading on IASCC cracks was investigated. In all samples, exclusive observations of grain boundary oxidation prior to the cracking was observed. This is in full agreement with the recently proposed quasi brittle fracture model based on the internal oxidation mechanism.
6. In chapter 6, we present the final conclusions and provide an outlook on further analyses that are deemed important to the microstructure and modelling aspects of irradiation-assisted SCC.

Chapter 2

Irradiation-assisted stress corrosion cracking

2.1 Introduction

2.1.1 Characteristics of (IA)SCC

Austenitic stainless steels are used in a variety of reactor pressure vessel (RPV) core components of nuclear power plants (NPPs). In addition to being influenced by the high temperature NPP operating conditions ranging between 270–340°C, these structural materials are subjected to an intense neutron-radiation field which not only alters the surrounding coolant water chemistry, but also the material's microstructure. These processes may induce material property changes that develop during service operation of NPPs. Lasting changes on the account of the material's microstructure or microchemistry may ultimately lead to a severely limiting degradation phenomenon known as irradiation-assisted stress corrosion cracking (IASCC) [17, 22–24, 37–44]. IASCC describes the sudden intergranular failure of core structural materials that occurs due to the interplay between many interdependent material degradation phenomena. A schematic of the primary parameters - stress, material microstructure, and aggressively corroding environment - and underlying degradation phenomena that affect IASCC is shown in Fig. 2.1.

Due to the multiplicity of the several interrelated parameters and mechanisms influencing the cracking of stainless steels, it becomes challenging to identify a uniform mechanism that describes IASCC and all its aspects of the material degradation. Many contemporary investigations have focused more on the interdependencies between the correlating factors related to IASCC. In studying these interdependencies, a complete understanding of the phenomenon may result in the development of a model that is capable of predicting or preventing upcoming failures. To that end, it is important for this chapter to first outline the aspect of materials being susceptible to IASCC. Within the interest of this thesis, section 2.2 presents an overview of the qualities and deformation mechanisms in stainless steels; most especially the cold-worked 316L alloy, which was and used as the structural material for susceptible BFBs. Consequently, the chapter continues by outlining the various metallurgical and microchemical changes that follow after continued neutron-irradiation of these materials, see section 2.3. Many of these processes are seen as precursors that increase the likelihood of intergranular crack initiation or assist in known intergranular crack growth rates. The additional factors that influence the cracking aspects and cracking regimes, most especially cold-work, stress intensity, loading paths

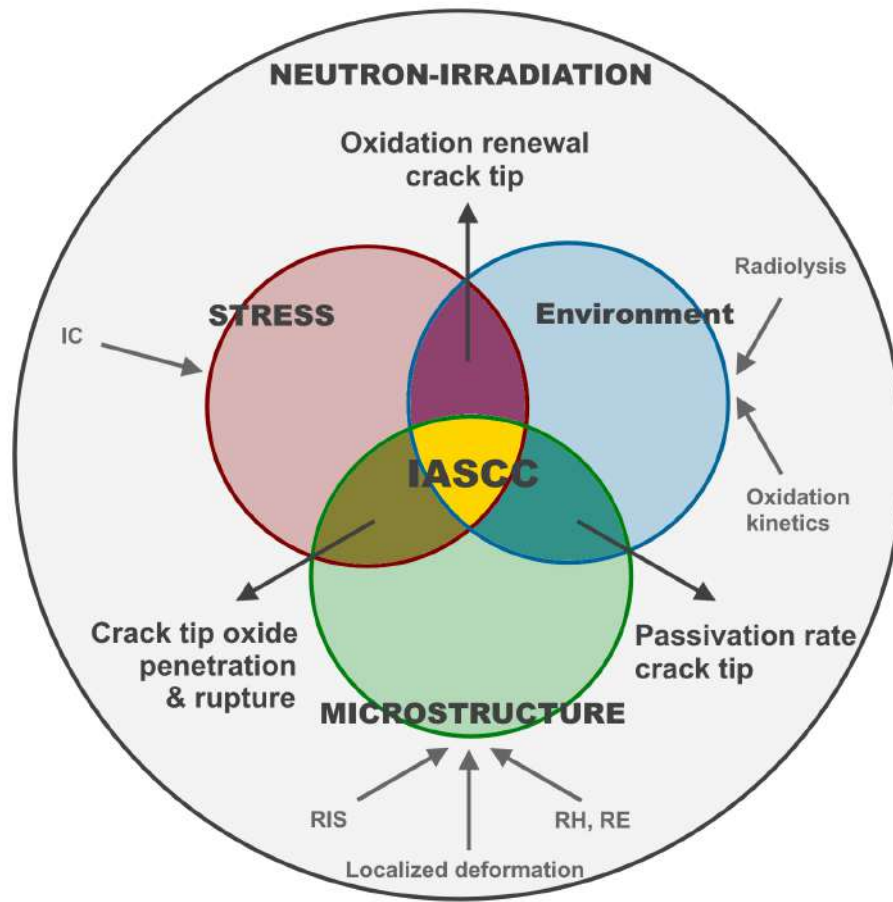


Figure 2.1: Schematic of the primary contributors that affect the underlying crack tip processes that control IASCC. The effects of neutron-irradiation is also shown, amongst which: (ir)radiation-induced segregation (RIS), -hardening (RH) and embrittlement (RE), and -creep (IC). Redrawn from reference [22].

and more, are discussed in section 2.4. Ultimately, the leading literature models that describe the cracking mechanisms are outlined in section 2.5. For each of these models, clear indicators are defined that may signal towards the model's validity when experimentally investigated.

2.2 Stainless steels

Stainless steel (SS) is a collective term for all alloys with a minimum concentration of about 10.5 wt. % Cr, giving them the ability to form a passivating chromium oxide layer on their surfaces. Depending on their crystallinity, SSs can exist either in an austenitic (γ), ferritic (α), duplex ($\gamma + \alpha$), or martensitic (α' or ϵ , respectively) form [45]. Austenitic SSs are the most familiar type of SSs for PWR practices. Forged 304L and 316L austenitic SSs (wherein L illustrates the lowered carbon content, improving corrosion resistance), their welds types 308L and 309L, and cast types CF3 and CF8(M), are the most common SS type alloys used in the primary loop circuits of PWRs and their auxiliary systems [46]. Besides iron as their basis element, the main alloying constituents of these steels are evidently chromium, nickel, and some other minor elements like manganese, molybdenum, silicon etc. Although these minor elements contribute little to the overall weight composition, their contribution to the steel's manufacturing qualities like steel weldability and formability, is immense.

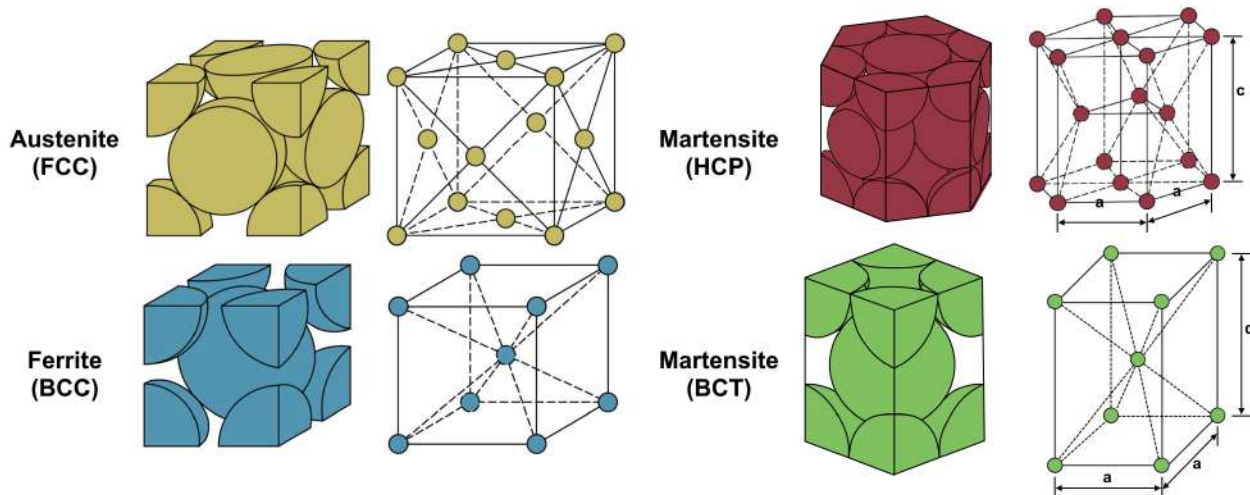


Figure 2.2: Ball-and-stick and hard-sphere representations of the unit cells for the austenite (FCC), ferrite (BCC), and martensite (HCP) and (BCT) lattices, respectively.

Other qualities found in SSs amount to a high ductility and increased fracture toughness. Because of their excellent corrosion resistance, effectuated by the growth of their oxide passivating film, SSs are among the first options for structural material in PWRs. Although, as will be discussed throughout this chapter, SSs are not free from corrosion – especially after breakdown of their passivating film.

2.2.1 Crystal structure

Austenite is characterized by a face-centered cubic (FCC) unit cell with a lattice parameter a_γ of about 3.57 \AA [47]. Due to its high cubic lattice symmetry, it contains a number of close-packed lattice planes whereupon the material can easily deform without tearing itself apart. Accordingly, austenite can withstand a great deal of lattice shear, giving it excellent ductile properties when being subjected to plastic deformation. Ferrite on the other hand possesses a body-centered cubic (BCC) unit cell with a lattice parameter around 2.86 \AA [47]. Some electrons within the BCC lattice typically remain unpaired and freely spinning, resulting in some magnetic properties adherent to ferrite. A BCC crystal structure will also exhibit less ductility in comparison to an FCC cubic structure, making it generally more prone to fracture especially at elevated temperatures. Martensite is another allotrope form of SS. It can nucleate in one of two forms: a hexagonally-close packed (HCP) type, also known as ϵ -martensite, or a body-centered tetragonal (BCT) type i.e., a stretched BCC unit cell in one primary direction, otherwise referred to as α' -martensite [48]. Both types of martensite may restrain the motion of dislocations under plastic deformation, thus contribute to the strength of the steel. The tetragonally shaped unit cell of α' -martensite has high strength qualities due to the large lattice distortion of its unit cell, causing it to become more brittle and consequently more susceptible to fractures. Lastly, duplex steel is composed of a blend microstructure between austenite and ferrite, which gives the material a mixture of both their properties. The unit cells for the different allotropes of SSs are shown in Fig. 2.2.

SSs can undergo phase transformations between their different allotropes under changing temperature or alloying conditions. For instance, at room temperature, SSs reside normally in the BCC ferrite phase, while at elevated temperatures above $910 \text{ }^\circ\text{C}$ or so, the crystal structure changes to FCC austenite instead. Austenite may transform into martensite following strong deformation or rapid cooling; a process which is normally expected to start at room or sub-zero temperatures [50]. On

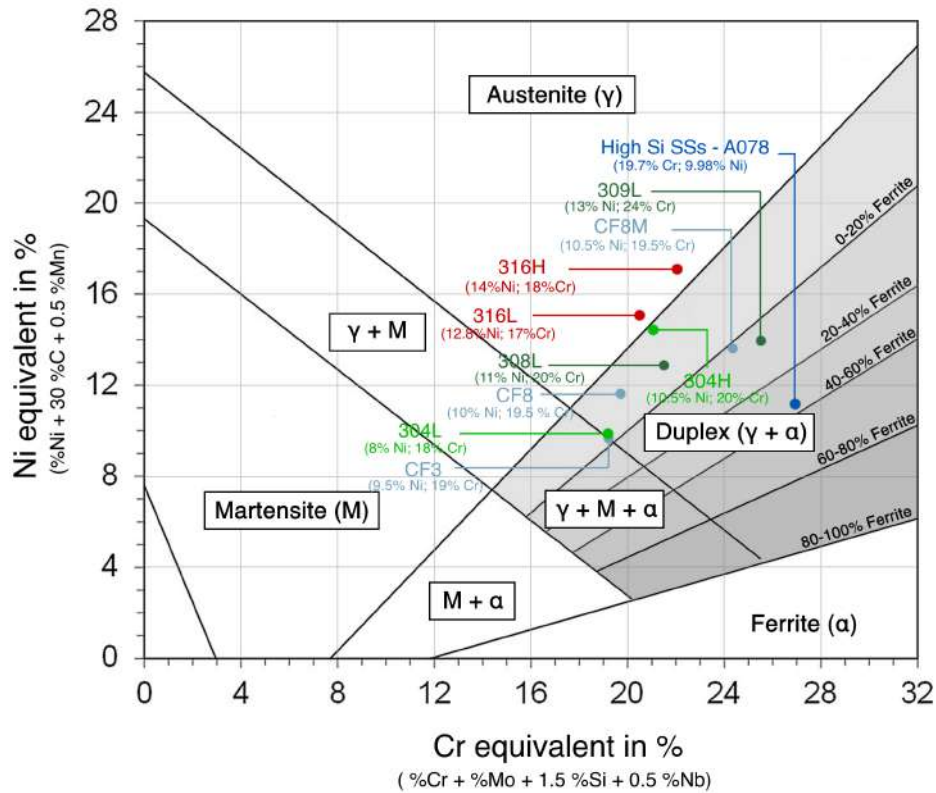


Figure 2.3: Schaeffler diagram illustrating the stable allotrope phases of SSs according to their equivalent ferrite and austenite stabilizers. Amongst others, types 316L and high-Si A078 duplex steel employed in this study are added for reference. Redrawn according to references [48, 49].

the other hand, their alloying composition may also influence the crystallographic structure of SSs. Whereas increased concentrations of Ni and Mn are known to stabilize the austenitic form; reliably stabilizing it down to room temperature depending on their critical concentration, Cr, Si and Mo on the other hand stabilize the ferrite structure instead. As we will see, there are quite a number of processes whereupon the alloying composition of steels can change at a local scale, potentially giving rise to such phase transformations. Although Cr is beneficial for the corrosion qualities of austenitic steels, depending on the concentration, it and some other ferrite stabilizers may induce an austenitic transformation in favor of ferrite or duplex structures instead. The effect of the different stabilizers is conventionally estimated by the Schaeffler diagram [49] illustrated in Fig. 2.3. This diagram illustrates the stability domains of the different stainless steel allotropes, depending their austenite and ferrite stabilizers.

2.2.2 Lattice structure and defects

Grain boundaries

Stainless steels are generally polycrystalline solids by nature. This implies that the entire steel's microstructure is composed of numerous crystal grains that coincide at interfaces known as grain boundaries. A single grain can be considered as one single crystal, wherein the atoms that compose that crystal are stacked in accordance to a fixed atomic unit cell. This unit cell is then repetitively translated across the entire metal volume to embody one complete crystal grain. The origin of these grains stem from the steel's manufacturing processes [51]. By managing the correct conditions of the

entire operation, one gains precise control over the grain's size and the grain boundary properties through a process called grain boundary engineering. Initially, when an alloyed steel is cast, it is allowed to cool down and solidify without any mechanical forces applied. The subsequent step in metalworking is to conduct the forming process of the steel. The metal is strongly deformed at elevated temperatures through processes like forging, rolling, or drawing, in order to increase its yield strength. Forming of the steel introduces a substantial amount of defects in the steel's microstructure; the deformation field now primarily subsists of large strains and dislocations. These defects require energy to be created. As such, they can be regarded as excited states of the metal which increase the steel's internal stored energy. Recovery of those defects from the deformed grains can be achieved through heat treatment. This process reduces some of the internal energy by rearranging parts of the crystal lattice through a process called recrystallization. The original deformed grains with internal defects are hereby replaced by a new set of un-deformed defect-free grains that nucleate and grow until the original grains have been completely replaced.

Microstructural characterization of the grain boundary, its structure, chemistry, and orientation, are considered to be of high importance to outline (IA)SCC susceptibility. Traditionally, grain boundaries are described using the coincident site lattice (CSL) model developed by Kronberg and Wilson [52,53]. Accordingly, the number of coincident atomic positions between the two opposing grains' orientations on either side of the interface is used as a measure of the energy of the grain boundary. A close match between two intersecting grains is found when a high number of coincident atomic positions intersect. Such grain boundaries have a relatively low internal energy and are referred to as coincident site lattice boundaries (CSLB). However, the CSL model does not take into account the grain boundary plane nor its orientation and is therefore found to be insufficient to properly describe its complete character. In reality, for a unique characterization, a full description of the orientation of the two adjacent grains and the parameters that define the grain boundary interface plane are required. Correspondingly, five degrees of freedom are necessary to characterize a grain boundary: two describing the rotation axis, a third describing the rotation angle, and another two defining the grain boundary interface plane [53]. Characterizing grain boundaries in this way based on their misorientation, or using the CSL model, has been found to be out of the scope of this thesis. Rather, priority has been given to the characterization of the deformation and the chemical aspects of grain boundaries, especially following the effects of cracking and neutron irradiation. Still, both methods provide interesting results in the field of SCC research. Alexandreanu [54,55] has shown that CSLBs with a low internal energy are generally more corrosion resistant and conserved from cracking. On the other hand, grain boundaries with a high internal energy known as high angle grain boundaries (HABs), are assumed to be more susceptible to preferential precipitation [56], pose a greater risk to cracking [55,57], and are more strongly affected by intergranular oxidation posing a risk of grain boundary embrittlement [58].

Dislocations

Deformation beyond the scope whereupon the material can still recover to its original state though not as significant in order to tear itself apart, must involve some kind of permanent change to the locations of atoms within the crystal lattice. This kind of deformation is deemed plastic deformation; the driving force of which, is reasoned because of the movement of dislocations [59]. A dislocation is a line defect within the stacking of a material, wherein one part of the material is offset by one atomic plane with respect of the rest of the material. Two distinct types of dislocations are considered depending on the relative orientation of their defining vector parameters. A dislocation is defined by its Burgers vector \vec{b} i.e., a measure of the lattice distortion caused by the dislocation, but also by its line vector \vec{l} i.e., the direction where the shear forces initiate at the dislocation site. These two vectors determine the kind of dislocation: an edge dislocation (often denoted by \perp), described by $\vec{b} \perp \vec{l}$, and

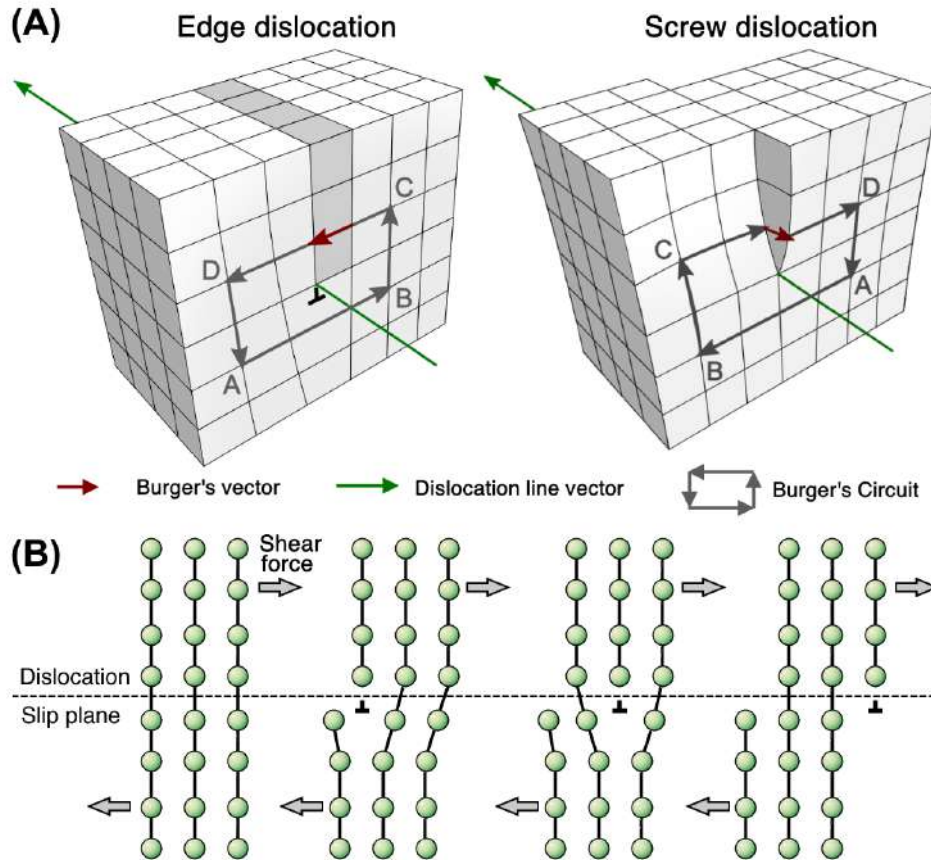


Figure 2.4: (A) Visual representation of the orientation of an edge- and screw dislocation, defined by their respective Burger \vec{b} and line vectors \vec{l} . (B) Atomistic representation of the process of dislocation slip. Redrawn according to reference [59].

a screw dislocation, whereat $\vec{b} // \vec{l}$ (see Fig. 2.4A). The circuit that encompasses the dislocation, and visualizes the amount of lattice distortion that is caused by that dislocation, is known as the Burgers circuit.

Due to the acting forces upon the material, atomic planes can easily slide over one another, a process referred to as the slippage of dislocations. Most of the dislocations that engage in slip are of a mixed character, both edge and screw dislocations. Material slip occurs at a very local scale between the most close-packed atomic planes of the lattice, also known as slip planes. The process of dislocation slip is schematically illustrated for edge dislocations in Fig. 2.4B. During tensile loading, the applied tensile stress on a material is attained when the shear stress resolved onto a slip plane increases up to the critical value to cause dislocations in that slip plane to move. This stress is known as Schmid's resolved shear stress, and is defined by:

$$\tau_R = \sigma \cos(\lambda) \cos(\phi) \tag{2.1}$$

wherein σ signifies the acting tensile stress, and λ and ϕ the angles between the loading direction with the slip plane and the normal of that slip plane, respectively. In conventional circumstances where the loading direction lies in between the slip plane and its normal, it can be thought of that these angles are each others complement. However, in three-dimensional space where more degrees of freedom are relevant, or under complex strain-paths where the loading direction is not in the general direction of

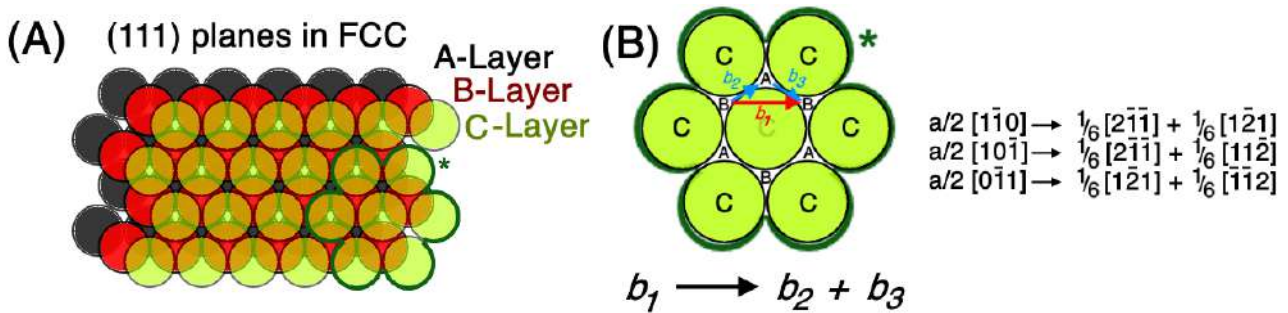


Figure 2.5: (A) Stacking sequence of $\{111\}$ -type FCC lattice planes, illustrating how (B) dislocations with a perfect Burgers vector b_1 may dissociate into two partial dislocations with vectors b_2 and b_3 . Redrawn in accordance to reference [59].

the slip, these angles need not be each others complement. Under these circumstances, it is required to characterize the resolved shear stress as equation 2.1.

Dislocations that move due to the applied shear stress are termed glissile, derived from the gliding over the slip plane. For FCC materials, dislocations that reside on the $\{111\}$ planes are deemed glissile. Activation of slip planes in accordance to Schmid's law tend to cause lateral displacements as well as axial extensions in the material. For illustrative purposes, this form of microstructural displacement is equivalent to the displacement that is caused when a common rope is constantly torsioned in between two hands. This microstructural displacement activates other slip systems in the vicinity, causing their Schmid factors to increase to the same value as that of the primary system.

There are some subtleties involved in characterizing dislocations. For example, if a Burgers vector of a dislocation takes on a single (or multiple) value of the material lattice parameter a , the lattice remains unaffected by the distortion and the corresponding dislocation is referred to as a perfect dislocation. However, if the dislocation is not equal to a lattice parameter, it is termed a partial dislocation instead. FCC crystals define perfect dislocations as those with a Burgers vector equal to $a/2\langle 110 \rangle$. It can happen that such a perfect dislocation may dissociate into two $\langle 112 \rangle$ partial dislocations, also known as Shockley partials, if it is more energetically favorable to do so [59]. This process is displayed for an FCC lattice e.g. austenite, in Fig. 2.5. It becomes evident that, upon dissociation, a stacking fault is introduced where the lattice locally changes from ABCABC (FCC stacking) to ABCA(**BCB**)C. The stacking of the crystal lattice is offset above and below the stacking fault by the length of the partial dislocations. This creates an attraction force within the stacking fault, counteracting the pre-existing repulsive force between the two Shockley partials [60] which favored dissociation of a perfect dislocation in the first place. The resulting energy equilibrium between the two partial dislocations dictates the spacing between them.

The dissociation of perfect dislocations is influenced by an inherent material property known as the stacking-fault energy (SFE) [61,62], denoted as γ_{SFE} (mJ/m^2). The SFE represents the required energy to create 1 m^2 of stacking faults within the material; these generated stacking faults carry a certain energy, hence the term stacking fault energy. Generally speaking, when a material's SFE is large, the dissociation of perfect dislocations is energetically unfavorable, allowing material to deform more easily through dislocation glide. Lower SFEs on the other hand, facilitate the dislocation dissociation and increases the separation distance between the two produced partials. This in turn may inhibit the dislocation motion on multiple slip planes and thus impede upon the dislocation glide [62]. The SFE is strongly determined by the material's composition [61]. In the case of austenitic steels, the SFE is considered to be low to medium, around the order of $10\text{-}50 \text{ mJ}/\text{m}^2$ [61]. The separation distance

between partial dislocations therefore tends to be of the order of a few up to 10 nm's [59]. The SFE determines to a large extent the deformation processes that take place in a material. As shall be discussed in the subsequent paragraphs, dissociation of a perfect dislocation and thus also the SFE, may lie at the basis of twinning and martensite phase transformations.

Twin Boundaries

One special kind of interface in FCC crystals that can be thought of as very similar to grain boundaries, is called a twin boundary [63]. During the growth of a crystal, e.g. during the recrystallization period of the metalworking process, parts of the crystal lattice may intergrow symmetrically over a shared interface to form twinned crystals. When this occurs, lattice points of one crystal are shared amongst the lattice points of the other, adding an apparent symmetry to both crystals within one single grain over an interface called a twin boundary. If twins nucleate during the crystal grain growth period without the application of a mechanical load, the twinning is described as annealing twins. Otherwise, if parts of the crystal lattice shear over one another as a consequence of an applied stress and strain, the induced twinning is known as either mechanical or deformation twinning, or sometimes referred to as Neumann Bands. Since twinning is regarded as a cooperative movement of the crystal lattice, twin formation should occur much faster in comparison to the common glide of dislocations. In fact, twin-formation is facilitated if the crystal is subjected to large strain-rates and shear forces. No thermal activation is required for the formation of deformation-twins, which otherwise does facilitate the dislocation movement. Therefore, it is typically regarded that deformation twinning becomes the more active plasticity mechanism at lower temperatures.

Twinning can be regarded in many different forms. There exist a *twist* twin boundary, wherein one crystal is rotated over an angle of 60° (or equivalently 180°) along a rotation axis normal to a $\{111\}$ twin boundary plane. On the other hand, there is also a *tilt* twin boundary, where one crystal is tilted by about 70.53° over a $\langle 110 \rangle$ direction perpendicular to the $\{111\}$ twinning plane. Alternatively, twinning may also mirror one part of the crystal over a $\{111\}$ *mirror* twin boundary. When the atoms of the $\{111\}$ twin boundary are shared by both twinned crystals, the twin boundary is referred to as being coherent. Otherwise, in the case when the twinned crystals do not share the $\{111\}$ planes, incoherent twin boundaries are formed. A typical example of twinning is illustrated in Fig. 2.6. Here, one example out of 12, of a $\{111\}\langle 112 \rangle$ twinning system is depicted, whereat the $\{111\}$ indicate the twinning plane and the $\langle 112 \rangle$ the twinning direction.

2.2.3 Deformation behavior

Tensile tests have revealed that different plasticity mechanisms may take place in austenitic SSs subjected to different stress and temperature conditions [48]. Those main mechanisms account to: (i) dislocation slip and (ii) dynamic strain ageing, mostly understood as the classical dislocation motion - mostly occurring at elevated temperatures between $200\text{--}400^\circ\text{C}$ [62,64]; and (iii) stacking-fault formation, (iv) twinning-induced plasticity, and (v) martensite phase transformation, categorized as displacive transformations - mostly playing a role at lower temperatures below 200°C [63,65–68]. Close competition exists between these five mechanisms, although some significant interaction may still take place. The competition is largely dependent on evidently the temperature range, but also the material composition (naturally, the SFE), grain size and orientation, and stress and strain conditions [48].

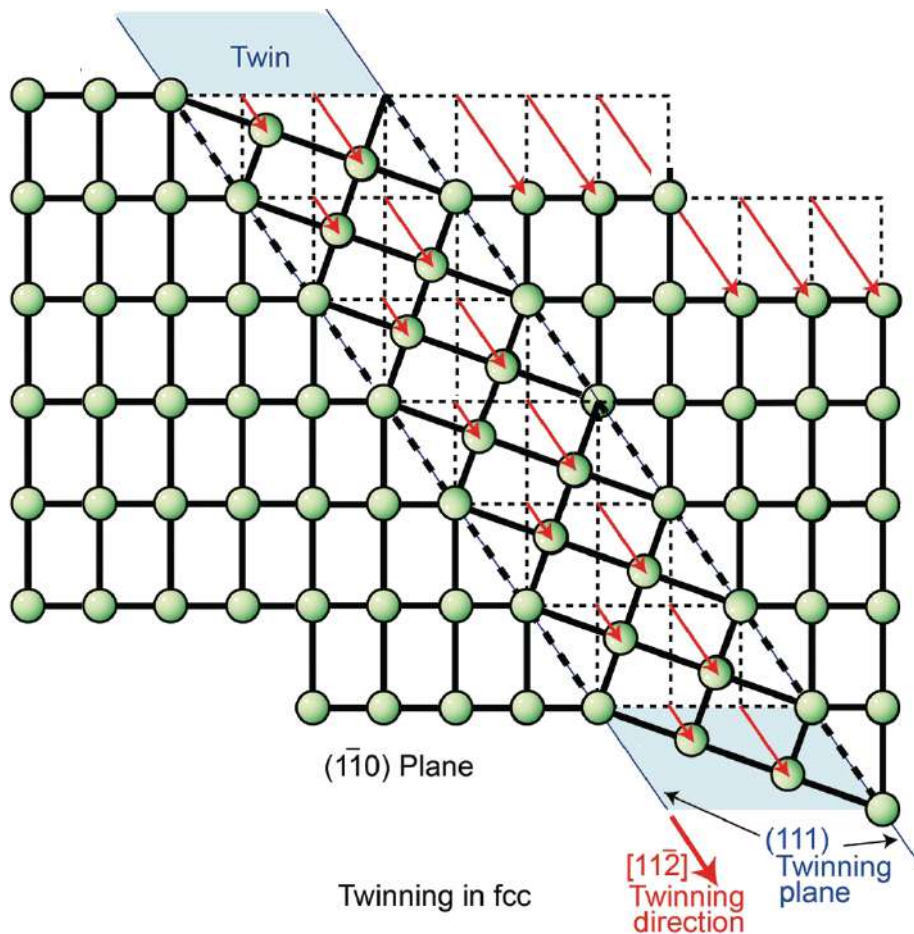


Figure 2.6: Atomistic model of the generation of a finite thickness coherent twin orientated in a $\langle 112 \rangle$ direction between two $\{111\}$ mirror twin boundaries. According to reference [59].

2.2.3.1 Strain-hardening

The way how dislocations increase the material strength may appear counterintuitive at first, given that dislocations are the carriers of plastic deformation and that an increased dislocation matrix may appear to facilitate the plastic deformation. However, associated to the presence of dislocations in a distorted lattice, is an elastic strain field which can create forces in between individual dislocations. This strain field may counteract the motion of all other dislocations in the distorted lattice, alleviating parts of the strain that is subjected onto the material. The inhibited motion of dislocations increases the material hardness and yield stress.

2.2.3.2 Deformation twinning

As readily illustrated in paragraph 2.2.2, homogeneous shear over large volumes of the material may cause the formation of reoriented phases in the parent crystal lattice, also known as mechanical or deformation twins. However, from an atomistic point of view, the onset of twinning is more complex. In FCC crystals like austenite, deformation twins develop as a consequence of the gliding of $a/6\langle 112 \rangle$ partial dislocations on each *successive* $\{111\}$ atomic planes [48, 63]. As illustrated in Fig. 2.7A, the ABCABCABC stacking of the FCC lattice locally changes to ABCA|CBACB when stacking faults

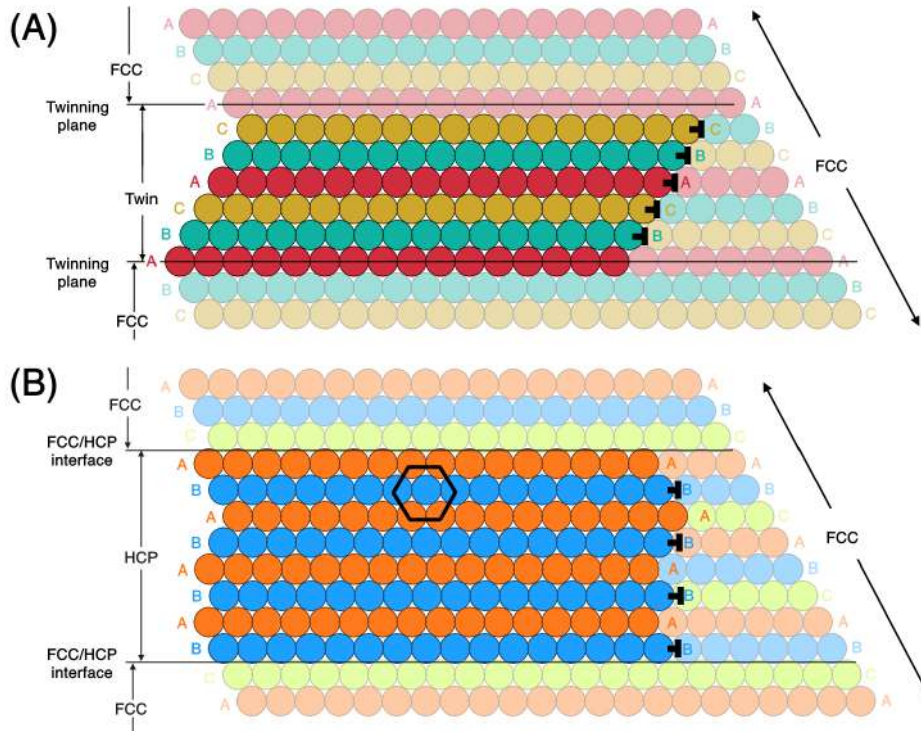


Figure 2.7: Schematic illustration of the stacking of an FCC lattice, leading to the formation of (A) twinning, and (B) HCP ϵ -martensite. Redrawn in accordance to the schematics in reference [48].

are successively introduced. Here, the notation “|” is equivalent to the twinning plane separating both crystal orientations. Some studies suggest that a nucleus containing a few stacking faults on adjacent close-packed $\{111\}$ planes is required in order to speak of a twin nucleation event [69]. Since dislocation glide is commonly accepted to be a stress-assisted mechanism, it is reasonable that the formation of twinning is as well. Twin nucleation at a certain stress is defined by the critically resolved twinning stress. Most nucleation models assume that this stress is reached at a very local scale through the pinning of dislocations. Stress concentration at dislocation pile-ups, inclusion particles, or grain boundaries may likely explain the origin of twinning [48]. Under continuous strains, it is even possible for the lattice to develop a secondary twin-system with a different orientation, other than the primary twin-system. Due to strain-hardening or possible grain reorientation, the resolved shear stresses reach the critical value for a secondary twinning-system to develop. Since twinning occurs much more easily in materials with a lower SFE (whereat the separation distance for stacking faults is commonly larger) [62, 70], it can be estimated that the critically resolved twinning stress is more easily attained in such materials.

Deformation twinning has a strong impact on the metallurgical properties of SSs, primarily on the hardness and brittleness qualities. The reasoning for this is that dislocation glide occurs more easily within the un-twinned phases of heavily twinned grains and that dislocation pile-up occurs at readily formed twin interfaces [48]. These effects may either be explained because the twinning interface serves as a hard obstacle for matrix dislocations to penetrate, or because present dislocations in the twinned regions are entangled or piled-up; restricting the glide of further dislocations [48]. The resultant of these entanglements is that twinning introduces new interfaces within the material grains that limit the dislocation mean free path and consequently promote the strain-hardening ability [65]. This material strengthening mechanism is more commonly known as the dynamic Hall-Petch effect [71].

2.2.3.3 Martensite transformation

Austenitic SSs may be subjected to another displacive transformation aside from twinning, known as the martensitic transformation [48, 72–78]. Whereas homogeneous shear can be responsible for the formation of a reoriented phase of the crystal lattice in the case of deformation twinning, martensitic transformations are characterized by the development of an entirely new crystal structure altogether. Since austenitic SSs are inherently thermodynamically unstable, they are known to be susceptible to martensitic transformations [72]. Two types of martensite can be distinguished within the parent crystal lattice, namely: (i) ϵ -martensite, characterized by a HCP crystal structure; and (ii) α' -martensite, consisting of a distorted BCC (i.e. BCT) crystal lattice. Both types are considered to be much harder than the parent austenite [73] and impede upon the mobility of dislocation within the austenite lattice [48]. Thus, martensitic phases contribute significantly to the material's strain-hardening ability. The extent of martensite transformation is determined by various parameters, the most important of which are the chemical composition of the susceptible material and the testing temperature at which the plastic deformation occurs. Driving mechanisms that may change the local alloy composition, say reduce the austenitic stabilizers such as Ni, may promote the formation of martensitic phases. Other major influencing parameters include the amount of plastic strain that is imposed, the deformation mode or stress state, and the grain orientations.

ϵ -Martensite

HCP ϵ -martensite is characterized by a HCP lattice structure with lattice parameters that are typically found to be around $a_\epsilon = 0.2532$ and $c_\epsilon = 0.4114$ nm. It may appear as very thin plates or lenses in austenitic SS, typically with a thickness of around 100 nm's in width [73]). In a similar fashion as was discussed for the case of deformation twinning, the ϵ -martensitic transformation follows from the gliding of $a/6 \langle 112 \rangle$ Shockley partials on close-packed austenitic planes. However, as displayed in Fig. 2.7B, the gliding occurs in this case on every *other* $\{111\}$ plane, resulting in a stacking that changes from the common ABCABC-stacking to the HCP stacking of ABABAB. The transformation from the parent austenitic lattice causes a material volume decrease of some 0.81%. This reduction in volume may inherently cause internal compressive stresses at localized regions in the material. The formation of ϵ -martensite typically follows the Shoji-Nishiyama (S-N) orientation relationships [75, 78], defined by: $\{111\}_\gamma // \{0002\}_\epsilon$ with $\langle \bar{1}10 \rangle_\gamma // \langle 11\bar{2}0 \rangle_\epsilon$. Hereby, the austenite unit cell normal to the close-packed atomic planes i.e. in the c-axis direction of the HCP lattice is contracted by only 1% or less [79]. What is considered to be an ϵ -martensitic nucleus is not fully understood, however Olsen and Cohen suggest that its formation may be due to overlapping stacking faults on every second $\{111\}$ austenitic planes analogously as for twinning [80]. Stress concentrations due to dislocation interactions with metallic interfaces such as grain or twin boundaries or inclusion particles may again be the driving mechanism for ϵ -martensitic nucleation. Experimental evidence of such stress-assisted nucleation is provided by TEM observations of in-situ tensile deformation tests [81].

α' -Martensite

On the other hand, α' -martensite is characterized by a distorted BCC lattice structure with a lattice parameter of $a_{\alpha'} = 0.2872$ nm. On the nucleation processes of α' -martensite in austenitic SSs under susceptible conditions, there is no common consensus on what processes lead to its formation. Though, it is described that α' -martensite may form either through a direct transformation of the parent lattice i.e. $\gamma \rightarrow \alpha'$, or an indirect transformation following the intermediary phase of HCP martensite i.e. $\gamma \rightarrow \epsilon \rightarrow \alpha'$ [48, 82]. Stress-assisted and strain-induced transformation of α' -martensite are two distinct mechanisms of direct transformation [82]. Of all the possible orientation relationships with the parent

austenite phase, namely the Bain (B), Pitsch (P), Kurdjumov-Sachs (K-S), and Nishiyama-Wasserman (N-W), only the K-S [77] and N-W [78] are widely reported [83]. These orientation relationships are defined as:

$$\{111\}_{\gamma} // \{110\}_{\alpha'} \quad (2.2)$$

$$\langle 112 \rangle_{\gamma} // \langle 110 \rangle_{\alpha'} \quad (\text{N-W}), \text{ and} \quad (2.3)$$

$$\{111\}_{\gamma} // \{110\}_{\alpha'} \quad (2.4)$$

$$\langle 110 \rangle_{\gamma} // \langle 111 \rangle_{\alpha'} \quad (\text{K-S}) \quad (2.5)$$

In the case of stress-assisted transformation, the martensitic phase primarily develops into irregularly shaped platelets upon cooling down below sub-zero temperatures [48]. Strain-induced martensitic transformation, on the other hand, develops purely on the account of plastic deformation into lath-shaped martensite bands on specific deformation-induced sites, e.g., on deformation slip- or twin-bands [68]; a process which becomes dominant in higher temperature regimes [48, 72]. The direct transformation of austenite into α' -martensite requires the dissociation and glide of dislocations at deformation-induced features. Experimental evidence of direct transformation of austenite into martensite is provided in the following works [74, 83, 84]. Direct transformation of the parent austenite with a lattice parameter of a_{γ} to $a_{\alpha'}$ causes a material volume increase of some 2.57%. This volume change may cause some considerable lattice friction stresses which may induce internal cracking as a result of the transformation. Alternatively, if this transformation specifically involves deformation-induced ϵ -martensitic bands, the martensite develops in an indirect manner from the parent austenite lattice. In the works of Shen et al. [85], this type of indirect transformation is also deemed to be stress-assisted. Olsen and Cohen [86] developed a mechanism for the nucleation of α' -martensite, based upon the works of Bogers' and Burgers' (B-B) [87], from the shear interaction between two ϵ -martensitic bands. Hereby, the martensite phases obey the following orientation relationship:

$$\{0002\}_{\epsilon} // \{011\}_{\alpha'} \quad (2.6)$$

$$\langle 11\bar{2}0 \rangle_{\epsilon} // \langle 1\bar{1}1 \rangle_{\alpha'} \quad (\text{B-B}) \quad (2.7)$$

Experimental evidence of the indirect transformation of austenite into martensite is presented in the works [88–90].

2.2.4 Oxidation kinetics

Stainless steels subjected to the high temperature PWR environments have the ability to form a passivating chromium oxide layer on their surfaces due to their relatively high concentration of alloying Cr. PWRs externalize a reducing environment in which metal atoms (M) lose their electrons (e^{-}) in anodic reactions i.e., $M \rightarrow M^{x+} + xe^{-}$. The produced metal ions tend to associate themselves with reactive oxide species from the environment. These oxides adhere and passivate the surface of the metal, formulating a chromium oxide barrier between the metal and the corrosive species in the environment. This process lies at the forefront of the significant corrosion resistance of SSs. The integrity of the passivating oxide film plays an integral part in any substantial corrosion or cracking mechanisms of the material.

Under standard PWR conditions, numerous studies [91–95] have indicated that the surface corrosion of SSs produce oxides that are composed of a duplex or bi-layer product. The typical chromite oxide layer described above is regarded as the inner oxide. This oxide embodies a spinel chemical structure (i.e. of the form AB_2O_4 ; whereat $A=Fe$ and $B=Cr$, respectively), growing into the metal and surface grain boundaries. The inner oxide is usually continuous and dense over the metal alloy substrate under un-irradiated conditions [91,92], displaying a nano-grained composition while averaging around 50 – 100 nm's in thickness. Post-irradiation [91], the inner oxide demonstrates porous features which can be interpreted as signs of embrittlement. Accompanied with the growth of the inner oxide, is the presence of a Ni-enrichment layer just below the substrate metal surface underneath the metal-oxide interface. In this layer, the local Ni concentration of the enriched area can reach up to twice the alloying concentration. The origin of the Ni-enrichment is still under dispute, although its nucleation is confirmed to be of several tens up to < 100 nm in thickness [93,94]. Its formulation is claimed to be associated with either a porosity forming de-alloying mechanism [96] or because of solid-state selective oxidation mechanisms [97–99]. On the other hand, the secondary layer of the duplex oxide is known as the magnetite layer which is also composed of a spinel form M_3O_4 (whereat $M=\{Fe,Cr,Ni\}$, individually formed as Fe, or otherwise assembled from set elements in variable proportions). While the inner oxide grows at a rate in accordance with the anodic dissolution of the substrate, the outer oxide forms due to the precipitation of metallic ions with hydroxides [92] formed during processes like radiolysis, see section 2.4.3.4. It is comprised of a mixture of sparsely distributed, coarse grained, particles that form atop of the inner oxide in the environmental medium [92]. Such particles embody crystallized geometric shapes and range from several hundreds to over one or more microns in size.

The growth of the oxide layers is described by the complex diffusion of reactive oxide species through the double barrier system between the environment with the inner oxide and the oxide-substrate metal interface. Diffusion of these species entails the kinetic transport of chemicals through the transpassive oxide barrier; a process which has been described and modeled by several studies [100,101]. Amongst the proposed oxidation mechanisms, the solid state mechanism by Wagner in 1933 [102] is a widely applied mechanism for the description of the kinetic oxidation laws in high temperature water environments¹ [103,104]. In this model, Wagner assumes that metallic ions and electrons from the corrosion processes are transported across the oxide layer. The growth of the oxide is modelled by ion diffusion through metallic defects created during the corrosion process at the substrate-oxide interface. By assuming that the migration of ions and electrons across the oxide barriers is a rate-controlling process balanced by the anodic dissolution reaction, and that thermodynamic equilibrium exists at both oxide interfaces [103], Wagner was able to derive a parabolic growth rate law of the surface oxidation [102]. Encapsulated in a generalized form, Wagner's theory of solid state oxidation can also be expressed under other oxidation kinetic growth regimes. The following equations illustrate Wagner's concept of solid state oxidation growth [104]:

$$L^{m_1} = k_1 t \quad (2.8)$$

$$L = k_p t^{1/m_1} \quad (2.9)$$

$$\frac{dL}{dt} = (1 - m) k_1^{1-m} t^{-m} \quad (2.10)$$

$$\text{whereat, } \begin{cases} k_p = k_1^{1/m_1} \\ m = \left(1 - \frac{1}{m_1}\right) \end{cases} \quad (2.11)$$

whereat L and dL/dt resemble the surface oxide thickness and growth rate over time, m and m_1 take

after growth rate exponents (which assume different values for different oxidation rates), and k_p and k_1 adhere to the oxide growth rate parameters (which are affected by local stress, grain or irradiation conditions). Due to the somewhat restrictive assumptions in the solid state oxidation mechanism, oxidation under certain conditions or environments may comply with different growth rate exponents. A higher growth value for m_1 implies a bigger tendency for the steel to develop a protective oxide. These exponents define different oxidation regimes e.g., (i) a linear growth law: $(m, m_1) = (0, 1)$, (ii) a parabolic growth law: $(m, m_1) = (1/2, 2)$, and (iii) a cubic growth law: $(m, m_1) = (2/3, 3)$. The parabolic growth rate of the surface oxidation resembles the form established in Wagner's theory of solid state oxidation [102].

Particularly in high temperature water conditions, e.g. in PWR environments, Ziemniak found the parabolic kinetic growth law to be valid for the surface oxidation of austenitic SSs [104,106]. However, evidently these kinetic growth laws may change depending on the reactor environment, the passivating material, the oxidation crystallographic structure, applied stress and so on. For example, it is likely that depending on the reactor conditions, these growth laws may transition into one another under various circumstances. Seyeux et al. reported that a logarithmic, or even an inverse logarithmic growth law, is valid for very thin oxides ≤ 10 nm. In high-temperature water conditions, these oxides are typically reported at the very early stages of oxidation in 316 SSs [91,95]. After longer immersion times, the kinetic growth law may develop into the expected parabolic law as confirmed by Ziemniak.

Wagner's solid state oxidation model is deemed important for several intergranular cracking mechanisms, including the film-rupture and internal oxidation based mechanisms discussed in section 2.5. Supporting evidence is provided by TEM investigations performed by, amongst others, Newman et al. [107]. However, other oxidation models like Macdonald's point defect model [108,109] or Castle's nanopores model [110] are also adopted for SSs in PWR environments.

2.3 Irradiation of stainless steels

In PWRs, austenitic SSs used as structural materials in RPV components, must be able to bare exceptionally strenuous and challenging conditions. Depending on the operation and reactor type, the steel must withstand the corrosive action of radiolytic species while being subjected to high-temperature water coolant environments varying between 50 – 370°C. Several of the microstructural and environmental degradation mechanisms mentioned throughout this chapter are also enhanced or induced by the effects of high-energetic neutron-irradiation. In fact, fission-released neutrons may be produced in a wide energy range, typically varying between a few eV to several MeV. Its neutron energy spectrum covers thermal and epithermal neutrons ($E < 100$ eV), to intermediate and fast neutrons ($100 \text{ eV} < E < 10 \text{ MeV}$), all the way up to high-energetic or relativistic neutron energies ($> 10 \text{ MeV}$). Because the neutron energies may vary tremendously between reactors and reactor operating conditions, the structural damage that is caused over time by irradiation is typically expressed in terms of displacements-per-atom (dpa). For comparison sake, in-core RPV materials irradiated by fast-neutron ($E > 0.1 \text{ MeV}$) up to about 7 dpa, would correspond to an impact factor of around 10^{22} neutrons irradiated per cm^2 of material. In practice, most of the structural damage that is caused, relates to epithermal to fast neutrons released during the fission process. Though typically speaking, it are the most energetic neutrons that cause the most impacting harm.

¹ In this and all following instances, "high temperature water" is used in the nuclear corrosion context as it considers the water in the primary water circuit which is being held under continuous pressure of roughly 150 bar at elevated PWR operating temperatures of about 260-360°C [105].

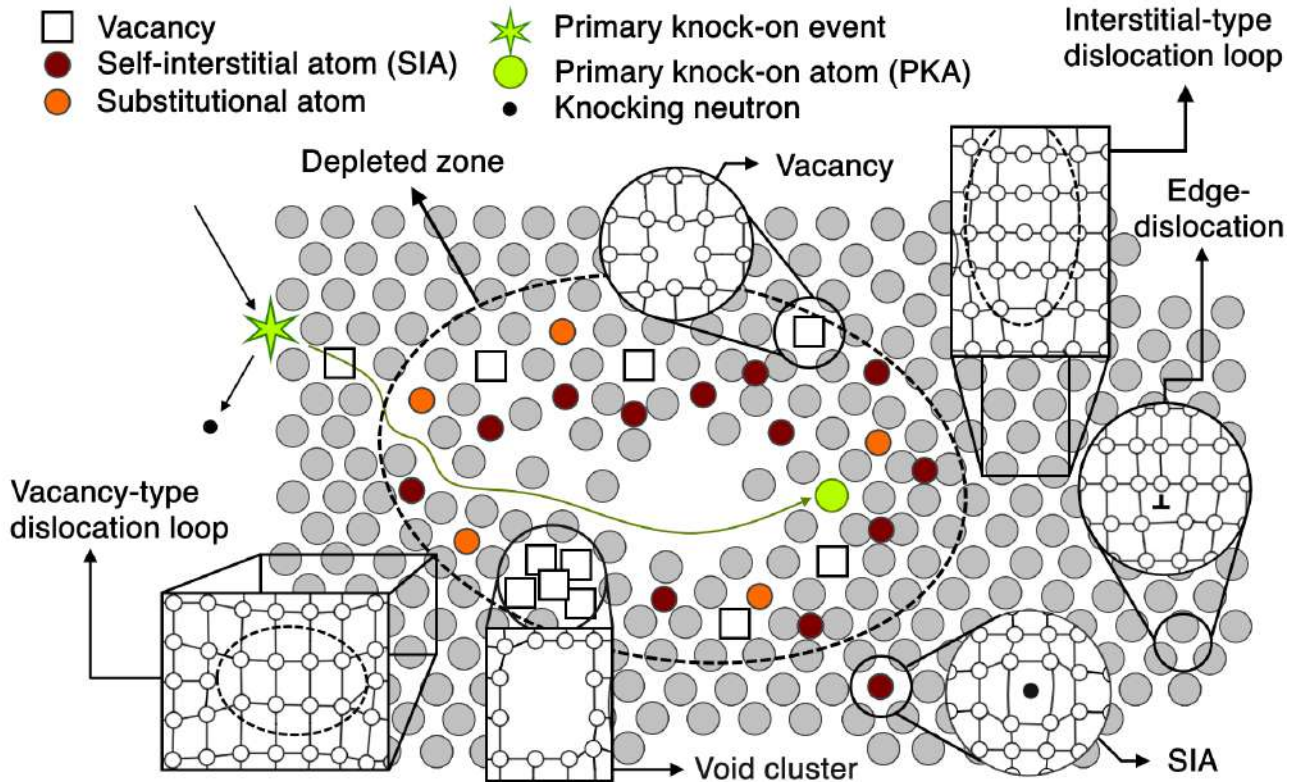


Figure 2.8: Schematic of the ballistic damage cascade following the impact of neutron irradiation in structural nuclear materials. Redrawn from references [111,112].

The meaning of displacements-per-atom is conceptualized following the impact of fission-released neutrons on structural materials subjected to radiation. Energetic neutrons may transfer their initial energy through elastic collisions with atomic nuclei and produce atomic displacements within the bulk crystalline metal matrix as a result, see Fig. 2.8. If the energy transfer exceeds a threshold value of several tens of eV, the atomic displacement results in the single ejection of an atom into an interstitial position of the lattice. The resultant displaced atom is typically referred to as a self-interstitial atom (SIA), while the lattice space it leaves behind is otherwise known as a common vacancy. SIAs and lattice vacancies are among the typical point-defects that are produced in materials subjected to neutron-irradiation. If the SIA remains electrostatically bound to its vacancy, the collective pair is referred to as a Frenkel defect. However, if the energy transfer from the neutron is insufficient to displace the atom instead, the excited atom will vibrate around its equilibrium lattice position without being displaced. Atomic displacements come in the form of single displacements resulting from a low-energy neutron collision, or following large displacement cascades from one high energetic neutron. More commonly instead, is the local displacement cascade that follows from atom-atom elastic collisions resulting from an initial large energy-transfer to produce a primary knock-on atom. The accumulated structural damage is therefore typically expressed in terms of dpa.

In the following stages after the initial ballistic phase, the damage cascade is characterized by a collection of dense interstitial atoms and lattice vacancies. At the center, a transient thermal spike is generated, induced by the collective energy deposited from the severe neutron-radiation. Driven by thermodynamics, most of the point-defects end up recombining shortly after their initial creation at vacant crystalline positions in the so-called coolant phase. Nonetheless, a relative percentage of defects remain supersaturated and evolve into microstructural defects of nanometer dimensions. In the final stage of the damage cascade, the irradiated microstructure resides within a quasi-equilibrium state

characterized by the primary damage defects existing at relatively fixed densities and size distributions.

2.3.1 Microstructural alterations

The main microstructural changes in irradiated steels come in the form of lattice dislocations, so-called Frank loops and black dots, and void cavities. Interstitial agglomerates remain two-dimensional, typically forming on high-symmetry cubic close-packed planes such as the 111 planes, while cavities may coalesce from defect vacancies in both two- and three-dimensions. These defects can impose changes on the material's microstructural and microchemical conditions, which in turn influence the overall metallurgical properties. Ultimately, the irradiation damage may lead to an increase in yield strength as well as a decrease in both material ductility (i.e., embrittlement) and fracture toughness.

Generally, the available literature around irradiated defects is centered around LWR operating temperatures and irradiation conditions [113–116]. Since neutron-irradiation is hard to replicate without in-situ tested material or access to material test reactors, contemporary studies usually perform ion-irradiation experiments under comparable reactor conditions to mimic the effects of neutron-irradiation. Reported densities and size distributions of irradiated defects typically yield similar results. Furthermore, tested under different dose-rates, the defect damage remains largely the same, i.e., not increasing beyond significant dose-rates. This indicates that the experiments tend towards a near saturated regime in terms of irradiation effects. Because the extent of these defects under different irradiation conditions is broadly known in the literature, the following section provides a general summary of their influence. However, within this thesis, no extensive study was performed regarding their density or size distribution. Rather, the induced consequences on IASCC cracking and the subsequent metallurgical changes on the account of irradiation are highlighted.

2.3.1.1 Radiation-induced microstructural defects

Frank loops

Point defects, generated by neutron-irradiation, induce an elastic strain field onto the microstructure in order to be locally accommodated by the surrounding metallic crystal structure. This strain field may stretch or compress the lattice depending on the type of defect. In order to decrease the stored lattice energy, such point defects may configure themselves into more favorable energetic configurations. In that respect, dislocation loops of either interstitials or vacancies may develop into nanometer-wide platelet-like defects situated on densely packed crystallographic lattice planes. These defects disrupt the lattice stacking order of the irradiated microstructure, and may therefore act as obstacles to dislocations under plastic deformation. To that end, dislocation loops typically lead to the hardening of the irradiated microstructure known as radiation hardening, discussed in paragraph 2.3.3.1.

One typical example of dislocation loops are Frank loops constituted from immobile SIAs, see Fig. 2.9. Frank loops are typically observed in the irradiated microstructure starting from a few dpa, only to saturate in more significantly irradiated materials beyond > 5 dpa. Typical size ranges may vary < 20 nm, with known densities, depending on environmental conditions like dose and temperature, between a few 10^{22} to $\times 10^{23}$ m^{-3} . The sizes and densities of Frank loops are heavily dependent on the material temperature. On the one hand may higher temperatures yield increased loop sizes due to an increased defect mobility, but on the other hand may it drive defect recovery and loop unfaulting, generally leading to a decrease in Frank loop densities.

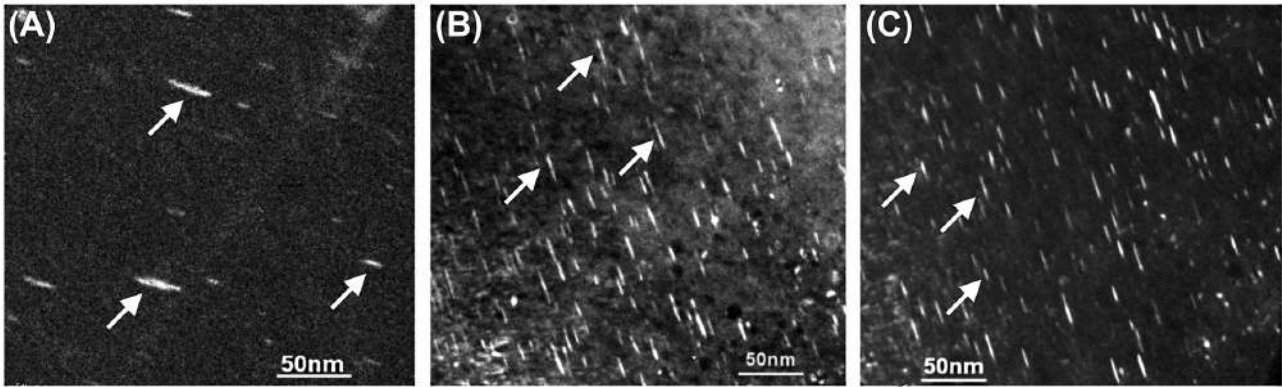


Figure 2.9: DF-TEM of typical Frank loops and precipitates observed within the microstructure of baffle bolt C47 at dose values and irradiation temperatures of (A) 18 dpa and 337-348 °C, (B) 27 dpa and 340-343 °C, and (C) 45 dpa and 340-345 °C. Figures adopted from reference [113].

Black dots

For a lack of a better term, early microscopists designated their observations of small spots as actual "black dots" in the irradiated microstructure. These black dots were later confirmed as small point defect clusters, ranging < 3 nm in size. Several studies have observed their formation in irradiated SSs [20, 42, 115–117]. Due to their limited size, it is difficult to ascertain what process is responsible for their nucleation. While some studies suggest that black dots are small or near edge-on orientated Frank loops [115, 116], other studies relate their existence with the collapse of vacancy or interstitial clusters [42]. Controversy exists whether black dots are in fact small immobile interstitial loops, likely in their early stages of formation (which seems reasonable because larger Frank loops are formed from coalesced interstitials), or directly formed from the collapse of point-defects after the primary irradiation damage cascade. Regardless, black dots are treated as part of the irradiated microstructure, and contribute to larger metallurgical effects.

Void clusters

Vacancy-type dislocation loops, otherwise known as common intrinsic stacking faults, may also form under irradiation although they are far less observed. This may be due to the fact that the binding energies between vacancy interstitials is not strong enough [116, 118], or the contribution of vacancy clustering is far larger. If observed, four intrinsic stacking faults may configure themselves into so-called stacking fault tetrahedrons (SFTs), with each main face of the tetrahedron on faulted 111 planes. SFTs are less-stable configurations which generally do not develop under PWR material conditions.

Instead, the contribution of vacancy point defects relates to the formation of cavities (void clusters), see Fig. 2.10. Cavities originate at operating temperatures of about 300°C and beyond, and form from the agglomeration of excess vacancies. Due to the large supersaturation of point-defect vacancies following neutron-irradiation, it is energetically more favorable to agglomerate into joint clusters rather than existing separately within the bulk. Collectively agglomerating into a single cavity, reduces the overall free surface area in the metal, which leads to more stable configurations. In that respect, voids are typically observed in the form of octahedral bubbles on the main close packed crystallographic lattice planes, but may grow three-dimensionally within the bulk. As such, void formation leads to macroscopic swelling of the irradiated material, typically referred to as void swelling [19, 20]. Typical

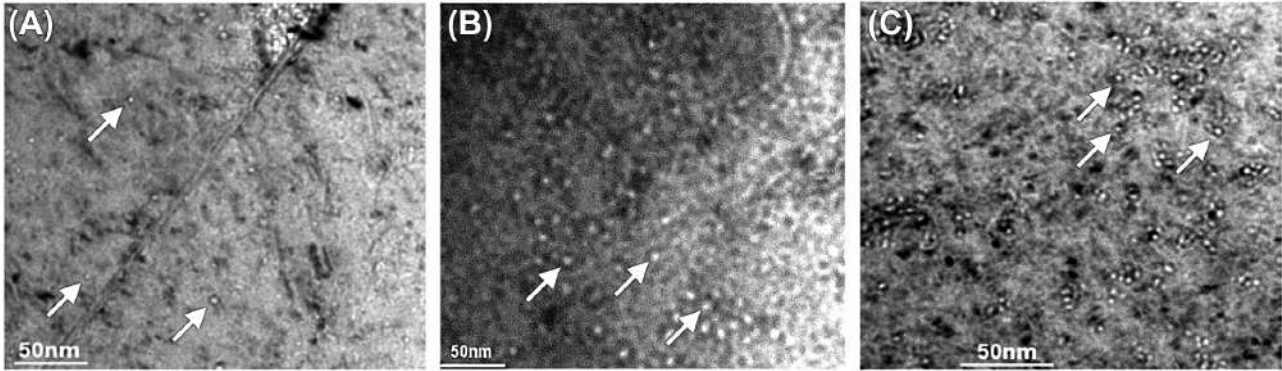


Figure 2.10: Under-focused BF-TEM of typical void clusters observed within the microstructure of baffle bolt C47 at dose values and irradiation temperatures of (A) 18 dpa and 337-348 °C, (B) 27 dpa and 340-343 °C, and (C) 45 dpa and 340-345 °C. Figures adopted from reference [113].

void swelling occurs in the following three-stage process: (i) incubation, where small voids initiate within the material; (ii) steady-state stage, where void nucleation causes the formation of cavities which grow uncontrollably; hence inducing material swelling, and (iii) saturation, where void nucleation is not the driving influence anymore for swelling. Large void clusters may ultimately grow to sizes of several tens of nm's, which collectively can induce a volumetric expansion of the material up to several percentages of its original size. Still, it is estimated that for austenitic steels, the transient regime may extend indefinitely up to very high dose rates i.e. practically suspending the saturation of material swelling [21]. In this respect, void swelling may be responsible for the generation of large tensile and shear loads within the material, which further assists other degradation phenomena. In addition, as discussed in the subsequent paragraphs, void clusters contribute to a reduced material strength and a decrease in material ductility. The reduced ductility makes the material more susceptible to brittle fracture under minor influence of plastic deformation, which from a safety perspective is intolerable.

2.3.2 Microchemical alterations

Included amongst the most important effects in neutron-irradiated materials, is the spatial redistribution of solute and impurity elements within the metal. Microchemical alterations in the material may include the localized enrichment or depletion, as well as the clustering and precipitation of structural elements at particular microstructural features or sinks. These sinks not only include grain boundaries, but also material defects such as lattice dislocations or immobile point-defect clusters such as dislocation loops and vacancy clusters induced by irradiation. Furthermore, following the impact of irradiation, the transmutation of certain structural elements generates the production of gaseous elements like hydrogen and helium, which together with the generated gamma-radiation, may accumulate material changes and heat-deposition, respectively. These microchemical alterations can alter metallurgical properties and increase susceptibility to material degradation, resulting in a deterioration of component integrity. Furthermore, it are the microchemical changes on the irradiation affected grain boundaries that are of main interest in terms of intergranular IASCC cracking. To that end, the influence of radiation-induced segregation (RIS), phase precipitate formation, and transmutation reactions, is discussed in the subsequent paragraphs. RIS is, first and foremost, believed to be among the main precursors to IASCC.

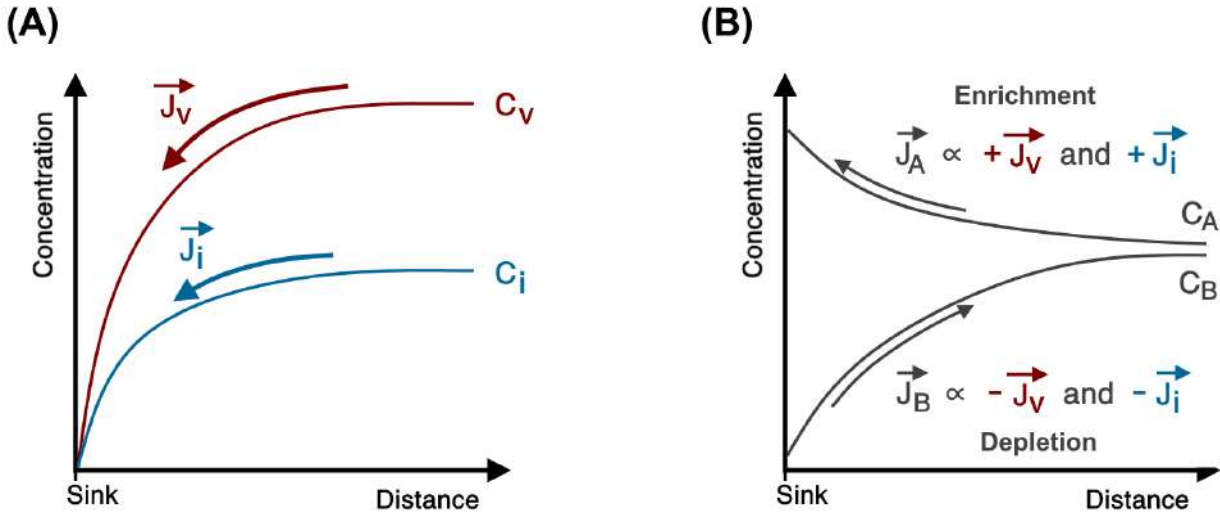


Figure 2.11: Illustration of the effects of radiation induced segregation. (A) Point defect concentrations profiles and fluxes of vacancies (C_v, \vec{J}_v) and interstitials (C_i, \vec{J}_i) in close vicinity to microstructural sinks. (B) Concentration profiles and corresponding element fluxes ($C_{A,B}, \vec{J}_{A,B}$) of elements A and B being enriched or depleted in association to the point defect flux.

2.3.2.1 Radiation-induced segregation

A great number of studies observed the preferential segregation or depletion of structural and solute elements at microstructural sinks following the effects of neutron- and proton-irradiation experiments [20,42,119–124]. Collectively, this redistribution of elements across the bulk metal is termed radiation-induced segregation (RIS). RIS is found to be dependent on the irradiated dose rate and the irradiation temperature of the material, and takes maximal effect at and around PWR operating temperatures in the early dpa irradiation regime [42,119]. Moreover, Fukuda [120] confirmed that the effects of RIS increased as the irradiation temperature was raised. Still, RIS is confirmed to reach a steady state condition after a certain irradiation dose. In austenitic steels, the saturation dose for RIS is estimated to be around 5 dpa [22]. Since IASCC cracking in irradiated SSs exclusively occurs at the grain boundaries, the microchemical effect on the cracking susceptibility following RIS is of great interest in the literature [22].

Two competing mechanisms are considered to be responsible to explain the transport of structural and solute elements to microstructural sinks [17,125]. The underlying driving force supporting both mechanisms is based on the mobility of radiation-induced point defects (vacancies and interstitials). Point defects tend to annihilate at the sinks, resulting in a strong concentration gradient in its near vicinity. The concentration of the point defects and its associated defect fluxes, (C_v, \vec{J}_v) for vacancies and (C_i, \vec{J}_i) for interstitials, are depicted in Fig. 2.11A. The influx of point defects is in accordance with Fick's laws of diffusion. Structural or solute elements that tend to be subjected to RIS, may associate themselves with the point defect flux and may wind up segregating or depleting at the microstructural sink. Such sinks may constitute of bulk metal grain boundaries, but also immobile nanoscale defects such as dislocation loops and void clusters or precipitate formations may be affected. On the one hand, some elements may preferentially bind to the vacancy point defect flux, while other elements associate themselves with the flux of interstitial atoms. The resultant of this coupling with the defect flux is depicted in Fig. 2.11B. Enrichment at the sink may occur when the point defect fluxes align in accordance to the element flux i.e., transportation to the sink, while depletion occurs in the reverse direction.

RIS is primarily affected by the diffusion rates of the point defects, but may also depend on the binding enthalpy between the affected solute and the vacancy, or even on the size factor of the solute atom in question. Solutes that typically bind with structural lattice vacancies engage in the so-called vacancy exchange mechanism, otherwise referred to as the inverse Kirkendall effect, while on the other hand, the elements that engage with the interstitial flux participate in the interstitial-solute transport mechanism. In relation to the vacancy exchange mechanism, solute atoms may feel electrostatic attraction to vacant lattice positions if the binding enthalpy between both elements is high. In this case, the solute may bind and diffuse along with the vacancy across the lattice i.e., solute drag. Otherwise, in the event that there is no electrostatic attraction, the vacancy and solute atom simply exchange position, hence moving in opposite directions away from one another, see Fig. 2.12A. Therefore, two separate flux directions are considered within the vacancy exchange mechanism based on the electrostatic attraction of the solute (s) with the vacancy defect (v) i.e., $\vec{J}_s// + \vec{J}_v$ or $\vec{J}_s// - \vec{J}_v$. These fluxes depicted in Fig. 2.12C, are responsible for either enrichment or depletion of the solute element in question, also see Fig. 2.11B. On the other hand, in consideration of the interstitial mechanism, the size factor of the solute atoms is paramount. While undersized atoms tend to preferentially exchange with interstitials, oversized atoms on the contrary preferentially exchange with vacancies. Indeed, smaller solute atoms are able to diffuse in relation to the interstitial mechanism simply by forming a so-called dumbbell configuration, see Fig. 2.12B. Interstitial-solute dumbbells may occur along the high symmetry lattice planes, or in the tetrahedral, octahedral, or even crowdion configurations. If stable, the mixed interstitial-solute dumbbell is responsible for the transport of the solute atom to a microstructural sink for interstitial atoms. In the event that the dumbbell formation is unstable, no solute transport may occur since the dumbbell does not transport the solute atom. Instead, it is expected that the interstitial sink is indirectly depleted from the solute atom in question, since the influx of other elements is more dominant. Therefore, similar as in the case of the vacancy-exchange mechanism, the interstitial transport mechanism is also responsible for an in- or outflux of the solute element (s) by an interstitial element (i) resulting in either enrichment or depletion at the microstructural sink, see Figs. 2.12D and 2.11B.

It is possible that, depending on the material and operating conditions, one mechanism valid to explain RIS is more dominant than the other. Indeed, according to Zinkle [122], the interstitial-solute transport mechanism is generally more dominant at lower temperatures and irradiation doses due to its high mobility with respect to lattice vacancies. On the other hand, the inverse Kirkendall mechanism prevails at high temperatures and dose rates because of the increased vacancy diffusion rate. Still, extreme temperature conditions may retard the effects of RIS because of decreased point defect mobility (low temperature) and enhanced recombination of point defects (high temperature). In addition, counterintuitively, highly irradiated materials may show diminishing signs of RIS due to an increased point defect concentration which promotes recombination, although no such studies have validly proven this matter. Nevertheless, it is estimated that the preferred mechanism, regarding irradiation and temperature as sole parameters, constitutes to the inverse Kirkendall effect under PWR conditions.

Generally affected elements in austenitic alloys due to RIS, enriching microstructural sinks under the influence of the interstitial drag mechanism, are Ni and Si, and to a lesser extent P [122]. This is due to the fact that these elements are undersized solutes which more easily configure in mobile interstitial dumbbell formations. Ni is the most characteristically affected element because its segregation occurs over a wide temperature and irradiation dose range. On the contrary, oversized substitutional elements like Fe, Cr and Mo, but also Mn, favorably deplete at microstructural sinks mainly due to the inverse-Kirkendall vacancy-exchange mechanism. The effects of most structural and concentrated solute elements is known, though uncertainty still remains regarding some minor and trace elements.

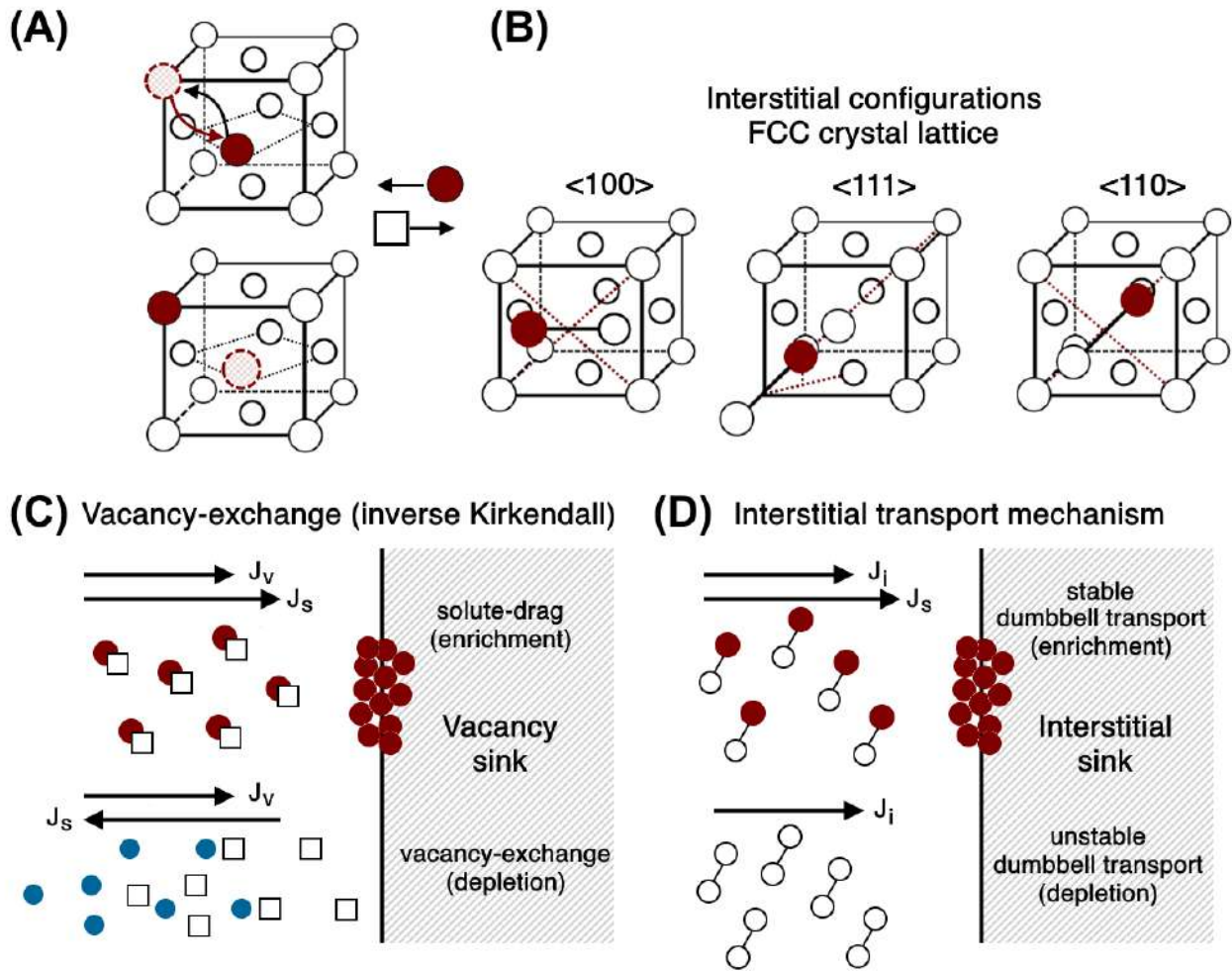


Figure 2.12: Radiation induced segregation mechanisms: (A) low binding enthalpy vacancy-exchange mechanism for FCC lattices, (B) formation of high symmetry interstitial dumbbells in FCC lattices, (C) solute drag vacancy-exchange mechanism, illustrating either enrichment or depletion respectively, depending on the vacancy-interstitial binding enthalpy, and (D) interstitial transport mechanism, illustrating either enrichment or depletion depending on the stability of the dumbbell configuration.

Undersized solutes like C, B, and N, are expected to segregate although little evidence has been presented so far [17]. If B does segregate, its transmutation may make He a potential segregant at sinks as well.

It is important to note that RIS is often implicated as one of the main precursors to IASCC in SSs [17, 22, 23, 38]. Bruemmer et al. [42, 126] showed strong correlations between low grain boundary Cr-content as a consequence of RIS and an increased susceptibility in intergranular SCC. Cr-depleted zones adjacent to the grain boundary can be of the order of several hundreds of nanometers, hence providing significant volume change of depleted material and therefore promoting the crack growth [17]. Additionally, the low Cr-content on the grain boundary may have deteriorating effects on the formation of passive oxide films which are more prone to cracking [127, 128]. The influence of minor solute elements like Si and P are implicated to lead to increased crack growth rates [121, 129]. Indeed, Yonezawa [130–132] and Li [129] provided extensive evidence showing that increased Si concentrations in alloys that are tailor-made to imitate the compositional effects of irradiated grain boundaries in an otherwise unirradiated sample, result in an increased cracking susceptibility. Chopra [23] also linked

the segregation of Si by RIS to an increased susceptibility to IASCC, expressing that Si under all relevant conditions may oxidize to SiO_2 , which is highly soluble in high temperature water. A similar argument can be made for B which is known to oxidize to BO_3 i.e., also soluble in high temperature water. The implications on IASCC of other impurity elements segregating to grain boundaries, like S, P, C and N, remains inconclusive [17].

2.3.2.2 Phase precipitation

In a similar fashion as to the formation of the interstitial-solute complex, the binding-enthalpy between some solutes can be considerably high. That is, for certain elements, it becomes energetically more favorable to initiate clustering so that their combined free energy is decreased. This clustering results in the formation of new phases present within the parent matrix, which is otherwise known as phase precipitation. Under irradiation, the presence of many irradiation-induced defects facilitates the precipitate reactions. Precipitation may either be enhanced or induced by the irradiation. Precipitates enhanced by radiation may form simply because the higher defect flux may enhance the transport mechanisms of structural and solute elements, thus accelerating the formation of precipitates. However, precipitates induced by the radiation, nucleate because the defect flux towards microstructural sinks increases the local solute concentration until the solubility limit is reached. Induced precipitates are modified or created in the parent metallic phase induced by irradiation, while enhanced precipitates are formed through accelerated precipitate kinetics as a consequence of irradiation. The difference lies in the fact that induced precipitates do not form without the influence of irradiation.

Many studies have indicated the formation of precipitates in stainless steels subjected to irradiation [20,42,122,123,133–135]. Precipitation is commonly reported at doses > 10 dpa and at relatively high irradiation temperatures $> 400^\circ\text{C}$ i.e., above PWR operating conditions. Still, evidence suggests that microchemical precipitation in various austenitic steels nucleated even at relatively low irradiation temperatures [136,137]. Precipitation was found to be dependent on the metallic composition, irradiation dose rate, or even to the stress that was applied during the formation [124,136–138]. Typical precipitates in 316 SS include carbides (MC , M_6C , M_{23}C_6 and intermetallic phases (σ , χ , and laves (η) phases) accelerated by irradiation, phosphides (M_xP with $x \geq 3$), or silicides (G and γ' phases); where the M stands for many possible metallic elements [135]. Carbides and intermetallic phases commonly occur in austenitic SSs during thermal ageing, and may form due to the supersaturation of alloying elements like Cr, Mo, Si and C dissolved in the matrix. The prime example of carbon precipitates in SSs is the formation of chromium carbides at the grain boundary, which sensitizes the stainless steel and may lead to a loss in alloy integrity, thus promoting intergranular cracking [139]. The silicides constitute to cubic structures rich in Si and Ni, which usually develop near microstructural sinks as a consequence of RIS (both Ni and Si are strongly enriched at grain boundaries due to RIS). The latter is also valid for the phosphide formations. The γ' precipitates are comprised of a M_3Si stoichiometry, while the G phases constitute of $\text{M}_6\text{Ni}_{16}\text{Si}_7$. The formation of each phase is typically associated with dislocation loops and may grow to several tens of nanometers.

2.3.2.3 Transmutation reactions

Of additional importance, is the absorption of neutrons by atomic nuclei and their subsequent energy excitation. Atoms may transfer their excess energy by undergoing transmutation reactions i.e., nuclear reactions leading to chemical changes through atomic transmutation into different elements. Typical examples involve the H and He production in (n, α)- and (n,p)-transmutation reactions [115], e.g. those involving alloying nickel and boron nuclei. Ni may follow the two-step process $^{58}\text{Ni}(n, \gamma)^{59}\text{Ni}(n, \alpha)^{56}\text{Fe}$ reaction, wherein ^{58}Ni after being subjected to high thermal neutrons quickly transforms into ^{59}Ni by releasing energetic gamma rays, which then readily transforms into ^{56}Fe after emitting He

(α -particles) [140]. Direct production of H may also occur at high neutron energies involving the transmutation of structural elements like Fe and Cr. Under continued operation, the accumulation of undissolved gases may start to affect the metallurgical properties of the irradiated material. In effect, gaseous He can lead to the filling of microstructural cavities formed by neutron irradiation, and may contribute to He-embrittlement or even swelling of the material. However, the contribution of H is often less considered to be of interest because it is not expected to significantly affect the mechanical properties of steels due to its high solubility and diffusion rate, especially at elevated temperatures. Following the transmutation reactions, the produced gamma rays may also contribute to local heat-deposition, termed gamma-heating. Due the photoelectric effect wherein gamma-rays interact with alloying atoms, energetic electrons may be produced which, although far less significantly than energetic neutrons, additionally contribute to atomic displacements. However, above all, the local-heat deposition drives the mobility of point defects, which facilitates the metallurgical changes in the material.

2.3.3 Metallurgical effects

As discussed in the prior sections, neutron-irradiation produces a significant network of defects within structural materials, which affects the dislocation and dislocation loop structures and produces nano-scale defect impurities and defect cluster complexes. In addition, segregation and depletion of structural and solute atoms at microstructural sinks such as grain boundaries may affect the microchemical conditions of the alloy, leading to significant volume changes at a localized scale. These irradiation-induced processes lead to metallurgical changes in the material, first and foremost towards radiation-induced hardening (RH) and embrittling (RE), but also to strain localization via dislocation channeling and irradiation-induced creep deformation. These effects have been implicated to facilitate the material's susceptibility to intergranular cracking.

2.3.3.1 Radiation hardening and embrittlement

Commercial steel alloys are described on the basis of their ability to strain under an applied stress in mechanical testing, resulting in a stress-strain response curve. The deformation under low levels of strain is described by the elastic regime of the alloy i.e., the regime wherein the deformation caused by straining the material remains reversible. Deforming the material under continued straining sets in the material yield, whereat the material elongation increases more rapidly than in the elastic regime. Additionally, when the deformation load is removed, some portion of the deformation is no longer reversible i.e., the material is plastically deformed. This point is also known as the yield point, which is the strength of the material whereat plastic deformation becomes relevant. On a crystalline scale, plastic deformation generates a number of dislocations which begin to slip along the crystalline close-packed directions in microstructural slip systems which lead to permanent deformation of the material [141]. Continued straining may lead to an increase in material strength caused by an impeded dislocation slip at high saturated dislocation pins (strain-hardening), after which a reduction on cross-sectional area (necking) leads to highly localized strains which are responsible for the specimen failure (fracture).

Following the impacts of a microstructure full of lattice defects, one consequence on the metallurgical properties of the material is hardening. If the hardening is facilitated by neutron-irradiation, it is referred to as radiation hardening (RH) [17, 18]. Otherwise, the process of hardening may occur as a consequence of dislocation interaction, which is described as strain-hardening in section 2.2.3.1. In the context of RH, solutes such as SIAs and substitutional atoms or impurities, have a shape-changing and dilatational-effect on the lattice structure. This makes them interact more easily with the inherently

large dislocation density improved by the aspect of radiation. The presence of solutes in the lattice, e.g. as the consequence of processes like RIS, may cause some lattice frictional stresses (also known as Peierls stresses) that inhibit the motion of dislocations [59]. In a much similar way, it is possible for other radiation-induced defects, such as dislocation loops (Frank- and black dots), point defect clusters, cavities, and precipitates, to serve as pinning points impeding the glide of dislocations. This inhibited motion acts as a stress concentrator in the matrix, which after a sufficiently acquired stress, may cause the dislocations to overcome the pinning-effect, only to interact once more with subsequent obstacles. The pinning of dislocations is known to increase the material hardness and yield stress. When this process is being caused by interstitial or substitutional atoms, it is often referred to as dynamic strain ageing (DSA) or solid solution strengthening. In irradiated conditions, the yield stress can reach up to 4 times the unirradiated yield strength, all the way up to > 1000 MPa under moderate dose rate PWR conditions [42]. Radiation hardening tends to saturate at and around 10 dpa. This is comparable to where intergranular cracking is first sighted in high-temperature water environments (around 5 dpa in PWR environments). Therefore, it is believed that RH, together with the localized plasticity (see following section), is a strong contributor to IASCC cracking in structural materials.

Accompanied by the increase in hardening, irradiated materials also experience a strong reduction in material elongation (ductility) and a reduction in fracture toughness [17, 42, 142]. The reduction in elongation may even drop down to less than 1% from its original value at doses and temperatures of around 4 dpa and 300°C [142]. In other words, under irradiation, the material becomes so brittle that it may break with minimal to even no prior deformation. From a safety perspective, severely embrittled materials are highly unstable because they can lead to sudden structural failures, much alike what is observed in intergranular cracking. To that end, radiation embrittlement (RE), accompanied with RH, is additionally considered as a precursor to IASCC.

As discussed in section 2.3.1.1, not only irradiation but also void swelling and gaseous He render a material invariably less ductile compared to normal circumstances [19]. While voids initially serve to harden the austenitic matrix, increased levels of swelling > 6% caused by void coalescence may lead to tensile fractures with negligible signs of ductility [143]. In addition, H but also He produced under radiation, may become trapped in void bubbles at the grain boundaries due to its high diffusivity [144]. Other mechanisms may also include the transformation reaction of segregated B under the influence of RIS, resulting in accumulated He at the grain boundaries through $^{10}\text{B}(n, \alpha)^7\text{Li}$. Grain boundary decohesion as a consequence of trapped He may lead to brittle fractures [145].

2.3.3.2 Localized deformation in irradiated steels

In addition to the increase in material hardening and embrittling, the deformation mechanisms in irradiated austenitic SSs start to change significantly. Unirradiated austenitic materials may display complex deformation mechanisms, mostly occurring along the close-packed crystallographic planes [62]. On the one hand, homogenous deformation can be expected in the form of multiple activated dislocation slip systems where dislocations glide under the influence of plastic deformation. Additionally, deformation may occur on the account of displacive finite-volume transformations such as mechanical twinning and phase transformations. Close competition may exist between one mechanism over the other, largely depending on the deformation temperature, which dictates the required strain under deformation. Low deformation temperatures typically promote the displacive transformation, while higher temperatures through thermal activation facilitates the motion of dislocations [62]. However, in irradiated materials, a significant number of defects are produced which tend to serve to a varying extent as obstacles to the dislocation motion under plastic deformation. Nanoscale defects such as cavities and faulted dislocation loops (interstitial Frank or vacancy loops), but also to a minor extent

smaller loops and void bubbles, tend to act as barriers to the dislocation slip [43]. Such barriers impede the motion of dislocations, which under normal circumstances tend to annihilate at microstructural free surfaces such as grain boundaries and twinned interfaces. As a consequence, the plastic deformation in irradiated materials becomes localized into narrow dislocation channels, which is also referenced as strain-localization [17, 22, 42, 43, 62, 146–148]. Dislocation channels represent a heterogeneous form of planar slip whereby dislocations remove or cut through nanoscale barriers across their path and glide over a limited amount of activated slip systems [149]. The shear force in which dislocations clear obstacles facilitates the path for subsequent dislocation glide, and as such, narrow channels of only tens of nanometers wide are created. To that end, the dislocation channels are also referred to as clear channels.

Strain-localization in the form of active dislocation channels has been implicated by many studies as a potential contributor to both IASCC initiation and propagation [17, 62, 147, 148, 150]. Dislocation channels often terminate at grain boundaries, where dislocations impinge and infuse on the grain boundary plane. The combination of very high stresses at the channel-grain boundary interaction due to the considerable infusion of dislocations and the reduction in strength of grain boundaries relative to the radiation hardened bulk material is estimated to promote intergranular cracking at PWR operating temperatures [17] and may result in grain boundary separation [147]. On the other hand, intergranular cracking has also been linked with localized plasticity in and around the grain boundary under the form of grain boundary sliding [148, 150]. Dislocation infusion creates a significant amount of stress on the grain boundary plane, where inherent grain boundary dislocations undergo glide, which results in sliding at the local grain boundary scale. Sliding has been implicated to be responsible for the formation of deformation ledges close to the grain boundary, which may appear as kinks or local migration of the grain boundary path. If sliding were to occur at the bulk specimen surface, it may be responsible for stressing the inherent SS oxide film and promote IASCC initiation. In that respect, sliding may be responsible for the deformation part of IASCC initiation, while corrosion is inaugurated by both crack tip oxidation and RIS.

It is well known that for SSs irradiated to doses approaching several dpa, most radiation effects such as the irradiated microstructure, RH, and RIS have the tendency to saturate. The deformation mechanisms at low irradiation doses typically show little to no plastic instability. However, for materials irradiated to higher doses, a strong decrease in material ductility and plastic instability is expected at the consequence of RE. Only a few studies have investigated the deformation behavior of LWR irradiated steels at significant dose rates [124, 148, 151]. While Nishioka et al. observed dislocation channeling and twinning to be the dominant forms of deformation in 35 dpa 316 SS at 320°C at low and fast strain-rates respectively [148], no observation of dislocation channeling was reported by Fukuya in 73 dpa 316 SS at the same temperature [124]. However, crack initiation at 125 dpa 316 SS also at 320°C was again found to be correlated with localized deformation channels by Du [151]. Together with prior grain boundary oxidation, localized deformation was found to facilitate the crack initiation by applying stress at the channel-grain boundary intersection. In addition, deformation twinning was commonly observed to accommodate high levels of localized stress at elevated doses.

2.3.3.3 Irradiation Creep

At elevated material temperatures, plastic deformation may additionally occur as a function of time at constantly imposed operation load or stress. This phenomenon is otherwise known as thermal creep [14]. Since creep occurs in load-bearing materials as a function of temperature, it is considered as a thermally activated process. Though, in accordance to irradiated materials, the generation of point defects may facilitate the overall creep rate significantly. The total irradiation creep (IC) rate may be

expressed as the sum of both the thermal creep and the contribution caused by the creep radiation component. This essentially means that, even at relatively lower temperatures where thermal aspect creep becomes negligible, structural deformation under the influence of IC may become relevant under certain operating conditions.

On a microstructural level, irradiation creep is best described by two accepted models [152–154]: (i) the climb-controlled glide of dislocations (CCG) [153] and (ii) the stress-induced preferential absorption (SIPA) of self interstitial atoms at Frank loops or at edge dislocations [154]. Under the CGB model, it is assumed dislocations may glide along the normal of their supposed slip plane i.e., dislocation climb [59]. This motion requires the addition of mobile point defects such as thermally-induced vacancies to carry the dislocations by diffusion. Vacancies in one lattice spacing may absorb with a dislocation in another, causing the dislocation to move up one atom spacing. Dislocations are also able to move down atom spacings by emitting vacancies, a process which is also referred to as dislocation climb. Climb is facilitated by large density point defects, e.g. as a consequence of irradiation, at high material temperatures where the defect mobility is increased. The glide of the dislocations between irradiation-induced obstacles, such as nanoscale interstitial loops, may produce a certain creep strain; the rate of which is responsible for the time-dependent strain under IC. On the other hand, the SIPA model explains the creep rate as the result of orientated dislocation loops with Burgers vectors aligned along the direction of the externally applied tensile stress. These dislocation loops grow preferentially in accordance to the applied stress direction and may be responsible for the preferential absorption SIAs. The stress-induced accumulation of SIAs onto the aligned dislocations and their consequent thermally-assisted climb controls the time-dependent creep deformation.

On the one hand, irradiation creep may be responsible for the relaxation of constant displacement stresses [22]; dislocation climb essentially removes dislocations from the matrix via diffusion processes, a deformation recovery process which is energetically more favorable than a fully dislocated structure. However, at the same time, the creep rate has also been implicated to cause large amounts of grain boundary sliding that can lead to localized deformation or even rupture, thus setting the stage for (IA)SCC initiation. Especially at elevated temperatures and doses of $> 350^\circ$ and > 30 dpa where the contribution of void swelling is high, IC may become a strong contributor to IASCC in irradiated materials. For PWRs, sensitive locations that conform with these conditions may be reactor core internal components such as the baffle-former bolt that screws together the baffle-former plates, particularly following the effects of gamma heating [22]. For instance, if the bolt were to swell under operating conditions, strong tensile stresses can be produced circumferentially along its symmetry axis at the points where it remains in contact with the surrounding plates. Thus, crack initiates may occur, facilitated under IC through the increased tensile load caused by differential swelling of the baffle bolt in its surrounding reactor core support structure.

2.4 (IA)SCC crack development

2.4.1 Stress intensity factor

Describing crack growth from first principles is a whole study on its own, namely the field of fracture mechanics [156,157]. Interesting reads include the works of Anderson [155] and Gross [158]. Knowing this, one renowned theoretical concept in fracture mechanics is the idea of a stress intensity factor (SIF). The SIF defines the global crack tip stress conditions which allows for the description of fundamental concepts like fracture toughness and failure criteria for specimens with brittle fractures. Furthermore, the SIF turns up multiple times in the description of the different crack growth stages (see the following section). Supposedly, as displayed in Fig. 2.13A, in the interest of a generic crack

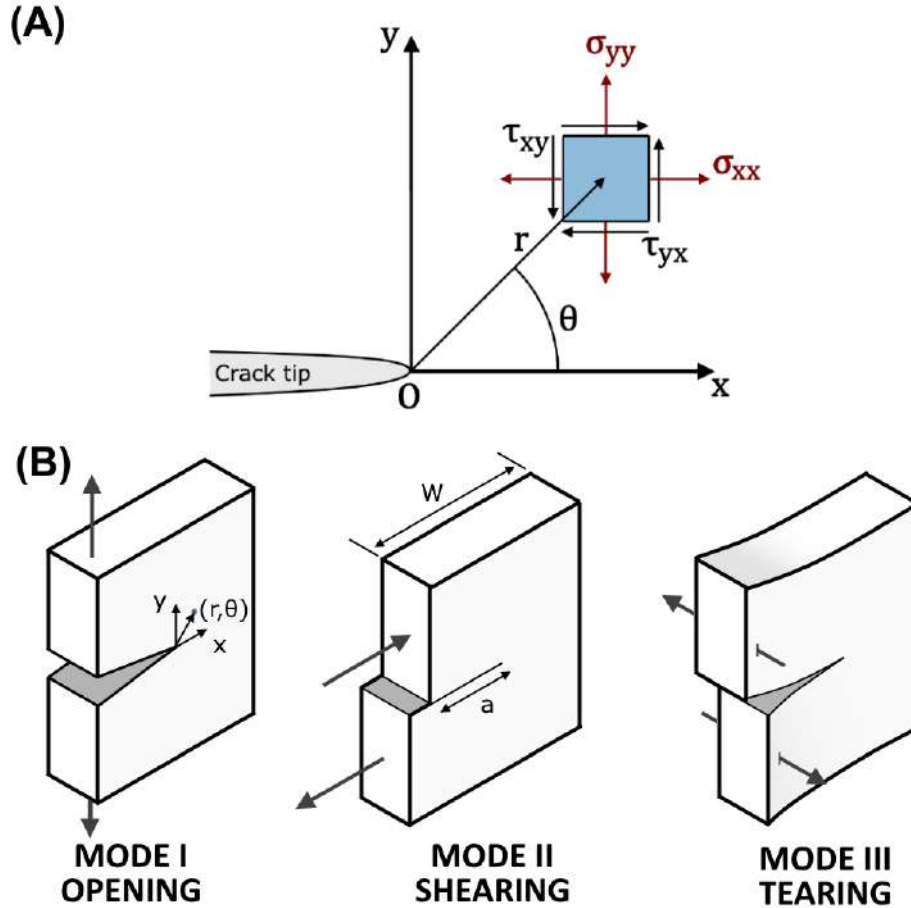


Figure 2.13: (A) First principle description of the stress distribution at the crack tip whereat σ and τ represent the normal and shear stress components in the (x,y) -directions at the crack tip. (B) Illustration of the distinct cracking modes for cracks subjected to external load. Redrawn from reference [155].

with crack length a and in a specimen with width W , the SIF K_I and the surrounding stress field σ around the crack is described as [155]:

$$K_I = f\left(\frac{a}{W}\right) \sigma \sqrt{\pi a} \quad (2.12)$$

$$\sigma_{ij}^{\iota}(r, \theta) = \frac{K_{\iota}}{\sqrt{2\pi r}} f_{ij}(\theta) + \underbrace{\sum_{m=0}^{\infty} A_m g_{ij}^{(m)}(\theta) r^{m/2}}_{\text{Higher order terms}} \quad (2.13)$$

whereby $\iota = \{I, II, III\}$ is dependent on the types of loading that the crack experiences. Fracture mechanics defines three distinct modes of loading, namely cleavage (opening), in-plane sliding (shearing), and out-of-plane sliding (tearing), see Fig. 2.13B. Each mode of loading produces different SIFs K_{ι} leading to a total stress distribution around the crack tip that is the sum of the individual σ_{ij}^{ι} components. Further terms in equations 2.12-2.13 are A_m and $g_{ij}^{(m)}$, defining the amplitude and the dimensionless tensor for the m 'th higher order terms which are completely dependent on the crack geometry. What is important to note about equation 2.13 is that the leading term is dependent on a factor $1/\sqrt{r}$, meaning that at the crack tip where r approaches 0, the stress meets a singularity point. In practice, this term leads to a stress concentration which produces a severe deformation field often referred to as the plastic zone around the crack tip. The size of the plastic zone is primarily dependent

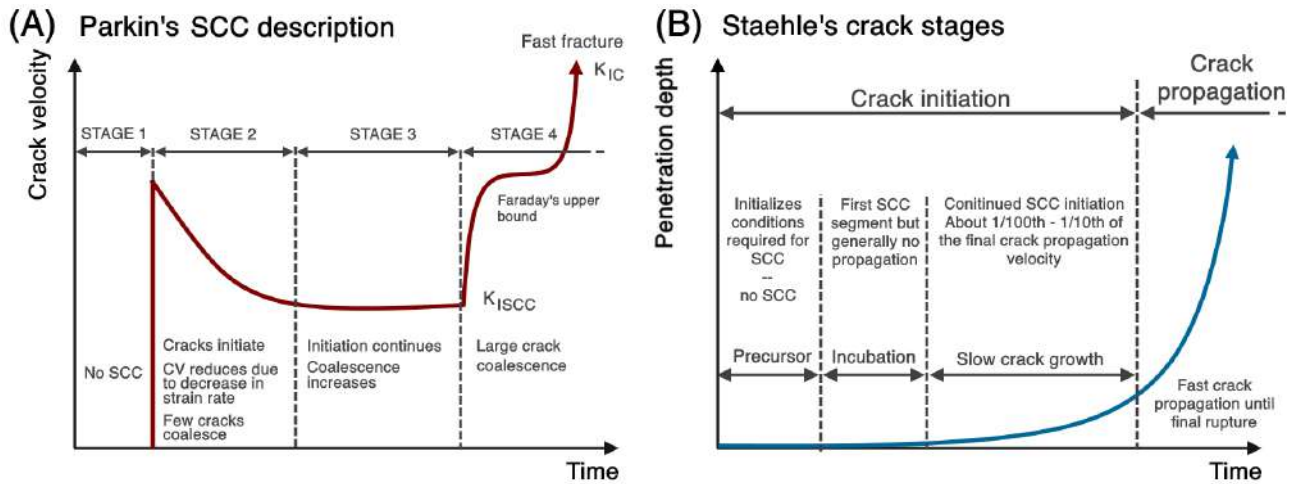


Figure 2.14: Description of SCC models according to (A) Parkin's model [159], (B) Staehle's model [160]. Redrawn according to each separate reference.

on the material parameters and the mode of loading. The deformation features that are caused by the stress concentration can be investigated with the use of electron microscopy.

2.4.2 Crack growth stages

Fracture behavior of stainless steel alloys depends on their ability to form passivating oxide films. Failures of such alloys primarily depend on the integrity of this oxide film. While pitting and crevice corrosion are largely determined by the chemical breakdown of the oxide due to its interaction with the corrosive environment, (IA)SCC crack initiation is, as a matter of principle, inherently governed by the impact of increasing strain and stress on the passive film. Studies indicated that, for the growth of SCC cracks, the time-to-failure (TTF) under relevant conditions is determined by: (i) a crack initiation period where crack growth rates are very minor, followed by a (ii) transient propagation period where high growth rates dominate the macroscopic specimen failure [159–162]. It is generally acknowledged that the majority of the time-to-failure is taken up by the crack initiation regime, followed by a short window of crack propagation that leads to the specimen failure. Therefore, it is within the interest of SCC, to fully understand the mechanisms that dominate the crack growth stages, especially the crack initiation regime.

A broad generalization of the different stages of crack development is not straightforward since crack initiation may occur differently within different materials, depending on the material composition and the environmental conditions. For example, Ni-based alloys like Alloy 600 may show sudden specimen failures after long periods of exposure time in SCC relevant conditions without showing great densities of initiated cracks [163], while the reverse may be true for SCC initiation in SSs [164]. Still, Parkins [159] and Staehle [160] proposed independently two separate models describing the various stages in crack development for stress corrosion cracking, see Fig. 2.14. Tab. 2.1 delineates a rough correspondence between both models according to the corresponding figure.

Table 2.1: Rough correspondence between Parkin's [159] and Staehle's [160] models for SCC initiation.

Crack growth stage	Remarks	Model description
Stage 1 / Precursor	Prerequisite conditions for SCC initiation are set.	Parkin's: Conditions for SCC initiation do not readily exist. Still, some deterioration mechanisms, which are best described according to probabilistic models depending on initiation stress, are in effect. Staehle's: Setting the necessary conditions for SCC crack initiation to occur, such as: surface wear, grain boundary oxidation, and depletion of alloy species.
Stage 2 / Incubation	Oxidation layer experiences damage processes, though the passivity is repeatedly restored.	Parkin's: Cracking initiates under prerequisite SCC conditions, though the CGR diminishes with time. Cracks become dormant partially due to (i) crack exhaustion i.e., loss of dynamic strain at the crack site, or (ii) crack shielding i.e., collective loss of crack-tip strain-rate due to the multiscale initiation of multiple SCC cracks. Initiated cracks may coalesce with prior dormant cracks. Staehle's: CGR increases with microscopic crack penetration in the bulk.
Stage 3 / Slow crack growth	SCC crack initiation events are no longer annulled, causing permanent cracks to initiate and coalesce.	Parkin's: Crack initiation and coalescence increases up to the point where the maximum stress intensity factor at the crack tip K_I exceeds $K_{I,SCC}$ i.e., the threshold for SCC propagation. Staehle's: Period of slow crack growth with relatively small crack penetration, where the rate of growth is much lower than in the final propagation stage.
Stage 4 / Fast crack propagation	Propagation of SCC cracks that lead to specimen failure.	Parkin's: Rapid crack propagation when the stress intensity factor at the crack tip K_I reaches the critical value for fast crack growth $K_{I,C}$, otherwise known as the fracture toughness, resulting in a short window of fast and unstable cracking that leads to specimen failure. Staehle's: Fast crack propagation period with high CGRs commences when the crack initiation regime has exceeded crack lengths of $> 500\mu\text{m}$.

2.4.3 Additional factors affecting crack growth rate

2.4.3.1 Stress

Tensile stresses are found to be a prerequisite for (IA)SCC occurrence, especially while acting upon a susceptible material placed in a corrosive environment. Acting stresses can either be externally applied or be constituted of residual stresses that remain internally effective within the material. Both account for the critical stress threshold needed for IGSCC to occur, which is usually close to the material's yield strength [165]. Externally applied stresses are commonly introduced by remote factors, such as being caused by an external load or because of a NPP's operational pressure; and are usually only considered to be a minor influence since they are comparatively low to the material's yield stress. However, residual stresses on the other hand, remain internally present and stem from the material's manufacturing processes or metallurgical degradation effects. Such residual stresses include those that come from material welding, cold-work, surface polishing or grinding, or from metallurgical degradation effects e.g. as being caused by neutron-irradiation (see section 2.3.3). Residual stresses are considered to be the most influential driving force for (IA)SCC, simply because the local stress concentration they impose is more comparable to the material's yield strength [166].

2.4.3.2 Cold-work

Cold-working is a metalworking process whereby a material is plastically deformed below its recrystallization temperatures resulting in the generation of a dislocation network, independent of the one induced by irradiation. The benefit of cold-working materials is that the additional dislocations may

accumulate and entangle with one another, thus serving as obstacles for subsequent dislocation motion under continuous deformation. In this respect, the parallel between cold-working and irradiation on material strength is equivalent i.e., both may increase the material's yield strength which translates into hardening [14,167]. In polycrystalline materials, slip systems across multiple grains can become affected, thus augmenting to the global result. To that end, cold-working may be applied to simulate to a certain extent the microstructural effect of in-service reactor components. Cold-working may be achieved through a variety of methods, though the most widespread use is found in cold rolling to certain level percentages (i.e. reduction in material thickness, usually around 20%).

It is widely accepted that prior cold-working leads to altered material tensile properties. In addition to that, cold-work has shown to have an implicate effect on deformation microstructure, passivation film, and crack growth rate [97,168–170]. Lozano-Perez [97,171] illustrated that work-hardening through cold-work may increase the density of twin deformation bands even in low stacking fault energy (SFE) alloys like austenitic SSs. Twin deformation band development in ordinary materials without the aspect of cold-work is rather uncommon since the resolved shear stress does not extend to the critical value that is required for twinning. Cold-worked microstructures can further develop high density regions of tangled dislocations characterized by a cellular substructure. In the aftermath of irradiation, Maziasz [123] concluded that this dislocation network competes with the dislocation loops induced by irradiation. It is assumed that cold-worked materials must first see its dislocated microstructure recover, before interstitial Frank loops nucleate. Moreover, in a subsequent study performed by Lozano-Perez [169], it was established that cold-work in SSs affected the surface oxidation. The increased defect density (dislocations and deformation bands) as a consequence of work-hardening can act as fast-diffusion paths for oxygen and iron, causing microstructural grain boundaries and deformation bands to preferentially oxidize more in cold-worked as opposed to non cold-worked samples. Especially when an external stress was applied, the effects of cold-work evidently increased the oxidation rates. The latter seemed to suggest some sort of stress-assisted oxidation model to allow for the increased oxidation kinetics. Cold-working also affected the thickness of the outer surface oxide under PWR conditions. On the other hand, several studies have also implicated prior cold-work to influence the cracking susceptibility in SSs under PWR conditions [97,172,173]. For instance, increased levels of cold-working noticeably increased the susceptibility to SCC in austenitic SSs [172]. Furthermore, as the yield strength increased by cold-working, a steady increase in crack growth rate in oxygenated BWR and hydrogenated PWR conditions was observed. This increase seemed to be magnified especially in the direction to which the cold-work was applied. It may be argued that, due to the increased material strength, an increase in the plastic zone around the crack tip is to be expected [170]. This local hardening would make it more and more difficult for the crack tip to deform the surrounding material, yielding a local increase in stress which is particularly undesirable at the crack tip.

2.4.3.3 Dynamic loading

The susceptibility to SCC initiation under PWR conditions in cold-worked unirradiated steels strained under different loading paths has been investigated by several authors [172,174]. In a comparison between static load (constant-load) and dynamic loading tests (CERT and cyclic loading), Raquet [172] observed SCC initiation in 304L SS and 316L SS under both conditions, though actual crack propagation only came into effect under more severe dynamic loading. The absence of crack propagation under constant load conditions was coupled with the low deformation mode, which is otherwise the case for dynamic straining. Constant loading exclusively gave rise to transgranular SCC (TGSCC) cracking, which was further confirmed by Couvant [174]. On the other hand, more severe strain paths following dynamic loading greatly enhanced IGSCC. Still, careful conclusions should be taken in regards to the specimen conditions. While Raquet [172] concluded that dynamic loading is a

prerequisite for intergranular SCC initiation, Bosch [161] observed intergranular cracking exclusively under constant load conditions. The difference between both experiments is correlated with the extent of neutron-irradiation. While in the former case no exposure to neutron-irradiation was exerted, the latter experiments were irradiated up to 80 dpa leading towards significant material hardening and embrittling; known to be precursors for intergranular cracking.

In the aftermath of variable loading-unloading cycles and operational thermal transients during LWRs operation, all structural materials including SSs, are known to endure non-monotonic cyclic loading conditions during their lifetime. Failure of such materials as being caused by the cyclic load is termed material fatigue [175]. The structural damage results in the initiation and propagation of fatigue cracks, typically driven by an experienced stress far below the material yield strength. Fatigue lifetimes of austenitic stainless steel specimens are decreased in LWR environments [176]; the reduction of which, is strongly dependent on the applied strain-rate and strain amplitude, temperature, and environmental conditions; primarily based on the dissolved oxygen concentration [90, 177]. A minimum threshold strain is required for a decrease in fatigue lives to be observed [178], while fatigue generally decreases at a decreasing strain-rate [179]. Fatigue lives are further decreased at increasing temperatures between a temperature range of 150-325 °C [180], and are also affected at low dissolved oxygen concentrations ≤ 0.01 ppm (valid for PWRs).

Crack growth of a fatigue crack is typically associated with tiny striation-marks recurring along the fracture surface [155]. The appearance of such striations is a strong confirmation that the cause of failure is by fatigue initiation [14]. Striations appear as microscopically small ridges and are produced perpendicular to the direction of crack propagation by the unloading of the stress during the cyclic deformation process. One proposed mechanism for striation formation is the plastic blunting model [181], wherein under the influence of an increasing tensile load, the fatigue crack blunts due to dislocation emission in newly generated slip planes from the crack tip after material separation. When the load decreases during the load cycle, the slip direction reverses and the compression causes the crack tip to fold inwards on itself. In the subsequent tensile part of the load cycle, the process repeats, thus producing a physical argument for the striation formation. According to this mechanism, the spacing between the striations is equal to the crack growth per cyclic load cycle (da/dN).

2.4.3.4 Corrosion potential

Intergranular corrosion from a chemical point of view is the electrochemical process that involves both an anodic metal dissolution (oxidation; i.e. reaction that produces electrons) and a cathodic (reduction; i.e. reaction that consumes electrons) reaction. These electrochemical reactions involve the transfer of charge and must balance each other out during the corrosion process. Typical reactions of each entail e.g., the dissolution of metal of which Fe is the prime constituent: $Fe \rightarrow Fe^{2+} + 2e^-$, versus the reduction of oxygen: $O_2 + 2H_2O + 4e^- \rightarrow 4 OH^-$ or water: $2H_2O + 2e^- \rightarrow H_2 + 2OH^-$. Since corrosion is associated with the flow of charged particles, the voltage, or rather the electrochemical potential (ECP) of the reactions will control the rate of corrosion. The ECP is a thermodynamic measure of the chemical potential that controls the thermodynamics and kinetics of the electrochemical reactions. ECP is typically expressed for each reaction as a logarithm dependent on the local oxidant, reductant and ionic concentrations via the Nernst relationship:

$$\phi = \phi_0 + \frac{RT}{nF} \ln \left(\frac{[\text{products}]}{[\text{reactants}]} \right) \quad (2.14)$$

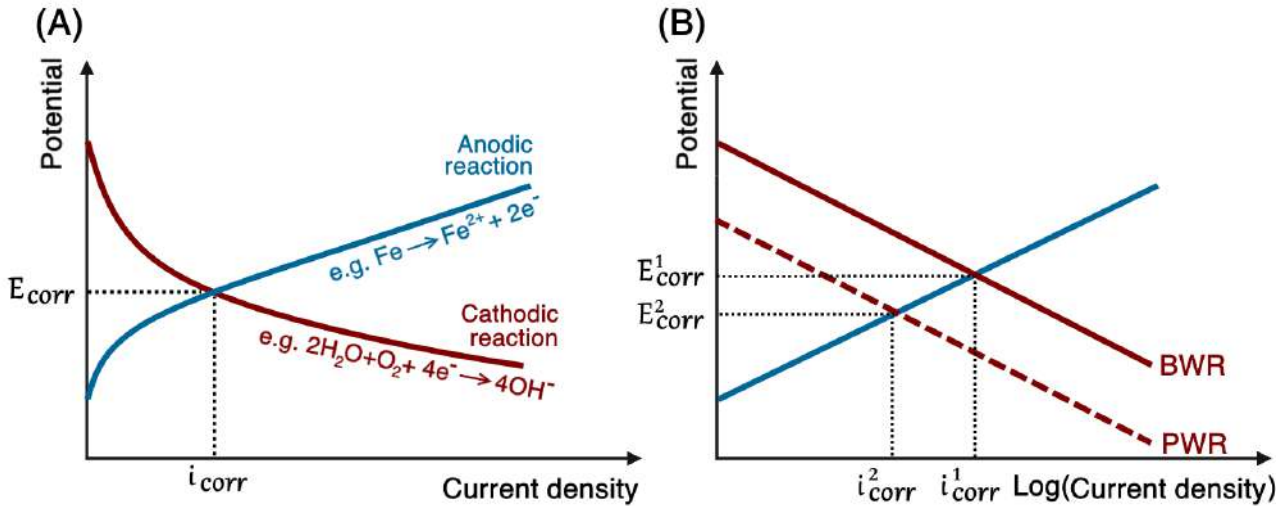


Figure 2.15: Evan's diagram for the corrosion of Fe in a cathodic solution. Redrawn from reference [182].

where ϕ is the ECP, R is the gas constant, T is temperature in Kelvin, n is the number of moles and F is Faraday's constant. In the case where only one anodic and cathodic reaction is considered, the ECPs of both are plotted as logarithmic functions in terms of their corrosion rate, expressed in terms of electric current density, in Fig. 2.15A. Corrosion is dictated by the balance of the anodic and cathodic reactions. Consequently, the corrosion rate occurs where the potential and current density associated with both reactions are equal to the corrosion potential E_{corr} and associated corrosion current i_{corr} , respectively.

A change in the ECP and current density changes the rate of the corrosion reaction, which is also known as polarization. Polarization may occur by: (i) activation i.e., catalyzing either the anodic or cathodic reaction so that a new equilibrium point is found, (ii) concentration i.e., changing the chemical concentration of reaction elements in order to change the corrosion rate, or (iii) resistance i.e., increasing the electrical resistance of the corroding components. The latter form of polarization may be achieved by separating the corroding component from the corrosive environment. This can be performed by one of two ways, namely through a passivation film (e.g. an oxide as is typically observed on SSs) or by coating the component with another metal which is comparatively less reactive than the substrate you wish to protect.

Polarization by concentration, especially following the impact of neutron irradiation, is considered highly consequential for several degradation phenomena depending on which reactor environment the corrosion occurs in. Indeed, corrosion of nuclear grade materials is not only determined by the short- and long-term effects of neutron-irradiation on the microstructure, but also by the effects of new species formed the radiolytic decomposition of water in high temperature water environments. The phenomenon of radiolysis can lead to the formation of new chemical reaction products, several of which are highly reactive free radicals and radiolytic species such as: $\cdot\text{OH}$, $\cdot\text{H}$, $\cdot\text{HO}_2$, H^+ , OH^- and O_2^- [14]. Many of these species are oxidants in the cathodic reactions, an increase in their global concentration may increase the corrosion potential i.e., accelerate corrosion reactions. Especially in BWRs where a lower hydrogen concentration (typically 10–40 ppb H_2) versus PWRs (typically 2–3 ppm H_2) is present, an increase in the corrosion rate can be expected. This is because a lower hydrogen concentration permits the radiolytic formation of oxidant species [22, 23], which effectuates in a larger corrosion current, see Fig. 2.15B. In PWRs, where the production of oxidants is suppressed due to the higher hydrogen concentration, the effect of radiolysis on corrosion rate is expected to be less severe.

In addition, the effect of the lower corrosion potential in PWRs vs. BWRs may have an effect on the different growth stages in crack development. The precursor period, wherein the prerequisite conditions for primary water SCC are being established, may be independent on the reactor environment. However, the duration of the crack incubation and slow growth periods wherein cracks first initialize and coalesce, may lengthen depending on the corrosion potential of the environment. For PWRs, less material is lost following the anodic metal dissolution reactions because of a lower corrosion potential compared to BWRs. To that end, it is expected that the lower corrosion rate in PWRs lengthens the crack incubation and slow growth periods accordingly. This is also confirmed by the later onset of IASCC cracking at higher fluences in PWRs compared to BWRs [42], simply because more initiation time is required in PWRs for IASCC cracking to occur. The effect of the corrosion potential is also proven by several studies which added oxide and hydrogen peroxide to increase the environment's corrosion potential under PWR relevant conditions [22]. An increased corrosion potential was shown to lead to a increased susceptibility to IASCC cracking in pre-irradiated 304 SS.

2.4.3.5 Passivation layer

As discussed in paragraph 2.2, nuclear materials such as austenitic SSs have the potential to form a self-healing and passivating oxide film onto their substrate surface. The formation of the oxide film is an example of the suppression of the corrosion rate by resistance polarization. In forming the passivation layer, the bare metal is shielded from the corrosive environment, impeding the charge transfer between both anodic and cathodic reactions to take place. This causes the anodic reaction rate to significantly drop down from the region where active corrosion occurs, see Fig. 2.16. The stability of the passive region is dependent on the initial Cr concentration of the affected alloy. Two curves relate the anodic behavior of steels with a different Cr concentration, one alloy with Cr comparable to 316SS (18% Cr) and the other with a lower Cr content (10% Cr) simulating the effects of Cr-depletion as a consequence of RIS at the grain boundaries [183]. The difference between both alloys is reflected by the increase in corrosion activity in the anodic and transpassive regions. Likewise, the shorter passive region indicates an increase in current density, which signifies that the passive layer is less stable at lower Cr contents. As confirmed by other studies, an increased Cr content in an oxide film formed under high temperature water conditions on austenitic alloys improves the stability of the passivation film [127, 128].

Control on the corrosion rate while in the passive state is determined by integrity of the passive oxidation film. Under long term exposure to the reactor environment, it may become difficult to maintain the full integrity of the passivating oxide film [14]. Numerous flaws can be introduced as a result of external imposed stresses or strains but also following the effects of neutron-irradiation or due to chemical break down reactions. This in turn may cause local initiation sites within the oxide at which cracks may nucleate to form small crack embryo's. It is believed that a balance is struck between coincident repetition of film breakdown mechanisms and the repassivation of the oxide film which self-heals many of the initiation sites (see also stage 2/Incubation in Tab. 2.1).

In order for (IA)SCC to occur, the balance must swing in the direction of the breakdown of the passivation film, which can be achieved through a number of processes.

1. Mechanical breakdown is facilitated under static stress in terms of irradiation or thermal creep. Creep may be considered as a uniform degradation mechanism occurring across the whole specimen surface, or site-specific, associated to microstructural features such as grain boundaries and deformation channels.

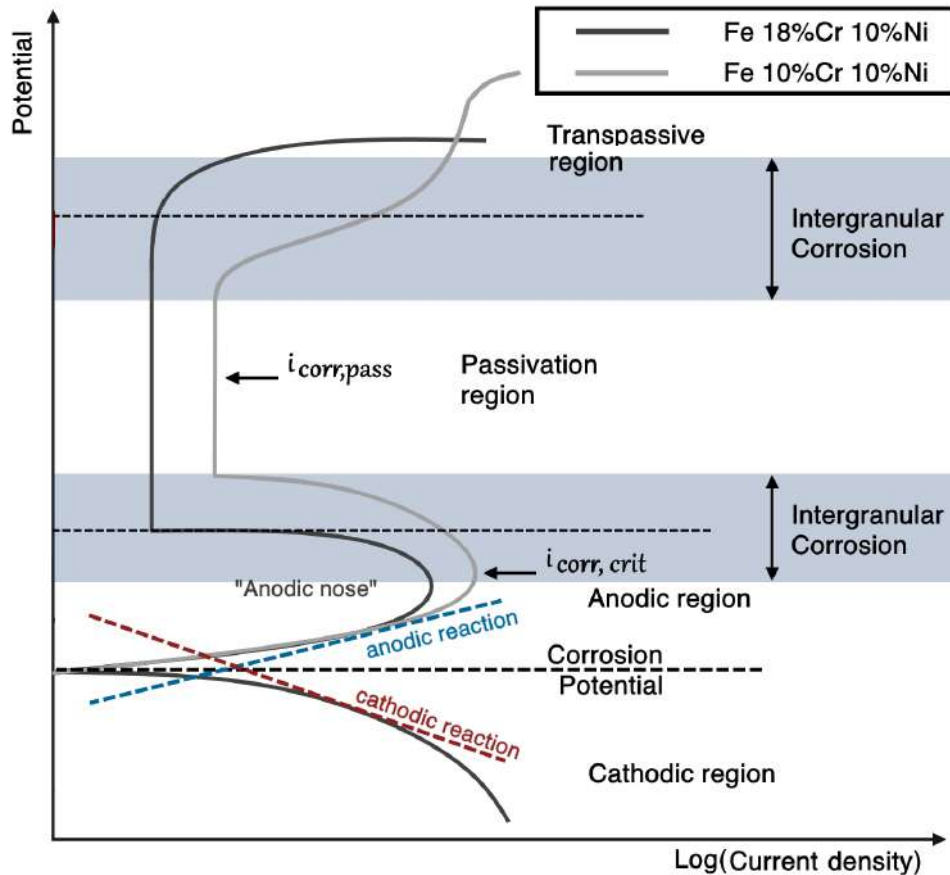


Figure 2.16: Evan's diagram illustrating the effect of passivation and Cr addition on the corrosion potential. Redrawn from reference [183].

2. In a similar fashion, oxide rupture by shear forces may also be considered as a mechanism for crack initiation. Step-like local deformation in the bulk or at the passivation layer may produce the necessary strain to shear the specimen to failure. Especially for irradiated materials where local deformation by clear channels and grain boundary sliding have been observed [147,148,150], planar deformation in shear bands may be responsible for crack initiation in the surface or grain boundary penetrative oxide.
3. Chemical breakdown of the oxide film may inherently follow from the growth of the oxide film on the metal substrate in the first place. Oxidation of bare metal causes vacancy injection from the passivation interface into the substrate under the same rate as metal ions are dissolved from anodic reactions. These vacancies join the vacancy flux which may already be present under the influence of neutron-irradiation and diffuse to microstructural vacancy sinks. Agglomeration of these vacancies to high-stressed areas can create local voids which impose a detrimental effect on the development of (IA)SCC embryos under a process known as vacancy condensation [108, 126, 184]. Voids could prevent the repassivation of the oxide film, which subjected to local deterioration, could cause it to break down chemically.

In addition to the film growth processes, Deng [128] concluded that the effects of irradiation dose scale with the thickness of the outer surface oxide on irradiated SSs subjected to simulated PWR conditions. The thickness of the passivation layer scales with the density of irradiation-induced defects within the affected material. These defects promote the diffusion of dissolute oxygen ions into the material

subsurface, accelerating the oxidation both on the material surface and along the grain boundaries. To that end, the vacancy condensation may also facilitate the transport of oxygen species in the process of internal oxidation.

2.5 (IA)SCC mechanisms

Considering the many different interdependencies between contributing factors that influence the CGRs, the various cracking appearances in different ambient environment, and the widespread variability in the failure times (from several hours up to many years, i.e. a wide experimental scatter), it becomes apparent that more than one mechanism can be responsible for the initiation of (IA)SCC. Therefore, contemporary investigations in the more recent literature have led to a more in-depth focus on the connection between the many different contributing mechanisms, rather than indicating one single responsible factor for the observed experimental and in-service failures. This rationale has produced different overarching models relating to crack initiation and propagation in order to reliably predict the susceptibility, initiation times, and CGRs for different reactor component materials.

The following section will focus on these different models suggested to describe crack initiation under the conditions that are relevant to PWR components. Amongst the proposed candidates, three different models have received considerable attention in the corrosion field regarding IASCC: (i) the film-rupture (FRM), or equivalently, the slip-dissolution model by Ford-Andresen [185, 186], (ii) the internal oxidation (IO) model by Scott and Le Calvar [187, 188], and (iii) several hydrogen-related cracking mechanisms, together encapsulated by the concept known as hydrogen-induced cracking (HAC) [189–193]. While each model has some controversial elements, all three have been used over the years to explain the experimental observations.

The FRM arguably finds strong support by many experimental and modelling studies, including by Vankeerberghen et al. [194]. This is because its primary advantage over all other models is that there is simply no other alternative model available that offers equally adequate expressions for the analytically derived CGRs equations. However, this model inherently fails at explaining some of the previously outlined (IA)SCC crack growth stages, e.g. the crack incubation and slow crack growth periods in section 2.4.2. Because the FRM only offers expressions for the anodic dissolution rate of the crack tip at the final stages of rupture, it fails to adequately predict the total time it takes for certain specimens to fail. This total time-to-failure is believed to be influenced by the close competition that exists between the crack nucleation events and the self-healing processes of the passivation layer, which are characterized by the length of the precedent growth rate stages i.e. the crack incubation and slow growth processes. Where the FRM falls short in predicting the failure time, the IO model and especially the subcritical crack propagation (SCP) model (which is based upon IO), find their strengths. Accordingly, crack growth is described by an oxide failure probability of the ingressed oxygen species along microstructural free surfaces like grain boundaries in front of the crack. The subsequent growth of the cracks may occur under a constantly applied stress well below the critical value for oxide rupture. Because it is not possible to certainly predict that the internally oxidized region determined by its failure probability will fail under a given stress, the SCP model also explains on a probabilistic basis, the inherent scatter that is found in many IASCC failure data; including the industrial component failures of BFBs [34]. The main benefits of IO and SCP lie therefore in their ability to predict the probabilistic aspect of cracking (including the inherent scatter in IASCC failure data), as well as make predictions for the total time it takes for crack propagation within the oxide to lead to a full specimen failure. However, the IO model only focuses on the role of the intergranular oxide ahead of the crack tip and consequently ignores all other potentially relevant factors nearby the crack tip location. Most importantly, these additional aspects include the localized plasticity which is

observed around the crack tip. Especially in hydrogenated PWR environments where an overpressure of hydrogen exists, potential ingress and diffusion of single hydrogen atoms within the microstructure of SSs may aid in the deformation processes and enhance the cracking susceptibility of IASCC. This form of hydrogen-induced deformation that facilitates the cracking is otherwise simply referred to as hydrogen-induced cracking (HAC).

From this representation, it becomes clear that each model has its merits to what concerns the development or predictiveness of IASCC. Still, the fact that there is no universal model that combines the positive traits from each mechanism into one, shows that IASCC is still considered a widely complex degradation phenomenon that is not yet fully understood. Corrosion experts have debated amongst themselves for several decades about which model earns more favor under which condition. In order to address this controversy, further experimental verification to what concerns intergranular cracking in irradiated materials under different environmental conditions is required. In particular, the characterization of the microstructure and morphology intergranular cracks and crack tips nucleated within the internal oxide is deemed important. It is therefore not surprising that this thesis attempts to address this missing link by investigating the failures of tested and industrial specimens. All measurements should be held accountable to each model's underlying roots in order to verify its validity under the given testing circumstances. To that end, Lozano-Perez et al. [24] issues some principle features that should be experimentally observed at the corresponding crack flanks and tips. In the following conceptualization of each individual cracking model, these principle features are highlighted in a boxed description which would aid in associating one's experimental findings to the related cracking mechanism.

Nonetheless, it is important to denote that all of the models described above are used to explain intergranular SCC (IGSCC) failures exclusively. Regarding transgranular SCC (TGSCC) in high temperature PWR water, there is somewhat surprisingly, also no common consensus on which is the most leading model to describe the observed phenomena. Still, in accordance to our observations, there is only one single mechanism that prevailed i.e. the film-induced cleavage (FIC) mechanism, discussed in the following chapter.

2.5.1 Film-induced cleavage

The film-induced cleavage (FIC) model by Sieradzki and Newman [184, 196, 197] is presented as a respectable candidate for TGSCC initiation. Historically, Edeleanu and Forty [198], continued by Pugh [199], observed cleavage-like TGSCC in α -brass and associated these fractures with a brittle-like crack initiation mechanism. Crack initiation could not be explained as the consequence of purely anodic dissolution of the substrate, because a dissolution based mechanism had to account for arguments as to (i) why the corrosion was only localized to a crack tip and not uniformly elsewhere, (ii) why the cracking appearance resembled cleavage-like surfaces, and (iii) why a certain symmetry to the crack opening formed during the cracking [195, 200]. Therefore, Galvele [201] suggested a mechanism based on the embrittlement of absorbed H atoms released during crack initiation. However, the role of H was disputed because it did not correlate well with the TGSCC cracking of other prime examples at the time, such as the cracking of Cu-Au and austenitic SSs. Furthermore, since SCC CGRs were very similar across a wide range of temperature variations, up until the critical point of water, hydrogen-assisted cracking remained controversial [197]. Rather, the believe shifted towards a mechanism with periodic crack initiation into some thin de-alloyed surface film affiliated with the substrate material susceptible to cracking. The other examples of TGSCC initiation similarly showed the existence of an epitaxial de-alloyed surface layer, which made this assumption more reasonable. To that end, it was concluded that de-alloying is a feature common to all TGSCC [184], which under oxidizing

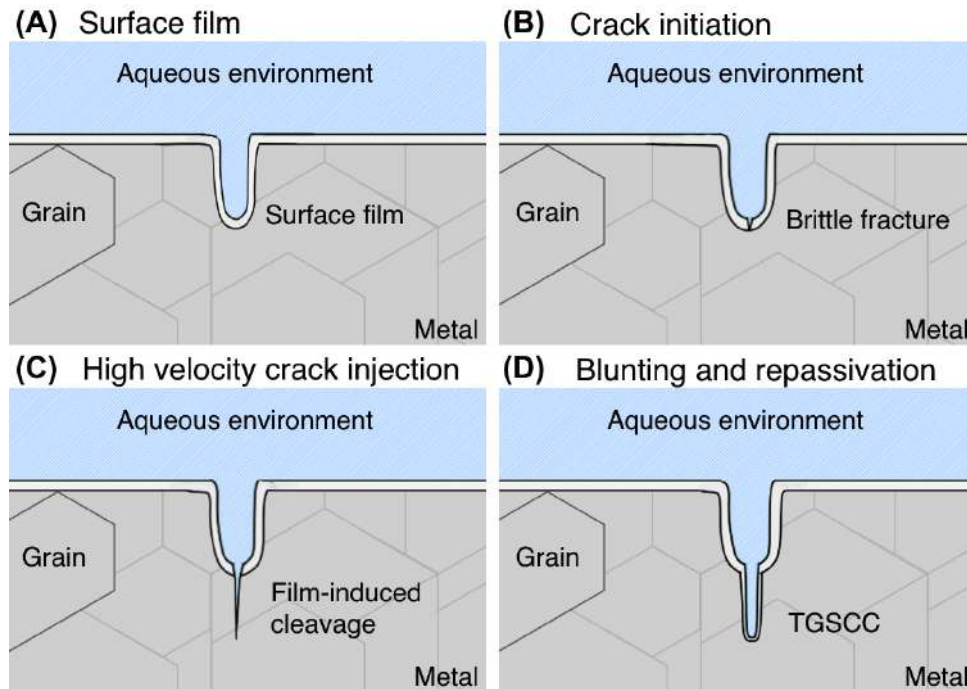


Figure 2.17: Schematic illustration of the successive events described by the film-induced cleavage (FIC) model for transgranular SCC. Redrawn according to references [184,195].

conditions usually resulted into the formation of a thin surface oxide film. There was no evidence of the mechanical properties of this de-alloyed oxide, though it was assumed that it had to be susceptible to brittle fracturing.

The FIC model has been applied on the TGSCC cleavage cracking of inherently ductile fcc materials such as austenitic SSs (alloys 304, 310 and 316), see Fig. 2.17. The basic premise of the model was the formation of a thin de-alloyed surface layer with brittle characteristics. For SSs which have the ability to repassivate, the de-alloyed layer can take the form of the thin chromite oxide surface film comprised of small nanocrystallite grains, see Fig. 2.17A. The nanocrystallites allow for nano-porosity, which is considered to be particularly effective in promoting cleavage fractures into the substrate film [202]. The resulting outcome of the de-alloying should mean that Fe and Cr other than Ni, being the less nobler elements in the austenite (Fe,Cr,Ni) alloy, should favorably dissolve in the formation of this surface film, leaving a Ni-enriched layer behind. The requirements of the surface film, other than it being susceptible to brittle fracture, should be that it is strongly adhered to the surface in order to allow for crack initiation into the substrate material and that it is sufficiently thin (around 200 Å) [196]. The sequential step in the FIC model is that the applied surface stress ruptures the de-alloyed surface film, see Fig. 2.17B. SCC can occur even at low levels of external stress, given the readily present internal contraction stresses of the substrate film following de-alloying. The fracturing of the brittle film leads to a sharp crack injection into the bulk substrate, with little loss of its initial growth rate, see Fig. 2.17C. The crack injects for a certain distance before exhausting in the surrounding ductile material substrate. Of critical importance when the crack enters the bulk, is the difference between the substrate and surface film lattice parameters [203]. Cleavage cracking of the substrate follows if the difference is positive. However, if the reverse were to be the case, significant dislocation emission following the crack injection occurs, effectively blunting and arresting the crack tip. The extent of crack advance is therefore dependent on the substrate film and the plasticity at the crack tip. Cracks may also encounter microstructural obstacles, such as grain boundaries or slip bands where extensive dislocation activity takes places, which may assist in crack blunting or arrest [202]. The crack advance

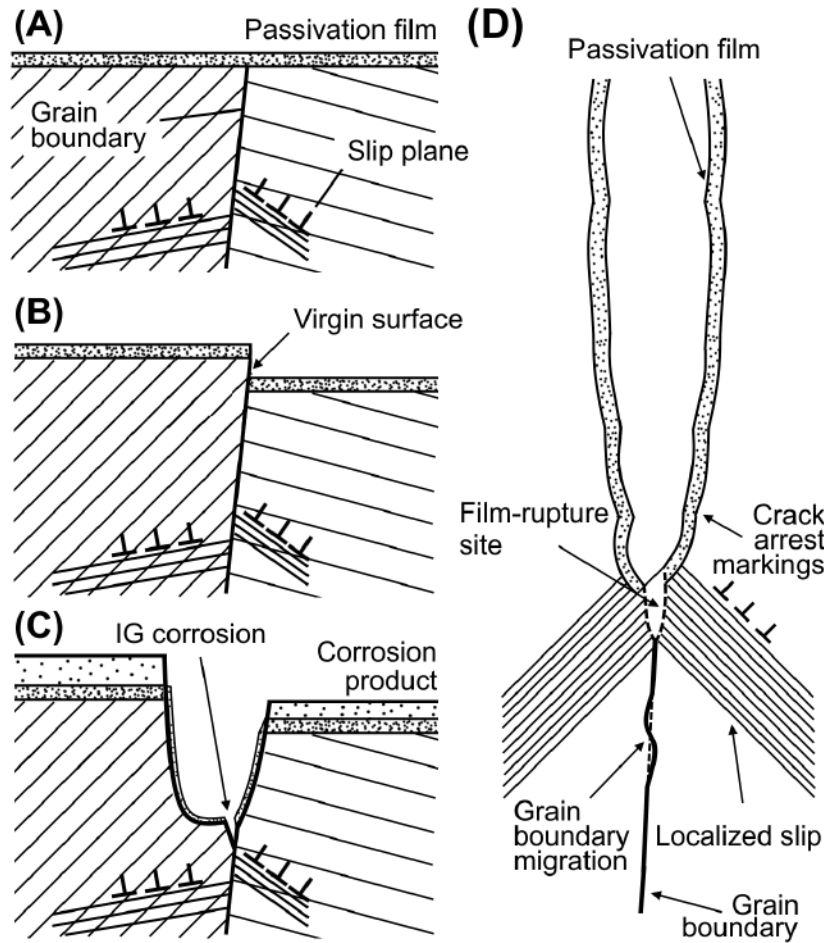


Figure 2.18: Schematic illustration of the successive events described by the film-rupture (slip-dissolution) model. Adopted and redrawn according to reference [204].

in a single discontinuous step is usually of the order of about $1 \mu\text{m}$ for austenitic steels [197]. Finally, after the crack exhausted into the substrate, the consequential blunting and repassivation seen in Fig. 2.17D set the conditions for repetition of the former steps.

2.5.2 Film-rupture or slip-dissolution model

The film-rupture model (FRM) or slip-dissolution model [205] was first suggested by Logan [206] after investigating stress corrosion on the surface films of a series of alloys, including type 302 SS. Since then, a number of models under different names have come to light [185,186,204,207,208], all describing SCC in stainless steel alloys from similar principles. Collectively, these models are categorized under the same FRM accordingly, which became among the most commonly accepted models for SCC after the adaptations performed by Ford and Andresen [185,186]. Slip dissolution, depicted in Fig. 2.18, involves the repeated cycle of (A) passivation film formation, (B) slip-based rupturing of this passivation film and therefore exposing a bare piece of the metal substrate to the corrosive environment, and finally the (C) repassivating of the corroded material. As the protective oxide film grows, it is expected that the oxidation rate drops significantly over time when approximating a certain saturation thickness. Under the continued action of stress, dislocation sources may become activated which results in a localized increase in stress that can promote the rupture of the oxide film. Such ruptures may briefly expose partial regions of the metal substrate which rapidly oxidize over time. Subsequent cycles repeat the

previous actions and lead to a subsequent increase in metallic corrosion. Crack advance is established due to the loss of ruptured oxidized material in front of the crack tip during each consecutive crack cycle. As is evident from 2.18A-C, dislocation sources within grain boundaries may act as preferential paths for dissolution, resulting in the characteristic intergranular form of SCC. In order to retain the long and tapering crack morphology of intergranular cracks, the rate of anodic dissolution at the crack flanks must be a considerable factor lower relative to the crack growth rate. This may be the result of high internal stresses caused by slip bands at the crack tip rather than at the crack flanks, see Fig. 2.18D. The repeated crack advance and arrest cycles may leave markings of crack arrest at the crack flanks under microscopical observations. Experimental results may also implicate strain-induced deformation and preferential segregation of elements (following the effects of e.g. RIS) to the slip-dissolution model.

Quantitative analysis based on the CGR for the FRM is based on Faraday's law of electrolysis. This law indicates that when the current density generated by anodic electrochemical dissolution reaction is known, the corrosion rate or equivalent mass loss rate may be calculated during the corrosion event. In terms of the FRM, the CGR depends on both the amount of dissolved material at the crack tip, and secondly, the frequency of the discontinuous rupture events t_d . To that end, the CGR may be expressed as [204, 205]:

$$\frac{da}{dt} = \left(\frac{M}{\rho z F} \right) \cdot \underbrace{\left(\frac{Q_d}{t_d} \right)}_{i(t)} \quad (2.15)$$

where M and ρ are the atomic mass and density of the dissolved metal respectively, Q_d the oxidation charge density of mechanical rupture of the oxide film cycle at the crack tip, t_d the repetition period between each consecutive film-rupture, F constitutes to Faraday's constant (9.65×10^4 C/mol), and z is the number of individual electrons lost per ion during the metal oxidation process. The fraction Q_d over t_d is an effective estimate of the corrosion current density at the crack tip $i(t)$, which is also the main feature on which the FRM relies on.

Now, the anodic dissolution process during a film-rupture event, i.e. the current density $i(t)$, is not constant over time (also see Fig. 2.16). During the transient dissolution of the bare metal, the corrosion current takes different values, see Fig. 2.19: (1) i_0 ; dissolution of the bare metal at the crack tip during time t_0 , and (2) i_p ; repassivation of the crack tip causes the dissolution rate to diminishes exponentially over time to which a full passive state is reached, indicated by point (i_p, t_p) . The following expressions are valid [104]:

$$Q_d = \int_0^{t_d} i(t) dt \quad (2.16)$$

$$i(t) = i_0 \left(\frac{t}{t_0} \right)^{-m} \quad (2.17)$$

$$Q_d = Q_I + Q_{II} + Q_{III} \quad (2.18)$$

$$\text{whereat, } \begin{cases} Q_I = i_0 \cdot t_0 \\ Q_{II} = \int_{t_0}^{t_p} i(t) dt \\ Q_{III} = i_p (t_d - t_p) \end{cases} \quad (2.19)$$

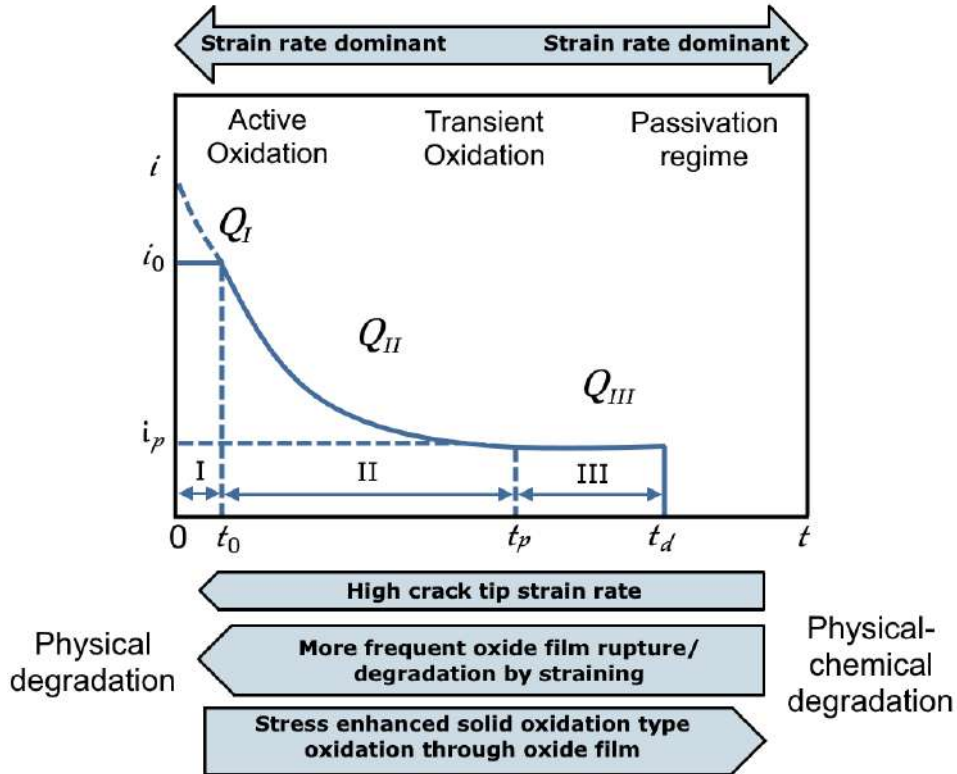


Figure 2.19: Schematic diagram of SCC sub-processes for quantitative analysis of the FRM. Adopted and redrawn according to reference [104].

where m is the exponent defined in Wagner’s solid-state oxidation laws and (i_0, t_0) are constants. Linear ($m = 1$), parabolic ($m = 2$) or cubic ($m = 3$) oxidation behaviors may typically apply under certain environmental conditions. The higher m , the bigger the tendency for the material to form a protective oxide. Particularly in high temperature PWR conditions, the parabolic growth law is found to be valid for solid state oxidation of austenitic SSs [104, 106].

In assuming that the local crack tip strain-rate $\dot{\epsilon}_{ct}$ is equal to the strain-rate of the passivation film at the crack tip, the period between each consecutive film-rupture event may be written in function of the critical threshold strain for oxide rupture ϵ_d , namely: $t_d = \epsilon_d / \dot{\epsilon}_{ct}$. Furthermore, since nuclear materials are subjected to a continuous load during operation, the SCC at the crack tip occurs continuously; thus it may be estimated that $t_d \gg t_0$ and $Q_d \approx Q_{II}$. These assumptions lead to the final CGR equations predicted for the FRM by combining all prior equations [104, 209, 210]:

$$\frac{da}{dt} = k_a^m \dot{\epsilon}_{ct}^m \quad (2.20)$$

$$k_a = \left(\frac{M}{z\rho F} \right) \left(\frac{i_0}{1-m} \right) \left(\frac{t_0}{\epsilon_d} \right) \quad (2.21)$$

Critique on the FRM has been presented on multiple accounts [205, 211–213]. Jones [211] expressed concerns about the anodic dissolution rates proposed in the FRM which do not sufficiently account for the known experimental CGRs in certain components made from brass and austenitic SS. Additionally, the FRM does not adequately explain the cases of brittle cleavage or intergranular failure where no

electrochemical dissolution was measured. Instead, the element of a brittle component responsible for crack propagation has been suggested. MacDonald on the other hand, who effectively developed a model closely related to the FRM model known as the Coupled Environmental Fracture Model (CEFM), argued that there is no strong dependence on the solution chemistry in the CGR equations [212]. This discrepancy is in effect accentuated by the exponent m in the solid-state oxidation laws. MacDonald argues that there is no theoretical justification for the value of this parameter, because as mentioned before in section 2.2.4, this value strongly depends on the chemical conditions determined by the corrosive environment. Furthermore, Gutman [205] postulated that no single mechanism can adequately explain the observed range of SCC failures across the literature. Arguably, some non-deformed materials in non-stressed conditions may show signs of IGSCC due to internal residual stresses. These experimental results could not be readily explained in accordance with the FRM since the internal stresses cannot cause film ruptures in a state of mechanical equilibrium and under constant conditions. Lastly, Hall [213] also concluded that the FRM cannot be considered as phenomenologically or fundamentally supported. Hall expressed several conceptual and mathematical problems relating with the fundamental equations of the FRM, amongst which one of the main points of critique is the fact that the current density in equation 2.17 is lacking a dependency on the crack tip strain-rate. In layman terms, in each consecutive step where the crack advances periodically determined by t_d , it should do so by having a crack tip strain-rate component. However, the current density, which is an indirect measure of the anodic dissolution rate, is not dependent on the intensity of the crack tip strain-rate at all. Hall considers that this discrepancy causes the FRM not to be fully phenomenologically accurate in describing the propagation of intergranular crack tips.

2.5: (IA)SCC Mechanisms — Film-rupture model

In order to associate crack propagation with the FRM, Lozano-Perez et al. [24] outlined the following features that should be experimentally observed at the corresponding crack flanks and tips:

1. A crack tip propagating within the bare metal substrate, ideally without any prior oxidation, relating the cracking to the final growth stage of the FRM. Nanometer thin oxidation at the crack tip may indicate subsequent repassivation.
2. Microstructural signs of a series of slip bands on the crack flanks, suggesting the repeated crack initiation and propagation nature.
3. Step-like crack flank appearances; associated with the above.

2.5.3 Internal oxidation

The internal oxidation (IO) model was first proposed by Scott and Le Calvar [187] in 1993 as a mechanism to explain the IGSCC in Ni-based alloys under PWR relevant conditions. The basic premise of the IO model was that the main alloy component remained metallic while all other alloying elements favorably oxidized under the ambient environmental conditions. For that reason, the IO model was almost exclusively used in association with the cracking of Alloy 600, simply because Ni, being the noblest prime constituent, remained resistant from oxidation while all other elements favorably oxidized through interaction with the environment. However, since then, the concept of internal oxidation has been expanded to SSs as well [214, 215]. Austenitic steels have the ability to form a passivating chromite layer that becomes, under the right conditions, brittle in nature and susceptible to fracture. Similar as were the case for Ni-based alloys, the internal diffusion of oxygen species into metallic grain boundary interfaces of austenitic SSs may embrittle the surrounding matrix and provide easier pathway for intergranular cracking to occur. In this process, the oxidized grain

boundary becomes more prone to sudden failure which facilitates the cracking.

The IO model specifically requires the physical diffusion of oxygen ahead of the crack tip prior to the cracking of that oxide itself. Intuitively, this can be achieved in one of two ways. Either, it can be demonstrated that the oxide grows faster in front of the crack tip than the crack tip itself [24], meaning that at all times, crack advancement is established within the oxidized region of the grain boundary. This would require very fast oxide growth rates, possibly comparable to or even much faster than the expected CGRs in austenitic stainless steels; estimated to be of the order of $1.00 \text{ E}-7 \text{ mm/s}$ in unirradiated 316L SS (20% CW) [173]. It is expected that these CGRs are one or several orders of magnitude faster in brittle irradiated materials, making this reasoning less likely. Alternatively, one could consider the case of a step-like crack growth model wherein crack growth is established by a continuous cycle of crack propagation followed by subsequent crack arrest. Crack tip oxidation extends for a certain depth in front of the crack tip after previous crack arrest event, after which the embrittlement has set up the conditions right for cracking. The oxidized material in front of the crack tip readily dissolves causing the arrest of the crack, beginning the continuous cracking cycle anew [105]. The step-like cracking mechanism finds evidence from observations of the microstructure close to the fracture surfaces and the crack propagation paths [104, 105, 216, 217]. The size and duration of the crack propagation steps determine the actual CGRs experienced in susceptible materials. Some of the microprocesses that influence the step-like crack growth include: (i) stress concentrations induced by strain localization of the material in front of the crack tip, (ii) enhanced oxidation along the dislocation networks in those strain localized regions, and (iii) local crack extension steps in the oxidized region in front of the crack tip [105].

Enhancing effects for an increased oxidation rate include the influence of (i) oxygen fast-diffusion paths [169, 218], be that as it may through the presence of ordinary microstructural grain boundaries that are filled with internal defects enabling the diffusion or through deformation-induced features such as dislocations and deformation slip-bands present at and around the crack and crack tip. Localized plasticity and dislocation activity in the vicinity of the crack tip or along the crack flanks may facilitate in such diffusion of oxygen. The dislocation matrix is generally increased by a significant amount through cold-work, neutron-irradiation, or through hydrogen, e.g. through the hydrogen-enhanced localized plasticity (HELP) model (see subsequent paragraph 2.5.4). Alternatively, (ii) the internal oxide may also be filled with internal oxygen defects, small pores or tiny voids, or even indications of brittle fracture bands, which could enhance the transport of oxygen [219, 220]. In fact, it is these defects that provide the main physical basis for the subcritical crack propagation (SCP) model and the stress-assisted oxidation effect (SAGBO), see subsequent paragraphs 2.5.3.1 and 2.5.3.2 respectively. On the hand, it may also be the case that (iii) grain boundary modification through chemical depletion, may assist in the oxidation kinetics. For example, Cr- and other elements depletion in the wake of RIS at microstructural grain boundaries, may act to widen the area where oxygen species can diffuse through interstitially [214].

In their work [187, 188], Scott and Le Calvar concluded that the IO model adequately reflects all known thermodynamic criteria and kinematic predictions for intergranular cracking and oxygen diffusion in Ni-based alloys at elevated PWR temperatures (within range of 300-400 °C). Rebak [221] further illustrated that the IO model provided fair predictions for experimental crack growth rates in Alloy 600. Intergranular embrittlement is established by the ingress of oxygen species, for which the fracture resistance of the corroded grain boundary is lowered. It is even established, through tensile experiments using microcantilever beam specimens of an Fe-based alloy, that the required stress to fracture an embrittled oxidized grain boundary may be as low as 360 MPa [222, 223]. However, concerning its validity for intergranular cracking under PWR environments, the IO model still faces substantial

critique - especially what regards the cracking of SSs [214]. Some studies [211, 214] cite that the grain boundary penetrative oxidation rate for SSs may be as much as up to two orders of magnitude less than the intergranular crack propagation rate. Additionally, Fukuya et al. claims not to have seen significant oxidation in front of SS crack tips, even suggesting that IASCC propagates without involvement of intergranular oxides [224]. Experimental investigations of active cracks should confirm the presence of brittle intergranular oxides ahead of propagating crack tips. Moreover, it should be established that, without the process of step-like cracking, the intergranular oxides grow faster than the propagation rate of the crack itself; thus contradicting prior observations [211, 214]. Considering specifically the case of SCC in SSs without the aspect of irradiation, no experimental verification in support of these reasonings has been presented so far. Intergranular oxides were observed in prior studies [99, 225, 226], but not to the extent to support arguments for IO. This casts some doubt about the model being applicable for SSs. However, in regards to irradiated steels, the as-irradiated microstructure not only enhances the dislocation density but also affects the leading grain boundary chemistry through processes like radiation-induced segregation (RIS). These effects may accelerate the oxidation kinetics in such a way that justifies reasonings for IO of leading grain boundary structures in irradiated materials.

2.5: (IA)SCC Mechanisms — Internal oxidation model

Experimental evidence for the IO model is very scarce [227], henceforth limiting the possibility to date to verify its validity for intergranular corrosion in SSs. However, Lozano-Perez et al. [24] has outlined the following aspects of cracking that should be experimentally observed with the internal oxidation of crack flanks and tips:

1. Each crack should exhibit a sufficiently thick oxidation layer ahead of its corresponding crack tip.
2. The internal oxide should demonstrate brittle fracture properties.
3. The oxide growth rate ahead of the crack tip should either be comparable or faster to known CGRs in susceptible materials, or, definite signs of a step-like cracking process should be observed along the crack path wherein the oxide repetitively grew beyond the crack tip to set up the conditions for cracking.

2.5.3.1 Subcritical crack propagation model

Following the notion of the IO model, Konstantinović [162] developed the basis of a probabilistic subcritical crack propagation (SCP) model² wherein the oxidized part of stainless steels plays the most essential role for crack initiation and consequent crack propagation. As readily established, intergranular oxides are responsible for embrittlement and the lowering of fracture resistance at the crack tip grain boundary. Failure of these oxides is governed by the idea of the weakest link. That is, cracking at any point in time is dictated by the inherent distribution of flaws and initiation points within the internal oxide. Such flaws at the crack tip can be constituted of internal oxide defects, pores, or multiscale fracture bands, which should be the main points of interest in subsequent microscopical studies that attempt to validate the SCP model. Nevertheless, if the cracking is entirely dictated by such flaws, it is reasonable to consider them in terms of the total probabilistic strength of the oxide. The more flaws are present, the weaker the strength of the oxide and the more prone it should be to failure. Additionally, the more voluminous the oxide is at the crack tip, the greater the chance to find an increased distribution of inherent flaws, and thus again, the more prone the oxide should be to failure. It is desirable to describe these effects quantitatively by incorporating them into a method of safe design and practical use. Therefore, because the Weibull probability distribution is often considered for its practicality in describing specimen failures dependent on statistical parameters [228], it makes

proper sense to use it here in terms of a probabilistic description of the oxide strength σ . As it would be for any probability distribution $p(\sigma)$, it should be normalized to a unit probability in terms of stress:

$$\int_0^{\infty} p(\sigma) d\sigma = 1 \quad (2.22)$$

However, when measuring the strength of the oxide, we expect that a cumulative failure probability $P_f(\sigma)$ describes the probability of failure at a specific failure stress $\sigma = \sigma_f$. The corresponding survival probability $P_s(\sigma)$ should be the complement of this:

$$P_f(\sigma) = \int_0^{\sigma_f} p(\sigma) d\sigma \quad (2.23)$$

$$P_s(\sigma) = 1 - P_f(\sigma) \quad (2.24)$$

Dedicated to the Weibull description, an expressive form of this cumulative failure probability can also be stated as [228]:

$$P_f(\sigma) = 1 - \exp \left[- \left(\frac{\sigma}{\sigma_i} \right)^m \right] \quad (2.25)$$

wherein m is the Weibull modulus or shape parameter; i.e. the inverse of the distribution width (typical values for Weibull moduli for thin film oxides range between 4.5 and 19.8, depending on the temperature and film thickness [229]), and σ_i the Weibull scale parameter; a measure of centrality of the distribution. As displayed in Fig. 2.20A, the probability of failure at no effective stress $\sigma = 0$ is zero, while when $\sigma = \sigma_i$ about 63% of the described specimens have failed.

In the SCP model, a volume-effect of the failure of the embrittled oxides can be established following the theory of the weakest link. Considering an SCC susceptible oxide subdivided into numerous individual elements n with individual volumes δV subjected to a stress σ , then the probability to failure of a single i th element is expressed as $P_f^i(\sigma, \delta V)$, while the survival probability is its inverse $1 - P_f^i(\sigma, \delta V)$. For each sub-element to survive, the survival probability of the entire volume $V = n\delta V$ is then:

$$1 - P_f(\sigma, V) = [1 - P_f(\sigma, \delta V)]^n \quad (2.26)$$

$$= \left[1 - \frac{V P_f(\sigma, \delta V)}{n \delta V} \right]^n \quad (2.27)$$

$$= \left[1 - \frac{V}{n} \varphi(\sigma) \right]^n \quad (2.28)$$

² The SCP model by Konstantinović should not be mistaken by evident notions of subcritical crack propagation in fracture mechanics, where a crack is stressed below the material's fracture strength until a critical crack length is reached, beyond which accelerating crack velocity and sudden unstable failure event are observed. SCP in accordance to Konstantinović does not consider the growth of a single crack, but rather the presence of various oxide defects at grain boundaries.

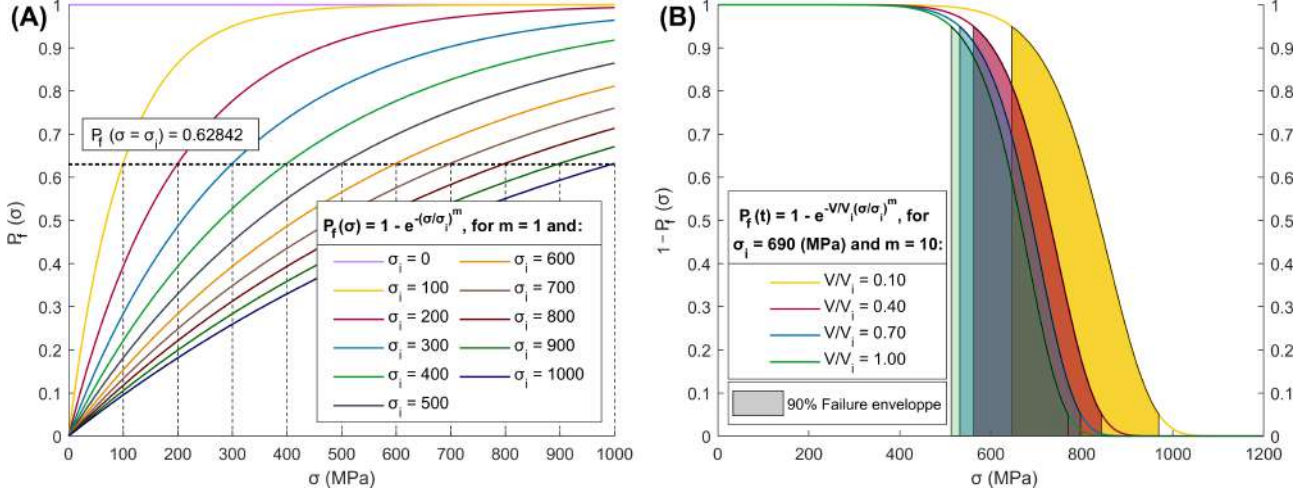


Figure 2.20: (A) Weibull cumulative failure distribution for several σ_i 's. (B) Depiction of the volume-thickness effect on the Weibull cumulative safety distribution calculated for several V/V_i 's. Calculated from equations 2.25 and 2.31.

where $\varphi(\sigma) = P_f(\sigma, \delta V)/\delta V$. When n approaches infinity, the sub-element volume δV approaches zero, so that we can make use of the following limit equality:

$$\lim_{n \rightarrow \infty} \left(1 - \frac{x}{n}\right)^n = \exp(-x) \quad (2.29)$$

so that:

$$P_f(\sigma, V) = 1 - \exp \left[-\frac{V}{\delta V} P_f(\sigma, \delta V) \right] \quad (2.30)$$

$$P_f(\sigma, V) = 1 - \exp \left[-\frac{V}{\delta V} \left(\frac{\sigma}{\sigma_i} \right)^m \right] \quad (2.31)$$

wherein equation 2.31, a typical Weibull risk function is used for $P_f(\sigma, \delta V)$ that is monotonically increasing in terms of stress. This equation provides an argument for the statistical analysis of the Weibull volume-effect based upon the weakest link theory. It takes into account how more voluminous oxides may be more susceptible to cracking, based on the probability of failure of individual oxide sub-elements. The probability of failure of a single link may lead to the fracture of the entire volume.

So far, the discussion on probabilistic crack propagation assumes an instantaneous failure of the internal oxide as being caused by the acting stress at the crack tip. However, as is discussed in paragraph 2.4.2, multiple stages of crack growth exist; e.g. the crack incubation and slow growth periods where initiated cracks are thought of as being dormant, but also the subsequent fast-growth regime where cracking occurs at substantially higher CGRs. Subcritical crack propagation [228] supposes that, just like in the case of the cracking of ceramic materials, those generally assumed "dormant" cracks instead grow slowly under a constantly applied stress until their stress intensity factor K_I reaches some critical value for the fracture i.e. K_{IC} . This slow growth continues at small crack growth rates, until at some point failure occurs characterized by fast crack growth some time after the stress was applied. The subcritical growth of cracking may occur throughout the internally oxidized material in front of the crack tip, or, set in after each crack arrest event during the step-like cracking processes discussed in section 2.5.3. Due to the subcritical growth of the crack, failure occurs not instantaneously but rather sets in a delayed form before the fast-growth regime sets in.

This reasoning presents the question what the total expected failure time of a susceptible brittle oxide subjected to a constantly applied stress could be. For that derivation, we assume the initiation of subcritical crack with crack length a under a static stress σ , for which the stress intensity factor was given by eqn. 2.12. Taking the time derivative yields:

$$K_I = \sigma f\left(\frac{a}{W}\right) \sqrt{\pi a} \quad (2.12)$$

$$\Rightarrow \frac{dK_I}{dt} = \frac{\sqrt{\pi}}{2} \sigma f\left(\frac{a}{W}\right) \frac{1}{\sqrt{a}} \frac{da}{dt} + \underbrace{\sigma \sqrt{\pi a} \frac{d}{dt} \left[f\left(\frac{a}{W}\right) \right]}_{f'(a/W) \rightarrow 0} \quad (2.32)$$

for which the last term in 2.32 can be neglected, considering that its change over time is insignificant for a subcritical crack with length a in substantially larger specimen with width W . Then, through substituting for K_I in equation 2.32, the required time for a crack to grow until fracture i.e. t_f can be derived as:

$$dt = \frac{2}{\pi \sigma^2 f\left(\frac{a}{W}\right)^2} \frac{1}{\dot{a}} K_I dK_I \quad (2.33)$$

$$t_f = \frac{2}{\pi \sigma^2 f\left(\frac{a}{W}\right)^2} \int_{K_{Ii}}^{K_{IC}} \frac{1}{\dot{a}} K_I dK_I \quad (2.34)$$

where the crack grows from its initial length whereat $K_I = K_{Ii}$ until fracture where $K_I = K_{IC}$. Then, using the relationship 2.12 in combination with the knowledge that a crack fractures at K_{IC} at stress σ_f (eqn. 2.35), the following relationship can be attained:

$$\left. \begin{array}{l} K_{Ii} = \sigma f\left(\frac{a}{W}\right) \sqrt{\pi a}, \\ K_{IC} = \sigma_f f\left(\frac{a}{W}\right) \sqrt{\pi a}, \end{array} \right\} \Rightarrow \frac{K_{Ii}}{K_{IC}} = \frac{\sigma}{\sigma_f} \quad (2.35)$$

Currently, we have found an expression of the total time for a crack to grow until specimen failure is attained, see equation 2.34. However, this expression is dependent on the CGR in the material i.e. \dot{a} , which can only be empirically estimated from experimental fracture data. The internal oxidation model does not offer an equivalent analytical expression for the CGR as the FRM does (see equation 2.20). Since the fundamentals between both models are completely different, one cannot simply insert this derived CGR equation into the IO model. Instead, the empirically derived Paris-Erdogan crack growth law $\dot{a} = CK_I^n$ is used, which is derived from experimental data [230]. In this equation, C is just a mere physical constant and n the SCC susceptibility parameter.

Substituting the Paris-Erdogan equation in the integral in eqn. 2.34, the following expression can be derived for t_d through some rigorous integral analysis:

$$t_f = \frac{2}{\pi C f\left(\frac{a}{W}\right)^2 (n-2)} \frac{1}{\sigma^n} \left(\frac{\sigma_f}{K_{IC}} \right)^{n-2} \quad (2.36)$$

where an assumption is made that for large values of n : $K_{Ii}^{n-2} \ll K_{IC}^{n-2}$. Equation 2.36 stipulates that the time-to-failure t_f of a crack under critical stress is proportional to σ^{-n} which is an important result for the SCP model. Not only does it illustrate how an increasing stress may lead to a decreasing

failure time, it may also be used to correlate any two failure times $t_1 = t_1(1/\sigma_1)$ and $t_2 = t_2(1/\sigma_2)$ with the same initial oxide strength to their respective failure stresses:

$$\frac{t_1}{t_2} = \left(\frac{\sigma_2}{\sigma_1} \right)^n \quad (2.37)$$

Equation 2.37 will become useful in the interpretation of the failure results of O-ring specimens in chapter 5. Typical expected values for the SCC susceptibility parameter n range from 15 to 40; the higher the value of n , the more reliable the material is in terms of preventing fractures. The susceptibility parameter for oxides formed on the fracture surfaces of SSs is assumed to be quite low since, in accordance to the IO mechanism, these oxides are considered brittle and thus inherently susceptible to fracture under the stressed conditions. Therefore, initial estimates of $n = 15$ as gauged by Konstantinović [162], was found to be an amendable result that indicated towards its brittleness.

Nevertheless, by combining equations 2.25 and 2.37, the final Weibull time-to-failure probability can be derived:

$$P_f(t) = 1 - \exp \left[- \left(\frac{t}{t_i} \right)^\tau \right] \quad (2.38)$$

wherein $\tau = \frac{m}{n-2}$.

Application of the probabilistic SCP model to IASCC failure data has indicated that the parameters governing the subcritical crack growth in the oxidized part of stainless steel play the most significant role towards cracking processes in IASCC. The model successfully explains several important experimental observations [162]:

1. Firstly, within the SCP model, it is established that the increase in TTF by decreasing the failure stress is best-described by the relevance of the cracking susceptibility parameter n . This parameter takes on typical values expected for transition metal oxides. Lower values for n indicate the oxide's susceptibility to brittle failure.
2. Secondly, the scatter in experimental IASCC TTF data originates from an intrinsic oxide failure probability, encapsulated by the statistical distribution of the oxide strength. Because it is not possible to certainly predict that the internally oxidized region determined in front of a crack tip will further fracture under a given stress, the SCP model explains on a probabilistic basis, the inherent scatter that is found in many IASCC failure data; including the industrial component failures of BFBs [34].
3. Furthermore, experimental observations show that there is no significant difference between the TTFs of IASCC fractured specimens irradiated from 40 up to 80 dpa samples [161]. In accordance to the SCP, this large spread in terms of irradiation dose may be explained because the oxidation has reached quasi steady state saturated thickness after these irradiation doses. Failure of these specimens is thus defined by an equivalent description of the probabilistic oxide strength.
4. Lastly, considering that relevant cracking parameters like the specimen exposure time to the corrosive environment and the applied failure stress provide conditions for subcritical crack growth, it can be assumed that the critical dpa dose for the cracking might be very low. Crack growth will be completely dependent on parameters governing the crack propagation within the

oxidized part of the SSs, if other parameters (such as exposure time and stress) provide conditions for subcritical crack growth (the cracking of NPP baffle bolts is observed to occur even at the dose of about 3 dpa. Most importantly, the failure stress threshold, even though theoretically expected for the oxide, is in practice extremely difficult to evaluate due to a very small crack velocities expected at the low stress values. Having in mind the large scatter in time-to-failures due to the stochastic nature of fracture, the concept of IASCC threshold, and the use of current estimates when assessing the component integrity, might not be a reliable methodology. The practical IASCC threshold could be defined as an acceptable cracking probability at certain times.

2.5.3.2 Stress-assisted grain boundary oxidation model

In support of the IO, intergranular oxide intrusions should be observed ahead of the crack tip intruding into the leading grain boundary, where they may embrittle the local metallic matrix and set-up the requirements for intergranular cracking. In that respect, prior studies have already denoted an intergranular oxide ingress in SSs subjected to PWR conditions [97, 220, 231, 232]. However, one interesting observation by Lozano-Perez et al. [169] illustrated that prior cold-work in addition to stress, enhanced the oxidation kinetics on the fracture surface by providing fast diffusion paths for oxygen through an increased matrix dislocation density. These observations point towards a trend of stress-assisted oxidation; allowing for a preferential transfer of mass-oxides to the fracture surface that can embrittle the local metallic matrix in setting up the right conditions for corrosion. If such stress-assisted oxidation could occur in leading grain boundaries ahead of oxidized crack tips, a phenomenon referred to as stress-assisted grain boundary oxidation (SAGBO) [233] may provide arguments for a facilitated method of intergranular corrosion. In support of this, Lu et al. [220] observed in their microscopical study of oxidized crack tips in SSs, two possible orders of oxide intrusion: (i) a long-range diffusion order ahead of the crack tip, facilitated by rapid oxide diffusion paths such as microstructural slip planes and grain boundaries, or a (ii) short-range diffusion order ahead of the crack tip, observed by the occurrence of tiny fracture bands in the intergranular oxide that can support the transfer of oxide species towards the furthest tip of intergranular oxide intrusion. Both orders are thought to be assisted by stress concentrations at the crack tip and the local deformed microstructure.

In deriving the SAGBO model, Evans [233] expanded upon the formalism of the solid state transport of oxygen species (eqns. 2.8 - 2.10) by developing stress-assisted oxidation crack growth rate equations in alloys subjected to high temperature water environments. For a stationary crack tip with an internal oxide leading into the uncracked grain boundary, the normal out-of-plane stress variation across the oxide intrusion tip is depicted in Fig. 2.21. Assuming parabolic oxidation kinetics ($m_1 = 2$ or $m = 0.5$ - valid for oxide growth under PWR environments in austenitic SSs [106]), the variation rate of the intergranular oxide length in front of the crack tip L (eqn. 2.10) is expressed as:

$$\frac{dL}{dt} = k_1^{1-m} t^{-m} \Big|_{m=0.5} \quad (2.39)$$

$$\Rightarrow \frac{dL}{dt} = k \frac{1}{L} \quad (2.40)$$

where k is the oxidation rate constant. At the crack tip, the oxidation is driven by the oxide vacancies inherently present within the oxide intrusion; the more vacancies correlates to an easier oxidation of the leading grain boundary interface. Upon oxidation, the oxygen species exchange volume with the metallic lattice; a parameter that is expressed by Ω , dependent on the total metal alloy volume Ω_M

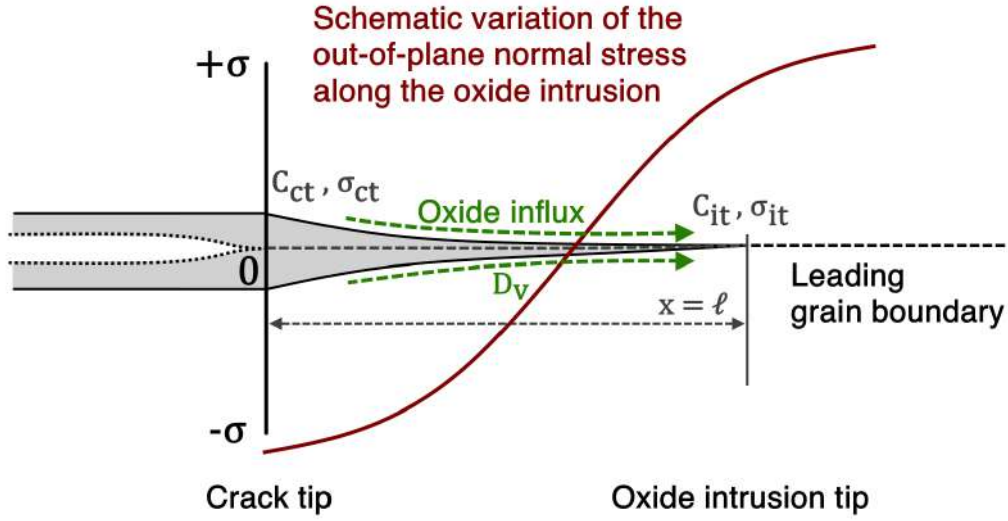


Figure 2.21: Schematic depiction of the normal stress-variation along an oxidized intrusion tip ($0 \gg x \gg \ell$) in front of a stationary crack ($x \leq 0$). Adopted and redrawn according to reference [233].

and the Pilling-Bedworth ratio ϕ_{PB} i.e. the volume exchange ratio between the formed oxide at the crack tip in exchange with the metallic matrix. The vacancy concentration in terms of a Boltzmann distributed stress $C_{v;\sigma}$ and the volume exchange parameter can be expressed as follows:

$$C_{v;\sigma} = C_{v,0} e^{\sigma \frac{\Omega}{k_B T}} \quad (2.41)$$

$$\Omega = \Omega_M (\phi_{PB} - 1) \quad (2.42)$$

$$\phi_{PB} = \frac{\text{volume of oxide}}{\text{volume of metal}} = \frac{1}{n} \frac{M_{\text{oxide}} \rho_{\text{metal}}}{M_{\text{metal}} \rho_{\text{oxide}}} \quad (2.43)$$

wherein $(C_v)_0$ is the equilibrium vacancy concentration in the absence of stress, M_i and ρ_i the molecular masses and densities of the metal and oxide species, n the number of atoms of the metal per molecule of the oxide, k_B the Boltzmann constant, and T the operating temperature. The oxide influx internally ahead of the crack is dependent on the concentration of oxide defects in the intrusion tip, driven by the stress gradient over that intrusion tip. To that end, the influx of oxide vacancies can be expressed in analogous manner of Fick's first law of diffusion:

$$J_v = -D_v \vec{\nabla} C_{v;\sigma} \quad (2.44)$$

$$= -D_v \left(\frac{\partial C_v}{\partial x} - \frac{\Omega}{k_B T} C_v \frac{\partial \sigma}{\partial x} \right) \quad (2.45)$$

with D_v the vacancies' diffusional constant and $\vec{\nabla} = \left(\frac{\partial}{\partial x} \right)$ defined over the coordinate x in the direction of crack propagation, see Fig. 2.21. In the presence and absence of stress, the influx of vacancies $J_{v;\sigma}$ and $J_{v;0}$ over the intrusion length ℓ depends on the vacancy concentrations and stress distributions at the crack tip C_{ct}, σ_{ct} and at the oxide intrusion tip C_{it}, σ_{it} :

$$J_{v;\sigma} \propto \frac{D_v}{\ell} \left[C_{it} e^{\sigma_{it} \frac{\Omega_M(\phi_{PB}-1)}{k_B T}} - C_{ct} e^{\sigma_{ct} \frac{\Omega_M(\phi_{PB}-1)}{k_B T}} \right] \quad (2.46)$$

$$J_{v;\sigma} \propto \frac{D_v}{\ell} [C_{it} - C_{ct}] \quad (2.47)$$

Because the oxygen partial pressure is much larger at the crack tip than at the oxide intrusion tip, it is expected that the oxide vacancy concentration is much lower at the crack tip than at the intrusion tip; in other words, $C_{it} \gg C_{ct}$. This concentration gradient is the foundation for the enhanced transport of oxygen species over the intrusion tip, which consequently grows over time as $\dot{\ell}_\sigma$.

$$\dot{\ell}_\sigma \propto J_{v;\sigma} \propto \frac{D_v C_{it}}{\ell} e^{\sigma_{it} \frac{\Omega_M(\phi_{PB}-1)}{k_B T}} \quad (2.48)$$

Ultimately, the SAGBO model evaluates the total stress-assisted intrusion length growth rate in the stressed state with respect to its growth under the stressed-free state over time. This evaluates in the stress-assisted enhanced oxidation parameter, otherwise known as the SAGBO parameter Φ_{SAGBO} :

$$\Phi_{SAGBO} = \left(\frac{\dot{\ell}_\sigma}{\dot{\ell}_0} \right) \quad (2.49)$$

$$\Leftrightarrow \Phi_{SAGBO} = e^{\sigma_{it} \frac{\Omega_M(\phi_{PB}-1)}{k_B T}} \quad (2.50)$$

2.5.3.3 The local model

Developed by Couvant et al. [234, 235], the so-called local model on the basis of the IO model should also not be overlooked for its relevance. It is a model dependent on a specific cracking scenario and various local parameters of the microstructure. The term 'local' relates to the grain boundary site cracking of IASCC cracks after the initial precursors are set during the crack initiation and incubation periods. The local model is originally developed for Ni-based alloys susceptible to grain boundary chromium carbides [234] but may find extensions to other material microstructures possibly be with reformulated equations such as stainless steels [235]. The local model is utilized through finite-element modelling of the three-dimensional microstructure with many different material parameters.

The strengths of the local model for IASCC cracking are its ability to predict (i) the necessary time to reach a critical oxidation depth necessary for rupture, (ii) the probability of a critical stress to fail a sufficiently oxidized grain boundary, and (iii) the ultimate crack extensions before reaching the fast crack propagation regime. The oxidation depth down the grain boundaries is modelled to be dependent on the exposure time, ambient temperature, and the dissolved hydrogen content within the primary water, as well as the grain boundary coverage of chromium carbides (specifically for the Ni-based Alloys 600 and 128), and the amount of material cold-work. Penetrative oxides are thought to lower the fracture resistance and the cohesive strength of the grain boundary by oxidation embrittlement. As is the case in all other models based on IO, this highlights the importance of the oxide grain boundary strength before fracture, estimated to be as low as 360 MPa [222, 223]. These experimental values are meant to be implemented in the finite-element calculations, that is the local

model. In accordance to the local model described in reference [234], the intergranular oxidation rate is expressed as:

$$p_{\iota} = a_{\iota} + \frac{1}{b_{\iota}} \text{Ln}(1 + c_{\iota} t) f(\Delta\text{ECP}) g(T) \quad (2.51)$$

$$\text{with, } \begin{cases} f(\Delta\text{ECP}) = H_1 + H_2 e^{-H_3 \Delta\text{ECP}} \\ g(T) = g_T e^{-\frac{Q_{ox}}{RT}} \end{cases} \quad (2.52)$$

where $\iota = \{\text{nominal, carbide, depleted}\}$ delineates the regime of intergranular oxidation rate p_{ι} in the chromium-nominal phase (dependent on the initial material Cr-content), the chromium-rich phase (at intergranular chromium-carbides), and the chromium-depleted phase (due to Cr-depletion adjacent of the carbide) respectively. Additionally, p_{ι} is modelled to be dependent on t i.e., the exposure time to the primary water environment, and three model parameters $\{a, b, c\}_{\iota}$ for the different phases. The additional function f depends on the electrochemical potential difference of the alloy and its oxide transition, as well as the dissolved hydrogen concentration H in the primary water. Lastly, the function g takes the form of an Arrhenius equation indicating the rate of the oxidation based its activation energy Q_{ox} and the local temperature T . All other parameters are deemed to be constants.

Fracturing of those grain boundaries while under the influence of stress is effectuated by crack extension dependent on the stress intensity factor K , in order to reach a slow CGR where the extensions arise from the coalescence of small initiated and incubated cracks. Crack propagation following the local model is defined as the failure of an oxidized grain boundary. Such a failure is assumed to be possible as soon as (i) the grain boundary is sufficiently oxidized up to a critical penetration value deeper than p_c (130–200 nm), and (ii) the local stress experienced at the grain boundary is higher than the critical opening stress σ_c (500–2000 MPa) required to fail the oxidized grain boundary. After a certain point, the cracking then transition into a fast CGR regime where the failure is determined by the extension of a single dominating crack.

2.5.4 Hydrogen-assisted cracking degradation

Cathodic reduction of water in the corrosive environment leads to the formation of molecular hydrogen which can partially enter, upon dissociating into mobile single hydrogen atoms, into the metal substrate and interact with the underlying microstructure. Other environmental sources of hydrogen production aside from the corrosion reactions include the radiolytic decomposition of water and the collisions of neutrons with the hydrogen atoms in water. Neutrons are very efficiently moderated by the coolant water since the nucleus of a hydrogen atom is a proton with an equal mass to that of a neutron and because the hydrogen scattering cross-section is typically quite large (about 20 barns). Also, in the case of PWR reactors, the maintained hydrogen-gas overpressure assists in the dissociation and absorption reactions of molecular hydrogen [140, 144]. On the other hand, hydrogen can also be produced directly from within the structural materials by exposure to the intense neutron-irradiation. Indeed, the main alloying components of these structural materials, which includes (Fe, Ni, Cr), all equally contribute to the formation of H (as well as He), under the exposure to the neutron-irradiation environment [144]. One typical example includes the transmutation of ^{58}Ni isotope after its interaction with fast neutrons with energies > 1 MeV, e.g. through $^{58}\text{Ni}(n,p)^{58}\text{Co}$. Other examples also include the transmutation of ^{58}Fe . Most generally, the nuclear (n,p) transmutation processes are effective in producing hydrogen, which, depending on the neutron activation energy and the nuclei involved, may be 14-20 times more efficient than (n, α) reactions are in producing helium [144].

The production of H either through environmental or through transmutation reactions may inadvert-

ently render the material susceptible to H-assisted cracking (HAC). H can be directly produced within the structural materials or through dissociation of molecular H_2 . Ingress of single H-atoms may be facilitated on several types of microstructural features and defects, including dislocations, slip planes, and grain boundary interfaces. Diffusible H may consequently become trapped at such sites, leading towards severe H-embrittlement (HE) in materials such as, amongst others, SSs. HE causes a global loss of material ductility which can, accordingly, lead to fracturing under residual or externally applied stress. HAC in susceptible materials becomes an issue of concern after being internally introduced during the metal manufacturing process or after being exposed to H-elevated PWR environments, rich in H products stemming from the radiolysis of high-temperature water.

Hydrogen degradation of susceptible materials can be summarized into the following categories: (i) hydrogen-dislocation interaction, (ii) lattice-bond interactions, (iii) internal hydrogen pressure formation, and (iv) hydride precipitation [189–193]. All four categories are considerably interrelated, though the first two mechanisms are attributed to solid solution hydrogen-interaction within the metallic lattice, while the latter two are caused by an excess concentration of H above the metal solubility limit. Relating to its interaction with metallic defects, H may considerably influence the mobility of lattice dislocations under plastic deformation, thereby altering the fracture toughness of the metal. On the one hand, H may interact with the strain-field around the dislocation and impede upon its motion, leading towards severe HE [189]; or, on the other hand, facilitate any deformation processes in regions of concentrated H that the local microstructure permits, and in the process enhance the dislocation motion under a mechanism known as H-enhanced localized plasticity (HELP) [190,191]. Lynch further proposed that the adsorption and consequent dissociation of H_2 along crack flanks may also facilitate the nucleation and mobility of dislocations [236]. The influence of H may therefore lead to both material embrittlement and softening at the same time. Secondly, on the basis of the works of Troiano and Oriani [192, 193], H ingress can also alter the metallic bond strength by material decohesion. Adsorption of H_2 may reduce the metal substrate bonds leading towards a facilitated mechanism of intergranular cracking under tensile stress. H may further diffuse into new dissociated positions at the crack front, whereupon the cracking process is repeated. This is strongly tied to the internal pressure mechanism [237] whereby single excess H-atoms recombine to form H_2 at internal free surfaces such as grain boundaries, deformation twins, or phase-transformed austenite interfaces. The building pressure of coalesced H-cavities may enhance the material decohesion and consequently facilitate the cracking mechanism. HE may suitably follow as the result of cavity formation within the bulk. Lastly, it is expected that H in excess concentrations above the metal solubility limit can interact with many metallic elements to form hydrogen-rich phases known as a metal hydrides [238]. Generally speaking,

2.5: (IA)SCC Mechanisms — Hydrogen-assisted cracking model

To associate intergranular cracking with hydrogen-related degradation, Lozano-Perez et al. [24] outlined the following aspects that should be experimentally observed in the vicinity of the cracks and crack tips:

1. Signs of trapped hydrogen, possibly in the form of hydrogen-filled bubbles, in and at the crack tip location. The concentration of H should be dependent on the local stress and chemistry at the crack tip.
2. Altered mechanical properties and/or diffusion rates.
3. Influence of the H availability on the crack growth rate.

Further aspects in favor of hydrogen-assisted cracking, include [202]:

1. Experimental observations of dimples, (nano-)voids, or cavities as evidence of H-enhanced plasticity and decohesion; especially, at the leading grain boundary interface.

such second-order phases are less dense and more susceptible to brittle fracture than the parent lattice, although for structural SSs, these phases are not observed [239].

2.6 Synthesis: (IA)SCC

The following summarizes the background literature study on SSs and their susceptibility to (IA)SCC. All known and found to be relevant LWR influential factors on cracking mechanisms and metallurgy aspects are discussed, including the effects of neutron-irradiation on the microstructure in section 2.3 and those factors affecting the crack development in section 2.4. The most leading (IA)SCC mechanisms were considered in sections 2.5 and onwards, including the film-rupture slip-dissolution mechanism, the internal oxidation mechanism, and the mechanisms related to hydrogen-assisted failure.

1 Irradiation-assisted stress corrosion cracking

1. Austenitic SSs are widely used in the primary loop circuits and auxiliary systems of PWR NPPs due to their strong manufacturing and corrosion resistant qualities. Deformation mechanisms of austenitic steels may be categorized under (i) dislocation slip and (ii) dynamic strain-ageing, (iii) stacking-fault formation, and displacive lattice transformations like (iv) deformation twinning and (v) martensitic phase transformations.
2. Neutron-irradiation strongly affects IASCC cracking, leading to both metallurgical alterations (RH/RE, localized deformation, IC) and microchemical changes (RIS, phase precipitation, transmutation) of the affected material.
3. (IA)SCC crack growth may be broadly generalized into different stages. According to Parkin's and Staehle's models, four cracking regimes can be delineated: (i) precursor, (ii) incubation, (iii) slow growth, and (iv) fast propagation.
4. Whereas film-induced cleavage is considered for transgranular SCC failures, the three most prominently considered IASCC failure models for intergranular failure include:
 - **Film-rupture model:** Crack propagation may occur after repeated breakdown of the passivation film at the crack tip, exposing bare metal to the corrosive environment, after which repassivation causes the process to begin anew.
 - **Internal oxidation model:** Fast-diffusion paths for oxygen species e.g. through leading grain boundaries, local plastic deformation, or internal oxide defects, assist the internal oxidation and embrittlement of metallic structures ahead of propagating crack tips. A probabilistic model describing crack growth in function of a Weibull distribution is the SCP model. On the other hand, considering the local stress concentrations at the crack tip, oxide ingress may also be described from first principles using a stress-assisted SAGBO model.
 - **Hydrogen-assisted cracking:** Ingress of H₂ may assist in the local metallic embrittlement. H may interact strongly with metallic defects leading towards H-enhanced localized plasticity (HELP), or affect the metallic bond strength, thus assisting in metallic decohesion.

Chapter 3

Experimental Methods

In this chapter, the experimental techniques that were employed and the investigated materials that were studied during this research for stress corrosion characterization are highlighted. While (IA)SCC often emerges as a macroscopic phenomenon observed in tested and industrial specimens, its origin entails degradation processes that initiate at a micro- to nanoscale level. For that purpose, the investigation techniques should have enough resolving power to image the specimen at appropriate magnifications. To that end, material characterization is primarily based on techniques involving electron microscopy. On the most elementary level, it is by virtue of the de Broglie wave-particle duality that electron microscopes differentiate themselves from ordinary visible-light microscopes. Postulated by de Broglie, the momentum p of an electron with mass m_0 is related to its wavelength λ by means of Planck's constant h :

$$p = \frac{h}{\lambda} \quad (3.1)$$

Electron microscopes make use an accelerating voltage V to accelerate an electron to a certain kinetic energy from an electron source filament. On the basis of conservation of energy, the acquired momentum of the electron can be written as a function of its acceleration energy:

$$eV = \frac{1}{2}m_0v^2 \quad (3.2)$$

$$\Rightarrow p = m_0v \quad (3.3)$$

$$\Rightarrow p = \sqrt{2m_0eV} \quad (3.4)$$

$$\Rightarrow \lambda = \frac{h}{\sqrt{2m_0eV}} \quad (3.5)$$

leaving underlying relativistic effects aside¹. Considering the classic Rayleigh criterion which proposes that the theoretical resolution of an instrument is directly proportional to its wavelength $\delta = \delta(\lambda)$, the preceding equations determine that an increase in resolution can be achieved through the use of imaging particles of increasing acceleration energies, and thus shorter wavelengths. In the field

of microscopy, standard visible-light microscopes operate within the visible light spectrum ranging between 750 – 380 nm. This offers a significant improvement in resolving power over regular eyesight, being able to resolve individual cellular organisms with thicknesses of a single human hair. However, for electrons accelerated by a standard of 300 kV operating voltage, the wavelength in equation 3.5 works out to about 10^{-12} m range, which is perfectly suited to resolve material features of sub-nanometer level. This gives microscopists the ability to probe individual atoms, given of course a tailored set-up that can manipulate electrons onto a specimen and translate the transmitted electron intensities to images that can be displayed on a viewing screen.

The use of electron microscopy is most effectively applied in material research, of which this work is no exception. This chapter offers an overview of the different characterization techniques that have been applied during this thesis. Scanning electron (SEM) and transmission electron microscopy (TEM) are discussed, in addition to the use of focused-ion beam (FIB) analysis. This chapter further covers the separate imaging techniques that were employed for each specific instrument. Furthermore, an explicit description of the investigated materials and their stress corrosion testing procedures are explained. The chapter not only discusses the applications of the materials themselves, but also the associated sample preparation methodologies for each specific sample. The focus is given on two sets of materials, namely the high duplex alloy and 316L SS alloy tapered and O-ring specimens, respectively.

On a separate note, when handling specimens with any degree of radioactivity, which was the case for the neutron-irradiated O-ring specimens, all analyses were performed using instruments that are located in a radiation (hot-)laboratory instead of the more commonplace cold-laboratory. All safety precautions stipulate that the operation of radioactive materials require a specific course of training. Since this was considered outside of the scope of this thesis, technical assistance is therefore provided by trained engineers and specialized technicians. These specialists were mainly of assistance in the process of sample preparation, or the loading and unloading of materials from technical instruments. SCKCEN employs radiation-shielded hot-cell facilities equipped with mechanically-controlled arms, which allow for the remote handling of radioactive sources. These hot-cell facilities are located within the radiation laboratory and play an integral part in the sample preparation processes and sample storage needs. In this regard, this chapter concludes on the description of the intricate mechanical operations that were performed by SCKCEN's technicians under the direction of the scientific research staff, which were essential to the investigation performed during this thesis.

3.1 Scanning Electron Microscopy

Conventional SEM utilizes either secondary- (SE) or backscattered electrons (BSE) that were created upon impact of a focused electron beam to form an image of the surface of a specimen of interest. The instrument accelerates an electron beam using an accelerating voltage typically around 20 – 30 kV and scans the beam across the specimen surface. In doing so, an array of the interaction products is created which entails most-importantly: (i) low-energy secondary electrons which primarily contain localized topographic information, (ii) more energetic back-scattered electrons emerging from elastic scattering events occurring from larger specimen volume interactions, and (iii) characteristic X-rays released from

¹ For simplicity, the relativistic aspect in equation 3.5 is omitted. Though, it is important to remark that electrons reach considerable fractions close to the speed of light when travelling down a TEM's electron column. Relativistic effects that change the electron properties may need to be taken into consideration, e.g. in the field of TEM image simulations. Through re-deriving the relevant expressions with Lorentz-transformations in mind, it becomes apparent that an electron's relativistic mass and energy may become significantly altered.

high-energy electrons filling the electron hole of inner shell ejected electrons caused by the impinging electron beam. The energy of the X-rays correlates with the discrete atomic energy levels and is thus deterministic for identifying chemical elements. Analysis of such characteristic X-rays is known as electron-dispersive X-ray spectroscopy (EDS or, sometimes also referred to as, EDX), which provides localized chemical information of the material composition and may be utilized appropriately.

SE imaging utilizes electron detectors that are optimized for the detection of mostly low-energy valence electrons produced from atomic ionization at the specimen surface. The image is formed from the collection of low-energy electrons typically emerging with only a few eV from the specimen surface layers. Therefore, SE imaging provides mostly topographical contrast information from shallow specimen surface layers only a few nanometers deep [240]. On the other hand, relatively high-energetic back-scattered electrons may be produced from single or more elastic scattering events originating of the impinging beam on the electric field of the array of atoms in the specimen volume. Such electrons preserve most of the original beam energy and produce contrast information correlating with a deeper interaction volume than previously with SE imaging. The SEM image signal is mostly dependent on the incident electron beam and specimen surface parameters, primarily including the beam energy and diameter but also the atomic number Z and the crystallinity of the investigated material. For instance, the higher the atomic number of the specimen, the more BSE will be produced although at a consequence of a decreased interaction volume. In contrast to TEM analysis, the specimen does not require to be of any specific thickness. Rather, SEM imaging may be employed on bulk samples and their surfaces.

SEM instruments employed within this research are the cold-laboratory situated LaB₆ JEOL JSM-6610 LV SEM and the hot-laboratory installed field-emission gun (FEG) JEOL JSM 7100 LV. Within the SCKCEN institute, transport of samples is sometimes preferred outside (respectively, cold-) of the radiation-controlled facility (respectively, hot-laboratory) , if at all possible, for reasons of radiation safety. The most striking difference between both SEM instruments, besides their situation in- or out-side the radiation zone, is the difference in their electron guns. The thermionic LaB₆ electron gun produces electrons upon heating the filament, giving them sufficient energy to overcome the natural barrier that prevents them from leaking out from the surface. This barrier is termed the work-function and has a value of a few eV. Alternatively, field-emission sources (FEGs) operate based on the strength of an electric field at the tip of the gun, produced by a positively charged cathode generating high accelerating voltages. A strong electric field effectively lowers the work-function barrier of the field-emission tip so that the electrons are able to tunnel out of the gun source. An overview of the different electron sources between both instruments is tabulated in Tab. 3.1. Overall, FEGs yield a general increase in brightness and lower energy spread in the electron beam but do require a more perfect electron source vacuum [241]. The produced electron beam from the electron gun travels down the SEM column and passes through a series of electron condenser lenses, which reduce the beam's crossover diameter and focuses the beam to a certain spot-size. Through the use of scanning coils, the beam is deflected and scanned across the specimen surface. Secondary and backscattered detectors are installed in the specimen chamber, which is held under vacuum by dedicated vacuum pumps after the sample has been loaded. Generally, a FEG electron source is preferred since it produces a higher current density in the focused beam spot and has a narrower energy spread compared to thermionic sources. An overview of the SEM instrumentation is found in Figure 3.1.

Table 3.1: Overview of general SEM instrumentation specifications obtained from JEOL specification sheets, with added information on the electron source performances of thermionic LaB₆ and Schottky FEG electron sources.

Operation parameters	JEOL JSM-6610 LV (Thermionic LaB ₆ gun)	JEOL JSM 7100 LV (Thermionic Schottky FEG)
Instrument specifications		
Acceleration Voltage (kV)	0.3 - 30	0.2 - 30
Resolution @ 1 kV (nm)	15	3.0
Resolution @ 30 kV (nm)	4.0	1.2
Magnification	× 5 - 300k	× 10 - 1000k
Electron source specifications		
Cathode Material	LaB ₆	ZrO/W(100)
Cathode radius at tip (nm)	10k	< 1k
Energy spread at source (eV)	1.3 - 2.5	0.35 - 0.7
Operating Temperature (K)	1800	1800
Life-time (h)	> 1k	> 5k
Brightness (A/cm ² sr)	× 10 ⁵	× 10 ⁷
Vacuum (mBar)	< 10 ⁶	< 10 ⁸

3.2 Focused-ion beam analysis

3.2.1 FIB-SEM instrument

On behalf of an accessible specimen chamber that is not limited by its own objective lens system, a SEM system allows for the incorporation of an additional instrument known as a focused ion beam (FIB) unit into the pre-existing design. Although exclusive FIB systems do exist, an extended FIB-SEM instrument is typically more common and has been employed throughout this thesis. The additional FIB instrument uses a gallium liquid-metal ion source (LMIS) to produce highly energetic Ga⁺ ions (2-30 keV), naturally using a similar accelerating anode-cathode design as employed in conventional SEM. The Ga⁺ ion beam can be scanned across the specimen surface, similar to the electron beams using scanning coils and beam deflectors. Accordingly, a so-called DualBeam FIB-SEM combines common SEM imaging capabilities with the added utility of probing the specimen surface using highly energetic ions. The benefit that the additional ion beam provides is primarily based on ion milling i.e., sputtering material away from the surface. Ion-milling can be useful for micro-machining site-specific regions up to the requirements meant for characterization techniques along the likes of electron backscatter diffraction (EBSD), or for which it has been primarily used for during this thesis, TEM sample preparation of tested and industrial specimens. Modern FIB-SEM systems additionally include a highly-stable micromanipulator tungsten needle in combination with a volatile gas injection system (GIS). Once inserted, the micromanipulator needle can be moved and rotated independently within the specimen chamber using precisely controlled stepper motors. This allows for the convenient interaction of the needle with inserted specimens. On the other hand, the GIS can sputter ion- or electron-beam controlled volatile metallic compounds in order to deposit small metallic layers onto the specimen surface. In combination with a micromanipulator needle GIS unit, the FIB-SEM is therefore considered to be a powerful and multifunctional instrument that can be employed in all sorts of research applications.

The FIB-SEM instrument available at SCKCEN laboratories is the ThermoFisher Scientific Scios DualBeam FIB-SEM. A generalized diagram of a DualBeam set-up is shown in Figure 3.2. The FIB column enters the specimen chamber under an angle of 52°. Or, in more explicit terms, the electron-

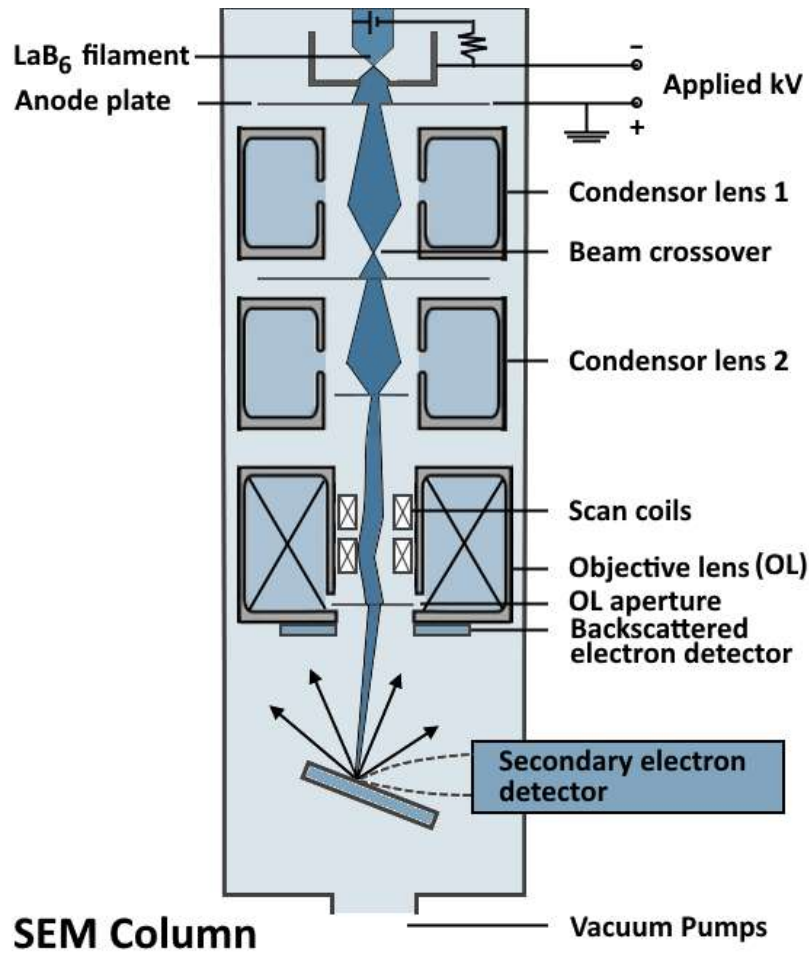


Figure 3.1: A diagram of a typical SEM illumination column. Adopted and redrawn in accordance to reference [242].

and ion beam columns intersect at the specimen plane under a 52° stage tilt orientation. This is particularly useful in the context of sample preparation, when imaging the specimen from different orientations. In this manner, the ion beam may also be used to generate a lower quality ion-image using the SEs generated from the interaction with the specimen surface, similar as to common SEM imaging.

3.2.2 Operational Techniques

In material characterization, it is often of interest to characterize a specimen feature from a different orientation other than the planar surface. In this case, energetic ion beams may be used to mill trenches around the feature of interest using site-specific milling patterns. Furthermore, it is possible to systematically extract that specimen feature using a consecutive trench undercut underneath it. Within the framework of this thesis, such a FIB-methodology was developed for the extraction of SCC and IASCC cracks in particular. Microstructural analyses were then performed using subsequent TEM analysis. The following section outlines the different approaches in crack tip extraction and describes the general guidelines of the methodology that was found to be the most effective.

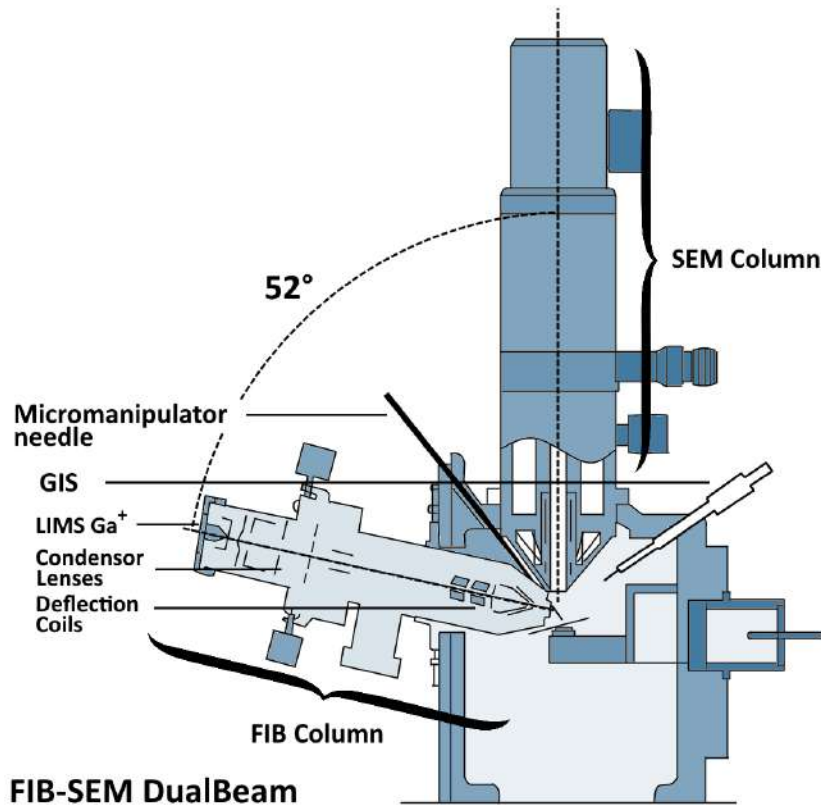


Figure 3.2: A diagram illustrating the individual components of the FIB-SEM DualBeam set-up. Adopted and redrawn from reference [243].

3.2.2.1 TEM-lamella preparation

The methodology for systematically preparing TEM specimens of (IA)SCC crack tips through FIB analysis has been outlined schematically in Figure 3.3. TEM specimens can be prepared in one of two ways, either in cross-sectional or in plan-view orientation. The former implicates a specimen orientation wherein a crack slice is extracted in perpendicular fashion from the specimen's fracture surface, while the latter entails a horizontal crack slice orientated parallel to the fracture surface. While both techniques have their benefits, the use of cross-sectional orientation was found to be more beneficial for the purposes of crack tip analysis. Primarily, in cross-sectional orientation [164, 232, 244, 245], one is able to extract the full three-dimensional configuration of a crack, which is ultimately thinned down to contain a final slice of a so-called propagating or leading crack tip. A cross-sectional specimen can be extracted within nanometer range of a designated area of interest without violating adjacent bulk material, in as short of a sample preparation time of only a few hours (up to three samples a day - without complications). On the other hand, in plan-view orientation [246, 247], only a surface crack can be extracted, which offers no possibility for the analysis of leading crack tips which drive the crack propagation. Plan-view specimens are considered more applicable in correspondence to surface characterization techniques like EBSD, which was not within the scope of this thesis.

Having established the benefit of cross-sectional orientated TEM-lamellae, the following describes the developed methodology for (IA)SCC crack tip extraction, which is based on the standard in-situ FIB lift-out technique:

- (i) A rectangular cross-section Pt preservation layer is deposited on top of a designated area of

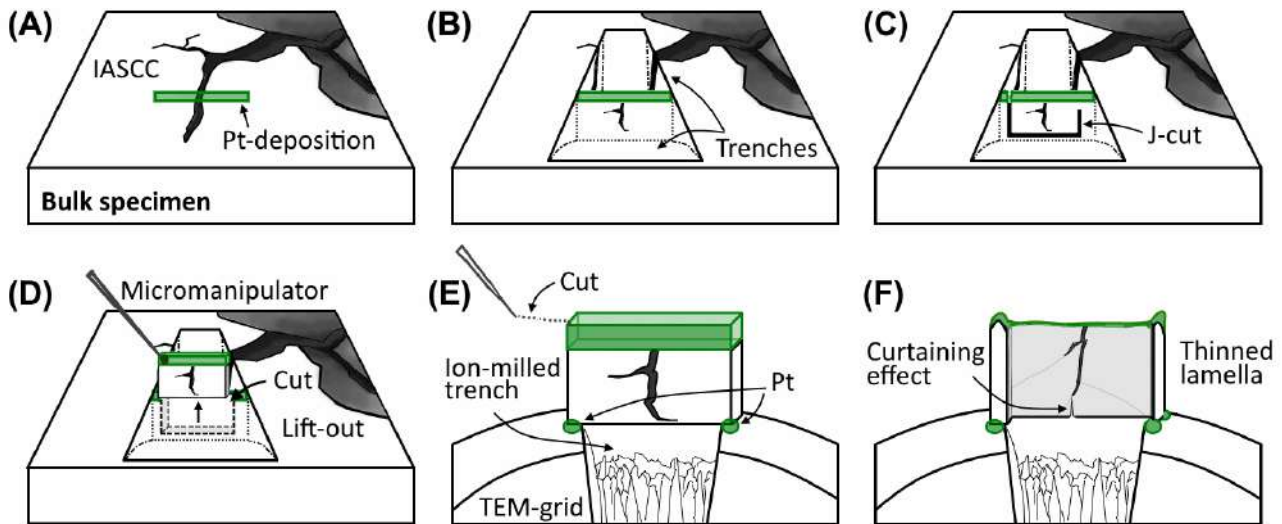


Figure 3.3: Schematic overview of the TEM-lamella FIB preparation of IASCC crack tips.

interest, see Figure 3.3A. In the context of this research, the specimen feature is generally a planar surface crack. Such a preservation layer allows for the protection of the crack, surface oxide layers, and underlying substrate material, from ion-damage in the consequent thinning phase. Pt is preferably deposited using low electron- or ion-beam currents to minimize sputtering inside the crack opening.

- (ii) Two equal trenches are milled on each opposing side of the deposition layer, see Figure 3.3B. Each lamella wall is consequently smoothed using a cleaning cross-section operation to remove back-sputtered material.
- (iii) A J-cut operation is performed to cut the lamella partially loose at an intermediate ion current, see Figure 3.3C.
- (iv) The lift-out needle is attached to the lamella side by sputtering a slight Pt deposit. The remaining material is cut loose from the lamella side, so that the lamella is loosened from the bulk material. The extraction of the lamella from the bulk is referred to as the lift-out procedure, see Figure 3.3D.
- (v) A standard or M-type TEM copper support grid is prepared according to the lamella size. Standard grid posts require readily milled pre-trenches, depending on the lamella's size dimensions, before it is mounted to the copper grid. The lamella is welded from one side to the grid post using slight Pt deposits, facing upwards to the ion-beam at an angle of 52° stage tilt.
- (vi) The lift-out needle is cut loose from the mounted lamella, see Figure 3.3E. In order to firmly secure the lamella in place, additional Pt may be sputtered on the opposing side of the lamella. A mechanically strong support is required in order for the lamella to not dislodge during the subsequent thinning operation.

The imposed specimen requirements for TEM investigation of crack embedded TEM-lamellae are such that the specimen thickness should be at least electron-transparent for the incoming electron beam to transmit through the sample. To that end, the final step in the preparation methodology entails high-precision thinning operations in order to produce samples up to the standard of TEM analysis,

Table 3.2: Practical guidelines for TEM-lamella thinning operation under ion-beam alignment of 52° stage tilt. Repetitive ion-milling steps successively thin the lamella to electron-transparency thickness, preferably sub 100 – 150 nm, in limitation of unavoidable ion-damage.

Operation mode	Voltage (kV)	i_{ion} (nA)	Tilt (52°)	Estimated thickness (nm)
Thinning	30	1	± 3	2000
	30	1	± 2	1000
	30	0.5	± 2	600
	16	0.25	± 2	300
	8	0.125	± 2	> 170
Cleaning	5	0.048	± 4	> 155
	2	0.027	± 4	> 150

see Figure 3.3F. Numerous ion milling steps over a range of various tilt angles, wherein the ion current is successively reduced, ensure a precise thinning operation. The steps outlined in Table 3.2 serve as a general guideline from which slight deviations may be taken, depending on the lamella morphology, estimated thickness, and increasing ion-damage.

Incontrovertibly, certain FIB-related artefacts may arise during the process of (IA)SCC TEM-lamellae sample preparation. Ion implantation of the milling species into lamella substrate material may occur due to metal deposition, ion-milling, or plainly as a consequence of ion-imaging using the SE signal generated from the impacting ion beam. The intensity of the ion damage may depend on the ion species, its current and accelerating voltage, the incidence angle, and the substrate material itself. Studies investigating the thickness of the ion-damaged subsurface layers reported several tens of nm impacted damage in crystalline silicon, irrespective of the beam parameters [248]. To that end, final low-energy broad ion beam milling is applied in order to reduce the thickness of the damaged material. On the other hand, the so-called curtaining effect may play an equally significant role in the preparation of TEM-lamellae. Local aggregated ion-milling may result in what appears as extended curtains across the lamella cross-section, which in principle relates to a change in lamella thickness as a consequence of a strong channeling effect. The curtaining effect may originate due to reasonable changes in the ion-milling rate from an irregular lamella topography, local crystal orientation, and/or material composition change [249, 250]. Because these reasons all contribute in the process of crack tip extraction, crack curtaining remained an inherent problem encountered in this approach. Productive steps to minimize the artefact included FIB-deposition of Pt prior to the thinning operation in order to level the milling surface, and the use of successively reduced ion-milling currents whenever the curtaining initiates. On several occasions, crack curtaining imposed a severe restriction on the ultimate lamella thickness during the thinning operation.

3.2.2.2 Low-voltage electron contrast imaging

In the context of intergranular cracking, the grain boundary orientation and morphology in front of the leading crack tip may illustrate important features related to crack initiation and propagation. To that end, characterization of the lamella's cross-section is an important aspect in the investigation of stress corrosion cracking. Low-voltage BSE-imaging is applied through utilizing FEI's OptiTilt function for the electron column. In this manner, primary beam electrons are accelerated to high energy by a strong potential in the electron column, and ultimately decelerated in-between the detectors and the sample. BSE- and SE-signals generated from the sample are collimated back into the electron lenses of the detectors, from which topographical and composite images can be inferred. The final deceleration of the electron beam before reaching the specimen may produce higher angles of BSEs, which further improves the compositional contrast. FEI's OptiTilt use function is optimized for FIB cross-section

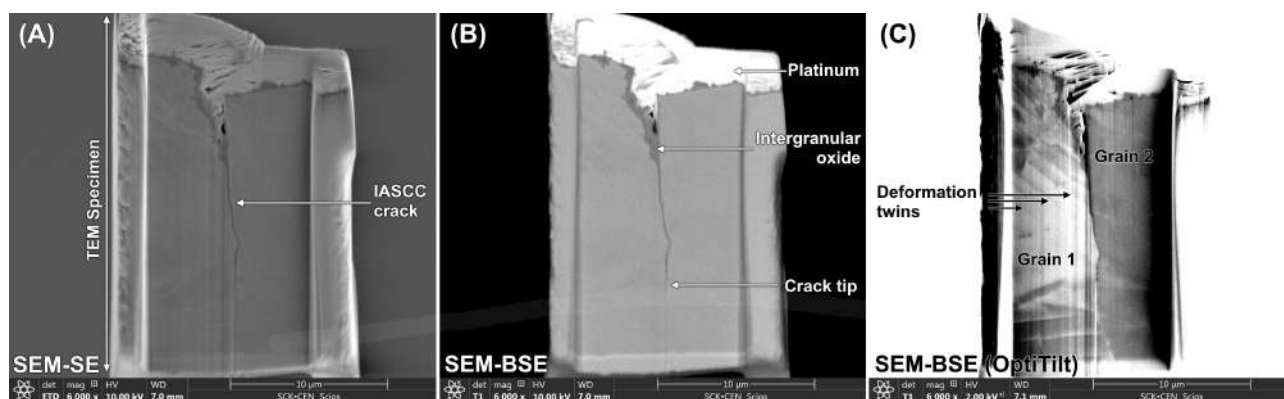


Figure 3.4: Comparison between the different imaging modes during the TEM specimen thinning operation: (A) SEM secondary electron using the ETD-detector, (B) SEM ordinary backscattered-secondary electron using T1-detector, and (C) SEM OptiTilt backscattered-secondary electron image using the T1-detector.

preparation and subsequent high resolution surface imaging at low accelerating voltages, usually up to 2 kV.

Low-voltage imaging has been primarily applied in regards of obtaining topographical information of the cross-sectional surface, see Fig. 3.4. Grain contrast is achieved due to varying backscattered electron count production, which is a factor of the substrate material and local crystal orientation. Hence, the contrast may demonstrate different bulk phases, underlying grain structures, grain-boundary triple junctions, and bulk-segregated particles in contemplation with subsequent TEM imaging. Grain sizes and indications of strong lattice deformation may additionally be inferred. The character of the signal further depends on the optical configuration of the electron column, mainly the working distance, vacuum conditions and stage bias deceleration potential.

3.3 Transmission electron microscopy (TEM)

TEM has been used as the primary tool for microstructural characterization throughout this research. On a similar principle as SEM, TEM employs an incident beam of high energetic electrons to image the sample. However, while SEM achieves a spatial resolution down to nanometer scale, TEM high-resolution imaging resolves sample features down to several Ångströms (Å) in size. This is achieved through electrons accelerated to higher voltages (up to 300 kV; a factor of 10 relative to SEM), impacting on an electron transparent specimen of the order of hundreds of nm in thickness, or less. Electron detectors above and below the sample detect the transmitted electrons, which carry information about the sample's microstructure, composition and crystallography.

First and foremost, this research employs SCKCEN's JEOL 3010 LaB₆ scanning (S)TEM microscope, equipped with an Oxford Instrument EDS link spectrometer with a corresponding Si(Li) electron detector, operated at a high voltage of 300 kV. TEM images were acquired using the Gatan Slow Scan Model 794 digital camera controlled by Gatan Inc.'s DigitalMicrograph™ software, which was later on used for subsequent characterization also. Further analytical analyses were acquired at EMAT, using their aberration-corrected X-FEG Thermo Fisher X-Ant-EM STEM instrument, primarily for the use of STEM-HAADF and spectral map imaging. Finally, several analytical STEM sessions were performed using SCKCEN's newly acquired JEM-ARM300F Grand ARM STEM operating also at 300 kV, specifically for samples which did not get clearance to leave the radiation controlled laboratory.

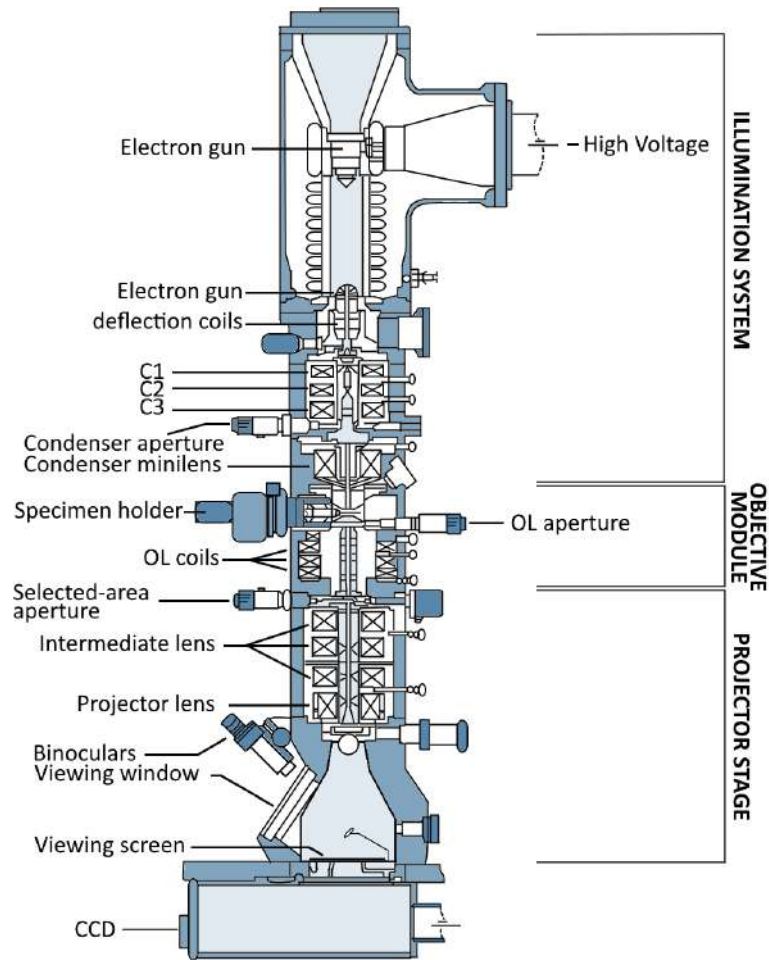


Figure 3.5: A schematic diagram of the JEOL 3010 LaB₆ (S)TEM. Redrawn in accordance to reference [251].

3.3.1 TEM instrument

The following entails an explicit description of a TEM's instrumentation, which is fundamental to the basic operation of the instrument. A schematic diagram of a typical TEM instrument is displayed in Figure 3.5. Its operation methods are described from an alignment perspective, with the functions and uses of each primary system component specified from top-to-bottom perspective. The separate stages of a TEM are highlighted, most specifically the illumination stage consisting of the electron source and subsequent condenser lenses, the objective module characterized by the objective lens surrounding the moveable sample stage, and finally the projector lens system which channels the transmitted electron beams to the appropriate detectors.

Initiation of a TEM session may begin when the TEM sample is mounted onto a clean double-tilt sample holder, the vacuum has settled after the sample was inserted, the column-valves have been opened, and the electron gun filament has been switched on for several minutes. In the case of thermionic emission, electrons are released from a heated electron gun filament and accelerated by the gun's acceleration voltage (usually 300 kV). Upon entering the electron column, one of the first elements the electron beam will interact with is a series of electromagnetic condenser lenses in the illumination stage. These, like all other electron lenses, consist of wiring coils which can apply an axially symmetric magnetic field \mathbf{B} by running a current through it. The magnetic field actively shapes the electron beam through an acting Lorentz-Force, \mathbf{F}_L :

$$\vec{\mathbf{F}}_L = q \left(\vec{\mathbf{E}} + \vec{\mathbf{v}} \times \vec{\mathbf{B}} \right) \quad (3.6)$$

with electron velocity \mathbf{v} and charge q , and electric field \mathbf{E} . Electrons passing through an electromagnetic lens will follow a ray path close to a helical trajectory down the optic axis, which can be controlled by inserting a lens aperture, changing the lens operating parameters, or through operating a series of lens deflection coils. Electron lens apertures may limit the collection and divergence angles of the electron beam, which allows for additional beam control. This operation becomes more important in relation to the second condenser lens C2. As for now, the electron beam originating from the electron gun needs to be aligned in relation to the first condenser lens, C1. Consequently, the first alignment of the illumination stage consists of both the gun tilt and the gun shift alignment.

Centering the gun tilt corresponds to aligning the gun tip with the gun aperture, so that the electron beam travels down along the optical axis in parallel onto the subsequent condenser lenses of the illumination stage. This is achieved simply by maximizing the beam current (or minimizing the exposure time). In this manner, all incoming electrons can be used for purposes of imaging with the possibility of having a maximal beam intensity. Secondly, the gun shift is aligned so that the electron beam from the gun impends on the center of the first illumination lens i.e., the C1 condenser lens. Adjustment of the gun shift is done by changing the beam spot size from high to low and vice versa, while iteratively centering the condensed beam in the viewing screen. Essentially, by changing the beam spot size, one alters the current through the sets of electron condenser lenses which may bring the beam cross-over closer (strong C1) or further away (weak C1) to the optic axis. The beam and gun shifts are consequently altered by changing the current through the set of double-deflection coils in the condenser stage, which improves the gun alignment significantly.

After the primary beam is correctly aligned with the first condenser lens C1, the next step consists of centering the second condenser lens C2 aperture on the optic axis. If the aperture is misaligned, the beam image may be distorted as one under- or over-focuses the C2 lens current i.e., the beam brightness. To center the C2 diaphragm, one iteratively changes the lens current to see the wobbling of beam image, and one mechanically moves the C2 aperture so that the wobbling is minimized. A lens artefact that may play an important role at this stage is the C2 astigmatism. Astigmatism is the most common defect in the TEM illumination system and arises because the C2 aperture is not centered appropriately or it is contaminated and is thus charging up, ultimately deflecting the electron beam. To counteract this artefact, condenser stigmators may be adjusted, which impose an additional magnetic field similar as an electron lens coil does, which corrects for the distortion. A correctly aligned C2 aperture is so that the spreading of the electron beam brings about a beam image which remains concentric when going in and out of focus.

In the context of the gun alignment, the condenser double-deflection coils in the illumination stage allow the user control over the shift of the electron beam. Of equal importance is control over the beam angle of illumination so that whenever the beam tilts, it does not induce a beam shift and correspondingly moves away from the area of interest. This alignment procedure is known as the adjustment of the beam tilt pivot points, and is achieved by minimizing the beam wobble between two values of opposite tilt by adjusting the pivot-point deflectors. This procedure concludes the alignment of the TEM illumination stage.

Moving down the electron column in Figure 3.5, the second stage of the TEM consists of the objective lens (OL) and the specimen stage. What is important during this stage of the alignment procedure, is that the specimen's height is adjusted to the eucentric plane on the optic axis. Essentially, the

eucentric height defines the position where the specimen does not move around laterally when tilted around the holder axis. While the eucentric plane could be specified earlier on, at this stage a good objective focus on the sample becomes important for that all consequent steps involve the alignment of the OL. For that, the OL must first be aligned with the optic axis through adjusting the rotation center deflectors. If the lens-field were to be off-center, then any electrons not traveling down the optic axis will suffer severe lens aberrations, and the image will rotate about a position as the OL focus is adjusted. Setting the final focus on the sample at high magnifications is done by finding the optimal OL current. However, in severe cases it can become apparent how the contrast differs in two opposite directions when going through focus. Therefore, as a final step in the alignment procedure, the OL stigmators are adjusted to correct for the most limiting aberration in TEM i.e., OL astigmatism.

3.3.2 Electron diffraction in TEM

The third and final stage of the TEM instrument consists of the projector and intermediate lens systems. These lenses essentially control the mode of operation of the TEM instrument after the electron beams exit the bottom surface of the specimen. Transmitted electron beams from a point of the specimen may converge by the objective lens to form a magnified image of the specimen in the image plane (distance d_i from the OL). Likewise, parallel beams transmitted from the specimen are brought to focus in the back-focal plane (BFP) of the objective lens (distance f from the OL). The projector stage functions to configure an image of either the image plane or the BFP of the objective lens onto the viewing screen or detector, see Figure 3.6. Typically, this is achieved by shifting the focus of the intermediate lens system to freely switch between image- and diffraction-mode. The projector lens is usually held at a constant focus and is only used to control the final diffraction appearance. The electrons finally detected by the charged-coupled device (CCD) camera will have their energies altered by elastically scattering on the sample's crystal potential. Operating the TEM in both configurations, image- and diffraction-mode, allows the user to collect these scattered electrons in the objective lens to form a magnified image or diffraction pattern (DP) of the specimen.

3.3.2.1 Bragg's Law

In the diffraction formalism introduced by Bragg, the primary incoming electron wave may be described as a planar wave with a constant wave-vector \vec{k}_0 using the form: $\Psi_0 = \Psi(\vec{k}_0)$. Electron diffraction of this planar wave on to a crystallographic plane of an electron-transparent specimen generates an outgoing diffracted wave $\Psi_s = \Psi(\vec{k}_s)$ with a transformed wave-vector \vec{k}_s . The parallel incident electron wave impinges on to the crystal that is oriented under an angle θ , and diffracts from a set of crystallographic planes with miller indices $\mathbf{H} = hkl$ with an intergranular spacing d , see Fig. 3.7A. The incident electron wave is considered in phase and parallel up to the point where diffraction occurs. However, only in the case when the path length difference δ between two consecutive planes is a multiple of the wavelength λ can constructive interference with the scattered beam take place. From basic trigonometry in the corresponding figure, one can derive Bragg's Law as:

$$2 d_{\mathbf{H}} \sin(\theta) = n\lambda \quad (3.7)$$

$$\Leftrightarrow \frac{1}{d_{\mathbf{H}}} = 2 \left(\frac{1}{\lambda} \right) \sin(\theta) \Big|_{n=1} \quad (3.8)$$

where commonly the integer multiple is set to 1, as to not make any distinction between the order of the diffracting plane. Extending Fig. 3.7A by drawing a sphere with radius $1/\lambda$ with its origin at

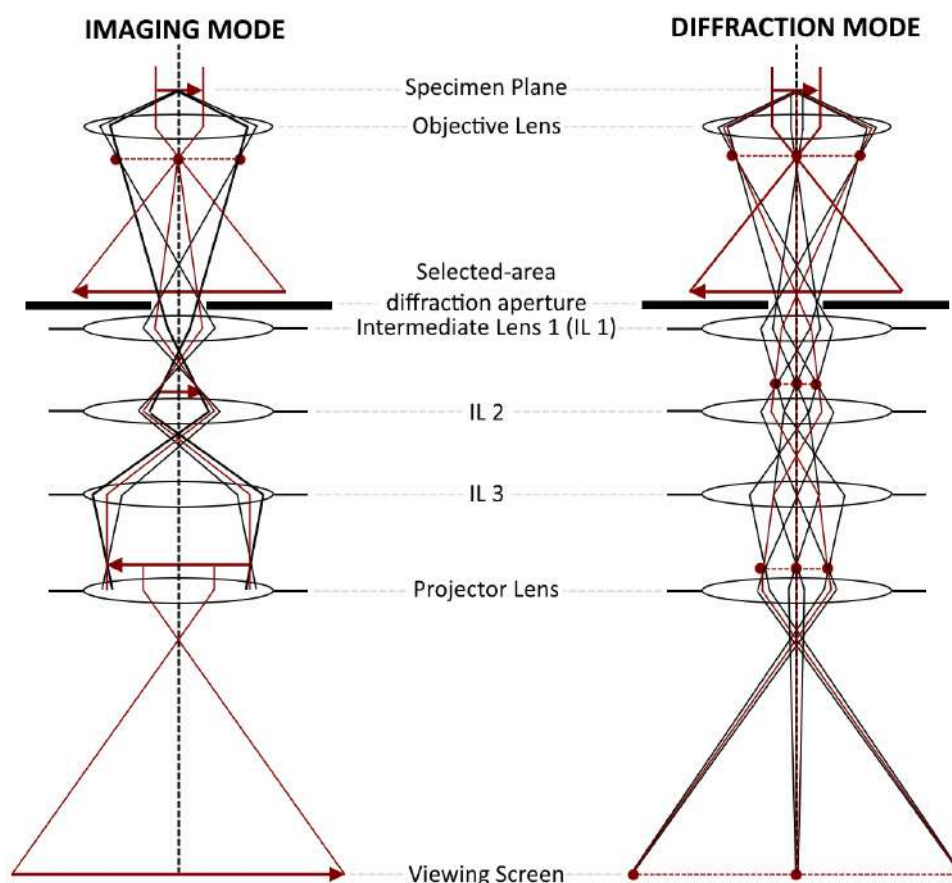


Figure 3.6: Schematic overview of the ray diagram projector stage consisting of the objective lens (OL), three intermediate lenses (ILs) and the projector lens (PL). Redrawn in accordance to reference [252].

the diffraction center O' , makes it so that this sphere intersects the direct beam at point O'' and the diffracted beam at P'' . The distance $O''P''$ is equal to $2\sin(\theta)/\lambda$, hence $O''P''$ is proportional to the inverse of the lattice spacing. This sphere is otherwise known as the Ewald sphere, and represents the geometrical construction where the Bragg condition for given reflections is satisfied.

In TEM diffraction-mode, the recorded DP may be displayed on the viewing screen, which lies perpendicular to the $O'O$ direction, see Fig. 3.7B. This distance is equal to the length between the specimen and recording plane, or otherwise known as the TEM's camera length L . The recorded diffraction spot extends from the diffracted beam along the $O'P'$ direction, and ultimately appears at position P . Because the wavelength λ and the scattering angle θ are generally small in TEM diffraction experiments, the Ewald's sphere with radius $1/\lambda$ is considered very large, so that its curvature is nearly flat.

3.3.3 Operational techniques

The following paragraphs will highlight the operation techniques that were used in this research. The focus is given on the technical aspect of each technique, as well as its application to the field of SCC research in general.

imaging simply because $Z(\text{O}) < Z(\text{Fe})$ and the local thickness near the crack flanks is less than the bulk metallic matrix (of which Fe is the main constituent). On the other hand, diffraction contrast may arise when the local diffraction conditions of the impending beam are changed within specific regions of the specimen. Contrary to BF-imaging, a dark-field (DF) image is formed from selecting a specific diffracted beam with the objective aperture, and the corresponding area associated to where this electron beam diffracted increases in image intensity, thus gets brighter. As shown in Fig. 3.8B, the objective aperture is displaced to select the scattered electrons from the diffracted electron beam. Electrons selected by such a displaced aperture travel off the optic axis, and thus experience more lens aberrations as a result. This operation is referred to as a displaced-aperture TEM-DF image (DADF) and is far from ideal, especially when the resultant image movement occurs as the objective-lens strength altered. To that end, the operation of bringing the scattered electrons from the DADF back to the optic axis, so that the lens aberrations are minimized but the resultant diffraction contrast is achieved, is referred to as a centered aperture dark-field (CADF/CDF) operation (see Fig. 3.8C). Because it is quite inconvenient to manually insert the SAED and objective apertures for every BF- and CDF-operation, the microscope is able to remember the positions of the electron beams simply by pressing the corresponding bright- and dark-field buttons.

Electron diffraction through TEM is considered very useful for the microstructural analysis, especially in terms of identifying crystallographic directions in the matrix around the crack as well as the examination of crystalline and amorphous oxides (see following section). Fig. 3.9 demonstrates the typical imaging modes which are essential for the purpose of determining crystallographic information. Through acquiring diffraction information, one can not only determine the crystallographic phase of the structure, but also identify certain microstructural defects and their orientation relationships with the parent matrix structure. Associated DPs may reveal structural information relevant for SCC research.

3.3.3.3 Ring-diffraction characterization

In diffraction analysis, one comes to expect that electron scattering from specific crystallographic planes results in typical spot-like DPs. Though, when diffraction occurs from a polycrystalline material (especially in the case of nanosized grains), numerous grains of different crystal orientations may accidentally diffract electron rays and satisfy the Bragg condition. In doing so, some grains diffract electron rays anywhere on the sphere represented by rotating O'P' around O'O in Fig. 3.7B. Intersecting these spheres with the Ewald sphere, which during TEM operation approximates a flat surface, may generate different concentric diffraction rings.

In practice, the oxidation layer for (IA)SCC is in fact polycrystalline, see Fig. 3.10C. In accordance to the diffraction formalism, the origin of its ring-like DP may be coupled with the construction of the Ewald's sphere. The DP may smear all diffraction reflections stemming from the different oxide grains into concentric circles. Interestingly, this smearing may become exacerbated for completely amorphous structures like the deposited Pt protection layer FIB-analysis, of which the DP is shown in Fig. 3.10D.

Experimental ring-DPs may give insight to the grain size of the diffracting crystallites. In fact, larger crystallite grain sizes typically yield more of a discrete spot pattern, while smaller crystallites produce a more continuous ring-like structure. It is possible to estimate the grain size through measuring the widths of the rings, but a more simple solution would be to image the nanograins directly instead.

Still, one difficulty that ring-DPs pose that is not easily overcome, is the multiple scattering from

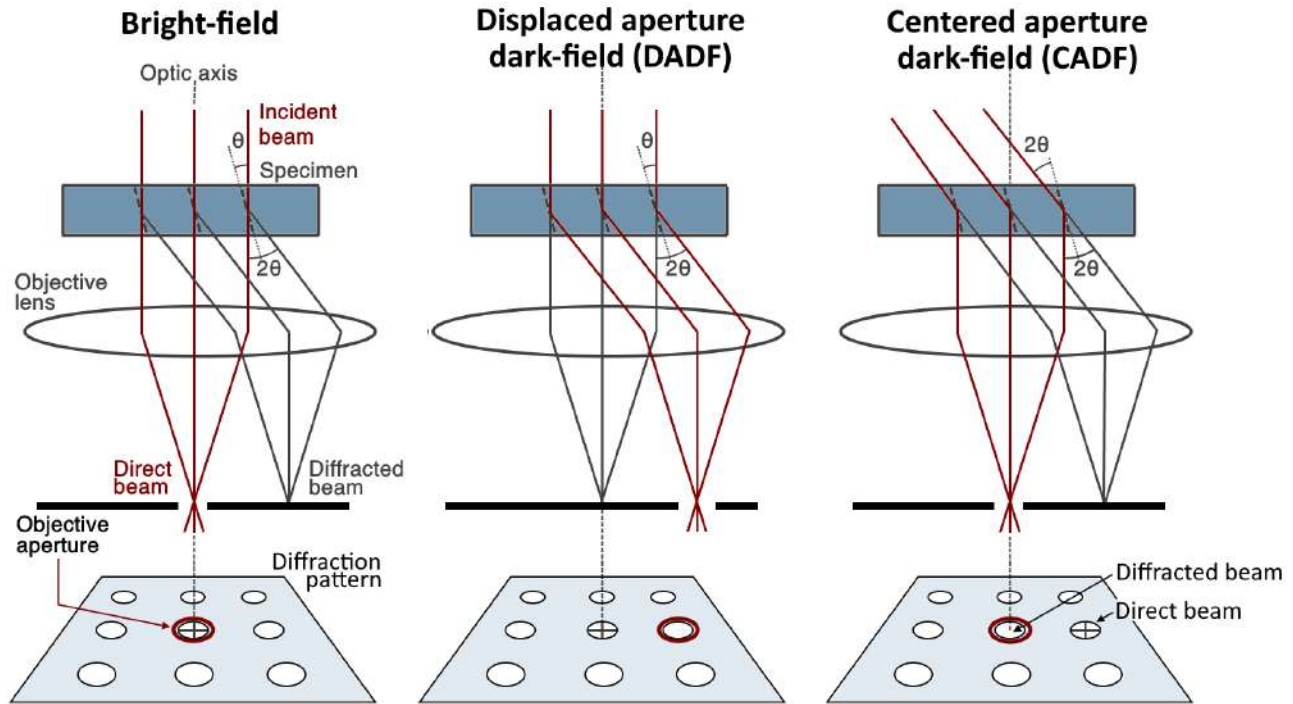


Figure 3.8: Ray diagram illustrating the operation to produce: (A) a BF-image, (B) a DADF-image from a specific off-axis scattered electron beam, and (C) a CDF image from a scattered electron beam onto the optic axis by tilting the primary incident beam onto the specimen. The DP seen on the viewing screen, is shown below each ray diagram. Redrawn from reference [252].

the abundantly reflecting nanograins leading to forbidden ring reflections. Forbidden reflections may prove identifying the exact polycrystalline structure difficult. In actuality, each crystal lattice, may it be one single crystal or multiple nanocrystals, specifies a set of extinction rules that determines whether certain diffraction reflections may be present or extinct (no diffraction spot is expected). In the previous treatment, we considered electron diffraction from a single atom only. However, many different diffracted waves from a series of (hkl) planes contribute to one given reflection. The sum of the total number of diffracted waves by all atoms in a single unit cell, for conditions specified by the equation 3.7 (Bragg's equation), is encapsulated by the structure factor $F(hkl)$ for a given crystal lattice. The geometrical expression of the structure factor is given by equation 3.9:

$$F(hkl) = \sum_i f_i e^{2\pi i(hx_i + ky_i + lz_i)} \quad (3.9)$$

wherein f_i is the scattering amplitude of the diffracted wave from a single unit cell atom, (x_i, y_i, z_i) the coordinates of that atom, and i looping over all atoms in that unit cell. The value of $|F(hkl)|$ is considered the amplitude of all waves contributing to a given diffraction reflection, while $|F(hkl)|^2$ corresponds to the intensity of the this reflection. Since this research exclusively encounters oxides with a face-centered cubic (FCC) lattice centers (also valid for metallic austenite), it may be shown that the structure factor equates to:

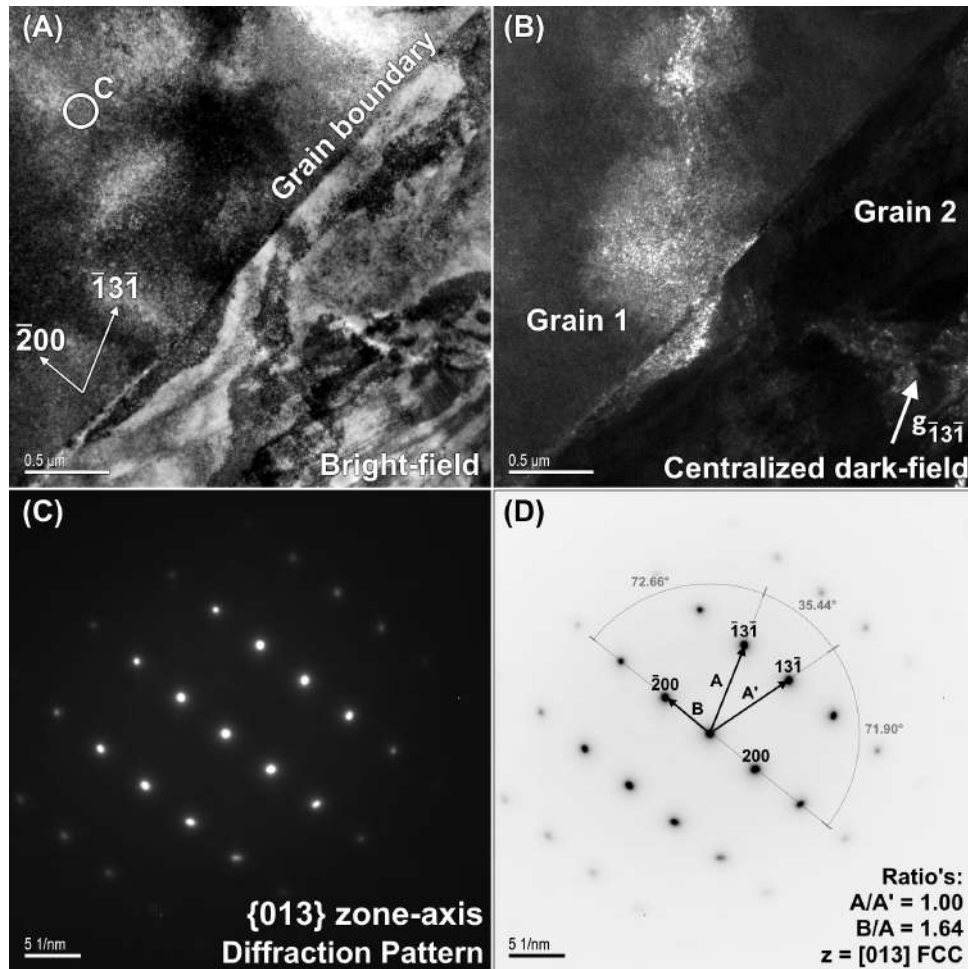


Figure 3.9: Electron diffraction through TEM investigation: (A) BF-TEM of grain boundary separating two opposing grains, (B) Centralized DF-TEM of grain 1, (C) corresponding DP, and (D) indexed DP, illustrating that the grain was tilted into the 013 austenitic zone axis.

$$F(hkl) = f \left(1 + e^{\pi i(h+k)} + e^{\pi i(h+l)} + e^{\pi i(k+l)} \right) \quad (3.10)$$

Meaning that, only in the case where h , k and l are all considered even or odd, diffraction reflections may be expected with an amplitude of $F = 4f$. If the parity of h , k and l is mixed, no reflections should be experimentally expected, unless of course they are measured as a forbidden reflection instead.

In order to correctly determine the crystalline structure of the oxides yielding a ring-like DP, the ring intensities were rotationally averaged and integrated. This produces a signal that is unique for the characterization of the crystal structure. Fig. 3.11 visualizes this process of ring-diffraction integration. Each peak in the corresponding spectrum relates to the diffracted ring intensity from which the interplanar spacing can be measured. Calculating the distance ratios from this signal, allows one to compare the experimental values to those ratio's calculated from simulated powder diffraction data. This in turn is the best way in order to determine the most likely structure from a known list of candidate structures for a given oxide crystal lattice in the literature. Using this method, we can reliably compare the experimental ring-diffraction ratio's, which may contain forbidden reflections due to the abundantly reflecting nanocrystals, to the theoretically expected values. This technique was

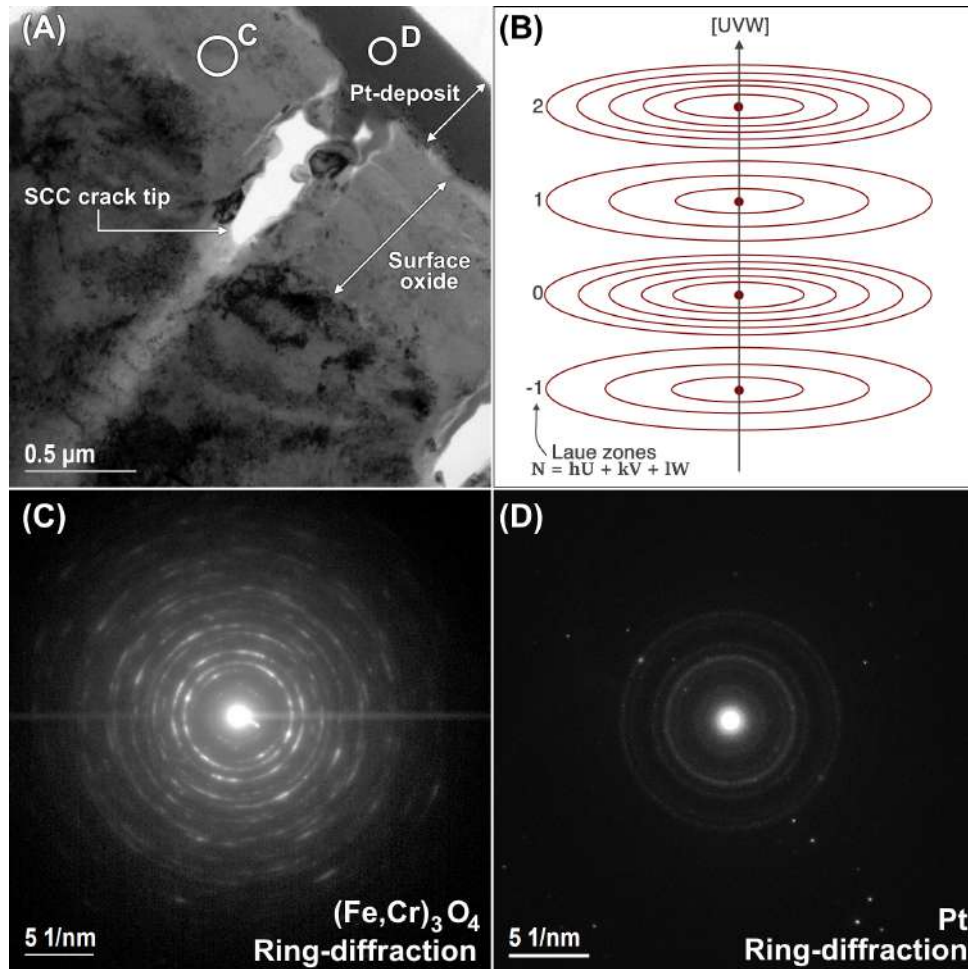


Figure 3.10: Electron ring-diffraction through TEM investigation: (A) BF-TEM of SCC arrested at the metal-oxide interface, (B) illustration of the different concentric circles of the Ewald's sphere represented in the reciprocal lattice (redrawn from reference [252]), (C) corresponding oxide DP, and (D) corresponding Pt DP in A.

most-often performed in the analysis of crystallite oxides found within crack flanks tips, through the assistance of the Crystbox MATLAB toolbox [254].

3.3.3.4 Energy dispersive X-ray Spectroscopy

In a similar principle as described in section 3.1, the transmission electron beam may generate interaction signals upon impinging onto the sample. Amongst others, the so-called Bremsstrahlung background radiation and characteristic X-ray radiation are significant in analytical TEM. Both types of radiation are the product of inelastic scatter-events, however only the characteristic X-ray signal will provide valuable information for the sake of energy dispersive spectroscopy (EDS). EDS-analysis may provide chemical information of the sample on three separate accounts: (i) qualitative analysis; probe-analyzes which indicate what specific elemental species are present at the sampled location, (ii) quantitative analysis; measurements regarding local quantified elemental compositions and ratio's, and (iii) line scans and two-dimensional spectral maps; indications on how the elements are distributed along a certain line or area. Due to the limited capabilities of our JEOL 3010 TEM set-up, only the first two methods were commonly practiced while leaving the acquisition of spectral maps for STEM-HAADF EDX imaging, described in section 3.4.

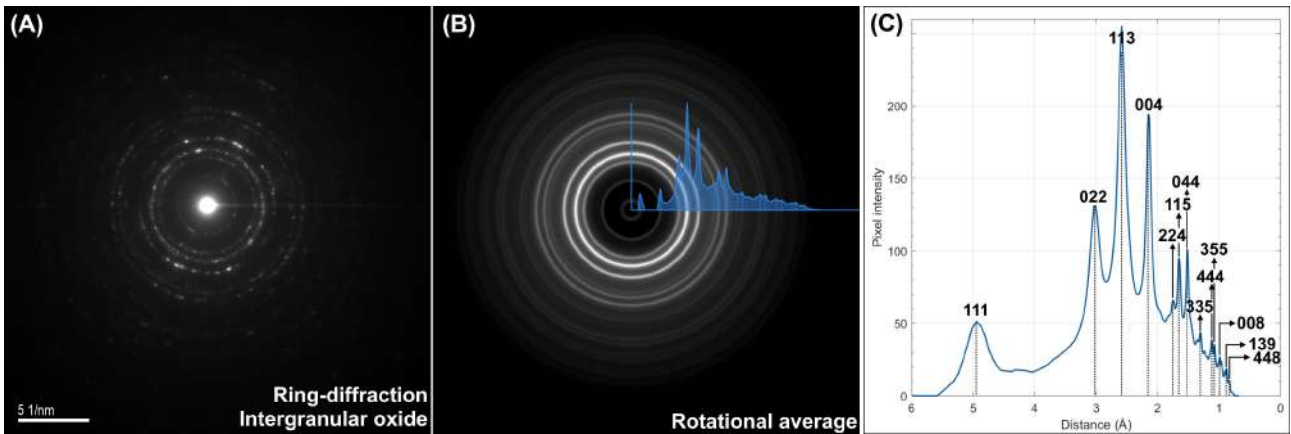


Figure 3.11: (A) Oxide ring-DP. (B) Application the rotationally averaging and integrating of the diffracted ring intensities, and (C) its corresponding signal ring intensity signal.

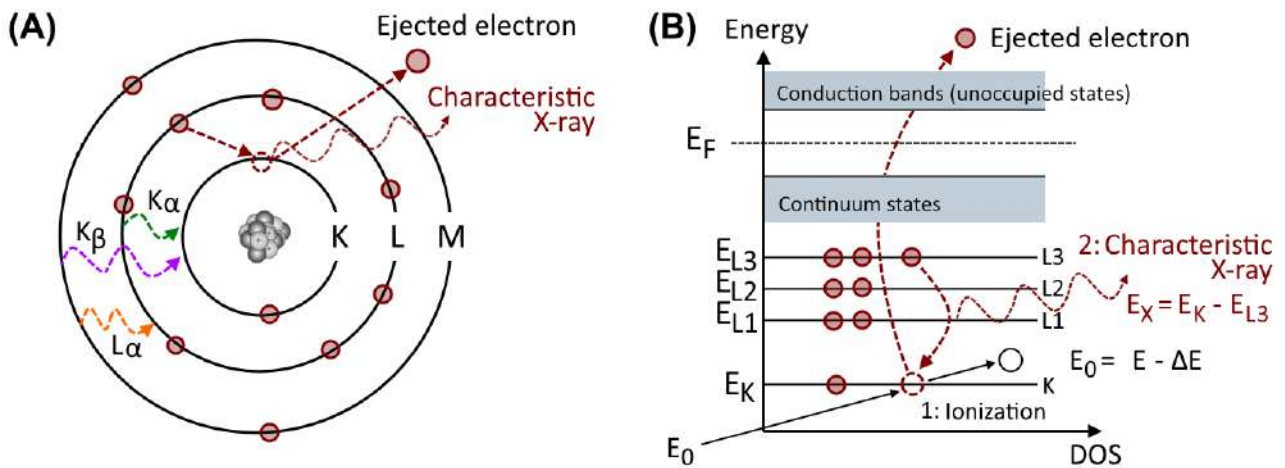


Figure 3.12: Schematic diagram of (A) Bohr's atomic model illustrating the principle of EDS, and (B) the electronic transitions related to X-ray emission. An electron hole in the inner K-shell is filled by an electron from an outer L₃-shell.

On each occasion, impinging beam electrons interact with the material atomic potential when transmitting through the sample, see Figure 3.12A. High energetic electrons may pass through atomic outer valance bands and scatter with inner-shell electrons. In this process, a certain energy is transferred from the impinging electron onto the atomic core electron, thus referred to as an inelastic scatter-event. If the energy transfer exceeds a certain critical value, the core-shell electron may become excited; giving it enough energy to eject from the atomic potential altogether, see Figure 3.12B. Having lost a core electron, the atom becomes ionized. High energetic outer-shell electrons may fill the electron-hole by emitting a discrete X-ray (or Auger electron) with the energy equivalent to energy difference between the two atomic energy levels. This energy difference is of the order of a few keVs, and is unique between the different energy levels for every atom; thus the X-ray is termed characteristic.

EDS spectra were acquired from various morphologies and phases of interest along the sample. Intensity peaks may indicate which elemental species are present, depending on the associated energy of the detected X-rays. The count-rates amongst various elements may signify the relative material composition of the species. Quantification of the EDS-spectra was achieved through the Cliff-Lorimer method (also called thin-film approximation) [255], indicated in equation 3.11. In a simplified case wherein two elemental species have relative detected X-ray intensities I_A and I_B , then the ratio of their

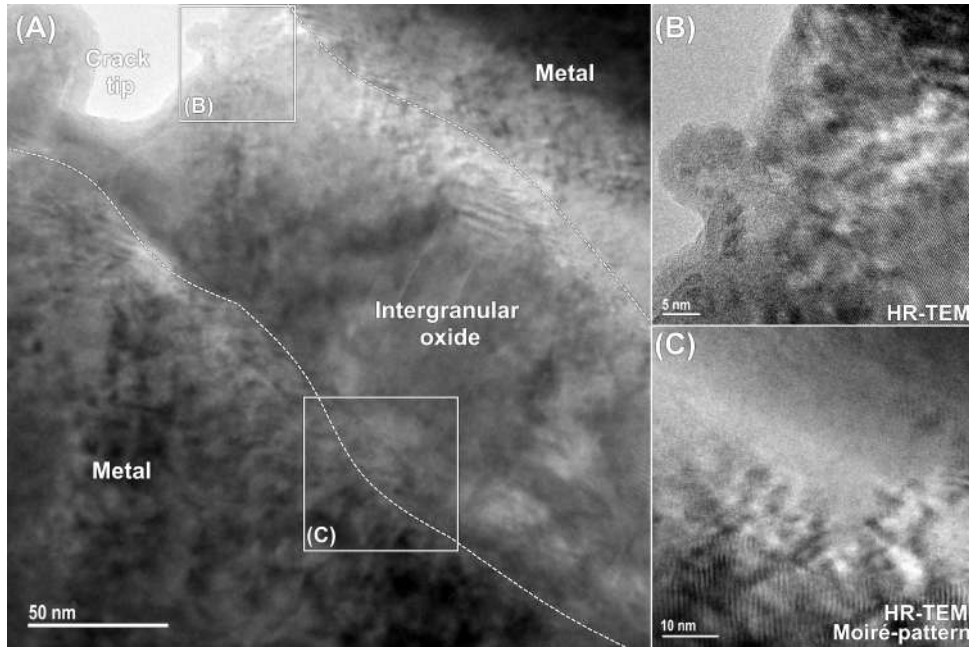


Figure 3.13: (A) BF-TEM image of an oxide intrusion leading into a grain boundary of an IASCC crack. (B) HR-TEM of the intergranular oxide at the crack tip. (C) HR-TEM Moiré pattern at the oxide-metal overlap.

concentrations C_A and C_B is dependent on a proportionality factor k_{AB} , where k_{AB} is determined by the various factors including the electron acceleration voltage, elemental ionization cross-sections, X-ray absorption etc. Because of the large variance of parameters, experimental determination of the k-factors is found limiting and time-consuming. To that end, analytical measurements often turn to theoretical approximations carried out by the commercial software equipped with the X-ray detectors, although an inaccuracy of $\pm 15 - 20\%$ can be expected [256].

$$\frac{C_A}{C_B} = k_{AB} \cdot \frac{I_A}{I_B} \quad (3.11)$$

3.3.3.5 Phase contrast and High-resolution TEM (HR-TEM)

High-resolution TEM (HR-TEM) allows for the direct imaging of atomic fringes, which may yield information about the local lattice crystal structure. Specifically, the separation between these atomic fringes may correlate to the largest lattice spacings, from which the crystal structure can be determined. The contrast in HR-TEM imaging is caused by interference between the forward-scattered and several other diffracted electron beams that are collected within the objective aperture. Usually, the largest or second-largest objective apertures are used in HR-TEM imaging. Thus, in principle, HR-TEM imaging is also viewed as phase contrast imaging, but only at substantially increased magnifications. Interference between all electron waves that are collected in a single objective aperture, may produce a superimposed resultant wave which depends on the separate phases of each wave specifically. The intensity of this resultant wave can be shown to be a sinusoidal oscillation with the same periodicity as the crystal lattice spacing. Essentially, this oscillation is directly representative to the bright-dark atomic lattice fringes typically observed in an HR-TEM image. As the lattice periodicity is highest in zone-axis orientation, direct observation of the lattice fringes comes most easily when tilted to high-symmetry zone axes. A typical example of a HR-TEM image is displayed in Fig. 3.13.

Of additional importance to HR-TEM, are the contrast fluctuations related to the performance of the objective lens. If not addressed, the OL may be strongly influenced by lens aberrations such as objective astigmatism and spherical aberration. The former implies a rotational streaking effect caused by an improper lens-field that becomes apparent when going through focus. On the other hand, spherical aberration suggests the improper focus of collected waves in the OL to spherical disks, rather than precise focal points. At high magnifications, said aberrations together with the objective focus may cause contrast variance, or otherwise limit the spatial resolution, that can be acquired during HR-TEM imaging.

Another matter to look out for when performing HR-TEM, or phase contrast imaging in general, is the occurrence of Moiré patterns, see Fig. 3.13C. Since corrosion along investigated crack tips may develop different overlapping crystallite phases, diffraction spots from those different phases may be collected together within the objective aperture. The resultant phase-contrasted image may contain additional Moiré fringes when certain crystals with a similar structure and orientation, but with a different lattice spacing, overlap each other. It can be proven that the spacing between these counterfeit fringes is given by:

$$d_{\text{Moiré}} = \text{abs} \left(\frac{d_1 d_2}{d_1 - d_2} \right) \quad (3.12)$$

wherein d_1 and d_2 are the lattice spacings of the crystal planes between two overlapping phases.

3.4 Scanning TEM (STEM)

While for most common practices a parallel beam illumination in TEM imaging is used, scanning transmission electron microscopy (STEM) focusses the electron beam at a larger angle and converges it onto the specimen surface. The primary electron beam is rastered across the sample and its transmitted signal is recorded as a function of its impinging location. The scanning of the primary electron beam is achieved through an additional set of deflection coils below the secondary condenser lens, while the converged beam onto the sample is managed by the C3 lens accordingly. In this respect, the spatial resolution that is achieved in STEM-mode is directly related to the electron beam's probe size that is rastered across the specimen plane.

3.4.1 STEM Image formation

The image formation in STEM is entirely different than compared to common TEM imaging. In order to produce diffraction contrast in TEM mode, an objective aperture is inserted to only allow the directly transmitted or a diffracted electron beam to continue into the projector stage. However, during STEM imaging, different electron detectors are inserted instead. Three different detectors are used to obtain STEM images, namely the BF-, annular DF- (ADF-), and high-angle annular DF- (HAADF-) STEM detectors are displayed in Fig. 3.14. In order to produce meaningful images, only the desired electrons are allowed to be detected by the corresponding STEM detectors. The detectors themselves are ring-shaped (or otherwise referred to as annular) and inserted to collect scattered electrons at specific angles (see θ_{1-3}). The STEM image intensity at every position is proportional to the amount of scattered electrons that were collected for every detector angle.

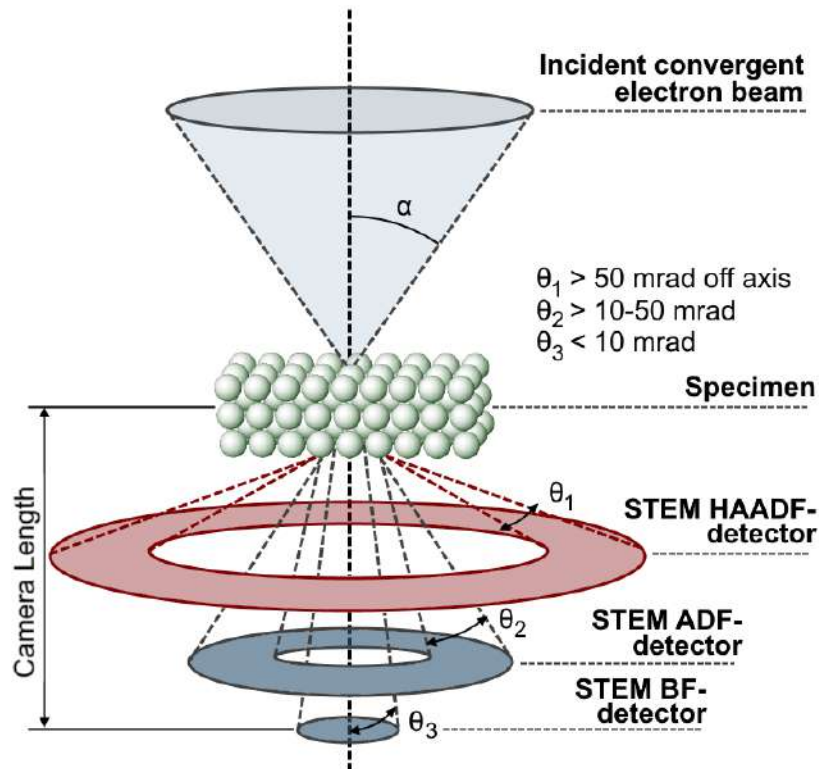


Figure 3.14: Schematic diagram illustrative of the geometric arrangement of the STEM-BF, -ADF and -HAADF detectors. The (semi-) collection angles of the BF- and DF-detector are representative for a 200 kV non-corrected STEM and may vary depending on the mode of operations. Redrawn from reference [257].

3.4.2 High-angle annular dark field (HAADF)

In principle, the transmitted electron beams scatter from the specimen plane onto the subsequent STEM detectors in the projector stage. These scattering events are directly related to the local thickness and atomic scattering amplitude of where the impinging electron beam was rastered across the specimen. In that sense, the contrast variation in STEM is similar to mass-thickness contrast in TEM. In fact, the scattering amplitude is linearly related to the atomic weight ($f \propto Z$), and thus modulus squared in relation the image intensity ($I \propto |Z|^2$). It is for that reason that STEM HAADF imaging is often also referred to as Z-contrast imaging. Without the detection of the transmitted electron beam, a HAADF-image is therefore only related to the chemical variation of the specimen, which makes it ideally suited to directly image the local elemental concentration in a specific region. As a general rule of thumb, it is perceived that heavier (respectively, thicker) rather than lighter (respectively, thinner) elements (respectively, regions), scatter more electrons and therefore produce more image contrast in STEM HAADF imaging than otherwise.

For the interest of STEM imaging in this research, Z-contrast imaging was employed to deliver chemically-sensitive information of crack tips and leading crack tip grain boundaries. STEM HAADF-EDS imaging was utilized to provide quantified spectral maps and line scans to characterize the chemical structural and influence of minor elements along the grain boundary, and relate those changes in view of probable cause of intergranular cracking. Of particular interest within the research, was the investigation the chemistry and oxidation of intergranular crack tip and the RIS profiles along their leading grain boundaries. A classical example of a crack that attracts interest is displayed in the BF-

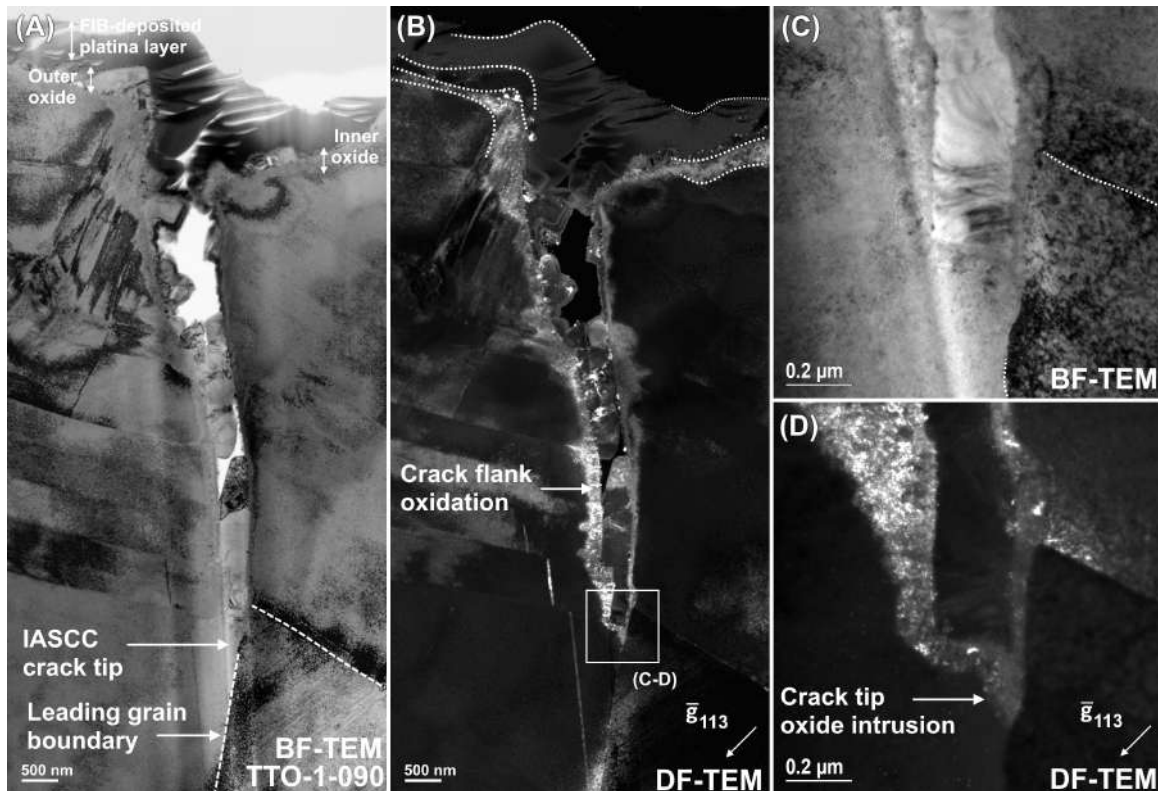


Figure 3.15: (A) BF-TEM and (B) CDF-TEM of an intergranular crack tip and its leading grain boundary. More magnified images are respectively displayed in images (C-D), which attract a lot of interest for analytical TEM and STEM investigations.

and CDF-TEM images in Fig. 3.15. The CDF-TEM images were taken with an objective aperture centered around an inner oxide reflection along the crack flanks.

3.5 Material investigation

In the first half of this chapter, sections 3.1 - 3.4 presented an overview of the experimental characterization techniques that were employed during this research. The focus was given to the imaging techniques that were employed for each specific instrument, in addition to their application to the field of stress corrosion characterization.

This second half goes on to discuss the double-set of investigated materials for which these experimental techniques were applied. The first set of materials concerns a series of tailor-made tapered tensile specimens made from a high Si SS duplex model alloy. SEM formed an integral part of the SCC characterization in said tapered specimens, especially in terms of crack initiation along the tested gauge length after prior corrosion-testing. The details of the crack initiation testing and the following analysis techniques are discussed in the subsequent sections of 3.5.1. The second testing material regards the intricate 316L cold-worked SS flux thimble tube i.e., an internal reactor component recently decommissioned from the commercial Belgian PWR NPP Tihange 2. The thimble tube is a long and slender steel tube that is mounted to the reactor fuel assembly from the lower internal component side of the RPV structure. Reactor coolant pressure and temperature act upon its outside surface, while the tube's internal volume is held under atmospheric conditions. Its function is to moderate the fission reaction by providing a way for the neutron flux detector to detect the neutron fluence of

Table 3.3: Elemental composition of duplex high Si SS tapered specimens and 316L cold-worked flux thimble tube O-ring specimens.

Test Material	Fe	Cr	Ni	Mn	Mo	Si	Co	Cu	Al	P	S	C
High Si SS alloy	Bal.	19.7	9.98	1.08	-	4.85	-	0.22	0.033	0.008	0.005	0.029
316L SS (20% cold-worked)	Bal.	17.0	12.8	1.79	2.68	0.53	0.07	-	-	0.022	0.009	0.044

the internal reactor core. The thimble tube that was acquired for this study was retrieved from the inside of a nuclear reactor and remained operational for about 25 years. To this end, the thimble tube is considered as unique test material for the characterization of IASCC. As explained in section 3.5.2 and beyond, FIB and TEM were the main tools of investigation for the specimens acquired from the thimble tube. The primary goal relates to the investigation of the microstructural and chemical aspects of intergranular crack tips, in order to elucidate the complex mechanism responsible for IASCC. The material composition of both the duplex SS model alloy and the 316L SS alloy can be found in Tab. 3.3.

3.5.1 High Si SS tapered specimens

In this section, we discuss the use of tapered tensile specimens tailor-made from a model alloy of high Si duplex SS, known to be susceptible to SCC in pressurized water reactor (PWR) primary water [35, 36, 258]. These specimens were made on account of the Euratom-funded FP6 project PERFECT [258] resembling 316 SS type baffle bolts. The model alloy contains high concentrations of Si, which (i) primarily mimics effects of RIS in an otherwise unirradiated material and (ii) secondarily increases the dislocation density which improves the ferrite matrix strength in duplex ferrite-austenite SSs [259, 260]. As discussed in section 2.3.2.1, RIS describes the radiation-induced composition changes of structural and solute elements at the local site of a grain boundary. Though, without the aspect of neutron-irradiation, it is difficult to simulate the driving forces that causes Si to segregate at the grain-boundaries. To that end, this un-irradiated model type alloy attempts to reflect the composition of a radiation-induced Si-segregated grain boundary by containing high concentrations of Si in and of itself. Therefore, this material is considered to be susceptible to SCC in the un-irradiated condition and, as such, deemed as a useful surrogate material for investigating the crack initiation in simulated PWR environments.

However, one initially unanticipated consequence of the high-Si addition is that the material has a duplex SS microstructure which is atypical for common austenitic structural materials. This duplex microstructure results in regions of elongated and vein-like austenite which resides in a continuous matrix phase of ferrite. The ferrite phase causes the model alloy to improve its general corrosion resistance, but otherwise also confines the initiation of SCC to the other possible material phase being the austenite matrix. Although the model alloy has useful properties as a surrogate material susceptible to SCC in high-temperature water without being irradiated, the cracking mechanism may not be entirely comparable to irradiated steels as initially predicted before this study initiated. More elaboration on this is presented in after the results of chapter 4.

3.5.1.1 Tapered specimens and CERT-testing

The high Si SS model alloy was shaped in the form of tapered dog bone specimens with gradually increasing cross sections, hence referred to as the tapered specimen gauge length, see Fig. 3.16A. Its

material composition can be found in Tab. 3.3. The tapered specimens have a double shoulder at each end of the gauge portion, so that when a tensile force is applied to the sample, the point of maximum stress is concentrated at the shoulder's smallest cross-section. This stress concentration increases the probability that the sample may fracture at this location. When this is the case, the failure is typically ascribed to the material reaching its maximum tensile strength, as is typically indicated in the load-elongation data. However if the sample ruptures at any other location, the failure may be attributed to inappropriate loading or a pre-existing fault in the material. To that end, tapered specimens are primarily used in tensile experiments because of their geometry.

In the interest of investigating SCC crack initiation, high Si SS tapered specimens were subjected to the combined action of an externally applied tensile load and a simulated corrosive PWR atmosphere. These corrosion experiments were performed at SCKCEN's corrosion laboratory in autoclave testing units. The autoclaves were equipped with an internal loading unit capable of performing slow strain-rate constant elongation rate tensile (CERT) tests at a constant temperature of 340° C, while maintaining an ambient simulated PWR-water (2 ppm of Li; 1000 ppm of B; 30 cc/kg H₂ i.e. equivalent to 2.66 ppm H₂) or an inert N₂ environment. An initial loading phase, under a pre-load of maximum 200 N at the given test temperature and water chemistry is typically carried out first. This pre-loading ensures the growth of a stable oxide film on the specimen, and sets the prerequisite conditions for SCC initiation. It has been demonstrated that pre-hardening promotes the initiation and propagation of SCC crack growth when conducted under PWR conditions [174]. The actual CERT-straining in the autoclaves is initiated in the second loading phase. Different strain-rates were applied for various tapered specimens in order to study the effect of loading on crack initiation. For an overview of the test specimen table and their applied loading conditions, see Tab. 3.4. Constant testing conditions were ensured through active load-control use in combination with high flowrate, recirculating, water conduct systems to maintain the water chemistry. Typical test durations varied between 10 and 34 days, respectively, for the fastest and slowest nominal strain-rates. The CERT-testing is performed until global specimen failure is achieved.

Because the local strain-rate varies as a function of the tapered cross-section, each section of the gauge length undergoes a different straining process that changes throughout the test. In this manner, a stress gradient across the specimen's fracture surface is created which is dependent on the local tapered cross-section. Hence, post CERT-testing, the specimen's gauge surface is completely covered with SCC cracks, see Fig. 3.16B; the density of which is determined completely by the combined impact of the stress gradient across the surface and the impact of the simulated PWR atmosphere. The following principle idea of these CERT-tests is then to correlate the exact location beyond which no stress corrosion cracks occur with the active stress value that is critical at this location. This critical location is linked with a critical stress value whereat no SCC cracks can initiate, simply because the driving impact stress is too low. Henceforth, the stress at this location is termed the critical stress threshold σ_{thr} . Determination of the stress threshold is performed by calculating the ratio between the maximum CERT-load that occurs during the tensile test i.e. F_M , with the respective critical cross-section whereat no SCC cracks are detected i.e. ϕ_c multiplied by the local specimen thickness at the fracture point t_c :

$$\sigma_{\text{thr}} = \frac{F_M}{\phi_c t_c} \quad (3.13)$$

In order to determine the stress threshold, an accurate methodology needs to be developed for the estimation of ϕ_c i.e. the critical threshold whereat no SCC cracks can be detected. This estimation

Table 3.4: Test results for tapered specimens CERT-strained under both a PWR and inert N₂ ambient environments.

Sample No.	Nominal $\dot{\epsilon}$ (s ⁻¹)	Thickness (mm)	F _M (N)	Ambient environment
1	5.00 E-8	1.51	3122	PWR
2	1.00 E-7	1.45	2909	PWR
3	5.00 E-7	1.33	3161	PWR
4	1.00 E-6	1.39	2903	PWR
5	5.00 E-6	1.48	3153	PWR
6	5.00 E-7	1.44	3464	N ₂
7	5.00 E-7	1.42	3378	N ₂
8	1.00 E-7	1.43	3370	N ₂

should both be standardized that is, free from human bias, and reproducible in subsequent analyzes. Furthermore, significant scatter in already existing threshold analyses [261–264] underline the need for additional tapered tensile testing and improved crack identification methodologies in order to increase the reliability of the obtained threshold evaluation. Therefore, the details of this newly developed methodology are described and further explained in the subsequent paragraph 3.5.1.2.

3.5.1.2 Crack detection algorithm

Post CERT-test analysis of the crack formation of the tapered specimens is executed with a JSM-6610 LV SEM. SEM images were iteratively taken along the gauge length starting from the main fracture surface. The crack detection is constrained by the SEM's spatial resolution at a specific accelerating voltage and magnification. An accelerating voltage of 30 kV at $\times 500$ magnification was found as a proper compromise between a spatial resolution of about 3 nm for accurate crack detection on the one hand, and a broad gauge field-of-view for reliable crack statistics on the other hand. BSE SEM imaging proved to be more representative than SE imaging as more extensive, oxide-penetrating SCC cracks are more properly visualised.

The crack detections on the individual SEM frames were carried out using a ridge-detector tool based on the detection of curvilinear structures from the open-source image processing software FIJI [265]. Such computer vision tools attempt to interpret visual imagery in an automated and humanly unbiased manner within a relatively short time-frame. In this respect, the ridge-detector employs Steger's effective and subpixel accurate line detection algorithm [266] to analyze the crack initiation in the CERT-strained SS tensile specimens. Mathematical operations involving the local approximation of the image pixel values with a higher-order Taylor expansion, the corresponding Hessian matrix, and its eigenvalues and eigenvectors define the local image topography of the analyzed SEM frame. The eigenvalues can be used as indicators to identify salient pixel lines of extreme grey values relating to actual cracks depicted in the SEM frames. In this manner, numerous imaged SCC cracks can be efficiently detected from a single SEM frame as valleys consisting of low pixel grey values surrounded by higher pixel-valued surface material regions.

Cracks of post CERT-tested tapered specimens are detected from the fracture surface according to a set of relevant detection parameters by means of FIJI's ridge-detector algorithm. However, inadequate crack detection from a single set of detection parameters calls for the need for varied parameter detections in order to gain a complete overview of all the crack profiles present in a single SEM frame. To that end, several crack detection runs were performed for varied parameters, primarily including a varied crack lengths and widths. These multiple detections ensure that the vast majority of all cracks in a series of SEM pictures across the gauge length are detected. The detected crack parameters, in-

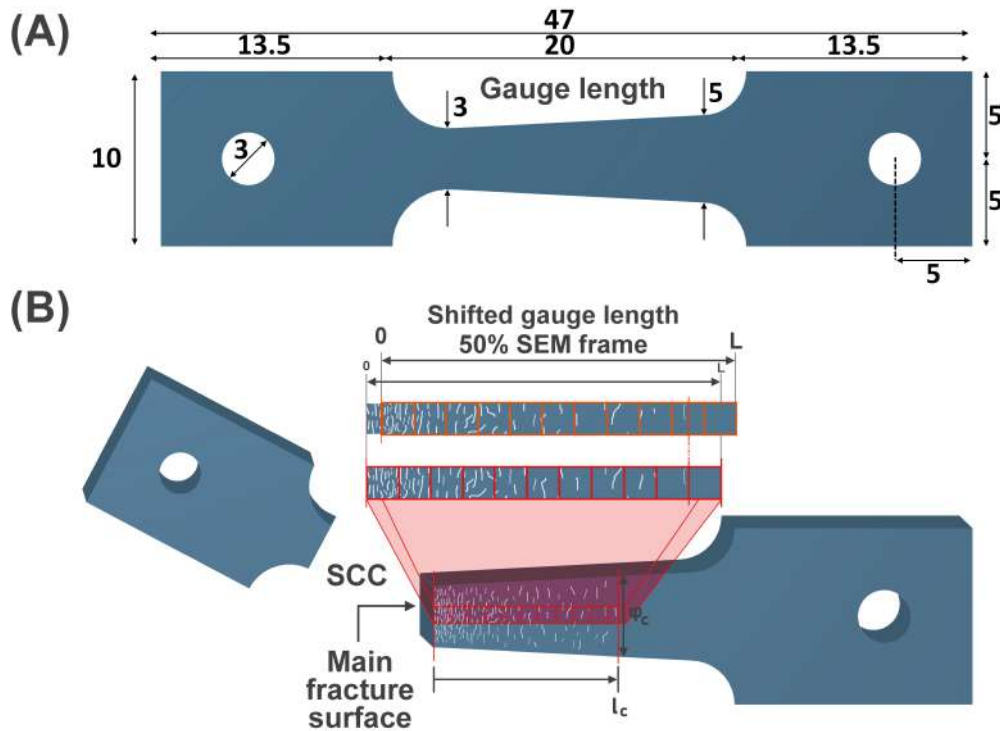


Figure 3.16: Overview of a typical tapered tensile specimen, (A) pre and (B) post CERT-testing after specimen failure. The distances are given in mm.

cluding their lengths, widths and relative angles, are consequently stored in large detection matrices. However, this methodology yields detections that are accompanied with distinct numerical problems, namely (i) the false detection of sample characteristics like the ferrite-austenite transitions, oxide crystals, and CERT deformation grooves, (ii) numerous identically detected cracks for different detection parameters, and (iii) of those identically detected cracks, certain ones may not be detected to their fullest extent. These problems contribute to over-counting and lead to deceitful interpretations of the density distributions.

For that purpose, a MATLAB script file was created to objectively filter out such false-detections, the key features of which are shown in the flowchart displayed in Fig. 3.17A. In order to overcome the first problem, additional filtering algorithms based on the crack detection parameters were devised in order to address the false detection of inherent sample features. Essentially, the first mean crack angle filter algorithm excludes those detections that do not correspond to a fixed angle interval centered around the perpendicular angle around the gauge length. In this manner, all indications of surface deformation are distinguished from true crack detections as these only occur perpendicularly (around 90°) to the loading axis, see Fig. 3.17B. On the other hand, a secondary segmented length filter was devised in order to exclude all detections that pertain to a significant line curvature. Such false detections typically entail the circular surface oxide crystals on the fracture surface, and are hence filtered out. Concerning the second and third problems relating to the identically detected cracks for various parameters, a specialized clustering algorithm is outlined based on the respective crack positions. Fig. 3.17C illustrates how multiple identically detected cracks can be categorized into one and the same cluster, and consequently differentiated from neighboring cracks based on their relative position. A distance threshold, which is typically of a subpixel to a few pixels in order, is empirically optimized on reference pictures with manually counted cracks. Since the vast majority of the cracks occur perpendicularly to the load-axis, the optimization scheme specifically clusters cracks

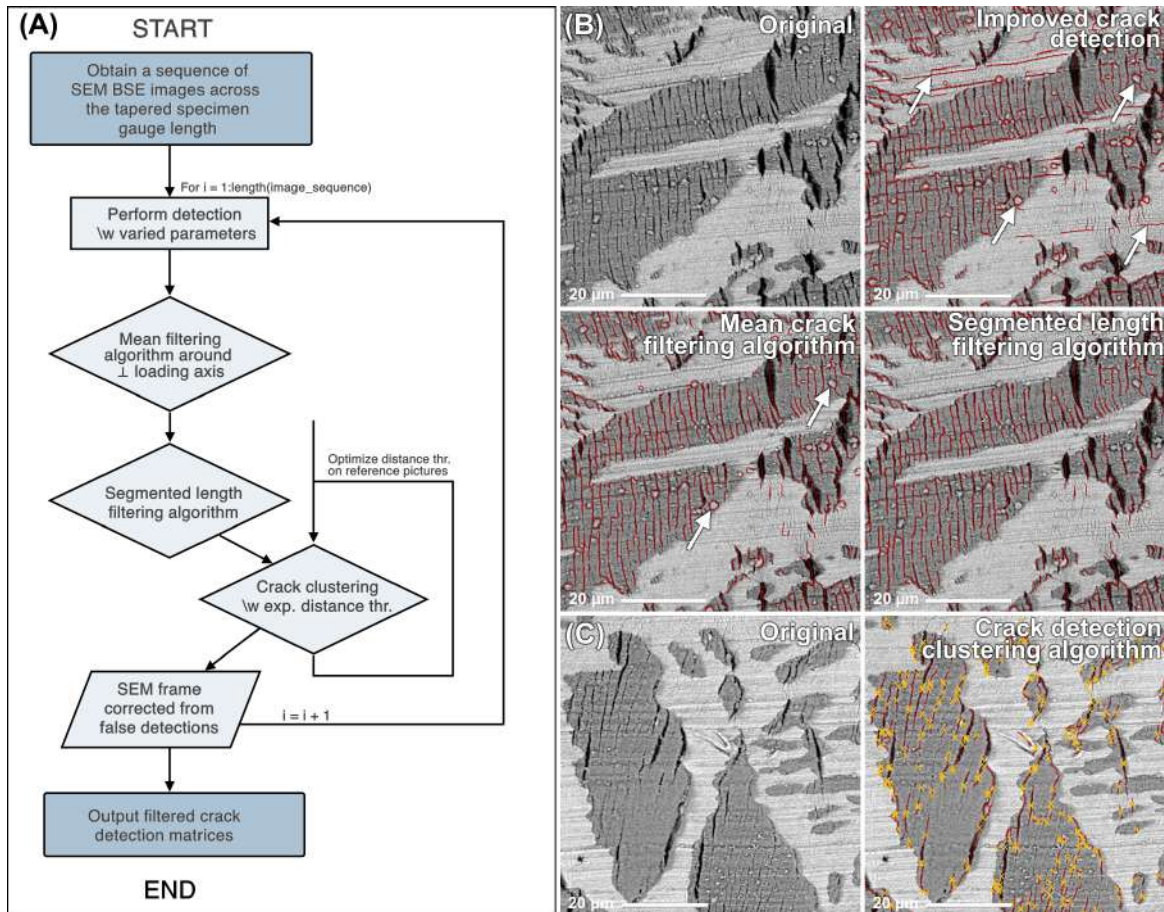


Figure 3.17: Functionality of the MATLAB script file handling the improved detection based on several filtering algorithms. (A) Flowchart of the algorithm. (B) Performance of the mean crack angle and segmented length filters on SEM BSE images. Indications highlight various false-detected surface features, excluded from the detection in the next filter (as indicated by arrows). (C) Performance of the crack clustering algorithm. Nearby clusters indicate similar and overcounted cracks (as indicated by crosses).

with slightly differentiating vertical positions. The distance threshold is determined when the crack clustering yields similar crack count rates after the final filtering is applied. Multiple detected cracks, and those that are not detected to their fullest extent, may therefore be categorized into one and the same cluster and are hence filtered out.

The crack densities obtained from the ridge-detection methodology are evaluated based on a preset crack length threshold, which was empirically chosen based on the initial microscope magnification settings. In this manner, only cracks with a crack length larger than this threshold are accounted within the density distributions. Based upon the operational settings of the employed JSM-6610 LV SEM, a length threshold of $10\ \mu\text{m}$ was found to be a good compromise between reliably representing the cracking initiations per specimen on the one hand, without too heavily affecting the results with the numerical problems associated with the multiple detections using the ridge-detection tool on the other hand. Error bars associated to the crack density distributions resemble the count errors that occur during the estimation of the undetected- or overestimated cracks in the crack detection algorithm. These count errors are evaluated by spatially shifting the initial gauge length SEM series by 50% of a SEM frame, see Fig. 3.16B. An average of the residuals between the crack detections of the first series with those detected on the shifted series estimates that the apparent count error for each frame of the crack density distribution. Typically, a crack count error of about 10 cracks per frame per specimen

strain-rate is obtained in this manner. Other methods employed to estimate the count error, such as varying crack detection parameters like the filtering angle and the cluster threshold parameters in Fig. 3.17B-C, yielded lower count errors. Also, since austenite is generally more susceptible to SCC than ferrite within the duplex structure of the high Si SS alloy [267], a weighing factor is used to account for the varying austenite-ferrite surface composition throughout the gauge length of each specimen. Application of this weighing factor on the linear crack density distributions allows for direct comparison of the cracking incidences per strain-rate for specimens which would otherwise differ in their duplex surface composition. The weighing factor is determined by image recognition of both austenite-ferrite phases within the SEM-frames of the tapered gauge lengths. In this manner, all compositional effects between the varying density distributions per strain-rate are eliminated.

3.5.2 Flux thimble tube

In recent times, a 316L cold-worked SS flux thimble tube was decommissioned from the Belgian Tihange PWR NPP T2, which remained operational for about 25 years. Tab. 3.3 illustrates the material composition, which is comparable to the ASTM specification standards and to other flux thimble tube materials reported within the framework of the international IASCC committee program [268]. The material is also comparable to the structural materials used in BFBs. The radiation dose along the length of the thimble tube linearly increased between 45 to 80 dpa. The closer the tube was to the PWR reactor core, the more radiation dose it accumulated during its operational lifetime. The tube itself was about 4 m in length, with an inner and outer diameter of 5.20 mm and 7.50 mm respectively. It was cut along its length in specialized hot-cell facilities in order to produce many O-ring specimens of various dosages, depending on where they were extracted from the tube. Subsequent machining of the O-ring specimens was applied so that any potential weak crack initiation sites were removed, while still preserving, to the best extent as possible, the original in-service reactor oxide layer. These ring specimens were primarily used for the purpose of destructive analysis in order to investigate their mechanical properties as a function of time-to-failure under various applied mechanical loads.

3.5.2.1 Constant load compression testing

In highly irradiated cold-worked SSs, the crack growth rates during the operational lifetime of industrial specimens can be considerably high. Such growth rates are predominantly determined by the first stages in the process of crack growth i.e., the crack incubation and initiation periods (see also section 2.4.2), where the prerequisites of the material degradation are being established. For these purposes, a specialized O-ring compression test rig has been developed that can be used to test different specimens of thimble tube to failure. These samples are loaded to different stress levels, typically of significant fraction of irradiated yield stress, in order to investigate their time-to-failure as a function of the applied stress. The compression test is performed by a loading rig installed in an autoclave pressure unit displayed in Fig. 3.18A. The details of the compression test are given below.

A photographic representation of the compression test rig is illustrated in Fig. 3.18B. A section of a tube is diametrically compressed, generating tensile stresses in the material, see Fig. 3.18C. The four rods are utilized to deliver a compressive load to the O-ring, causing tensile and compressive stresses to be introduced at the material's inner and outer surfaces. Preliminary stress calculations in COMSOL Multiphysics [269] were carried out to calculate the maximal material stress as a function of the applied load and mounted O-ring widths, see 3.18D. It is apparent that, given wider O-ring sections, the specimen is able to bare more load resulting in a less maximally applied tensile surface stress. On the other hand, given stronger loads, higher surface tensile stresses were achieved that generally resulted in faster time-to-failures. The set-up has been designed in such a way that 5 different O-ring

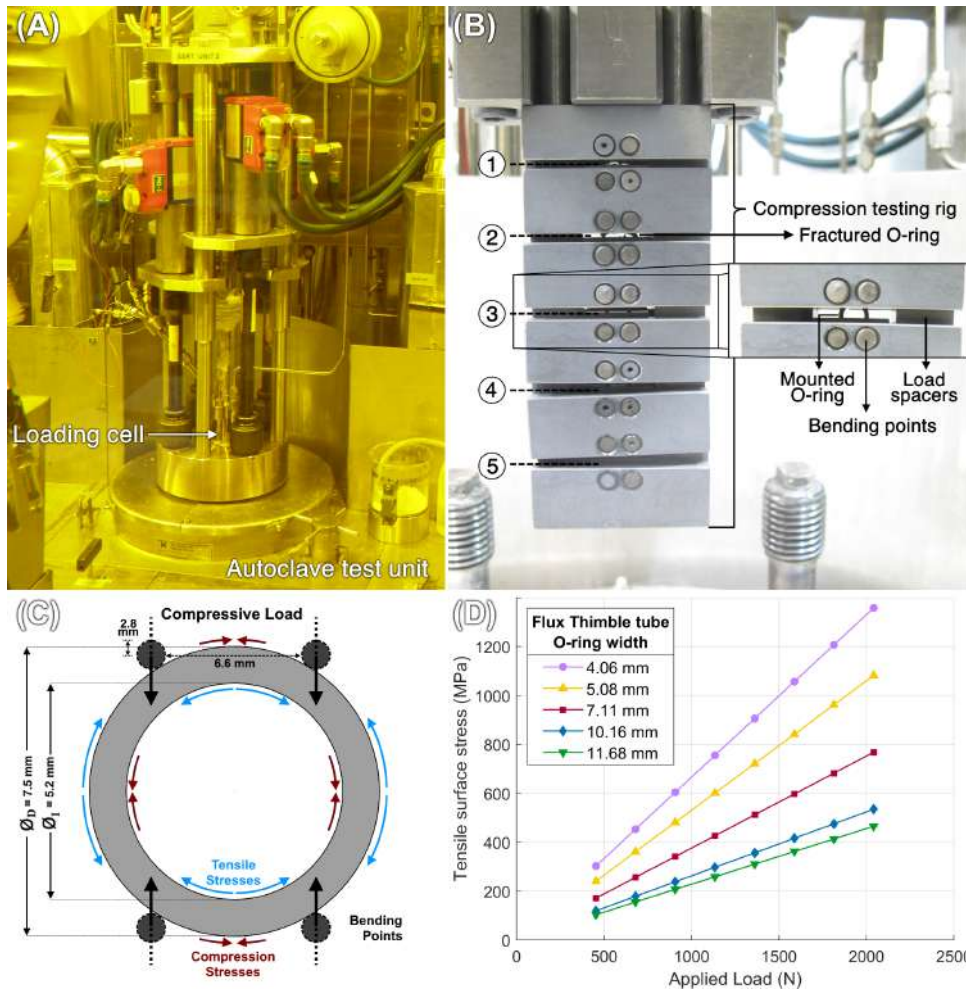


Figure 3.18: O-ring compression test rig. (A) Autoclave pressure unit installed in one of SCKCEN’s hot-cell facilities. (B) The compression loading unit capable of compressing five O-rings to failure. (C) Schematic representation of the tensile and compressive surface stresses on the inner and outer surfaces of the O-ring. Fracture typically occurs in the middle plane in between the bending points. (D) COMSOL Multiphysics stress calculations.

specimens may be tested simultaneously, with the same force applied to each ring by the loading unit, within an autoclave cell capable of simulating an ambient corrosive PWR atmosphere. Given the fact that each ring may have a varying specimen width, the advantage of this set-up allows the coincidental testing of these different rings at different stress levels. By compressing each ring with the same loading force, the yielded tensile stresses are inversely proportional to the ring length. In the event of a sudden failure of one of the five mounted O-ring specimens, the set-up is immediately compressed until the compressive load is taken up by the spacers on both side of the failed ring. In this way, the test can continue with the same load applied to the remaining rings without prematurely interrupting the test. The length of the spacers is different for every ring position, so that the compression distance is characteristic for the failure of every individual ring. In this way, the time to failure can be determined for each ring from the mechanical load data of the test.

In view of the fact that one O-ring specimen failure, depending on the compressive load and maximal tensile stress, may last for several weeks or even months, the prime benefit of this test rig is that multiple O-ring specimens may be tested at once without interruption. In this way, the compression test rig is another form of accelerated corrosion testing for the purpose of understanding crack growth, in a similar way as the accelerated CERT tensile testing was applied for the purpose of SCC investigation

Table 3.5: Flux thimble tube O-ring (TTO) specimen table. The yield stress of the irradiated SSs at PWR operating temperature (320°C) is determined to be 1000 MPa.

Specimen	Length (mm)	Dose (dpa)	Load (N)	Stress (MPa)	Fractured pieces	TTF (h)	Exposure time (h)	Surface condition	Loading path
TTO-1-053	10.425	60	3350	390	5	1910	4350	PWR oxide	Constant
TTO-1-071	8.32	80	3350	500	4	190	350	PWR oxide	Constant
TTO-1-001	5.94	80	3350	690	3	14.8	120	PWR oxide	Constant
TTO-1-090	5.89	80	3350	700	5	155.2	1102	Non-native oxide	Constant
TTO-1-066	14.66	80	1880 - 3000 - 4700	280 ±120	4	1680	1680	PWR oxide	Cyclic

in tapered specimens.

During the course of SCKCEN's thimble tube testing program, over 80 O-ring specimens were readily cut from the flux thimble tube and correspondingly tested to failure according to the methodology described above [161]. For the purposes of this study, especially in correspondence to the analyses performed in chapter 5, five different O-rings were selected for microscopical analysis of IASCC cracks, see Tab. 3.5. Three prime specimens were taken to study the effect of tensile stress and exposure time on the microstructure around intergranular cracks. These include different O-rings that were loaded to different stress levels, expressed in terms of the irradiated yield stress of the material. It is noteworthy that the time-to-failure, which is proportional to the exposure time to the PWR environment, drastically decreases in increasingly stressed specimens. On the other hand, two O-ring specimens were separately selected with specialized treatment to conclude the effects of surface oxidation and of the applied loading mode. In the first specimen, the O-ring was mechanically polished in order to remove its outer surface oxide layer prior to testing. The oxide removal was performed in a hot-cell autoclave with the O-ring mounted to a drill chuck while carefully spinning it against gritted sandpapers. Abrading the oxide layer prior to the compression testing would demonstrate the effect of oxide on the initiation and propagation of intergranular cracks in a sensitive material. Conversely, the final specimen was cyclically loaded to failure instead of the conventional constant loading applied to all other specimens. Cyclic loading consecutively removes and re-applies the compressive load to the O-ring in a systematic manner. This loading mode is expected to lead to a faster time-to-failures as the sample is essentially fatigued to failure during the compression test.

3.5.2.2 Sample preparation for microstructural analysis

Post compression testing, the irradiated O-ring specimens typically failed into several majorly connected pieces. Of these pieces, typically one was selected for the purpose of IASCC crack extraction using FIB-analysis. However, in order to comply with the dose limit of the FIB set-up, it was required to reduce the sample's radioactivity level down to a threshold value of around several mSv/h in contact or less, before it could be safely loaded into the instrument. For that purpose, the piece was cut by SCKCEN's trained engineers and specialized technicians in according to specific cutting schemes presented in Figs. 3.19 and 3.20. The final cut was performed in parallel to the fracture surface at a distance of about 1 mm. The remaining piece was slightly polished from both sides while still preserving the branched IASCC cracks on the fracture surface.

Interesting fractured O-ring pieces were generally selected for microstructural analysis in view of the fact that the primary fracture surfaces exhibited a full intergranular fracturing mode under prior scanning electron microscopy (SEM) investigation. Additionally, the observation of substantially branched

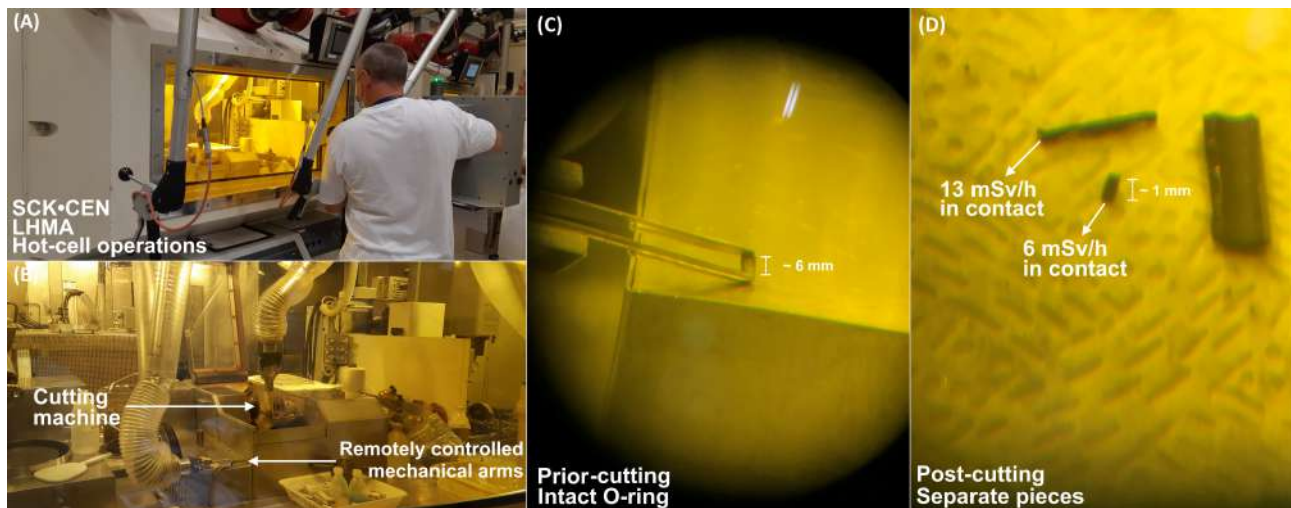


Figure 3.19: O-ring cutting procedure. (A) Operation of the hot-cell mechanical arms during the process of sample preparation. (B) Inside view of SCKCEN's hot-cell 37. (C) Irradiated O-ring prior to cutting, and (D) post-cutting.

cracking appearance on the O-ring's outer surface was considered a positive affirmation. This intergranular cracking is demonstrated in cross-sectional and edge-on orientation for one piece of interest, see Figs. 3.20D-E respectively. BSE SEM imaging provides excellent channeling contrast for the visualization of the individual grains which were typically of the order of several square micrometers.

3.6 Synthesis: Experimental Techniques

The following summarizes the techniques of interest that were performed in relation to the study of (IA)SCC crack tips. Each technique and its application was briefly described in the above paragraphs.

2 Experimental Methods

1. **Scanning electron microscopy (SEM)** was mainly utilized in the study of SCC initiation in tapered high Si SS specimens. Its uses were found in:
 - the development of a new methodology to obtain accurately detected crack density distributions from still SEM pictures along the gauge length of tapered specimens;
 - employment of a crack detection algorithm for planar surface cracks, primarily based on FIJI's ridge-detector functionality, in order to achieve said crack density distributions;
 - separately, to investigate the main fracture surface of tapered and neutron-irradiated O-ring specimens.
2. **Focused-ion beam (FIB)** analysis was employed for the following reasons:
 - sample preparation, primarily in the production on electron-transparent TEM-lamellae, valuable for subsequent TEM analyzes;
 - the study of SCC and IASCC cracks through low-voltage imaging.
3. **(Scanning) Transmission electron microscopy ((S)TEM)** was the main tool of investigation to study the morphology and microstructural aspect involving SCC and IASCC cracking.
 - TEM diffraction contrast, BF- and centralized DF-imaging demonstrates the extent of deformation in the bulk microstructure and the oxidation within fully developed, intergranular IASCC or transgranular SCC, crack tips;
 - Diffraction pattern analysis was useful in the study of oxide and microstructural defects

- within and adjacent to trans- and intergranular crack tips;
- STEM HAADF contrast originating from elastic scattering of primary beam electrons with atomic nuclei was primarily utilized for the sake of EDS mapping and line scans, in order to provide localized chemically-sensitive information around cracks and crack tips.

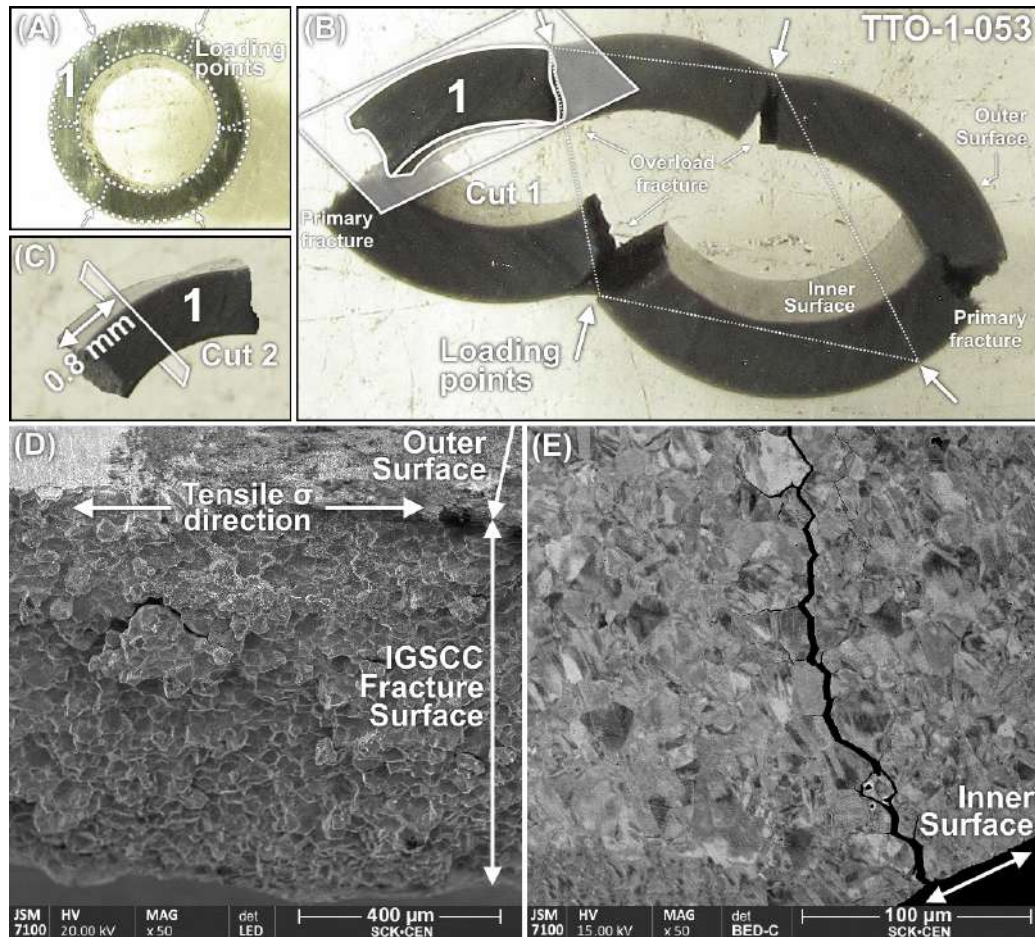


Figure 3.20: TTO-1-053 O-ring cutting scheme. (A) Intact O-ring specimen prior to constant load testing. (B) O-ring post constant load compression testing. Indications of the loading points and transversal cut along the middle of the specimen are depicted. (C) Second cut of the remaining piece, close to the primary fracture surface. (D) Secondary electron SEM view of the fracture surface illustrating the full intergranular mode. (E) Backscattered electron SEM view in edge-on orientation illustrating the extent of branched cracking from the inner surface.

Chapter 4

Tapered Specimens

This first results chapter is divided into two separate parts. The first half of this investigation presents the analysis of SCC crack initiation on the fracture surfaces of tapered specimens following CERT-tests at different strain-rates (see section 4.1). The details and goals of these tests are discussed in paragraph 3.5.1. Investigation of the initiated cracks is performed through iteratively taking SEM images along single strips of the specimens' gauge surfaces using the JSM-6610 LV SEM instrument. A crack detection algorithm is consequently applied to attain linear crack density distributions which show the onset of cracking along the specimens' lengths. These distributions indicate accurate estimations of the so-called critical gauge lengths, which can be correlated through equation 3.13 to a critical stress threshold. These values represent the gauge width at which no SCC cracking under the given stress value occurs. Additionally, a number of finite-element modelling (FEM) stress-analyses are performed using the software Ansys Workbench 2019 R2 to associate some of the prominent peaks in the crack density graphs with local stress concentrations. The results of this work have been reported in the following first-author publication [164]. The second half of this chapter proceeds to investigate the crack initiation from a more detailed microscopical point of view (see section 4.3). FIB is employed to extract cross-sectional slices of SCC cracks from the same subset of specimens after which TEM analysis is employed to investigate the cracks' morphology and surrounding microstructure. Detailed examinations of the SCC cracks, that include crack tip oxidation and surrounding deformation field analyzes, indicate towards the existence of an interplay between corrosion- and deformation-driven failure mechanisms as a function of the active strain-rate applied during the CERT-testing. Slow strain-rate crack tips exhibit a narrow cleavage failure which can be linked to the film-induced failure mechanism, while rounded shaped crack tips for faster strain-rates could be related to a strain-induced failure mechanism. These findings were reported in a succeeding first-author publication [270].

4.1 SEM investigation

4.1.1 CERT load-elongation curves

CERT-testing of high Si duplex stainless steel model type alloy tapered specimens was performed under both a corrosive simulated PWR and an inert N_2 environment. The details of the CERT-testing are displayed in Tab. 3.4 of the previous chapter. The load versus elongation curves obtained during the individual CERT-tests are represented in Fig. 4.1. It is clear from each curve that the elongation increases linearly with an increasing load in the first regime of the straining process. This regime is signified by an elastic deformation process whereat the imposed tensile load is directly proportional to

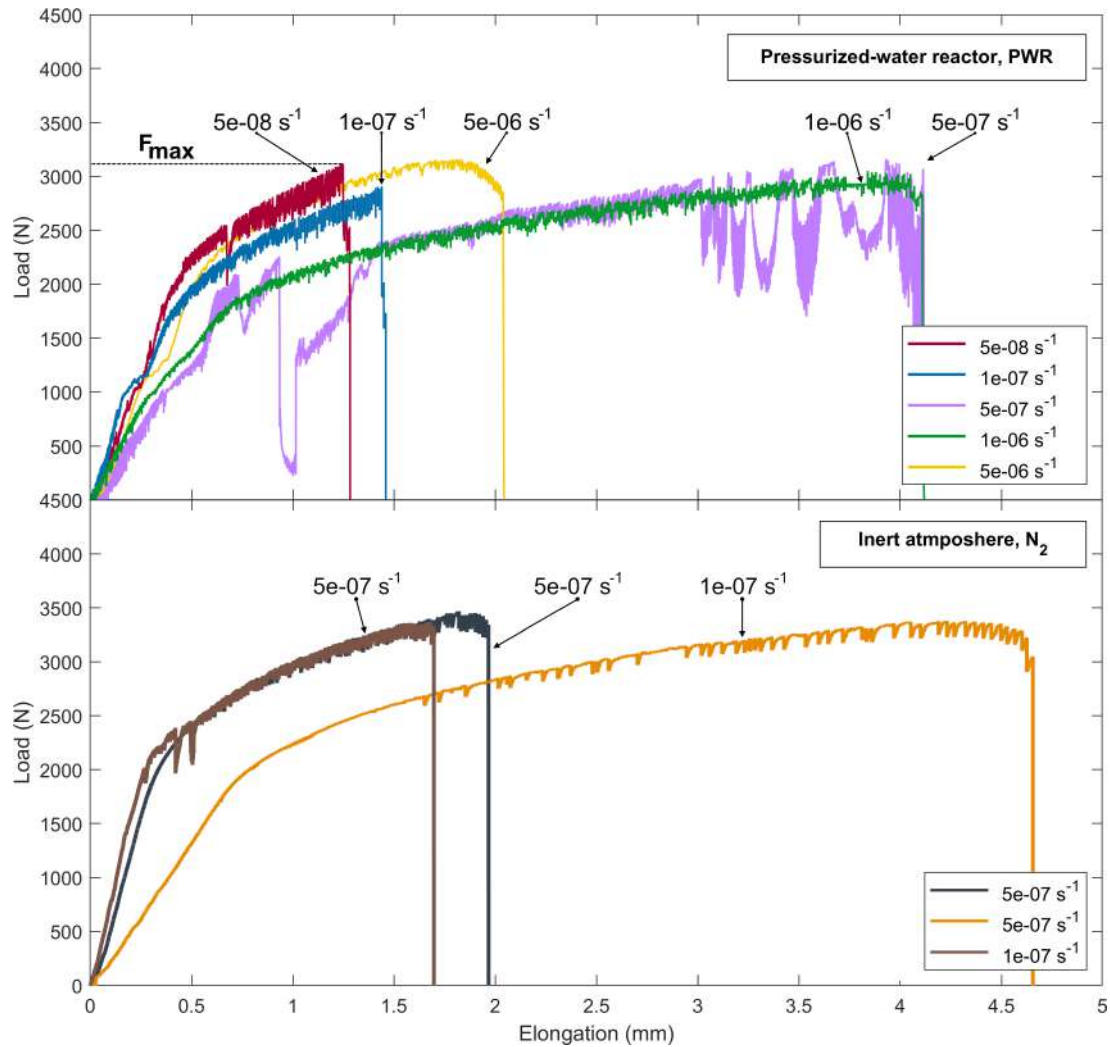


Figure 4.1: Autoclave load-elongation curves for high Si stainless steels obtained after CERT-testing, under (a) PWR and (b) inert N₂ conditions. The curves are corrected for an initial load offset due the small load oscillations before the CERT deformation.

the specimen strain. However, after the material's yield point is reached, a secondary regime of plastic behavior sets in. This regime is characterized by a uniform plastic deformation process determined by a increase in material elongation without a significant increment in applied tensile load. After the material's ultimate strength is obtained i.e., the maximally attained tensile load F_M , a non-uniform regime of plastic deformation known as necking leads to the final rupture of the specimen.

It is evident that for PWR tested specimens in Fig. 4.1A, the necking region is nearly non-existent for strain-rates below $1.00 \text{ E}-6 \text{ s}^{-1}$. This type of specimen failure is reminiscent of the abrupt cracking that occurs under SCC failure. Higher strain-rates however above $1.00 \text{ E}-6 \text{ s}^{-1}$ clearly show the onset of specimen necking which may indicate towards some type of strain-induced failure. For the tapered specimens tested under N₂ atmosphere in Fig. 4.1B, the necking region is apparent at all strain-rates; indicating that no SCC-type failure occurred under the inert environment. PWR tested specimens show a maximally attained tensile load within the range of $< 3200 \text{ N}$ while N₂ tested specimens reach to some extent higher loads. This implies that the load-bearing area of the PWR-tested specimens decreases more rapidly under the consequence of an SCC-type failure which is otherwise non-existent under N₂ conditions [271]. Interestingly, all specimens failed at varying elongations regardless of the

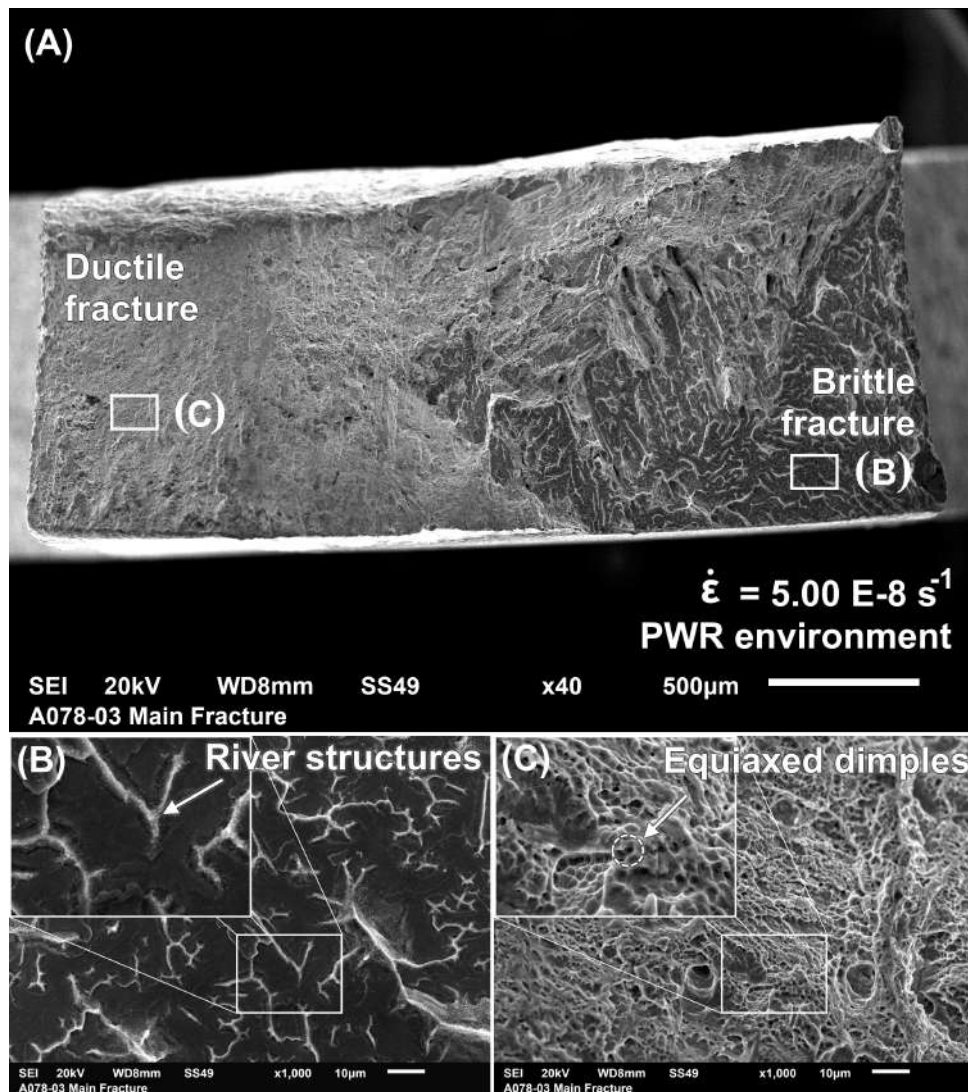


Figure 4.2: Main fracture surface of a tapered specimen tested under $\dot{\epsilon} = 5.00 \text{ E-}8 \text{ s}^{-1}$ in a simulated PWR environment. (A) General overview of the transgranular fracture, with (B) its brittle- and (C) its ductile-aspect of the fracture regions.

imposed strain-rate value or the applied environment. The yield- and maximal load points that were found are independent of the applied tensile strain-rate. Each specimen was subjected to rapid load variations originating from temperature and pressure fluctuations that occur during inconsistencies of the autoclave loading unit that performs the CERT-tests. Some small shoulders can be observed in the elastic regime of the PWR load-elongation curves which are inherently due to similar experimental artefacts of the load cell. The pressure in the autoclave unit may cause some brief compressive forces, typically of around 1000 N, which renders an overcorrected trace in the mechanical load data when accounting for this transition. Specifically for specimen $\dot{\epsilon} = 5.00 \text{ E-}7 \text{ s}^{-1}$, these inconsistencies may uniquely lead to large load drops at irregularly timed intervals. While its load-elongation curve is not consistent with the other specimens, the sample is still retained for the analysis purposes since the single interruption intervals are much shorter than the total test duration time. Aside from the load drops, its overall shape still represents a proper load-elongation measurement curve.

4.1.2 Main fracture surface investigation

In studying the main fracture surfaces of the failed tapered specimens, SEM images are taken to determine the principle failure mode of the specimens under the various environments. The load-elongation curves described in the previous paragraph signified a distinction in failure mechanism between PWR-tested specimens at a strain-rate of about $1.00 \text{ E}-6 \text{ s}^{-1}$. SEM investigation of the main fracture surfaces where the abrupt necking of the SCC and strain-induced failures occurred, underlines this result. Fig. 4.2A shows an exemplary fracture surface of a PWR-tested specimen at a strain-rate lower than $\text{E}-6 \text{ s}^{-1}$. For slow strain-rates, the main fracture surfaces displayed a mixed fracture mode between both brittle- and ductile-like fracture appearances. For the brittle-aspect of the fracture surface seen in Fig. 4.2B, macroscopically the surface reflectivity was remarkably high, and microscopically the fracture surface appearance demonstrated a smooth cleavage-like appearance. According to Becker [175], brittle-fractures are typically characterized by such a smooth cleavage fracture appearance while ductile fractures embody more strongly a dimple-like rough surface appearance. Brittle fractures as observed at lower strain-rates signify an abrupt and fast crack propagation reminiscent of a typical SCC type failure. Under SEM view, the brittle fracture displays the appearance of river lines along the cleavage surface. Such lines display the localized directions of crack growth during the failure process [175]. Most especially, at the brittle site of the main fracture surface, the austenitic phase of the duplex structure was observed. This can be reasoned because the surface roughness is typically smoother for higher strength materials, while a rougher surface can be expected for lower strength materials [175]. Hardness measurements of duplex stainless steels have indicated that austenite exemplifies a higher averaged hardness than ferrite [272], which supports this result.

Adjacent to the brittle-aspect of the fracture lies a large region showing extensive plastic deformation as seen in Fig. 4.2C. Macroscopically, this part of the fracture surface was more matte in visual appearance, while microscopically its appearance was distinguished predominantly by a completely covered dimple surface. Microscale dimples typically represent a ductile overload part of the fracture surface in most engineering materials [175]. Dimples arise on the fracture surface because of the microscale mechanism known as microvoid coalescence [175, 273, 274]. Microvoid coalescence occurs when void defects are formed around tiny inclusions in the material as it deforms plastically under stresses beyond the material's yield stress. During the necking process, these microvoids tend to combine together to coalesce into larger material voids embodied by dimples. At the final stages of rupture, material decohesion occurs at the ridges of these dimples. Ductile fractures are initiated by a process wherein dimples develop in size either from pre-existing cracks or from void-like defects or large void structures [175]. Dimples can be seen as incipient cracks within the material along the fracture surface. They appear equiaxed in shape under tensile loading conditions, as is the case for most of the fracture appearances in these type of samples, while under shear- or torsional loading, they often appear more elliptical instead.

On the other hand, for strain-rates above $1.00 \text{ E}-6 \text{ s}^{-1}$, the load-elongation curves expected a full strain-induced failure mechanism characterized by signs of ductile necking without showing any signs of an abrupt SCC failure. For such specimens, Fig. 4.3A displays an exemplary overview of the main fracture surface. Fast-strained specimens showed exclusively ductile fracture surface appearances as exemplified by the abundant dimples seen most prominently in Figs. 4.3B-C. This is because void formation within the process of microvoid coalescence, and thus as a result also ductile crack propagation as a whole, is more favored at high strain-rates instead. The numerous dimples at the ductile-aspect of the fracture surface are uniformly filled by small precipitated oxides.

Alternatively, for specimens subjected to inert N_2 atmospherical conditions, large necking was observed

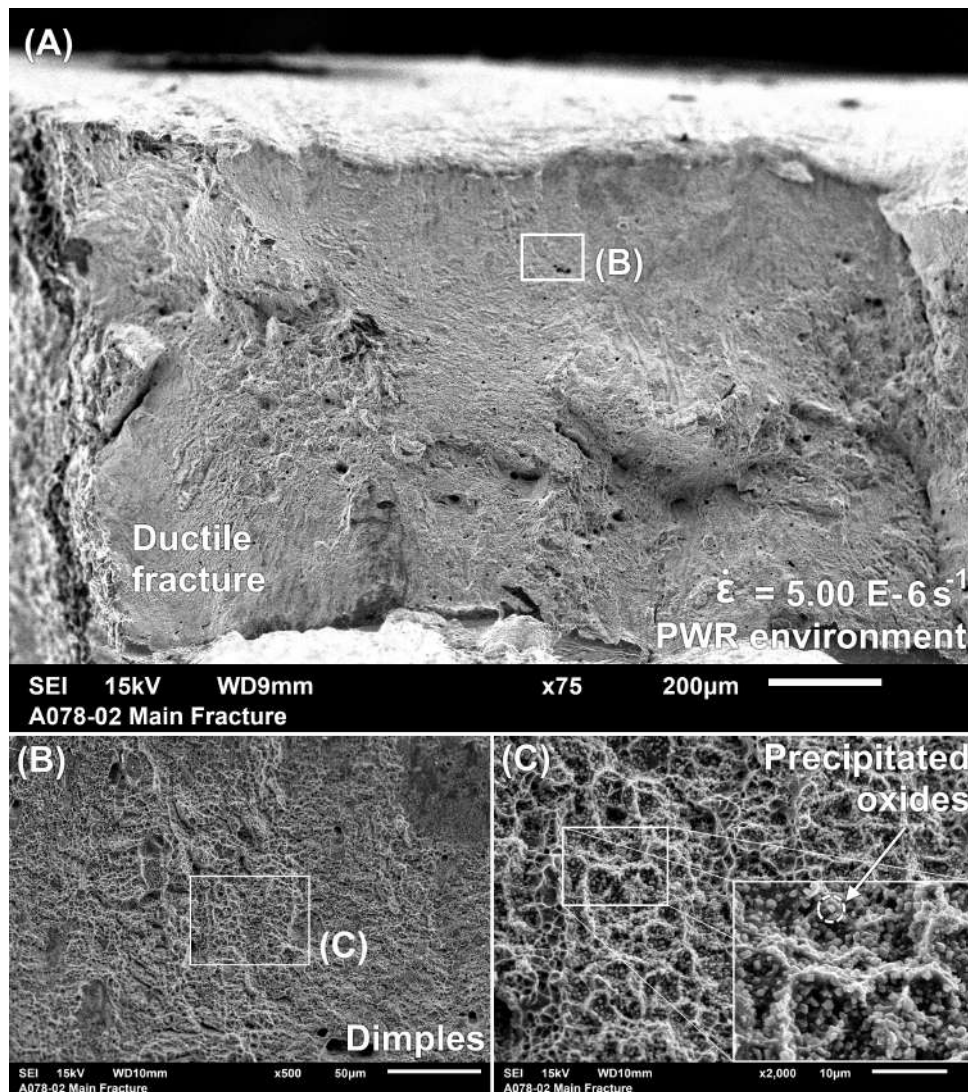


Figure 4.3: Main fracture surface of a tapered specimen tested under $\dot{\epsilon} = 5.00 \text{ E-}6 \text{ s}^{-1}$ in a simulated PWR environment. (A) General overview of the transgranular fracture with (B-C) its ductile-aspects of the fracture regions.

in the load-elongation curves in a similar fashion as for high strain-rate PWR failures. This necking was also observed in the reduced load-bearing area of Fig. 4.4A, which displays an exemplary main fracture surface of a N_2 -tested specimen at a strain-rate of about $5.00 \text{ E-}7 \text{ s}^{-1}$. As expected, the specimen's fracture surface is completely covered by equiaxed dimples seen in Figs. 4.4B-C. Such dimples can be attributed to a ductile mechanical overload failure [175], reminiscent of what is observed at high strain-rates in common PWR environments. The fractures for specimens tested in the inert environment remained completely ductile regardless of the applied strain-rate.

4.1.3 EDS-spectra

Investigation of the cracking appearance on the main fracture surface is performed at first hand by means of the FIB-SEM's EDS utilities. Fig. 4.5 depicts the main most-relevant EDS spectral maps of the duplex microstructure for a specimen strained to failure at a strain-rate of $\dot{\epsilon} = 5.00 \text{ E-}7 \text{ s}^{-1}$. These maps reveal a clear distinction between the austenitic and ferritic phases of the gauge length. The austenite phase, wherein the cracking almost exclusively occurred, is characterized by enriched signals

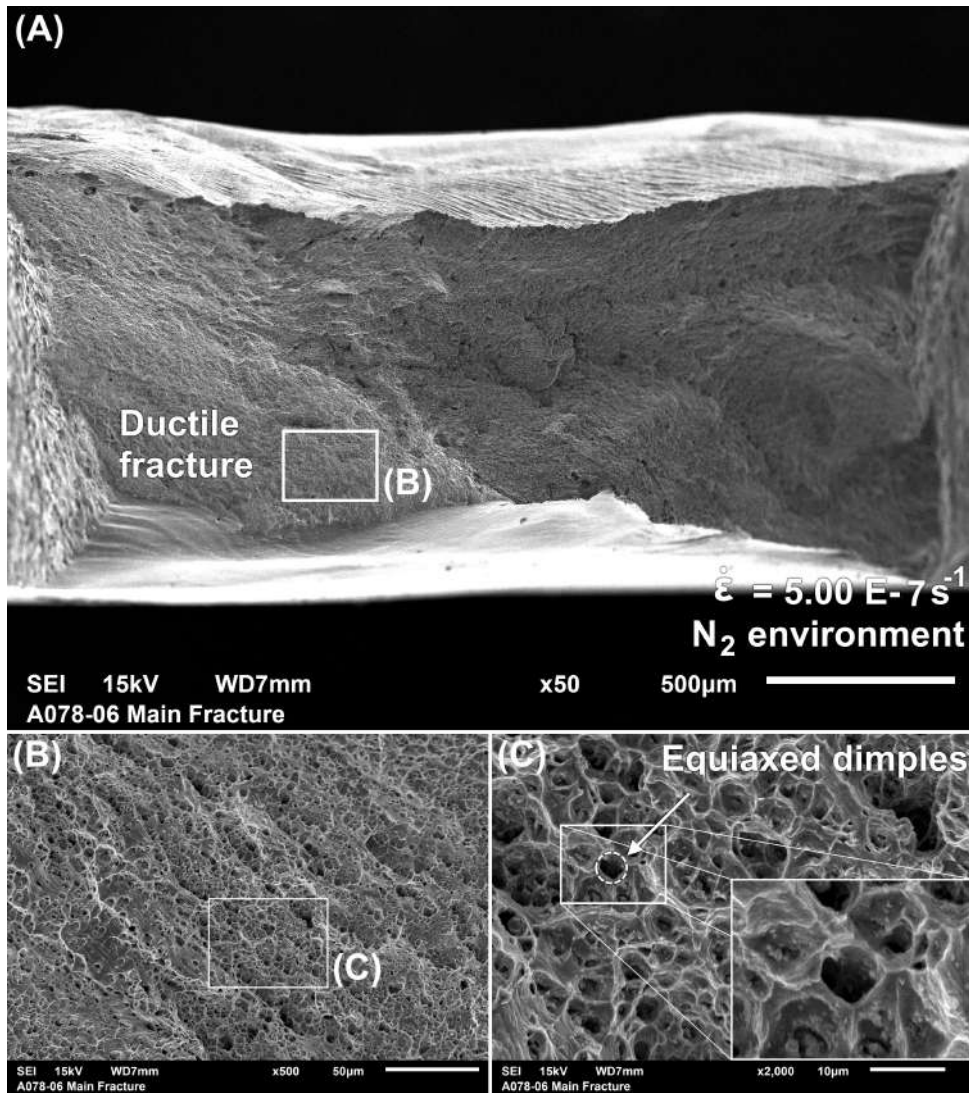


Figure 4.4: Main fracture surface of a tapered specimen tested under $\dot{\epsilon} = 5.00 \text{ E-}7 \text{ s}^{-1}$ in an inert N_2 environment. (A) General overview of the transgranular fracture with (B-C) its ductile-aspects of the fracture regions.

of Ni and Mn. As for ferrite, which was found to be preserved from crack initiation, a marked increase in composition for Cr and Si was observed. As discussed within paragraph 2.2.1, these elements are known to stabilize the austenitic and ferritic phases respectively. A marked increase in Fe is also observed in the ferrite phase over the austenite. Interestingly, as for the surface oxidation of the gauge length, oxides are found to adhere mostly onto the austenite over the ferrite phase instead. This result is noteworthy as it may indicate that crack initiation requires a stabilized oxide surface of sufficient oxide thickness. Since this oxide was only observed on the austenite phase, the reasoning of crack initiation coupled with oxidized surfaces may explain the austenite's tendency to almost exclusively exhibit the cracking. Another reasoning for the confined cracking in austenite is because the ferrite phase is typically more stabilized by the high amount of Si content within the model alloy. This is evident from the increased Si concentration in ferrite over austenite in the EDS maps in Fig. 4.5, but also from respective EDS point-analysis spectra in Fig. 4.6. Silicon is a known solid-solution strengthening element for ferrite [267], which automatically makes austenite more prone to cracking.

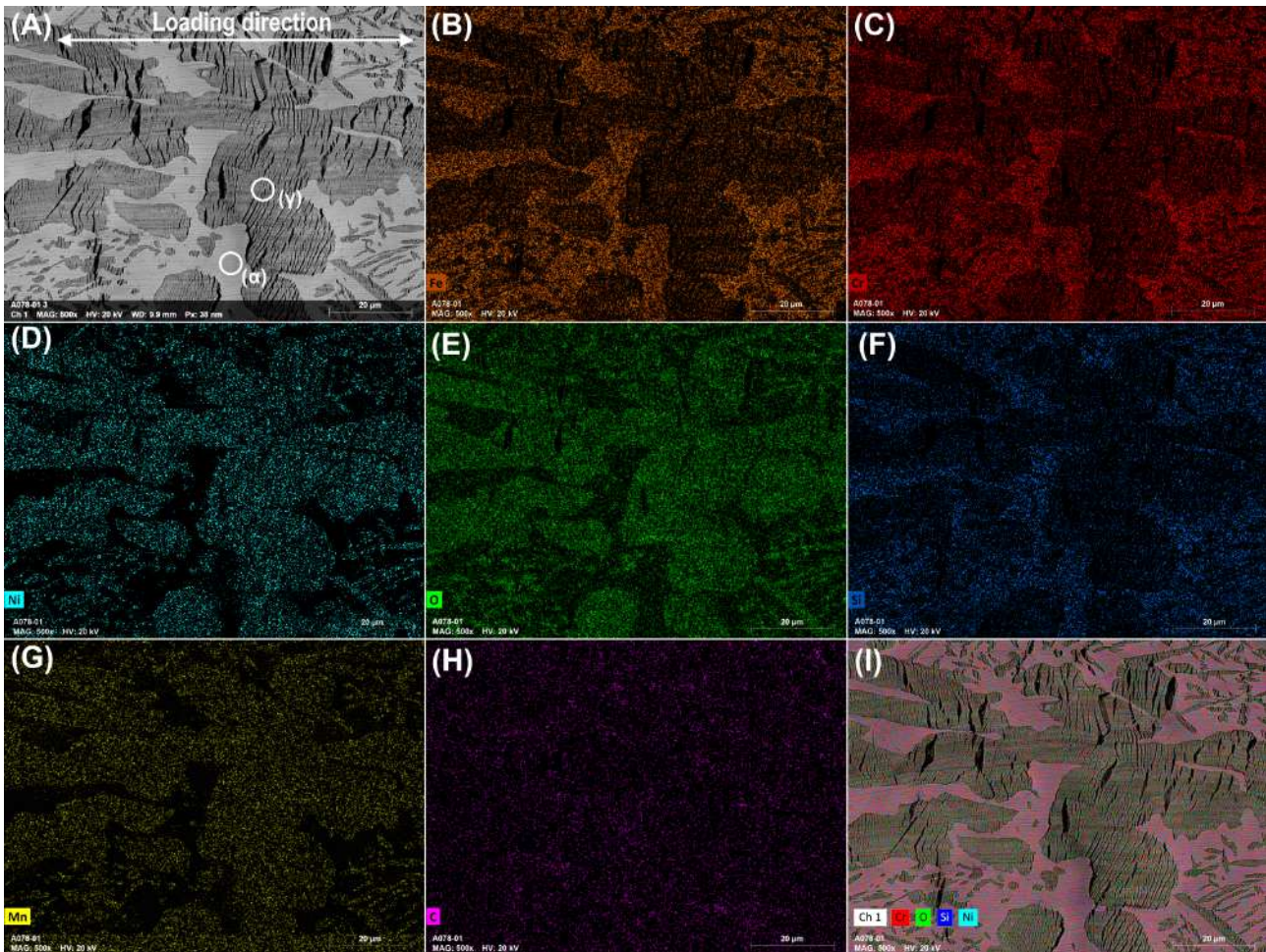


Figure 4.5: Overview of several EDS spectral maps of the tapered gauge length of a specimen tested to $\dot{\epsilon} = 5.00 \text{ E-}7 \text{ s}^{-1}$.

4.1.4 SCC crack detection

A typical examination of the SCC crack initiation along a tapered gauge length is presented in Fig. 4.7. In the process that leads up to the formulation of a crack density distribution, numerous cracks are detected per SEM frame for which several detection parameters are examined. Based upon these parameters, multiple crack filtering algorithms are applied to single out only those cracks relevant for subsequent analysis, see Fig. 4.7B-C. The effect of the individual filtering algorithms is outlined in section 3.5.1.2. For instance, a typical crack angle distribution (CAD) can be composed in Fig. 4.7D, for which the mean crack angle filter algorithm excludes those detections that do not correspond to a fixed angle interval of $\pm 55^\circ$ centered around the perpendicular angle of the loading axis direction. This allows for all surface deformation marks to be differentiated from actual crack detections, which can only initiate at an angle of about 90° perpendicular to the loading direction. Post-filtering, which also includes the segmented length filter, may ultimately lead to a true crack detection frame for which Figs. 4.7E-F illustrate the crack length distribution (CLD) and CAD, respectively. Subsequent use of a crack length threshold, typically considering solely those cracks larger than $> 10 \mu\text{m}$ leads to the crack density distributions outlined in the subsequent paragraph.

However, as was previously noted, austenite is typically more prone to SCC than ferrite within the duplex structure of this high Si SS alloy. This observation necessitates the application of a weighting

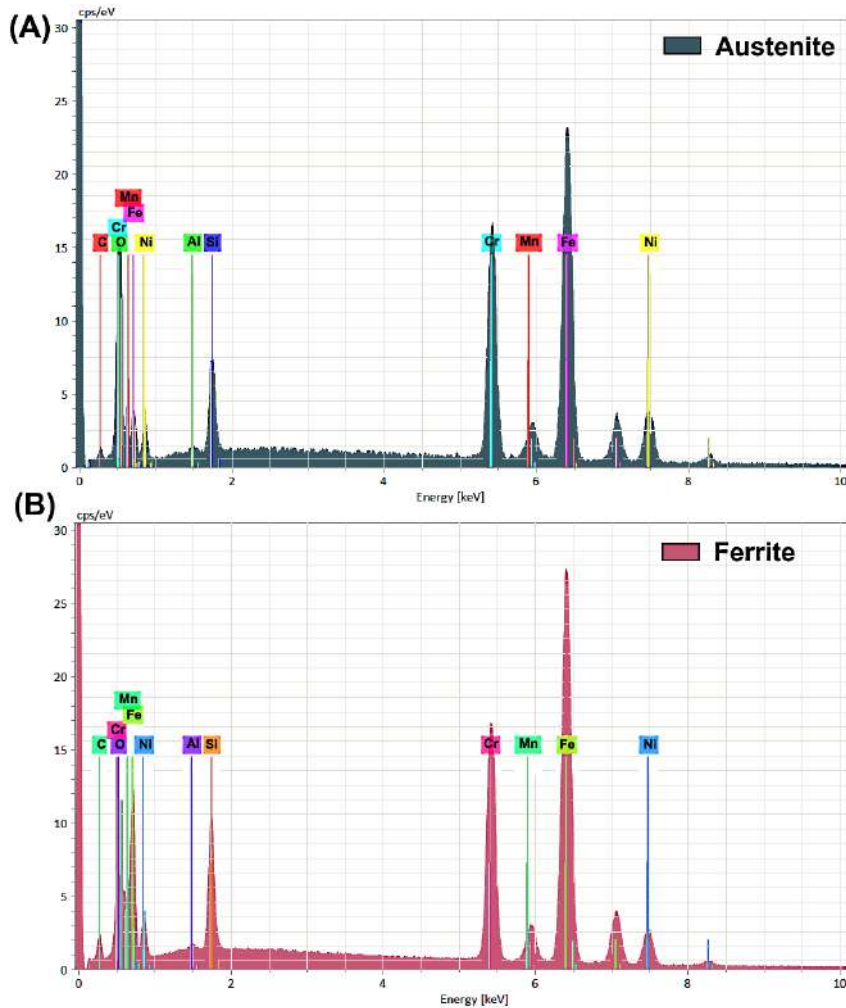


Figure 4.6: Point EDS spectra of the (A) austenite (γ) and (B) ferrite (α) phases of the tapered gauge length of a specimen tested to $\dot{\epsilon} = 5.00 \text{ E-}7 \text{ s}^{-1}$.

factor in order to account for variations in the austenite-ferrite duplex composition throughout the gauge lengths of each investigated specimen. Utilizing MATLAB's Computer Vision Toolbox, this weighing factor is attained for each SEM frame along the strip of the gauge length by means of image recognition of the duplex phases, see Figs. 4.8 and 4.9. Training the utility functions on the image contrast between austenite and ferrite, MATLAB is able to independently calculate a probability map of what it considers the difference between austenite and ferrite, see Fig. 4.8. Applying a valid probability threshold produces a mask whereupon the different duplex phases can be identified, see Figs. 4.8C-D. The change in compositional ratio across the tapered gauge length produces weighing factors per SEM frame, displayed in Fig. 4.9.

4.1.5 Crack density distributions

Figs. 4.10A-C depict typical linear crack density distributions of the SCC crack detections along the surface gauge lengths of several tapered tensile specimens tested under PWR conditions. Using the weighing factor obtained for a tapered gauge length using the methodology displayed in section 4.1.4, variable compositions of the austenite per specimen strain-rate are taken into account over the specimen's gauge length. Any compositional differences between the specimens are therefore adjusted, which makes the crack density distributions mutually comparable per strain-rate.

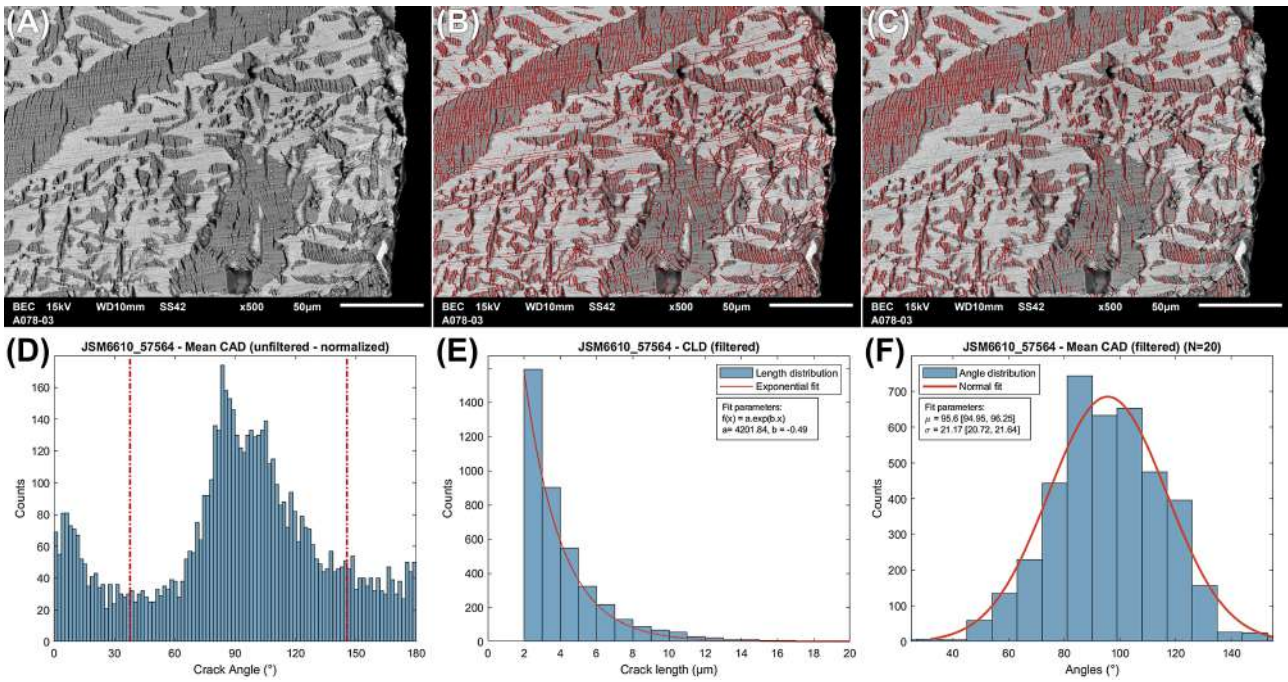


Figure 4.7: SCC crack detection on a tapered gauge length of a specimen strained to $\dot{\epsilon} = 5.00 \text{ E}^{-8} \text{ s}^{-1}$. (A) Original SEM frame, (B) crack detection (prior to filtering), (C) crack detection (post filtering), (D) crack angle distribution (prior to filtering), (E-F) crack length and crack angle distributions (post filtering).

The SCC cracking is far most substantial near the main fracture at the smallest gauge width where the highest strains occurred. An exponential decrease from the main fracture surface towards a negligible amount of cracking is observed at larger gauge cross-sections. On top of the cracking distribution, several prominent peaks are superimposed. These density peaks are nearly uniformly spaced; a feature that was observed for every strained specimen. Given that the detected cracking incidences were systematically higher and more refined at lower strain-rates, these distributions may underline the previous reasoning that corrosion processes play a more significant role at lower strain-rates. Presumably, crack initiation within the surface oxide of the tapered gauge length is more facilitated due to the longer testing duration time at lower strain-rates. For specimens strained under N_2 conditions, little to no SCC cracking was observed along the specimens' gauge lengths. This result underlines the importance of the water chemistry aspect to SCC crack initiation.

4.1.6 Finite-element analysis

Following the methodology for crack density analyses outlined in section 3.5.1.2, potential surface artefacts in the detection algorithm or varying surface compositions of the duplex material are ruled out as a possible origin of the crack density peaks. Therefore, the assumption is made that the crack density peaks occur due to elevated localized stresses imposed on the tapered geometry. Relief of these stresses may occur in the vicinity of dense SCC regions which take place during the crack initiation phase. In order to validate this assumption, the stress behavior along the tapered gauge length needs to be simulated. To that end, Fig. 4.11 reports the FEM calculations performed in ANSYS Workbench 2019 R2.

The temporal stress intensity response of a general tapered specimen CERT-strained to failure was simulated on an at scale tapered specimen model without any prior SCC, see Fig. 4.11A. The stress intensity variation is modelled after the experimental load history of the specimen strained to a strain-

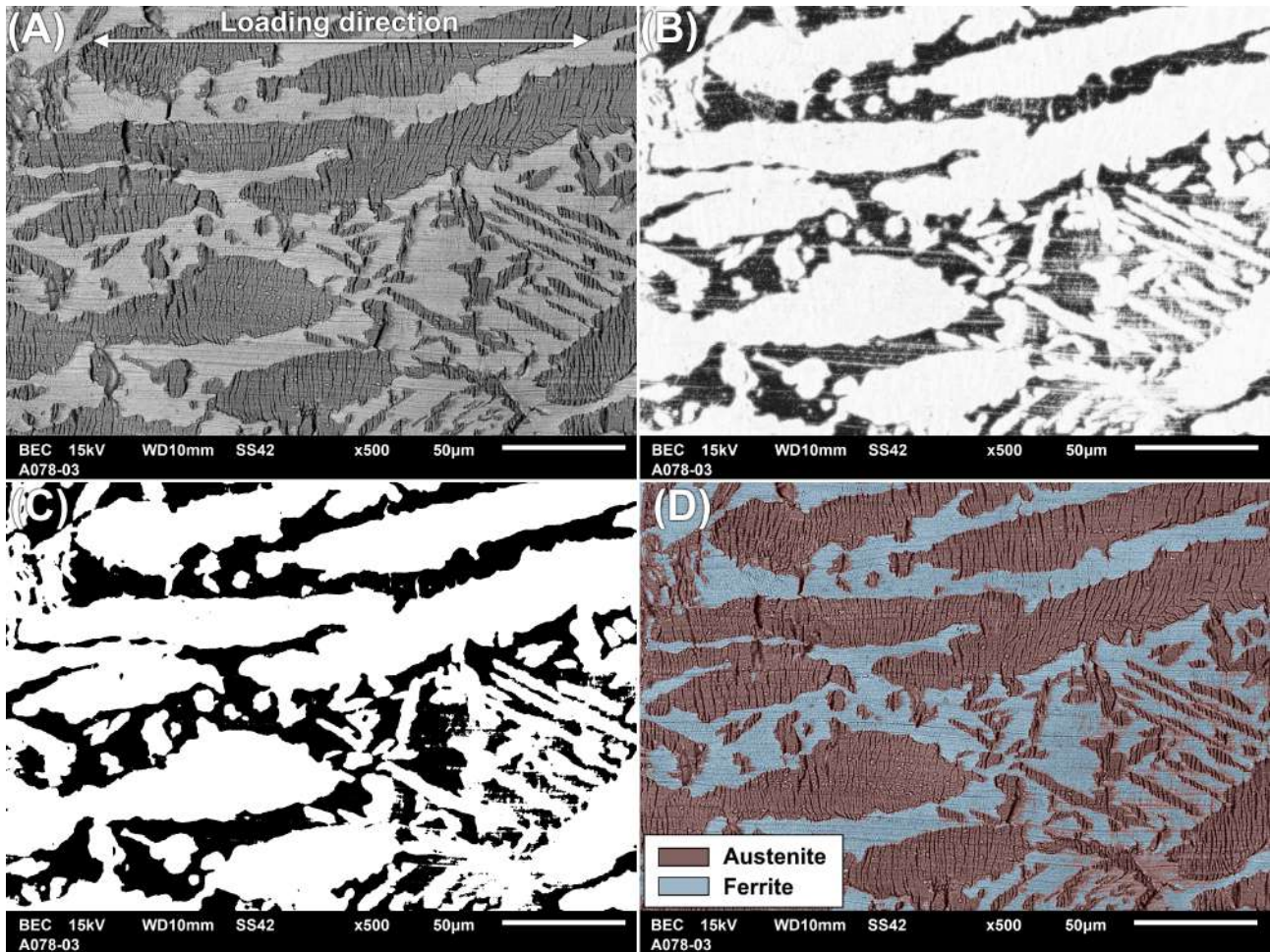


Figure 4.8: Process of phase recognition of the duplex surface composition of a single SEM frame in the crack detection algorithm. (A) Original SEM frame, (B) probability map, (C) threshold masked map and (D) phase recognition map of the austenite-ferrite phases.

rate of $\dot{\epsilon} = 5.00 \text{ E}-8 \text{ s}^{-1}$. It is clear that, because of the tapered geometry, stress concentrates at the region of the smallest cross-section where necking and ultimately specimen failure occurs. By briefly interrupting the stress calculation, a single FEM crack was introduced in the mesh according to the dimensions of about 150 maximally detected SCC cracks at the previous site's highest stress point, see Fig. 4.11B. This simulative crack may represent a local dense concentration of SCC cracks as is observed at the density peaks seen in Fig. 4.10C. Again, the stress calculation is resumed with the same loading conditions applied. The newly calculated stress intensities along the gauge length were obtained on a re-meshed model of a cracked specimen. The mesh was refined especially around the crack tip to ensure reliable values of the stress intensities where the stress typically concentrates. A following calculation demonstrates a new region of stress build-up beyond the latest FEM crack, while otherwise the regions adjacent to the densely simulated crack regions show signs of local stress-relief. In a similar process, several FEM cracks with constant crack-depths and opening-widths were simulated at the specimen's peak stress intensities across the gauge length, see Figs.4.11C-D. For multiple densely simulated crack regions, the stress variation along the tapered gauge length from FEM calculations is compared to the corresponding crack density graph of the specimen with the same loading history, see Fig. 4.10C-D. The calculated stress intensities along the gauge length agree well with the experimental cracking incidences measured in the crack density analysis. The FEM simulations show: (i) a partial stress relief in the vicinity of the simulated FEM cracks during the

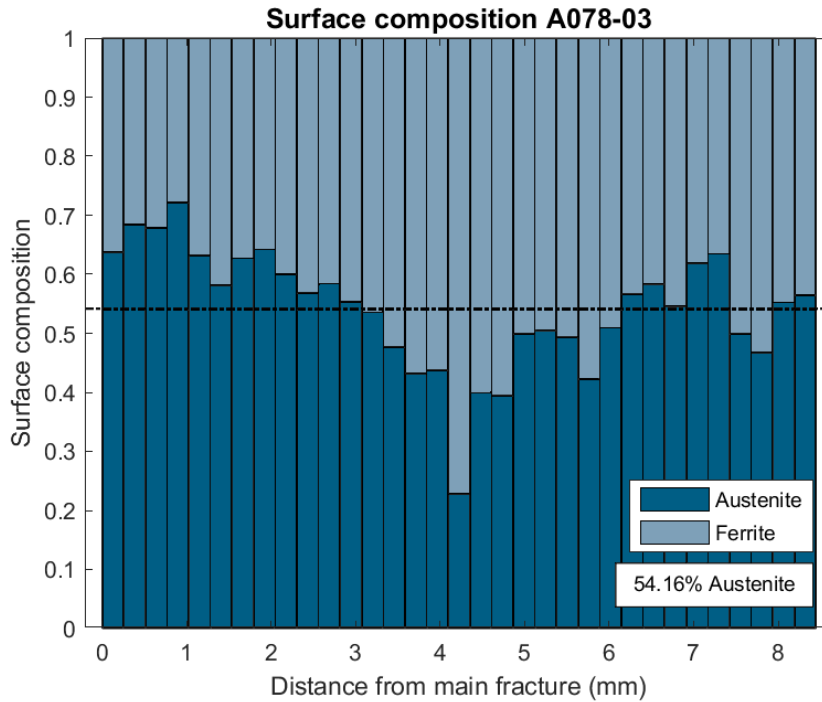


Figure 4.9: Total variation of the duplex surface composition of a typical tapered specimen's gauge length.

initiation phase, (ii) local stress concentration at the FEM crack tips, suggesting the feasible onset of crack growth and (iii) stress build-up beyond the simulated cracked region along the tapered gauge length. From these results, it is reasonable to assume that the nearly equidistant density peaks appear as a consequence of the repetitive stress variations with an effective crack size being much smaller than the size of the gauge cross section. The FEM simulation is halted when the microstructurally obtained critical gauge length is reached, which yields an indication of the stress threshold derived in section 4.1.7.

4.1.7 Critical stress threshold

Explicit assessments of the crack densities along the gauge length of the tapered specimens based on the statistical method of crack detection leads to the estimation of a so-called stress threshold $\sigma_{thr,i}$ for each nominal strain-rate. Below these thresholds, the tapered specimens are conceivably preserved from any initiation of SCC under the given stress conditions. The individual stress thresholds are determined according to the ratio of the maximum CERT-load obtained during testing F_M with the critical sample thickness at the necking point t_c multiplied by the respective critical cross-sections of the specimen at which no SCC is detected i.e. ϕ_c , see equation 3.13. Some of these parameters are presented in Tab. 3.4 of the previous chapter. However, the critical cross-sections are completely reliant on the critical gauge length ℓ_c obtained from the crack density analysis displayed for several specimens in Fig. 4.10A-C. Evidently, the critical gauge length is subjected to the count error of the cracks in each frame of the crack detection algorithm. This count error determines the error bars on each individual stress threshold, and is noticeably smaller at lower strain-rates whereat better-determined critical gauge lengths ℓ_c are obtained.

Ultimately, the extrapolation of the critical threshold through the individual thresholds as a function of strain-rate is shown in Fig. 4.12. No significant strain-rate effect larger than the estimated error bars is

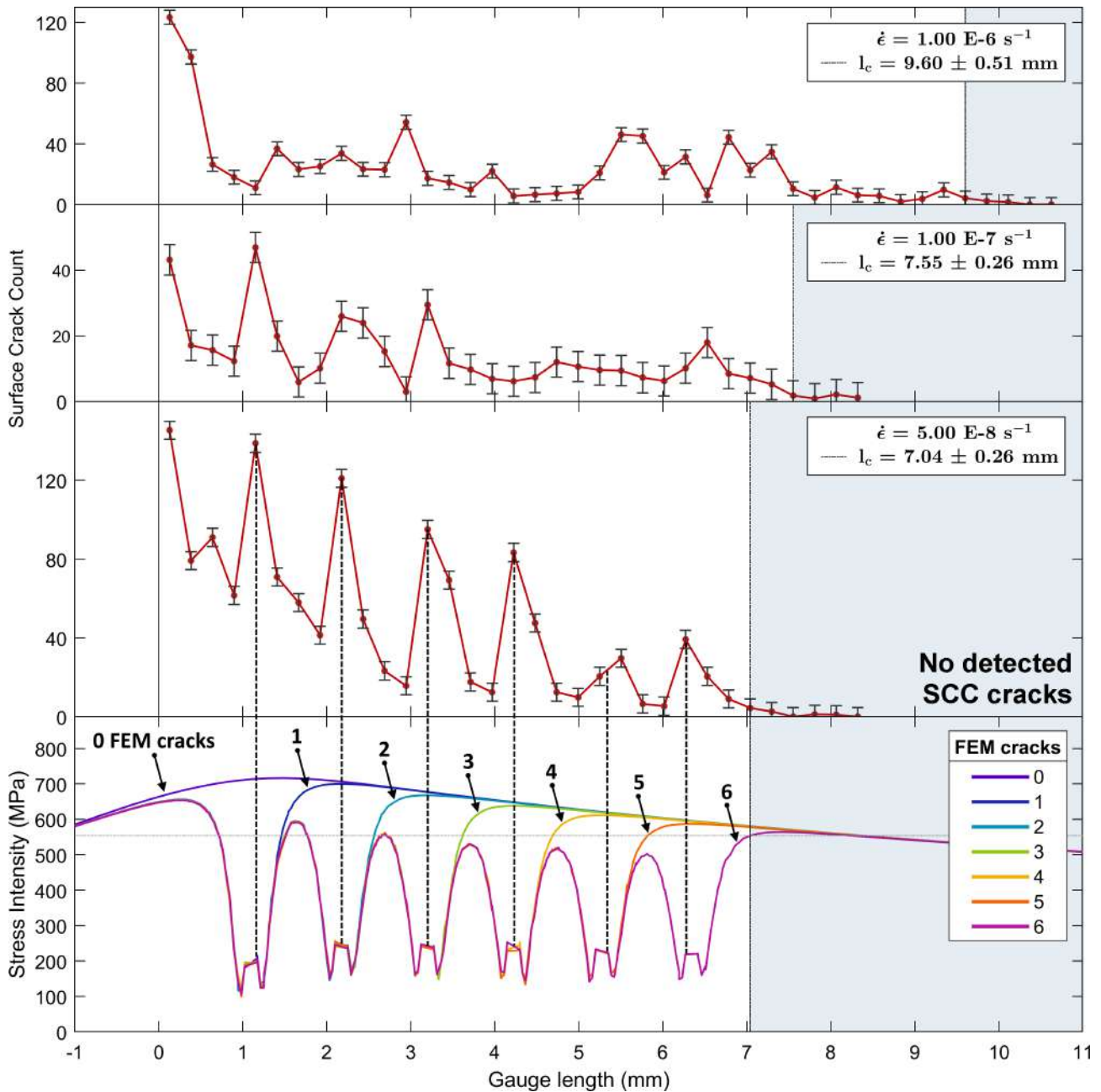


Figure 4.10: Crack density distributions of CERT-strained tapered specimens with strain-rates: (A) $\dot{\epsilon} = 1.00 \text{ E-}6 \text{ s}^{-1}$, (B) $\dot{\epsilon} = 1.00 \text{ E-}7 \text{ s}^{-1}$ and (C) $\dot{\epsilon} = 5.00 \text{ E-}8 \text{ s}^{-1}$ and (D) FEM stress intensity after simulating the load history of the sample tested under $\dot{\epsilon} = 5.00 \text{ E-}8 \text{ s}^{-1}$. The critical gauge lengths ℓ_c and the FEM simulated critical stress threshold are shown.

observed at low and intermediate strain-rates below $1.00 \text{ E-}6 \text{ s}^{-1}$, while an increase in strength at high strain-rates is clearly observed otherwise. The data scatter is in accordance with the specimens failure at varying elongations regardless of the strain-rate value. In other words, the intrinsic scatter suggests that SCC is independent of the strain-rate for strain-rates lower than $1.00 \text{ E-}6 \text{ s}^{-1}$. The critical threshold value for the duplex high Si stainless steel, based upon the extrapolation to constant load conditions, yields in total $581 \pm 16 \text{ MPa}$. This value is in a very good agreement with known literature values for stress thresholds for similar types of alloys [35,262]. The stress threshold results agree well with both mechanical data and fracture surface appearance. Additionally, the experimentally acquired

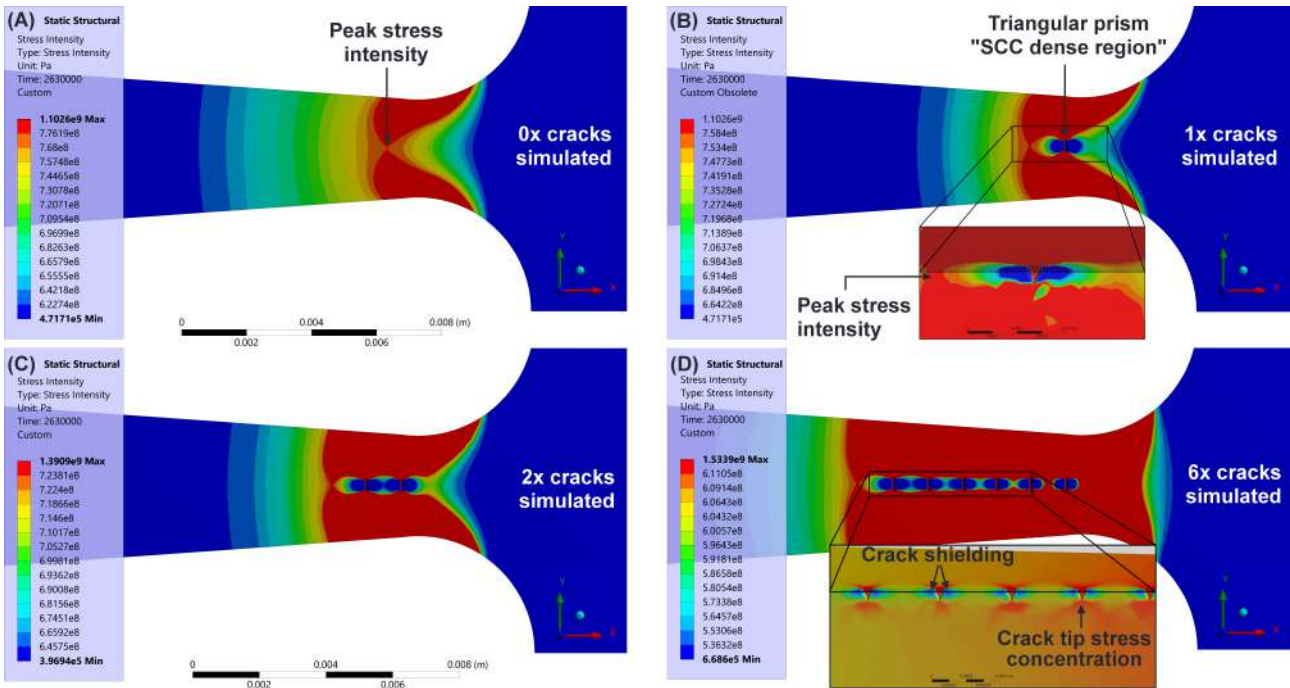


Figure 4.11: FEM calculations of the stress intensities along the tapered gauge length. (A) Zero, (B) one, (C) two, and (D) ultimately six triangular crack prisms of size $0.4 \times 0.15 \times 0.15 \text{ mm}^3$ were consecutively simulated in the mesh as being representative of dense crack regions.

stress threshold substantiates the results of FEM calculated stress variation across the gauge length in Fig. 4.10C-D. Indeed, it is apparent that the FEM stress intensities dip below the stress threshold at about 7 mm along the gauge length. This measurement is comparable to the experimentally confirmed critical cross-section where no more cracking is detected. The driving stress intensities simulated by FEM are not sufficient enough to cause crack initiation below the estimated threshold stress.

Despite the application of an accurate crack detection algorithm that is both free from human bias and fully reproducible, the individual thresholds per specimen still showed a scatter that remained inherent to the dataset. Since this scatter was also observed in previous literature studies attempting to estimate a stress threshold for cracking [261–263], it suggests that the origin of this scatter is intrinsic to SCC initiation process. The accuracy in determining the critical length ℓ_c in the crack density graphs lies at the basis of this scatter, because the error on the critical lengths further determines the error bars of the individual thresholds. However, because of the tapered geometry, the local strain-rate varies as a function of the tapered cross-section. Accordingly, any error that is correlated to the uncertainty of ℓ_c must also be correlated to an uncertainty to the local strain-rate across the tapered gauge length. This suggests that there is a probabilistic aspect involved in the initiation processes of SCC, which will also be further discussed in the light of the SCP model in the cracking of intergranular oxides in the subsequent chapter.

Interestingly, as a prelude to results obtained in section 4.3, the observed SCC cracks have almost exclusively initiated within the surface oxide of the high Si SSs model type alloy only. Minor crack propagation of the SCC cracks was observed in the underlying bulk material. This may cast some doubt upon the essence of the critical stress threshold, which has been ascribed as a property specifically for the alloy. In fact, it may be argued that this value is not characteristic for the alloy itself, but rather for the surface oxide that forms atop of it wherein the SCC cracks initiate. Indeed, the observation of $\sigma_{\text{thr}} = 581 \pm 16 \text{ MPa}$ is also in good agreement with the microcantilever experiments performed

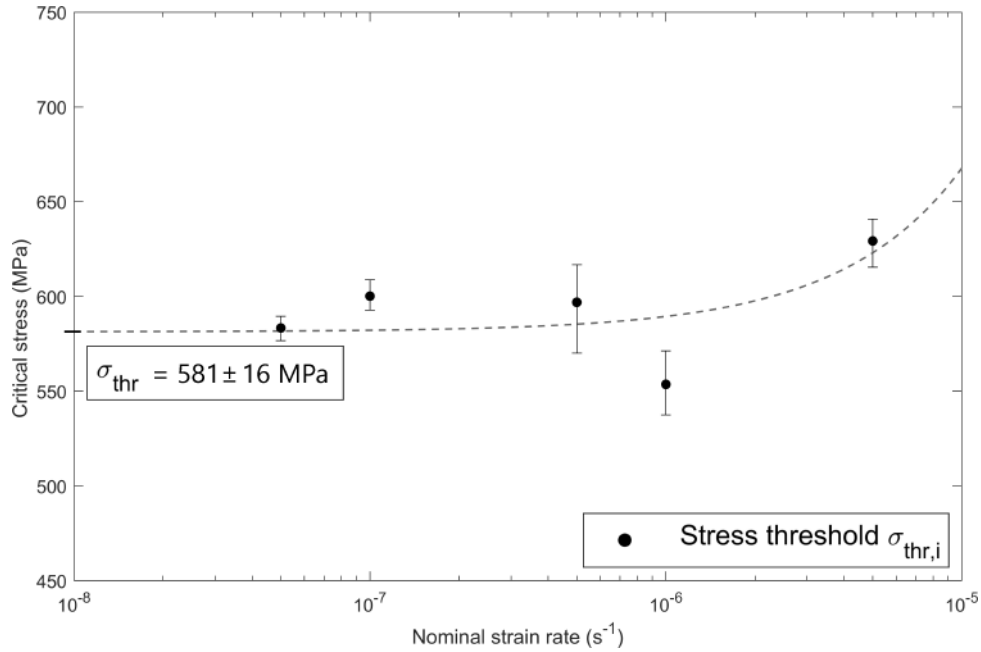


Figure 4.12: Stress thresholds $\sigma_{\text{thr},i}$ for high Si stainless steel tapered specimens in a simulated PWR environment. Extrapolation through the individual stress thresholds determines the stress threshold under which constant load conditions are independent of the applied nominal strain-rate i.e., the critical stress threshold which is evaluated as $\sigma_{\text{thr}} = 581 \pm 16$ MPa.

on Fe-based oxidized grain boundaries by Fujii et al. [222]. In this investigation, it was shown that the nominal stress required for an intergranular oxide to fracture may be as low 360 MPa whereas the stress normal to the oxidized grain boundary causes it to fail at a value of around 540 MPa. These values are relatively similar to our measurements, even though the acting environment in the microcantilever experiments was vacuum instead of high temperature PWR water. It is also important to denote that, grain boundary oxide strengths should be inherently stronger than the oxides that are formed on top of the bulk material. This is because in the consideration of the volume-effect in the SCP model, it is expected that thinner oxides found at the grain boundaries exhibit less inherent flaws and are thus stronger than more voluminous oxides found on top of the bulk. However, the values of the oxide strengths in our PWR environment versus the vacuum experiment of Fujii et al. should only be tentatively compared. Since the corrosive environment and the ambient temperature in the two experiments are different, direct correlation between the two experiments is perhaps not without error. Both parameters are believed to play a significant role towards the probabilistic oxide strength. Estimation of the critical oxide strength is invaluable when considering that intergranular oxides tend to lower the fracture resistance through metallic embrittlement.

4.2 FIB analysis

4.2.1 SCC crack extraction

In the second half of this chapter, fully developed SCC crack tips were readily extracted from the high Si duplex SS tapered specimens' gauge lengths by means of the ThermoFisher Scientific Scios DualBeam FIB-SEM. These cracks, embedded within a TEM-lamellae, were consequently thinned to electron-transparency thicknesses according to the methodology described in section 3.2.2.1. The lamellae were prepared in cross-sectional orientation i.e., along the crack propagation direction. In

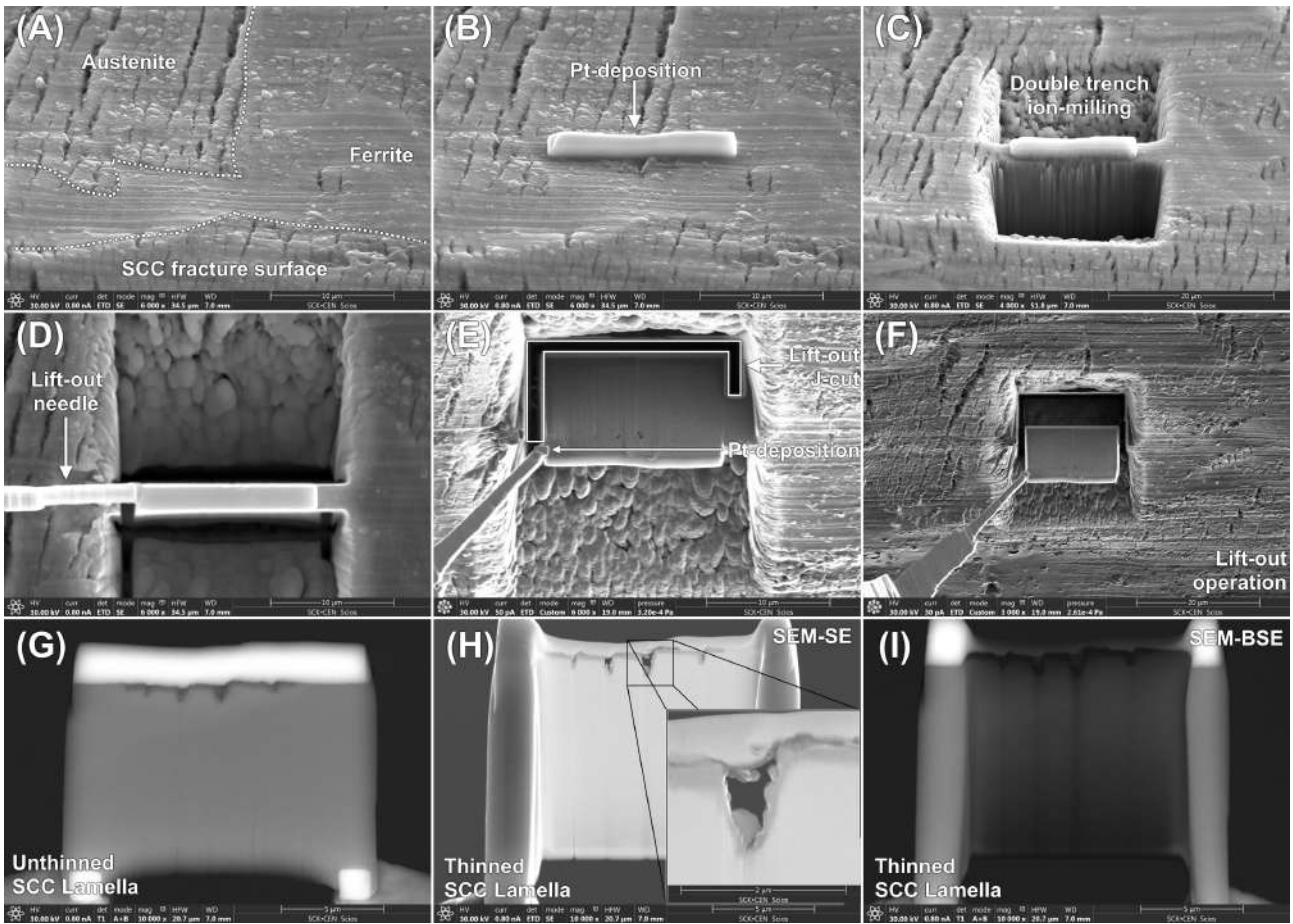


Figure 4.13: FIB-SEM images illustrating the methodology of SCC crack tip extraction from a bulk specimen surface.

this manner, one slice of an SCC crack tip is definitely guaranteed to be extracted and preserved after final thinning, which is otherwise not the case in plan-view orientation [246]. SCC cracks were typically extracted from the specimen gauge surface in a region of about 1 mm away from the smallest tapered cross-section. This is due to the local peak in surface stresses which produced the highest density of fractures at this location. Depending on the local crack density, it was possible to extract a multitude of SCC crack tips simultaneously in one lamella by adjusting the length of the lamella (averaging 1 – 2 for regions of low crack density up to 5 – 10 for densely cracked regions). A typical example of the FIB extraction procedure is displayed in Fig. 4.13.

4.2.2 Grain contrast imaging

Prior to beginning the TEM study, it is typically considered useful to first understand the lamella cross-sectional duplex composition. This allows for a better characterization of the different austenite and ferrite grains in a subsequent TEM session. Therefore, FEI's FIB-SEM OptiTilt function described in section 3.2.2.2 is employed to visualize the grain composition using low BSE voltages. A typical example for an SCC fractured lamella is displayed in Fig. 4.14. Clear contrast variation along the cross-section unveils the subsequent FIB platinum protection layer, oxide, and bulk metal layers. The oxidation film varies slightly in thickness along the gauge length and appears darker under SEM view because of the lower BSE count production. The grain contrast demonstrates a shallow transgranular cracking nature in the duplex stainless steel at the top part of the TEM-lamella. As was previously confirmed in prior observations, SCC cracks primarily initiated within the austenite phase structure.

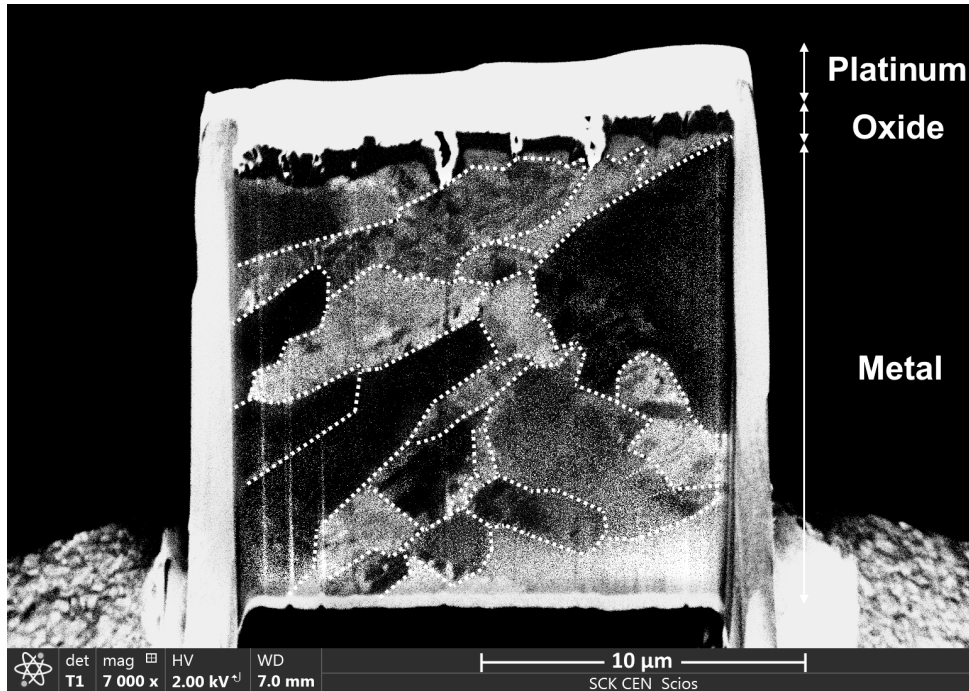


Figure 4.14: Low-voltage BSE grain contrast imaging of a TEM-lamella with SCC cracks. The dashed lines illustrate the compositional grain structure of the lamella cross-section.

From the present grain contrast imaging it becomes apparent that the crack propagation was halted at grain interfaces of which presumably the impeding grains are of high Si solid-solution hardened ferrite nature. The duplex matrix composition is further characterized by visually elongated grains which are no more than a few square micrometers in size.

4.3 TEM investigation

Regardless of the local surface crack density, crack opening widths/lengths, crack orientation, or location of the cracks along the gauge length, all extracted cracks were visibly similar for each of their respective strain-rate. The most striking differences between the specimens across the different strain-rates were differences in crack tip morphologies, surrounding deformation fields, and oxidation thicknesses along the gauge surfaces. These aspects of the crack initiation process were primarily investigated by means of TEM using the JEOL 3010 LaB₆ scanning (S)TEM instrument. Additional STEM spectral maps were also obtained by SCKCEN's scientific collaborator Dr. W. Van Renterghem during several initiation sessions on the JEM-ARM300F Grand ARM STEM (which was later acquired and employed at subsequent research) in Tokyo, Japan. The chemical composition of the SCC crack tips at their point of initiation in the duplex SS microstructure is clearly outlined by these additional measurements, and is hereby also discussed within the results.

4.3.1 Low-magnification imaging

Subsequent conventional TEM investigation of SCC cracks is performed in BF-imaging mode in low-indexed zone axes. Low-magnification micrographs of the entire lamella can be seen for slow $\dot{\epsilon} = 5.00 \text{ E-}8 \text{ s}^{-1}$ and fast $\dot{\epsilon} = 5.00 \text{ E-}6 \text{ s}^{-1}$ strain-rates, see Figs. 4.15A-B respectively. BF-TEM imaged cracks reveal a sequencing of platinum, various oxide and metal layers, and transgranular cracks that either propagate shortly into the bulk metal or arrest within the oxide. Deformation slip bands are

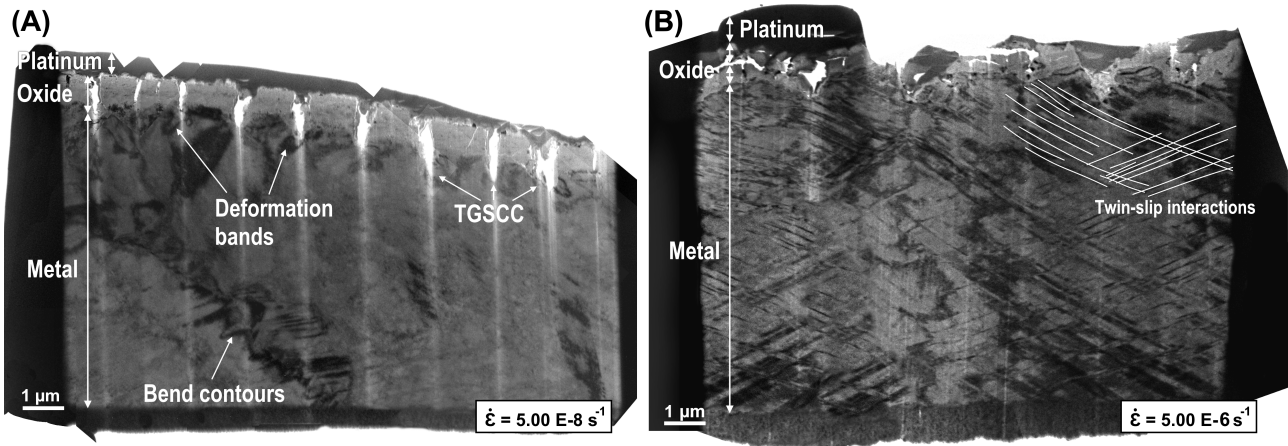


Figure 4.15: Low-magnification BF-TEM image of the lamella cross-sections of strained tapered specimens with respective strain-rates of (A) $\dot{\epsilon} = 5.00 \text{ E-}8 \text{ s}^{-1}$ (slow) and (B) $\dot{\epsilon} = 5.00 \text{ E-}6 \text{ s}^{-1}$ (fast).

observed as indicators for increased strain concentration in the vicinity of the crack tips. Furthermore, various twin-systems extending deep ahead of the crack tips are distinctly observed for faster strain-rate lamellae, see below. Artefacts stemming from the FIB thinning, such as the occurrence of bend contours and curtaining, cause contrast variation as the lamella is buckled or locally thinner near the crack tip. The curtaining artefact may remain visible in all subsequent TEM images.

4.3.2 SCC crack tips

Two types of crack tip morphologies were commonly observed depending on the applied nominal strain-rate. Slower strained specimens such as $\dot{\epsilon} = 5.00 \text{ E-}8 \text{ s}^{-1}$ and $\dot{\epsilon} = 5.00 \text{ E-}7 \text{ s}^{-1}$ entailed oxidized cleavage-mode crack tips which partially propagated into the bulk austenite before the final arrest, see Fig. 4.16A. Reasonably long and narrow crack openings were common features at slower strain-rates. The SCC tips were completely oxidized and arrested within the metal substrate. Contrastingly, more blunted shaped crack tips with wider cleavage-mode openings were observed for faster strained specimens of $\dot{\epsilon} = 1.00 \text{ E-}6 \text{ s}^{-1}$ and beyond, see Fig. 4.16B. The SCC cracks extracted from fast-strained specimens routinely blunted at the point of arrest within the surface oxide layers near the metal interface or further within the surrounding bulk material in high tensile stressed regions. Fast-strained crack tips are characterized by an increased roundness and a wider opening mode of the crack tip. Consequently, the crack tip is typically covered by platinum deposition stemming from the FIB extraction procedure.

In support of the observation of the increased roundness, different crack tip morphologies are distinguished based on the crack length-to-width ratio. A comparison is shown for different strain-rates in Fig. 4.17. It was found that this ratio steadily decreases with an increasing strain-rate, implying that the crack blunting increased under increased tensile deformation. Most likely, this blunting is related with deformation-induced features in the bulk microstructure during the crack initiation process.

Irrespective of the loading conditions, one can also observe small crack embryo's that initiate at the surface underneath the outer oxide layer. Such cracks generally follow a ragged path and may be filled with outer oxide deposit due to the anodic corrosion processes that take place. The irregular shape suggests that they are the result of brittle oxide fracturing under the applied stress conditions. This observation is more exemplified by the debonding of the metallic-oxide interface along the tapered gauge length. Debonding is especially seen at high strain-rates as shown in Fig. 4.16B.

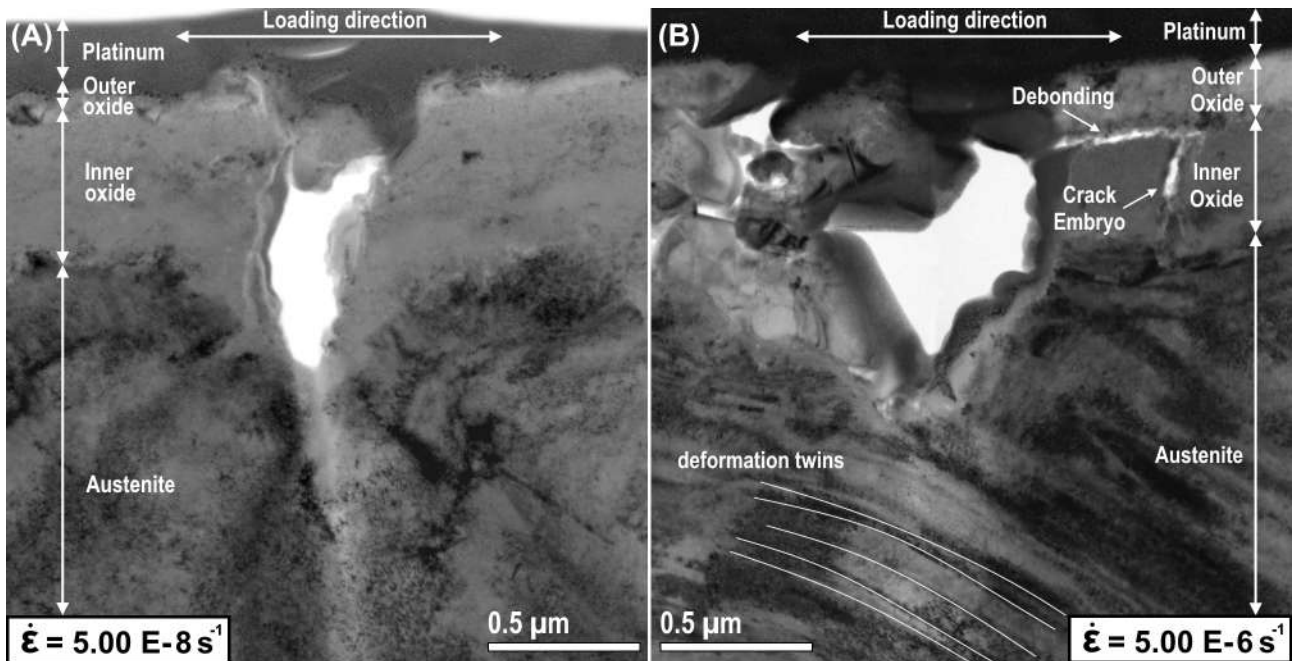


Figure 4.16: Cross-sectional crack morphologies of SCC cracks appertaining to (A) $\dot{\epsilon} = 5.00 \text{ E-}8 \text{ s}^{-1}$, and (B) $\dot{\epsilon} = 5.00 \text{ E-}6 \text{ s}^{-1}$.

Fig. 4.18 displays the case of a microcleavage event that occurred exclusively for slow strained specimens. The crack tip propagates for a short distance parallel to the crack growth direction in the inherent inner oxide layer ahead of the pre-existing crack tip, see Fig. 4.18B. Because the reciprocal lattice spacing between the diffraction spots of the metal and the adherent oxide film is small, one cannot easily distinguish between both phases in a corresponding DF-TEM micrograph of the crack tip, see Fig. 4.18C. Still, the occurrence of microcleavage events is evidently seen in BF-TEM and should be considered as experimental evidence that the crack initiates first within the adherent crack tip oxide layer, and that the substrate surface oxidation precedes the next crack penetration within the bulk. In this manner, the crack tip resembles a short-range crack injection event which is characteristic to the film-induced cleavage (FIC) model [184,196] described in section 2.5.1. Indeed, the crack tip morphology is a clear example of a transgranular microcleavage injection shown in the illustrative diagrams of the FIC model [195]. In order for the crack to grow progressively with each cleavage injection into the bulk, the FIC model proposes that the crack should first blunt into the bulk material ahead of the pre-oxidized crack. Consecutive surface oxidation around the blunted crack tip occurs while the crack remains in contact with the corroding environment. Subsequently, small cleavage fractures may initiate in a thin surface film whenever the crack velocity exceeds the oxide repassivation rate. This is what is shown in 4.18B-C. These injections are reasoned to be related to a more developed crack front under influence of strong tensile stresses at the crack tip. The critical aspects of the FIC model are the strong bonding of a brittle oxide film on the one hand, and de-alloying of a nano-porous film (usually of the order of about 200 Å) wherein the crack initiates on the other hand [196]. Crack growth in the surrounding metal substrate is a consequence of small cleavage injections which are subjugated to the initial crack entry velocity. Depending on the initial crack length, these crack injections may extend in the range of tens to hundreds of nm; an estimation which is supported by these findings.

Based upon the applied strain-rates per specimen, it appears that dissimilar cracking morphologies suggest that different cracking mechanisms take place for slow and fast strained specimens respectively. Primarily, with concern to the plastic deformation field in front of the respective crack tips, it becomes

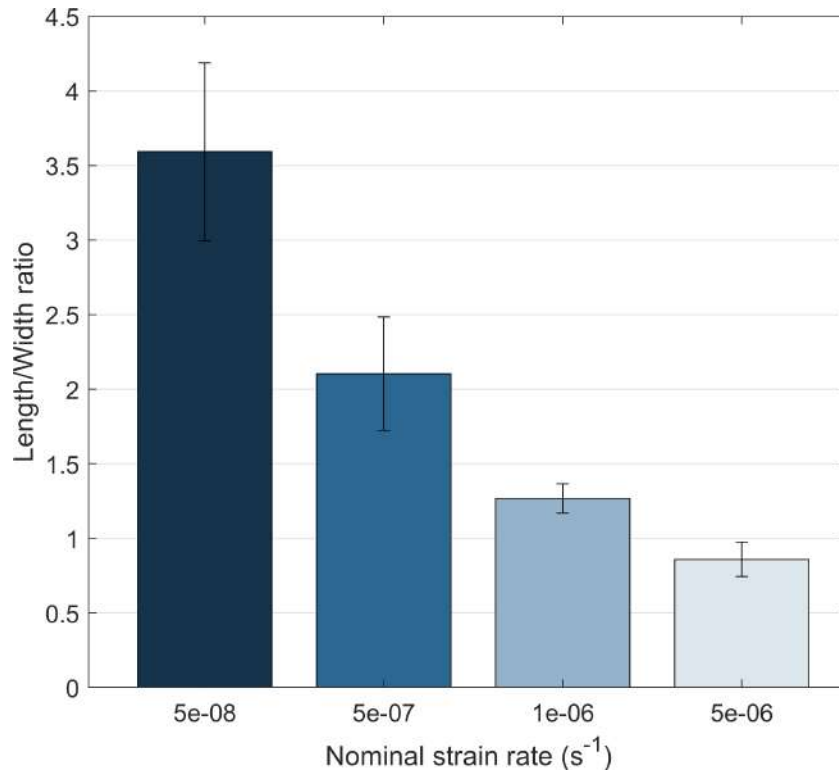


Figure 4.17: Comparison of the SCC crack length-to-width ratio as an indicator for the crack morphology variation in terms of the applied nominal strain-rate. The morphology of the crack tip becomes more rounded with increasing strain-rate.

clear that mechanical twinning becomes more activated under increased levels of externally applied load. At slow strain-rates, plastic strain is typically concentrated in the form of deformation bands near the grain boundaries and around the SCC crack tips. This is typically illustrated by the plastic zone in the bulk metal around the crack tip where the highest stresses occurred. However, for fast strain-rates, the intensity of mechanical twinning becomes much more apparent as seen in Fig. 4.19. The indexing of the diffraction pattern illustrates that common twinning occurs along the close-packed austenitic $\{111\}$ planes. Twin-slip interactions have been commonly observed, especially in the vicinity of crack tips appertaining to fast-strained specimens. At intermediate strain-rates, a balance between these two extremes in terms of plastic deformation was noted.

4.3.3 Crack tip oxidation

With respect to the external and crack tip oxidation films, a double-layered oxide was confirmed using both diffraction and EDS point analyzes, see Figs. 4.20 and 4.20 (continued) and also 4.21 respectively. The BF- and CDF-TEM images clearly illustrate the extent of oxidation in front of the crack tip and along the external gauge surface. The oxidation film is found to be duplex by nature. Whereas the inner oxide typically consists of randomly oriented nanocrystallite grains, the outer oxide exclusively consists of large crystallites, see Fig. 4.20A,C and 4.20B,D respectively. The thicknesses of these oxidation films are measured and presented per nominally applied strain-rate in Fig. 4.22. A significant trend regarding the crack tip oxidation in terms of the applied strain-rate was not observed. The apparent increment at high strain-rates is still below the precision of the measurement, making a stress-assisted oxidation trend difficult to verify. However, in contrast to slow strain-rates, fast-strained specimens do exemplify a more significantly oxidized gauge surface due to the increase of the

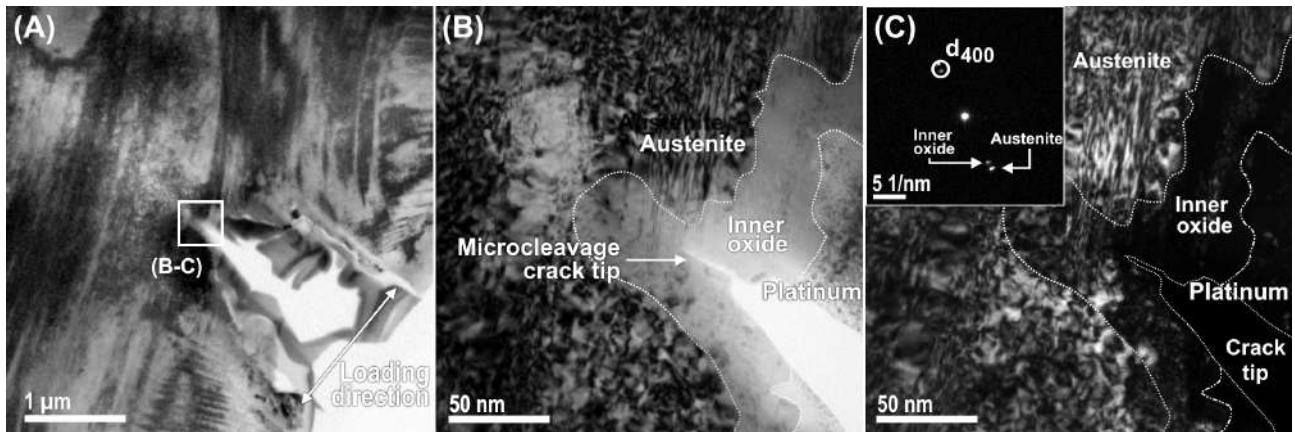


Figure 4.18: Two-beam micrographs of an embedded microcleavage crack tip for a lamella belonging to a specimen slowly strained to $\dot{\epsilon} = 5.00 \text{ E-}7 \text{ s}^{-1}$. (A) BF-TEM overview, (B,C) respective BF- and CDF-TEM of the magnified crack tip. The metal and oxide reciprocal reflections are indexed in the inset diffraction pattern, and the experimental objective aperture is illustrated with the small circle.

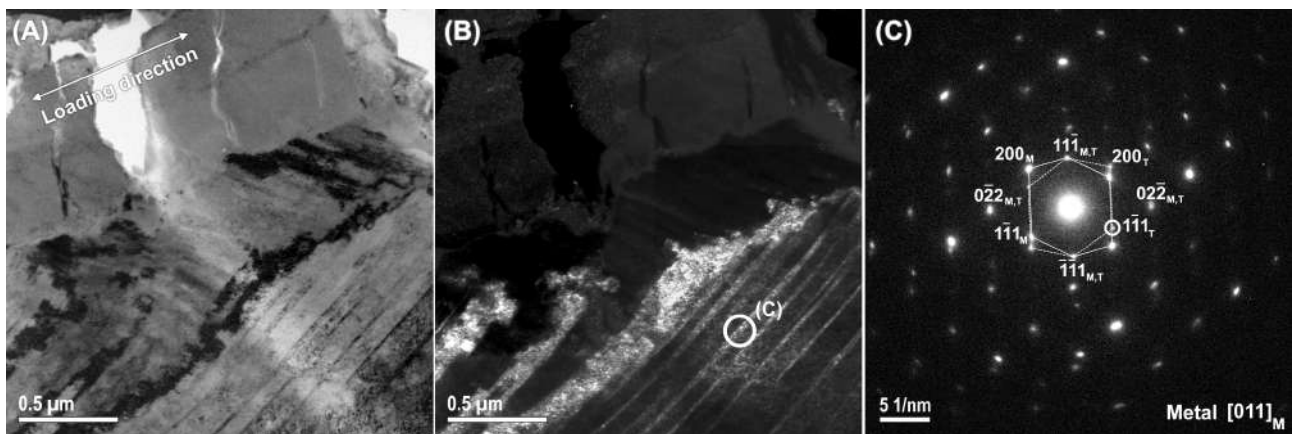


Figure 4.19: Twinned microstructure of the deformed metal matrix for a specimen pertaining to the sample strained to $\dot{\epsilon} = 5.00 \text{ E-}6 \text{ s}^{-1}$. (A) BF-TEM, (B) CDF-TEM and (C) corresponding SAED diffraction pattern of twinned structure. The objective aperture is shown by the small circle. The indexing of the matrix (M) and twin (T) diffraction spots demonstrates that the twins predominantly occur along the $\{111\}$ austenitic planes.

outer oxide thickness. Moreover, an increasing trend of outer oxidation at the expense of the inner oxide can be observed. This is in agreement with previous studies which have shown that external stresses can have an increasing effect of the surface oxidation under PWR conditions [168,169].

EDS point analyses were conducted in order to determine the chemical composition of the double-layered oxide structure for a crack tip extending into the bulk metal pertaining to a specimen strained at $\dot{\epsilon} = 5.00 \text{ E-}7 \text{ s}^{-1}$, see Fig. 4.21A. The EDS spectra of the oxides at the crack tip are consistent with the external surface oxide and are presented in Fig. 4.21B. The inner oxide has been verified as a de-alloyed Ni-depleted iron-chromium oxide, while the outer oxide is solely iron enriched. This is in agreement with the respective inner and outer oxide studies on stainless steels under PWR conditions [92,99]. However, small traces of Ni and Si found in the EDS spectra suggest that the inner oxide is not completely homogeneous. Observations of silicates may potentially substitute within the inner oxide to form SiO_4 . The presence of Si in the inner oxide is not totally surprising due to the high Si content of the substrate matrix. Strained silicate bonds are typically more prone to rupture under aqueous environments, as has been suggested by silicate fracturing models [275]. If this were the case,

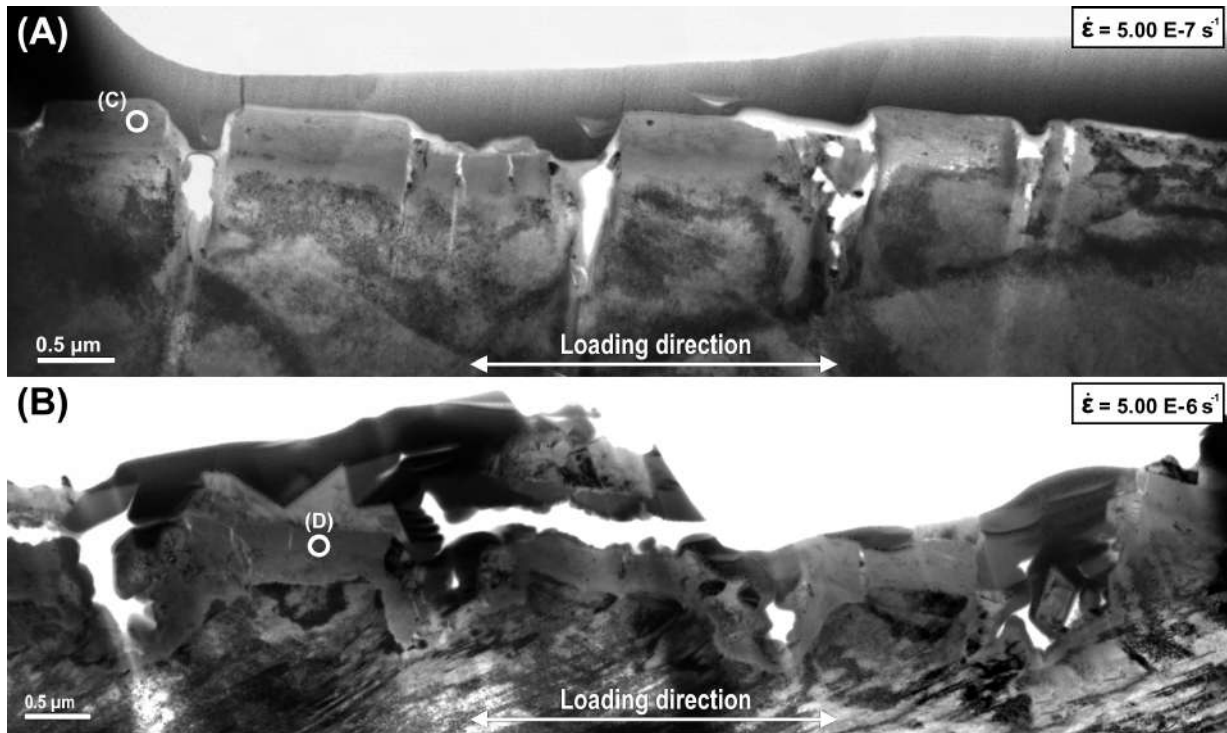


Figure 4.20: BF-TEM appertaining to specimens strained to (A,B) $\dot{\epsilon} = 5.00 \text{ E-}7 \text{ s}^{-1}$, and (C,D) $\dot{\epsilon} = 5.00 \text{ E-}6 \text{ s}^{-1}$. See also Fig. 4.20 (continued).

it implies that Si may generally have an adverse effect to the SCC resistance of this type of model alloy. Also, results indicate that the outer oxide is typically more continuous at the gauge surface and at crack flanks while the inner oxide is of a fine-grained porous nature at the crack tip. Based on these results, it can be considered that the inner oxide is the resultant of Cr-selective diffusion-corrosion oxidation mechanism while the outer oxide is solely redeposited in retrospect of the anodic matrix dissolution processes. The latter is supported by the evidence that the outer oxide precipitates appear non-homogenously along the crack flanks and external surfaces.

Visualization of how the inner and outer oxides adhere along the tapered gauge length patterns and compose along the crack flanks is presented in Figs. 4.24 and 4.25 respectively. Analysis of the inner oxide diffraction pattern is performed through an integrated ring intensity profile, see Fig. 4.23. The ring diffraction pattern was rotationally sampled and normalized in Fig. 4.23B, which generates a signal composed of the interplanar ring spacings that is unique for the characterization of the oxide phase, see Fig. 4.23C. Based upon this signal, a comparison between the experimental interplanar ring spacings and theoretical distances for known potential candidate structures of the inner oxide diffraction pattern can be made, see Tab. 4.1. The candidate structures were selected from previous investigations on SSs [94, 276–278] in unison with the elemental analysis in the acquired EDS data. The experimental interplanar ratio's stipulate that the main oxide component must correspond to a FCC-type spinel structure. Therefore, the most probable structure matching the experimental data amounts to FeCr_2O_4 , otherwise known as chromite, with a known lattice constant of 0.8365 nm [279]. Theoretical ring intensities from X-ray powder diffraction (XRD) simulations strongly support the observed experimental ratio's for this structure. Other oxide structures were considered, but can be ruled out on the basis of missing intense theoretical reflections. For example, the most prominent theoretical peak for Cr_2O_3 , which more commonly forms along Ni-based alloys [280], is the peak corresponding to $d[01\bar{4}] = 2.66 \text{ \AA}$. However, when taking its largest interplanar distance

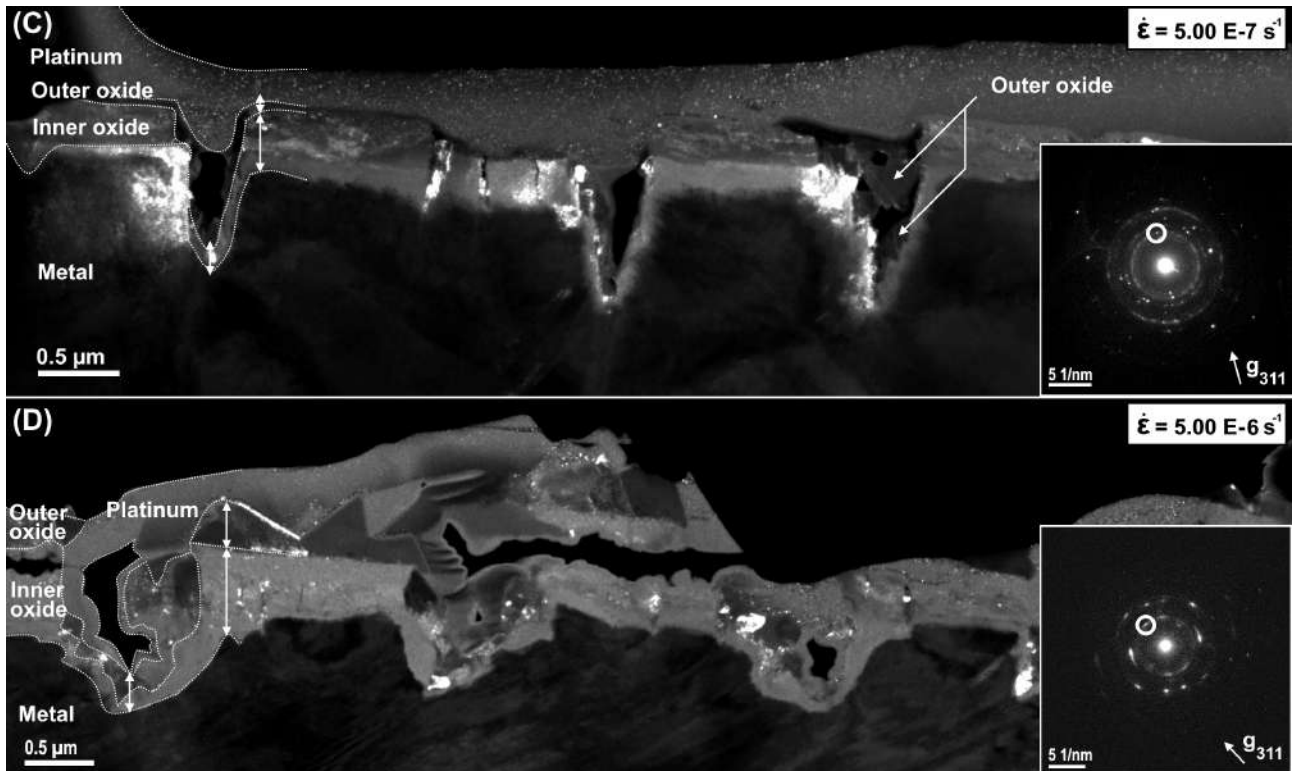


Figure 4.20: (continued) Corresponding DF-TEM of the specimens strained to (A,B) $\dot{\epsilon} = 5.00 \text{ E-}7 \text{ s}^{-1}$, and (C,D) $\dot{\epsilon} = 5.00 \text{ E-}6 \text{ s}^{-1}$. The inset diffraction patterns correspond to the SAED locations are shown as white circles in the respective BF-TEM micrographs. Indexing of the diffraction patterns corresponds to the verified main oxide component FeCr_2O_4 .

$d[012] = 3.62 \text{ \AA}$ into account, Cr_2O_3 can be disregarded since the ratio $d[012]/d[01\bar{4}] = 1.36 \text{ \AA}$ is clearly not represented within the experimental data set.

Concerning the outer oxide shown in Fig. 4.25, its structure is only loosely connected to the material substrate due to a brittle fracture occurring at the interface with the inner oxide. Its experimentally obtained spot-like diffraction pattern is analyzed in Fig. 4.26A. The interplanar ratio and angle between the non-linear basis reflections yield $d_1/d_2 = 1.72$ and $\angle d_1 d_2 = 73.3^\circ$, respectively. These measurements strongly correspond to another FCC-type spinel structure as listed in the FCC indexing table of reference [282], with a zone-axis of $[113]$, determined by the reflections $(2\bar{2}0)$ and $(42\bar{2})$ correspondingly. To that end, the outer oxide strongly agrees with the spinel oxide $(\text{Fe,Ni})_3\text{O}_4$, otherwise referred to as magnetite, with a known literature lattice constant of 0.8338 nm [281]. Simulation of this structure along the same zone-axis is presented as a close match in Fig. 4.26B. Quantitative differences between the iron-nickel ratio may vary slightly depending on the outer oxide morphology. However, these changes should have minimal impact on the corresponding lattice structure. In fact, variations between $2.6\text{Fe-}0.4\text{Ni}$ to 2Fe-Ni (relative changes between 6.5:1 to 2:1) produce still the same crystal structure. In these experiments, typical variations that were obtained using EDS analysis were measured to be about 4:1. Therefore, in each encounter of the outer oxide structure, its structure remained the same.

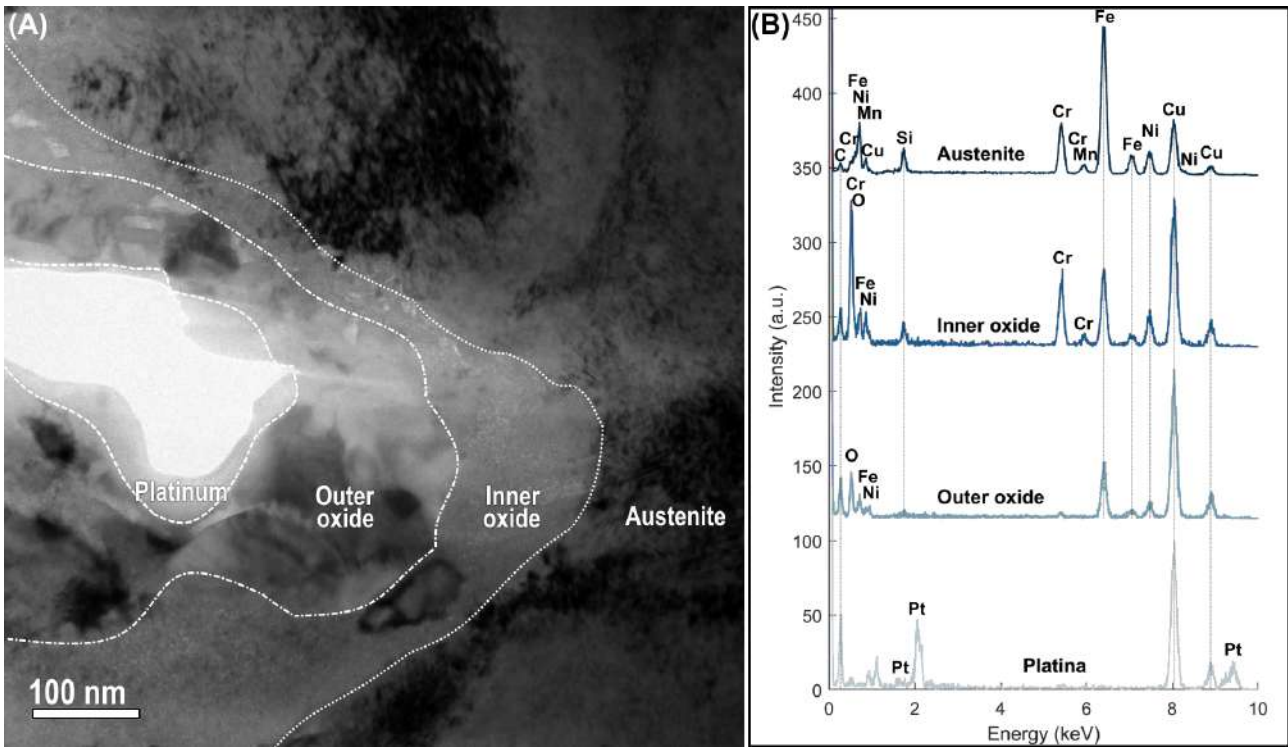


Figure 4.21: (A) BF-TEM SCC crack from a specimen strained to $\dot{\epsilon} = 5.00 \text{ E-}7 \text{ s}^{-1}$. (B) Corresponding EDS spectra of different features surrounding the crack tip. The Cu signal originates from the TEM support grid.

4.3.4 STEM-HAADF analysis

Additional STEM-HAADF EDS chemical composition maps of SCC crack tips were also acquired. Many of the interesting spectral maps are shown in Figs. 4.27 and 4.28. In a global overview of the duplex microstructure, a clear separation between both austenite and ferrite can be observed. Whereas austenite is clearly enriched by Ni, ferrite can be distinguished from the matrix by an evident enrichment in both Si and Cr. These elements are considered as stabilizers for their respective phases [49]; the influence of which can be observed in the Schaeffler diagram in Fig. 2.3. Contrast within the STEM-HAADF view is influenced by the mass-thickness variation in the microstructure. Since austenite and ferrite clearly differ in their elemental composition, delineation between both phases is also evident in terms of the image contrast. Turning towards the aspect of crack initiation, SCC cracking is again observed preferably within austenite. Two reasons for this occurrence were previously outlined, namely because of the austenite's tendency to form a more stabilized oxide on its gauge surface and because of the high solid-solution strengthened ferrite on the account of the high concentration of Si within the matrix [267]. Interestingly, both depicted cracks progress only so far up to the grain boundary separating the austenite and ferrite phases. Likely, the strengthened ferrite is considered more resistant to SCC fracturing as none of the cracks were observed to transition across the interface.

In a more detailed view in Fig. 4.28, the SCC crack morphology is seemingly composed out of various oxide and metallic phases. Indeed, from top to bottom, Pt can be first off observed which is inherently due to the FIB preparation process of the SCC crack extraction. Subsequently, the outer oxide phase of magnetite $(\text{Fe,Ni})_3\text{O}_4$ can be recognized on several instances along the crack morphology. Directly underneath in the crack opening, chromite FeCr_2O_4 can be distinguished along the crack flanks and along the metallic surface substrate, associated to which is also Si-enrichment observed. Thereafter,

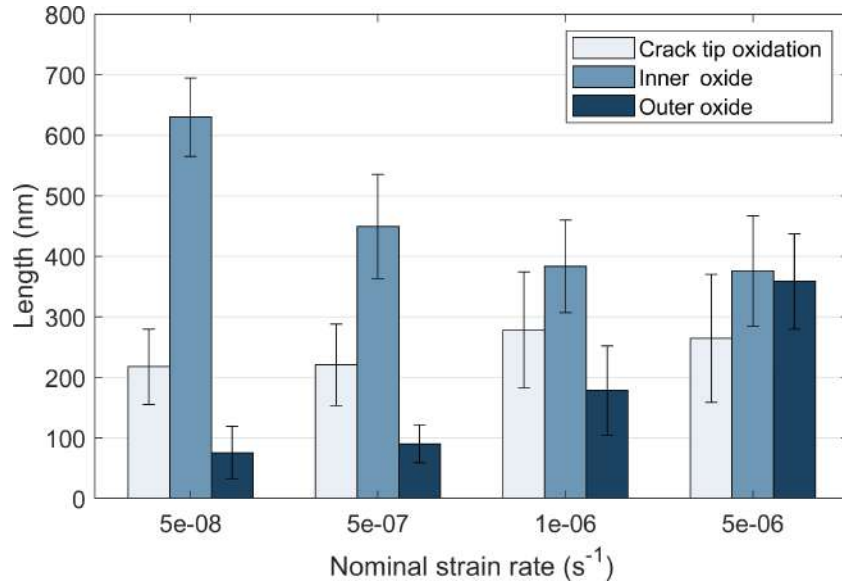


Figure 4.22: External and crack tip oxide thickness measurements obtained from the BF- and CDF-TEM images for the varying strain-rates.

Table 4.1: Comparison between experimental radial reflections and theoretical interplanar spacing ratios of possible candidate structures for the inner oxide diffraction pattern illustrated in Fig. 4.23. The theoretical reflections were selected based on meaningful simulated powder diffraction intensities ($I/I_{\max} > 5\%$). The prominent reflections are highlighted according to the coloring scheme representing reflections from, most weak to most bright, between 20-50%, > 50% and 100% (I_{\max}), respectively.

Ratio index	Measured ratio	Theoretical interplanar spacing $d[h\ k\ l]$ (Å) of structures of interest											
		FeCr ₂ O ₄			FeCrO ₃			Cr ₂ O ₃		Cr ₂ (SiO ₄)		Fe ₃ Cr ₂ (SiO ₄) ₃	
R1/R1	1,00	d[1 1 1]/d[1 1 1]	1,00	d[0 0 3]/d[0 1 2]	1,25	d[0 1 2]/d[0 1 2]	1,00	d[1 1 1]/d[1 1 1]	1,00	d[1 1 2]/d[1 1 2]	1,00		
R1/R2	1,63	d[1 1 1]/d[0 2 2]	1,63	d[0 0 3]/d[0 1 -4]	1,70	d[0 1 2]/d[0 1 -4]	1,36	d[1 1 1]/d[0 2 2]	1,23	d[1 1 2]/d[0 0 4]	1,63		
R1/R3	1,90	d[1 1 1]/d[3 1 1]	1,91	d[0 0 3]/d[1 1 0]	1,83	d[0 1 2]/d[1 1 0]	1,46	d[1 1 1]/d[0 4 0]	1,61	d[1 1 2]/d[0 2 4]	1,83		
R1/R4	2,30	d[1 1 1]/d[2 2 2]	2,00	d[0 0 3]/d[0 0 6]	2,00	d[0 1 2]/d[0 0 6]	1,60	d[1 1 1]/d[1 1 3]	1,66	d[1 1 2]/d[2 3 3]	1,91		
R1/R5	2,98	d[1 1 1]/d[0 0 4]	2,31	d[0 0 3]/d[0 2 -2]	2,22	d[0 1 2]/d[1 1 3]	1,67	d[1 1 1]/d[2 2 0]	1,77	d[1 1 2]/d[2 2 4]	2,00		
R1/R6	3,25	d[1 1 1]/d[2 2 4]	2,83	d[0 0 3]/d[0 2 4]	2,50	d[0 1 2]/d[0 2 4]	2,00	d[1 1 1]/d[0 0 4]	1,87	d[1 1 2]/d[1 3 4]	2,08		
R1/R7	4,41	d[1 1 1]/d[1 1 5]	3,00	d[0 0 3]/d[1 1 6]	2,71	d[0 1 2]/d[1 1 6]	2,17	d[1 1 1]/d[1 5 3]	2,57	d[1 1 2]/d[1 2 5]	2,24		
		d[1 1 1]/d[0 4 4]	3,27	d[0 0 3]/d[1 1 -6]	2,71	d[0 1 2]/d[1 2 2]	2,30	d[1 1 1]/d[3 1 3]	2,78	d[1 1 2]/d[4 4 4]	2,83		
		d[1 1 1]/d[0 2 6]	3,65	d[0 0 3]/d[0 1 8]	2,87	d[0 1 2]/d[1 2 -4]	2,48	d[1 1 1]/d[2 6 0]	2,88	d[1 1 2]/d[0 4 6]	2,94		
		d[1 1 1]/d[2 4 6]	4,32	d[0 0 3]/d[1 2 -4]	3,10	d[0 1 2]/d[0 3 0]	2,54	d[1 1 1]/d[1 7 1]	2,96	d[1 1 2]/d[2 4 6]	3,06		
		d[1 1 1]/d[3 5 5]	4,43	d[0 0 3]/d[0 3 0]	3,18	d[0 1 2]/d[0 3 6]	3,00	d[1 1 1]/d[1 7 3]	3,24	d[1 1 2]/d[0 0 8]	3,27		
		d[1 1 1]/d[1 3 7]	4,43	d[0 0 3]/d[0 2 -8]	3,40	d[0 1 2]/d[1 3 4]	3,23	d[1 1 1]/d[3 1 5]	3,35	d[1 1 2]/d[4 6 6]	3,83		
		d[1 1 2]/d[2 4 10]	4,47	d[0 0 3]/d[0 4 -4]	4,44	d[0 1 2]/d[3 3 0]	4,39	d[1 1 1]/d[4 8 0]	4,50	d[1 1 2]/d[4 6 8]	4,40		

thin enriched layers of metallic Si and Ni can be observed which jointly separate the oxide from the austenite metallic substrate. These layers are approximately around 20 – 50 nm in thickness and were not previously observed from previous EDS point analyzes. The different layers of the SCC morphology are also evident from the RGB overlay image included with the spectral composition maps.

The presence of enriched Ni was also observed in 316 SS SCC crack tips by Terachi et al. [94, 276], however the origin of which is since still under dispute. Lozano-Perez [97, 98] postulated that Ni was rejected from the chromite oxidation on the surface of stainless steels causing it, to some extent, to cluster around the metal-oxide interface. This postulation fits our observations since it is apparent that no close-at-hand depletion of Ni occurs from inside the bulk matrix. Selective oxidation at the surface may cause the formation of the chromite oxide, while Fe- and to some extent Ni-ions diffuse outwards to form the secondary nickel-bearing magnetite oxide. Remaining Ni is then pushed back to form an enriched layer at the metal-oxide interface. On the other hand, Arioka et al. [283] postulated that the increased concentration of Ni may be due to different diffusion velocities of alloying components

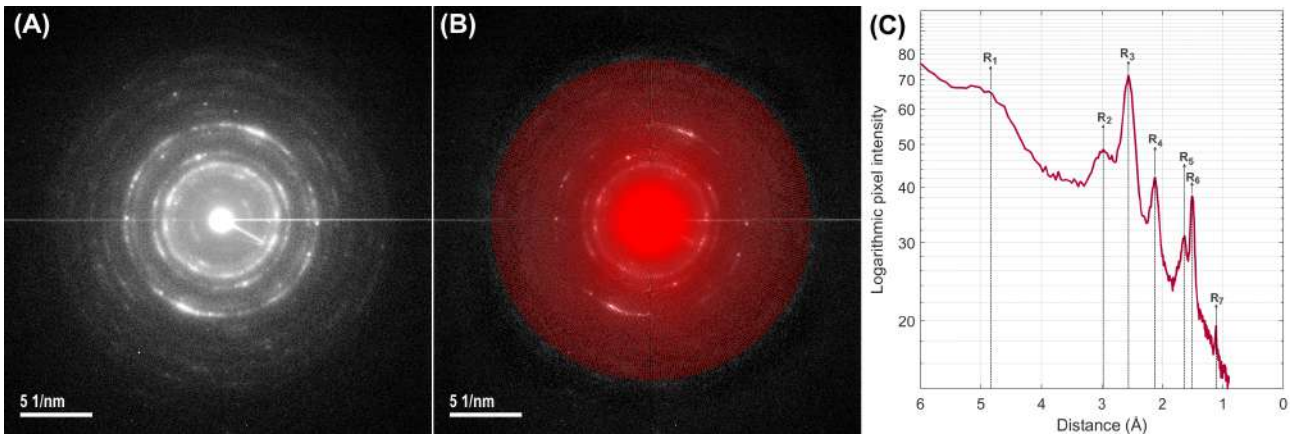


Figure 4.23: (A) Inner oxide experimental ring diffraction pattern. (B) Application of the radial sampling method i.e. taking rotational integrations of the diffraction pattern and subsequently normalizing the resulting intensities. (C) Corresponding line trace of the radial sampling method.

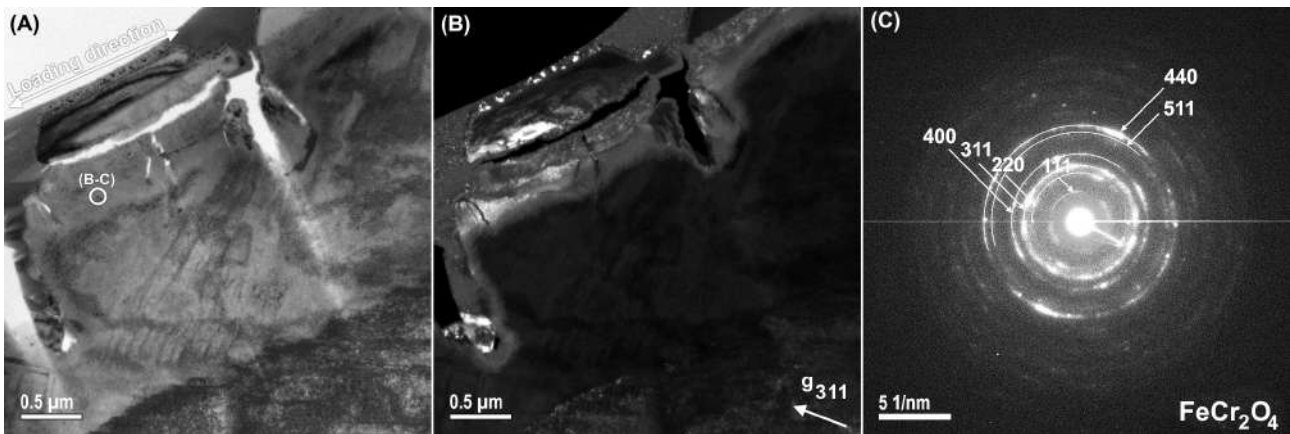


Figure 4.24: Inner oxide for a specimen strained to $\epsilon = 1.00 \text{ E-}6 \text{ s}^{-1}$. (A) BF- and (B) corresponding CDF-TEM of the inner oxide in between two crack tips, with (C) their indexed ring-like diffraction pattern matching FeCr_2O_4 .

in a creep-like crack growth mechanism associated with internal vacancy fluxes, rather than being the result of any selective oxidation processes. This process could be enhanced in the wake of the crack tip due to the local stress gradients and the formation of vacancies of advancing cracks. Alternatively, the Ni could also arise from classical porosity forming de-alloying mechanisms [284] which is known to lead to FIC [184, 196], especially in systems other than stainless steel. The origin of the enriched Si around the crack tips is likely attributable to similar kind of mechanisms as postulated for Ni, although no indicative observations to support this have been made so far. These mechanisms are likely also enhanced when the matrix concentration of Si is increased, as is the case within this model alloy.

4.3.5 Transgranular SCC mechanism

In all SCC mechanisms of stainless steel operating in PWR temperature water, oxidation plays a detrimental role. Therefore, it is expected that the information on crack morphology, and in particular the crack tip oxidation, should help to elucidate the dominant SCC mechanism. Since re-oxidation may occur after the initial crack is formed, it is of crucial importance to deduce under which conditions the oxide kinetics govern the crack initiation and propagation processes. In contrast to stainless steels at ambient temperature where passivation films have thicknesses within the nanometer range [285],

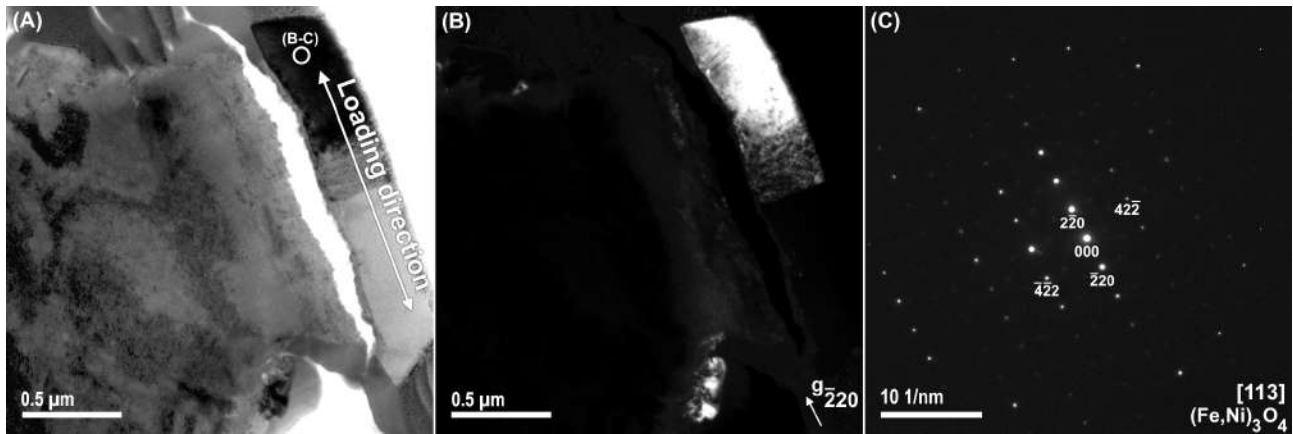


Figure 4.25: Outer oxide for a specimen strained to $\dot{\epsilon} = 1.00 \text{ E-}6 \text{ s}^{-1}$. (A) BF- and (B) corresponding CDF-TEM of an outer oxide grain in between two crack tips, with (C) their indexed spot-like diffraction pattern matching $(\text{Fe,Ni})_3\text{O}_4$.

PWR temperature oxide layers are of the order of about one to several micrometers thick.

One renowned SCC mechanism is based on slip-dissolution [185,186] where a sufficient thick oxide film at the crack tip is required for oxide film rupture to occur. A second example is the internal oxidation model [24, 187] where oxidation of the grain boundary at the crack tip is imperative as oxidation alone is responsible for the lowering of fracture toughness embrittled interfaces, leading towards the subsequent initiation and propagation of the crack. These two examples are typically applicable only for IGSCC of metallic grain boundaries in irradiated steels. However, as is perceived within this study, transgranular cracking is the observed dominant failure mode on the gauge surface of the specimens. This signifies that the cracking mechanism for these tapered specimens may not be entirely comparable to what is expected for irradiated steels. Unfortunately though, for TGSCC in PWR temperature water, there is no consensus on which model best describes the observed phenomena. To that end, we discuss the following observations in the light of two separate models i.e., the film-induced cleavage and the strain-induced failure mechanism.

The presence of strong deformation fields in close vicinity of the crack tips indicates that one needs to consider the interplay of both corrosion- and deformation-driven cracking mechanisms. In our observations, different sample exposure times occurring at different strain-rates play a role in favor of one mechanism over the other. On the one hand, at long exposure times with slow strain-rates up to $\dot{\epsilon} = 5.00 \text{ E-}7 \text{ s}^{-1}$, a diffusion-based oxidation process precedes the crack formation. This observation is embodied by the abrupt failure of slow-strained specimens in the load-elongation curves of Fig. 4.1, the cleavage-like main fracture surface in Fig. 4.2, the increased amount of cracking incidences with prominent peaks along the crack density distributions in Fig. 4.10, and the different morphology and deformation features at and around the SCC crack tip in Figs. 4.17 and 4.16 respectively. However, for shorter exposure times at faster strain-rates starting from $\dot{\epsilon} = 1.00 \text{ E-}6 \text{ s}^{-1}$ and beyond, intrinsic failure is not as much dominated by corrosion but rather induced by the high external deformation rates. SCC cracks propagating within the brittle oxide at increased strain-rates typically show an increase in crack tip roughness [286, 287]. Rounded shaped crack tips can be related to the strain-induced dislocation slipping in the surrounding microstructure under the influence of the high external deformation rates. Strain-induced crack tip failure is hence associated with the dislocation dynamics and stress-strain profiles in the near vicinity of the crack tips [92]. As the straining ensues, the localized deformation becomes more severe and additional microstructural defects such as twin systems are introduced. Primary mechanical twins initiate along favorable austenitic crystallographic $\langle 111 \rangle$ directions in the early stages of deformation. Secondary twinning systems may become activated under

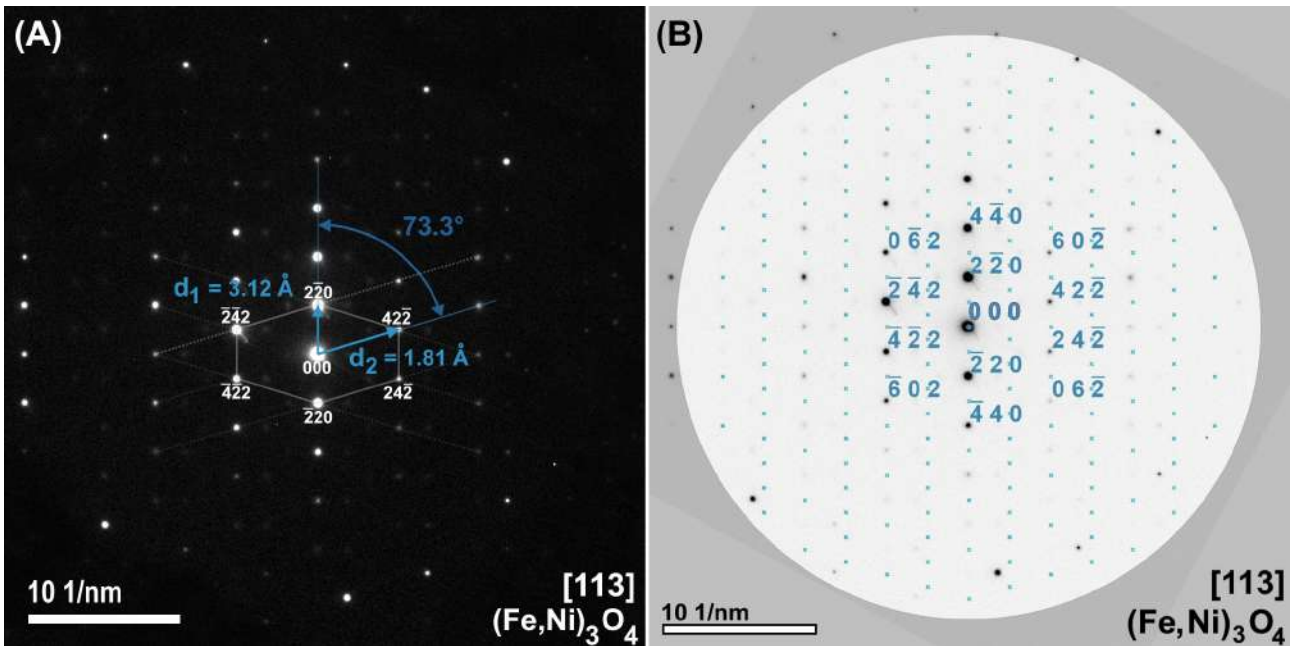


Figure 4.26: Outer oxide (A) experimental, and (B) simulated diffraction pattern analysis of the FCC-type spinel oxide $F\bar{d}3m$ (227) $(\text{Fe,Ni})_3\text{O}_4$ [281]. All systematic absences of the space group along the zone-axis $[1\bar{1}3]$ are indicated with little blue crosses.

the increased degree of deformation, deeper within the bulk specimen, although this was less observed in the present work. Twin-slip interactions are known to induce strain-hardening as the dislocation slip is inhibited due to the increase in twin interfaces [288,289]. This process is commonly understood as the dynamical Hall-Petch effect [71].

Respectively, the dominant SCC observed failure mechanisms at low and high strain-rates have been linked to the FIC and strain-induced failure mechanisms. The FIC model [184,196] is presented as a respectable candidate that requires a material covered with a sufficiently thick surface layer that is sensitive to brittle fracture. Thus far, the FIC model has not been applied to transgranular SCC in PWR temperature water, although it applies well to experimental results observed for SCC cracks in stainless steels at low strain-rates for long exposure times. Accordingly, it is required that a sufficiently thick Ni de-alloyed nano-porous film develops as a result of anodic diffusion-dissolution processes that is susceptible to brittle fracture. These prerequisites for the FIC are typical for stainless steels in PWR environments and are supported by our findings. Internal microcleavage cracking within the porous layer may occur on the account of several actors, primarily being the externally applied surface stress. The FIC mechanism further postulates that small successive cleavage cracks are introduced, much alike the sharp crack illustrated in Fig. 4.18 in the de-alloyed (nickel-depleted) oxide film. After propagation, surface re-oxidation of the exhausted crack tip occurs while in contact with the primary water. Evidence of Ni-enrichment ahead of the crack tips in Figs. 4.27 and 4.28, which has also been reported for stainless steels in high-temperature water [94,97,98,276], may be the resultant of this de-alloying process. Hence, the FIC can potentially induce transgranular crack growth in stainless steels under PWR conditions [197]; a process which has so far more been linked only to SCC failures in other corrosive environments [195,200].

A final point of discussion involves the role of the inherent data scatter observed in the stress threshold analyses in section 4.1.7. Despite the application of an accurate crack detection algorithm, the individual thresholds per specimen still showed a scatter that remained inherent to the dataset. The fact

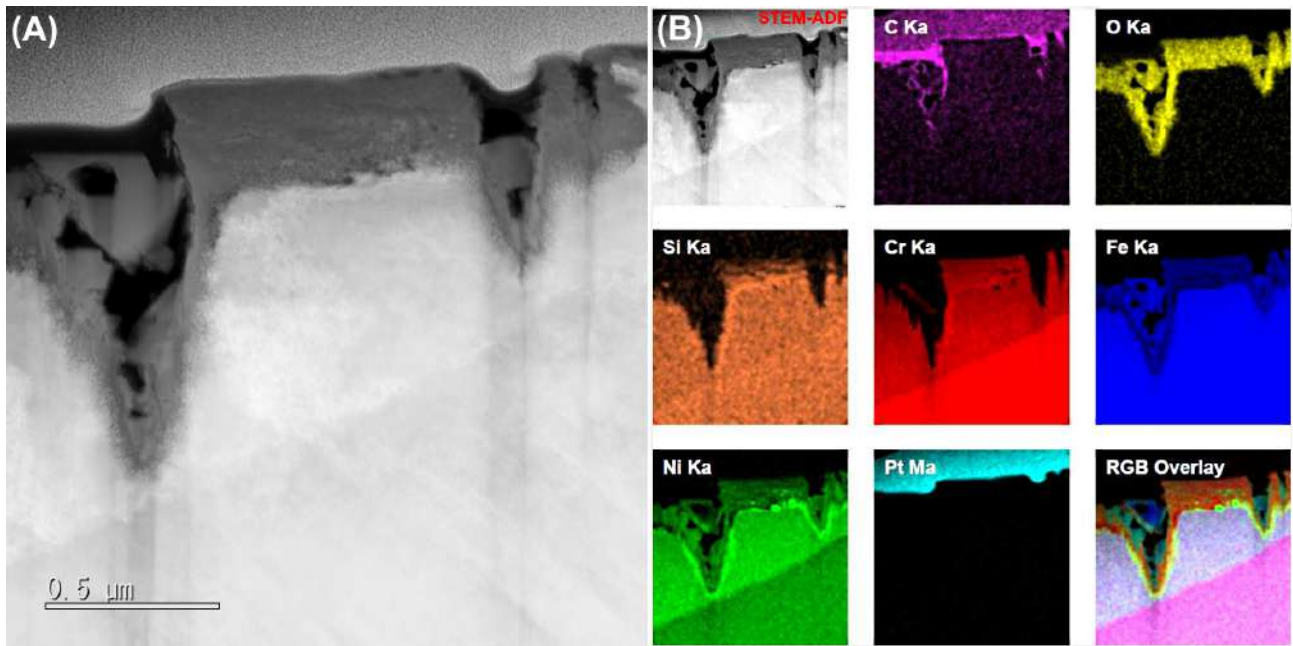


Figure 4.27: STEM-HAADF EDS spectral maps acquired from a $\dot{\epsilon} = 5.00 \text{ E-}7 \text{ s}^{-1}$ CERT-strained tapered specimen illustrating the SCC initiation within the austenite phase of the duplex microstructure.

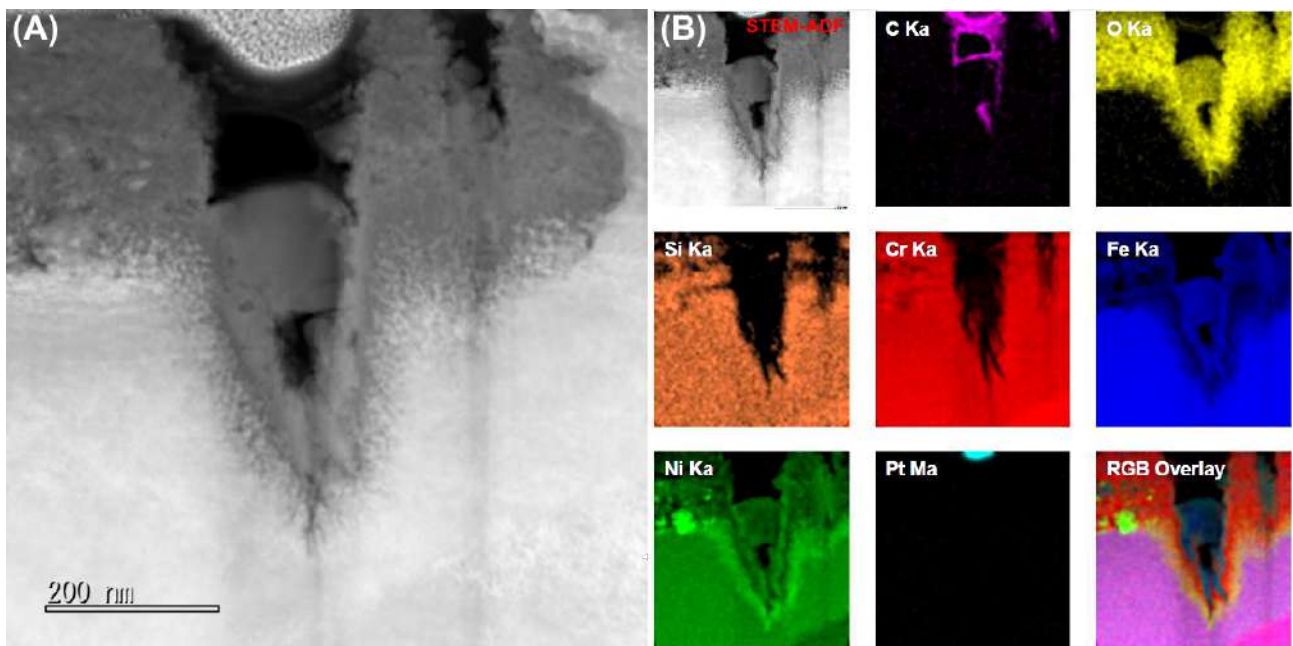


Figure 4.28: STEM-HAADF EDS spectral maps acquired from a $\dot{\epsilon} = 5.00 \text{ E-}7 \text{ s}^{-1}$ CERT-strained tapered specimen illustrating the different metallic and oxide composition of a typical SCC crack.

of the matter is that, any error that is correlated to the uncertainty of the critical gauge length l_c in the crack density distributions, which lies at the basis of the scatter in the stress threshold analyzes, must also be correlated to an uncertainty to the local strain-rate that varies across the tapered gauge length. In easier words, the scatter found in the threshold analyzes naturally stems from a local strain-rate distribution along one particular cross-section of the tapered gauge length. This suggests that SCC cracking is driven by a probability distribution of stress, effectuated by local strain on the tapered geometry. Since the cracking almost exclusively occurred within the surface oxide of the

tapered specimens, this probabilistic stress distribution likely affects also the cracking of the oxide. Considering that an oxide may have a certain fracture stress, deemed the total strength of the oxide, it will never be possible to exactly determine when the oxide will fail when it is placed under a variable stress. Therefore, it is inferable that the whole initiation of SCC may be linked with the uncertainty of cracking of the surface oxide, determined by the total strength of the oxide of the oxide itself. A weaker oxide strength may be more vulnerable to failure when it is placed under constant stress. This is very reminiscent the SCP model developed on the notion of IO by Konstantinović [162]. If indeed a probabilistic nature is involved in the crack initiation processes, it shows that the parameters governing the strength of the oxide must play a crucial role towards the cracking of steels.

Chapter 5

Thimble Tube O-ring Specimens

Over the course of the ENGIE SCKCEN corrosion convention program, some 80 neutron-irradiated O-ring specimens were cut from a 316L SS cold-worked flux thimble tube redeemed from the commercial Tihange PWR in Belgium [161]. These O-ring specimens were subjected to constant load compression tests in order to investigate the IASCC cracking in a controlled set-up environment. The O-ring's compression stresses were recorded over a period of time while being subjected to a simulated PWR-environment. An overview of the test results of the applied stresses in function of the O-rings' time-to-failures (TTFs) is presented in Fig. 5.1. In these types of tests, the O-rings are typically loaded to different stress levels ranging between significant fractions of the irradiated yield stress; estimated to be around 1000 MPa. The experimental results demonstrated that: (i) the O-ring samples failed faster when being subjected to higher stress values, (ii) with an increasing neutron dose, the applied compression stresses required for the O-rings to fail tended to decrease, and (iii) estimation of the stress threshold under which no IASCC cracking occurred, yielded about 40% of the irradiated yield stress [161]. However, one factor that limits the application of the mechanical load testing, is the large scatter observed throughout all the TTF data of the tested O-rings. For all specimens tested under relatively similar conditions, the scatter of the failure data remains inherent to the dataset while its origin is not fully understood. For instance, as seen in Fig. 5.1, the O-ring failure times ranged between 100 – 2000 h under an applied stress of 55% of the irradiated yield stress. Recent rendition of these failures by Konstantinović [162], one of SCKCEN's promoters of this thesis, indicated that this scatter may be correlated with the parameters that govern the IASCC crack initiation solely within the oxidized part of the stainless steels. As we know from section 2.5.3, the intergranular oxides can be responsible for metallic embrittlement and the lowering of the material's fracture resistance as a consequence of oxide diffusion leading into the crack tip grain boundary. This grain boundary embrittlement makes the material much more prone to sudden intergranular failure as it would be otherwise. In a probabilistic approach following the idea of the weakest link principle, failure at any point in time in the oxidized grain boundary is governed by a certain distribution of flaws or initiation points within the naturally established oxide. The probability of total failure tends to increase in more voluminous oxides where the possibility of existing oxide flaws is far greater. If the cracking is entirely dictated by the failure of the oxide, it is reasonable to consider probabilistic oxide strengths in association with the internal oxidation model in order to determine the cracking probability. In this regard, Konstantinović [162] developed a probabilistic fracture model on the grounds of the statistical Weibull treatment of oxide strength and described the subsequent growth of cracking in terms of a subcritical crack propagation (SCP) process, see also section 2.5.3.1.

Validation of the SCP mechanism for intergranular cracking requires distinct observations of IASCC

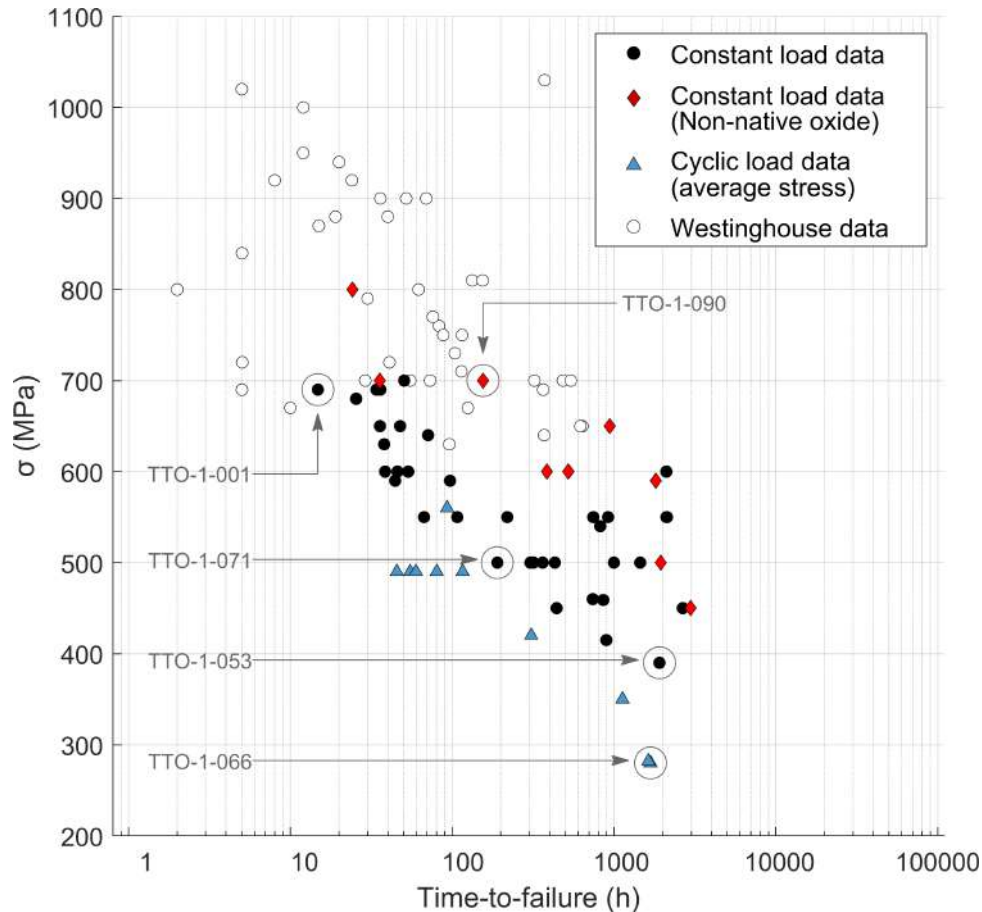


Figure 5.1: Mechanical load O-ring compression testing. Stress versus time to failure of O-rings tested under the constant load condition. Time to failure of O-rings that are investigated in this study are indicated in the figure.

cracks and crack tips formed under various applied stress and initial material surface state conditions. Furthermore, since it is based upon the internal oxidation model, experimental investigations should confirm the presence of brittle intergranular oxides ahead of propagating crack tips. Moreover, it should be observed that, the intergranular oxides grow faster than the propagation rate of the crack itself, or, a step-like cracking process is evident wherein the intergranular oxide repetitively grows beyond the crack tip to set up the conditions for cracking. In the cracking processes, both stress [290] and surface oxidation [162] are believed to play a crucial role for brittle intergranular cracks, in particular when the nature of probabilistic cracking is considered. Therefore, for the analysis of the specimens within this chapter, specifically O-rings with (i) steadily increasing stress states, (ii) different oxidized surface states, and (iii) varying loading conditions are considered. Details on the testing parameters of these O-rings were outlined in the overview table, listed in Tab. 3.5. Three of these specimens, namely TTO-1-053, -071, and -001 were tested under constant load conditions by increasing the stress, ranging from 390 to 690 MPa, well below the irradiated yield stress. A fourth sample, i.e., TTO-1-090 was prepared with a different oxide surface state in order to investigate its implication on the crack initiation. Its initial native PWR oxide, which was established naturally when the thimble tube was in service in the Tihange PWR NPP, was abraded prior to the initiation of the constant load test by mechanical soft grinding. In this way, the metallic surface quickly establishes a non-native oxide layer, composed of an oxide that formed under aerated and under simulated PWR conditions during testing. Implication of this non-native oxide to the initiation of IASCC cracks and overall time-to-failure of the O-ring specimen could indicate some of the prerequisites required for cracking and shed light on the cracking mechanisms itself. Lastly, an additional fifth specimen i.e. TTO-1-066 was

subjected to low-cycling fatigue (LCF) testing conditions, instead of the more conventional constant load conditions subjected to all other O-ring specimens in this study. The loading cycle consisted of a triangular waveform with a transient time of about 60 minutes, wherein the compressive stresses are systematically cycled between 40 to 100 % of its maximum stress value, averaging around 70 % stress overall. LCF failure is characterized by high amplitudes of applied tensile stress effectuated by a load that varies over long frequencies. Both elastic and plastic strains are created in this manner of loading. In contrast to high-cycle fatigue (HCF), failure by LCF occurs in far fewer loading cycles as a result of the permanent deformation that may eventually lead to cracking. Individually, these specific O-rings were selected from the large data pool of specimens outlined in Fig. 5.1.

5.1 Prior SEM investigations

Before moving on to the extraction and subsequent investigation of IASCC cracks using FIB-SEM and TEM analysis, it is worth to outline some of the priorly obtained results from SEM investigations on fractured O-rings. These investigations were performed by Dr. Konstantinović. The obtained SEM results were recorded in internal SCKCEN reports in references [291–293], before or during the early start of this Ph.D. project.

From the large pool of investigated O-rings, SEM images of especially the lowest and the highest stress-tested O-rings, i.e., TTO-1-053 (390 MPa) and TTO-1-001 (690 MPa), are selected. Figs. 5.2 and 5.3 illustrate the reconstructions of the failures post constant load testing, which are added to this thesis for the sake of completion. These results effectively support some of the conclusions that come forth from other analyses acquired after the investigation of IASCC crack tips. Most remarkably is the fact that crack initiation was observed from both the outer as from the inner surface of the O-ring. Crack initiation is normally expected to occur only from the O-ring's outer surface, because: (i) it exhibits a saturated oxide that formed during service under PWR conditions instead of a thinner oxide formed under aerated conditions along the inner surface, and (ii) higher tensile stresses are expected along the outside of the O-ring according to preliminary finite-element modeling (FEM) Von Mises stress analyses [294]. On the other hand, Fig. 5.4 presents SEM images of the fracturing mode along the primary fracture surface. Cracking at lower stresses exclusively exhibited intergranular SCC (IGSCC), whereas at higher stresses a mixed fracture mode with some transgranular SCC (TGSCC) is also observed.

5.1.1 O-ring crack initiation studies

5.1.1.1 TTO-1-053

SEM images of O-ring specimen TTO-1-053 (390 MPa) are presented in Fig. 5.2. This specimen fractured into five individual pieces post constant load testing; the two largest pieces, A and B, were embedded in edge-on orientation in a mounting resin and subsequently polished. The following SEM investigation showed that a large macroscopic crack initiated from the inner surface along the opposite side of the loading bearing point, see Fig. 5.2B (blue). BSE-SEM images provide possibility to observe channeling contrast, which is very useful for visualization of individual grains and grain boundaries. The average grain size is found to be around 20-50 μm 's, which is typical for stainless steel used for making the thimble tube. Clearly, the crack propagated fully intergranularly through the bulk material towards the O-ring's outer surface, illustrating severe branching at multiple grain boundary triple junctions. Evidently, it propagated not sufficiently long enough to lead to the full fracture with a total of six pieces. However, its extended propagation does suggest that intergranular cracking from the inner surface could lead to a main O-ring failure. Numerous other smaller cracks have been

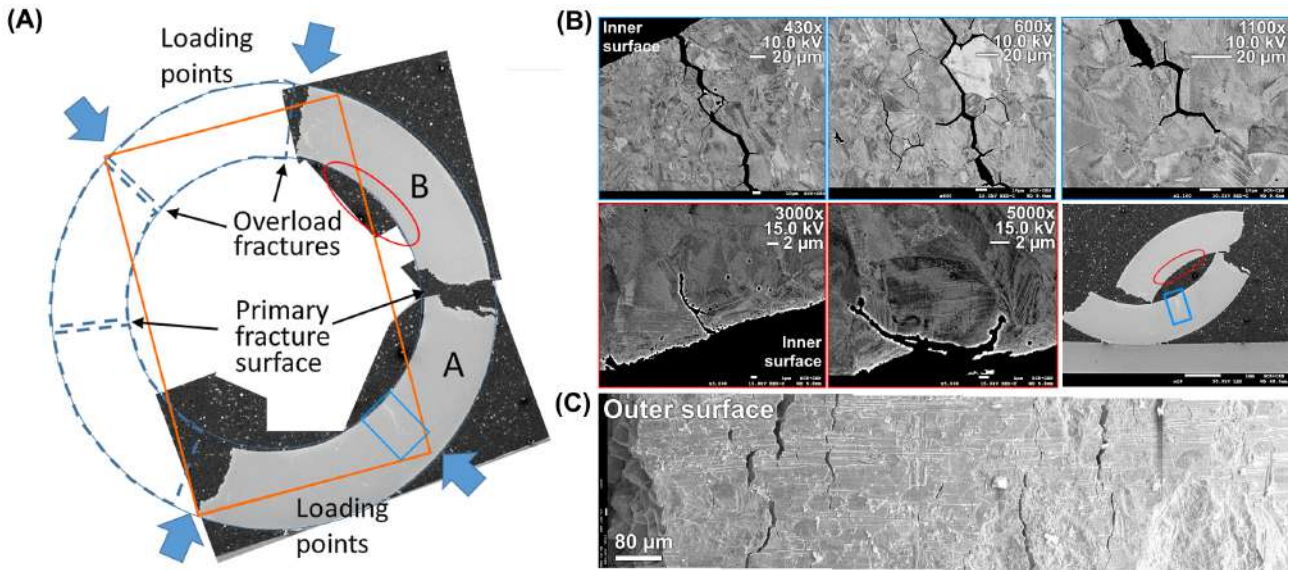


Figure 5.2: (A) Reconstruction of the failure of TTO-1-053 (390 MPa). (B) BSE-SEM imaging of the crack initiation along the inner surface. (C) SE-SEM of the as-received O-ring's outer surface.

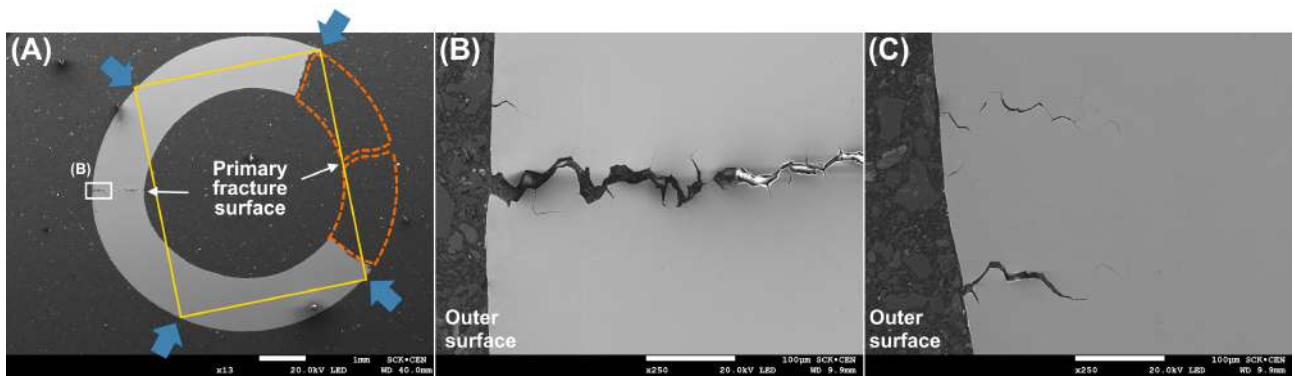


Figure 5.3: (A) Reconstruction of the failure of TTO-1-001 (690 MPa). (B-C) SEM imaging of the crack initiation along the outer surface.

observed equally at the inner surface on other locations, see Fig. 5.2B (red). The typical size of these smaller cracks is of the order of several micrometers instead of the near full O-ring specimen width. Their positions could not be associated to the regions where large tensile stresses are expected, see also prior FEM analyses [161] and Fig. 3.18. Moreover, their fracturing mode was not always linked with a complete intergranular mode either.

On the as-received specimen, crack initiation along the outer surface was equally observed, see Fig. 5.2C. It is expected that most of the cracks responsible for O-ring failure initiate along this outer surface. The crack distribution is in a very good agreement with the stress distribution across the surface. On the contrary to the inner surface, the outer surface exhibited the formation of thicker oxide with cracks that could be directly related to large tensile stress. A fully saturated oxide is expected to be due to the acting in-service PWR environment which affected only the outer flux thimble tube surface.

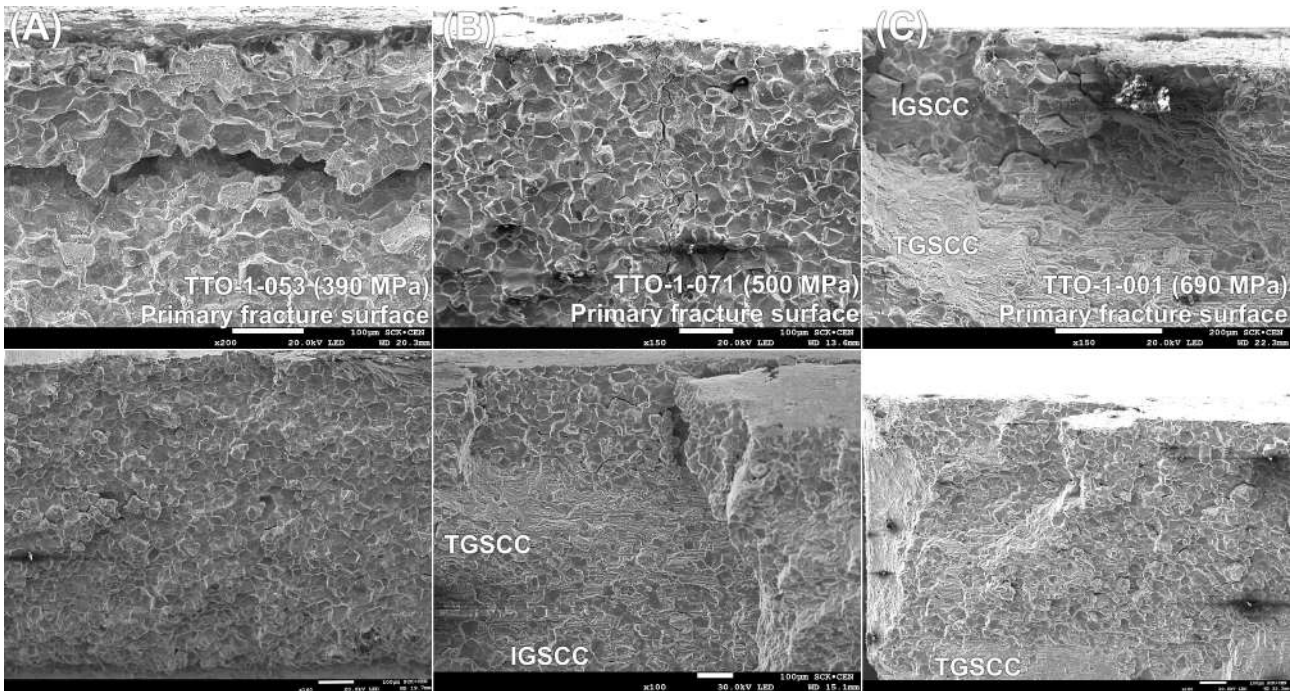


Figure 5.4: SEM SE investigation of the primary fracture surface of specimens (A) TTO-1-053 (390 MPa), (B) TTO-1-071 (500 MPa), (C) TTO-1-001 (690 MPa).

5.1.1.2 TTO-1-001

SEM images of the crack initiation in O-ring TTO-1-001 (690 MPa) are presented in Fig. 5.3. The O-ring tore in three individual pieces post testing; the largest part was embedded and polished for subsequent SEM analysis. The initiated cracks are located in the region where the highest tensile stresses are expected from prior FEM analyses [161]. Most cracks from the outer surface are thus distributed along the primary fracture that lead to failure, see Fig. 5.3B. In comparison to specimen -053 (390 MPa) presented above, the primary crack seems to be extended much broader than in the other case. It is possible but rather unlikely that the sample handling, including embedding and polishing processes, have caused a broader opening of the main crack. However, it is far more likely that the acting tensile stresses caused a broader opening mode at the point of crack initiation. All observed cracks were equally branched, although much less than previously observed in specimens subjected to lower stress, like -053 (390 MPa). The branching developed along several grain boundary triple junctions, but its extension is less invasive.

5.1.1.3 Primary fracture surface analyses

Post constant load compression testing SE-SEM images of the primary fracture surface of several investigated O-ring specimens are presented in Fig. 5.4. Lower stressed specimens exclusively exhibited an IGSCC fracturing mode. This was especially visible for specimen TTO-1-053 (390 MPa), as can be seen in the close-up and broader overview images in Fig. 5.4A. Many individual grains can be visualized, with numerous IASCC cracks propagating into the bulk specimen. However, for specimens tested to larger stresses like -071 (500 MPa) and in particular -001 (690 MPa), the fracture surface exhibited a mixed fracture mode with both IGSCC and substantial TGSCC cracking. In specimen -001 (690 MPa), some additional ductile fracture regions were discovered, which may have indicated towards an overload-type failure at higher stresses. Transgranular and ductile fracture surfaces are responsible for the formation of uneven and non-flat surfaces. Specimen -071 (500 MPa) exhibited

surfaces appearances that somewhat lie in between both extremes. Thus, it is expected from the crack tip investigation, that some evidence towards more significant deformation is also expected at higher stresses.

5.2 FIB analysis

The following results discuss the scope of IASCC cracking, the cracking morphologies, and the surrounding deformation field of intergranular cracks extracted from O-rings tested to different stress-, surface oxide-, and loading states using TEM analysis. The aim of this investigation is three-fold: (i) to illustrate a working FIB methodology for crack tip extraction, (ii) to identify microstructural features that can be related to crack initiation and propagation by performing a detailed study of the crack and crack tip morphologies, and (iii) to provide additional data to help elucidate on existing cracking mechanisms, especially in relation to the different sample and loading conditions subjected to the O-ring specimens during testing. Microstructural investigations of the crack's deformation field are performed on numerous cracks; the extent of which is interpreted in relation to the acting stress intensity. The effect of the non-native oxide surface and the cyclic loading states are interpreted in relation to mechanical TTF data of common native-oxide constant load O-rings. Results achieved within this investigation may facilitate in the development of predictive methodologies and mitigation strategies related to IASCC cracking, especially for the industrial failures of BFB cracking in particular. This work has led to the publication of two peer-reviewed first-author publications, cited as [232] and [295].

5.2.1 IASCC crack extraction

Fig. 5.5 depicts a typical overview of the extraction steps of an IASCC crack described in section 3.2.2.1. Most of the cracks were extracted from the O-ring's primary fracture surface using the Thermo Scientific Scios DualBeam FIB-SEM according to the standard in-situ FIB lift-out technique, except for those appertaining to samples TTO-1-001 (690 MPa) and some cracks of TTO-1-066 (280 MPa - cyclic loading). Hard-lining restrictions on the FIB pieces appertaining to these O-rings, such as the samples' activity levels and their size dimensions, made it sometimes very difficult to practically tilt their primary fracture surface facing upwards towards the FIB's electron beam. Therefore, in all cases where the FIB's crack extraction was not feasible from the O-ring's primary intergranular fracture surface, it was opted to extract the cracks from the O-ring's outer surface instead. Cracks extracted from the primary fracture surface generally attract a lot of interest due to the fact that the fracture surface closely resembles an IASCC-like fracture appearance which clearly does not correspond to any of the ductile overload fractures near the external loading points of the compression procedure. However, extraction of such crack tips was considered to be quite challenging given the large branching nature along multiple grains of the cracks; especially for samples tested to lower stress conditions. Alternatively, cracks extracted from the O-ring's outer surface have some positive merit as well. Indeed, in studying outer surface cracks, one gains more information on the effect of the tensile stress orientation in relation to the crack propagation. Therefore, the restriction on the FIB sample's orientation still offers some value in regards to this investigation. For reference, typical examples of the primary fracture and outer surfaces of O-rings are respectively shown in Figs. 5.6A and 5.6B.

Tab. 5.1 presents a complete overview of all the cracks that were extracted and subsequently investigated using TEM analysis. A multitude of crack embedded lamellae were prepared for each individual specimen. Ultimately, a total of 24 fully developed crack tips were completely extracted and investigated. Some recurrent features that can be identified from the cracks after first impression post FIB-extraction from figures like Figs. 5.5H-I, include:

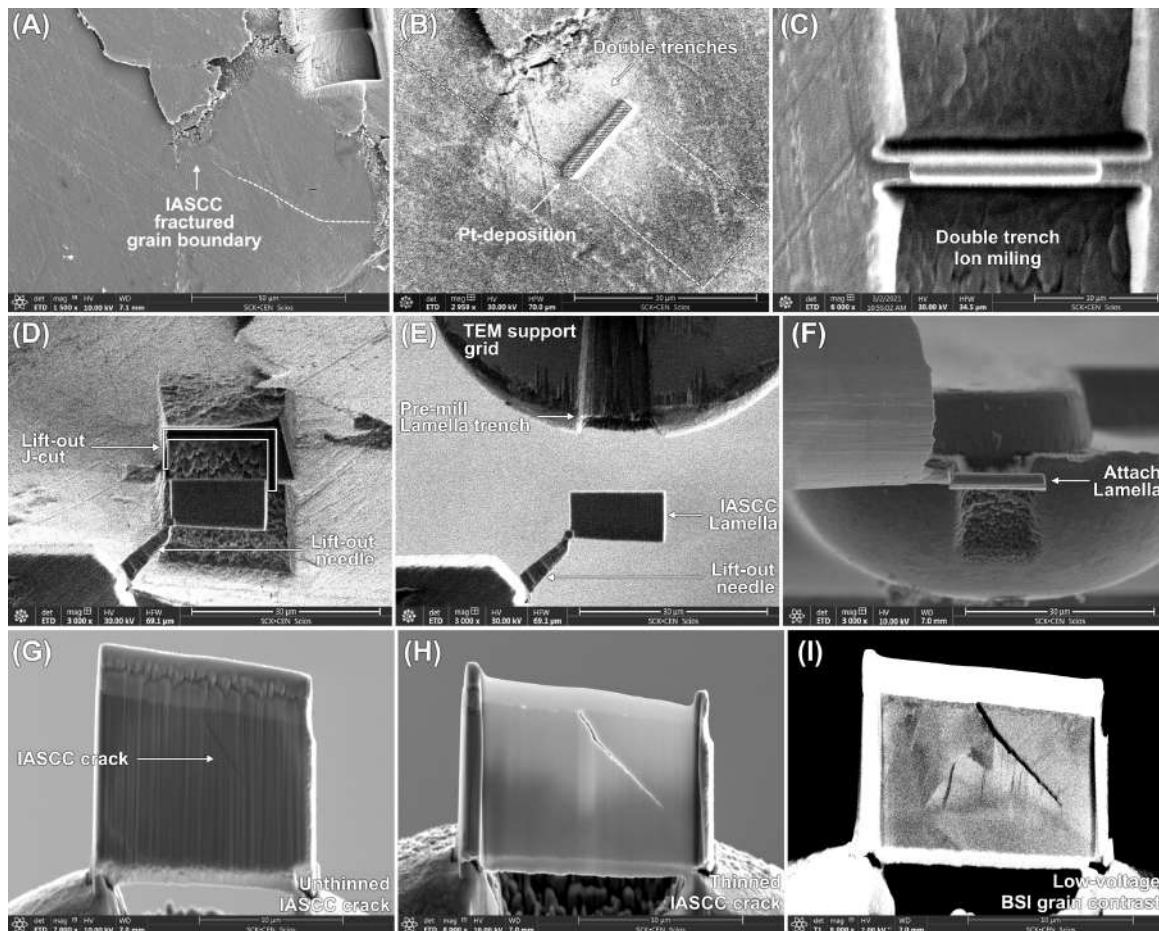


Figure 5.5: FIB-SEM images illustrating the methodology of IASCC crack tip extraction from an O-ring's specimen piece polished primary fracture surface.

1. Cracks extended typically from a fully oxidized grain boundary triple junction, branching off towards a single crack, that ultimately resulted in a fully oxidized crack tip. On some other occasions, narrow intergranular cracks could be observed that developed perpendicular from the lamella surface without showing any existential branching. From the select collection of cracks, the branching nature of IASCC cracks was more frequently observed at generally lower stresses.
2. It is apparent from the collected crack tips that the tensile stress orientation plays an important role for crack initiation in all sets of specimens. On each occasion, the imposed stress direction is aligned in parallel for crack tips extracted from the O-ring's outer surface while it acts in the in-plane direction into the bulk when facing the primary fracture surface. This implies that cracks extracted in cross-sectional orientation from the outer surface initiate in cleavage-mode (mode I), while those extracted from the primary surface initiate in shearing-mode instead (mode II).
3. The effective stress orientation at the crack tip naturally depends on the crack path along the leading grain boundary, which correspondingly affects the ultimate crack length of the cracks that were extracted. Cracks that continuously propagated in a shear-orientation generally resulted in much shorter developed crack lengths, while cleavage-orientated cracks generally extended much deeper within the bulk. To some extent, such cleavage cracks could develop beyond the size that could be feasibly extracted with FIB. This is evident by the much greater success rate in extracting a shearing-mode crack tips, simply because the crack length was typically shallower.
4. Crack arrest was more commonly observed whenever the tensile stress acted in shearing-mode orientation at the propagating crack tip. This observation is related to the preceding one.

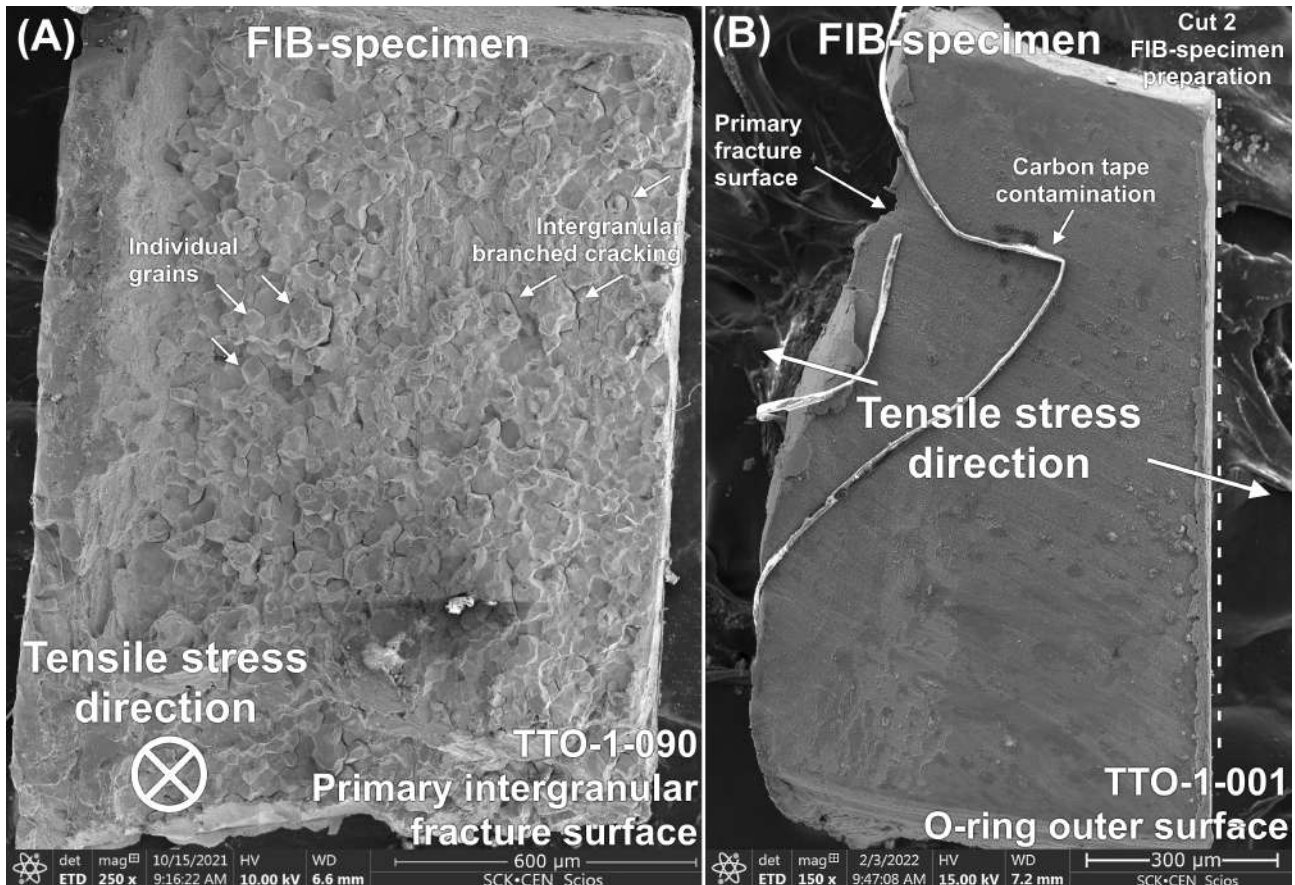


Figure 5.6: SEM images of IASCC crack initiation at the (A) primary fracture surface of TTO-1-090 and (B) at the outer surface of TTO-1-001.

5.3 TEM investigation

The following portion of this chapter present a detailed examination of the IASCC cracks listed in Tab. 5.1 from a top-down approach. Firstly, within section 5.3.1, the global structures of the IASCC cracks as a whole are investigated. The aspects of crack branching, which was most commonly observed in the lower stressed specimens like TTO-1-053 (390 MPa), is discussed in detail. The oxides that form along the inner structures of the IASCC cracks are characterized for both native and non-native oxide specimens. Subsequently, in section 5.3.2, the investigation moves on to discuss the deformation fields that are induced due to the crack propagation. A distinction is made between specimens that are stressed to low and high stress conditions. Also, the remarkable deformation field associated with cyclic loading is presented. Section 5.3.3 then goes on to discuss the characterization of the IASCC crack tips themselves. This section provides arguments for a stress-driven internal oxidation mechanism that describes oxide embrittlement of the leading grain boundary of an advancing crack. Investigations of the crack tip structure show how the crack continuously propagates within a brittle oxide intrusion in front of its tip. In section 5.3.4, the chemical composition of these crack tips and their leading grain boundary structures are studied in more detail. STEM-HAADF EDS spectral maps are obtained of both the crack tip and of some close by grain boundary interfaces. For their assistance in acquiring these maps in joint STEM sessions, a special appreciation is extended to T. Yang as an associate Ph.D. student at the University of Antwerp, and to Dr. W. Van Renterghem as a scientific collaborator at SCKCEN. Within section 5.3.5, some interesting cases of crack arrest are discussed. Amongst other examples, this discussion includes the intriguing case of intergranular cracking along

Table 5.1: Overview of all TEM-lamellae which contain active IASCC crack tips extracted from the primary fracture surface (PFS) or outer surface (OS) of failed O-rings tested under varying conditions. Partially extracted cracks without crack tips are not listed. (θ i.e. angle between crack propagation direction and tensile stress direction).

Specimen ID	Lamella ID	Surface	θ	Remarks
TTO-1-053 (390 MPa - Native oxide - Constant load)	L01	PFS	14°	Shear crack extracted close to an intergranular MnS inclusion particle.
	L03	PFS	1°	Completely branched and oxidized grain boundaries, of which one branch features a shear crack tip from an oxidized triple junction.
	L05	PFS	39°	Narrow shear crack propagating straight down oxidized grain boundary, tapering towards extended oxidized crack tip.
	L06	PFS	10°	Shear crack tip extracted from a heavily corroded grain boundary close to the fracture surface.
	L08	PFS	88° & 2°	Separate extracted cracks: (i) one featuring a non-branched shearing crack tip, while (ii) the other displays a fully branched cleavage crack, featuring multiple oxidized branch points.
TTO-1-071 (500 MPa - Native oxide - Constant load)	L03	PFS	74°	Fractured grain boundary tapering down towards shear crack tip. Branching observed at oxidized triple junction.
	L07	PFS	47°	Similar as L03.
	L11	PFS	2°	Similar as L03.
TTO-1-001 (690 MPa - Native oxide - Constant load)	L05	OS	107°	Shallow cleavage crack extending from oxidized OS. No branching.
	L07	OS	95°	Cleavage crack tapering straight down towards oxidized cleavage crack tip. No branching.
	L16	OS	4° & 131°	Wide cleavage crack arrested at oxidized triple junction, two crack tips extracted: (i) one in cleavage-, and (ii) the other in shear-mode orientation.
	L23	OS	1° & 101°	Similar as L16.
TTO-1-090 (700 MPa - Non-native oxide Constant load)	L01	PFS	1°	Wide shear crack tapering down to oxidized shear crack tip. No branching.
	L06	PFS	2°	Similar as L01.
	L07	PFS	0°	Shear crack partially impeded by oxidized MnS particle, but ultimately arrested at a grain boundary triple junction. No branching.
	L08	PFS	16°	Similar as L01.
TTO-1-066 (280 ± 120 MPa - Native oxide - Cyclic load)	L02	OS	100°	Narrow cleavage crack tapering down to oxidized triple junction. No branching.
	L07	PFS	16°	Narrow shear crack following curvature of grain boundary. Branching at triple junctions resulting in one extracted crack tip.
	L08	PFS	4°	Similar as L07.
	L09	PFS	20°	Similar as L07.

a grain boundary whereat a MnS inclusion particle has segregated.

5.3.1 Intergranular oxidation

5.3.1.1 Overview of grain boundary cracking

The extent of intergranular oxidation throughout a typical IASCC crack branch leading up to a grain boundary triple junction is shown for the low-stress tested sample TTO-1-053 (390 MPa) in Fig. 5.7A. The crack path is characterized by extensive branching and initiation points within the internal oxide structure. Straight sections of the crack branch are often followed by abrupt changes in the crack propagation direction. These jagged features in the cracking nature are interpreted as forms of brittle crack propagation within the intergranular oxide. The crack mainly follows the metal-oxide interface,

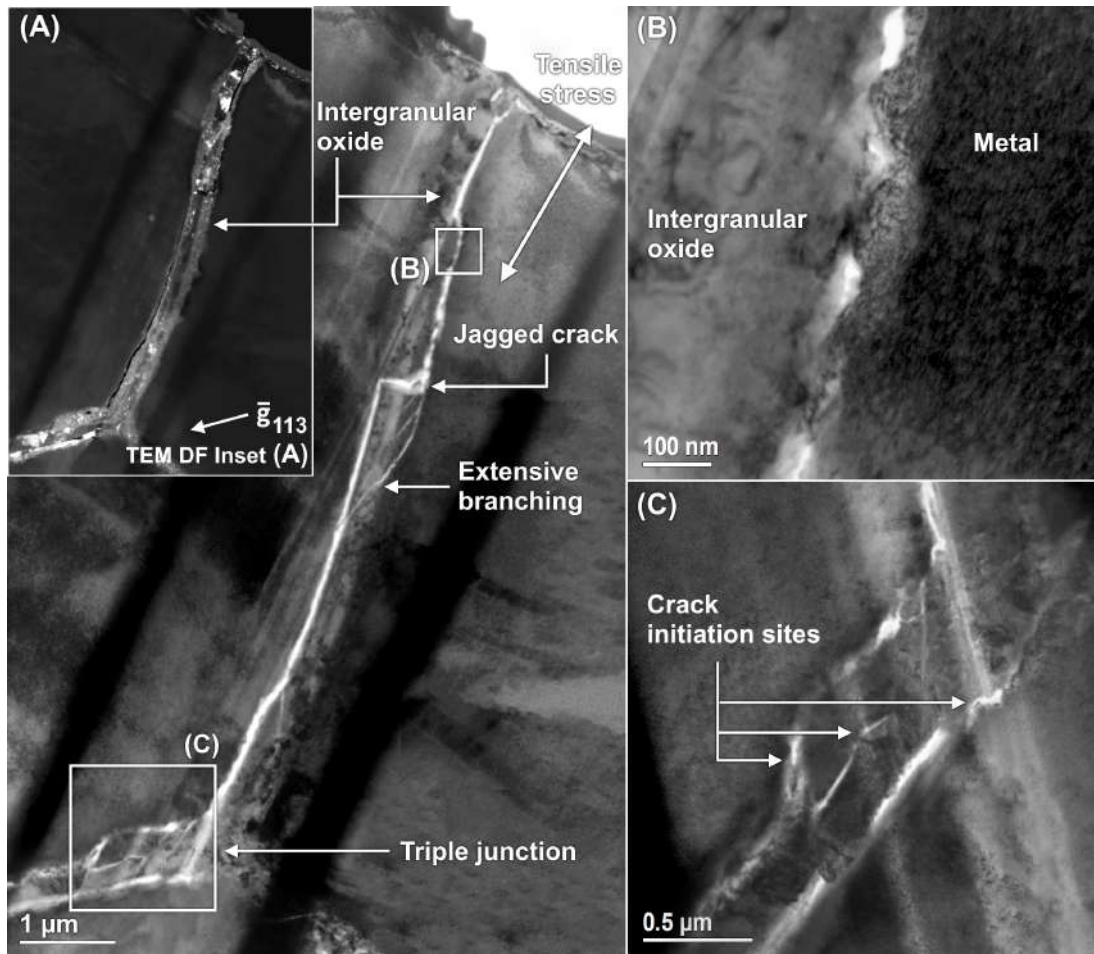


Figure 5.7: TTO-1-053 (390 MPa) L03 (A) BF-TEM overview of a main IASCC branch leading up to a completely oxidized grain boundary triple junction. Inset image depicts the corresponding low-magnification CDF-TEM view of the oxidized grain boundary. (B) Magnified view of the metal-oxide interface cracking. (C) Representation of the strong crack branching nature within the intergranular oxide. Darker contrast bands represent intentionally thicker strokes of material that are left behind during the process of FIB-milling in order to mitigate the strong curtaining effect underneath the oxidized triple junction.

as demonstrated in more detail in Fig. 5.7B. Presumably, the applied external stress caused the crack to propagate alongside its weakest interface i.e. strained metal-oxygen bonds, which are inherently more chemically active and thus more prone to cracking than non-strained bonds. Additionally, it is important to express the significance of the three-dimensional aspect of the crack morphology. Certain sections of the crack may subside and/or re-emerge within perspective of the lamella. Fig. 5.7C emphasizes on the formation of multiple crack initiation sites within the dense oxidized triple junction. Under closer inspection, these initiation sites may nucleate into numerous brittle microcracks which are formed mostly parallel to the main intergranular crack propagation direction. While under the influence of the external load, these microcracks coalesce into the formation of a fully developed crack front.

Alternatively, crack branches in high-stress tested specimens such as TTO-1-001 (690 MPa) show a much broader crack morphology filled with far less intergranular oxides, see Fig. 5.8. From the associate BF-TEM view, it is apparent that the opening of the crack is assisted by the acting cleavage orientation of the tensile stress at the initiation point. Comparatively less crack branching within the intergranular oxide is observed, as were still the case for lower stressed specimens, simply because the

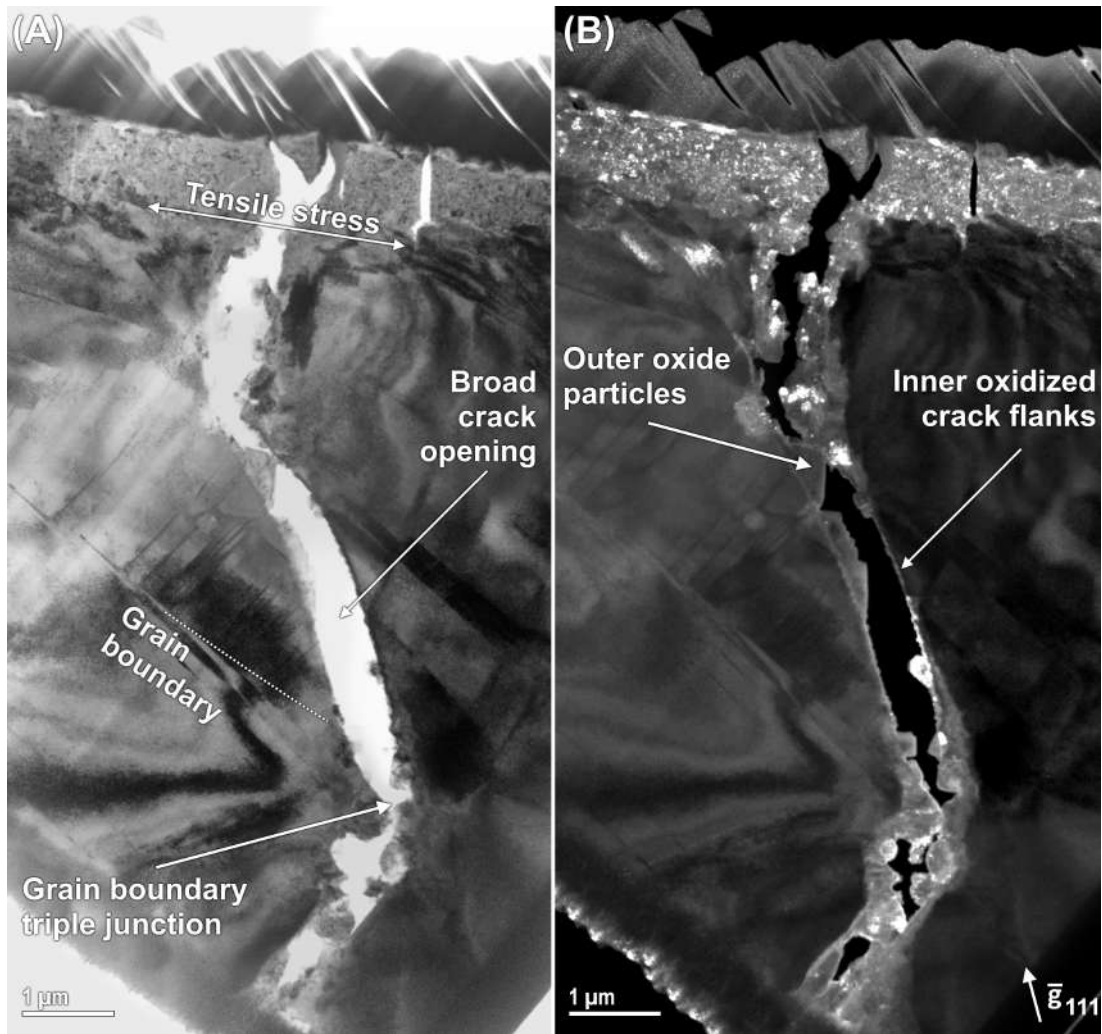


Figure 5.8: TTO-1-001 (690 MPa) L06 (A) BF-TEM and (B) corresponding CDF-TEM overview of a main completely oxidized IASCC branch.

crack flanks are less oxidized at high stresses. Arguably, the higher stresses have not only affected the crack opening, but also deteriorated the inner oxide filled within the crack branch. The corresponding CDF-TEM view reveals to some extent the difference between continuously oxidized crack flanks with some other round oxide precipitates. The oxide composition thus consists of an inner oxide along the external crack surfaces and inner crack flanks, along with a different, sparsely precipitated outer oxide with a more granular structure at wide open regions within the crack.

5.3.1.2 Native oxide characterization

Additional demonstration of an IASCC crack propagating along the metal-oxide interface is presented in the BF-TEM and CDF-TEM overview images presented in Figs. 5.9A-B. From the CDF-TEM view of the intergranular oxide, it is apparent that the crack favorably propagates alongside the metal-oxide interface, leaving one particular side of the crack flank progressively more oxidized than the other. Its intergranular oxide structure has been examined through diffraction- and EDS-analyses, see Figs. 5.9C-E. From these results, it can be concluded that there is a separation between two different oxides. The entire oxide assembly is constituted of a primary nanograined crystallite Cr-oxide enriched with a strong Fe-rich signal, and a coarse-grained secondary oxide revealing mainly signals of Fe and Ni.

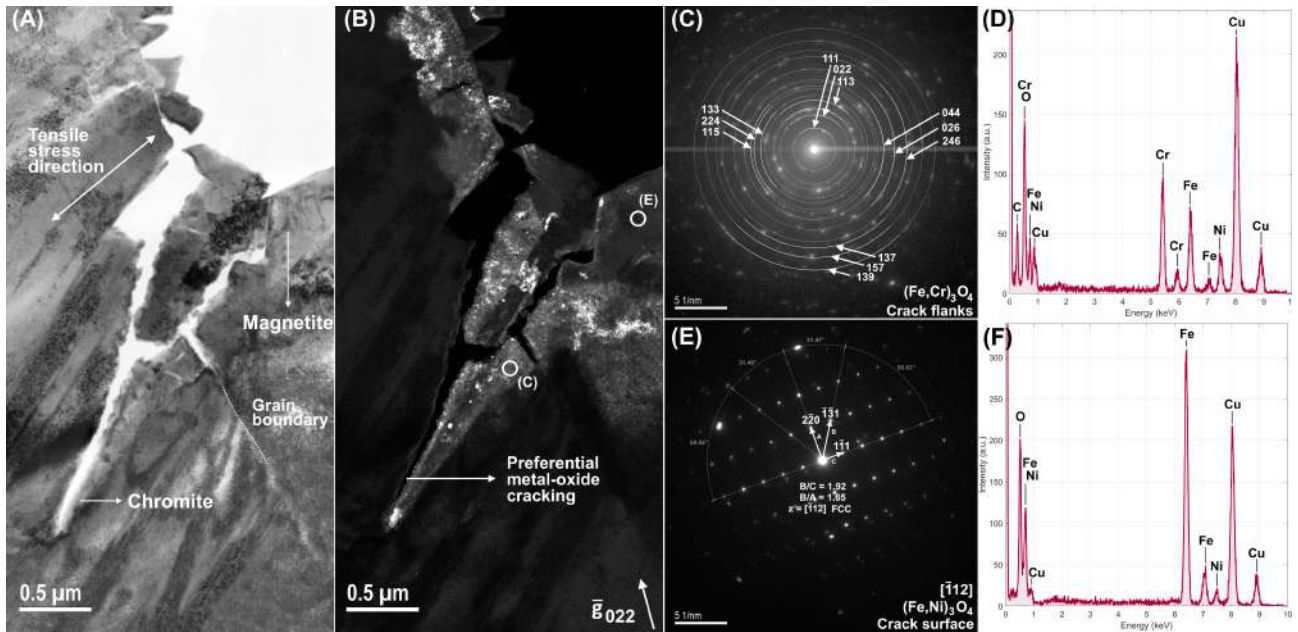


Figure 5.9: TTO-1-053 (390 MPa) L06 (A) BF-TEM and (B) CDF-TEM of an IASCC crack imaged from an intergranular oxide reflection. Respectively, the (C,E) DPs and (D,F) EDS spectra of the corresponding chromite spinel $(\text{Fe,Cr})_3\text{O}_4$ and the magnetite deposit $(\text{Fe,Ni})_3\text{O}_4$ oxides are depicted. The strong Cu-signal originates from the TEM grid holder.

Whereas the Cr-rich oxide is homogeneously found around the crack flanks and crack tip, as concluded from the distribution of diffracting nanograins in the TEM-DF image of Fig. 5.9B, the secondary Fe-rich oxide remains sparsely precipitated along the crack flank merely within wide open crack regions. Considering the sole observations of the Fe-rich oxide deposits, it is reasoned that this oxide is the resultant of bulk dissolution processes and is consequently precipitated at accessible crack regions exposed to the environment [92].

The most plausible structure corresponding to the main oxide component along the crack flanks is found to be chromite spinel $(\text{Fe,Cr})_3\text{O}_4$ with a known lattice parameter of 0.8378 nm [296]. This result is supported by the observed ring-like DP originating from the nano-grained structure, featuring a spinel FCC centering with an experimentally obtained lattice constant of 0.8339 nm, see Fig. 5.9C. Furthermore, given the strong Cr- and Fe-signals in the corresponding EDS spectrum of Fig. 5.9D, other candidate oxide structures such as Cr_2O_3 which has been experimentally observed in stainless steels under BWR environments [220], may be disregarded. Regarding the secondary oxide, the EDS signal demonstrates a sole Fe-rich oxide with slight traces of Ni. Therefore, the single reasonable candidate structure is the Ni-bearing magnetite spinel oxide $(\text{Fe}_{1-x}\text{Ni}_x)_3\text{O}_4$, likewise featuring an FCC lattice with a lattice constant of 0.8338 nm [281], see Figs. 5.9E-F. The iron-nickel ratio may vary between 2Fe - Ni ($x \approx 0.33$) to 2.6Fe - 0.4Ni ($x \approx 0.13$) without reasonable change in the lattice structure. This change may be related to the local alloy composition, the oxygen diffusion and metal dissolution rates. The oxide compositions are in complete agreement with previous observations regarding SCC cracking in stainless steels [92,99].

5.3.1.3 Non-native oxide characterization

BF-TEM investigation of IASCC cracks belonging to the non-native oxide specimen generally displayed a crack morphology that gradually tapers down from a uniformly oxidized triple junction or fracture surface. Crack flanks at the metal interface are consistently oxidized by a thin primary nanocrystallite

oxide film, while a coarse-grained secondary oxide is typically observed in more wide open crack regions. Void spaces may be observed in between the duplex oxide assembly near the fracture surface where crack opening is consistently wider. The tapering of the crack may continue for several tens of μm , leading to a fully developed intergranularly oxidized crack tip. Cracks may establish branch points at microstructural grain boundaries along the way, typically in a cleavage relation to the applied tensile stress direction. Intergranular oxidation at these branch points recurs at every interaction. As the crack narrows, less of the corrosion product and more of the nanograined oxide is observed until only a uniformly oxidized crack tip remains.

Figs. 5.10A,B display an overview of a typical IASCC shear crack propagating from a uniformly oxidized fracture surface, extending up to a bulk grain boundary triple junction. The crack propagates alongside a completely oxidized MnS particle segregating close to the grain boundary, ultimately arresting at a grain boundary triple junction orientated near perpendicularly upon the crack propagation direction. Major characteristics are the long and tapered crack appearance and its duplex oxide formation within the crack opening. Regarding the oxides found within non-native oxidized cracks, it is evident how the crack is comprised of a nanograined oxide with a thickness close to 100 nm on both opposing sides filled by a coarse-grained oxide deposit, see Fig. 5.10C. EDS spot- and SAED diffraction analyses respectively shown in Figs. 5.10D and 5.10E-F demonstrate that the crack flank oxide corresponds to a Fe- and Cr-rich spinel with a ring-like DP signifying its nanograined crystallite structure, while Figs. 5.10G-H show that the deposited oxide solely exhibits an Fe-rich spinel with a disparate spot-like DP. Both DPs correspond to a FCC crystal structure with similar lattice constants experimentally valued to be 0.8372 nm and 0.8396 nm, respectively. To that end, it may be considered

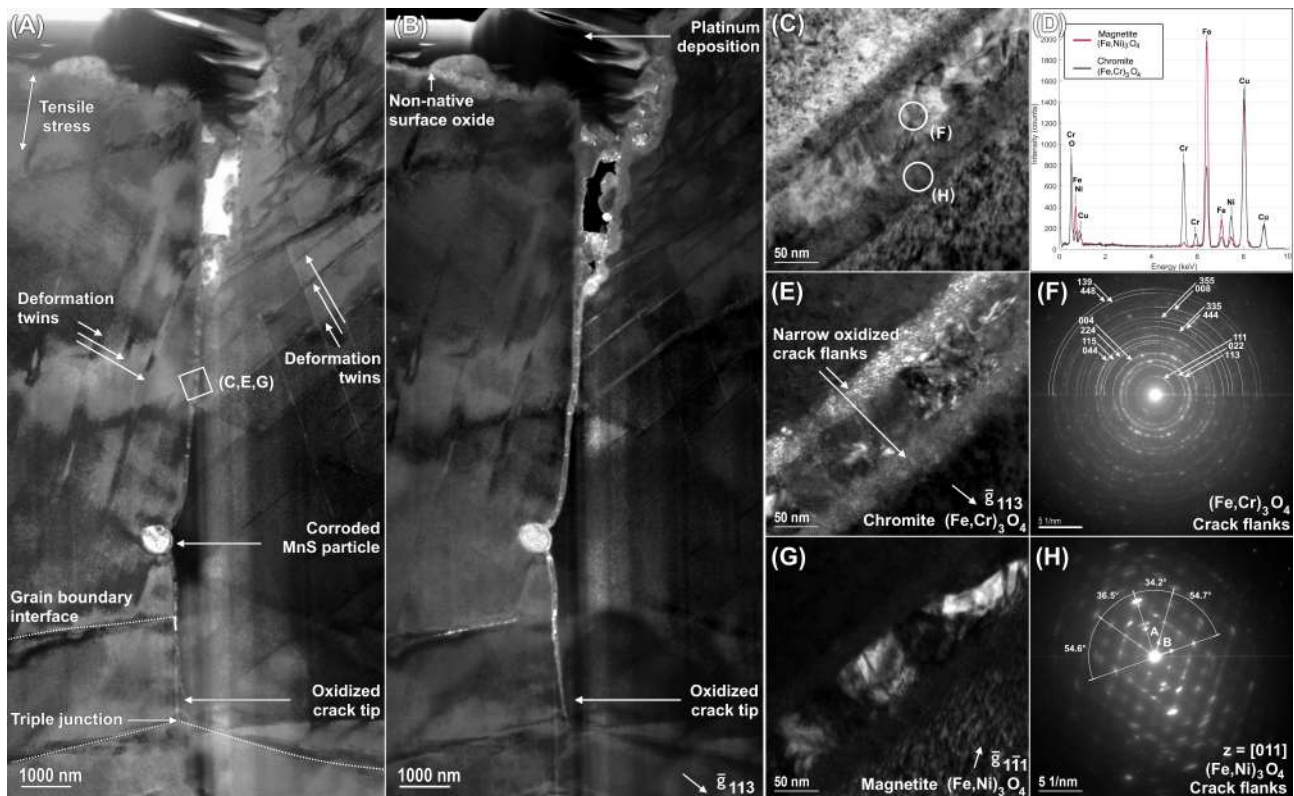


Figure 5.10: TTO-1-090 (700 MPa - non-native oxide) L06 (A) BF-TEM and (B) corresponding CDF-TEM of the general crack morphology imaged from an internal chromite reflection. (C) BF-TEM of narrow oxidized crack flanks. (D) EDS spectra of the duplex oxide formation inside the crack flank of C. (E-F) Chromite $(\text{Fe,Cr})_3\text{O}_4$ and (G-H) Magnetite $(\text{Fe,Ni})_3\text{O}_4$ CDF-TEM and corresponding DPs relating to C.

that the non-native duplex oxide is composed of the $(\text{Fe,Cr})_3\text{O}_4$ chromite [296] and the $(\text{Fe}_{1-x},\text{Ni}_x)_3\text{O}_4$ magnetite ($0.13 < x < 0.33$) [281], and that it is structurally no different from the oxides previously investigated in other O-ring specimens seen in section 5.3.1.2.

5.3.2 Microstructural characterization

5.3.2.1 Crack deformation field

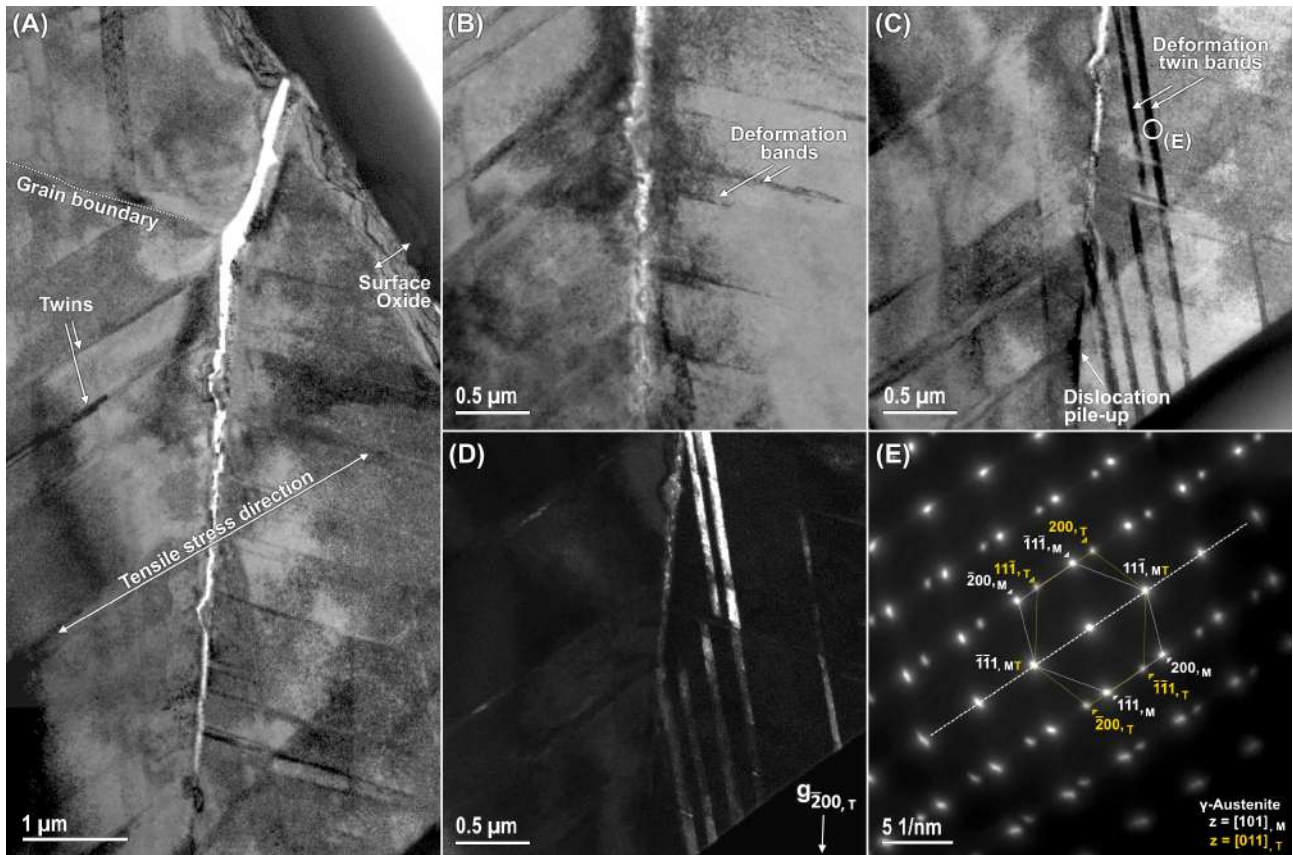


Figure 5.11: TTO-1-053 (390 MPa) L05 (A) BF-TEM overview of a typical intergranular IASCC crack extending into the bulk. (B,C) BF-TEM deformation structures identified as deformation band and twin bands, respectively. (D,E) Corresponding CDF-TEM and DP of the deformation twin bands, respectively.

Propagating cracks produce a deformation field that remains consistent for all cracks appertaining to each specimen tested at separate stress levels. In analyzing the deformed microstructure for low stress levels, long-running parallel deformation bands may be observed extending from the crack flanks and crack tips towards nearing grain boundaries, see Figs. 5.11B and 5.11C appertaining to TTO-1-053 (390 MPa). Analysis of these deformation structures was performed through common SAED imaging. When tilted into a suitable orientation, it was observed that certain bands extending from the crack flanks could not be related to twinning, while others that extended from the crack tip typically showed twin-related streak DPs. Consequently, these deformation structures seen in Figs. 5.11B–E respectively, were identified as general deformation- and deformation twin-bands accordingly. The crack within the intergranular oxide appears jagged along several intersections of the crack path, especially closer towards the crack tip. Dense dislocation contrast that signify strain-localization is evident around these jagged crack paths as seen in Fig. 5.11B. These type of appearances may be interpreted as signs of step-like cracking, prominently featured with the film-dissolution and internal oxidation models.

On the other hand, relating to the microstructure of cracks extracted from specimens tested at high stress levels, similar but increased deformation features were observed within specimens TTO-1-001 (690 MPa) and TTO-1-090 (700 MPa - non-native oxide). In both cases, large sets of deformation twins were found to extend essentially in parallel from crack tip location into the bulk interior. The increased density of twinning at higher stress levels appears consistent with the grain boundary's ability to accommodate stress in the surrounding lattice. Fig. 5.12A shows an exemplary case for TTO-1-001 (690 MPa) of a high-stressed IASCC crack arrested at a grain boundary triple junction that displays a broad open crack morphology filled with intergranular oxides. Extensive deformation twins with a twin face parallel to the (111) crystallographic planes can be observed adjacent to the crack. Under the influence of the stress exerted by the crack, the twin plane exemplifies a mirror section of the parent lattice; the crystallographic indices of which can be calculated from Hirsch's textbook formulae [297]. The twin-indexing is in agreement with the inset DPs displayed in Figs. 5.12C,D. Equivalently for TTO-1-090 (700 MPa - non-native oxide), another illustrative example for high stressed specimens is shown in Fig. 5.13A. Broad twin bands nucleate at the end of a tapered intergranular IASCC crack and extend for long distances across the grain. Interaction of the expanding deformation twin with the crack may even kink the crack tip as observed in Fig. 5.13B. The twin plane occurs along a similar (111) crystallographic plane, in agreement with the previous figure, calculated by equations 5.1-5.3.

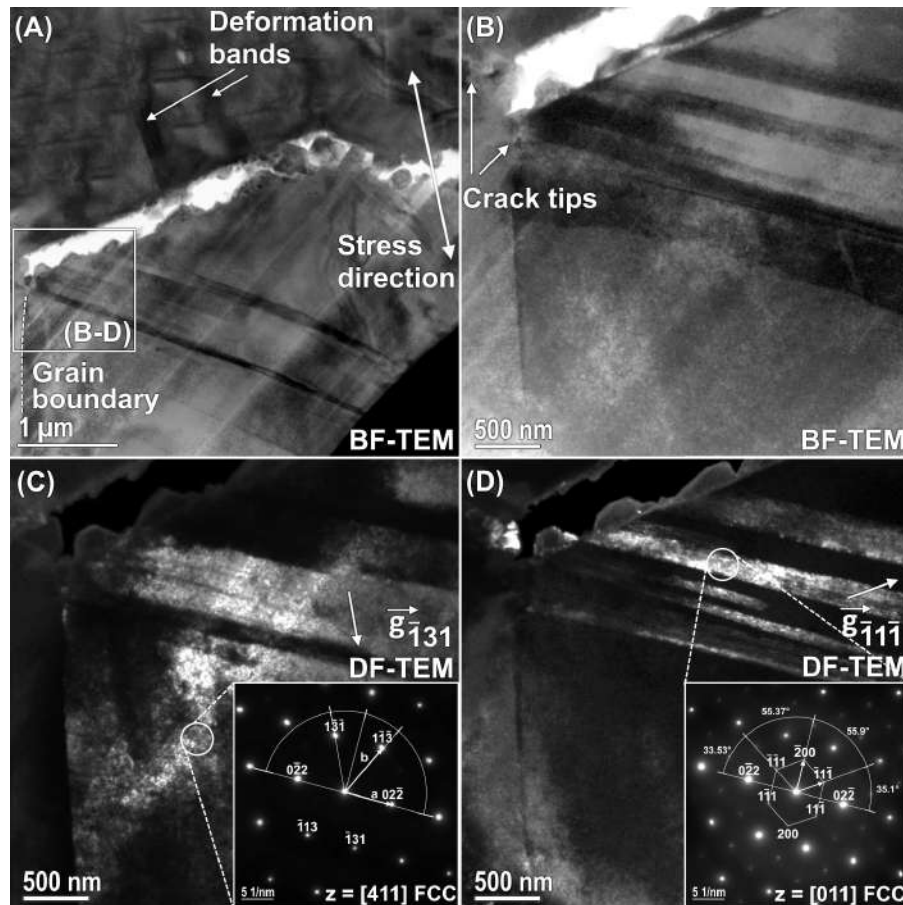


Figure 5.12: TTO-1-001 (690 MPa) L16 (A) Magnified BF-TEM overview of a broad IASCC crack. (B) BF-TEM of (111) orientated deformation twins extending from the crack tip. Corresponding CDF-TEM of (C) parent austenite and (D) deformation twin.

Application of these equations to the DPs of Figs. 5.12C-D and 5.13C-D indicates that, between the parent matrix and twinned crystallographic phase, at least one (111) orientated twin plane is

present. Indeed, indexing the DP of the parent austenite matrix shows that it is orientated along a typical $\langle 411 \rangle$ zone-axis. The twinned crystal which shows a $\langle 011 \rangle$ zone-axis is only attainable through mirroring the parent austenite over a $\{111\}$ orientated twinning plane.

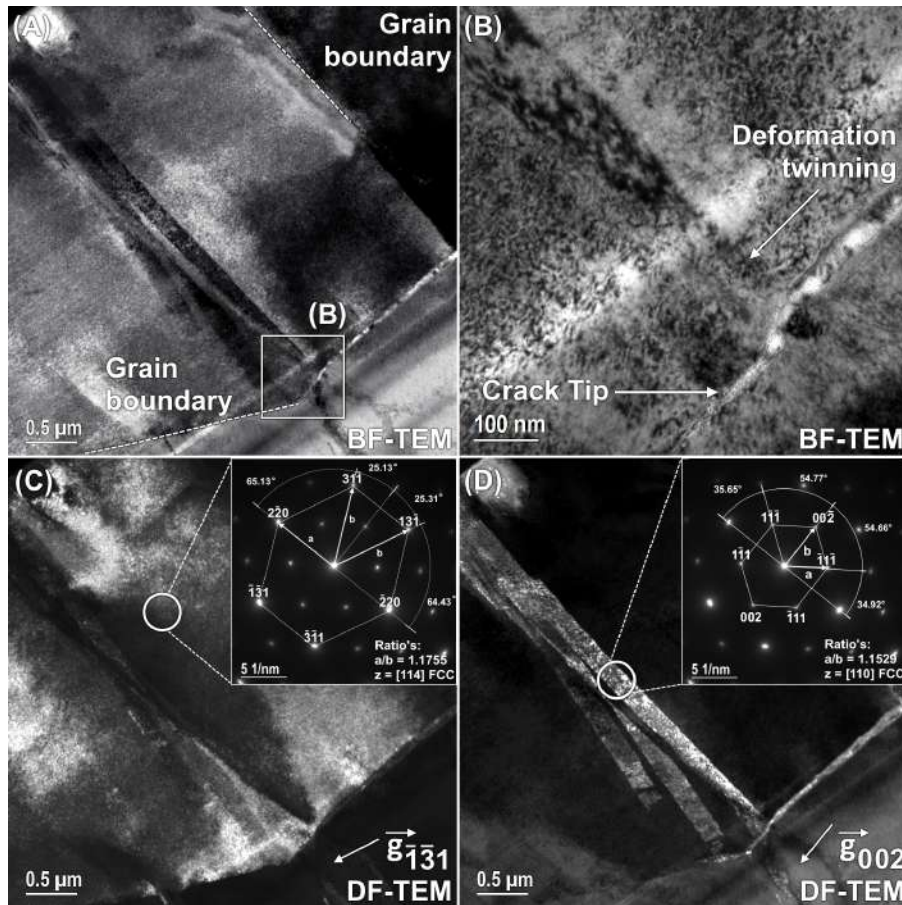


Figure 5.13: TTO-1-090 (700 MPa - Non-native oxide) L06 (A) BF-TEM overview of tapered IASCC crack. (B) Magnified BF-TEM of $\{111\}$ orientated deformation twins extending from the crack tip. Corresponding CDF-TEM with inset DPs shown for (C) the parent austenite and (D) the deformation twin structures.

For TTO-1-090 (700 MPa - non-native oxide) displayed in Fig. 5.14A-B, another set of parallel twins propagating across the grain are shown, this time intersecting solely with the leading grain boundary. Adjacent to the grain boundary interface, a secondary twin system is also seen to nucleate, see Fig. 5.14C. Stress build-up at the grain interface may even cause a limited migration of the grain boundary itself, a phenomenon that seems consistent with diffusion-induced grain boundary migration (DIGM). The evolution of a grain boundary under the influence of stress, corrosion-enhanced diffusion or finite-volume displacive transformations, can cause it to locally propagate through one particular grain causing the simultaneous growth of the other adjacent grain [24,298]. Effectively, this migration seems to be occurring only when two twin systems intersect simultaneously on either side of the interface with the grain boundary. Analysis of the set of twins customarily results in the typical twin-related DP, see Fig. 5.14D. Both twin systems consist of a $\langle 111 \rangle$ orientated twin plane as indicated by the demonstrated pattern indexation.

From Hirsch: When a twinning plane lies parallel to the electron beam, the corresponding twinning axis is then also parallel to the reciprocal lattice plane. Diffraction from a twin structure is then easily recognizable since the twinned reflections form mirror image of the matrix reflections, similar as in Fig. 5.11E. However, in dealing with cases where the twinning axis is perpendicular to the reciprocal lattice plane such as in Figs. 5.12 and 5.13, twinning may not be so evident if not for some crystallographic formulae defined in reference [297]. Indeed, considering a twinning plane with indices (hkl) that separates two crystallographic phases on either side of the twin orientated to $[uvw]$ - and $[u'v'w']$ zone-axes, the indices of the latter phase can be expressed in the basis of the former using the indices of the mirroring twin:

$$u' = \frac{(h^2 - k^2 - l^2)u + 2hkv + 2hlw}{(h^2 + k^2 + l^2)} \quad (5.1)$$

$$v' = \frac{(k^2 - h^2 - l^2)v + 2hku + 2klw}{(h^2 + k^2 + l^2)} \quad (5.2)$$

$$w' = \frac{(l^2 - h^2 - k^2)w + 2hlu + 2klv}{(h^2 + k^2 + l^2)} \quad (5.3)$$

Equations 5.1-5.3 are only valid for cubic crystals.

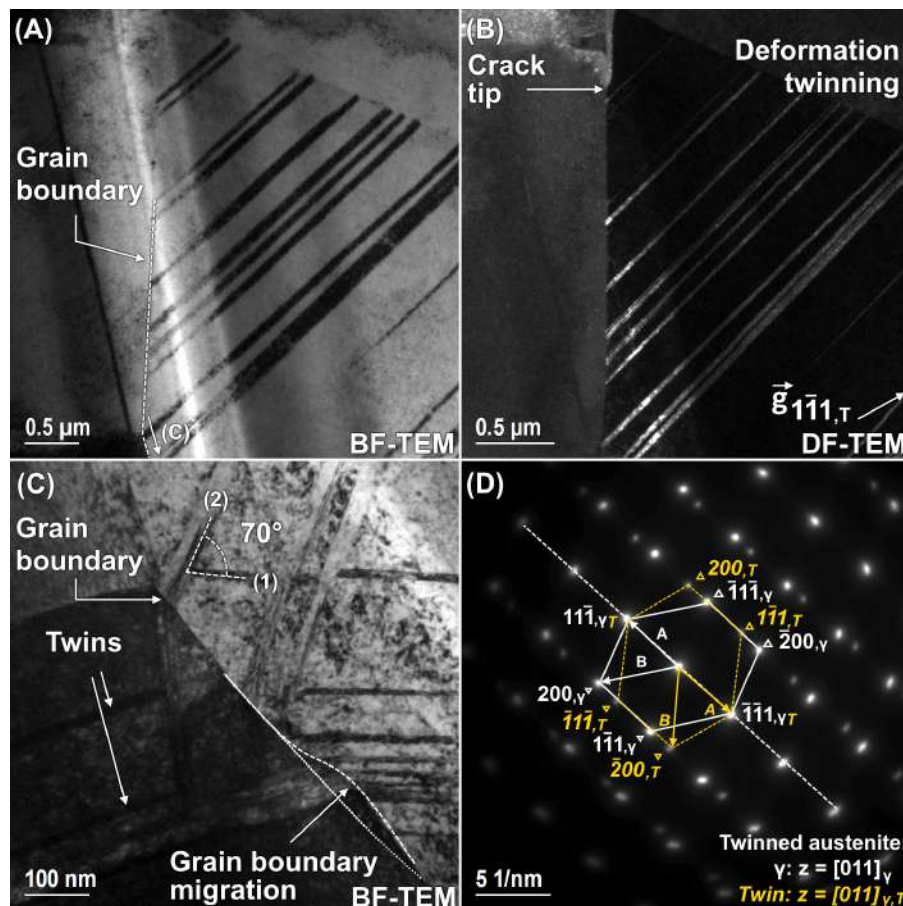


Figure 5.14: TTO-1-090 (700 MPa - non-native oxide) L01 (A) BF-TEM, and (B) CDF-TEM of twinned microstructure ahead of an IASCC crack tip. (C) BF-TEM of double twin-systems leading to grain boundary migration. (D) Corresponding twin-related DP.

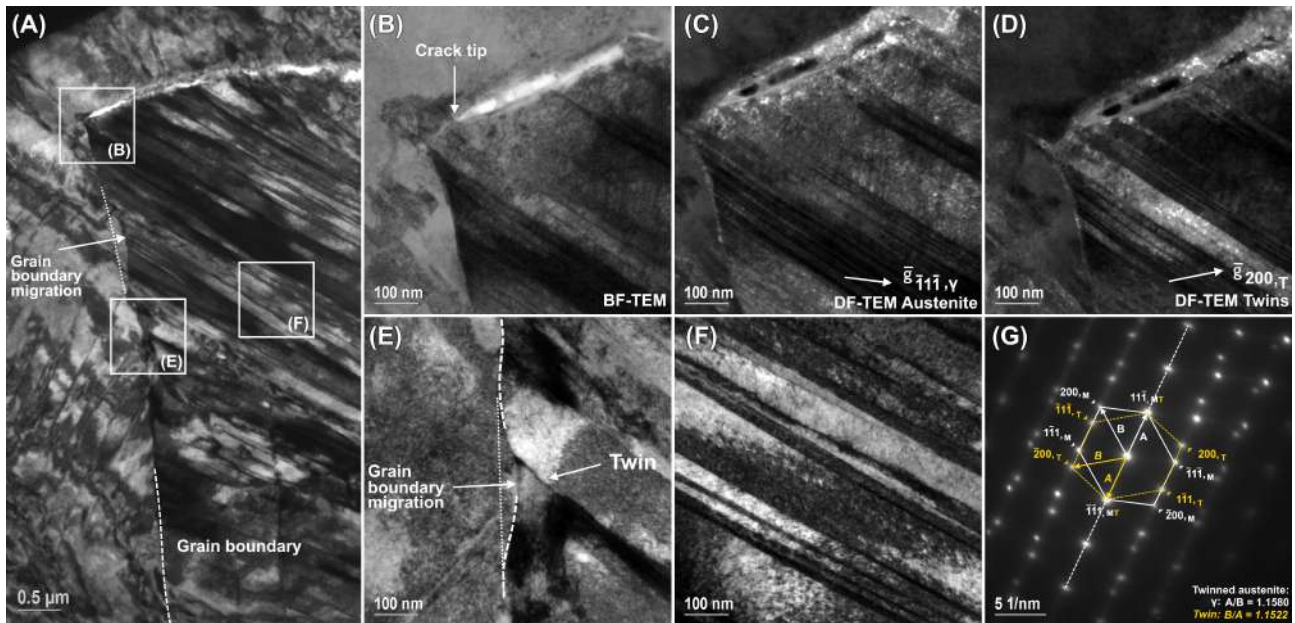


Figure 5.15: TTO-1-066 (280 MPa - cyclic loading) L09 (A) BF-TEM overview of twinned microstructure in the crack's vicinity. (B) BF-TEM and (C,D) CDF-TEM of the austenitic and twinned microstructure, respectively. (E) Grain boundary migration. (F) BF-TEM of twins and (G) its corresponding DP.

5.3.2.2 LCF-induced deformation field

Examination of the microstructure in close vicinity of fatigue cracks appertaining to the cyclic loaded sample indicated a severely twinned deformation field with evidence of shear and stress-induced martensite bands. Fig. 5.15A illustrates a global overview of the impact of twinning on the crack and its leading grain boundary interface. Regions of strain contrast indicating stacked dislocation pile-up at sheared regions in between deformation twins are evident adjacent to the crack. Figs. 5.15B-D illustrate the extent of the twinning on the cracked grain boundary interface. Deformation twins may also have a displacive impact on the austenitic microstructure which can result in the curvature of a propagating crack, or the effective migration of its leading grain boundary, as observed in Fig. 5.15E. Grain boundary migration is again observed in association with a secondary twin system nucleated in the opposing grain. To that end, the microstructural evolution surrounding fatigue cracks is similar, although substantially more intensified, as observed in highly stressed specimens. SAED imaging of the microstructure revealed the typical twin-related DP, see Fig. 5.15G.

5.3.2.3 Martensite transformation

Interestingly, aside a typical intergranular crack belonging to specimen TTO-1-053 (390 MPa), notable microstructural defect structures can be observed. On the one hand, Figs. 5.16A-C depicts the formation of a microstructural twin system and its corresponding DP. On the other hand, thick deformation laths are occasionally present both within the bulk matrix and extending from the crack tip into the grain interior, see Figs. 5.16D and 5.16E-F respectively. Closer inspection of these laths was performed through SAED imaging. Fig. 5.16F indicates that the thick laths do not resemble any DP that can be related to deformation twinning. Rather, it is perceived that the lattice locally transformed from the parent austenitic FCC structure towards a BCC centering, which is suggested by the altered interplanar ratios indicated within the DP. In that sense, the microstructure sustained a structural transformation to a lattice that correlates well with deformation-induced martensite. Such martensitic laths were commonly observed to extend from the crack flanks or tips to any of the adjacent

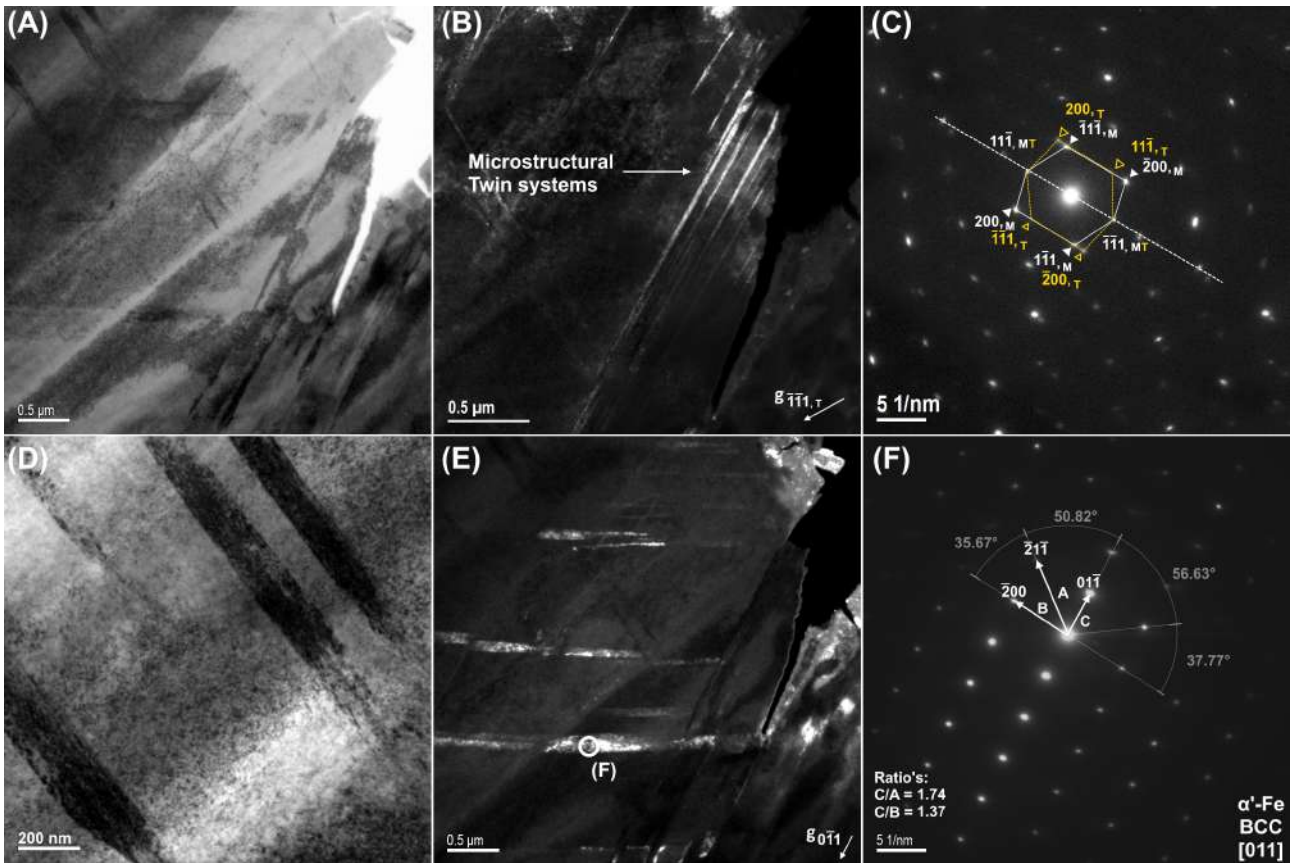


Figure 5.16: TTO-1-053 (390 MPa) L06 (A) BF-TEM overview of the microstructure alongside a crack. (B) CDF-TEM of microstructural twins extending from the crack flanks. (C) Corresponding DP of twinned structure. (D) Magnified BF-TEM of stress-induced martensitic laths. (E) CDF-TEM of laths extending from the crack tip. (F) Corresponding martensitic DP illustrating the BCC nature of the stress-induced α' -martensite from a [011] zone-axis.

grain boundaries; hence, propagating across the grain away from the crack. This way of nucleation gives the impression that the martensitic laths can be related to the crack propagation, as they were exclusively observed close to IASCC cracks.

Other instances of these martensitic phases are displayed in Figs. 5.17 and 5.18. Thick laths are formed across the grain which intersect on either side of the grain boundary, see Fig. 5.17A. The following martensitic transformation occurs in close vicinity of the crack initiation point at the specimen surface. Suggested by the darker contrast regions at the grain boundary, dislocation pile-up in-between the intersections of the martensite with the grain boundary is present. The latter may suggest an impeding dislocation motion which may well induce local stress at the grain boundary. The additional reflections that appear in the DP illustrated in Fig. 5.17C closely match the well-known Nishiyama-Wasserman (N-W) orientation relationship [76, 78] between FCC γ -austenite and BCC α' -martensite. Correspondingly, this shows that deformation-induced martensite nucleates along the close-packed crystallographic planes of austenite since both phases appear parallel in the zone-axis DP:

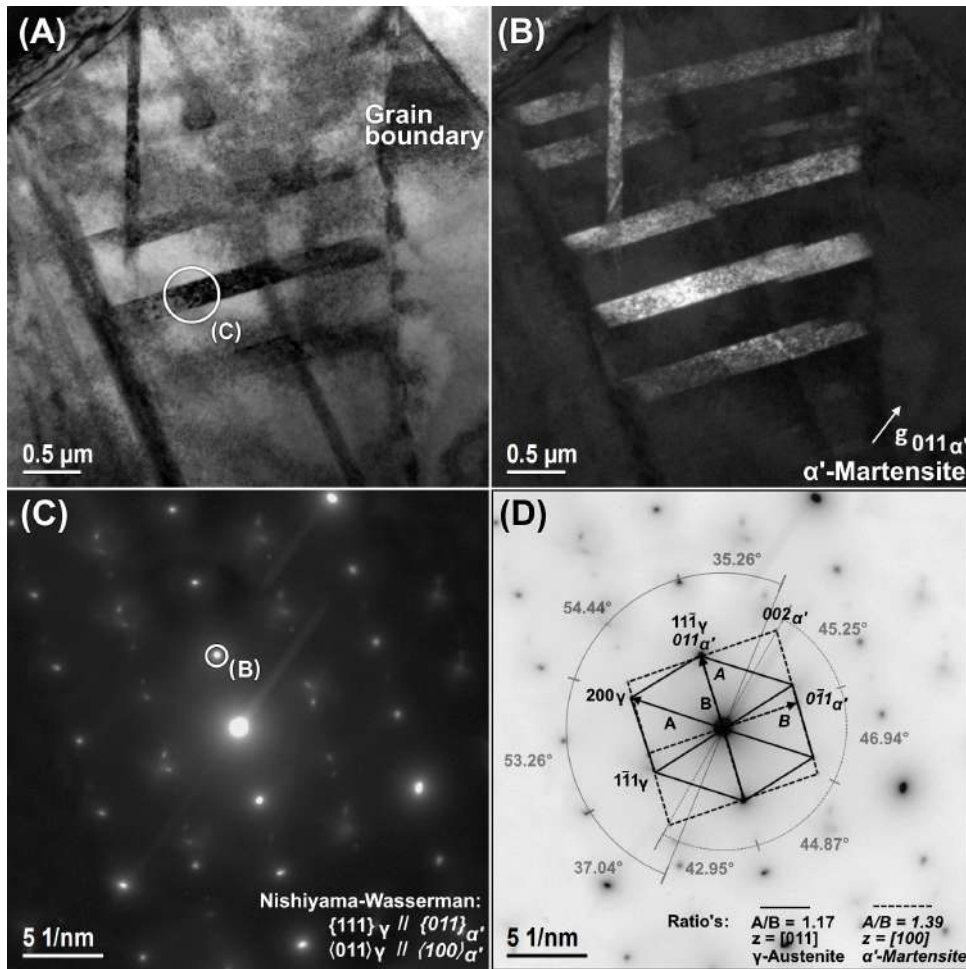


Figure 5.17: TTO-1-053 (390 MPa) L05 (A) BF-TEM and (B) corresponding CDF-TEM of martensitic laths extending across the grain close to the crack initiation. (C) Corresponding DP of the martensitic laths. (D) Analyzed DP matching the Nishiyama-Wasserman orientation relationship between FCC γ - austenite and BCC α' -martensite. This figure corresponds to the top-left grain beside the crack displayed in Fig. 5.11.

Phase transformed austenite to martensite orientation relationships, appertaining to Fig. 5.17D:

$$\begin{aligned} \{111\}_{\gamma} // \{011\}_{\alpha'}, & \quad (\text{N-W}) \\ \langle 011 \rangle_{\gamma} // \langle 100 \rangle_{\alpha'} \end{aligned}$$

Displayed in Fig. 5.18A-B, similar martensitic lath structures are unmistakably observed extending from the propagating crack tip and leading grain boundary. Once again, the high density of dislocation regions in-between the parent austenite phase at the grain boundary seem to be a reoccurring characteristic. SAED imaging confirms the $[\bar{1}11]$ BCC nature of the martensite in Fig. 5.18C. However, in this instance, it is apparent from the corresponding CDF-TEM view that an additional phase structure is present. As shown in Figs. 5.18F, analysis of the complementary DP reveals the presence of an additional $[100]$ α' -martensitic lath accompanied by reflections corresponding to thin retained austenite. As depicted in Fig. 5.18D using the $(\bar{1}1\bar{1})_{\gamma}$ reflection, the FCC austenite phase is located at the interfaces of the martensitic transformation. Considering one martensitic crystal at a time, Fig. 5.18F demonstrates the previously observed N-W orientation relationship between $[011]_{\gamma} // [100]_{\alpha'}$

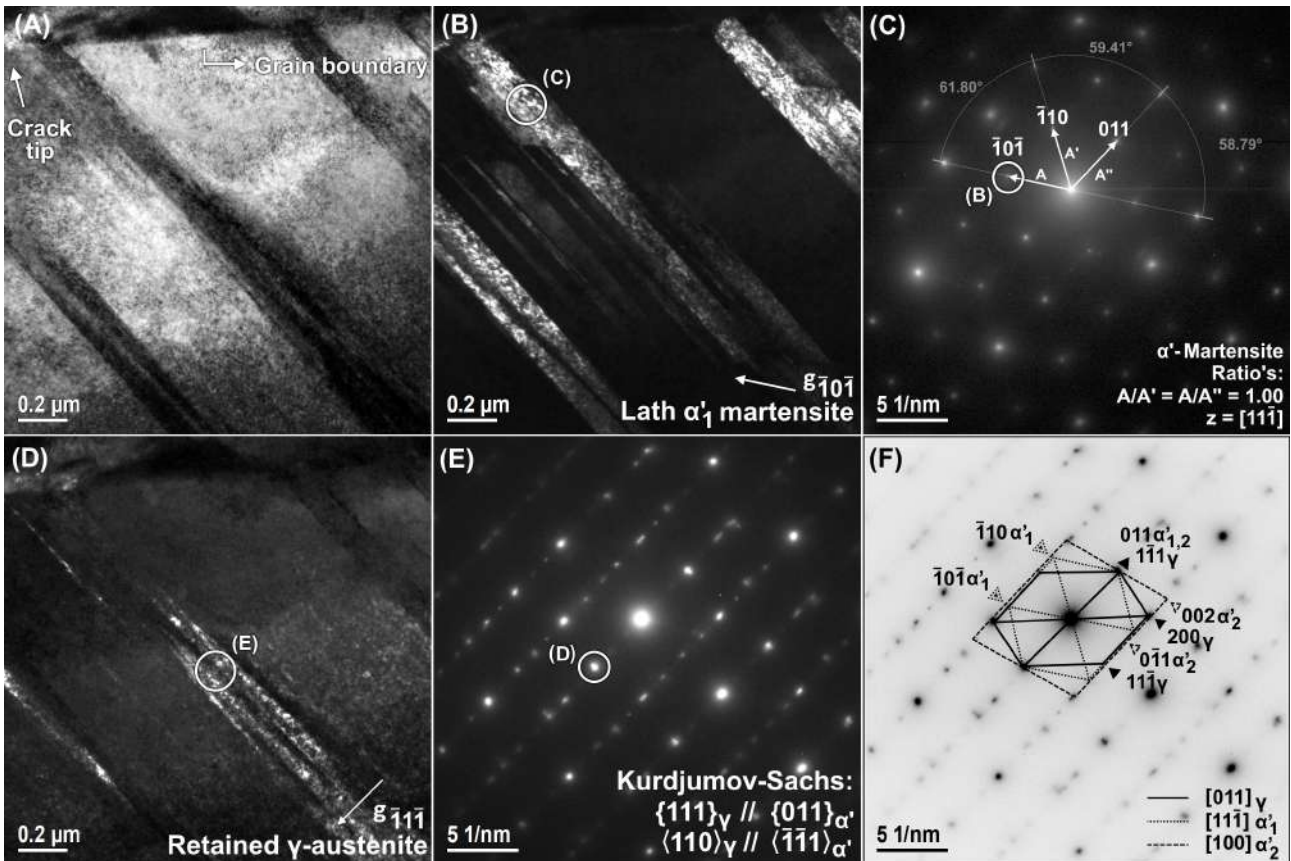


Figure 5.18: TTO-1-053 (390 MPa) L05 (A) BF-TEM and (B,C) corresponding CDF-TEM with associated DP of α' -martensite extending from the leading grain boundary in $[\bar{1}11]\alpha'$ zone-axis orientation. (D,E) Retained γ -austenite located at martensite interfaces with associated DP. (F) Analyzed DP matching the Kurdjumov-Sachs orientation relationship between FCC γ -austenite and BCC α' -martensite. This figure depicts the leading grain boundary imaged in Fig. 5.11.

and the Kurdjumov-Sachs (K-S) orientation relationship between $[011]_{\gamma} // [11\bar{1}]_{\alpha'}$. Since the N-W and K-S orientation relationships are related by only a 5.26° rotation, it is not surprising to observe both orientation relationships together in one DP [83].

Phase transformed austenite to martensite orientation relationships, appertaining to Fig. 5.18F:

$$\begin{aligned} \{111\}_{\gamma} // \{011\}_{\alpha'}, & \quad (\text{K-S}) \\ \langle 110 \rangle_{\gamma} // \langle \bar{1}\bar{1}1 \rangle_{\alpha'} \end{aligned}$$

Regarding specimen TTO-1-066 (280 MPa - cyclic loading), other notable deformation structures that too resemble phase-transformed austenite to martensite are observed within the microstructure close to propagating cracks. Fig. 5.19A shows two characteristic HCP ϵ -martensite deformation laths extending from a fatigue crack flank, for which one forms adjacent to a deformation slip band extending into the bulk. The angle between both ϵ -laths is equivalent to the angle of the close-packed high-symmetry crystallographic 111-planes of the parent austenite (i.e. around 70°) on which ϵ -martensite laths are known to preferentially nucleate [48]. Interestingly, attributed to the high dislocation density within the adjacent deformation slip band, a preferential intrusion of intergranular oxides can be observed into the bulk matrix. Further into the bulk, other instances of austenite to

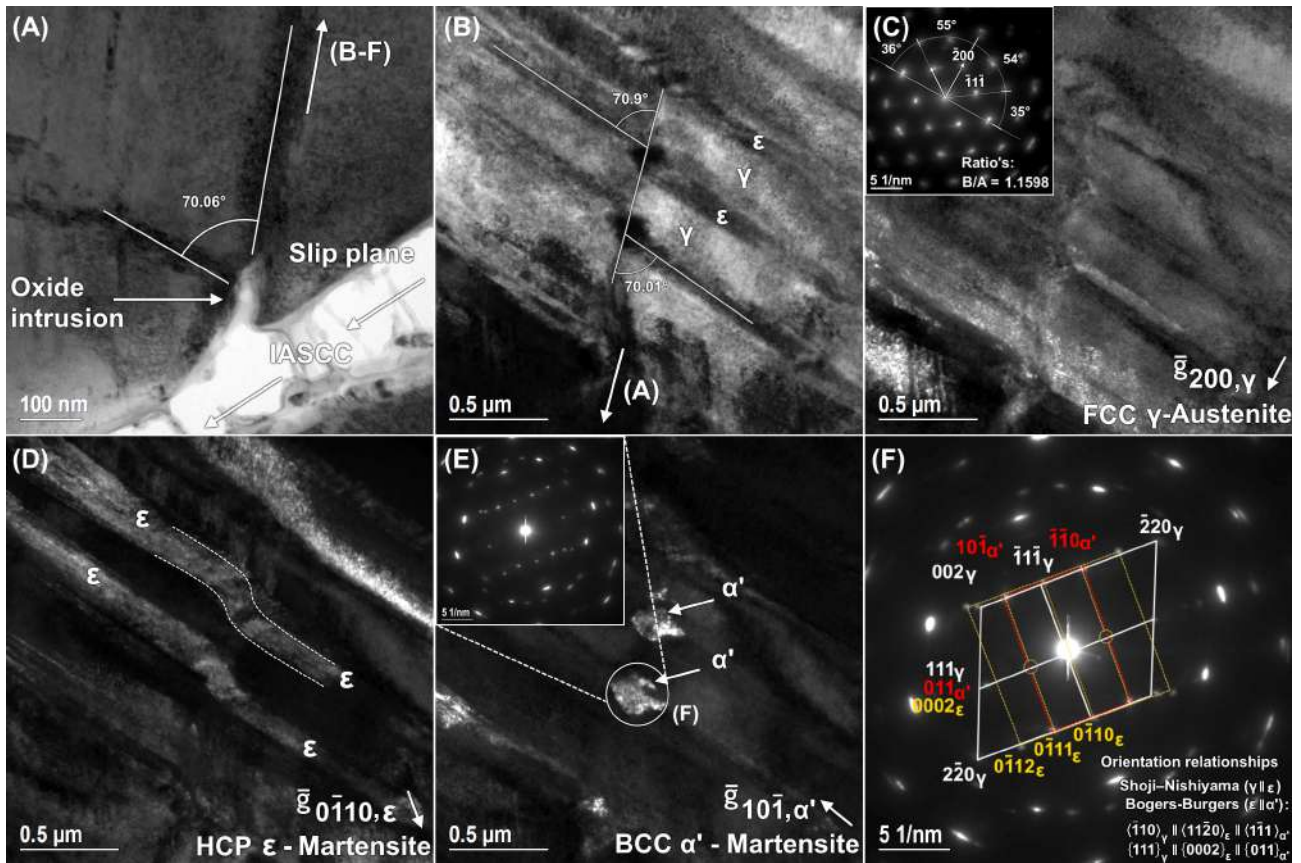


Figure 5.19: TTO-1-066 (280 MPa - cyclic loading) L08 (A) BF-TEM of ϵ -martensite laths extending from the crack flanks into the bulk interior. Deeper into the bulk, phase transformation of austenite to martensite is observed in accordance to Olsen-Cohen’s model [86] from a (B) BF-TEM, and (C-E) CDF-TEM γ -austenite, ϵ -martensite and α' -martensite perspective. The overall DP is illustrated and indexed in (F).

martensite phase transformations may be observed adjacent to microstructural slip bands, see Figs. 5.19B-D. The ϵ -martensite laths make the typical wavy shear interaction described in the Olsen-Cohen model for martensitic transformations [86]. At this shear interaction, Fig. 5.19E shows the stress-induced nucleation of BCC α' -martensitic islands in the parent austenite. CDF-TEM images in the current showcase were made by means of diffraction spots belonging to the different phases, from which Fig. 5.19F reveals the schematic representation of the Shoji-Nishiyama (S-N) $\gamma//\epsilon$ and Bogers-Burgers (B-B) $\epsilon//\alpha'$ orientation relationships:

Phase transformed austenite to martensite orientation relationships, appertaining to Fig. 5.19F:

$$\begin{aligned} \{111\}_{\gamma} // \{0002\}_{\epsilon}, \quad (\text{S-N}) & \quad \{0002\}_{\epsilon} // \{011\}_{\alpha'}, \quad (\text{B-B}) \\ \langle \bar{1}10 \rangle_{\gamma} // \langle 11\bar{2}0 \rangle_{\epsilon} & \quad \langle 11\bar{2}0 \rangle_{\epsilon} // \langle 1\bar{1}1 \rangle_{\alpha'} \end{aligned}$$

5.3.3 Crack tip characterization

5.3.3.1 SAED investigations of several IASCC tips

IASCC crack tips were either observed extending from beyond branched oxidized triple junctions, or at the end of converged intergranular cracks, see Figs. 5.20A-B and 5.20A respectively. Most crack tips

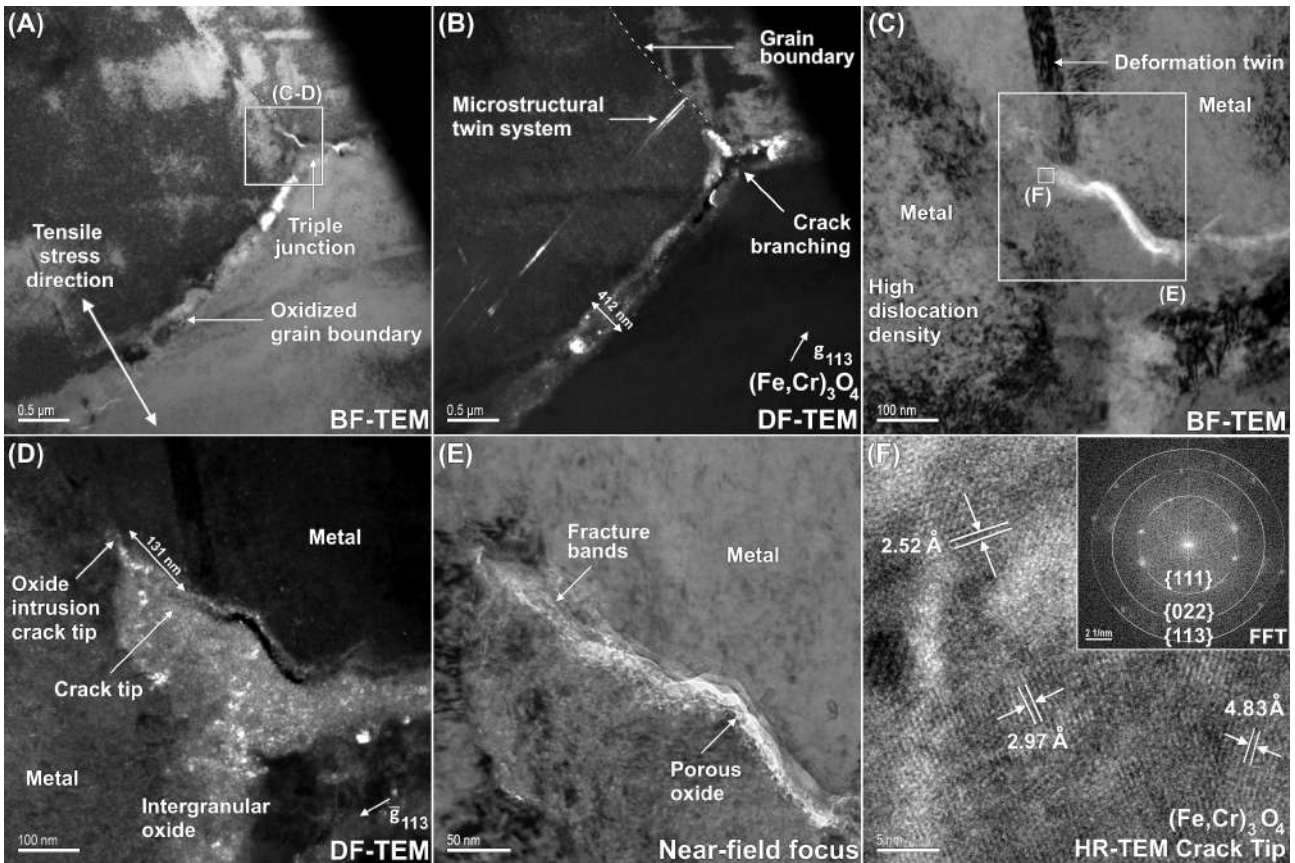


Figure 5.20: TTO-1-053 (390 MPa) L03 (A) BF-TEM imaged IASCC intergranular crack propagating along an oxidized grain boundary. (B) Corresponding CDF-TEM from an inner oxide reflection. (C) BF-TEM crack tip extending from the triple junction illustrating the presence of deformation twinning at the crack tip. (D) Corresponding CDF-TEM illustrating the extent of intergranular oxide penetration in front of the crack tip. (E) BF-TEM underfocus Fresnel contrast image of the same crack tip from edge-on orientation. (F) HR-TEM of the oxide near the crack tip seen in C, with a reduced FFT diffractogram as an inset matching the largest d-spacings of the chromite.

showed similar characteristics in terms of morphology and surrounding microstructure. Oxide-filled grain boundaries taper down towards the advanced crack tip, often accompanied by strong deformation fields on either side of the grain boundary. Extensive deformation structures such as microstructural twins are visible when the adjacent grain boundary is tilted in a suitable orientation for imaging, see Fig. 5.20C. These twins are observed to extend from the crack tip location, therefore giving the impression that their nucleation is induced by the deformation induced by the crack propagation. Distinctive features include the oxide intrusion from the leading grain boundary facing the crack tip towards one of the neighboring grains, and the preferential cracking of the oxide along the metal-oxide interface. These leading oxide intrusions extended beyond the actual crack tip, for each investigated crack tip. Oxidation at crack tip was found to be asymmetric. The crack advances more extensively into one of the two adjacent grains along the metal-oxide interface made possible by this asymmetric oxidation. This asymmetry may be caused by a higher local dislocation density close to the crack tip, which can also be observed in the global overview images further away from the tip, just as well as by the grain orientation, which may potentially favor a more extensive grain oxidation. Asymmetric oxidation at crack tips is also supported in the other literature observations of SCC cracking [97].

Intergranular oxide intrusions in front of the crack tip were consistently observed by performing SAED imaging of the crack tip oxide, see Figs. 5.20D and 5.21B. This oxide ingress may span distances of a hundred(s) of nm's in front of the propagating crack tip for specimen TTO-1-053 (390 MPa). Several

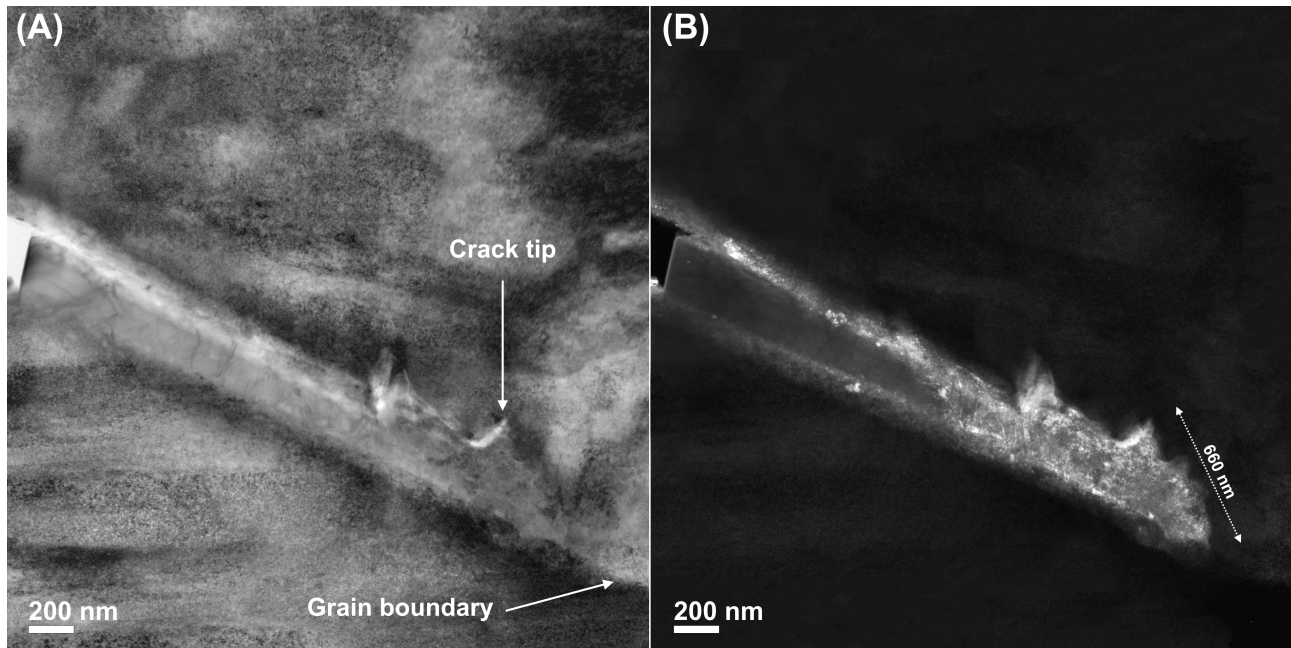


Figure 5.21: TTO-1-053 (390 MPa) L08 (A) BF-TEM and (B) corresponding CDF-TEM of the integral chromite oxide, of an IASCC crack tip propagating along an oxidized grain boundary.

crack tips additionally showed porous features within this leading oxide intrusion. Consequently, further investigation was performed from edge-on orientation using near-field Fresnel contrast imaging. Fig. 5.20E illustrates the porosity of the intergranular oxide which can be clearly seen adjacent to the crack flanks and leading crack tip edges near the metal interface. In front of the crack tip, noticeable fine fracture bands may be observed that represent the formation of brittle microcracks within the oxide-filled regions. These fracture bands nucleate completely within the integrated oxide and are interpreted as signs of oxide porosity in front of the crack tip. The fracture bands tend to propagate to the furthest point of the oxide intrusion tip. At the oxide intrusion tip, a high density of dislocation signified by the BF-TEM contrast is observed. HR-TEM examination close by these porous oxide structures revealed that the leading crack tip oxide matches the previously found chromite observed along the crack flanks, see Fig. 5.20F. The inset FFT diffractogram illustrates reflections that match the largest lattice spacings of said chromite along the crack flanks.

Another typical example of an oxidized crack tip is shown for specimen TTO-1-066 (280 MPa - cyclic loading) in Fig. 5.22A. The fatigue crack displays a fully oxidized crack tip wherein porous structures are observed, see Figs. 5.22C. To that end, this observation is very similar as observed previously within specimen TTO-1-053 (390 MPa) and subsequently within all other IASCC cracks. Closer inspection from edge-on orientation using near-field Fresnel imaging shows that these porous structures consist again of small oxidized fracture bands in front of the crack tip. It appears that these bands penetrate the oxidized region of the crack in such a manner that they may be associated with brittle cracking of the oxide. Following the crack path, it is evident how the internal oxide closely intrudes the grain boundary interface following a very narrowly oxidized intrusion. The oxide extends for over 200 nm in length and broadens the grain boundary for only several nm in width. This needle-like intrusion results into a final oxidized crack tip as shown in Fig. 5.22C. Arguably, due to the narrow width of the oxide intrusion, one may reason that the oxidation in front of the crack tip occurs before the propagation of the actual crack. Otherwise, in the event that the cracking precedes the intergranular oxidation, it would be expected that the crack cleaved through the grain boundary, leading to an oxide intrusion morphology that was much wider than the several nanometer wide intrusion width that was

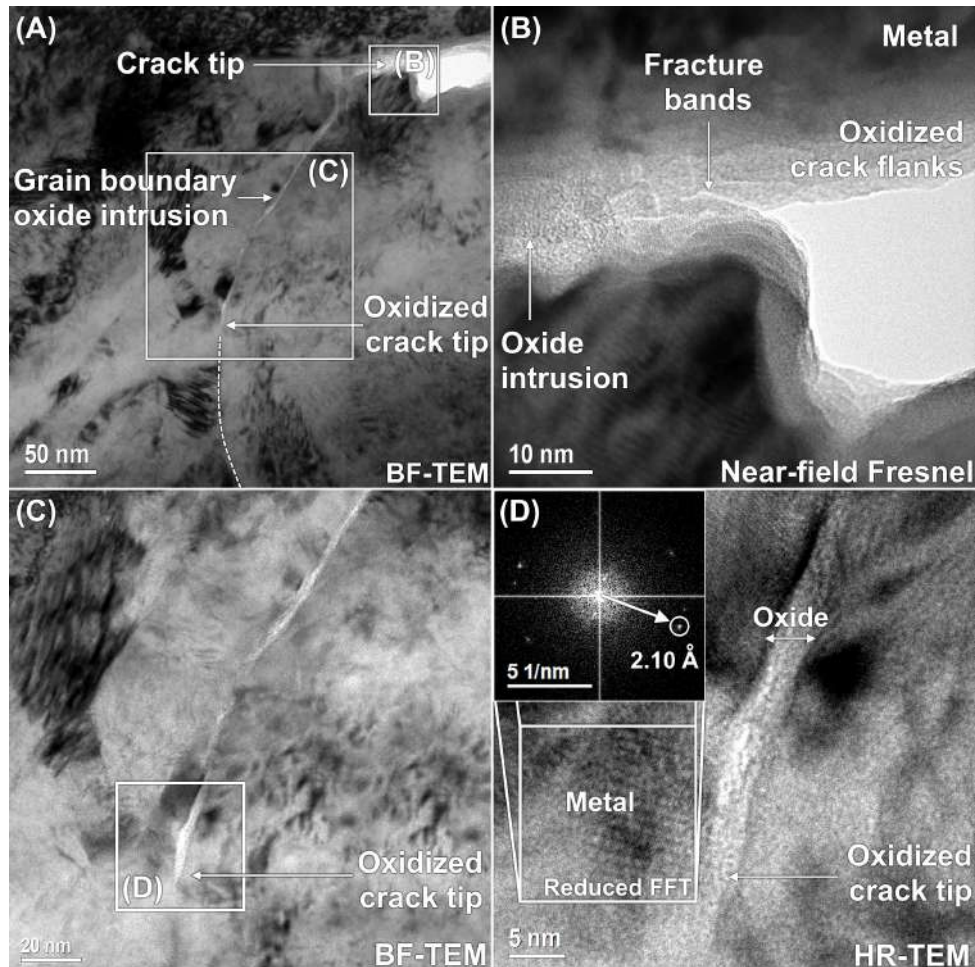


Figure 5.22: TTO-1-066 (280 MPa - cyclic loading) L09 (A) BF-TEM overview of grain boundary cracking where the oxide intrusion is seen to penetrate the leading grain boundary in front of the propagating crack tip. (B) BF-TEM underfocus Fresnel contrast image illustrating apparent fracture bands within the intergranular oxide. (C) BF-TEM of oxidized crack tip. (D) Corresponding HR-TEM of the crack tip. Inset FFT diffractogram illustrates the 111_{γ} austenite planes, while the oxidized tip remained amorphous.

observed within Fig. 5.22C. Due to this narrow intrusion width, it remained difficult to fully isolate diffraction reflections from the internal oxide from those of the neighboring bulk metal within a single TEM objective aperture during SAED imaging. Additional investigation using HR-TEM imaging reveals the metallic crystal lattice at atomic resolution while the oxidized crack tip remained fully amorphous, see Fig. 5.22D.

5.3.3.2 Oxide intrusions comparison

Cracks extracted from the fracture and O-ring's outer surfaces generally resulted into a fully converged crack tips readily available for TEM investigation. Numerous crack tips were examined from all different specimens; several of which are placed side by side in a BF- and inner oxidized CDF-TEM comparison in Figs. 5.23 and 5.23 (continued). Recurring characteristics for these crack tip morphologies were partially discussed before within section 5.3.3.1, and include: (i) an asymmetrically oxidized crack front at low to intermediate stress levels as seen in Figs. 5.23A,B; facilitating the crack propagation in one of the adjacent grains more favorably than the other. Cracking was observed to occur preferentially along the metal-oxide interface, presumably because the strained metal-oxygen bonds are inherently more chemically active and thus more prone to cracking. This observations at

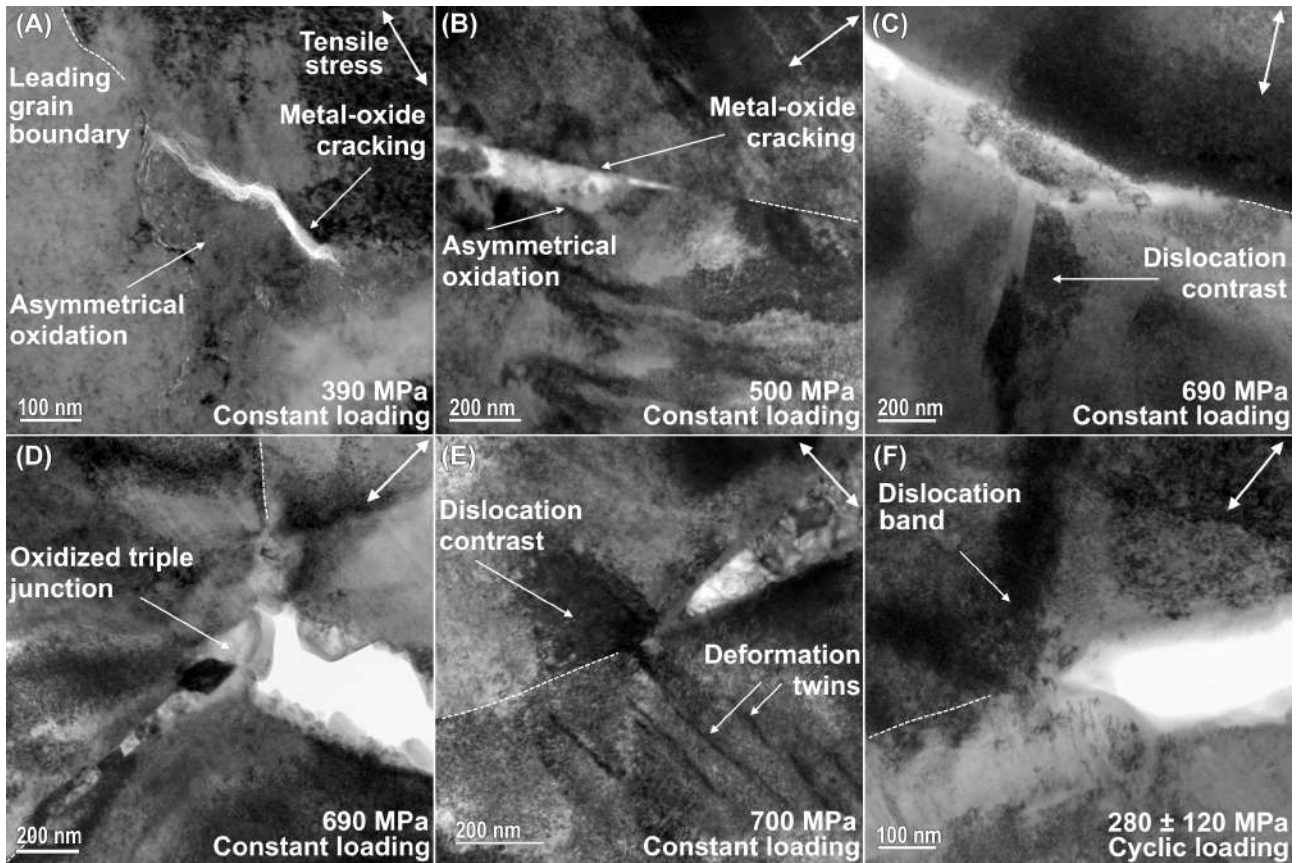


Figure 5.23: BF-TEM of the oxidation in front of several crack tips corresponding to (A) TTO-1-053 (390 MPa) L03, (B) TTO-1-071 (500 MPa) L07, (C,F) TTO-1-001 (690 MPa) L16 and L23, (D) (A) TTO-1-090 (700 MPa - non-native oxide) L08, and (E) TTO-1-066 (280 MPa - cyclic loading) L07.

low stress levels appears consistent with prior literature observations [97]. On the other hand, cracks extracted from highly stressed and cyclic loaded specimens as seen in Figs. 5.23C-F, display more widened crack opening morphology without showing any preferential cracking at the crack tip. Each crack illustrated (ii) thin oxidized crack flanks, often filled with a secondary corrosion product. These observations are compatible with other microscopical examinations of IASCC cracks [284]. Furthermore, (iii) each crack converged into a fully oxidized crack tip with narrow oxidation lengths intruding into the leading grain boundary that seemingly increased with the applied stress. Indeed, as illustrated in Tab. 5.2, evident intrusion lengths at low levels of applied stress were measured to vary between hundred(s) of nanometers up to the order of about $1 \mu\text{m}$ in specimens subjected to higher stress. On par with the increased oxidation at one of the two neighboring grains, these oxide intrusions appeared to be correlated with strong deformation fields adjacent to the crack front near the grain boundary. It is reasonable that the lattice deformation and the local dislocation activity at the crack tip facilitated the intergranular oxidation, in addition to the known enhancing effects caused by the irradiated neutron-dose [128, 226] and applied levels of cold-work [169]. Observations of these oxide intrusions trigger a redefinition of what is implied by an intergranular crack tip; that is, it being referred to as the beginning of the cracked oxide or the end of the oxide intrusion tip observed in the leading grain boundary.

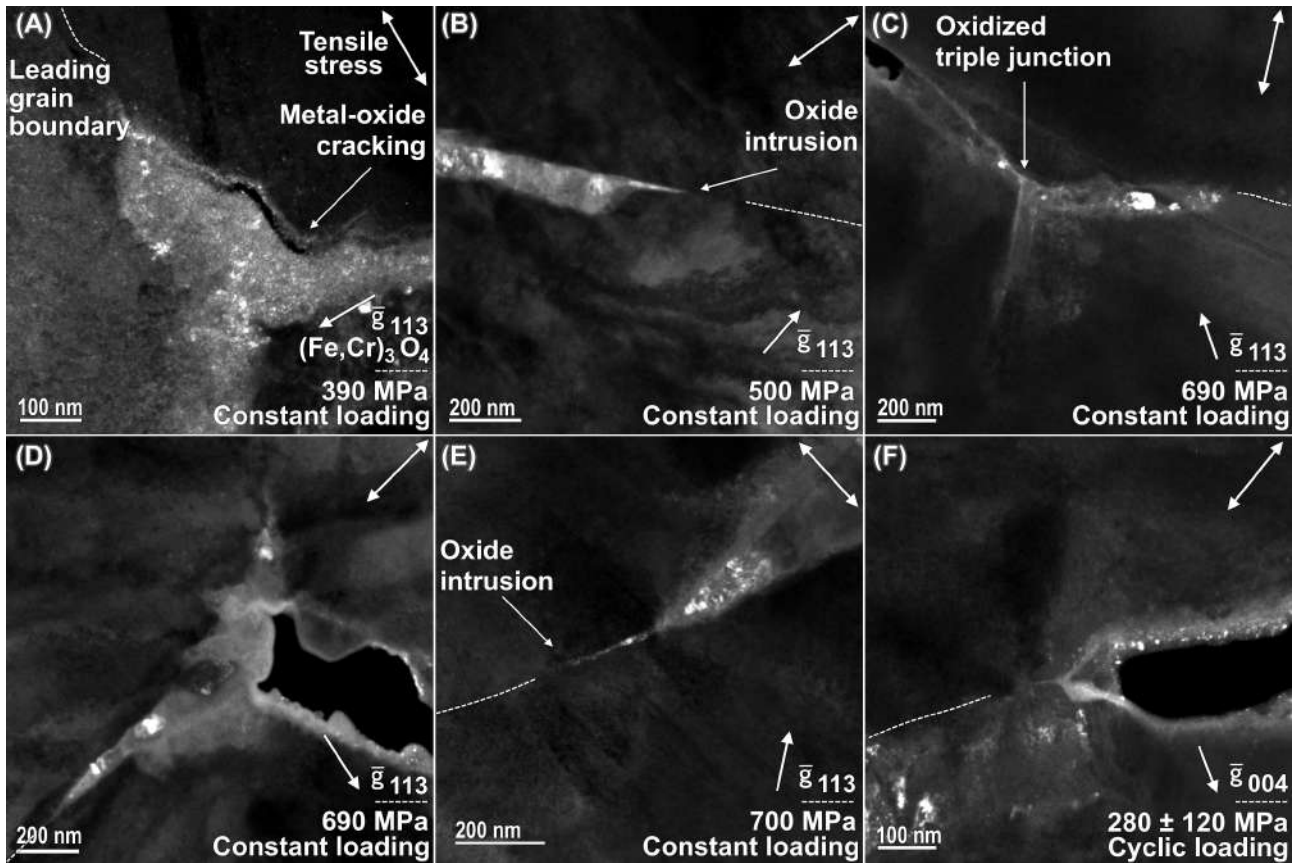


Figure 5.23: CDF-TEM of the oxidation in front of several crack tip (continued).

Table 5.2: Overview of the intergranular chromite oxide intrusion depths measured for edge-on imaged crack tips appertaining to lamellae extracted from different stress-tested specimens (θ : angle between crack propagation direction and tensile stress direction).

TTOs Specimen IDs	Mean (nm)		Maximum (nm)			Minimum (nm)		
	Intrusion Length	Intrusion Length	Intrusion Length	Lamella IDs	θ	Intrusion Length	Lamella IDs	θ
TTO-1-053 (390 MPa)	236	660	L08	88°	68	L08	2°	
TTO-1-071 (500 MPa)	321	403	L11	2°	261	L03	74°	
TTO-1-001 (690 MPa)	695	1259	L23	101°	305	L05	107°	
TTO-1-090 (700 MPa - non-native oxide)	222	301	L08	16°	120	L06	2°	
TTO-1-066 (280 MPa - cyclic loading)	154	199	L09	20°	109	L07	16°	

5.3.4 STEM-HAADF analysis

In what follows, the chemical composition of a crack tip along an impaired grain boundary is analyzed using STEM-HAADF EDS line scans and spectral mapping. These investigations may then be compared to the measurements along unimpaired grain boundaries to visualize the effects of a changing crack chemistry against radiation-induced segregation (RIS). With the focus on IASCC cracking, these measurements may provide arguments for what makes the grain boundary susceptible to fracture.

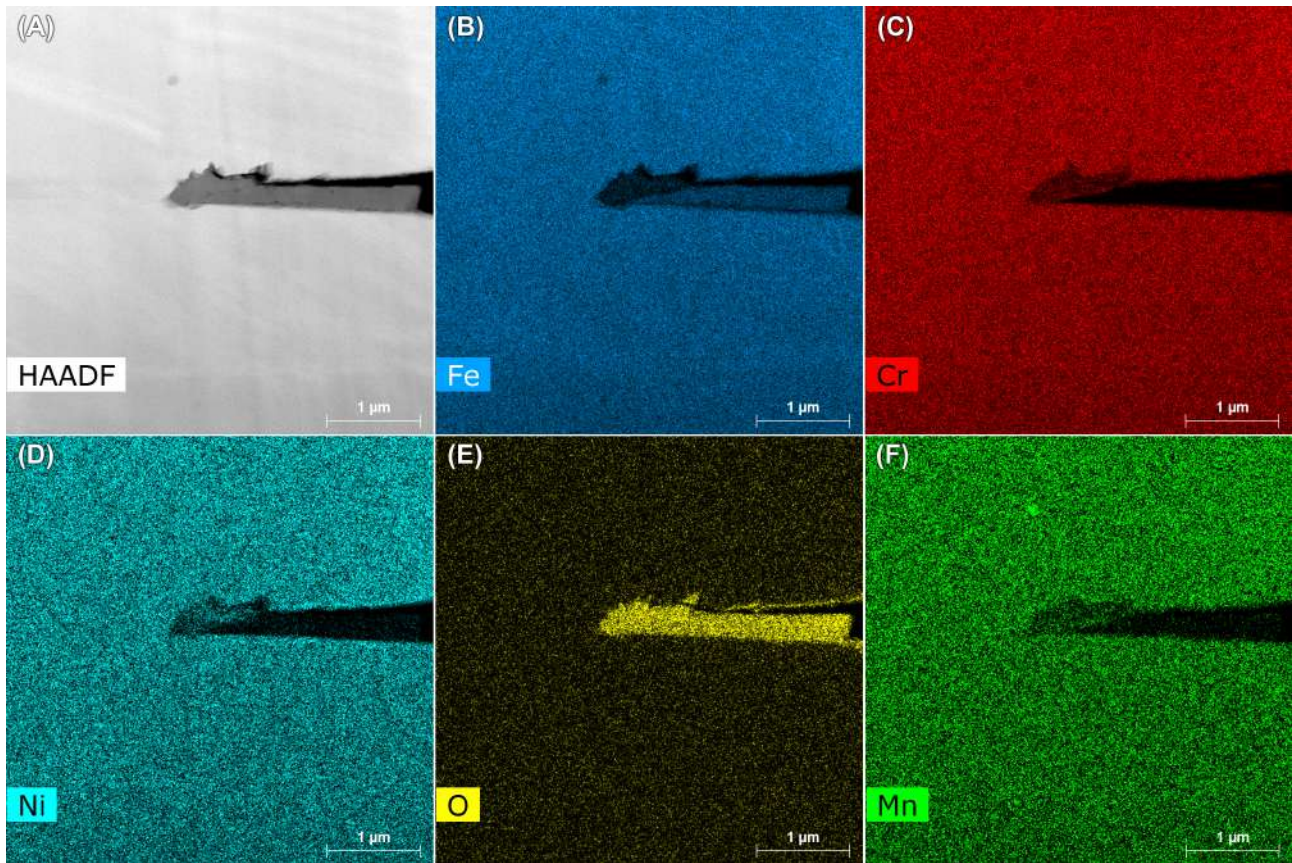


Figure 5.24: TTO-1-053 (390 MPa) L08 HAADF-STEM EDS chemical mapping of a selected IASCC crack tip.

5.3.4.1 Crack tip mapping

Fig. 5.24 presents an overview of the most relevant STEM-EDS maps of an IASCC cracked grain-boundary in specimen TTO-1-053 (390 MPa) shown in Fig. 5.21. Clear separation between the chromite and magnetite oxide spinels can be observed. Whereas the magnetite is deposited inside the crack opening, the chromite extends beyond the crack tip into the leading grain boundary. Evident segregation and depletion of metallic elements is not observable from this magnification. To that end, Fig. 5.25 depicts the most relevant chemical maps of the impaired GB structure from another IASCC crack belonging to TTO-1-053 (390 MPa). A highly Ni-enriched metallic zone on one specific side of the grain boundary was observed in Fig. 5.25D, spanning a range of approximately 70 nm wide and 75 nm in front of the crack tip. Additionally, preferential segregation of solute elements such as Si is apparent close to the crack tip. In that respect, the element composition of the leading grain boundary in front of the crack tip is expected to be highly altered.

Indeed, as becomes evident from the investigation of IASCC cracks appertaining to specimen TTO-1-066 (280 MPa - cyclic loading), a highly altered crack tip and leading grain boundary composition is observed in Fig. 5.26. The investigated crack is the same one depicted in Fig. 5.14. Clear depletion of Fe and Cr may be observed in front of the crack tip, while evident enrichment of Ni is apparent at the crack tip location. Ni is observed to enrich adjacent to the crack flanks and further along at a distance of several tens of nm in front of the crack tip. Additionally, elemental spectra of Mn and Mo show an evident depletion in front of the crack tip in agreement with previous observations [299]. Furthermore, small Ni and Si clusters were also observed throughout the matrix in equal densities close and far away from the crack tip. This observation signifies that their presence is unrelated to

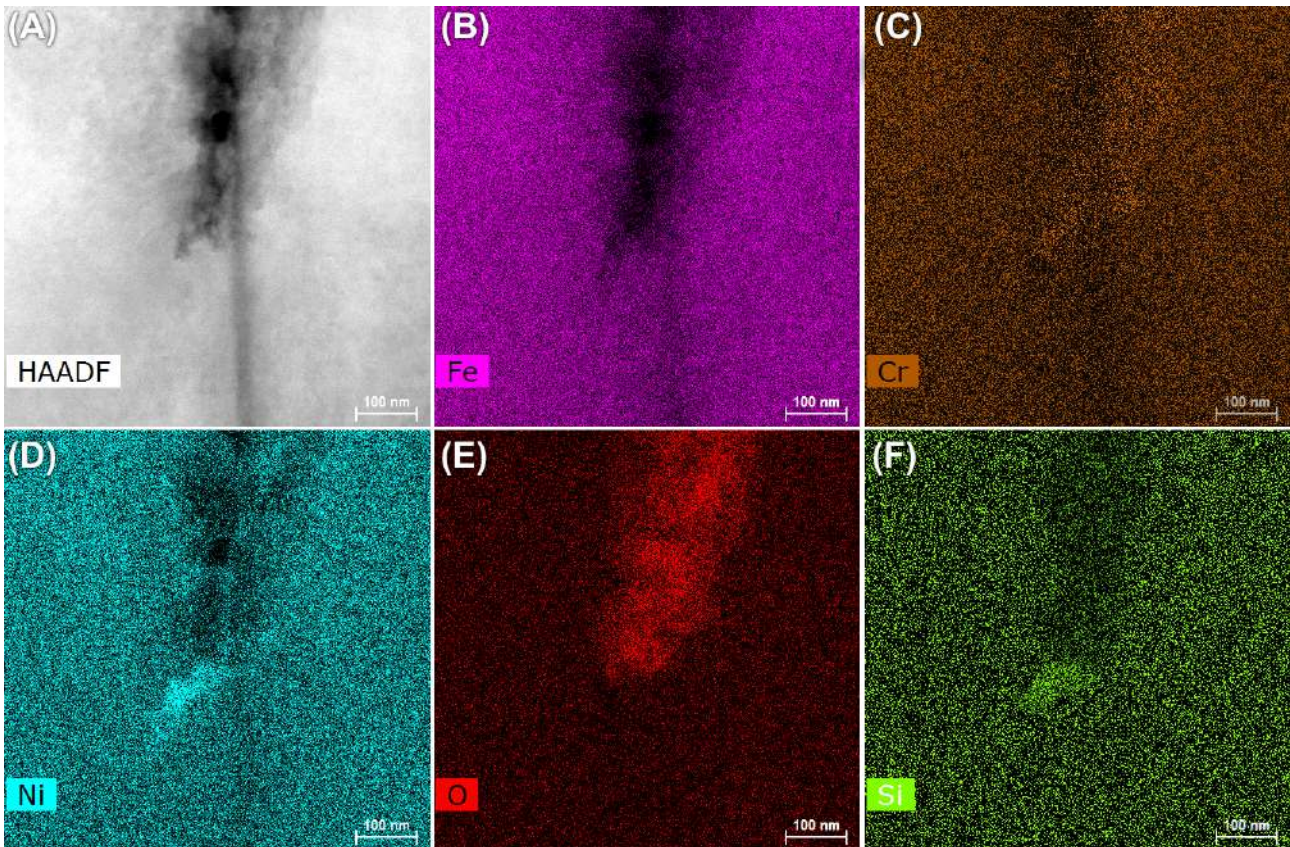


Figure 5.25: TTO-1-053 (390 MPa) L08 HAADF-STEM EDS chemical mapping of enriched and depleted elements closer to a selected IASCC crack tip.

any of the deformation mechanisms relating to the crack propagation. Rather, their origin can be related to the small coherent diffusion of structural elements following the intense effects of neutron-irradiation. Indeed, rough estimated diffusion distances of RIS tend to show that elemental diffusion lengths are of the order of around several to tens of nm's [20, 232], which reasonably corresponds to the clusters' approximate size distributions. Moreover, the deformation field is also seen to cause some inhomogeneous segregation and depletion of structural elements at the grain boundary interface. Indeed, Ni but also more evidently Si, are observed to effectively enrich at separate locations along the grain boundary corresponding to the local impact of intersecting twin systems. Chemical enrichment of these elements is also evident at the twin interfaces themselves. Pertaining solely to oxide concentration map, it is evident how the crack tip itself is completely filled by the chromite oxide. It is unmistakable how oxide intrusions extend into the leading grain boundary in the form of a nm-wide needle-like oxide intrusion, similar to what has been observed in Figs. 5.20E, 5.21, and 5.22C. Since oxidation in front of the crack tip was evident from all crack tips observed in Fig. 5.23, this additional result signifies that oxidation embrittlement may contribute significantly towards the genuine propagation of the IASCC crack.

Fig. 5.27 reports the chemical concentrations following the crack tip propagation and opening directions of the crack displayed in Fig. 5.26. Following the propagation direction of the crack, it is evident from the structural element profiles that Fe and Cr transition from their oxidized form prior to the crack tip to their bulk concentration values, in a rather inconsistent manner. This suggests that there is a complex chemical interaction between other contributing elements at the crack tip. Indeed, first and foremost, clear depletion of Fe and Cr may be observed at the crack tip location, while Ni

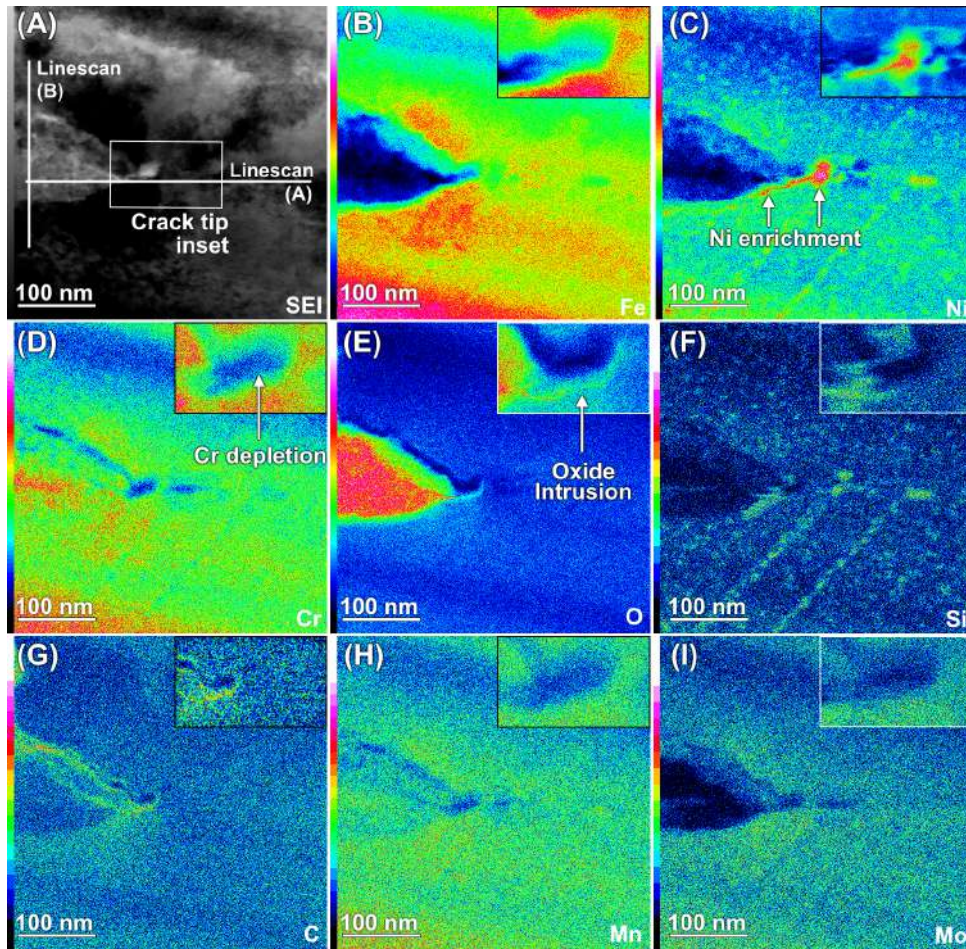


Figure 5.26: TTO-1-090 (700 MPa - non-native oxide) L01 HAADF-STEM EDS chemical mapping of enriched and depleted elements close to a selected IASCC crack tip. Regions of high to low STEM intensities are indicated by the color scheme varying from white to black, respectively.

enriches to values of near 26 wt.% (+103% vs. metallic concentration). Secondly, it is observed that the crack tip oxide concentration drops at a steeper rate compared to the corresponding Cr concentration, and that lower values of Cr are detected close to the crack tip location. This may indicate the crack tip's ability to form a poorer Cr-oxide susceptible to brittle fracture. Furthermore, it is apparent that local deformation close to the grain boundary greatly influences the chemical composition of the grain boundary itself. For instance, Si is enriched at three separate locations in the oxidized part (+144% vs. oxidized concentration) and at the metallic part (+189% and +109% vs. metallic concentration) of the crack, each corresponding to the local impact of twins intersecting with the grain boundary interface. As seen in Fig. 5.26F, Si may enrich just as equally at twinned interfaces, as they may act as microstructural sinks for RIS. Similarly for Mn and Mo, their concentrations show some depletion behind the crack tip consistent to what has been observed in prior analyses seen for specimen TTO-1-053. Alternatively, along the opening direction, a steep drop in the Fe-signal (−71% vs. metallic concentration) is observed when transitioning from its metallic form to the intergranular oxide. Alternatively, amidst the intergranular oxide, the Cr signal is seen to enrich to about twice as much the bulk concentration (+61% vs. metallic concentration). Regarding the signals of Ni and Si, it is somewhat evident how firstly a Ni-enriched layer closely followed by a Si enriched layer is observed adjacent to the oxidized crack. The Ni-enrichment layer is observed at the transition point from the intergranular oxide to the metallic matrix composition. Interesting spectra are seen for Mn and Mo as well. Whereas Mn remains approximately similar across the entire line scan, Mo engages in

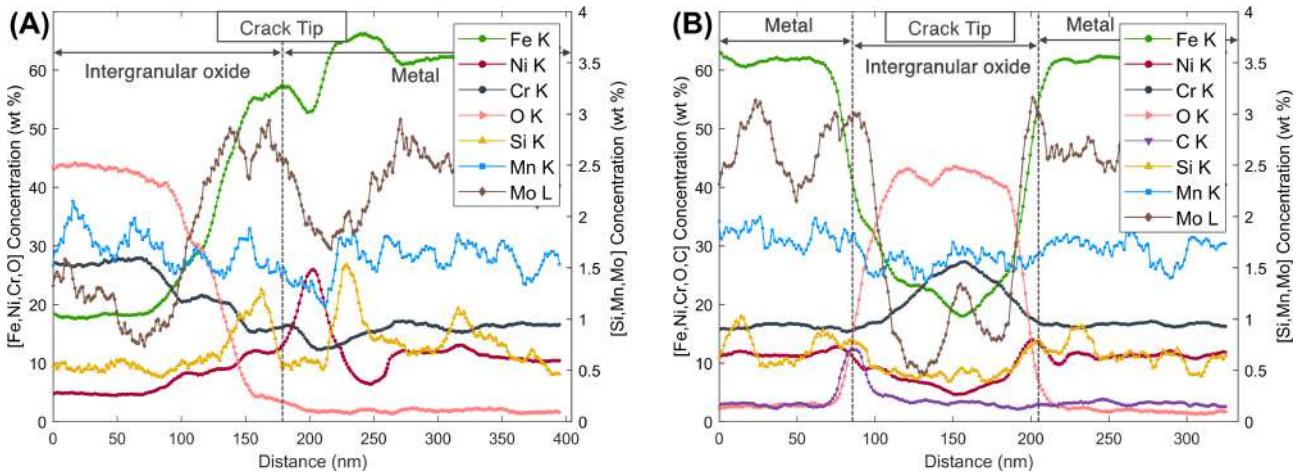


Figure 5.27: TTO-1-090 (700 MPa - non-native oxide) L01 HAADF-STEM EDS line scan along the IASCC crack tip (A) propagation direction and (B) opening direction illustrated in Fig. 5.26A.

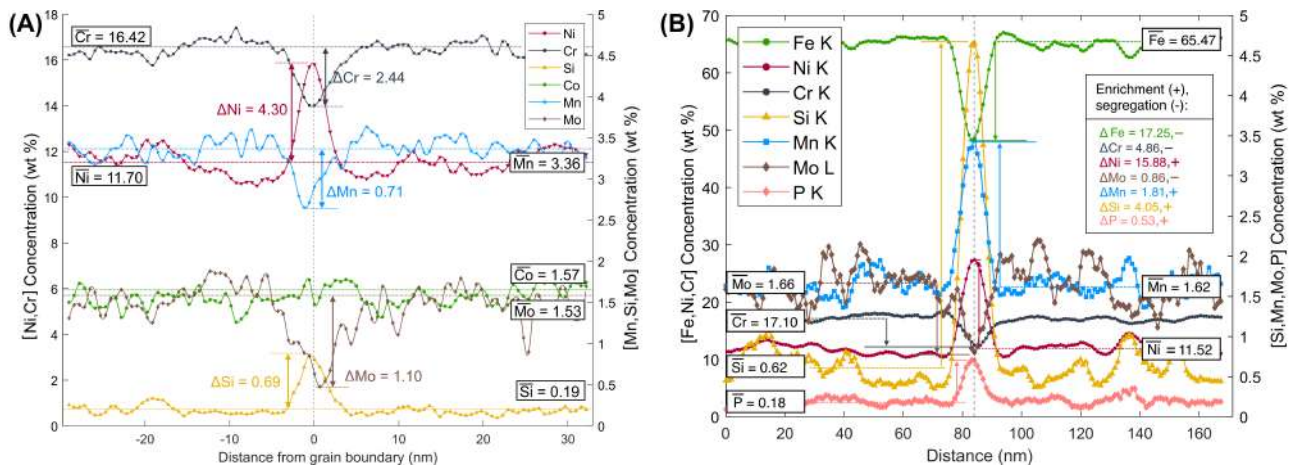


Figure 5.28: HAADF-STEM EDS line scans of edge-on unimpaired grain boundaries appertaining to specimens (A) TTO-1-053 (390 MPa) L08 and (B) TTO-1-090 (700 MPa) L01.

chemical interactions with the crack exemplified by a typical W-shaped profile. Slight Mo-enrichment is observed adjacent to the crack, followed by a step drop within the intergranular oxide, only to increase again in the midst of the crack. This interaction has not been previously observed. Although the changing signals in the Fe- and Cr-spectra do not clearly support this, it is possible that this transition is the result of a layer stacking between the chromite and magnetite oxide within the intergranular crack.

5.3.4.2 RIS at unimpaired grain boundaries

Thorough analysis of the chemical composition of an unimpaired grain boundary close to a triple junction of specimen TTO-1-053 (390 MPa) is displayed in Fig. 5.28A. These scans present a complete profile of the extent of RIS along a typical grain boundary structure of a specimen that was irradiated up to 60 dpa. Segregation and depletion of several elements are evident from the edge-on orientated grain boundary profile. Ni and Si are unmistakably enriched versus the clear depletion of Cr, Mn and Mo. Ni is considered as the slowest diffusing element, reaching segregation levels of up to 16 wt.% enrichment at the grain boundary (+36% vs. metallic concentration). On the other hand, Cr depletes to a value of about 14 wt.% compared to the structural matrix composition (−15% vs.

metallic concentration). Pre-depletion and -segregation of respectively Ni and Cr are apparent by the narrow regions of change adjacent to the grain boundary. This becomes evident by the somewhat inverse and direct W-shaped profile respectively. Considering the high irradiation exposure, this pre-depletion and pre-segregation may suggest an interaction between other co-diffused elements. Indeed, correspondingly the depletion of other alloying elements like Mn (-21% vs. metallic concentration) and Mo (-72% vs. metallic concentration) is also observed. Bruemmer et al. [42] argued that Mn, similarly as to Mo, deplete on the basis of both strong diffusion and transmutation at high fluence levels but neither has been implicated to play a major role for crack initiation. With respect to the role of Si, which was found to be enriched up to significantly along the current grain boundary ($+363\%$ vs. metallic concentration), its implication on crack initiation is not yet fully understood [121]. The rate of change of the RIS profile is consistent with the inverse Kirkendall (vacancy-exchange) and interstitial-solute transport mechanisms [300,301], and is slightly enhanced compared to the segregation profiles presented for low-to-moderate fluences in the literature [42,121]. As for reference, the average element composition distant from the grain boundary closely corresponds to the bulk matrix composition. In that sense, it is estimated that the diffusion length of both structural and solute elements is of the order of tens of nm.

Comparatively, Fig. 5.28B presents a similar measurement of the RIS profiles along an unimpaired grain boundary structure, this time stemming from specimen TTO-1-090 (700 MPa - non-native oxide). This specimen foresaw a slightly increased irradiation dose, up to 80 dpa instead. Each respective element is seen to match the enrichment and depletion profiles of the previous investigation in TTO-1-053. Their profiles signify the extent of RIS as a measure of the susceptibility of the grain boundary interface to intergranular cracking. Equivalently, Ni ($+138\%$ vs. metallic concentration) and Si ($+653\%$ vs. metallic concentration) are seen to significantly enrich, whereas Cr (-28% vs. metallic concentration) and Mo (-52% vs. metallic concentration) are observed to deplete to great extents at the interface. Additional spectra's are shown for the typical Fe-depletion (-26% vs. metallic concentration) and P-enrichment ($+294\%$ vs. metallic concentration). Interestingly, Mn is seen to enrich at the grain boundary ($+112\%$ vs. metallic concentration), which stands in contrast with previous observations in Fig. 5.28A for specimen TTO-1-053. Pre-segregation and pre-depletion profiles resulting into the priorly observed W- or inverse W-shaped concentration profiles were not perceived in great detail. The segregation and depletion of structural and minor elements are mostly consistent with the inverse Kirkendall (vacancy-exchange) and interstitial-solute transport mechanisms [300,301]. These results are encapsulated within Tab. 5.3.

Table 5.3: Quantified results of the RIS profiles investigated by means of STEM-HAADF EDS line scans across unimpaired grain boundaries shown in Figs. 5.28A and 5.28B (\pm stands for segregation and depletion, NE = no measurable effect).

Specimen ID	Fe	Ni	Cr	Co	Mn	Mo	Si	P
TTO-1-053 (390 MPa - 60 dpa)	-	+36%	-15%	NE	-21%	-72%	+363%	-
TTO-1-090 (700 MPa - 80 dpa)	-26%	+138%	-28%	-	+112%	-52%	+653%	+294%

5.3.5 Interesting cases surrounding IASCC cracking

5.3.5.1 MnS inclusion particles

Fig. 5.29A depicts an overview of an IASCC crack that has clearly arrested at an intergranular inclusion particle. Close consideration of the chemical structure of the inclusion particle is presented by the corresponding EDS spectrum in Fig. 5.29B. The spectrum exhibits strong peaks which can be assigned to Mn, S and Cu. As a result, the particle is further referred to as being a MnS inclusion particle, in correspondence to the literature nomenclature [302–304]. The inclusion particle has segregated close

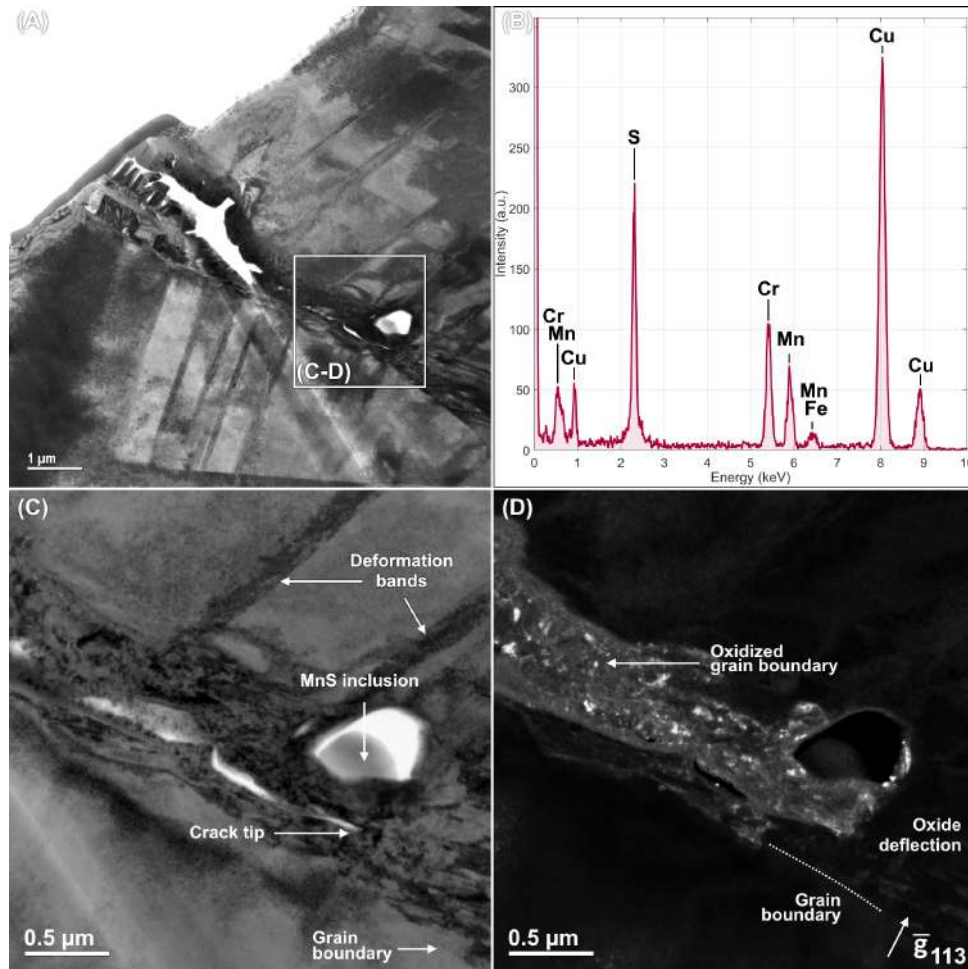


Figure 5.29: TTO-1-053 (390 MPa) L01 (A) BF-TEM of an intergranular IASCC crack arrested at a (B) EDS-confirmed MnS inclusion particle in close vicinity to the grain boundary. (C) BF-TEM of the crack tip illustrating a heavy deformation field in close vicinity to the particle. (D) CDF-TEM displaying the intergranular oxide deflection away from the grain boundary towards the inclusion particle.

to the grain boundary, altering the crack path and ultimately arresting the IASCC crack. As shown in Figs. 5.29C-D, it is evident how the oxidation deflects from the leading grain boundary, encapsulating the inclusion. The arrest is accompanied with strong lattice deformation, suggested by the dense deformation field ahead of the crack and the propagation of deformation slip bands from the crack flanks. Interestingly, the intersections of the deformation bands with the crack led to a discontinuous ingress of oxide into the bulk matrix. In association with earlier findings [97,98,218], deformation bands may act as fast-diffusion paths for intergranular oxidation. The ingress along the deformation slip bands is reasonably facilitated by the localized dislocation flow in the highly deformed microstructure close to the crack flanks.

5.3.5.2 Intergranular inclusion particles

In specimen TTO-1-090 (700 MPa - non-native oxide), some interesting findings were discovered along an impaired grain boundary in front of an IASCC crack tip depicted in Fig. 5.30A-C. Indeed, it is evident how metallic inclusion particles are found to segregate along the grain boundary in front of the tip. These particles segregate in series along the grain boundary and average in width of about 10–50 nm. Due to their relative small size and the neighboring twin-systems intersecting with the grain

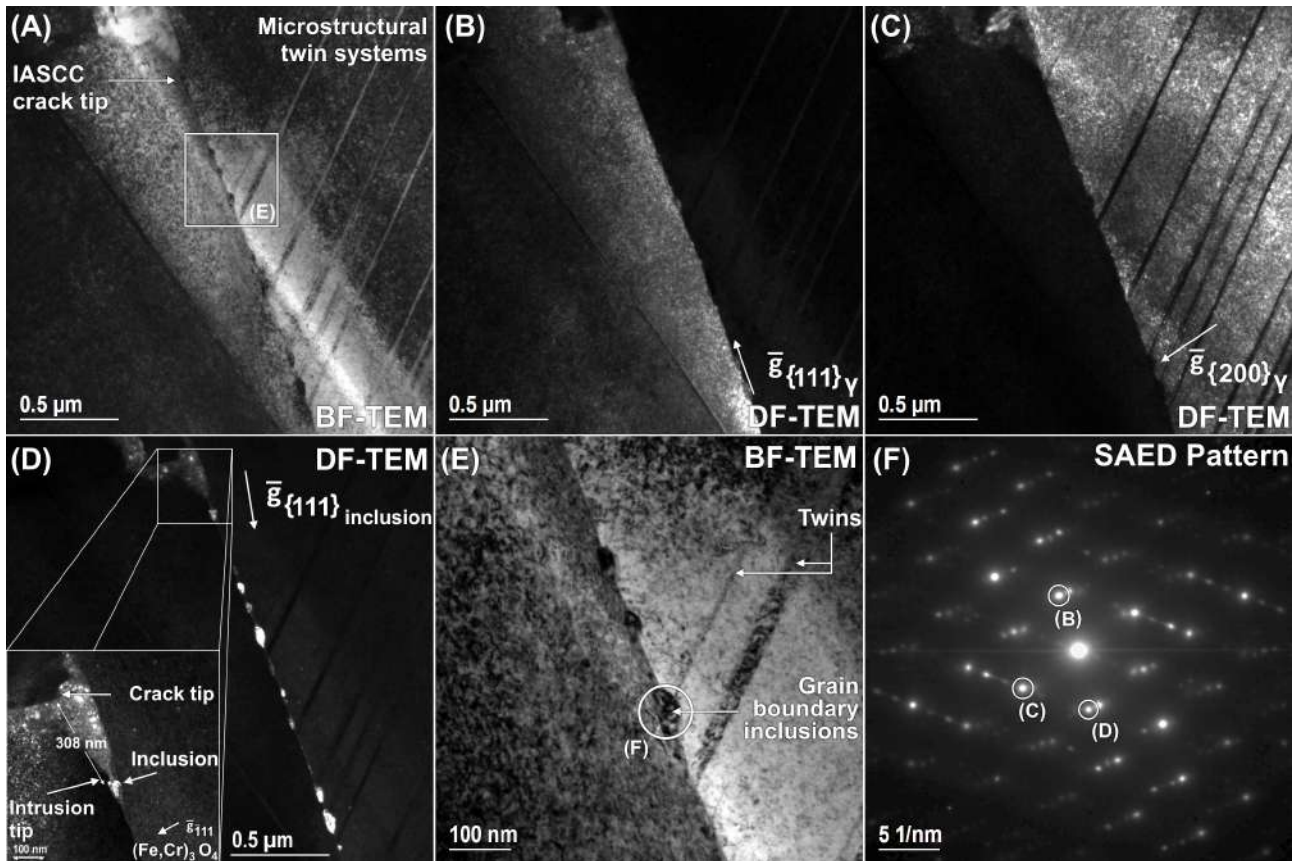


Figure 5.30: TTO-1-090 (700 MPa - non-native oxide) L01 (A) BF-TEM overview of IASCC leading grain boundary. (B-C) CDF-TEM of adjacent grain boundary structures. (D) CDF-TEM of intergranular inclusion particles. Inset shows a CDF-TEM from a CT oxidation reflection, illustrating oxide intrusion up to the inclusion particle. (E) Magnified BF-TEM of intergranular inclusions. (F) Corresponding DP.

boundary, it was difficult to attain an appropriate DP of solely the inclusion particles. Instead, the obtained DP depicted in Fig. 5.30F, contains reflection elements of not only the inclusions, but also from both opposing austenitic grains and the impacting twin systems adjacent to the grain boundary. Fig. 5.30D depicts a CDF-TEM from one of the inclusions, taken from a reflection with d-spacing of 1.99 Å (a value that lies in-between the {111} and the {200} lattice planes of the expected austenitic lattice). A series of particles is seen segregate along the grain boundary, possibly having affected the initiation and propagation processes of the crack. According to the CDF-TEM inset in Fig. 5.30D, taken with an objective aperture centered around an inner oxide reflection at the crack tip, the oxide intrusion of the tip is seen to protrude all the way up to one of the grain boundary inclusion particles. A closer view of a few of the inclusions from an edge-on orientation of the grain boundary is depicted in Fig. 5.30E.

Closer inspection of one of these grain boundary inclusions is performed by STEM-HAADF and HR-TEM analyses with the JEM-ARM300F STEM, operating with a better chemical and spatial resolution, see Fig. 5.31. The line scan across one of the particles is illustrated in Fig. 5.31B. Evidently, persistent Fe- and Si-enriched signal are attained, while the inclusion otherwise strongly depletes in signals appertaining to Ni, Cr, Mn and Mo. The changes in the transition metals and Si that align with diffusion processes of RIS should be considered carefully as they cannot be solely attributed to the presence of the inclusion only. The HR-TEM image and its corresponding spot-like FFT diffractogram is depicted in Fig. 5.31C. These analyses illustrate that the inclusion particle displays a

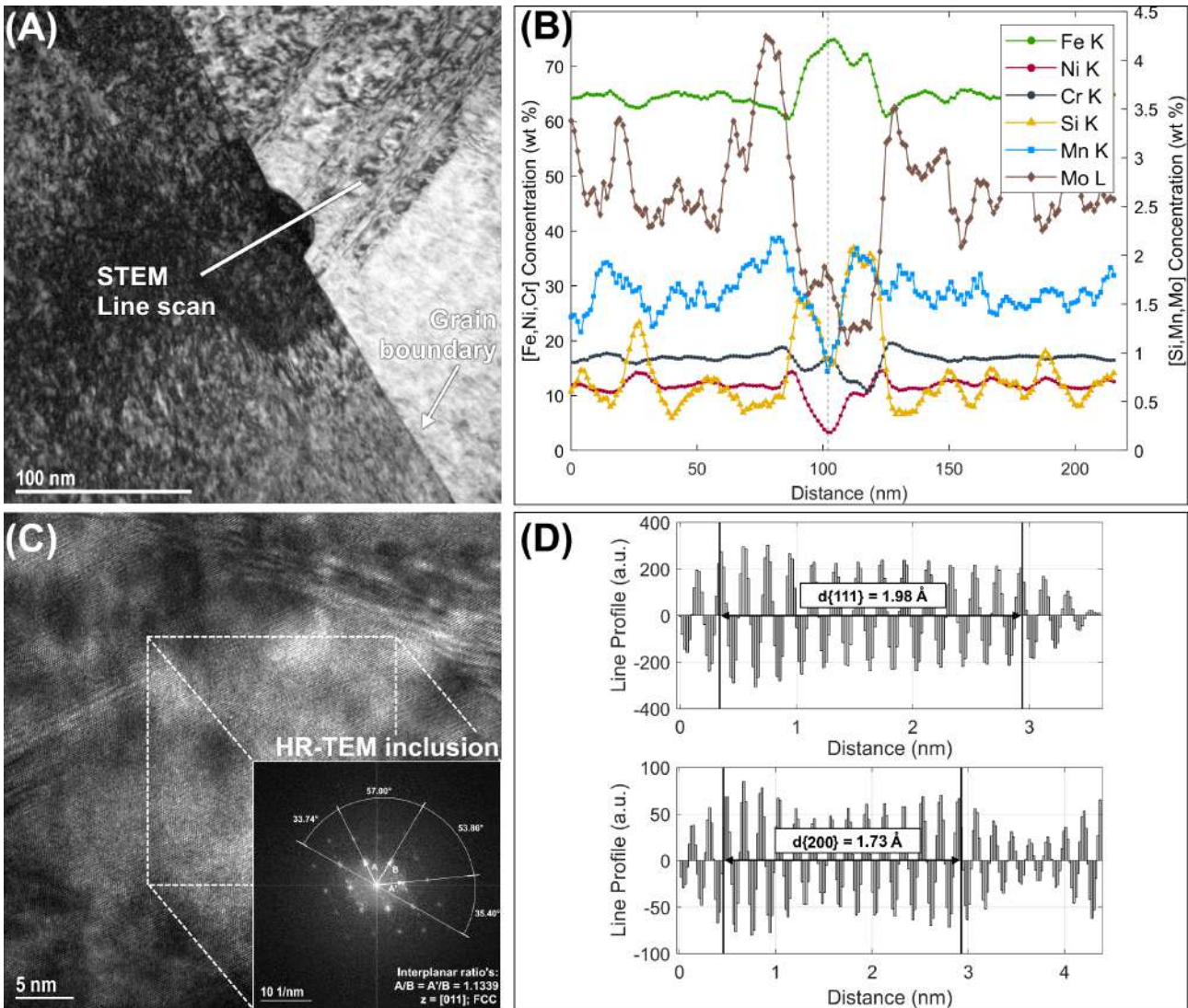


Figure 5.31: TTO-1-090 (700 MPa - non-native oxide) L01 (A) BF-TEM image of, and (B) STEM-HAADF line scan across, the intergranular inclusion particle. (C) HR-TEM and (D) reduced FFT of C of the inclusion particle.

crystallographic structure that best-matches a typical $[0\ 1\ 1]$ zone-axis with an FCC centering. Through the inverse FFT diffractogram of the of the masked primary lattice reflections, Fig. 5.31D displays that primal lattice spacings of the intergranular inclusion result in $d_{\{111\}} = 1.98\ \text{\AA}$ (similar to what was obtained before through diffraction analysis) and $d_{\{200\}} = 1.73\ \text{\AA}$. Determination of the lattice parameter yields a value of about $a = 3.46\ \text{\AA}$, which is close to the unit cell parameter of common austenite. What is surprising, is that from all the investigated crack tips within this study, these particles were only specifically observed along this leading grain boundary only.

5.3.5.3 Tensile stress direction

Generally, the role of the external tensile stress with respect to intergranular cracking is made evident under general examination of several fractured grain boundaries. Relative to the orientation of the grain boundary, especially following triple junctions where one of the boundaries failed preferentially compared to the other, it was observed that the cracking typically aligned perpendicular towards the external tensile stress direction. As observed in Fig. 5.32A-B and Tab. 5.1, cracks propagating beyond

an oxidized triple junction tend to always follow a crack path in cleavage mode orientation, even though the adverse grain boundary was equally oxidized. In agreement with previous studies associating the tensile stress to crack propagation [70], this result indicates external tensile stress assists intergranular cracking most effectively whenever both the grain boundary normal and the stress orientation are aligned in parallel. In all other cases, the crack propagation was shortly followed by a full crack arrest.

5.3.5.4 Preferential oxidation

Fig. 5.33 depicts the crack initiation process along the outer surface oxide for specimen TTO-1-001 (690 MPa). Evidently, the crack did not propagate to considerable lengths because of a missing leading grain boundary interface in front of the crack tip, see Fig. 5.33C. Preferential oxidation is observed ahead of the tip, which ingressed transgranularly into the bulk. Possible explanations may be due to cumulative deformation near the fracture surface. The presence of pre-established dislocation shear bands or microstructural (nano-)twins could explain this occurrence [305]. Microstructural defects may act as short-circuit fast-diffusion paths for oxidizing species, allowing them to penetrate deeper within the bulk material. The oxides are additionally seen from a CDF-TEM oxide perspective to ingress sideways between a double microstructural interface, see Fig. 5.33D. This interface can be regarded as either a grain boundary or another twin interface developing closely to the surface. However, another valid explanation may be because of the enhanced oxidation along martensitic phase structures, as observed by Chang et al. [72]. Albeit, it was not possible to definitively prove the presence of the martensites by diffraction analyses. All things considered, it is difficult to draw conclusions from the rather heterogeneous microstructure caused by prior cold-work and neutron-irradiation so closely present at the fracture surface.

In Figs. 5.34A-B, a typical overview of an IASCC crack appertaining to specimen TTO-1-001 (690 MPa) is depicted. From the CDF-TEM of an inner oxide reflection stemming from the crack flanks, it is evident that the crack flanks themselves are narrowly oxidized along the complete length of the

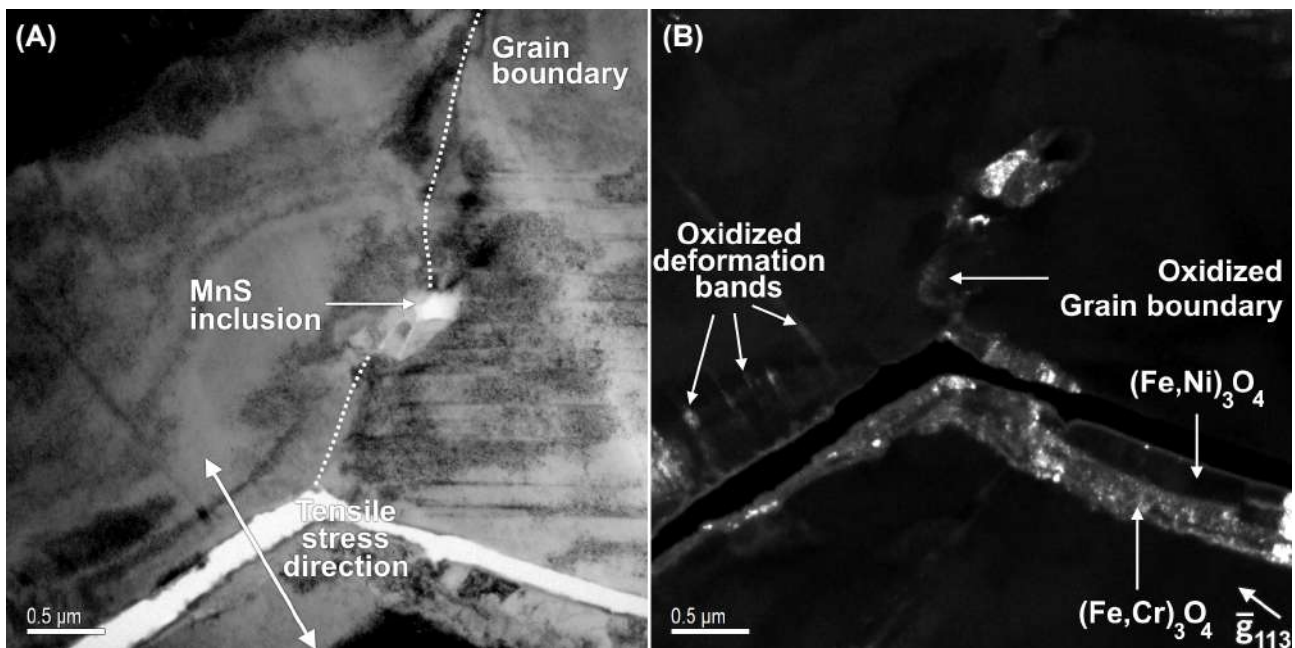


Figure 5.32: TTO-1-053 L03 (A) BF-TEM of an intergranular crack propagating in cleavage mode in relation to the tensile stress direction. (B) CDF-TEM of oxidized grain boundary triple junction. (C-D) CDF-TEM of the opposing grains.

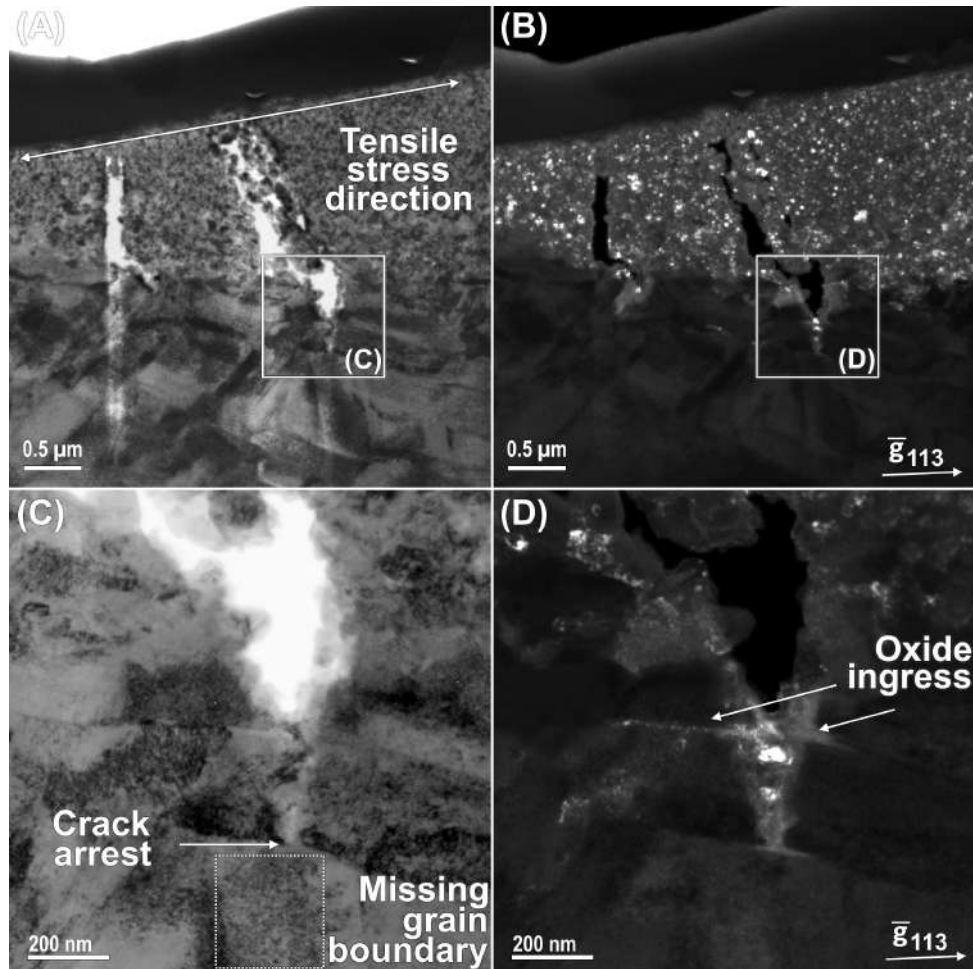


Figure 5.33: TTO-1-001 (690 MPa) L20 (A) BF-TEM and (B) corresponding CDF-TEM of inner oxide reflection along oxidized outer surface. (C) Magnified BF-TEM with (D) corresponding CDF-TEM of oxidized crack tip arrested at microstructural interface.

crack. However, several preferential oxide ingresses are observed to penetrate in the form of finger-like structures into the adjacent bulk material. These oxide-fingers were found to follow the orientation of nearby microstructural deformation structures as observed in the BF- and CDF-TEM images in Figs. 5.34C-D. SAED investigation of the associated deformation structures is performed in Figs. 5.34E-F. Interestingly, the contrast difference in the associated BF-TEM image suggests these phases are considered to be different from the parent austenitic phase of the metallic lattice. Also, the equivalent DP illustrates a $[001]$ zone-axis DP with metallic reflections that form under a ratio and corresponding angle that is not common for ordinary FCC lattices. Instead, the DP illustrates a seeming BCC structure, similar to α' -martensite as observed otherwise in section 5.3.2.3, although again not fully confirmed according to the suitable orientation relationships with the parent austenite lattice. The preferential oxidation along these structures may be a very similar process as described in Fig. 5.33 above.

Additionally, within the BF- and corresponding CDF-TEM images earlier in Figs. 5.32A-B and now presently in Figs. 5.34G-H, noticeable deformation bands are seen to nucleate aside of the oxidized crack flanks close to the ultimate crack tip. As becomes evident from the corresponding CDF-TEM images, these deformation bands are susceptible to preferential oxidation. The oxidation along such deformation bands reached transgranular lengths of up to several hundreds of nm, following

an orientation where the bands nucleate in parallel towards the external stress. This observation is in full agreement with the findings of Lozano-Perez [97], who illustrated that the oxidation is favored along any deformation band that intersects the crack path which is orientated in parallel to the applied stress direction. This phenomenon may be explained physically by the fact that the dislocation densities within the deformation bands are larger while their distribution is thought to be complicated; i.e. existing of closely distributed intersecting dislocations that generated during the deformation process, as is the case for highly deformed metals. In this manner, the dislocation bands are considered as stress-concentrated regions which provide fast-diffusion paths for oxide species. This form of oxidation may be additive towards the enhanced oxidation observed at the oxide intrusion tip.

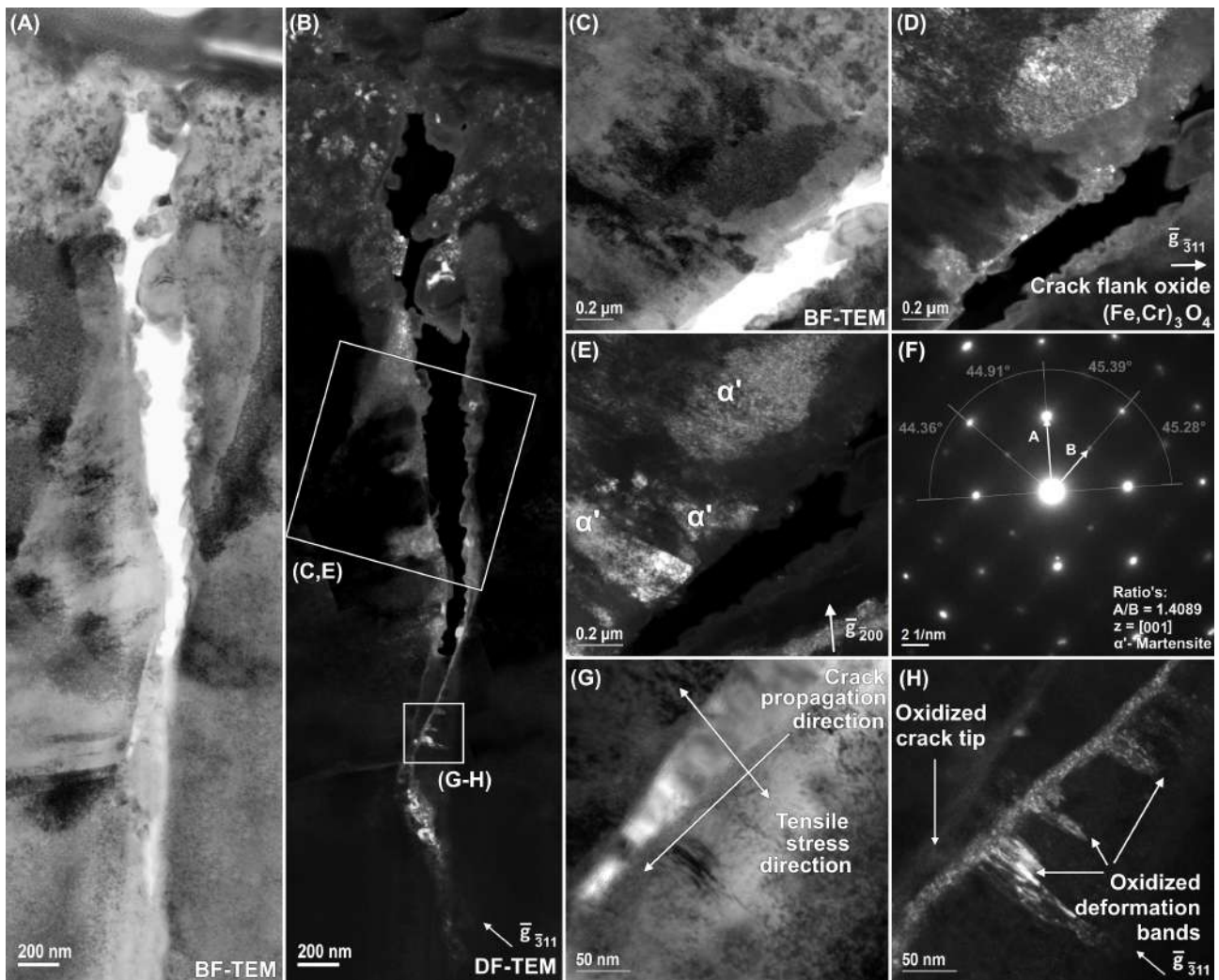


Figure 5.34: TTO-1-001 (690 MPa) L23 (A) BF-TEM and (B) corresponding oxide reflection CDF-TEM of the overview of a typical IASCC crack. (C-D) CDF-TEM and corresponding oxide DP of the crack flank oxide. (E-F) CDF-TEM and corresponding DP of adjacent metallic phase aside of the crack. (G-H) BF-TEM and corresponding oxide CDF-TEM of preferential oxidation along deformation bands.

5.4 Discussion

5.4.1 On the effect of applied external stress

Influence of the active stress state on the initiation and propagation of IASCC cracks may first be derived from the crack overview table listed in Tab. 5.1. Primarily, it is evident that crack propagation was facilitated by the applied tensile stress while it acted upon the crack in cleavage-mode orientation. Contrastingly, crack tips propagating in the otherwise shearing-mode orientation were found to be arrested far more frequently. These observations are reminiscent of previous studies where an influence of the tensile stress was also found to play a role [70]. Likewise, in consideration of the acting stress value, it was evident that crack branching at oxidized triple junctions occurred more frequently in lower stressed specimens compared to otherwise higher stressed specimens. Moreover, as was observed from TTO-1-053 (390 MPa), branching occurred more frequently at triple junctions where one grain boundary was orientated favorably with respect of the tensile stress. It is possible that crack branching at lower stresses occurs more easily within specimens exposed longer to the corroding environment where the crack is given more time to develop.

5.4.1.1 Deformation twinning

Consistent with previous studies [70, 306], the observations of deformation- and deformation twin-bands as linear defects adjacent to cracks within the microstructure of specimen TTO-1-053 (390 MPa) are reasoned to be related to initiation and propagation of cracks along the grain boundary. Deformation bands accumulate a high number of dislocations along specified crystallographic planes of the crystal lattice, and may nucleate as a result of increased external stresses induced by the crack propagation. To that respect, the deformation bands are frequently observed adjacent to the crack flanks. At the same time, deformation twins are generally observed; their density tends to increase the closer towards the propagating intergranular crack. Considering the higher active tensile stresses at the crack tip, this observation suggests the nucleation of deformation twins occurs at the crack tip as a consequence of the crack propagation. Indeed, observations of twinning well-below the irradiated yield stress (≈ 1000 MPa) close to the tips suggests that the nucleation of deformation twins occurs as a consequence of the lattice deformation induced by the propagation of the crack.

Relating to specimens TTO-1-001 (690 MPa) and TTO-1-090 (700 MPa - non-native oxide), it is also observed that deformation twins extend from the crack flanks into the bulk matrix. Especially at higher stresses, larger densities of deformation twins were empirically observed in close vicinity of the crack tip, see Figs. 5.12 and 5.13. Apart from the twinning at the crack tip, multiple twin systems were also seen to interact with the leading grain boundaries further away from the tip, see Fig. 5.14. These transformations are often accompanied with the abrupt migrations of the grain boundary interface, which is induced by the deposition or removal of solutes from the matrix [307]. This phenomenon is otherwise described as DIGM [307, 308]. The growth of one crystal grain at the expense of the other in association to DIGM, has been observed in previous investigations involving crack growth under the influences of external stresses [24, 298]. DIGM may hint towards the contribution of IASCC-relevant phenomena such as grain boundary sliding [147] and separation [148]. Indeed, stress build-up in a mobile segment of the grain boundary enhanced by the diffusion of solutes contributes to this migration. To that end, DIGM may promote several dissociation reactions of the grain boundary interface, ultimately leading the way for possible intergranular crack initiation.

DIGM should also be contemplated with respect to the chemical composition of the grain boundary interface, especially in relationship with the intersecting twinning systems that were observed ahead

of the crack tip in Fig. 5.14. These twins were found to be enriched by Ni and Si while also inhomogeneously affecting the local grain boundary chemistry ahead of the crack, see Fig. 5.26. If the enrichment of twin interfaces is due to the processes of RIS, then this signifies that they already nucleated prior to the initiation of the crack and therefore do not stem from the crack propagation itself. In this respect, it is important to note that local stress caused by the lattice deformation of the expanding deformation twin can concentrate at the grain boundary interface. In association with DIGM, this stress build-up may further enhance the susceptibility to intergranular cracking [70,306]. In other words, deformation twins intercepted by a grain boundary prior to the initiation of the crack can act as preferential crack initiation sites at the grain boundary, or otherwise, serve as means to facilitate the crack propagation when the crack has already nucleated. To that end, distinction between twins that have formed on the account of crack propagation, or those that were priorly present and may have induced the crack in the first place, is sometimes difficult. In agreement with the study on twinning systems in FCC metals, Rémy [309] indicated that readily present twins interacting with the grain boundary may lead to crack initiation sites as well as facilitate the propagation of already nucleated cracks. Such twins may have formed to a moderate degree during the manufacturing and annealing steps of the metal, under prior cold-working of the material, or perhaps due to the bearing of plasticity to form nano-twins induced by the intense neutron-irradiation [148,310]. An additional factor to consider is that deformation twins may forcefully lead to potential transgranular propagation of cracks, although this was not observed.

Apart from the nucleation of deformation twins, an additional characteristic to consider is also that dislocations may pile-up at the leading grain boundary in front of the crack tip or sometimes interact with readily present twin-structures, see Fig. 5.11C. Especially in highly irradiated materials where defects play a significant role, dislocation build-up may produce additional internal stresses at the grain boundary due to their slip-interaction with the grain boundary. This localized stress may come into effect as a consequence of grain boundary sliding due to dislocation absorption in front of the leading crack tip, which may then be regarded as a prelude to intergranular failure [150]. Otherwise, the movement of dislocations may become hampered at local twin-interfaces, leading to an increased strain-hardening ability of the material [48,65]. This way of material strengthening is otherwise understood as the dynamic Hall-Petch effect [71].

5.4.1.2 Martensite transformation

In the case of austenitic steels, plastic deformation generally occurs either through the classic dislocation motion or through displacive lattice translations such as deformation-induced twinning and phase transformations. The competition is considered largely to be a thermodynamical driven process which is dependent on the material properties. The observation of martensite in close vicinity to intergranular crack at high-temperature water conditions is a remarkable feature in the sense that such phase transformations are more commonly reported at and below room temperatures [62]. However, in agreement with the literature, martensite transformations were observed either in relation to LWR environments or associated with intergranular cracking in both irradiated [37,284,311–313] and non-irradiated materials [72,90,314,315]. Interesting facts from these works include the findings of Bruemmer et al. [284], who reported possible martensite formation consistent with their microstructural findings of intergranular cracks in irradiated 304 SS and 316 SS exposed to simulated BWR environments. Karlsen et al. [311] observed the indirect formation of α' -martensite through the intermediate HCP ϵ -martensite in strained irradiated SUS 304 exposed to a simulated PWR environment. In that context, the nucleation of martensite has been largely attributed to the loss of Ni as an austenitic stabilizer in the matrix as a consequence of RIS at the grain boundaries. Other studies have also pointed out the stress-assisted dependency of the martensite phase-transformations [84,316,317]; an

aspect that is under the current circumstances relevant close to crack initiation and propagation. After nucleation, the finite-volumes of martensite may significantly affect the bulk mechanical properties. Martensitic transformation is known to impede on the dislocation motion which can imply a localized increase in hardening. The pile-up of dislocations at impenetrable interfaces such as phase-transformed martensite may cause an effective increase in strain-hardening that can lead to an increased cracking susceptibility [74, 311].

In the current observations, martensitic transformations were perceived and discussed in section 5.3.2.3. Microstructural characterization of these martensitic phases were performed in specimens TTO-1-053 (390 MPa) and TTO-1-066 (280 MPa - cyclic loading) within Figs. 5.16, 5.17, 5.18 and Fig. 5.19 respectively. Some studies have linked their formation to the initiation or propagation of intergranular cracks, however, rarely though were these phase transformations associated with the appropriate diffraction orientation relationships that uniquely distinguished their presence. To that end, the analysis of some of the DPs that defined the formation of ϵ - and α' -martensitic phases is considered somewhat revolutionary within this investigation.

Specifically relating to specimen -053, α' -martensitic laths were primarily observed extending from the crack tip and leading grain boundary without evidence for the intermediary HCP ϵ -martensite. It is unlikely that the observed martensite formation is related to initial cold-work or as an artefact of the specimen preparation. Rather, it is reasoned that its formation is associated with large lattice deformations inherent to the crack propagation; a process which is stress-assisted at the crack tip where most martensite structures were observed. The deformation may have resulted in the direct transformation of austenite into martensite ($\gamma \rightarrow \alpha'$) in close vicinity to the crack tip. It is known that strain-induced α' -martensite not only has a higher strength [85] but also a larger volume per atom [88] than the parent austenite matrix. This may create a considerable amount of internal coherency strains, which increases the susceptibility to fatigue cracking overall [90]. Additionally, Figs. 5.17A and 5.18A clearly illustrate substantial regions of highly dislocated structures in-between the intersections of the martensitic laths with the grain boundaries. The following can be linked to the lack of dislocation glide and the inadequate strain to nearby slip planes. In that sense, martensitic transformation may lead to an increase in local stresses the grain boundary interface; thus promoting intergranular cracking as a result. Additionally, the interfaces between the austenite and martensite phase structures can provide low energy paths promoting further cracking [37].

An alternative explanation aside from the intense deformation may be found in the high irradiation exposures (60 – 80 dpa; neutron-irradiated) to which these thimble tube materials were subjected to. STEM-HAADF EDS investigations of the as-irradiated microstructure shown in Fig. 5.26, demonstrate that a significant withdrawal of the amount of structural Ni from the matrix. This change in Ni concentration is effectuated by the processes associated with RIS, which manifests itself through the elemental segregation of Ni at the grain boundary interfaces and through the nucleation of densely populated Ni and Si clusters within the matrix adjacent to the grain boundary. Surrounding such precipitates, a Ni depleted region typically of the order of the RIS elemental diffusion distance (estimated to be around several to ten(s) of nm) was found. Additionally, adjacent to the grain boundaries and alongside intergranular cracks, a typical W-shaped may be observed within the Ni spectral map specifically, see Fig. 5.27. It is possible that these forms of Ni-depletion, may affect the structural lattice into a metastable state following the effects of neutron-irradiation. Using the Schaeffler diagram in Fig. 2.3 as a reference, it becomes evident that reducing the equivalent Ni concentration would cause 316L SS to move ever closer to a greater austenite instability. That is, a reduction in Ni on the accounts of neutron-irradiation, may promotes the formation of BCC-stable lattices like α' martensite and α -ferrite correspondingly. This reasoning is strongly supported by the evidence provided by Gusev

et al. [318], who showed that the formation of α' -martensite was promoted to a great extent in already low Ni-based stainless steels exposed to high neutron doses under PWR-relevant operating conditions.

As illustrated in Figs. 5.33 and 5.34, some preferential oxidation along microstructural features and interfaces adjacent to the crack tips were discovered. In the latter case, the oxides seemed to nucleate in the form of finger-like configurations along the orientation of deformation phases that were reminiscent of BCC martensite. To that extent, these results are reminiscent of the findings of Chang et al. [72] in his investigation of the effects of martensites on the oxidation processes of 316L SS (20% CW). Preferential oxidation of strain-induced α' -martensite was deemed to be possible due to its lower atomic packing factor (larger volume per atom) than the parent austenite or due to its higher defect density, suggesting an easier ingress of oxides through its widened metallic configuration. The ingress may be made possible along the martensitic phase resulting in the typical oxide fingers or in-between its interface with the parent austenite. It is noted that earlier studies [97, 218] have also seen the development of oxide fingers along the crack sides of CW SSs in high-temperature water, however these features were solely attributed to the oxidation of the slip bands, which was equally observed on similar occasions.

5.4.2 Stress-assisted oxidation at the crack tip

Intergranular oxidation ahead of propagating crack tips in stainless steels subjected to PWR conditions has been observed on several occasions [97, 220, 231, 284]. Although it was readily predicted that the effective stress concentration at the crack tip facilitated the crack tip oxidation [97, 104], to the best of our knowledge, no such stress-dependent effect has yet been empirically revealed. To that end, Figs. 5.24, 5.25, and 5.26 demonstrate prime examples of IASCC crack tips showcasing oxide intrusions into the leading grain boundary; the lengths of which, for crack tips appertaining to specimens tested under increasing stress conditions, are displayed in Tab. 5.2. At low levels of applied macroscopic stress, oxidation in front of the crack tips remains moderately comparable to known literature data [299]. Under these conditions, the oxidation is mainly determined by the effects of the high neutron-irradiation doses [128, 226] and prior cold-work treatment [169], both have shown to increase the oxidation rates in laboratory experiments. However, as the applied macroscopic stress increases, an effective increase in mean oxidation length in front of the crack tips can be observed. In Fig. 5.35, the average oxide intrusion lengths in front of the crack tip is displayed, normalized to the average value of the sample with the lowest stress as a function of stress. The normalization of the data is performed in order to solely illustrate the increase as a consequence of increasing tensile stress. This trend demonstrates an exponential effect; a phenomenon which is reminiscent of Evans's stress-assisted grain boundary oxidation model (SAGBO) [233]. Accordingly, the acting stress at the crack tip may assist in the transport of diffusive corroding species within the intergranular oxide along diffusion paths constituted of internal oxide defects. Empirical observations of thin fracture bands within the intergranular oxide at the crack tip, as seen in Fig. 5.22B, may be deemed as such fast-diffusion paths for the intergranular oxide species [220].

To assess the stress-assisted oxidation along the crack tip, the SAGBO model evaluates the growth rate of the oxide intrusion in the stressed state $\dot{\ell}_\sigma$ with respect to its growth under a stress-free condition $\dot{\ell}_0$. To that end, a SAGBO ratio parameter Φ_{SAGBO} is derived which is explained in more detail within section 2.5.3.2:

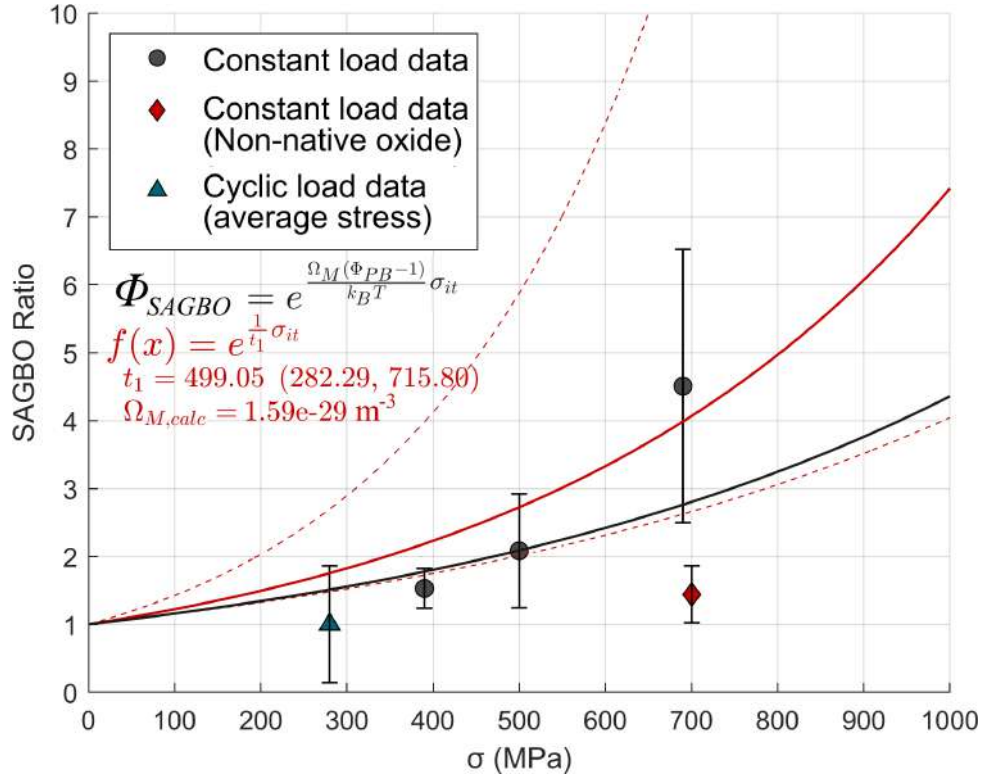


Figure 5.35: Mean intergranular oxidation lengths with corresponding standard errors on the oxide intrusions measurements, normalized to the specimen with the lowest macroscopic stress, for crack tips extracted from O-rings tested under increased stress conditions.

In retrospect of equations 2.48-2.50 in the stress-assisted grain boundary oxidation (SAGBO) model:

$$\dot{l}_\sigma \propto \frac{D_v C_{it}}{\ell} \exp \left[\frac{\sigma_{it} \Omega_M (\Phi_{PB} - 1)}{k_b T} \right] \quad (5.4)$$

$$\Phi_{SAGBO} = \left(\frac{\dot{l}_\sigma}{\dot{l}_0} \right) = \exp \left[\frac{\sigma_{it} \Omega_M (\Phi_{PB} - 1)}{k_b T} \right] \quad (5.5)$$

whereat σ_{it} represents the tensile stress at the oxide intrusion tip in front of the crack tip, Ω_M the total metal alloy volume (calculated from 316 SS's molar volume [319] as $1.16e - 29 \text{ m}^{-3}$), Φ_{PB} the Pilling-Bedworth ratio (known to be 2.07 for chromium oxides at the crack tip [320]), k_B Boltzmann's constant, and $T = 593 \text{ K}$ the ambient PWR testing temperature.

Extrapolating the stress-assisted oxidation effect from a state of zero-effective stress in accordance to equation 2.50 is displayed by the black trendline in Fig. 5.35. In first approximation, the stress intensities at the oxide intrusion tips σ_{it} are evaluated equal to the O-ring's macroscopic tensile stresses along the fracture surface. However, stress concentration at the crack tip, as a consequence of the deformation-induced twinning plasticity, local dislocation activity, or surrounding grain orientation, may lead to an even more increased effect as is currently predicted. Still, by taking the standard material input parameters, the stress-assisted enhancement factor correlates well with the increase in the normalized average intrusion lengths displayed in Tab. 5.2. The oxide intrusion lengths markedly increase by a factor of 5 with a local stress of 1000 MPa predicted at the oxide inclusion tip. However,

the distinct outlier corresponding to the intrusion lengths of TTO-1-090 (700 MPa - non-native oxide) does not stroke with the trend curve and is possibly related to an overestimated stress at the crack tip (see the discussion in the subsequent paragraph). Another way to interpret these results is to perform a best-fit exponential regression analysis with corresponding 90% confidence intervals on the intrusion lengths dataset, displayed by the red trendlines. Correspondingly, the fitting parameter $1/t_1$ can be equated to the exponential parameters within the stress-free SAGBO factor. Assuming a high-temperature water environment of $T = 613.15\text{K}$ forming a chromite oxide with $\Phi_{PB} = 2.07$ at the crack tip, a calculated total metal alloy volume $\Omega_{M,calc} = 1.59E - 29$ can be derived. The latter parameter is close to the actual metal alloy of 316L SS, indicating a good match of stress-assisted oxidation for stainless steels.

5.4.3 In broader perspective with the literature

Our observations of stress-assisted grain boundary intrusions could be differentiated from the limited available literature data on crack tip oxidation in stainless steels [224, 284, 299, 305]. Typically, the reported oxide penetration depths ahead of propagating tips are of the order of hundreds of nm. However, in this study a record value of over $1 \mu\text{m}$ is reported within the highest stressed specimen TTO-1-001 (690 MPa). This variation could be reasoned in terms of varying material and testing conditions, exposure times to the corrosive environment, and due to the effective stress concentration at the crack tip. It is further assumed that the high irradiated doses of the flux thimble tube material (60 – 80 dpa) and its applied level of cold-work (20% CW) have significant impacts on the oxidation rates at the IASCC crack tip [128, 169, 226].

Observations of the crack tips have also shown some similarities with respective works in the literature. Some oxidized tips indicated features ahead of the crack tip that could be considered as evidence of fast-diffusion paths for oxygen species [220]. Most significantly, these features relate to the high densities of defect clusters signified by the increased dislocation contrast around the crack tips and the evidence of brittle fracture bands within the oxide intrusions. On the other hand, in studying the morphology of the crack path, cracks typically showed considerable evidence of the step-like cracking phenomena featured prominently within the leading IASCC mechanisms. When every observation including the stress-assisted oxidation at the crack tip is taken into account, these findings together clearly demonstrate evidence for all the mechanisms associated with the internal oxidation model.

Promptly, this questions immediately the oxide diffusion rates at the crack tip in consideration of the fast CGRs observed in stainless steels. Arioka et al. [173] illustrated that on the basis of un-irradiated 316L SS (20% CW) compact tension-type specimens, the intergranular SCC CGR is of the order of about $1.00 E-7 \text{ mm/s}$. On the account of the irradiation-induced processes like RH and RE, it is expected that the CGR in irradiated 316L SS (20% CW) is going to be faster than this, perhaps of one or several magnitudes difference. However, such CGR data for irradiated SSs are generally considered to be in short supply. In terms of averaged cracking rates in other materials, it can be said that these estimates are generally reviewed as very fast in the literature. Thus, evidently proving that the oxide intrusion rate is faster than the CGR is challenging when solely based upon microscopy within this work. However, as one may also consider the step-like cracking process, which is generally assumed to be the more prevalent phenomenon based upon other works [104, 105, 216, 217], providing evidence for fast oxide diffusion rates in favor of the internal oxidation model is typically not required. In the step-like cracking model, crack tip oxidation occurs solely within the time when the crack has arrested after dissolving all the oxidized material at the tip. The size and duration of the crack propagation steps determine the actual CGRs experienced in susceptible materials. Some of the microprocesses that influence the step-like crack growth include: (i) stress concentrations induced by strain localization of

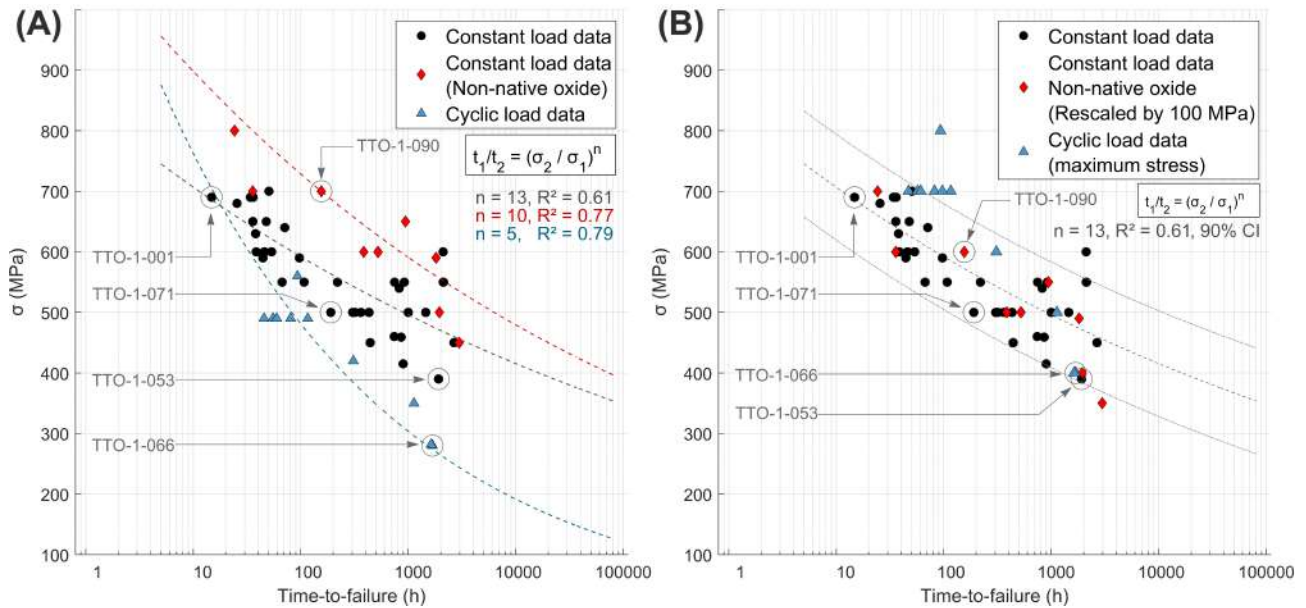


Figure 5.36: (A) Overview of the TTFs of the constant load native, non-native, and cyclic loaded O-ring data in terms of stress [294]. Model analysis of data is performed through equation 2.37, statistically optimized to match the most ideal SCC corrosion susceptibility parameter n . (B) Adjusted stress interpretation of the non-native oxide and cyclic loaded O-ring failures on the account of possible crack initiation from the O-ring's inner surface and peak stress intensity values, respectively.

the material in front of the crack tip, (ii) enhanced oxidation along the dislocation networks in those strain localized regions, and (iii) local crack extension steps at the oxidized region in front of the crack tip [105]. All three of these features in favor of step-like cracking have been observed.

The final CGR values in un-irradiated 316L SS (20% CW) of Arioka et al. [173] are only estimates of the final stage of rupture in the fast-propagation regime, which is known to be characterized by fast propagation rates. They do not however, take into account the total time that is required for preceding growth stages of the crack i.e., the crack incubation and slow growth processes, and the time between each crack rupturing event following step-like cracking. As issued before [159,160], these stages may require a long time for them to set-up the prerequisite conditions before the final rupture of IASCC can take place. Indeed, Mayuzumi et al. [321] tentatively concluded that for 316L SS the SCC incubation time was of the order of hundreds of hours, 490 h to be exact. This prerequisite time for just the incubation period alone may already significantly lengthen to complete failure time of the crack. This also does not yet take into account the slow growth processes wherein the crack grows under an applied stress well below the critical value for the fracture. Arguably, when taking into account the time that is required for the preceding crack growth stages, the known CGRs may reduce by several orders of magnitude when considering the total failure time. Additionally, when taking into account the aspect of stress-assisted oxidation in front of the crack tip, experimental measurements indicate that, at all times, the intergranular cracking grows within the pre-established oxide intrusion in front of the crack tip. This representation provides strong support for all mechanisms associated to the internal oxidation mechanism that describes the oxide embrittlement of the leading metallic matrix ahead of an advancing crack [24, 187, 188, 214, 227]. Intergranular oxides are then reasoned to be responsible for the lowering of the fracture resistance at the grain boundary, providing a facilitated means for intergranular crack propagation within the leading oxide intrusion.

5.4.4 Mechanical failure data

The following discusses how the previous findings on crack tip oxidation lengths contribute to the failures of O-rings with an abraded outer oxide surface and those being subjected to cyclic loading, respectively TTO-1-090 (700 MPa - non-native oxide) and TTO-1-066 (280 MPa - cyclic loading). Fig. 5.36A displays the O-ring failure times as a function of stress in correlation with the other constant-load stress tested O-rings. The corresponding model curves are drawn for each dataset represented by dashed lines, calculated in accordance to the proportionality ratio between TTFs and failure stress, given by equation 2.37. Initial guesses for the (t_1, σ_1) values are taken from tested O-rings within that group. This ratio is developed in relation to the subcritical crack propagation model by Konstantinović [162], and is dependent on the cracking susceptibility parameter n . Fundamentally, this parameter stems from the empirical power law for crack growth and essentially denotes a material's susceptibility to cracking [228]. Within the SCP model, the higher the value of n , the more reliable a material's resistance to fracture. To that end, the cracking susceptibility parameter is a good measure for correlating the TTFs for specimens tested to different sample conditions. Respectively, each curve is drawn for the statistically optimized cracking susceptibility parameter n , correlating the TTFs at any point with the respective failure stress.

In retrospect of equation 2.37 described in the subcritical crack propagation (SCP) model:

$$t \propto \frac{1}{\sigma^n} \quad (5.6)$$

$$\frac{t_1}{t_2} = \left(\frac{\sigma_2}{\sigma_1} \right)^n \quad (5.7)$$

5.4.4.1 On the effect of oxide abrasion

As observed in Fig. 5.36A, the apparent shift rightwards to higher TTFs reveals that the non-native oxide specimens are less susceptible to IASCC failure after the removal of the native PWR oxide layer on the outer O-ring's surface. The best-fit cracking susceptibility parameter also lowers to $n = 10$ in comparison to other constant load compression tested O-rings with their native oxide intact. Non-native oxide specimens are seen to fail at a later point in time under a given stress state, or equally, at higher stresses under a preset TTF compared to other native oxide specimens. This change indicates that the removal of the outer surface oxide has altered some aspect of the cracking mechanism in relation to the other constant-load specimens. In the sense that a less established oxide layer should expectedly be more susceptible tear-down and thus to IASCC failure, this apparent TTF shift appears counterintuitive at first sight. However, this discrepancy may be reasoned from two separate point of views: (i) one relating to the possibility of crack initiation from the inner fracture surface where a more established oxide still remains, (ii) or second, from a SCP point of view wherein the probability of cracking in a less voluminous oxide tends to be greater instead.

- (i) From the microstructural investigation, Fig. 5.10 revealed that the duplex oxide formed along the crack flanks of TTO-1-090 (700 MPa - non-native oxide) constitutes of the same oxide morphology as observed in other specimens [232]. Fig. 5.13 revealed the nucleation of broad deformation twinning as similarly observed in other high stressed specimens. However, as illustrated in Fig. 5.35, one big difference for cracks resulting from the non-native oxide specimen TTO-1-090 (700 MPa - non-native oxide) is that the crack tips produced far less oxidized intrusion lengths as should be expected in accordance to the SAGBO model [320]. Intergranular oxidation in the

non-native oxide specimen therefore does not stroke with the expected oxidation lengths at the given stress state in comparison to other specimens.

Accordingly, this difference could be related to a lower stress-enhanced oxidation at the crack tip; possibly in relation to the initiation of cracking in regions of the O-ring where lower effective stresses occurred. Indeed, finite-element modelling of the Von Mises stresses have shown that the inner part of the O-ring constituted to a lower effective maximum stress during the compression testing than the outer surface [161]. Arguably, following the abrasion of the outer surface oxide, crack initiation may have occurred from the lower stressed inner surface as opposed from the anticipated outer surface instead. The probability of crack initiation from the inner surface whereat a sufficiently saturated oxide formed under aerated conditions still remained, may have increased during testing. This observation is explicated from the view of the SCP process wherein crack initiation in brittle oxides is dominated by the inherent structural flaws that exist within these oxides. The probability of cracking tends to be effectively greater in more voluminous oxides. Consequently, following the initiation from the inner surface, the lowered oxide intrusion lengths are thus interpreted by the reduced stresses that take place near the crack tips at the point of initiation. In this reasoning, it can be argued that the O-ring failures with the non-native oxide surface must be plotted against an overestimated critical stress in the mechanical failure data displayed in Fig. 5.36B. Indeed, by lowering the stresses by an arbitrary value of about 100 MPa, all TTFs of the non-native oxide specimens shift into the confidence interval of the other constant-load O-ring specimens.

Consistent with the observation of crack initiation from the O-ring's inner surface following the abrasion of the outer surface oxide, is that the onset of cracking at all times could not be ruled out in either failed or non-failed O-ring specimens [294]. This observation is in agreement with evidence from the available literature, which shows that crack initiation within O-ring specimens was seen either from the anticipated outer surface, from the less anticipated inner surface, or within both [322]. Section 5.1 additionally provided clear examples of inner surface initiated cracks underneath the load bearing points which nearly caused structural failure of tested O-rings.

- (ii) Alternatively, from a stochastic SCP viewpoint, the probability of crack initiation tends to be greater in a less voluminous non-native oxide than in a thicker and more saturated native oxide. As argued within section 2.5.3.1, there is a higher statistical probability to find inherent flaws in a thicker oxide which may then present a higher probability of failure through the weakest-link argument as a result. More voluminous oxides are therefore reasoned to crack more easily under a given stress state. When low stresses and thus larger time-to-failures are in effect, arguably the more voluminous oxide fails faster simply because more time is allowed for the crack to stochastically initiate within the passive oxide layer. Therefore, brittle materials such as crack-susceptible oxides on stainless steel in a similar fashion as ceramic oxides [228], may be subjugated to a so-called volume-effect dependent on their initial oxide strength.

Since the Weibull probability distribution is frequently used to describe specimen failures that are reliant on statistical parameters, it is reasonable to apply it here in terms of a probabilistic description of the oxide strength σ :

In retrospect of the subcritical crack propagation (SCP) model described in section 2.5.3.1 [162], the volume-effect is given by equation 2.31:

$$P_f(\sigma, V) = 1 - \exp \left[-\frac{V}{\delta V} \left(\frac{\sigma}{\sigma_i} \right)^m \right] \quad (5.8)$$

The essence of the volume-effect is represented by the ratio V/V_i , wherein V represents the non-native oxide volume obtained post abrasion of the oxide surface and V_i the saturated oxide surface volume under common conditions, see equation 2.31. The volume-effect ratio is incorporated within the exponential probability function. However, with respect to the failure times, it is considered very difficult to equate the TTFs both in terms of stress and in terms of volume. That is, there is currently no analytical expression that incorporates both directly within the model curves as expressed by equation 2.37. Still, within first approximation, the volume-effect may be effectively estimated from the 90% failure envelopes of the native and non-native oxide specimens in Fig. 5.37. Fundamentally, the effect stems from the difference in SCC susceptibility parameters n between native and non-native specimens. Essentially, those differences indicate the steepness of the model curves which creates a wedge-effect from lower to higher TTFs. In quantitative agreement as indicated by the model curves, the volume-effect is expected to decrease at low levels of applied stress or for samples subjected for longer times in the corrosive environment, simply because of the surface oxide tends to saturate to thicknesses that are expected for native oxide specimens after longer exposure times. Indeed, after long TTFs, it is expected that for saturated oxides the volume-effect tends to disappear when $V/V_i = 1$. However, for lower TTFs instead where $V/V_i \ll 1$, the volume-effect may be used to reasonably explain the reduced susceptibility to failure for non-native oxide specimens like for TTO-1-090 (700 MPa - non-native oxide), merely because there will be less predicted oxidation in front of the crack tip. Rough estimates of the volume-effect on the TTF data result in a reduction of about 50% oxidation for non-native oxide specimens; an estimate which is in reasonable agreement with the reduced intrusion lengths for specimen -090 in Fig. 5.35.

Both viewpoints are believed to play a role in the crack initiation for non-native oxide specimens. Their validity is dependent on whether the crack initiates from the inner (mechanism (i)) or outer (mechanism (ii)) O-ring fracture surface. However, in the experimental compression procedure, it is often difficult to determine the exact onset of cracking and thus which mechanism tends to be preferred. To that end, two possible viewpoints of discussing the effect of non-native oxide specimens are presented.

5.4.4.2 On the effect of cyclic loading

Concerning the TTFs of cyclic loaded O-rings, it was observed by Bosch et al. that the stress threshold below which no IASCC failure occurs under constant loading, shifts from about 40% [161] down to only 19% of the irradiated yield stress under transient cyclic loading [323]. In that regard, cyclic loading was argued to have a detrimental effect on the component lifetime and thus on the IASCC susceptibility of tested O-rings. Similar conclusions can be drawn from the TTFs and the corresponding model curves for constant and cyclic loaded O-rings displayed in Fig. 5.36A. Evidently, the cyclic failures occur at a significantly lower stress as compared to constant loaded specimens. This decrease is encapsulated by a much steeper model curve in the analysis of the specimen TTFs. Expressed in terms of the SCC susceptibility parameter n , a drastic change from constant ($n = 13$) to cyclic loading conditions ($n = 5$) can be observed. This transition suggests that material fatigue may influence the cracking in ways under cyclic loading that were not the observed under common constant load conditions.

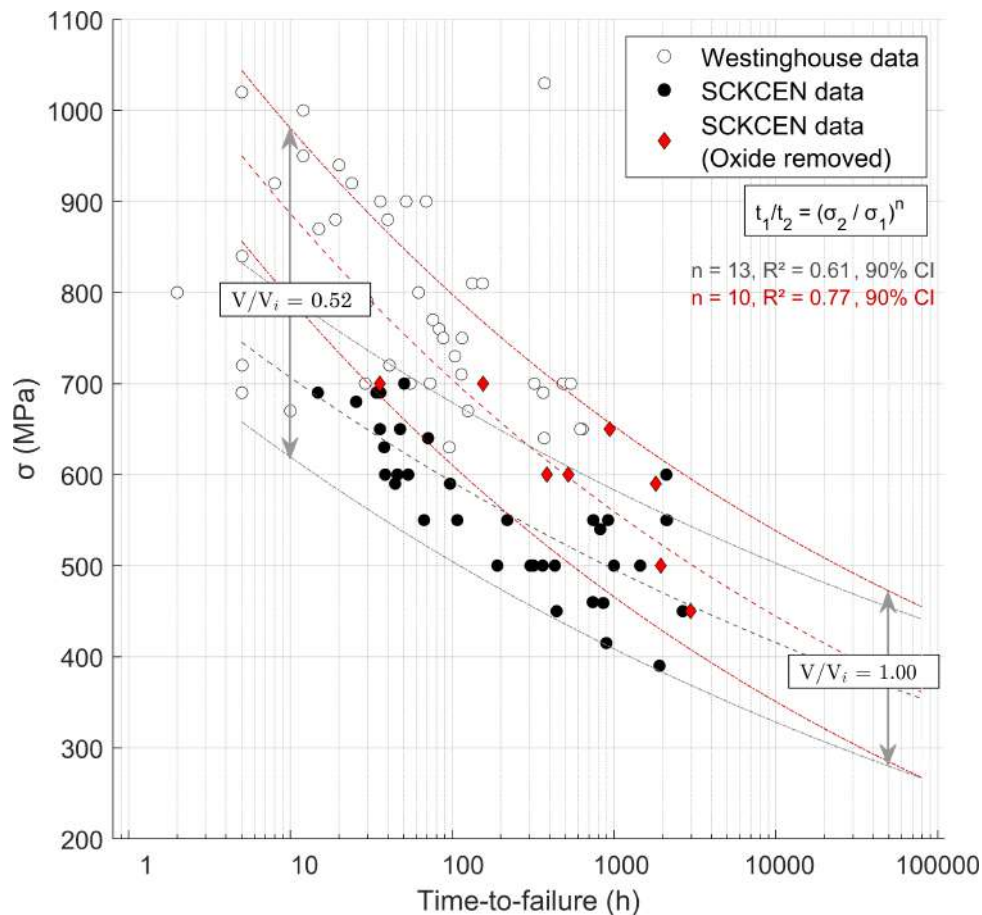


Figure 5.37: Time-to-failure data of constant vs. non-native oxide O-ring data in evaluation of the oxide strength volume-effect. Model curves and corresponding 90% coincidence intervals are drawn to both native and non-native oxide specimens relating to equation 2.37, optimized to match the most ideal SCC corrosion susceptibility parameter n .

However, one has to take into account the fact that the TTF of the samples tested under cyclic loading are represented by an average stress. Since the crack tip oxidation results discussed in the previous sections indicate that stress plays the most significant role for oxide formation, one can safely assume that maximum stress during each transient load cycle needs to be taken into account as a proper parameter to interpret the failures under cyclic loading. Indeed, by plotting TTF data under cyclic loading against maximum stress, all data shift upwards in stress into the predicted failure regime delineated by the confidence intervals of constant loaded specimens, see Fig. 5.36B. To that end, it may be argued that crack propagation is facilitated at the peak stresses, which may then lead to shorter TTF during cyclic loading.

From the microstructural analysis, the change in cracking mechanism under cyclic loading becomes evident from the analysis of IASCC cracks stemming from specimen TFO-1-066 (280 MPa - cyclic loading). Indeed, cyclic crack propagation has been linked to hydrogen-assisted fatigue cracking [90], especially in relation to the formation of susceptible martensite phases adjacent to crack flanks. Microstructural analyses have shown stress-induced austenite to martensite phase transformations adjacent to fatigue cracks in accordance to the Olsen-Cohen model, see Fig. 5.19. Martensite phases are typically promoted under high stressed conditions [84, 312, 316, 317] in association to presence of hydrogen [90, 324]. Especially following the exposure to a PWR environment, mobile hydrogen may diffuse into the crack and segregate at leading crack tip grain boundaries. Its presence promotes and increases the formation of HCP ϵ -martensite laths while under the influence of straining [90].

In accordance to Bogers formalism [87], aggregated BCC α' -martensite islands may then nucleate following the shear interactions of two ϵ -martensite bands within the parent austenitic phase. Prior observations of martensite phases at the crack tips of fatigue cracks in 304L SS are in support of this reasoning [90] and fully correspond to the findings displayed in Fig. 5.19. In regards to the influence of martensites on the cracking aspects of stainless steels, please refer to the argumentation provided in section 5.4.1.2. In agreement with the mechanical load testing, the martensitic phase transformation following cycling fatigue leads to a decreased fatigued life-time.

Further microscopical investigations have also shown a substantially more deformed microstructure near the crack tip and along its leading grain boundary. Fig. 5.15 shows the neighboring grain's ability to bear large amounts of shear by developing deformation-induced twins in close vicinity to the intergranular crack. At sufficiently high stresses, these deformation products are known to form along finite-volumes of the close-packed $\{111\}$ high symmetry austenitic planes. The displaced lattice volumes that they induce, can effectively impede on the dislocation glide path and thus contribute to the transformation strengthening of the material [62, 325]. When the critical twinning stress is reached, dislocations may pile up at deformation-induced twin interfaces, leading to consequent strain hardening [85] and an increased susceptibility to brittle fracturing. This process is expected to be enhanced by the peak stress intensities at the crack tip occurring during each consequent load cycle. Reasonable estimates of the SAGBO parameter at these maximum stress intensities still show a good agreement with the expected oxidation lengths in Fig. 5.35.

5.4.5 Microchemical investigations

5.4.5.1 Regarding the role of RIS

RIS is believed to be amongst the main contributors to IASCC intergranular cracking. As investigated in Figs. 5.27 and 5.28, the STEM-HAADF EDS line scans present highly altered material compositions across unimpaired grain boundaries in comparison to the adjacent as-irradiated microstructure. Previous studies have shown that RIS reaches a steady state condition after an irradiation dose of about 5 dpa in austenitic SSs [22]. However, after high irradiation doses up to 60 (TTO-1-053; Fig. 5.27) or even 80 dpa (-090; Fig. 5.28), the elemental segregation and depletion profiles are seen to be moderately more enhanced in comparison to other investigations in materials irradiated to low-to-moderate doses [42, 121]. Especially for specimen TTO-1-090, some strong enrichment profiles for Ni, Si and P were observed. Depletion of Fe and Cr is also considerably evident from the elemental spectra. The roles of the individual elements are briefly outlined below:

- **Fe and Cr:** The depletion of Fe and Cr may cause some significant volume change of structural material at the grain boundary, therefore strongly implicating both the initiation or propagation of intergranular cracking. Many studies have shown that Cr-depletion has an enhancing effect towards IASCC [17, 127, 128], the main conclusions of are mainly the fact that less concentrated Cr may leave the grain boundary less susceptible to global oxidation, possibly by forming a poorer quality chromite that is more sensitive to brittle cracking [127, 128].
- **Ni:** Ni-enrichment at the grain boundary as a consequence of RIS should be differentiated from the enrichment that takes place due to the the propagation of (IA)SCC cracks. In the latter case, reasonable explanations for the enriched Ni layers were already provided in section 4.3.4 for the subset of high Si SSs tapered specimens. Ni-enrichment through irradiation of structural materials is very common as it occurs over a wide temperature range at various irradiation doses. Busby [121] concluded Ni cannot be considered as a mitigating factor for IASCC as the cracking

steadily increased to approximately twice the bulk concentration at low doses along with an ever increasing cracking susceptibility. The role of Ni may also be important in the nucleation processes of martensites, as readily explained in section 5.4.1.2.

- **Mn and Mo:** Regarding some transition elements, the influence of Mn and Mo is investigated by Bruemmer et al. [42]. Manganese expectedly depletes because of its strong diffusivity. However, its depletion has been shown to cause some degree of phase instability and property degradation in austenitic stainless steels [326,327]. The strong depletion of Mo is observed in other relevant studies [42], although no strong conclusions regarding its influence are drawn. Mo is known to cause some significant volume change due to its depletion because of its large misfit size in regards to base alloy elements.
- **Si and P:** In performing annealing studies on SSs, Busby [121] concluded that the enrichment of Si and P were removed at a pace similar to that of the cracking susceptibility; therefore implicating both elements to some degree as contributors to IASCC. However, the role of Si regarding intergranular cracking is still under dispute. While Yonezawa [130–132], Li [129] and Chopra [23] provide extensive evidence that shows that the increased Si concentration results in an increased cracking susceptibility in irradiated alloys, other studies performed by Chung [328] report exactly the opposite trend in alloys irradiated to the same conditions. Si tends to favorably oxidize to SiO₂ under all LWR-relevant conditions which is deemed to be considerably soluble in high-temperature water [17,121]. As a result, its presence at sufficiently high grain boundary concentrations is expected to be extremely susceptible towards IASCC. However, contemporary research has not yet brought to light the necessary concentrations of these species at the grain boundaries for such deteriorating effects to take place. Regarding the role of P, several studies reported that its effect on IASCC is either immeasurable or minor [329,330].

Tab. 5.3 presents an overview of the elemental concentrations measured at the grain boundaries for specimens TTO-1-053 (390 MPa) and -090 (700 MPa - non-native oxide). The rate of change of the elements is mostly consistent with the inverse Kirkendall (vacancy-exchange) and interstitial-solute transport mechanisms [300,301]. However, one discrepancy remains the interesting observation of Mn-enrichment at the unimpaired grain boundary of specimen -090. In truth, Mn is expected to deplete at the interface due to its rapid diffusivity following the effects of RIS and due to several transmutation reactions that take place under the effects of neutron-irradiation [42]. Its strong enrichment in this specific case is therefore unanticipated; an observation for which no rationale at this time can be provided. In some other cases, direct- or inverse-shaped W-profiles in the RIS spectra could be observed. Considering other elemental spectra during the same observations, these forms of pre-depletion and pre-segregation close by the grain boundary may suggest a strong interaction between other co-diffused elements. The shape of these profiles suggest that the elemental diffusion distance is of typically of the order of several to ten(s) of nm. This estimate is in agreement with the Ni and Si clusters observed within Fig. 5.26. The average element composition far away from the grain boundary closely corresponds to the bulk matrix composition known for 316L SS listed in Tab. 3.3.

5.4.5.2 Regarding the role of MnS inclusions

Throughout the extraction of IASCC crack tips by means of FIB-SEM, segregated MnS particles were routinely observed within the bulk material of the lamellae. Some evident examples of these particles segregating close to impaired grain boundaries were observed in Figs. 5.29 and 5.10. Manganese is added to steel to stabilize the austenitic structure since it, together with Ni, guarantees a complete austenite formation during the austenization treatment [331]. Both elements are regarded as austenite

stabilizers in the steelmaking processes. Sulfur on the other hand, commonly binds with Mn in the form of manganese sulfides, to act as a source of stress concentrator which favors the steel's machinability by reducing the cutting force [332]. However, considering the recurrent observations of surface pitting corrosion at MnS particles [29, 303, 333], degrading corrosion properties should be expected as a consequence of an increasing sulfur content. Therefore, the addition of S should be considered as a trade-off between the material's performance and its corrosion qualities.

Nonetheless, regarding intergranular crack propagation, the role of bulk segregated MnS inclusions remained thus far undetermined. Since MnS inclusions are in principle less noble than the surrounding matrix [302], it can be expected that these particles would preferentially oxidize and dissolve under high-temperature water conditions when coming into contact with an intergranular crack. Indeed, as observed within Fig. 5.29, coupled with the localized deformation slip bands close to the crack, the intergranular oxide is seen to deflect towards and surround the MnS particle. The presence of the closely segregated inclusion particle effectively changed the crack path and impeded the grain boundary failure. A similar result is observed within Fig. 5.10 for the specimen TTO-1-090 (700 MPa - non-native oxide). The demonstrated intergranular crack ultimately did not come to a full arrest at the particle. It is therefore expected that a MnS particle only impedes upon the crack propagation, but due to prolonged exposure, cracking is allowed to continue until some other type of arrest occurs. Altogether, from these observations, it is clear that MnS inclusions have a retarding effect what concerns intergranular crack propagation.

5.4.5.3 Regarding the role of intergranular inclusions

In Figs. 5.30 and 5.31, evident intergranular inclusions particles averaging between 10–50 nm in width, with a typical FCC lattice structure, were discovered along an impaired leading grain boundary in front of an IASCC crack tip. At first glance, these particles may have resembled the appearance of carbides like Cr_{23}C_6 or Cr_6C , which are known to sensitize the grain boundary [139, 314], making it more prone to IASCC cracking as a result of the locally depleted Cr concentration. However, due to the strong (Fe-, Si-) enriched signals and the fact that carbides generally have a lattice parameter that equals a third of the parent austenite phase [135], the inclusion particles are otherwise thought to be as phase-precipitated intermetallic particles, possibly induced by exposure of the material to the intense neutron-irradiation. Common intermetallic particles that arise in irradiated 316L are either the sigma- (σ), chi- (χ), or laves-phases (η) [135]. However, none of these particles are represented by the observed FCC lattice structure that was attained from the diffraction analysis of the inclusion particle. Neither do these particles nucleate at temperatures below the typical PWR operating temperature of 320–340° or are they represented by a stoichiometry that strokes with the depleted Ni and Mo signals. Alternatively, the inclusions could be related to the characteristic G-phase particles which ordinarily form in low-carbon austenitic and duplex SSs. G-phase precipitates are known nickel-silicides with a complex FCC lattice structure, possibly forming intergranularly or within the bulk material during metal ageing processes at high processing temperatures between 500 – 850°C. Their nucleation can also be induced by the austenitic stainless steel exposure to neutron irradiation [334]. This would meet every requirement for its characterization, except for the fact that the inclusion is otherwise depleted in Ni and that its lattice parameter should also expectedly be a third of that from common austenite.

To that end, it is possible that some element of the puzzle is missing in identifying these inclusion particles. Regardless, their nucleation at the grain boundary is normally considered undesirable in terms of intergranular corrosion. Intergranular inclusions may effectively cause (i) local lattice frictions and (ii) chemical volume change and inhomogeneity at the grain boundary, but also (iii) a general decrease in material ductility and fracture toughness. On the other hand, some evidence in particular

for carbides suggests that [135], processes like grain boundary separation [148] and sliding [147] are suppressed when intergranular particles are present.

5.4.6 IASCC cracking mechanisms

Given the direct observations of (i) porous features and brittle oxidized fracture bands, but also (ii) the inhomogeneous and (iii) stress-assisted oxidation ahead of propagating crack tips, it is reasoned that the internal oxide parameters play a dominant role in terms of general IASCC initiation and propagation. These findings are in good agreement with all associated mechanisms of the IO model, and most-especially the subcritical crack propagation proposed to be relevant for IASCC by Konstantinović [162]. Accordingly, intergranular cracking is best-described by a slow crack growth process occurring under an applied stress well below the critical value for oxide rupture. The stress-assisted oxidation in front of the crack tips demonstrate that the intergranular oxides grow comparable if not faster than the crack propagation rate. At all times, failure occurs within the internal oxide, determined by the probabilistic oxide strength and the bonding strength with the metal interface. Observations of multiple crack initiation sites within the oxide, and the existence of brittle fracture bands ahead of the tips, make the underlying assumption for an oxide strength dependent failure probability rather conceivable. The failure probability successfully explains the observation of multiscale fracture bands within the oxide, as is displayed in unison with the fine oxide porosity. The internal oxides are then reasoned to be responsible for the lowering of the fracture resistance at the grain boundary, providing a facilitated means for intergranular crack propagation within the leading oxide intrusion. Probability analyses illustrating the validity of the SCP model also fit well with the mechanical loading dataset of O-ring TTFs in function of their failure stress, see section 5.4.4. To that end, our results provide strong support for a stress-driven internal oxidation mechanism that describes the oxide embrittlement of the leading metallic matrix ahead of an advancing crack [24,187,188,214,227].

Chapter 6

Conclusions

Structural materials for nuclear engineering purposes are always selected through a compromise between achieving excellent metallurgical qualities (including material strength, ductility, hardness, fracture toughness etc.) on the one hand and yielding the best corrosion resistant properties on the other. This trade-off becomes increasingly more evident from the fact that the so-called strongest material is not always the most safest (i.e., free from material degradation) [22,142]. In fact, under high temperature water corroding conditions in a neutron-irradiated environment, the material properties may quickly degrade depending on a number of essential factors, most especially, the acting stress conditions.

In order to better understand the phenomenological models surrounding trans- and intergranular (irradiation-assisted) stress corrosion cracking ((IA)SCC) in stainless steels, experimental verification of the morphology and surrounding microstructure of cracks formed within the oxide along the fracture surface and within oxidized grain boundaries is required. Therefore, the purpose of this study was to extract localized regions of interest close to and beyond the crack tips of failed specimens by means of FIB-SEM analysis. Crack tips were extracted from both tested model alloys and irradiated industrial specimens subjected both to a simulated PWR-environment during testing. Microstructural investigations by means of (S)TEM illustrated that these regions close to the crack tip provided crucial information in order to elucidate the mechanisms driving the crack initiation and further crack propagation.

In the view of the fact that an experimental study such as this requires a number of essential requirements, amongst which: (i) access to unique test material, preferably stemming from in-situ NPP components, (ii) the ability to safely operate with heavily irradiated materials and (iii) access to the proper instrumentation for the required analyses, little microscopical studies on (neutron-irradiated) materials and most especially (IA)SCC cracks, have been presented thus far in the literature. Therefore, it should be noted that the results obtained within this investigation are considered to be extremely relevant for both industrial standards and for innovative material research. This work is considered as a first step in understanding the essentials surrounding IASCC cracking.

Several of the presented tools and models employed within this thesis support the development of predictive methodologies for a more secure and economically viable operation of structural materials and reactor components. With many of the world's fleet Gen II NPPs slowly transitioning towards the end of their lifetime, possibly facing operational LTE up to 60 years and beyond, the ability of predicting component failures following material degradation becomes an evermore worrying concern

for secure plant management.

6.1 Research outcomes

6.1.1 Tapered specimens

A lot of literature studies have been devoted to determining a stress threshold for crack initiation in both un-irradiated [35,36,261–263] and neutron-irradiated materials [161,322,335]. However, the large uncertainties in estimating this stress threshold, especially following the application of the constant load tests in irradiated materials, somewhat restrict this concepts' reliability. To that end, a new and improved method of stress threshold determination was developed, based on the accelerated tapered tensile test specimens and an accurate crack detection methodology on iteratively displaced SEM images, with the intent to improve some of the inherent scatter associated with the existing literature data.

Detailed crack density distributions were obtained from the detection of SCC cracks along the tapered gauge lengths of differently strained tapered specimens. These distributions yielded the critical cross-section whereat no more SCC cracks were detected, which then provided reasonable estimates for the individual stress threshold under given strain conditions. Based on the extrapolation of these thresholds to constant load conditions, the critical stress threshold for the duplex high Si stainless steel alloy was attained. Additional analyses included finite-element analysis, wherein the prominent peaks in the crack density graphs were demonstrated to be related to stress relief and stress build-up during the crack initiation phase. Intrinsic scatter related to the crack detection suggests that stress corrosion cracking is independent of the strain-rate for strain-rates lower than $1.00 \text{ E}-6 \text{ s}^{-1}$.

After investigating the crack initiation along the tapered gauge length, several of these SCC cracks were extracted and subsequently investigated by means of FIB-SEM and TEM analysis. The microstructural investigation in the near vicinity of SCC crack tips illustrates a strain-rate dependency in SCC mechanisms. Detailed analyses of the crack tip morphology, that includes crack tip oxidation and surrounding deformation field, indicated the existence of an interplay between corrosion- and deformation-driven failure as a function of the strain-rate. Slow strain-rate crack tips exhibited a narrow cleavage failure which can be linked to the film-induced failure mechanism, while rounded shaped crack tips for faster strain-rates could be related to the strain-induced failure. As a result, two nominal strain-rate-dependent failure regimes dominated either by corrosion or deformation-driven mechanisms were distinguished.

Ultimately, these results have led to two first-author publications, cited as references [164,270]. The following paragraphs summarize some of the main conclusions and open discussions that remain after the investigation in chapter 4.

↔ Crack detection algorithm

Literature estimates of the critical stress thresholds for cracking based on the tapered specimen methodology were not considered as standardized. This means that the employed methodology was not free from human bias and was not accurately reproducible in subsequent analyses. Furthermore, a significant scatter remained in the literature data which called into question the validity of the employed methodology [261–263]. To that end, a methodology for accurate detection of SCC cracks in order to analyze the crack initiation process along the gauge lengths of CERT-tested tapered specimens was developed. This methodology was vulnerable to false-detections of SCC cracks, over-counting, and

surface imperfections along the material substrate, which were addressed by a series of crack filtering algorithms. These algorithms were specifically designed for the purpose of yielding true crack density distributions which were corrected for any compositional differences in the duplex microstructure. This allows for the crack density distributions to be mutually comparable per tapered specimen tested strain-rate. The adopted methodology in this work provides the means for a true estimation of the critical stress threshold for cracking.

↔ **On the importance of the stress threshold for cracking**

Extrapolation of the individual stress thresholds for all strained tapered specimens to constant load conditions determined the critical stress threshold for SCC cracking, obtained to be $\sigma_{\text{thr}} = 581 \pm 16$ MPa. This stress threshold can arguably be considered as either a material parameter of the high Si stainless steel, or otherwise as the overall strength of the oxide formed on the surface of the material.

Despite the application of an optimized crack detection algorithm, the scatter to individual thresholds remained intrinsic to the data set. The origin of this scatter was linked to a probabilistic stress distribution along the critical cross-section of the tapered gauge length. Since the cracking almost exclusively occurred within the surface oxide, this probabilistic stress is closely tied to the fracture strength of the oxide. If σ_{thr} may indeed be considered as a measurement of the oxide strength, it is important to denote that any of the parameters that affect this value may likely play a crucial role towards the crack initiation in the oxidized part of SSs.

↔ **Regarding the SCC crack tip chemistry**

Based on diffraction pattern analyses, STEM-HAADF spectral maps and EDS point analyses, the oxide composition on the fracture surface and in the SCC cracks themselves was shown to comprise of a chromite FeCr_2O_4 together with a magnetite $(\text{Fe,Ni})_3\text{O}_4$ spinel oxide structure. Layers enriched with metallic Ni followed by segregated Si were observed at the metal-oxide interface, typically illustrating thicknesses of about 20 – 50 nm. The origin of the enriched Ni layer can be traced back to different possible mechanisms, amongst which: (i) a preferential oxidation suggested by Lozano-Perez [97, 98], (ii) a de-alloying mechanism put forward by Bruemmer [284], or a different diffusion velocity mechanism proposed by Arioka [283]. The origin of the enriched Si around the crack tips is possibly attributable to similar kinds of mechanisms as postulated for Ni, although no indicative observations to support this have been made so far.

↔ **Regarding the TGSCC cracking mechanism**

Tapered tensile specimens subjected to CERT tests demonstrated an interplay between corrosion-driven failures typically observed at lower strain-rates up to $\dot{\epsilon} = 5.00 \text{ E}-7 \text{ s}^{-1}$, and deformation-driven cracking observed at strain-rates of $\dot{\epsilon} = 1.00 \text{ E}-6 \text{ s}^{-1}$ and beyond. Under the corrosion-driven regime, the TGSCC cracking demonstrated a narrow cleavage-like morphology which was found to be best-described by the film-induced cleavage mechanism (FIC). Prominent peaks in the crack density graphs could also be linked with FEM analyses to stress relief and stress build-up during the crack initiation phase. Alternatively, under the deformation-driven regime, crack initiation showed signs of strain-induced overload failure instead. The distinction between both mechanisms was indicated by the main fracture surface appearance, the abrupt SCC-like failure in the load-elongation curves, the prominent peaks in the crack density distributions, and the overall crack tip morphologies. The ferrite phase was solution-strengthened by the high addition of alloying Si, causing the SCC cracks to exclusively initiate within the duplex austenite phase instead.

6.1.2 Thimble tube O-rings

In a subsequent investigation, the microstructural features of intergranular IASCC cracks were investigated from a series of stress-tested O-ring specimens acquired from a redeemed flux thimble tube of the Belgian Tihange PWR NPP T2. The O-ring specimens were comprised of a 20% cold-worked neutron-irradiated 316L stainless steel material and were tested to different stress-, surface- and loading conditions in a PWR simulated environment. The experimental techniques employed during this research include FIB-SEM analysis for the accurate extraction of IASCC cracks from the bulk specimen and subsequent (S)TEM microscopy for the microstructural characterization.

Close examination of the various crack morphologies and surrounding deformation features were performed as a function of applied macroscopic stress, surface oxidation state, and loading path - constant versus cyclic loading. Higher stressed specimens exhibited a greater density of deformation twinning adjacent to the cracks and equally moving closer towards the crack tip. Evidence of stress-induced martensitic transformation extending from the crack tips is presented. Cyclic loading was found to have a more pronounced effect on the crack tip microstructure, demonstrating a significantly increased amount of deformation twinning and martensitic transformations. The oxide assembly within the crack openings and along the crack flanks were found to be the same between specimens with a native and non-native oxide surface layer. (S)TEM analyses provided chemical segregation and depletion profiles of leading impaired and un-impaired grain boundaries in front of the crack tips. These measurements provided an overview of the elemental composition in close vicinity to intergranular cracks, in addition to the extent of RIS at the grain boundary interfaces.

All investigated IASCC cracks exhibited prevalent grain boundary oxidation in front of the crack tip. Crack propagation was found to be driven by the occurrences and coalescence of multiscale fracture bands in front of the oxidized crack tip intrusions. Some evidence of jagged crack paths within the intergranular oxide, in addition to the dense dislocation contrast signifying strain-localization around the crack, suggests that crack may grow in accordance to a step-like cracking mechanism. The results on the morphology and chemistry of crack tips provide strong support for the IO mechanism, known to be relevant for IASCC cracking in stainless steels. Key aspects of the cracking such as the microscopic fracture bands that are observed within the most porous regions of the oxide intrusion, in addition to the coalescence of these fracture bands into the nucleation of small microcracks extending from the crack tip itself, and the overall brittle nature of the intergranular oxide, agree well with several of the derived models based on IO. Such models discussed within this thesis include the probabilistic SCP mechanism based on the densities of oxide defects constituting the microscale fracture bands, and the local model where intergranular oxidation plays the most-important role for consecutive step-like crack extensions. Of special importance is also the fact that the intergranular oxidation depth scales exponentially with the applied macroscopic tensile stress intensity. This exponential increase in oxidation exemplifies the relevance of stress-assisted oxidation at the crack tip, best-described by the SAGBO model.

Crack tips appertaining to specimens with an initially abraded oxide layer at the outer surface showed comparatively less oxidation at the crack tip as should be predicted by the SAGBO model. This observation could indicate towards the initiation of cracking from regions of the O-ring that exemplify lower stresses e.g., along the O-ring's inner fracture surface. These regions generally exhibit a different stress intensity than along its outer surface and the onset of cracking is not always fully determined. Alternatively, if cracking does originate from the O-ring's outer fracture surface for oxide-removed specimens, it is postulated that the reduced oxide thickness that grows during testing exemplifies a higher fracture strength as thicker oxide scales. This phenomenon is commonly understood as the

volume-effect within the probabilistic SCP model, and aligns well with the macroscopic fracture data that correlates the time-to-failure with the applied fracture stress. On the other hand, in consideration of crack tips that stem from cyclic loaded specimens, it is observed that the extent of crack tip oxidation does properly agree with expected values predicted by the SAGBO model. However, this is only the case for the maximum stress values that are applied during each consecutive loading cyclic. To that end, it is concluded that the peak maximum stresses during cyclic loading play the most prominent role for stress-driven crack tip oxidation.

This section concludes the results obtained from the characterization of IASCC cracking and crack tips extracted from neutron-irradiated TTO specimens tested under different stress and specimen conditions. Similarly as the work on tapered specimens, this investigation led to two additional first-author publications in addition to a third-author conference proceedings article, respectively cited as [232, 294, 295]. The following paragraphs summarize some of the main conclusions and open discussions that remain after the investigation in chapter 5.

↔ **On the significance of sample preparation**

Complete extraction and investigation of IASCC crack tips has been made achievable by the high spatial resolution characterization techniques used in electron microscopy. The FIB-SEM instrument allows for a site-specific extraction and preparation of crack tip samples from irradiated materials. While a cross-sectional lift-out methodology within this thesis was developed to extract crack tips to a very high success rate, it was not always considered to be without failure. First and foremost, the FIB-specimen was found to impose severe limitations on the possibility of crack extraction. Indeed, the FIB-specimen must abide to a very low dose threshold of some several mSv/h while being in contact (preferably less) in order to ensure safe operation of the instrument. Crack extraction from the primary fracture surface may also limit the angle interval to which one can tilt the specimen. Indeed, the intergranular primary fracture surface is very rough, which limits the specimen tilting when performing in-situ-lift out experiments. Furthermore, extracted FIB lamellae with embedded cracks within them are especially prone to artefacts like fracturing or being buckled when the thinning operation towards electron-transparency commences. Local aggregated ion-milling underneath extracted crack tips, a phenomenon known as the curtaining-effect, may also cause considerable difficulties in keeping the lamella walls equally thinned. Crack curtaining was considered as an inherent problem within this research and imposed severe restriction on the ultimate lamella thickness during the thinning operation. These artefacts could only be minimized by taking numerous consecutive ion-milling steps over a wide range of large tilt angles with repeatedly reduced the ion-milling currents whenever an artefact was visible. Final low-energy cleaning was found to be essential in reducing the extent of Ga⁺ ion implantation in the resultant TEM lamella.

↔ **On the difference between PFS and OS extracted crack tips**

Working with tiny specimens that stem from heavily irradiated materials is generally considered to be very difficult. This problem was most prevalent when inserting the TTO specimens into the FIB-SEM chamber. Hard-lining restrictions on the FIB pieces made it practically very difficult to tilt the IASCC primary fracture surface (PFS) facing upwards towards the FIB's electron beam. This predicament resulted in the fact that all cracks of specimens TTO-1-001 (600 MPa) and some of -066 (280 MPa - cyclic loading) were extracted from the specimen's outer surface (OS), whereas others stemming from specimens TTO-1-053 (390 MPa), -070 (500 MPa), -090 (700 MPa - non-native oxide) and the remaining cracks of -066 (280 MPa - cyclic loading) were extracted from the O-rings' PFSs instead. The position from where the cracks are extracted has a major influence on the crack morphology,

especially in relation with the acting tensile stress orientation. Indeed, cracks that were extracted from the PFS initiated in a shear-mode stress orientation, whereas all others from the OS initiated in cleavage-mode. The resulting influence of this difference in orientation was compared in the overview table of all extracted crack tips in Tab. 5.1, from which it became evident that: (i) cracks showed definite branching when extracted from the PFS whereas no branching was observed from the OS, but also the (ii) opening-width and (iii) propagation lengths of shear-mode extracted cracks from the PFS was generally smaller/shallower than those extracted in cleavage-mode from the OS; the extent of these points is generally assumed to be influenced by other properties, mainly being the stress-intensity difference between both surfaces. It is important to note that the effective stress orientation is not implied to be the same at the fracture surface as at the crack tip itself. Naturally, the stress orientation versus the crack tip orientation varies along the crack path following the leading grain boundary, which correspondingly affects the cracking-mode orientation. Cracks that continuously propagated in a shear-orientation generally resulted in much shorter developed crack lengths, while cleavage-orientated cracks generally extended much deeper within the bulk. To some extent, such cleavage cracks could develop beyond the size that could be feasibly extracted with FIB. This is evident by the much greater success rate in extracting shearing-mode crack tips from the PFS versus those extracted from the O-ring's OS, simply because the crack length was typically a lot shallower for those in shear-mode.

↔ Crack tip and grain boundary chemistry

The oxide assembly associated with intergranular cracking was found to be comparable to known literature observations of surface oxidation on 316L SS [91–95], illustrating an inner chromite spinel $(\text{Fe,Cr})_3\text{O}_4$ oxide along the crack flanks and ahead of the crack tips, and an outer nickel-bearing magnetite spinel $(\text{Fe}_{1-x},\text{Ni}_x)_3\text{O}_4$ with $(0.13 < x < 0.33)$ in wide-open accessible crack regions. At all times, the crack flanks and especially the crack tip were found to be oxidized. Around the crack tip, a small Ni-enriched layer was detectable, extending for several tens of nm aside to and in front of the crack tip. From crack tips that were asymmetrically oxidized, it became evident that the Ni-enrichment may be the result of a selective oxidation process. According to Lozano-Perez et al. [97,98], Ni may become rejected from the chromite oxidation of the metallic matrix along the crack causing it, to some extent, to cluster around the metal-oxide interface. Alternative explanations may still include the possibility of different diffusion velocities of alloying Ni in comparison to other structural elements as suggested by Arioka [283], or through matrix de-alloying as suggested by Bruemmer et al. [284].

In investigating the effects of RIS, significant volume changes were measured along elemental line scans across un-impaired grain boundaries away from the crack tips. Significant depletion of elements like Fe, Cr and Mo were observed, whereas on the other hand, strong enrichment of Ni, Si and P were found as well. Interestingly, Mn was found to be significantly reduced in the elemental profile linked with specimen TTO-1-053, whereas it strongly segregated in specimen TTO-1-090. The extent of RIS after exposure up doses of 60 to even 80 dpa was found to be a moderately more enhanced in comparison to other investigations in materials irradiated to low-to-moderate doses [42,121]. The rate of change of the elements is mostly consistent with the inverse Kirkendall (vacancy-exchange) and interstitial-solute transport mechanisms [300,301].

↔ Stress-assisted internal crack tip oxidation

All investigated IASCC cracks exemplified narrow oxide intrusions of several nm wide leading into the grain boundaries ahead of their tips. The extent of oxidation in front of the crack tips was found to be proportional to applied levels of macroscopic stress; an effect which was found to be best-described

by Evan's SAGBO model. In low stressed specimens, the crack tip oxidation lengths were found to be of the order of several hundreds of nm, whereas in the high stressed specimens, the oxide intrusions extended for over 1 μm in total. This increased amount of oxidation should be differentiated from the limited available literature data on crack tip oxidation in stainless steels [224, 284, 299, 305]. In summary, the increase in oxidation kinetics in front of the crack tip was reasoned to be enhanced by: (i) the effective stress concentration at the crack tip, (ii) the varying material and testing conditions, (iii) the exposure times to the corrosive environment, (iv) the high irradiated doses of the material, (v) the applied level of cold-work to the material, and finally (vi) the effects of short-circuit fast-diffusion paths for oxidizing species, including the existence of multiscale brittle fracture bands in the oxide intrusions, as well as the localized plasticity, especially dislocation activity and slip deformation, adjacent to the crack tip.

↔ **Subcritical crack propagation**

Crack tip advancement was seemingly driven by thin oxidized fracture bands that nucleated within the most porous regions of the oxide intrusions leading into the grain boundary interface. Additional observations of nanometer wide oxide intrusions, asymmetrical oxidation along the crack tip, preferable cracking of the metal-oxide interface, and brittle crack propagation, all support mechanisms that are based upon the IO model, known to be relevant for IASCC cracking in stainless steels. These mechanisms include the SCP developed by Konstantinović [162] and the local model by Couvant et al. [234, 235]. Moreover, our results provide strong support for a stress-driven internal oxidation mechanism that describes the oxide embrittlement of the leading metallic matrix ahead of an advancing crack. Intergranular oxides are then reasoned to be responsible for the lowering of the fracture resistance at the grain boundary, providing a facilitated means for intergranular crack propagation within the leading oxide intrusion.

↔ **Native-oxide versus non-native oxides**

O-rings with abraded oxide surfaces prior to testing typically developed a renewed surface oxide under aerated and simulated PWR conditions during the autoclave compression testing. These so-called non-native oxide specimens were seen to fail at a later point in time under a given stress state which was comparable to common native oxide specimens. Arguably, this difference is related to the fact that: (i) the samples were plotted against an overestimated critical failure stress, or (ii) because of the probabilistic volume-effect described by the SCP model. In the former case, it is possible that the ultimate crack that led to failure initiated from the O-ring's inner surface where, according to FEM analyses, lower critical stresses are observed. This suggests that the true failure stress may indeed be lowered to match the critical stress along the O-ring's inner surface, which is typically lower than along the O-ring outer surface. Alternatively, in the latter case, it is hypothesized within the SCP model that less voluminous oxides on the outer surface of the non-native O-ring have an inherently stronger oxide strength which is less prone to failure. This suggests that more stress is required to fracture these O-rings, matching the trends that are observed within the experimental data. Both viewpoints are believed to play a role in the crack initiation for non-native oxide specimens. Their validity is dependent on whether the crack initiates from the inner (mechanism (i)) or outer (mechanism (ii)) O-ring fracture surface.

↔ **Constant versus cyclic loading**

In comparing the O-ring specimens tested to constant versus cyclic load conditions, it is concluded that cyclic loading resulted into a substantially more deformed microstructure near the crack tips and along

their leading grain boundaries. The increased amount of deformation twinning effectively impeded on the dislocation glide path and contributed to a deformation strengthened microstructure [62,325]. This increase in hardening is then argued to lead to an increased susceptibility to brittle fracturing, which may reduce the component's lifetime by a significant amount. This observation is in general good agreement with the reduced TTFs of cyclic loaded O-rings in comparison to the otherwise constant loaded specimens. Strong evidence of martensitic transformations adjacent to the crack tip were also reasoned to be associated to HAC.

It is further concluded that the maximum stresses during each transient load cycle of the cyclic loaded O-rings play the most essential role for crack tip propagation. This is supported by the fact that the extent of crack tip oxidation in front of cyclic loaded tips still agreed well with expected values for maximum stress applied during the transient load cycle. Furthermore, by refitting the O-ring TTFs in accordance to these maximum stresses, it was observed that all data shifted upwards in stress into the predicted failure regime delineated by the confidence intervals of constant loaded specimens.

6.2 Future outlook

One of the clear outcomes from this research, is that the properties of the brittle oxides ahead of the crack tip play an essential role for crack propagation along microstructural grain boundaries. Crack incubation and subsequent subcritical crack propagation may really take effect in poorer quality oxides which show a weaker probabilistic strength when they are exposed to subcritical stress levels. To that end, it is imperative to know under which conditions oxidized grain boundaries may come to fracture (e.g., metal-oxide cracking, asymmetrical crack tip oxidation, fracture bands coalescence etc.) and exactly how brittle they may be (i.e., what is the critical magnitude of imposed stresses that leads to failure).

Since the main rebuttal towards IO in stainless steels is still the discrepancy between the oxide intrusion rates and the known CGRs, upcoming studies should definitely incorporate the effects that influence the oxidation rates around the crack tip. This includes the incorporation of fast oxide diffusion paths, e.g. dislocations and deformation-slip bands, that may greatly increase the oxidation kinetics [214,218]. Furthermore, other enhancing effects include the aspects of stress, material cold-work, and neutron-irradiation. In favorable conditions, crack tip oxidation may become largely comparable if not exceedingly faster than the known CGRs observed in experimental material studies. In contemplation with the observations of brittle microscale cracking such as by oxidized fracture bands, these results could definitively prove the internal oxidation mechanism for stainless steels, as was put forward within the context of this thesis.

In the notion of the SCP model, it becomes of interest how cracks nucleate in underdeveloped passivation layers at the very early stages of oxidation. This can be achieved by surface polishing the pre-existent oxide layer from the material and then subjecting it to specific oxidation loops in simulated high-temperature PWR autoclave experiments. After oxidation periods of less than 24 hours, the surface oxide is still only as thick as several tens of nm [95]. From a probabilistic viewpoint, such oxides may show considerable strength due to the fact that there is less oxide volume available where internal flaws may nucleate. Early oxidation experiments may therefore be considered as the ideal method to analyze the volume-effect of the probabilistic oxide strength. Such experiments could also provide estimates of what the critically required oxide thickness could be for crack nucleation under the SCP regime. Current estimates based on the results from SCC experiments show that cracks may grow under stresses less than about 1% of K_{IC} , i.e. the critical SIF for rupture [336]. Using the analytical expressions for the SIF, this leads to a theoretical upper limit of nucleated crack lengths within

an oxide with a thickness of about 20 nm. This under limit value may be considered as a threshold parameter where the SCP model is valid [162]. The fact that this result is considerably lower than the average oxide thicknesses observed in neutron-irradiated stainless steel (of the order of hundreds of nanometers) may indicate the SCP model's viability. Regardless, this threshold thickness should still be verified by the experiment. Because of the volume-effect, a significant amount of stress would also be required to fracture such thin nanoscale oxide layers. This brings forward the concept of a threshold stress in view of the SCP model to fracture the nanoscale oxides. Also, when looking at the very low exposure times in the O-ring overview TTF plot in Fig. 5.1, it becomes evident that quite a substantial vertical scatter remains in the dataset in terms of fracture stress. Arguably, at such low exposure times when the nanoscale oxides are subjected to high stresses, a close competition could arise between SCP failures on the one hand, and a stress-induced overload failures on the other. This competition between the two mechanisms may lie at the base of the observed scatters at low TTFs. It can also be assumed that at low exposure times, simply not enough time has passed to reach a steady-state oxide thickness ingressed at the grain boundaries (some hundred(s) of nm [169]), making overload failure which is not driven by internal oxidation a more likely scenario. This reasoning is already supported by the fact that the primary fracture surface of TTO-1-001 (690 MPa) exemplified a considerable overload failure. In view of this close competition, it remains speculative but worthy of interest what the threshold stress for SCP to overload failure may be.

In furtherance of the analyses performed on TTO specimens, it is important to elucidate the discrepancy between onset of cracking from the inner or the outer O-ring's fracture surface. As was shown from prior FEM analyses [161], crack initiation along the outer surface is usually considered as the preferred method of failure due to the higher acting tensile stresses that occur along the O-ring specimen's outside surface. Also, because the inner surface of the thimble tube has been oxidized considerably less during its service life (while not being in contact with PWR environment as was the case for its outer surface), crack initiation is usually indeed asserted predominantly within the outer oxide. This may also be considered in view of the SCP model where inner oxides may show a considerable increase in strength. However, SEM studies of failed and non-failed O-rings specimens in section 5.1 and reference [294], have shown that intergranular cracking at the inner surface cannot be excluded - in particular at the regions where high simulated Von Mises stresses associated to the applied load are present. This observation is in line with prior Japanese crack initiation studies of fractured O-rings where crack initiation was seen from either the outer or inner surface, or from both [322]. This discrepancy needs to be further investigated as it may considerably influence the interpretation of the failure stresses of the TTO specimens. A starting point for this investigation is to perform additional FEM calculations and simulate the stress intensities along both surfaces under different conditions. These analyses may confirm the hypothesis of inner surface cracking as was put forward in this thesis for non-native oxide specimens.

Considerable attention in the literature has gone to analyzing a stress threshold for crack initiation below which no IASCC failure may exist. In unirradiated materials, estimation of the stress threshold is typically performed on the basis of CERT-testing of tapered tensile specimens [35,36,261–263]. For irradiated specimens, constant load experiments showed that the threshold stress for irradiated 316L dropped to about 40% of the irradiated yield stress [161]. However, the concept of a threshold for cracking may also be applied in terms of the irradiated microstructure in order to get an analogue dpa-threshold. In view of the SCP model, the effect of neutron-irradiation is quite essential in terms of grain boundary oxidation, in particular to what concerns the weakening of the probabilistic oxide strength by producing inherent oxide flaws. Alternative effects also include the aspects of RH and RE, and of course the influence of an altered grain boundary chemistry through RIS. Since many irradiation-induced microstructural alterations tend to saturate in 316L SS after only a few dpa [22,23], this may

be the critical dpa-threshold level needed to weaken the grain boundary and enable the propagation of brittle oxide cracking.

6.2.1 IASCC-resistant alloys

Future mitigation strategies to reduce the susceptibility of structural materials towards IASCC may start by re-engineering the alloy composition in order to improve the general corrosion resistance [22,142]. Many studies have correlated the fact that Cr-depletion through RIS at grain boundary interfaces has a strong impact on IASCC [17,38,42,126]. Therefore, the likelihood that the grain boundary Cr-levels may fall below a substantial threshold level important for grain boundary cracking may thus be reduced by increasing the general bulk Cr concentration. Additionally, higher Cr-concentrations may also improve the quality of the passivation layer on the fracture surface and along oxide ingressed grain boundaries. As was shown within this thesis, crack propagation was driven by the occurrence of multiscale fracture bands within the leading oxide intrusions ahead of the crack. These fracture bands typically nucleated within the oxide porous regions of the internal chromite, which may have been due to the depleted levels of ambient Cr. In the light of the SCP model, an increased Cr concentration may potentially also increase the probabilistic oxide strength by reducing the amount of internal defects. Increased oxide strengths may consequently show less overall susceptibility to internal cracking. Alternatively, an increase in the material's SFE achieved through e.g. an increased concentration of bulk Ni, may significantly change the deformation modes and localized plasticity associated to cracking. Higher SFEs reduce the material's ability to deform through displacive transformations by making the dissociation of perfect dislocations less energetically favorable. This causes the material to deform more easily through common dislocation glide, most-especially wavy slip, which could reduce the levels of localized deformation that enhances intergranular cracking. A third option could be to reduce the bulk concentrations of Si in structural materials susceptible to cracking. Several studies have shown that there is a correlation between high levels of concentrated Si, e.g. at RIS-affected grain boundaries, and the initiation and propagation of intergranular cracking in high-temperature water environments [121,129].

Material changes that occur as a consequence of neutron-irradiated, i.e., RIS, dislocation loop nucleation, void formation and radiation-induced precipitation, can be traced back to the excess production of vacancies and interstitials in the as-irradiated microstructure. Therefore, in order to minimize the effects of neutron-irradiation, the concentration of irradiation-induced point-defects should be reduced. This can be achieved by developing materials with the ability to either greatly enhance the mutual point-defect recombination, or, by increasing the chance for them to be lost to the matrix at microstructural point defect sinks. This can be achieved by increasing the density of microstructural trap-sites for point defects generated within the matrix. Point defects may thermodynamically diffuse towards these trap-sites, such as coherent precipitates or oversized solute atoms, where their motion may be impeded as a result. This generally increases the likelihood for them to recombine with their complementary defect whenever it also diffuses towards the trap-site. The effectiveness of the point-defect trap is determined by its relative size compared to the diffusion distance of the defects in the irradiated material. Possible choices therefore are between: (i) dispersion-strengthened materials; which generally contain a high level of precipitated particles, (ii) grain-engineered materials with typical grain sizes down to the order of tens of nm; this increases the density of grain boundaries where defects may annihilate, or (iii) increase the density of dislocations e.g. through material cold-work, which may also act as point-defect sinks.

Bibliography

- [1] IPCC, 2018: Impacts of 1.5°C of Global Warming on Natural and Human Systems. In: Global Warming of 1.5°C. An IPCC Special Report on the impacts of global warming of 1.5°C above pre-industrial levels and related global greenhouse gas emission pathways, in the context of strengthening the global response to the threat of climate change, sustainable development, and efforts to eradicate poverty [Masson-Delmotte, V., P. Zhai, H.-O. Pörtner, D. Roberts, J. Skea, P.R. Shukla, A. Pirani, W. Moufouma-Okia, C. Péan, R. Pidcock, S. Connors, J.B.R. Matthews, Y. Chen, X. Zhou, M.I. Gomis, E. Lonnoy, T. Maycock, M. Tignor, and T. Waterfield (eds.)]. In Press.
- [2] IEA (2019), Nuclear Power in a Clean Energy System, IEA, Paris <https://www.iea.org/reports/nuclear-power-in-a-clean-energy-system>.
- [3] A. Lima, E. Romero, Y. Piña, A. Gens, X. Li, Water retention properties of two deep belgian clay formations, *Unsaturated Soils: Res Appl* (2012) 179–184 [doi:10.1007/978-3-642-31116-1_24](https://doi.org/10.1007/978-3-642-31116-1_24).
- [4] A. Berckmans, D. Boulanger, S. Brassinnes, M. Capouet, C. Depaus, E. D. Lopez, A. Gambi, R. Gens, X. Sillen, H. V. Baelen, M. V. Geet, P. V. Marcke, W. Wacquier, L. Wouters, L. Harvey, S. Wickham, V. Pirot, *ONDRAF/NIRAS Research, Development and Demonstration (RD&D) Plan for the geological disposal of high-level and/or long-lived radioactive waste including irradiated fuel if considered as waste*, Tech. Rep. Niron-d-tr 2013-12 E, Niras/ondraf (12 2012). URL <https://www.niras.be/sites/default/files/ONDRAF/NIRAS%20Research%20Development%20and%20Demonstration%20%28RD%26D%29%20Plan.pdf>
- [5] D. Woitrin, F. Possemiers, *Voorlopige rapport van de Commissie Energie 2030, met als titel "Belgium's Energy Challenges Towards 2030"*, Tech. Rep. (F) 070301-cdc-661, Creg (03 2007). URL <https://www.creg.be/sites/default/files/assets/Publications/Studies/F661NL.pdf>
- [6] A. Henry, *Quelle énergie pour un développement durable?*, Tech. Rep. Working Paper 14-05, Bureau fédéral du Plan (06 2005). URL <https://www.plan.be/uploaded/documents/200605091448115.WP0514fr.pdf>
- [7] Fanc-afcn, *Doel 3 and Tihange 2 reactor pressure vessels - Final Evaluation Report*, Tech. Rep. Final evaluation report, Afcn - Fanc (05 2013). URL https://afcn.fgov.be/fr/system/files/rapport_intermediaire_afcn_d3-t2_2013.pdf
- [8] Fanc-afcn, *Doel 3 – Tihange 2: RPV issue – Final Evaluation Report*, Tech. Rep. Final evaluation report, Afcn - Fanc (11 2015). URL https://fanc.fgov.be/de/system/files/final_evaluation_report_fanc_d3-t2_2015.pdf
- [9] Pwc, *SUCCESSEN IN DE ENERGIETRANSITIE - De rol van kernenergie en hernieuwbare energie in België.*, Tech. rep., Pwc Enterprise Advisory (2016). URL https://www.nucleairforum.be/uploads/docs/FOR00029_PWC_rapport_NL_HR.pdf

- [10] W. Séverine, [Energy Key Data - februari 2022](#), Tech. rep., Fod Economie, K.M.O., Middenstand en Energie (02 2022).
URL <https://economie.fgov.be/nl/publicaties/energy-key-data-februari-2022>
- [11] E. Commission, [Belgium – Capacity remuneration mechanism](#), Tech. Rep. Final evaluation report, European Commission (07 2021).
URL https://ec.europa.eu/competition/state_aid/cases1/202137/288236_2313671_226_2.pdf
- [12] IPCC, 2018: Summary for Policymakers. In: Global Warming of 1.5°C. An IPCC Special Report on the impacts of global warming of 1.5°C above pre-industrial levels and related global greenhouse gas emission pathways, in the context of strengthening the global response to the threat of climate change, sustainable development, and efforts to eradicate poverty [Masson-Delmotte, V., P. Zhai, H.-O. Pörtner, D. Roberts, J. Skea, P.R. Shukla, A. Pirani, W. Moufouma-Okia, C. Péan, R. Pidcock, S. Connors, J.B.R. Matthews, Y. Chen, X. Zhou, M.I. Gomis, E. Lonnoy, T. Maycock, M. Tignor, and T. Waterfield (eds.)]. World Meteorological Organization, Geneva, Switzerland, 32 pp.
- [13] F. Cattant, D. Crusset, D. Féron, Corrosion issues in nuclear industry today, *Materials Today* 11 (10) (2008) 32–37. doi:[https://doi.org/10.1016/S1369-7021\(08\)70205-0](https://doi.org/10.1016/S1369-7021(08)70205-0).
- [14] K. Murty, I. Charit, [An Introduction to Nuclear Materials: Fundamentals and Applications](#), Physics Textbook, Wiley, 2013.
URL <https://books.google.be/books?id=rZvWGzLn-u4C>
- [15] Ökobüro, [Lifetime Extension of Nuclear Power Plants](#), Tech. Rep. Public Participation Toolkit, Ökobüro (01 2022).
URL https://www.oekobuero.at/files/717/toolkit_public_participation_lte_okoburo_2022_fin.pdf
- [16] T. Allen, J. Busby, M. Meyer, D. Petti, Materials challenges for nuclear systems, *Materials Today* 13 (12) (2010) 14–23. doi:[https://doi.org/10.1016/S1369-7021\(10\)70220-0](https://doi.org/10.1016/S1369-7021(10)70220-0).
- [17] G. S. Was, P. L. Andresen, 3 - mechanisms behind irradiation-assisted stress corrosion cracking, in: S. Ritter (Ed.), *Nuclear Corrosion*, European Federation of Corrosion (EFC) Series, Woodhead Publishing, 2020, pp. 47–88. doi:<https://doi.org/10.1016/B978-0-12-823719-9.00003-2>.
- [18] B. Singh, A. Foreman, H. Trinkaus, Radiation hardening revisited: role of intracascade clustering, *Journal of Nuclear Materials* 249 (2) (1997) 103–115. doi:[https://doi.org/10.1016/S0022-3115\(97\)00231-6](https://doi.org/10.1016/S0022-3115(97)00231-6).
- [19] F. A. Garner, Recent insights on the swelling and creep of irradiated austenitic alloys, *Journal of Nuclear Materials* 122 (1-3) (1984) 459–471. doi:[10.1016/0022-3115\(84\)90641-x](https://doi.org/10.1016/0022-3115(84)90641-x).
- [20] D. Edwards, E. Simonen, F. Garner, L. Greenwood, B. Oliver, S. Bruemmer, Influence of irradiation temperature and dose gradients on the microstructural evolution in neutron-irradiated 316ss, *Journal of Nuclear Materials* 317 (1) (2003) 32–45. doi:[https://doi.org/10.1016/S0022-3115\(03\)00003-5](https://doi.org/10.1016/S0022-3115(03)00003-5).
- [21] F. A. Garner, M. L. Hamilton, C. R. Eiholzer, M. B. Toloczko, A. S. Kumar, Influence of cold work level on the irradiation creep and creep rupture of titanium-modified austenitic stainless steels, Vol. 1175, 1992, p. 696–713. doi:[10.1520/stp23967s](https://doi.org/10.1520/stp23967s).
- [22] G. S. Was, Y. Ashida, P. L. Andresen, Irradiation-assisted stress corrosion cracking 29 (2011) 7–49. doi:[10.1515/corrrev.2011.020](https://doi.org/10.1515/corrrev.2011.020).

- [23] O. K. Chopra, A. S. Rao, A review of irradiation effects on LWR core internal materials - IASCC susceptibility and crack growth rates of austenitic stainless steels, *Journal of Nuclear Materials* 409 (3) (2011) 235–256. doi:10.1016/j.jnucmat.2010.12.001.
- [24] S. Lozano-Perez, J. Dohr, M. Meisnar, K. Kruska, Sec in pwr: Learning from a bottom-up approach, *Metallurgical and Materials Transactions E* 1 (2) (2014) 194–210. doi:10.1007/s40553-014-0020-y.
- [25] P. L. Andresen, A brief history of environmental cracking in hot water, *Corrosion* 75 (3) (2018) 240–253. doi:10.5006/2881.
- [26] V. Kain, S. Roychowdhury, T. Mathew, A. Bhandakkar, Flow accelerated corrosion and its control measures for the secondary circuit pipelines in indian nuclear power plants, *Journal of Nuclear Materials* 383 (1) (2008) 86–91, *advances in Nuclear Materials: Processing, Performance and Phenomena*. doi:https://doi.org/10.1016/j.jnucmat.2008.08.024.
- [27] J. Singh, U. Kumar, N. Kumawat, S. Kumar, V. Kain, S. Anantharaman, A. Sinha, Flow accelerated corrosion of carbon steel feeder pipes from pressurized heavy water reactors, *Journal of Nuclear Materials* 429 (1) (2012) 226–232. doi:https://doi.org/10.1016/j.jnucmat.2012.05.045.
- [28] J. He, S. Xu, W. Ti, Y. Han, J. Mei, X. Wang, The pitting corrosion behavior of the austenitic stainless steel 308L-316L welded joint, *Metals* 10 (9) (2020). doi:10.3390/met10091258.
- [29] J. Stewart, D. Williams, The initiation of pitting corrosion on austenitic stainless steel: on the role and importance of sulphide inclusions, *Corrosion Science* 33 (3) (1992) 457–474. doi:https://doi.org/10.1016/0010-938X(92)90074-D.
- [30] S. Peter, J. Anders, B. Martin, *SMILE - Studsvik Material Integrity Life Extension Project*, Tech. Rep. STUDSVIK/N-19/010 Rev.2, Studsvik (10 2020).
URL <https://www.studsvik.com/contentassets/df5c7977dc06474991d110ff2120b3ee/smile-executive-summary.pdf>
- [31] K. Fukuya, K. Fujii, H. Nishioka, K. Takakura, K. Nakata, A prediction model of iascc initiation stress for bolts in pwr core internals, *Nuclear Engineering and Design* 240 (3) (2010) 473–481. doi:https://doi.org/10.1016/j.nucengdes.2009.10.022.
- [32] M. Shen, X. Peng, L. Xie, X. Meng, X. Li, Deformation characteristics and sealing performance of metallic o-rings for a reactor pressure vessel, *Nuclear Engineering and Technology* 48 (2) (2016) 533–544. doi:https://doi.org/10.1016/j.net.2015.11.009.
- [33] J. Vidal, J. Stodolna, F. Sefta, C. Pokor, 2018. Engineering Models Used For PLIM [PowerPoint presentation]. SOTERIA Training School, 3-7 September, Valencia.
- [34] F. Somville, R. Gerard, R. W. Bosch, D. Bertolis, S. Vissers, *Ageing management of baffle former bolts in belgian nuclear power plants*, Fontevraud 8: Conference on Contribution of Materials Investigations and Operating Experience to LWRs' Safety, Performance and Reliability, France, 2015, specific Nuclear Reactors And Associated Plants.
URL http://inis.iaea.org/search/search.aspx?orig_q=RN:46087905
- [35] R.-W. Bosch, S. Ritter, M. Herbst, R. Kilian, M. G. Burke, J. Duff, F. Scenini, Y. Gu, A. Dinu, U. Ehrnstén, A. Toivonen, R. Novotny, O. Martin, F.-J. Perosanz, A. Legat, B. Zajec, Stress corrosion crack initiation testing with tapered specimens in high-temperature water – results of a collaborative research project, *Corrosion Engineering, Science and Technology* 56 (2) (2021) 103–118. doi:10.1080/1478422x.2020.1815460.

- [36] R.-W. Bosch, S. Ritter, M. Herbst, R. Kilian, M. G. Burke, J. Duff, F. Scenini, Y. Gu, A. Dinu, U. Ehrnstén, A. Toivonen, R. Novotny, O. Martin, F.-J. Perosanz, A. Legat, B. Zajec, Stress corrosion crack initiation testing with tapered specimens in high-temperature water – results of a collaborative research project, *Corrosion Engineering, Science and Technology* 56 (2) (2021) 103–118. doi:10.1080/1478422x.2020.1815460.
- [37] A. Hojná, Overview of intergranular fracture of neutron irradiated austenitic stainless steels, *Metals* 7 (10) (2017). doi:10.3390/met7100392.
- [38] G. S. Was, J. T. Busby, Role of irradiated microstructure and microchemistry in irradiation-assisted stress corrosion cracking, *Philosophical Magazine* 85 (4-7) (2005) 443–465. doi:10.1080/02678370412331320224.
- [39] P. Scott, 2000 F.N. speller award lecture: Stress corrosion cracking in pressurized water reactors interpretation, modeling, and remedies, *Corrosion* 56 (08 2000). doi:10.5006/1.3280580.
- [40] P. L. Andresen, Emerging Issues and Fundamental Processes in Environmental Cracking in Hot Water, *Corrosion* 64 (5) (2008) 439–464. doi:10.5006/1.3278483.
- [41] G. S. Was, P. L. Andresen, Stress Corrosion Cracking Behavior of Alloys in Aggressive Nuclear Reactor Core Environments, *Corrosion* 63 (1) (2007) 19–45. doi:10.5006/1.3278331.
- [42] S. M. Bruemmer, E. P. Simonen, P. M. Scott, P. L. Andresen, G. S. Was, J. L. Nelson, Radiation-induced material changes and susceptibility to intergranular failure of light-water-reactor core internals, *Journal of Nuclear Materials* 274 (3) (1999) 299–314. doi:10.1016/s0022-3115(99)00075-6.
- [43] O. Chopra, A. Rao, Degradation of LWR core internal materials due to neutron irradiation, *NUREG/CR-7027* (2010).
- [44] K. Fukuya, H. Nishioka, K. Fujii, M. Kamaya, T. Miura, T. Torimaru, Fracture behavior of austenitic stainless steels irradiated in pwr, *Journal of Nuclear Materials* 378 (2) (2008) 211–219. doi:https://doi.org/10.1016/j.jnucmat.2008.06.028.
- [45] W. F. Hosford, *Iron and Steel*, Cambridge University Press, 2012. doi:10.1017/cbo9781139086233.
- [46] M. Le Calvar, I. De Curières, 15 - corrosion issues in pressurized water reactor (pwr) systems, in: D. Féron (Ed.), *Nuclear Corrosion Science and Engineering*, Woodhead Publishing Series in Energy, Woodhead Publishing, 2012, pp. 473–547. doi:https://doi.org/10.1533/9780857095343.5.473.
- [47] S.-J. Lee, Y.-K. Lee, Quantitative analyses of ferrite lattice parameter and solute nb content in low carbon microalloyed steels, *Scripta Materialia* 52 (10) (2005) 973–976. doi:https://doi.org/10.1016/j.scriptamat.2005.01.028.
- [48] G. Meric de Bellefon, J. van Duysen, Tailoring plasticity of austenitic stainless steels for nuclear applications: Review of mechanisms controlling plasticity of austenitic steels below 400 °c, *Journal of Nuclear Materials* 475 (2016) 168–191. doi:https://doi.org/10.1016/j.jnucmat.2016.04.015.
- [49] A. L. Schaeffler, *Constitution Diagram for Stainless Steel Weld Metal*, *Metal Progress* 56 (11) (1949) 680 and 680–B.
URL <https://cir.nii.ac.jp/crid/1570009751069526400>
- [50] Y. Xiong, Y. Yue, Y. Lu, T. He, M. Fan, F. Ren, W. Cao, Cryorolling impacts on microstruc-

- ture and mechanical properties of aisi 316 ln austenitic stainless steel, *Materials Science and Engineering: A* 709 (2018) 270–276. doi:<https://doi.org/10.1016/j.msea.2017.10.067>.
- [51] T. Ishikawa, 1 - understanding and controlling microstructural evolution in metal forming: an overview, in: J. Lin, D. Balint, M. Pietrzyk (Eds.), *Microstructure Evolution in Metal Forming Processes*, Woodhead Publishing Series in Metals and Surface Engineering, Woodhead Publishing, 2012, pp. 3–16. doi:<https://doi.org/10.1533/9780857096340.1.3>.
- [52] M. L. Kronberg, F. H. Wilson, Secondary recrystallization in copper, *Jom* 1 (8) (1949) 501–514. doi:[10.1007/bf03398387](https://doi.org/10.1007/bf03398387).
- [53] D. Brandon, 25 year perspective defining grain boundaries: an historical perspective the development and limitations of coincident site lattice models, *Materials Science and Technology* 26 (7) (2010) 762–773. doi:[10.1179/026708310x12635619987989](https://doi.org/10.1179/026708310x12635619987989).
- [54] B. Alexandreanu, B. Capell, G. S. Was, Combined effect of special grain boundaries and grain boundary carbides on igsc of ni–16cr–9fe–xc alloys, *Materials Science and Engineering: A* 300 (1) (2001) 94–104. doi:[https://doi.org/10.1016/S0921-5093\(00\)01705-6](https://doi.org/10.1016/S0921-5093(00)01705-6).
- [55] B. Alexandreanu, G. S. Was, The role of stress in the efficacy of coincident site lattice boundaries in improving creep and stress corrosion cracking, *Scripta Materialia* 54 (6) (2006) 1047–1052, viewpoint set no. 40: Grain boundary engineering. doi:<https://doi.org/10.1016/j.scriptamat.2005.11.051>.
- [56] H. Liu, M. Gao, D. G. Harlow, R. P. Wei, Grain boundary character, and carbide size and spatial distribution in a ternary nickel alloy, *Scripta Metallurgica et Materialia* 32 (11) (1995) 1807–1812. doi:[https://doi.org/10.1016/0956-716X\(95\)00015-N](https://doi.org/10.1016/0956-716X(95)00015-N).
- [57] Z. Zhai, M. Olszta, M. Toloczko, S. Bruemmer, Precursor corrosion damage and stress corrosion crack initiation in alloy 600 during exposure to pwr primary water, in: *17th International Conference on Environmental Degradation of Materials in Nuclear Power Systems - Water Reactors*, Springer International Publishing, 2015, pp. 1477–1490.
- [58] L. Fournier, O. Calonne, P. Combrade, P. Scott, P. Chou, R. Pathania, Grain boundary oxidation and embrittlement prior to crack initiation in alloy 600 in pwr primary water, in: J. T. Busby, G. Ilevbare, P. L. Andresen (Eds.), *Proceedings of the 15th International Conference on Environmental Degradation of Materials in Nuclear Power Systems — Water Reactors*, Springer International Publishing, Cham, 2016, pp. 1491–1501.
- [59] T. W. Clyne, J. E. Campbell, *Mechanisms of Plastic Deformation in Metals*, Cambridge University Press, 2021, p. 43–80. doi:[10.1017/9781108943369.005](https://doi.org/10.1017/9781108943369.005).
- [60] G. P. Haviland, K. Ono, Short-range interactions between two parallel dislocations, *Journal of Applied Physics* 42 (1) (1971) 238–246. doi:[10.1063/1.1659574](https://doi.org/10.1063/1.1659574).
- [61] G. Meric de Bellefon, J. van Duysen, K. Sridharan, Composition-dependence of stacking fault energy in austenitic stainless steels through linear regression with random intercepts, *Journal of Nuclear Materials* 492 (2017) 227–230. doi:<https://doi.org/10.1016/j.jnucmat.2017.05.037>.
- [62] W. Karlsen, G. Diego, B. Devrient, Localized deformation as a key precursor to initiation of intergranular stress corrosion cracking of austenitic stainless steels employed in nuclear power plants, *Journal of Nuclear Materials* 406 (1) (2010) 138–151. doi:[10.1016/j.jnucmat.2010.01.029](https://doi.org/10.1016/j.jnucmat.2010.01.029).
- [63] I. J. Beyerlein, X. Zhang, A. Misra, Growth twins and deformation twins in metals, *Annual Review of Materials Research* 44 (1) (2014) 329–363. doi:[10.1146/annurev-matsci-070813-](https://doi.org/10.1146/annurev-matsci-070813-)

113304.

- [64] W. Karlsen, M. Ivanchenko, U. Ehrnstén, Y. Yagodzhinskyy, H. Hänninen, Microstructural manifestation of dynamic strain aging in aisi 316 stainless steel, *Journal of Nuclear Materials* 395 (1) (2009) 156–161. doi:<https://doi.org/10.1016/j.jnucmat.2009.10.047>.
- [65] X. Wu, X. Pan, J. Stubbins, Embrittlement and flow localization in reactor structural materials (10 2006). doi:[10.2172/892910](https://doi.org/10.2172/892910).
- [66] H. Fujita, S. Ueda, Stacking faults and f.c.c. (γ) \rightarrow h.c.p. transformation in 188-type stainless steel, *Acta Metallurgica* 20 (5) (1972) 759–767. doi:[https://doi.org/10.1016/0001-6160\(72\)90104-6](https://doi.org/10.1016/0001-6160(72)90104-6).
- [67] M. Gussev, J. Busby, T. Byun, C. Parish, Twinning and martensitic transformations in nickel-enriched 304 austenitic steel during tensile and indentation deformations, *Materials Science and Engineering: A* 588 (2013) 299–307. doi:<https://doi.org/10.1016/j.msea.2013.08.072>.
- [68] F. Lacroisey, A. Pineau, Martensitic transformations induced by plastic deformation in the fe-ni-cr-c system, *Metallurgical and Materials Transactions B* 3 (2) (1972) 391–400. doi:[10.1007/bf02642042](https://doi.org/10.1007/bf02642042).
- [69] S. Kibey, J. Liu, D. Johnson, H. Sehitoglu, Predicting twinning stress in fcc metals: Linking twin-energy pathways to twin nucleation, *Acta Materialia* 55 (20) (2007) 6843–6851. doi:<https://doi.org/10.1016/j.actamat.2007.08.042>.
- [70] M. Koyama, E. Akiyama, K. Tsuzaki, D. Raabe, Hydrogen-assisted failure in a twinning-induced plasticity steel studied under in situ hydrogen charging by electron channeling contrast imaging, *Acta Materialia* 61 (12) (2013) 4607–4618. doi:<https://doi.org/10.1016/j.actamat.2013.04.030>.
- [71] G. Laplanche, A. Kostka, O. Horst, G. Eggeler, E. George, Microstructure evolution and critical stress for twinning in the crmnfeconi high-entropy alloy, *Acta Materialia* 118 (2016) 152–163. doi:<https://doi.org/10.1016/j.actamat.2016.07.038>.
- [72] L. Chang, M. G. Burke, K. Mukahiwa, J. Duff, Y. Wang, F. Scenini, The effect of martensite on stress corrosion crack initiation of austenitic stainless steels in high-temperature hydrogenated water, *Corrosion Science* 189 (2021) 109600. doi:<https://doi.org/10.1016/j.corsci.2021.109600>.
- [73] K. Spencer, J. Embury, K. Conlon, M. Véron, Y. Bréchet, Strengthening via the formation of strain-induced martensite in stainless steels, *Materials Science and Engineering: A* 387–389 (2004) 873–881, 13th International Conference on the Strength of Materials. doi:<https://doi.org/10.1016/j.msea.2003.11.084>.
- [74] J. Talonen, H. Hänninen, P. Nenonen, G. Pape, Effect of strain rate on the strain-induced $\gamma \rightarrow \alpha'$ -martensite transformation and mechanical properties of austenitic stainless steels, *Metallurgical and Materials Transactions A* 36 (2) (2005) 421–432. doi:[10.1007/s11661-005-0313-y](https://doi.org/10.1007/s11661-005-0313-y).
- [75] H. Shöji, Geometrische beziehungen unter den strukturen der modifikationen einer substanz, *Zeitschrift für Kristallographie - Crystalline Materials* 77 (1-6) (1931) 381–410. doi:[doi:10.1524/zkri.1931.77.1.381](https://doi.org/10.1524/zkri.1931.77.1.381).
- [76] K. Koumatos, A. Muehleman, A theoretical investigation of orientation relationships and transformation strains in steels, *Acta Crystallographica Section A Foundations and Advances* 73 (2) (2017) 115–123. doi:[10.1107/s2053273316020350](https://doi.org/10.1107/s2053273316020350).

- [77] G. Kurdjumow, G. Sachs, Der mechanismus der stahlhärtung, *Naturwissenschaften* 18 (22) (1930) 534–534. doi:[10.1007/bf01513427](https://doi.org/10.1007/bf01513427).
- [78] Z. Nishiyama, 2 - crystallography of martensite (general), in: M. E. Fine, M. Meshii, C. Wayman, Z. Nishiyama (Eds.), *Martensitic Transformation*, Academic Press, 1978, pp. 14–134. doi:<https://doi.org/10.1016/B978-0-12-519850-9.50007-7>.
- [79] S. Takaki, H. Nakatsu, Y. Tokunaga, Effects of austenite grain size on ϵ martensitic transformation in fe-15mass%mn alloy, *Materials Transactions, JIM* 34 (6) (1993) 489–495. doi:[10.2320/matertrans1989.34.489](https://doi.org/10.2320/matertrans1989.34.489).
- [80] G. B. Olson, M. Cohen, Kinetics of strain-induced martensitic nucleation, *Metallurgical Transactions A* 6 (4) (1975) 791. doi:[10.1007/bf02672301](https://doi.org/10.1007/bf02672301).
- [81] B. Jiang, T. Tadaki, H. Mori, T. Y. H. X. Zuyao, In-situ tem observation of $\gamma \rightarrow \epsilon$ martensitic transformation during tensile straining in an fe-mn-si shape memory alloy, *Materials Transactions, JIM* 38 (12) (1997) 1072–1077. doi:[10.2320/matertrans1989.38.1072](https://doi.org/10.2320/matertrans1989.38.1072).
- [82] C. Huang, G. Yang, Y. Gao, S. Wu, S. Li, Investigation on the nucleation mechanism of deformation-induced martensite in an austenitic stainless steel under severe plastic deformation, *Journal of Materials Research* 22 (3) (2007) 724–729. doi:[10.1557/jmr.2007.0094](https://doi.org/10.1557/jmr.2007.0094).
- [83] B. V. N. Rao, On the orientation relationships between retained austenite and “lath” martensite, *Metallurgical Transactions A* 10 (5) (1979) 645–648. doi:[10.1007/bf02658328](https://doi.org/10.1007/bf02658328).
- [84] V. Tsakiris, D. V. Edmonds, Martensite and deformation twinning in austenitic steels, *Materials Science and Engineering: A* 273-275 (1999) 430–436. doi:[https://doi.org/10.1016/S0921-5093\(99\)00322-6](https://doi.org/10.1016/S0921-5093(99)00322-6).
- [85] Y. Shen, X. Li, X. Sun, Y. Wang, L. Zuo, Twinning and martensite in a 304 austenitic stainless steel, *Materials Science and Engineering: A* 552 (2012) 514–522. doi:<https://doi.org/10.1016/j.msea.2012.05.080>.
- [86] G. Olson, M. Cohen, A mechanism for the strain-induced nucleation of martensitic transformations, *Journal of the Less Common Metals* 28 (1) (1972) 107–118. doi:[https://doi.org/10.1016/0022-5088\(72\)90173-7](https://doi.org/10.1016/0022-5088(72)90173-7).
- [87] A. Bogers, W. Burgers, Partial dislocations on the 110 planes in the b.c.c. lattice and the transition of the f.c.c. into the b.c.c. lattice, *Acta Metallurgica* 12 (2) (1964) 255–261. doi:[https://doi.org/10.1016/0001-6160\(64\)90194-4](https://doi.org/10.1016/0001-6160(64)90194-4).
- [88] L. Bracke, L. Kestens, J. Penning, Transformation mechanism of α' -martensite in an austenitic fe-mn-c-n alloy, *Scripta Materialia* 57 (5) (2007) 385–388. doi:<https://doi.org/10.1016/j.scriptamat.2007.05.003>.
- [89] S.-I. Baik, Y.-W. Kim, A transmission electron microscopy study of strain-induced secondary twin and epsilon-martensitic transformation in fe-15mn-2cr-0.6c-0.06n austenitic steel, *Materialia* 10 (2020) 100677. doi:<https://doi.org/10.1016/j.mtla.2020.100677>.
- [90] Z. Que, C. Huotilainen, T. Seppänen, J. Lydman, U. Ehrnstén, Effect of machining on near surface microstructure and the observation of martensite at the fatigue crack tip in PWR environment of 304L stainless steel, *Journal of Nuclear Materials* 558 (2022) 153399. doi:[10.1016/j.jnucmat.2021.153399](https://doi.org/10.1016/j.jnucmat.2021.153399).
- [91] M. Boisson, L. Legras, E. Andrieu, L. Laffont, Role of irradiation and irradiation defects on the

- oxidation first stages of a 316l austenitic stainless steel, *Corrosion Science* 161 (2019) 108194. doi:<https://doi.org/10.1016/j.corsci.2019.108194>.
- [92] X. Liu, W. Hwang, J. Park, D. Van, Y. Chang, S. H. Lee, S.-Y. Kim, S. Han, B. Lee, Toward the multiscale nature of stress corrosion cracking, *Nuclear Engineering and Technology* 50 (1) (2018) 1–17. doi:<https://doi.org/10.1016/j.net.2017.10.014>.
- [93] S. Perrin, L. Marchetti, C. Duhamel, M. Sennour, F. Jomard, Influence of irradiation on the oxide film formed on 316 l stainless steel in pwr primary water, *Oxidation of Metals* 80 (5) (2013) 623–633. doi:[10.1007/s11085-013-9401-3](https://doi.org/10.1007/s11085-013-9401-3).
- [94] T. Terachi, K. Fujii, K. Arioka, Microstructural characterization of scc crack tip and oxide film for sus 316 stainless steel in simulated pwr primary water at 320°C, *Journal of Nuclear Science and Technology* 42 (2) (2005) 225–232. doi:[10.1080/18811248.2005.9726383](https://doi.org/10.1080/18811248.2005.9726383).
- [95] R. Soulas, M. Cheynet, E. Rauch, T. Neisius, L. Legras, C. Domain, Y. Brechet, Tem investigations of the oxide layers formed on a 316l alloy in simulated pwr environment, *Journal of Materials Science* 48 (7) (2013) 2861–2871. doi:[10.1007/s10853-012-6975-0](https://doi.org/10.1007/s10853-012-6975-0).
- [96] J. Deakin, Z. Dong, B. Lynch, R. C. Newman, De-alloying of type 316 stainless steel in hot, concentrated sodium hydroxide solution, *Corrosion Science* 46 (9) (2004) 2117–2133. doi:<https://doi.org/10.1016/j.corsci.2004.01.011>.
- [97] S. Lozano-Perez, T. Yamada, T. Terachi, M. Schröder, C. English, G. Smith, C. Grovenor, B. Eyre, Multi-scale characterization of stress corrosion cracking of cold-worked stainless steels and the influence of cr content, *Acta Materialia* 57 (18) (2009) 5361–5381. doi:<https://doi.org/10.1016/j.actamat.2009.07.040>.
- [98] S. Lozano-Perez, D. W. Saxey, T. Yamada, T. Terachi, Atom-probe tomography characterization of the oxidation of stainless steel, *Scripta Materialia* 62 (11) (2010) 855–858. doi:<https://doi.org/10.1016/j.scriptamat.2010.02.021>.
- [99] K. Kruska, S. Lozano-Perez, D. W. Saxey, T. Terachi, T. Yamada, G. D. W. Smith, Nanoscale characterisation of grain boundary oxidation in cold-worked stainless steels, *Corrosion Science* 63 (2012) 225–233. doi:<https://doi.org/10.1016/j.corsci.2012.06.030>.
- [100] A. Fattah-alhosseini, A. Saatchi, M. Golozar, K. Raeissi, The transpassive dissolution mechanism of 316l stainless steel, *Electrochimica Acta* 54 (13) (2009) 3645–3650. doi:<https://doi.org/10.1016/j.electacta.2009.01.040>.
- [101] G. Song, Transpassivation of fe–cr–ni stainless steels, *Corrosion Science* 47 (8) (2005) 1953–1987. doi:<https://doi.org/10.1016/j.corsci.2004.09.007>.
- [102] C. Wagner, Beitrag zur theorie des anlaufvorgangs, *Zeitschrift für Physikalische Chemie* 21b (1) (1933) 25–41. doi:[doi:10.1515/zpch-1933-2105](https://doi.org/10.1515/zpch-1933-2105).
- [103] N. Birks, G. H. Meier, F. S. Pettit, *Introduction to the High Temperature Oxidation of Metals*, 2nd Edition, Cambridge University Press, 2006. doi:[10.1017/cbo9781139163903](https://doi.org/10.1017/cbo9781139163903).
- [104] T. Shoji, Z. Lu, H. Murakami, Formulating stress corrosion cracking growth rates by combination of crack tip mechanics and crack tip oxidation kinetics, *Corrosion Science* 52 (3) (2010) 769–779. doi:<https://doi.org/10.1016/j.corsci.2009.10.041>.
- [105] A. Hojná, Environmentally assisted cracking initiation in high-temperature water, *Metals* 11 (2) (2021). doi:[10.3390/met11020199](https://doi.org/10.3390/met11020199).

- [106] S. Ziemniak, M. Hanson, Zinc treatment effects on corrosion behavior of 304 stainless steel in high temperature, hydrogenated water, *Corrosion Science* 48 (9) (2006) 2525–2546. doi:<https://doi.org/10.1016/j.corsci.2005.10.014>.
- [107] R. Newman, T. Gendron, P. Scott, *Internal Oxidation and Embrittlement of Alloy 600*, John Wiley & Sons, Ltd, 1999, pp. 79–93. doi:<https://doi.org/10.1002/9781118787618.ch8>.
- [108] D. D. Macdonald, The point defect model for the passive state, *Journal of The Electrochemical Society* 139 (12) (1992) 3434–3449. doi:[10.1149/1.2069096](https://doi.org/10.1149/1.2069096).
- [109] D. D. Macdonald, The history of the point defect model for the passive state: A brief review of film growth aspects, *Electrochimica Acta* 56 (4) (2011) 1761–1772. doi:<https://doi.org/10.1016/j.electacta.2010.11.005>.
- [110] J. Castle, H. Masterson, The role of diffusion in the oxidation of mild steel in high temperature aqueous solutions, *Corrosion Science* 6 (3) (1966) 93–104. doi:[https://doi.org/10.1016/S0010-938X\(66\)80001-X](https://doi.org/10.1016/S0010-938X(66)80001-X).
- [111] V. K. Verma, K. Katovsky, *Radiation Damage and Development of a MC Software Tool*, Springer Singapore, Singapore, 2019, pp. 123–144. doi:[10.1007/978-981-10-7503-2_7](https://doi.org/10.1007/978-981-10-7503-2_7).
- [112] W. Hoffelner, *Irradiation Damage in Nuclear Power Plants*, Springer New York, New York, NY, 2015, pp. 1427–1461. doi:[10.1007/978-1-4614-5589-9_36](https://doi.org/10.1007/978-1-4614-5589-9_36).
- [113] R.-W. Bosch, W. Van Renterghem, S. Van Dyck, R. Chaouadi, R. Gérard, F. Somville, Microstructure, mechanical properties and iascc susceptibility of stainless steel baffle bolts after 30 years of operation in a pwr, *Journal of Nuclear Materials* 543 (2021) 152615. doi:[10.1016/j.jnucmat.2020.152615](https://doi.org/10.1016/j.jnucmat.2020.152615).
- [114] W. Van Renterghem, R.-W. Bosch, R. Gérard, F. Somville, Transmission electron microscopy study of long-term irradiated baffle bolts, *Fontevraud 9: Contribution of Materials Investigations and Operating Experience to Light Water NPPs' Safety, Performance and Reliability*, Avignon, France, 2018.
- [115] P. J. Maziasz, C. J. McHargue, Microstructural evolution in annealed austenitic steels during neutron irradiation, *International Materials Reviews* 32 (1) (1987) 190–219. doi:[10.1179/095066087790150331](https://doi.org/10.1179/095066087790150331).
- [116] C. Pokor, Y. Br chet, P. Dubuisson, J.-P. Massoud, A. Barbu, Irradiation damage in 304 and 316 stainless steels: Experimental investigation and modeling. part i: Evolution of the microstructure, *Journal of Nuclear Materials* 326 (2004) 19–29. doi:[10.1016/j.jnucmat.2003.11.007](https://doi.org/10.1016/j.jnucmat.2003.11.007).
- [117] W. Van Renterghem, M. J. Konstantinovi c, M. Vankeerberghen, Evolution of the radiation-induced defect structure in 316 type stainless steel after post-irradiation annealing, *Journal of Nuclear Materials* 452 (1-3) (2014) 158–165. doi:[10.1016/j.jnucmat.2014.04.024](https://doi.org/10.1016/j.jnucmat.2014.04.024).
- [118] N. M. Ghoniem, D. D. Cho, The simultaneous clustering of point defects during irradiation, *physica status solidi (a)* 54 (1) (1979) 171–178. doi:<https://doi.org/10.1002/pssa.2210540122>.
- [119] P. Scott, A review of irradiation assisted stress corrosion cracking, *Journal of Nuclear Materials* 211 (2) (1994) 101–122. doi:[https://doi.org/10.1016/0022-3115\(94\)90360-3](https://doi.org/10.1016/0022-3115(94)90360-3).
- [120] T. Fukuda, M. Sagisaka, Y. Isobe, A. Hasegawa, M. Sato, K. Abe, Y. Nishida, T. Kamada, Y. Kaneshima, Microstructural changes of austenitic steels caused by proton irradiation under

- various conditions, *Journal of Nuclear Materials* 283-287 (2000) 263–267, 9th Int. Conf. on Fusion Reactor Materials. doi:[https://doi.org/10.1016/S0022-3115\(00\)00356-1](https://doi.org/10.1016/S0022-3115(00)00356-1).
- [121] J. Busby, G. Was, E. Kenik, Isolating the effect of radiation-induced segregation in irradiation-assisted stress corrosion cracking of austenitic stainless steels, *Journal of Nuclear Materials* 302 (1) (2002) 20–40. doi:[https://doi.org/10.1016/S0022-3115\(02\)00719-5](https://doi.org/10.1016/S0022-3115(02)00719-5).
- [122] S. Zinkle, P. Maziasz, R. Stoller, Dose dependence of the microstructural evolution in neutron-irradiated austenitic stainless steel, *Journal of Nuclear Materials* 206 (2) (1993) 266–286. doi:[https://doi.org/10.1016/0022-3115\(93\)90128-L](https://doi.org/10.1016/0022-3115(93)90128-L).
- [123] P. J. Maziasz, Overview of microstructural evolution in neutron-irradiated austenitic stainless steels, *Journal of Nuclear Materials* 205 (1993) 118–145. doi:[10.1016/0022-3115\(93\)90077-c](https://doi.org/10.1016/0022-3115(93)90077-c).
- [124] K. Fukuya, K. Fujii, H. Nishioka, Y. Kitsunai, Evolution of microstructure and microchemistry in cold-worked 316 stainless steels under pwr irradiation, *Journal of Nuclear Science and Technology* 43 (2) (2006) 159–173. doi:[10.1080/18811248.2006.9711078](https://doi.org/10.1080/18811248.2006.9711078).
- [125] A. Ardell, Radiation-Induced Solute Segregation in Alloys, 1970, pp. 285–310. doi:[10.1007/978-1-4020-8422-5_15](https://doi.org/10.1007/978-1-4020-8422-5_15).
- [126] S. M. Bruemmer, G. S. Was, Microstructural and microchemical mechanisms controlling intergranular stress corrosion cracking in light-water-reactor systems, *Journal of Nuclear Materials* 216 (1994) 348–363. doi:[https://doi.org/10.1016/0022-3115\(94\)90020-5](https://doi.org/10.1016/0022-3115(94)90020-5).
- [127] Y. Han, J. Mei, Q. Peng, E.-H. Han, W. Ke, Effect of electropolishing on corrosion of nuclear grade 316L stainless steel in deaerated high temperature water, *Corrosion Science* 112 (2016) 625–634. doi:<https://doi.org/10.1016/j.corsci.2016.09.002>.
- [128] P. Deng, Q. Peng, E. Han, W. Ke, C. Sun, Z. Jiao, Effect of irradiation on corrosion of 304 nuclear grade stainless steel in simulated pwr primary water, *Corrosion Science* 127 (2017) 91–100. doi:<https://doi.org/10.1016/j.corsci.2017.08.010>.
- [129] G. F. Li, Y. Kaneshima, T. Shoji, Effects of Impurities on Environmentally Assisted Crack Growth of Solution-Annealed Austenitic Steels in Primary Water at 325°C, *Corrosion* 56 (5) (2000) 460–469. doi:[10.5006/1.3280550](https://doi.org/10.5006/1.3280550).
- [130] T. Yonezawa, K. Fujimoto, T. Iwamura, S. Nishida, Improvement of iascc resistance for austenitic stainless steels in pwr environment, 2000, pp. 224–238. doi:[10.1520/stp10221s](https://doi.org/10.1520/stp10221s).
- [131] T. Yonezawa, T. Iwamura, K. Fujimoto, K. Ajiki, Optimized chemical composition, working and heat treatment condition for resistance to irradiation assisted stress corrosion cracking of cold worked 316 and high-chromium austenitic stainless steel, *Journal of the Japan Institute of Metals* 64 (2000) 413–422. doi:[10.2320/jinstmet1952.64.5_413](https://doi.org/10.2320/jinstmet1952.64.5_413).
- [132] T. Yonezawa, Irradiation Assisted Stress Corrosion Cracking of Austenitic Stainless Steels in Water Reactors, *Corrosion Science and Technology* 7 (2) (2008) 77–84.
- [133] D. J. Edwards, E. P. Simonen, S. M. Bruemmer, Evolution of fine-scale defects in stainless steels neutron-irradiated at 275 °C, *Journal of Nuclear Materials* 317 (1) (2003) 13–31. doi:[10.1016/S0022-3115\(03\)00002-3](https://doi.org/10.1016/S0022-3115(03)00002-3).
- [134] A. Renault, J. Malaplate, C. Pokor, P. Gavaille, TEM and EFTEM characterization of solution annealed 304L stainless steel irradiated in PHENIX, up to 36 dpa and at 390 °C, *Journal of Nuclear Materials* 421 (1-3) (2012) 124–131. doi:[10.1016/j.jnucmat.2011.10.049](https://doi.org/10.1016/j.jnucmat.2011.10.049).

- [135] A. Padilha, P. Rios, Decomposition of austenite in austenitic stainless steels, *ISIJ International* 42 (4) (2002) 325–327. doi:[10.2355/isijinternational.42.325](https://doi.org/10.2355/isijinternational.42.325).
- [136] A. Renault-Laborne, J. Malaplate, C. Pokor, B. Tanguy, Characterization of precipitates in 316 Stainless Steel neutron-irradiated at $\sim 390^\circ\text{C}$ by the combination of CDF-TEM, EF-TEM, and HR-TEM, *ASTM Special Technical Publication Stp 1572* (October) (2014) 74–97. doi:[10.1520/stp157220130096](https://doi.org/10.1520/stp157220130096).
- [137] H. Brager, L. Blackburn, D. Greenslade, The dependence on displacement rate of radiation-induced changes in microstructure and tensile properties of AISI 304 and 316, *Journal of Nuclear Materials* 122 (1-3) (1984) 332–337. doi:[10.1016/0022-3115\(84\)90620-2](https://doi.org/10.1016/0022-3115(84)90620-2).
- [138] A. Renault, J. Malaplate, P. Gavaille, J. Garnier, C. Pokor, J. Massoud, Effects of chemical composition, metallurgical state and stress during irradiation on microstructure of neutron-irradiated austenitic stainless steels: comparison of pwr and bor-60 irradiations (Jul 2011).
- [139] K. Chen, J. Wang, D. Du, X. Guo, L. Zhang, Characterizing the effects of in-situ sensitization on stress corrosion cracking of austenitic steels in supercritical water, *Scripta Materialia* 158 (2019) 66–70. doi:<https://doi.org/10.1016/j.scriptamat.2018.08.041>.
- [140] L. Greenwood, Neutron interactions and atomic recoil spectra, *Journal of Nuclear Materials* 216 (1994) 29–44. doi:[https://doi.org/10.1016/0022-3115\(94\)90004-3](https://doi.org/10.1016/0022-3115(94)90004-3).
- [141] D. Hull, D. Bacon, Chapter 3 - movement of dislocations, in: D. Hull, D. Bacon (Eds.), *Introduction to Dislocations* (Fifth Edition), fifth edition Edition, Butterworth-Heinemann, Oxford, 2011, pp. 43–62. doi:<https://doi.org/10.1016/B978-0-08-096672-4.00003-7>.
- [142] G. S. Was, *Irradiation Hardening and Deformation*, Springer New York, New York, NY, 2017, pp. 669–733. doi:[10.1007/978-1-4939-3438-6_12](https://doi.org/10.1007/978-1-4939-3438-6_12).
- [143] F. Garner, *Irradiation Performance of Cladding and Structural Steels in Liquid Metal Reactors*, *Materials Science and Technology* (2006). doi:[10.1002/9783527603978.mst0110](https://doi.org/10.1002/9783527603978.mst0110).
- [144] F. Garner, E. Simonen, B. Oliver, L. Greenwood, M. Grossbeck, W. Wolfer, P. Scott, Retention of hydrogen in fcc metals irradiated at temperatures leading to high densities of bubbles or voids, *Journal of Nuclear Materials* 356 (1) (2006) 122–135, proceedings of the Seventh International Workshop on Spallation Materials Technology. doi:<https://doi.org/10.1016/j.jnucmat.2006.05.023>.
- [145] H. Schroeder, H. Ullmaier, Helium and hydrogen effects on the embrittlement of iron- and nickel-based alloys, *Journal of Nuclear Materials* 179-181 (Part 1) (1991) 118–124. doi:[10.1016/0022-3115\(91\)90025-3](https://doi.org/10.1016/0022-3115(91)90025-3).
- [146] T. S. Byun, N. Hashimoto, [Strain localization in irradiated materials](#) 38, research Org.: Oak Ridge National Lab. (ORNL), Oak Ridge, TN (United States). High Flux Isotope Reactor (HFIR); Oak Ridge National Lab. (ORNL), Oak Ridge, TN (United States). Shared Research Equipment Collaborative Research Center (Jan 2006). URL <https://www.osti.gov/biblio/1003606>
- [147] Z. Jiao, G. Was, Localized deformation and iascc initiation in austenitic stainless steels, *Journal of Nuclear Materials* 382 (2) (2008) 203–209, microstructural Processes in Irradiated Materials. doi:<https://doi.org/10.1016/j.jnucmat.2008.08.032>.
- [148] H. Nishioka, K. Fukuya, K. Fujii, Y. Kitsunai, Deformation structure in highly irradiated stainless steels, *Journal of Nuclear Science and Technology* 45 (4) (2008) 274–287. doi:

- [10.1080/18811248.2008.9711437](https://doi.org/10.1080/18811248.2008.9711437).
- [149] T. S. Byun, N. Hashimoto, K. Farrell, Deformation mode map of irradiated 316 stainless steel in true stress-dose space, *Journal of Nuclear Materials* 351 (1-3) (2006) 303–315. doi:[10.1016/j.jnucmat.2006.02.033](https://doi.org/10.1016/j.jnucmat.2006.02.033).
- [150] B. Alexandreanu, G. S. Was, Grain Boundary Deformation-Induced Intergranular Stress Corrosion Cracking of Ni-16Cr-9Fe in 360°C Water, *Corrosion* 59 (8) (2003) 705–720. doi:[10.5006/1.3277600](https://doi.org/10.5006/1.3277600).
- [151] D. Du, K. Sun, G. S. Was, Iascc of neutron irradiated 316 stainless steel to 125 dpa, *Materials Characterization* 173 (2021) 110897. doi:<https://doi.org/10.1016/j.matchar.2021.110897>.
- [152] W. Hoffelner, Development and application of nano-structured materials in nuclear power plants, Woodhead Publishing Limited, 2010. doi:[10.1533/9781845699956.3.581](https://doi.org/10.1533/9781845699956.3.581).
- [153] C. H. Henager, Jr, E. P. Simonen, [Critical assessment of low fluence irradiation creep mechanisms](#), in: Conference: 12. international symposium on effects of radiation on materials, 1984. URL <https://www.osti.gov/biblio/6678354>
- [154] P. T. Heald, M. V. Speight, Irradiation creep and swelling, *Philosophical Magazine* 30 (4) (1974) 869–875. doi:[10.1080/14786437408207240](https://doi.org/10.1080/14786437408207240).
- [155] T.L. Anderson, (2017). *Fracture Mechanics: Fundamentals and Applications* (4th ed.). CRC Press. <https://doi.org/10.1201/9781315370293>.
- [156] A. A. Griffith, G. I. Taylor, The phenomena of rupture and flow in solids, *Philosophical Transactions of the Royal Society of London. Series A, Containing Papers of a Mathematical or Physical Character* 221 (582-593) (1921) 163–198. doi:[10.1098/rsta.1921.0006](https://doi.org/10.1098/rsta.1921.0006).
- [157] G. R. Irwin, Analysis of stresses and strains near the end of a crack traversing a plate, *Journal of Applied Mechanics* 24 (3) (1957) 361–364. doi:[10.1115/1.4011547](https://doi.org/10.1115/1.4011547).
- [158] D. Gross, T. Seelig, *Fracture mechanics: With an introduction to micromechanics*, Fraunhofer IWM (01 2011). doi:[10.1007/b22134](https://doi.org/10.1007/b22134).
- [159] R. N. Parkins, Strain Rate Effects in Stress Corrosion Cracking, *Corrosion* 46 (3) (1990) 178–189. doi:[10.5006/1.3585089](https://doi.org/10.5006/1.3585089).
- [160] R. Staehle, Introduction to initiation, in: *Proceedings of the Workshop on Detection, Avoidance, Mechanisms, Modelling, and Prediction of SCC Initiation in Water-Cooled Nuclear Reactor Plants*, Beaune, France, 2008.
- [161] R. Bosch, M. Vankeerberghen, R. Gérard, F. Somville, Crack initiation testing of thimble tube material under pwr conditions to determine a stress threshold for iascc, *Journal of Nuclear Materials* 461 (2015) 112–121. doi:<https://doi.org/10.1016/j.jnucmat.2015.02.038>.
- [162] M. J. Konstantinović, Internal oxidation and probabilistic fracture model of irradiation assisted stress corrosion cracking in stainless steels, *Journal of Nuclear Materials* 495 (2017) 220–224. doi:[10.1016/j.jnucmat.2017.08.018](https://doi.org/10.1016/j.jnucmat.2017.08.018).
- [163] R. Newman, Aspects of Stress Corrosion Cracking Relevant to Irradiation-Assisted Stress Corrosion Cracking (IASCC), Tech. Rep. 1003421., Epri (05 2002).
- [164] A. Penders, M. Konstantinović, R. Bosch, D. Schryvers, Crack initiation in tapered high si stain-

- less steel specimens - stress threshold analyses, *Corrosion Engineering, Science and Technology* 55 (8) (2020) 721–728. doi:10.1080/1478422x.2020.1785651.
- [165] S. Majumdar, *Assessment of Current Understanding of Mechanisms of Initiation, Arrest, and Reinitiation of Stress Corrosion Cracks in PWR Steam Generator Tubing*, Tech. Rep. Nureg/cr-5752, Anl-99/4 ((2000).)
URL <https://www.nrc.gov/docs/ML0036/ML003688205.pdf>
- [166] R. W. Staehle, Quantitative micro-nano (qmn) approach to scc mechanism and prediction-starting a third meeting, in: J. T. Busby, G. Ilevbare, P. L. Andresen (Eds.), *Proceedings of the 15th International Conference on Environmental Degradation of Materials in Nuclear Power Systems — Water Reactors*, Springer International Publishing, Cham, 2016, pp. 1535–1629.
- [167] E. P. DeGarmo, *Materials and processes in manufacturing*, 12th Edition, Wiley, Hoboken, NJ, 2017.
- [168] K. Kruska, S. Lozano-Perez, D. W. Saxey, T. Terachi, T. Yamada, G. D. W. Smith, 3d atom-probe characterization of stress and cold-work in stress corrosion cracking of 304 stainless steel (2016) 939–951.
- [169] S. Lozano-Perez, K. Kruska, I. Iyengar, T. Terachi, T. Yamada, The role of cold work and applied stress on surface oxidation of 304 stainless steel, *Corrosion Science* 56 (2012) 78–85. doi:<https://doi.org/10.1016/j.corsci.2011.11.021>.
- [170] H. Yang, H. Xue, F. Yang, S. Wang, Effect of cold working on the driving force of the crack growth and crack growth rate of welded joints under one overload, *Advances in Materials Science and Engineering* 2020 (2020) 4972589. doi:10.1155/2020/4972589.
- [171] C. Donadille, R. Valle, P. Dervin, R. Penelle, Development of texture and microstructure during cold-rolling and annealing of F.C.C. alloys: Example of an austenitic stainless steel, *Acta Metallurgica* 37 (6) (1989) 1547–1571. doi:10.1016/0001-6160(89)90123-5.
- [172] O. Raquet, E. Herms, F. Vaillant, T. Couvant, Scc of cold-worked austenitic stainless steels in pwr conditions, *Advances in Materials Science* Vol. 7, nr 1(11) (2007) 33–46.
- [173] K. Arioka, T. Yamada, T. Terachi, G. Chiba, Cold Work and Temperature Dependence of Stress Corrosion Crack Growth of Austenitic Stainless Steels in Hydrogenated and Oxygenated High-Temperature Water, *Corrosion* 63 (12) (2007) 1114–1123. doi:10.5006/1.3278329.
- [174] T. Couvant, F. Vaillant, J. Boursier, D. Delafosse, Effect of strain-path on stress corrosion cracking of aisi 304l stainless steel in pwr primary environment at 360 ° c, in: *EUROCORR 2004 - European Corrosion Conference: Long Term Prediction and Modelling of Corrosion*, Vol. 11, 2004, p. 11. doi:10.1533/9781845693466.2.87.
- [175] W. Becker, S. Lampman, *Fracture Appearance and Mechanisms of Deformation and Fracture*, in: *Failure Analysis and Prevention*, ASM International, 2002. doi:10.31399/asm.hb.v11.a0003537.
- [176] O. Chopra, *Mechanism of Fatigue Crack Initiation in Austenitic Stainless Steels in LWR Environments*, Vol. *Pressure Vessel and Piping Codes and Standards of Pressure Vessels and Piping Conference*, 2002, pp. 133–142. doi:10.1115/pvp2002-1230.
- [177] R. Alain, P. Violan, J. Mendez, Low cycle fatigue behavior in vacuum of a 316l type austenitic stainless steel between 20 and 600°C part i: Fatigue resistance and cyclic behavior, *Materials Science and Engineering: A* 229 (1) (1997) 87–94. doi:[https://doi.org/10.1016/S0921-5093\(96\)10558-X](https://doi.org/10.1016/S0921-5093(96)10558-X).

- [178] K. Tsutsumi, T. Dodo, H. Kanasaki, S. Nomoto, Y. Minami, T. Nakamura, Fatigue behavior of stainless steel under conditions of changing strain rate in PWR primary water, Asme, New York, NY, 2001, pp. 135–141.
- [179] O. Chopra, [Effects of LWR Coolant Environments on Fatigue Design Curves of Austenitic Stainless Steels](#), Tech. Rep. Nureg/cr-5704, Anl-98/31 ((1999).).
URL <https://www.nrc.gov/reading-rm/doc-collections/nuregs/contract/cr6583/index.html>
- [180] M. Higuchi, K. Iida, Reduction in Low-Cycle Fatigue Life of Austenitic Stainless Steels in High-Temperature Water, Asme, New York, NY, 1997, pp. 79–86.
- [181] P. Chowdhury, H. Sehitoglu, Mechanisms of fatigue crack growth – a critical digest of theoretical developments, *Fatigue & Fracture of Engineering Materials & Structures* 39 (6) (2016) 652–674. doi:<https://doi.org/10.1111/ffe.12392>.
- [182] B. Cottis, 2015. Introduction to Corrosion [Conference notes]. NuCoSS-15, 7-12 July, Gozd Martuljek, Slovenia.
- [183] P. Pedefferri (Deceased), Intergranular and Selective Corrosion, Springer International Publishing, Cham, 2018, pp. 297–311. doi:[10.1007/978-3-319-97625-9_15](https://doi.org/10.1007/978-3-319-97625-9_15).
- [184] K. Sieradzki, R. C. Newman, R. C. Newman, Brittle behavior of ductile metals during stress-corrosion cracking, *Philosophical Magazine A: Physics of Condensed Matter, Structure, Defects and Mechanical Properties* 51 (1) (1985) 95–132. doi:[10.1080/01418618508245272](https://doi.org/10.1080/01418618508245272).
- [185] F. P. Ford, P. W. Emigh, The prediction of the maximum corrosion fatigue crack propagation rate in the low alloy steel-de-oxygenated water system at 288°C, *Corrosion Science* 25 (8) (1985) 673–692.
- [186] P. L. Andresen, Environmentally Assisted Growth Rate Response of Nonsensitized AISI 316 Grade Stainless Steels in High Temperature Water, *Corrosion* 44 (7) (1988) 450–460. doi:[10.5006/1.3583961](https://doi.org/10.5006/1.3583961).
- [187] P. M. Scott, M. Le Calver, [Some possible mechanisms of intergranular stress corrosion cracking of alloy 600 in pwr primary water](#) (1993).
URL http://inis.iaea.org/search/search.aspx?orig_q=RN:25067219
- [188] P. M. Scott, An overview of internal oxidation as a possible explanation of intergranular stress corrosion cracking of alloy 600 in pwr (1999) 1–14 doi:<https://doi.org/10.1002/9781118787618.ch1>.
- [189] H. G. Nelson, Hydrogen embrittlement, in: C. Briant, S. Banerji (Eds.), *Embrittlement of Engineering Alloys*, Vol. 25 of *Treatise on Materials Science & Technology*, Elsevier, 1983, pp. 275–359. doi:<https://doi.org/10.1016/B978-0-12-341825-8.50014-3>.
- [190] C. D. Beachem, A new model for hydrogen-assisted cracking (hydrogen “embrittlement”), *Metallurgical and Materials Transactions B* 3 (2) (1972) 441–455. doi:[10.1007/bf02642048](https://doi.org/10.1007/bf02642048).
- [191] H. Birnbaum, P. Sofronis, Hydrogen-enhanced localized plasticity—a mechanism for hydrogen-related fracture, *Materials Science and Engineering: A* 176 (1) (1994) 191–202. doi:[https://doi.org/10.1016/0921-5093\(94\)90975-X](https://doi.org/10.1016/0921-5093(94)90975-X).
- [192] A. R. Troiano, The role of hydrogen and other interstitials in the mechanical behavior of metals, *Metallography, Microstructure, and Analysis* 5 (6) (2016) 557–569. doi:[10.1007/s13632-016-0319-4](https://doi.org/10.1007/s13632-016-0319-4).

- [193] R. A. Oriani, Whitney Award Lecture–1987: Hydrogen–The Versatile Embrittler, *Corrosion* 43 (7) (1987) 390–397. doi:[10.5006/1.3583875](https://doi.org/10.5006/1.3583875).
- [194] M. Vankeerberghen, G. Weyns, S. Gavrilov, B. Martens, J. Deconinck, Crack propagation rate modelling for 316ss exposed to pwr-relevant conditions, *Journal of Nuclear Materials* 384 (3) (2009) 274–285. doi:<https://doi.org/10.1016/j.jnucmat.2008.11.034>.
- [195] R.E. Ricker, J. Fink, E. Escalante. Evidence of film-induced cleavage by electrodeposited Rh. *Corros Deformations Interact.* 1993; (January 1993):733–740.
- [196] R. C. Newman, K. Sieradzki, *Film-Induced Cleavage During Stress-Corrosion Cracking of Ductile Metals and Alloys*, Springer Netherlands, Dordrecht, 1987, pp. 597–611. doi:[10.1007/978-94-009-3665-2_37](https://doi.org/10.1007/978-94-009-3665-2_37).
- [197] R. Newman, R. Corderman, K. Sieradzki, Evidence for dealloying of austenitic stainless steels in simulated stress corrosion crack environments, *Corrosion Engineering Science and Technology* 24 (2) (1989) 143–148, funding Information: This research was supported at BNL by the US Department of Energy, Office of Basic Energy Sciences, Division of Materials Sciences, under contract no. DE-Ae02-76eH0016. doi:[10.1179/000705989798270261](https://doi.org/10.1179/000705989798270261).
- [198] C. Edeleanu, A. J. Forty, Some observations on the stress-corrosion cracking of α -brass and similar alloys, *The Philosophical Magazine: A Journal of Theoretical Experimental and Applied Physics* 5 (58) (1960) 1029–1040. doi:[10.1080/14786436008235881](https://doi.org/10.1080/14786436008235881).
- [199] U. Bertocci, E. N. Pugh and R. E. Ricker, Environment-induced cracking of copper alloy. *Environment-induced Cracking of Metals* (eds. R. P. Gangloff and M. B. Ives), pp. 273-285, NACE, Houston (1990).
- [200] R. Ricker, J. Fink, J. Harris, A. Shapiro, Evidence for film-induced cleavage in rhodium plated nickel 26 (4 1992).
- [201] J. Galvele, A stress corrosion cracking mechanism based on surface mobility, *Corrosion Science* 27 (1) (1987) 1–33. doi:[https://doi.org/10.1016/0010-938X\(87\)90117-X](https://doi.org/10.1016/0010-938X(87)90117-X).
- [202] S. Lynch, 1 - mechanistic and fractographic aspects of stress-corrosion cracking (scc), in: V. Raja, T. Shoji (Eds.), *Stress Corrosion Cracking*, Woodhead Publishing Series in Metals and Surface Engineering, Woodhead Publishing, 2011, pp. 3–89. doi:<https://doi.org/10.1533/9780857093769.1.3>.
- [203] A. Turnbull, Modelling of environment assisted cracking, *Corrosion Science* 34 (6) (1993) 921–960. doi:[https://doi.org/10.1016/0010-938X\(93\)90072-0](https://doi.org/10.1016/0010-938X(93)90072-0).
- [204] Z. Li, Y. Lu, X. Wang, Modeling of stress corrosion cracking growth rates for key structural materials of nuclear power plant, *Journal of Materials Science* 55 (2) (2020) 439–463. doi:[10.1007/s10853-019-03968-w](https://doi.org/10.1007/s10853-019-03968-w).
- [205] E. Gutman, An inconsistency in “film rupture model” of stress corrosion cracking, *Corrosion Science* 49 (5) (2007) 2289–2302. doi:<https://doi.org/10.1016/j.corsci.2006.10.023>.
- [206] H. L. L., *Film-Rupture Mechanism of Stress Corrosion*, *Journal of Research of the National Bureau of Standards* 48 (2) (1952) 99–105.
URL https://nvlpubs.nist.gov/nistpubs/jres/048/jresv48n2p99_A1b.pdf
- [207] T. Nakayama, M. Takano, Application of a Slip Dissolution-Repassivation Model for Stress Corrosion Cracking of AISI 304 Stainless Steel in a Boiling 42

- % MgCl₂ Solution, Corrosion 42 (1) (1986) 10–15. doi:10.5006/1.3584873.
- [208] F. P. Ford, Quantitative Prediction of Environmentally Assisted Cracking, Corrosion 52 (5) (1996) 375–395. doi:10.5006/1.3292125.
- [209] T. Hashimoto, M. Koshiishi, Modification of the fri crack growth model formulation from a mathematical viewpoint, Journal of Nuclear Science and Technology 46 (3) (2009) 295–302. doi:10.1080/18811248.2007.9711533.
- [210] M. Koshiishi, S. Tanaka, R. Obata, Formulation of irradiation assisted stress corrosion crack growth rates for neutron-irradiated stainless steels under hydrogen water chemistry conditions of boiling water reactors, Journal of Nuclear Science and Technology 59 (9) (2022) 1107–1116. doi:10.1080/00223131.2022.2030261.
- [211] D. A. Jones, A unified mechanism of stress corrosion and corrosion fatigue cracking, Metallurgical Transactions A 16 (6) (1985) 1133–1141. doi:10.1007/bf02811682.
- [212] D. D. Macdonald, On the modeling of stress corrosion cracking in iron and nickel base alloys in high temperature aqueous environments, Corrosion Science 38 (6) (1996) 1003–1010. doi:https://doi.org/10.1016/0010-938X(96)00048-0.
- [213] M. Hall, Critique of the ford–andresen film rupture model for aqueous stress corrosion cracking, Corrosion Science 51 (5) (2009) 1103–1106. doi:https://doi.org/10.1016/j.corsci.2009.02.022.
- [214] S. Lozano-perez, M. Meisnar, J. Dohr, Reviewing the internal oxidation mechanism as a plausible explanation for SCC in PWR primary water. In proceedings of the 16th international Conference on Environmental Degradations of Materials in Nuclear Power Systems-Water Reactors (August 2013).
- [215] Y. Behnamian, A. Mostafaei, A. Kohandehghan, B. S. Amirkhiz, J. Li, R. Zahiri, E. Aghaie, W. Zheng, D. Guzonas, M. Chmielus, W. Chen, J. L. Luo, Internal oxidation and crack susceptibility of alloy 310s stainless steel after long term exposure to supercritical water at 500°C, The Journal of Supercritical Fluids 120 (2017) 161–172. doi:https://doi.org/10.1016/j.supflu.2016.09.007.
- [216] R. Parkins, Metallography of environment sensitive fracture, Materials Characterization 26 (4) (1991) 303–323, failure Analysis: From Large Structures to Small Components. doi:https://doi.org/10.1016/1044-5803(91)90019-Z.
- [217] T. Magnin, R. Chieragatti, R. Oltra, Mechanism of brittle fracture in a ductile 316 alloy during stress corrosion, Acta Metallurgica et Materialia 38 (7) (1990) 1313–1319. doi:https://doi.org/10.1016/0956-7151(90)90203-S.
- [218] F. Scenini, A. Sherry, Stress Corrosion Cracking of Sensitized Type 304 Stainless Steel in High-Temperature Water with Anionic Impurities Contamination, Corrosion 68 (12) (2012) 1094–1107. doi:10.5006/0690.
- [219] C. Guerre, P. Laghoutaris, J. Chêne, L. Marchetti, R. Molins, C. Duhamel, M. Sennour, Stress corrosion cracking of alloy 600 in pwr primary water : Influence of chromium, hydrogen and oxygen diffusion, in: J. T. Busby, G. Ilevbare, P. L. Andresen (Eds.), Proceedings of the 15th International Conference on Environmental Degradation of Materials in Nuclear Power Systems — Water Reactors, Springer International Publishing, Cham, 2016, pp. 1477–1490.
- [220] Y. Lu, Q. Peng, T. Sato, T. Shoji, An aem study of oxidation behavior of scc crack tips in 304l stainless steel in high temperature oxygenated water, Journal of Nuclear Materials 347 (1)

- (2005) 52–68. doi:<https://doi.org/10.1016/j.jnucmat.2005.07.006>.
- [221] R. Rebak, Z. Szklarska-Smialowska, The mechanism of stress corrosion cracking of alloy 600 in high temperature water, *Corrosion Science* 38 (6) (1996) 971–988. doi:[https://doi.org/10.1016/0010-938X\(96\)00183-7](https://doi.org/10.1016/0010-938X(96)00183-7).
- [222] K. Fujii, K. Fukuya, Development of micro tensile testing method in an fib system for evaluating grain boundary strength, *Materials Transactions* 52 (1) (2011) 20–24. doi:[10.2320/matertrans.M2010320](https://doi.org/10.2320/matertrans.M2010320).
- [223] T. Miura, K. Fujii, K. Fukuya, H. Seto, Micro-mechanical investigation about degradation of grain boundary cohesive strength of neutron-irradiated stainless steels, *Journal of Nuclear Science and Technology* 59 (10) (2022) 1251–1265. doi:[10.1080/00223131.2022.2041125](https://doi.org/10.1080/00223131.2022.2041125).
- [224] K. Fukuya, H. Nishioka, K. Fujii, Y. Kitsunai, Characterization of iascc crack tip in highly irradiated stainless steels, *14th International Conference on Environmental Degradation of Materials in Nuclear Power Systems Water Reactors 2009 2* (2009) 1248–1258.
- [225] R. Matthews, R. Knusten, J. Westraadt, T. Couvant, Intergranular oxidation of 316l stainless steel in the pwr primary water environment, *Corrosion Science* 125 (2017) 175–183. doi:<https://doi.org/10.1016/j.corsci.2017.06.023>.
- [226] T. Fukumura, K. Fukuya, K. Fujii, T. Miura, Y. Kitsunai, Grain boundary oxidation of neutron irradiated stainless steels in simulated pwr water, in: J. H. Jackson, D. Paraventi, M. Wright (Eds.), *Proceedings of the 18th International Conference on Environmental Degradation of Materials in Nuclear Power Systems – Water Reactors*, Springer International Publishing, Cham, 2019, pp. 2153–2163.
- [227] H. Dugdale, D. E. Armstrong, E. Tarleton, S. G. Roberts, S. Lozano-Perez, How oxidized grain boundaries fail, *Acta Materialia* 61 (13) (2013) 4707–4713. doi:<https://doi.org/10.1016/j.actamat.2013.05.012>.
- [228] J. Wachtman, W. Cannon, M. Matthewson, *Statistical Treatment of Strength*, John Wiley & Sons, Ltd, 2009, Ch. 7, pp. 119–150. doi:<https://doi.org/10.1002/9780470451519.ch7>.
- [229] J. Yang, J. A. Gaspar, O. Paul, Fracture properties of lpcvd silicon nitride and thermally grown silicon oxide thin films from the load-deflection of long Si_3N_4 and $\text{SiO}_2\text{Si}_3\text{N}_4$ diaphragms, *Journal of Microelectromechanical Systems* 17 (5) (2008) 1120–1134. doi:[10.1109/jmems.2008.928706](https://doi.org/10.1109/jmems.2008.928706).
- [230] P. Paris, F. Erdogan, A Critical Analysis of Crack Propagation Laws, *Journal of Basic Engineering* 85 (4) (1963) 528–533. doi:[10.1115/1.3656900](https://doi.org/10.1115/1.3656900).
- [231] Z. Shen, D. Du, L. Zhang, S. Lozano-Perez, An insight into pwr primary water scc mechanisms by comparing surface and crack oxidation, *Corrosion Science* 148 (2019) 213–227. doi:<https://doi.org/10.1016/j.corsci.2018.12.020>.
- [232] A. Penders, M. Konstantinović, T. Yang, R.-W. Bosch, D. Schryvers, F. Somville, Microstructural investigation of iascc crack tips extracted from thimble tube o-ring specimens, *Journal of Nuclear Materials* 565 (2022) 153727. doi:<https://doi.org/10.1016/j.jnucmat.2022.153727>.
- [233] H. Evans, H. Li, P. Bowen, A mechanism for stress-aided grain boundary oxidation ahead of cracks, *Scripta Materialia* 69 (2) (2013) 179–182. doi:<https://doi.org/10.1016/j.scriptamat.2013.03.026>.
- [234] T. Couvant, J. Caballero, C. Duhamel, J. Crépin, T. Maeguchi. Calibration of the Local IG-

- SCC Engineering Model for Alloy 600. In Proceedings of the 18th International Conference on Environmental Degradation of Materials in Nuclear Power Systems-Water Reactors, Portland, Oregon, USA, 13-17 August 2017.
- [235] T. Couvant, E. Burger, C. Thaury, C. Rainasse. Simulating the Susceptibility to IGEAC of Cold-Work 316 Austenitic Stainless Steel Exposed to Primary Water. In Proceedings of the 19th International Conference on Environmental Degradation of Materials in Nuclear Power Systems-Water Reactors, Boston, MA, USA, 18–22 August 2019.
- [236] S. P. Lynch, Mechanisms of h-assisted cracking, *Metals Forum* 2 (3) (1979) 189–200.
- [237] B. Bilby, J. Hewitt, Hydrogen in steel—the stability of micro-cracks, *Acta Metallurgica* 10 (6) (1962) 587–600. doi:[https://doi.org/10.1016/0001-6160\(62\)90048-2](https://doi.org/10.1016/0001-6160(62)90048-2).
- [238] D. G. Westlake, *Generalized model for hydrogen embrittlement.*, ASM (Amer. Soc. Metals), Trans. Quart. 62: 1000-6(Dec 1969). (1 1969).
URL <https://www.osti.gov/biblio/4173745>
- [239] M. D. Dolan, M. A. Kochanek, C. N. Munnings, K. G. McLennan, D. M. Viano, Hydride phase equilibria in v–ti–ni alloy membranes, *Journal of Alloys and Compounds* 622 (2015) 276–281. doi:<https://doi.org/10.1016/j.jallcom.2014.10.081>.
- [240] N. Brodusch, H. Demers, R. Gauvin, Imaging with a commercial electron backscatter diffraction (ebstd) camera in a scanning electron microscope: A review, *Journal of Imaging* 4 (7) (2018). doi:[10.3390/jimaging4070088](https://doi.org/10.3390/jimaging4070088).
- [241] M. Szyrkowska, Microscopy techniques | scanning electron microscopy, in: P. Worsfold, A. Townshend, C. Poole (Eds.), *Encyclopedia of Analytical Science* (Second Edition), second edition Edition, Elsevier, Oxford, 2005, pp. 134–143. doi:<https://doi.org/10.1016/B0-12-369397-7/00385-X>.
- [242] D. Stokes, *Principles of SEM*, John Wiley & Sons, Ltd, 2008, Ch. 2, pp. 17–62. doi:<https://doi.org/10.1002/9780470758731.ch2>.
- [243] J. Kuba, J. Michels, M. Hovorka, P. Erdmann, L. Berka, R. Kirmse, J. Köning, J. De Bock, B. Goetze, A. Rigort, Advanced cryo-tomography workflow developments – correlative microscopy, milling automation and cryo-lift-out, *Journal of Microscopy* 281 (2) (2021) 112–124. doi:<https://doi.org/10.1111/jmi.12939>.
- [244] R. M. Langford, A. K. Petford-Long, Preparation of transmission electron microscopy cross-section specimens using focused ion beam milling, *Journal of Vacuum Science & Technology A* 19 (5) (2001) 2186–2193. doi:[10.1116/1.1378072](https://doi.org/10.1116/1.1378072).
- [245] Y. Z. Huang, S. Lozano-Perez, R. M. Langford, J. M. Titchmarsh, M. L. Jenkins, Preparation of transmission electron microscopy cross-section specimens of crack tips using focused ion beam milling, *Journal of Microscopy* 207 (2) (2002) 129–136. doi:<https://doi.org/10.1046/j.1365-2818.2002.01050.x>.
- [246] S. Lozano-Perez, A guide on fib preparation of samples containing stress corrosion crack tips for tem and atom-probe analysis, *Micron* 39 (3) (2008) 320–328. doi:<https://doi.org/10.1016/j.micron.2007.12.003>.
- [247] R. M. Langford, Y. Z. Huang, S. Lozano-Perez, J. M. Titchmarsh, A. K. Petford-Long, Preparation of site specific transmission electron microscopy plan-view specimens using a focused ion beam system, *Journal of Vacuum Science & Technology B: Microelectronics and Nanometer Structures Processing, Measurement, and Phenomena* 19 (3) (2001) 755–758. doi:

[10.1116/1.1371317](https://doi.org/10.1116/1.1371317).

- [248] N. I. Kato, N. Miura, N. Tsutsui, A plasma-polymerized protective film for transmission electron microscopy specimen preparation by focused ion beam etching, *Journal of Vacuum Science & Technology A* 16 (3) (1998) 1127–1130. doi:[10.1116/1.581245](https://doi.org/10.1116/1.581245).
- [249] T. Ishitani, K. Umemura, T. Ohnishi, T. Yaguchi, T. Kamino, Improvements in performance of focused ion beam cross-sectioning: aspects of ion-sample interaction, *Journal of Electron Microscopy* 53 (5) (2004) 443–449. doi:[10.1093/jmicro/dfh078](https://doi.org/10.1093/jmicro/dfh078).
- [250] T. H. Loeber, B. Laegel, S. Wolff, S. Schuff, F. Balle, T. Beck, D. Eifler, J. H. Fitschen, G. Steidl, Reducing curtaining effects in fib/sem applications by a goniometer stage and an image processing method, *Journal of Vacuum Science & Technology B* 35 (6) (2017) 1–7. doi:[10.1116/1.4991638](https://doi.org/10.1116/1.4991638).
- [251] W. Van Renterghem, User Manual JEOL 3010 STEM, Sckcen: Nms-nma, Boeretang 200, B-2400 Mol (November 2016).
- [252] D. B. Williams, C. B. Carter, *The Instrument*, Springer US, Boston, MA, 2009, pp. 141–171. doi:[10.1007/978-0-387-76501-3_9](https://doi.org/10.1007/978-0-387-76501-3_9).
- [253] K. W. Andrews, D. J. Dyson, S. R. Keown, *Fundamentals of electron diffraction*, Springer US, Boston, MA, 1967, pp. 5–7. doi:[10.1007/978-1-4899-6475-5_2](https://doi.org/10.1007/978-1-4899-6475-5_2).
- [254] M. Klinger, *CrysTBox - Crystallographic Toolbox*, Institute of Physics of the Czech Academy of Sciences, Prague, 2015.
URL <http://www.fzu.cz/~klinger/crystbox.pdf>
- [255] G. Cliff, G. W. Lorimer, The quantitative analysis of thin specimens, *Journal of Microscopy* 103 (2) (1975) 203–207. doi:<https://doi.org/10.1111/j.1365-2818.1975.tb03895.x>.
- [256] M. Watanabe, D. B. Williams, The quantitative analysis of thin specimens: a review of progress from the Cliff-Lorimer to the new zeta-factor methods, *J Microsc* 221 (Pt 2) (2006) 89–109.
- [257] J. Liu, Scanning transmission electron microscopy and its application to the study of nanoparticles and nanoparticle systems, *Journal of Electron Microscopy* 54 (3) (2005) 251–278. doi:[10.1093/jmicro/dfi034](https://doi.org/10.1093/jmicro/dfi034).
- [258] R. Kilian, B. Devrient, Experimental data on crack initiation, Tech. Rep. deliverable C35c, FP6 project PERFECT (2008).
- [259] W.-T. Tsai, Y.-N. Wen, J.-T. Lee, H.-Y. Liou, W.-F. Wang, Effect of silicon addition on the microstructure and corrosion behavior of sintered stainless steel, *Surface and Coatings Technology* 34 (3) (1988) 209–217. doi:[https://doi.org/10.1016/0257-8972\(88\)90113-2](https://doi.org/10.1016/0257-8972(88)90113-2).
- [260] J. C. Pang, B. Y. Xu, G. D. Wang, Q. Lu, J. F. Wang, H. L. Yi, Effect of silicon and aluminium in ferrite on tensile and impact properties, *Materials Science and Technology* 33 (15) (2017) 1806–1810. doi:[10.1080/02670836.2017.1320085](https://doi.org/10.1080/02670836.2017.1320085).
- [261] Zajec B., Hojna A., Bosch R.W., et al. DELIVERABLE D6.2 – Applied experimental procedures, 2018.
- [262] J. Bai, S. Ritter, H.-P. Seifert, S. Virtanen, Using tapered specimens to study the effect of hydrogen and surface finish on scc initiation in alloy 182 under boiling water reactor conditions, *Corrosion Engineering, Science and Technology* 52 (8) (2017) 558–566. doi:[10.1080/1478422x.2017.1340245](https://doi.org/10.1080/1478422x.2017.1340245).

- [263] J. Bai, S. Ritter, H.-P. Seifert, M. Vankeerberghen, R.-W. Bosch, The use of tapered specimens to evaluate the scc initiation susceptibility in alloy 182 in bwr and pwr environments, in: J. H. Jackson, D. Paraventi, M. Wright (Eds.), *Proceedings of the 18th International Conference on Environmental Degradation of Materials in Nuclear Power Systems – Water Reactors*, Springer International Publishing, Cham, 2019, pp. 1929–1948.
- [264] M. Vankeerberghen. Some Effects of Surface Finish and LWR Environment on Environmentally-assisted Crack Initiation in Alloy 182, In *Proceedings of the 20th International Conference on Environmental Degradation of Materials in Nuclear Power Systems-Water Reactors, USA, July 2022*.
- [265] J. Schindelin, I. Arganda-Carreras, E. Frise, V. Kaynig, M. Longair, T. Pietzsch, S. Preibisch, C. Rueden, S. Saalfeld, B. Schmid, J.-Y. Tinevez, D. J. White, V. Hartenstein, K. Eliceiri, P. Tomancak, A. Cardona, Fiji: an open-source platform for biological-image analysis, *Nature Methods* 9 (7) (2012) 676–682. doi:[10.1038/nmeth.2019](https://doi.org/10.1038/nmeth.2019).
- [266] C. Steger, An unbiased detector of curvilinear structures, *IEEE Transactions on Pattern Analysis and Machine Intelligence* 20 (2) (1998) 113–125. doi:[10.1109/34.659930](https://doi.org/10.1109/34.659930).
- [267] P. J. Jacques, E. Girault, A. Mertens, B. Verlinden, J. van Humbeeck, F. Delannay, The developments of cold-rolled trip-assisted multiphase steels. al-alloyed trip-assisted multiphase steels, *ISIJ International* 41 (9) (2001) 1068–1074. doi:[10.2355/isijinternational.41.1068](https://doi.org/10.2355/isijinternational.41.1068).
- [268] Tech. rep., materials Reliability Program: Characterizations of Type 316 Cold Worked Stainless Steel Highly Irradiated Under PWR Operating Conditions (International IASCC Advisory Committee Phase 3 Program Interim Report) (MRP-202). EPRI, Palo Alto, CA: 2006. 1013418. 11303336.
- [269] R. W. Bosch, Design of an O-ring compression test device for in a hot cell, Tech. Rep. Restricted contract report R-4791, Sckcen (April 2009).
- [270] A. Penders, M. J. KonstantinoviÄ†, W. V. Renterghem, R. Bosch, D. Schryvers, Tem investigation of scc crack tips in high si stainless steel tapered specimens, *Corrosion Engineering, Science and Technology* 56 (8) (2021) 767–777. doi:[10.1080/1478422x.2021.1961665](https://doi.org/10.1080/1478422x.2021.1961665).
- [271] Z. Shen, L. Zhang, R. Tang, Q. Zhang, Scc susceptibility of type 316ti stainless steel in supercritical water, *Journal of Nuclear Materials* 458 (2015) 206–215. doi:<https://doi.org/10.1016/j.jnucmat.2014.12.014>.
- [272] P. Tao, J. ming Gong, Y. fei Wang, Y. Jiang, Y. Li, W. wei Cen, Characterization on stress-strain behavior of ferrite and austenite in a 2205 duplex stainless steel based on nanoindentation and finite element method, *Results in Physics* 11 (2018) 377–384. doi:<https://doi.org/10.1016/j.rinp.2018.06.023>.
- [273] P. Moore, G. Booth, 8 - failure modes and analysis in metals, in: P. Moore, G. Booth (Eds.), *The Welding Engineer's Guide to Fracture and Fatigue*, Woodhead Publishing, Oxford, 2015, pp. 95–110. doi:<https://doi.org/10.1533/9781782423911.1.95>.
- [274] R. Wanhill, R. Byrnes, C. Smith, 16 - stress corrosion cracking (scc) in aerospace vehicles, in: V. Raja, T. Shoji (Eds.), *Stress Corrosion Cracking*, Woodhead Publishing Series in Metals and Surface Engineering, Woodhead Publishing, 2011, pp. 608–650. doi:<https://doi.org/10.1533/9780857093769.4.608>.
- [275] T. A. Michalske, S. W. Feiman, A molecular mechanism for stress corrosion in vitreous silica, *Journal of the American Ceramic Society* 66 (4) (1983) 284–288. doi:<https://doi.org/10.1111/j.1151-2916.1983.tb15715.x>.

- [276] T. Terachi, T. Yamada, T. Miyamoto, K. Arioka, K. Fukuyama, Corrosion behavior of stainless steels in simulated pwr primary water—effect of chromium content in alloys and dissolved hydrogen—, *Journal of Nuclear Science and Technology* 45 (10) (2008) 975–984. doi:[10.1080/18811248.2008.9711883](https://doi.org/10.1080/18811248.2008.9711883).
- [277] S. Ziemniak, M. Hanson, Corrosion behavior of 304 stainless steel in high temperature, hydrogenated water, *Corrosion Science* 44 (10) (2002) 2209–2230. doi:[https://doi.org/10.1016/S0010-938X\(02\)00004-5](https://doi.org/10.1016/S0010-938X(02)00004-5).
- [278] M. da Cunha Belo, M. Walls, N. Hakiki, J. Corset, E. Picquenard, G. Sagon, D. Noël, Composition, structure and properties of the oxide films formed on the stainless steel 316l in a primary type pwr environment, *Corrosion Science* 40 (2) (1998) 447–463. doi:[https://doi.org/10.1016/S0010-938X\(97\)00158-3](https://doi.org/10.1016/S0010-938X(97)00158-3).
- [279] D. Lenaz, H. Skogby, F. Princivalle, U. Hålenius, Structural changes and valence states in the $\text{MgCr}_2\text{O}_4\text{--FeCr}_2\text{O}_4$ solid solution series, *Physics and Chemistry of Minerals* 31 (9) (2004) 633–642. doi:[10.1007/s00269-004-0420-0](https://doi.org/10.1007/s00269-004-0420-0).
- [280] M. Sennour, P. Laghoutaris, C. Guerre, R. Molins, Advanced tem characterization of stress corrosion cracking of alloy 600 in pressurized water reactor primary water environment, *Journal of Nuclear Materials* 393 (2) (2009) 254–266. doi:<https://doi.org/10.1016/j.jnucmat.2009.06.014>.
- [281] K. N. Subramanyam, Neutron and x-ray diffraction studies of certain doped nickel ferrites, *Journal of Physics C: Solid State Physics* 4 (15) (1971) 2266–2268. doi:[10.1088/0022-3719/4/15/012](https://doi.org/10.1088/0022-3719/4/15/012).
- [282] Z. Luo, A practical guide to transmission electron microscopy : fundamentals / Zhiping Luo., first edition. Edition, Materials characterization and analysis collection, Momentum Press, New York, [New York] (222 East 46th Street, New York, NY 10017), 2016.
- [283] K. Arioka, T. Yamada, T. Terachi, T. Miyamoto, Dependence of Stress Corrosion Cracking for Cold-Worked Stainless Steel on Temperature and Potential, and Role of Diffusion of Vacancies at Crack Tips, *Corrosion* 64 (9) (2008) 691–706. doi:[10.5006/1.3278507](https://doi.org/10.5006/1.3278507).
- [284] S. M. Bruemmer, L. E. Thomas, High-resolution characterizations of stress-corrosion cracks in austenitic stainless steel from crack growth tests in bwr-simulated environments (7 2005).
- [285] D. Ramachandran, R. Egoavil, A. Crabbe, T. Haufman, A. Abakumov, J. Verbeeck, I. Vandendael, H. Terryn, D. Schryvers, Tem and aes investigations of the natural surface nano-oxide layer of an aisi 316l stainless steel microfibre, *Journal of Microscopy* 264 (2) (2016) 207–214. doi:<https://doi.org/10.1111/jmi.12434>.
- [286] M. J. Buehler, F. F. Abraham, H. Gao, Hyperelasticity governs dynamic fracture at a critical length scale, *Nature* 426 (6963) (2003) 141–146.
- [287] M. J. Buehler, H. Gao, Dynamical fracture instabilities due to local hyperelasticity at crack tips, *Nature* 439 (7074) (2006) 307–310. doi:[10.1038/nature04408](https://doi.org/10.1038/nature04408).
- [288] I. Karaman, H. Sehitoglu, Y. I. Chumlyakov, H. J. Maier, The deformation of low-stacking-fault-energy austenitic steels, *Jom* 54 (7) (2002) 31–37. doi:[10.1007/bf02700983](https://doi.org/10.1007/bf02700983).
- [289] H. Idrissi, K. Renard, D. Schryvers, P. Jacques, On the relationship between the twin internal structure and the work-hardening rate of twip steels, *Scripta Materialia* 63 (10) (2010) 961–964. doi:<https://doi.org/10.1016/j.scriptamat.2010.07.016>.

- [290] K. Fukuya, Current understanding of radiation-induced degradation in light water reactor structural materials, *Journal of Nuclear Science and Technology* 50 (3) (2013) 213–254. doi:[10.1080/00223131.2013.772448](https://doi.org/10.1080/00223131.2013.772448).
- [291] R. Bosch, J. V. Eyken, M. Konstantinović, Crack initiation tests thimble tube Tihange - Constant load tests under PWR conditions to study effect of oxide layer, Tech. Rep. 40796796, R-8149, Sck Cen (12 2020).
- [292] M. J. Konstantinović, J. V. Eyken, W. V. Renterghem, R. W. Bosch, SEM and TEM characterization of the oxide formed in O-ring and baffle bolt specimens, Tech. Rep. 20295305, R-6225, Sck Cen (12 2016).
- [293] M. J. Konstantinović, A. Penders, W. V. Renterghem, J. V. Eyken, R. W. Bosch, Microstructural analysis of cracks and crack tips in support of the probabilistic fracture model, Tech. Rep. 36393580, R-7135, Sck Cen (12 2019).
- [294] R. W. Bosch, M. Konstantinović, A. Penders, M. Vankeerberghen, F. Somville, Iascc crack initiation testing of thimble tube material under pwr conditions: effect of oxide layer, stress and load form (2022) 1–102022 - FONTEVRAUD 10; Conference date: 19-09-2022 Through 22-09-2022; Avignon - France.
- [295] A. Penders, M. Konstantinović, W. Renterghem, R.-W. Bosch, D. Schryvers, F. Somville, Characterization of iascc crack tips extracted from neutron-irradiated flux thimble tube specimens in view of a probabilistic fracture model, *Journal of Nuclear Materials* (2022) 154015 doi:<https://doi.org/10.1016/j.jnucmat.2022.154015>.
- [296] G. Shirane, D. E. Cox, S. J. Pickart, Magnetic structures in fcr2s4 and fcr2o4, *Journal of Applied Physics* 35 (3) (1964) 954–955. doi:[10.1063/1.1713556](https://doi.org/10.1063/1.1713556).
- [297] P. B. Hirsch, A. Howie, R. B. Nicholson, D. W. Pashley, M. J. Whelan, L. Marton, Electron microscopy of thin crystals, *Physics Today* 19 (10) (1966) 1–563. doi:[10.1063/1.3047787](https://doi.org/10.1063/1.3047787).
- [298] M. Meisnar, A. Vilalta-Clemente, A. Gholinia, M. Moody, A. J. Wilkinson, N. Huin, S. Lozano-Perez, Using transmission kikuchi diffraction to study intergranular stress corrosion cracking in type 316 stainless steels, *Micron* 75 (2015) 1–10. doi:<https://doi.org/10.1016/j.micron.2015.04.011>.
- [299] L. Legras, M. Boisson, E. Fargeas, P. Cu villier, R. Mercier, S. Miloudi, J. Tarabay, M. Roch, Tem investigations of the microstructure and oxides at the tip of intergranular cracks of a baffle former bolt irradiated up to 10 dpa, in: *Contribution of Materials Investigations and Operating Experience to Light Water NPPs' Safety, Performance and Reliability*, Fontevraud 9, Avignon, France, 2018.
- [300] G. Was, T. Allen, J. Busby, J. Gan, D. Damcott, D. Carter, M. Atzmon, E. Kenik, Microchemistry and microstructure of proton-irradiated austenitic alloys: toward an understanding of irradiation effects in lwr core components, *Journal of Nuclear Materials* 270 (1) (1999) 96–114. doi:[https://doi.org/10.1016/S0022-3115\(98\)00897-6](https://doi.org/10.1016/S0022-3115(98)00897-6).
- [301] T. R. Allen, G. S. Was, Radiation-enhanced diffusion and radiation-induced segregation, in: K. E. Sickafus, E. A. Kotomin, B. P. Uberuaga (Eds.), *Radiation Effects in Solids*, Springer Netherlands, Dordrecht, 2007, pp. 123–151.
- [302] G. Wranglen, Pitting and sulphide inclusions in steel, *Corrosion Science* 14 (5) (1974) 331–349. doi:[https://doi.org/10.1016/S0010-938X\(74\)80047-8](https://doi.org/10.1016/S0010-938X(74)80047-8).
- [303] R. S. Lillard, M. A. Kashfipour, W. Niu, Pit propagation at the boundary between manganese

- sulfide inclusions and austenitic stainless steel 303 and the role of copper, *Journal of The Electrochemical Society* 163 (8) (2016) C440–c451. doi:10.1149/2.0461608jes.
- [304] M. P. Ryan, D. E. Williams, R. J. Chater, B. M. Hutton, D. S. McPhail, Why stainless steel corrodes, *Nature* 415 (6873) (2002) 770–774. doi:10.1038/415770a.
- [305] A. Herbelin, T. Couvant, L. Legras, D. Delafosse, G. Ilbevare, Oxidation of austenitic stainless steels in PWR primary water, in: C. F. de l'Anticorrosion (CEFRACOR) (Ed.), *European Corrosion Congress 2009 (EUROCORR 2009)*, Vol. 3, Curran Associates, Inc. 57 Morehouse Lane Red Hook, NY 12571 USA, Nice, France, 2010, pp. 1592–1608.
- [306] T. Onchi, K. Dohi, N. Soneda, J. Cowan, R. Scowen, M. Castaño, Fractographic and microstructural characterization of irradiated 304 stainless steel intergranularly fractured in inert gas, *Journal of Nuclear Materials* 320 (3) (2003) 194–208. doi:https://doi.org/10.1016/S0022-3115(03)00105-3.
- [307] A. H. King, Diffusion induced grain boundary migration, *International Materials Reviews* 32 (1) (1987) 173–189. doi:10.1179/095066087790150304.
- [308] H. Lopez, Role of dislocations and generation of twins during diffusion induced grain boundary migration, *Materials Science and Technology* 7 (8) (1991) 681–685. doi:10.1179/mst.1991.7.8.681.
- [309] L. Rémy, The interaction between slip and twinning systems and the influence of twinning on the mechanical behavior of fcc metals and alloys. *Metall Mater Trans A* 12, 387–408 (1981).
- [310] N. Hashimoto, S. Zinkle, A. Rowcliffe, J. Robertson, S. Jitsukawa, Deformation mechanisms in 316 stainless steel irradiated at 60°C and 330°C, *Journal of Nuclear Materials* 283-287 (2000) 528–534, 9th Int. Conf. on Fusion Reactor Materials. doi:https://doi.org/10.1016/S0022-3115(00)00087-8.
- [311] W. Karlsen, J. Pakarinen, A. Toivonen, U. Ehrnstén, Deformation microstructures of 30 dpa aisi 304 stainless steel after monotonic tensile and constant load autoclave testing, in: J. T. Busby, G. Ilbevare, P. L. Andresen (Eds.), *Proceedings of the 15th International Conference on Environmental Degradation of Materials in Nuclear Power Systems — Water Reactors*, Springer International Publishing, Cham, 2016, pp. 1429–1446.
- [312] W. Karlsen, A. Toivonen, P. Efsing, Baseline examinations and autoclave tests of 65 and 100 dpa flux thimble tube o-ring specimens, *Corrosion and Materials Degradation* 2 (2) (2021) 248–273. doi:10.3390/cmd2020014.
- [313] A. Hojna, J. Duchon, P. Halodova, H. K. Namburi, Effect of strain rate and high temperature water on deformation structure of vver neutron irradiated core internals steel, in: J. H. Jackson, D. Paraventi, M. Wright (Eds.), *Proceedings of the 18th International Conference on Environmental Degradation of Materials in Nuclear Power Systems – Water Reactors*, Springer International Publishing, Cham, 2019, pp. 549–563.
- [314] L. Tsay, S. Yu, R.-T. Huang, Effect of austenite instability on the hydrogen-enhanced crack growth of austenitic stainless steels, *Corrosion Science* 49 (7) (2007) 2973–2984. doi:https://doi.org/10.1016/j.corsci.2007.01.008.
- [315] I. Park, E.-Y. Kim, W.-J. Yang, *Microstructural investigation of stress corrosion cracking in cold-formed aisi 304 reactor*, *Metals* 11 (1) (2021). doi:10.3390/met11010007. URL https://www.mdpi.com/2075-4701/11/1/7
- [316] L. Yongfeng, B. Fuming, W. K., H. P., Deformation-induced martensitic transformation beha-

- rior in cold-rolled aisi304 stainless steels, *Materials and Manufacturing Processes* 28 (3) (2013) 256–259. doi:[10.1080/10426914.2012.667897](https://doi.org/10.1080/10426914.2012.667897).
- [317] G. B. Olson, M. Cohen, Stress-assisted isothermal martensitic transformation: Application to trip steels, *Metallurgical Transactions A* 13 (11) (1982) 1907–1914. doi:[10.1007/bf02645934](https://doi.org/10.1007/bf02645934).
- [318] M. N. Gusev, D. A. Toktogulova, O. P. Maksimkin, and F. A. Garner, "A new deformation mode observed in austenitic low-nickel stainless steels irradiated to high neutron exposure at 310-432°C," Proc. of 14th International Conference on Environmental Degradation of Materials in Nuclear Power Systems - Water Reactors. Virginia Beach, Virginia, August 23–27, 2009. American Nuclear Society (ANS) (2010), 1385-1391.
- [319] J. L. Straalsund, J. F. Bates, Partial molar volumes and size factor data for alloy constituents of stainless steel, *Metallurgical and Materials Transactions B* 5 (2) (1974) 493–498. doi:[10.1007/bf02644119](https://doi.org/10.1007/bf02644119).
- [320] H. E. Evans, Stress effects in high temperature oxidation of metals, *International Materials Reviews* 40 (1) (1995) 1–40. doi:[10.1179/imr.1995.40.1.1](https://doi.org/10.1179/imr.1995.40.1.1).
- [321] M. Mayuzumi, N. Ishiyama, Y. Mizutani, J. ichi Tani, K. Kako, Incubation time of stress corrosion cracking for type 316l and type 316 stainless steels by cbb method in high temperature water, *Zairyo-to-Kankyo* 57 (5) (2008) 230–234. doi:[10.3323/jcorr.57.230](https://doi.org/10.3323/jcorr.57.230).
- [322] H. Nishioka, K. Fukuya, K. Fujii, T. Torimaru, Iascc initiation in highly irradiated stainless steels under uniaxial constant load conditions, *Journal of Nuclear Science and Technology* 45 (10) (2008) 1072–1077. doi:[10.1080/18811248.2008.9711894](https://doi.org/10.1080/18811248.2008.9711894).
- [323] R. Bosch, M. Konstantinovic, M. Vankeerberghen, R. Gérard, F. Somville, Effect of cyclic loading on iascc stress threshold of thimble tube material with a dose up to 80 dpa under pwr conditions, in: *International Symposium Contribution of Materials Investigations and Operating Experience to Light Water NPPs' Safety, Performance and Reliability*, 2018, pp. 1–11, 3; 2018 - FONTEVRAUD 9 ; Conference date: 17-09-2018 Through 20-09-2018.
- [324] Y. Murakami, S. Matsuoka, Effect of hydrogen on fatigue crack growth of metals, *Engineering Fracture Mechanics* 77 (11) (2010) 1926–1940, international Conference on Crack Paths 2009. doi:<https://doi.org/10.1016/j.engfracmech.2010.04.012>.
- [325] D. R. Steinmetz, T. Jäpel, B. Wietbrock, P. Eisenlohr, I. Gutierrez-Urrutia, A. Saeed-Akbari, T. Hickel, F. Roters, D. Raabe, Revealing the strain-hardening behavior of twinning-induced plasticity steels: Theory, simulations, experiments, *Acta Materialia* 61 (2) (2013) 494–510. doi:<https://doi.org/10.1016/j.actamat.2012.09.064>.
- [326] J. McCarthy, F. Garner, Phase instabilities in irradiated simple fe-cr-mn low activation alloys, *Journal of Nuclear Materials* 155-157 (1988) 877–882. doi:[https://doi.org/10.1016/0022-3115\(88\)90433-3](https://doi.org/10.1016/0022-3115(88)90433-3).
- [327] J. McCarthy, Phase evolution during neutron irradiation of commercial fe-cr-mn alloys, *Journal of Nuclear Materials* 179-181 (1991) 626–628. doi:[https://doi.org/10.1016/0022-3115\(91\)90166-5](https://doi.org/10.1016/0022-3115(91)90166-5).
- [328] H.M. Chung, W.E. Ruther, J.E. Sanecki, T.F. Kassner, in: D. Cubicciotti (Ed.), *Proceedings of Fifth International Symposium On Environmental Degradation Of Materials in Nuclear Power Systems-Water Reactors*, ANS, Monterey, CA, 1992, p. 795.
- [329] K. Fukuya, K. Nakata, A. Horie, in: D. Cubicciotti(Ed.), *Proceedings of Fifth International Symposium On Environmental Degradation Of Materials in Nuclear Power Systems-Water Re-*

- actors, ANS, Monterey, CA, 1992, p. 814.
- [330] T. Tsukada, Y. Miwa, J. Nakajima, in: Gold R.E., E.P. Simonen (Eds.), Proceedings of Seventh International Symposium On Environmental Degradation Of Materials in Nuclear Power Systems – Water Reactors, Breckenridge, CO, 1999, 1995, p. 1009.
- [331] H. Bhadeshia, R. Honeycombe, Chapter 4 - solutes that substitute for iron, in: H. Bhadeshia, R. Honeycombe (Eds.), Steels: Microstructure and Properties (Fourth Edition), fourth edition Edition, Butterworth-Heinemann, 2017, pp. 101–134. doi:<https://doi.org/10.1016/B978-0-08-100270-4.00004-4>.
- [332] Y.-N. Wang, J. Yang, Y.-P. Bao, Effects of non-metallic inclusions on machinability of free-cutting steels investigated by nano-indentation measurements, Metallurgical and Materials Transactions A 46 (1) (2015) 281–292. doi:[10.1007/s11661-014-2596-3](https://doi.org/10.1007/s11661-014-2596-3).
- [333] K. J. Stephenson, G. S. Was, [The role of dislocation channeling in iascc initiation of neutron irradiated stainless steel](https://doi.org/10.1016/j.jnucmat.2016.09.001), Journal of Nuclear Materials 481 (2016) 214–225. doi:<https://doi.org/10.1016/j.jnucmat.2016.09.001>.
URL <https://www.sciencedirect.com/science/article/pii/S0022311516306912>
- [334] T. Williams, J. Titchmarsh, D. Arkell, Void-swelling and precipitation in a neutron-irradiated, niobium-stabilised austenitic stainless steel, Journal of Nuclear Materials 107 (2) (1982) 222–244. doi:[https://doi.org/10.1016/0022-3115\(82\)90423-8](https://doi.org/10.1016/0022-3115(82)90423-8).
- [335] J. Conermann, R. Shogan, K. Fujimoto, T. Yonezawa, Y. Yamaguchi, Irradiation effects in a highly irradiated cold worked stainless steel removed from a commercial pwr, in: Proceedings of the Twelfth International Conference on Environmental Degradation of Materials in Nuclear Power Systems-Water Reactors, Proceedings of the Twelfth International Conference on Environmental Degradation of Materials in Nuclear Power Systems-Water Reactors, 2005, pp. 277–287, 12th International Conference on Environmental Degradation of Materials in Nuclear Power Systems-Water Reactors ; Conference date: 14-08-2005 Through 18-08-2005.
- [336] J. West, Basic Corrosion and Oxidation, Ellis Horwood series in corrosion and its prevention, E. Horwood, 1986.

